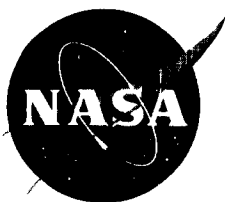# Annual Research Briefs – 1995

Center for Turbulence Research

December 1995

Ames Research Center

Stanford University

Annual Research Briefs – 1995
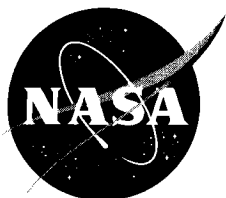
Center for Turbulence Research

December 1995

Dedicated to the memory of

Otto Zeman
(1936 - 1995)

and

Dean Chapman
(1922 - 1995)

Ames Research Center

Stanford University

CONTENTS

iii

Preface

This report contains the 1995 annual progress reports of the Research Fellows and students of the Center for Turbulence Research. In addition to this and the Summer Program reports, each year several CTR manuscript reports are published to expedite the dissemination of research findings by the CTR Fellows.

In 1995 CTR continued its concentration on the development and application of large-eddy simulation to complex flows, development of novel modeling concepts for engineering computations in the Reynolds averaged framework, and turbulent combustion. In large-eddy simulation, a number of numerical and experimental issues have surfaced which are being addressed. Almost all fundamental studies of turbulence physics were carried out by the senior visitors. Last year CTR also took on a new role by supporting Akiva Yaglom in writing the second edition of the classic book, "Statistical Fluid Mechanics" by Monin and Yaglom, which has been invaluable for the serious students of turbulence. We plan to continue this support for as long as possible.

The first group of reports in this volume are on large-eddy simulation. A key finding in this area was the revelation of possibly significant numerical errors that may overwhelm the effects of the subgrid-scale model. We also commissioned a new experiment to support the LES validation studies. The remaining articles in this report are concerned with Reynolds averaged modeling, studies of turbulence physics and flow generated sound, combustion, and simulation techniques. Fundamental studies of turbulent combustion using direct numerical simulations which started at CTR will continue to be emphasized. These studies and their counterparts carried out during the summer programs have had a noticeable impact on combustion research world wide.

Last year CTR lost two very special people. Dr. Otto Zeman, a Senior Fellow of CTR and one of the world's most creative turbulence modelers, died last March. Professor Dean Chapman, a visionary who fostered the development of the turbulence simulation programs at Stanford and Ames and who served on the CTR's Steering committee from its inception, passed away in October. We dedicate this volume to the memory of their enormous contributions.

As always, we are indebted to Debra Spinks, the Center's Administrative Assistant, for her skillful compilation of this report and the day-to-day management of the Center.

Parviz Moin
William C. Reynolds

Analysis of discretization errors in LES

By Sandip Ghosal[1]

1. Motivation and objectives

All numerical simulations of turbulence (DNS or LES) involve some discretization errors. The integrity of such simulations therefore depend on our ability to quantify and control such errors. In the classical literature (see e.g. Chu 1978) on analysis of errors in partial differential equations, one typically studies simple linear equations (such as the wave equation or Laplace's equation). The qualitative insight gained from studying such simple situations is then used to design numerical methods for more complex problems such as the Navier-Stokes equations. Though such an approach may seem reasonable as a first approximation, it should be recognized that strongly nonlinear problems, such as turbulence, have a feature that is absent in linear problems. This feature is the simultaneous presence of a continuum of space and time scales. Thus, in an analysis of errors in the one dimensional wave equation, one may, without loss of generality, rescale the equations so that the dependent variable is always of order unity. This is not possible in the turbulence problem since the amplitudes of the Fourier modes of the velocity field have a continuous distribution. The objective of the present research is to provide some quantitative measures of numerical errors in such situations. Though the focus of this work is LES, the methods introduced here can be just as easily applied to DNS. Errors due to discretization of the time-variable are neglected for the purpose of this analysis.

2. Accomplishments

In this report, analytical expressions for the power spectra of errors due to the spatial discretization of the Navier-Stokes equations are derived. In § 2.1, an expression for the numerical error is presented as the sum of "finite-differencing", "aliasing", and "modeling" errors that have different origins. In § 2.2, expressions for the power spectra of the first two kinds of errors are derived as well as the corresponding expressions for the subgrid and total nonlinear terms. The essential tool that makes the derivation of such an analytical expression possible is the "joint-normal hypothesis" for turbulent velocities. The essential technique is identical to that used by Batchelor in his derivation of the pressure spectrum of turbulence from the energy spectrum (Batchelor 1951, 1953). These results are applied to the LES of turbulence in § 2.3 to obtain some measure of numerical errors in finite-difference schemes, which are increasingly being used in turbulence computations on flows with complex boundaries. This report summarizes the essential results, the details of the mathematical development will be presented elsewhere (Ghosal 1995 - henceforth referred to as "paper 1").

1 Present address: CNLS (MS-B258), LANL, Los Alamos, NM 87545

2.1 Calculation of discretization errors

Any representation of the true velocity field in a turbulent flow on a finite grid is necessarily approximate. One must be careful to distinguish between errors due to the finiteness of the representation and the "discretization error" of a numerical scheme. In a numerical simulation, the velocity field at any time-step can be regarded as an element of a vector space with a finite number of dimensions (N) where N is the number of variables retained in the computation. This is an approximate representation in a subspace of the larger vector space that contains the true solution. The best possible approximation to the true solution in the subspace is the projection onto the subspace (in fact that is the definition of a projection operator — see e.g. Helmberg 1969). The "ideal" or "best approximation" to the Navier-Stokes operator in the finite subspace is that operator that ensures that the numerical solution remains "locked" to the projection of the true solution at all times as both vectors move around in their respective vector spaces. It may be shown (see paper 1) that this condition is achieved by spectral methods (or properly dealiased pseudo-spectral methods) in the absence of subgrid modeling errors. By "discretization error", $\mathbf{E}$, of a numerical method we mean the deviation of the right hand side evaluated with the method from what would have been obtained if the right-hand side of the full Navier-Stokes equation were projected into the computational subspace. Thus, for a spectral method used in conjunction with an 'exact' subgrid model, $\mathbf{E} = 0$.

In order to evaluate the formal expression for the error $\mathbf{E}$, one needs to introduce a basis. The most advantageous choice is the 3D Fourier-basis since in Fourier space differentiations reduce to multiplication by wavevectors and numerical differentiation reduces to multiplication by modified wave vectors (see e.g. Vichnevetsky 1982). We now restrict our attention to flows in a periodic cubical box. Further, while considering finite-difference methods, the grid will be assumed uniform in every direction. Let $E_i(\mathbf{k})$ denote the components of $\mathbf{E}$ in the Fourier-basis with $i = 1$ to 3 corresponding to the x, y, and z directions respectively. Then $E_i(\mathbf{k})$ can be written as

$$E_i(\mathbf{k}) = E_i^{(\mathrm{FD})}(\mathbf{k}) + E_i^{(\mathrm{alias})}(\mathbf{k}) + E_i^{(\mathrm{model})}(\mathbf{k}). \tag{1}$$

The first term arises because of the inability of the finite-differencing operator, $\delta/\delta x_k$, to accurately compute the gradient of short-wavelength waves. We call this the "finite-differencing error." It vanishes for a spectral method that can differentiate waves of all wavelengths exactly. The second term arises due to the method of computation of the nonlinear term by taking products in physical space on a discrete lattice. This is called the "aliasing error" and is well known in the literature on pseudo-spectral methods (Canuto *et* al. 1988, Rogallo 1981). The last term is the difference between the true subgrid force and that computed using a subgrid model. We call this the "modeling error".

In the following analysis, the magnitude of the error $\mathbf{E}$ will be characterized by statistical properties such as its power spectral density. Such statistical measures can be precisely defined only in the limit where the wavevector can assume a continuum rather than a discrete set of values. In physical space this implies that we

are considering the grid size Δ and some characteristic scale of turbulence λ fixed and taking the limit as the size of the box $L \to \infty$. In actual simulations, of course, the box size L is finite. However, L is taken much larger that Δ or λ so that smooth power spectra can be defined and computed statistical quantities are not changed when the box size is increased further. This ensures that the computed quantities are indistinguishable from the ideal limit, $L \to \infty$. For the purpose of theoretical analysis it is advantageous to take the limit $L \to \infty$ first rather than at the end of the computation. Thus, in the Fourier-basis, the exact solution will be characterized by a continuum of wave vectors $\mathbf{k} \in \mathbf{R}^3$ and the numerical solution will be characterized by the subset $\mathbf{k} \in \mathcal{B}$ where $\mathcal{B} \equiv [-k_x^{\max}, k_x^{\max}] \times [-k_y^{\max}, k_y^{\max}] \times [-k_z^{\max}, k_z^{\max}]$. We will assume for simplicity that the grid length Δ is the same in all three directions so that $k_x^{\max} = k_y^{\max} = k_z^{\max} = k_m = \pi/\Delta$. Further, we will consider the LES "filter-width" and the grid length to be identical. This condition will be relaxed in § 2.3.3. In the limit of infinite box size, the discrete Fourier transform and its inverse take the form (a factor of $L^3/8\pi^3$ is 'absorbed' in the definition of the transform)

$$\hat{\phi}(\mathbf{k}) = \frac{\Delta^3}{8\pi^3} \sum_{\mathbf{x}} \phi(\mathbf{x}) \exp(-i\mathbf{k} \cdot \mathbf{x}) \quad \phi(\mathbf{x}) = \int_{\mathcal{B}} d\mathbf{k} \hat{\phi}(\mathbf{k}) \exp(i\mathbf{k} \cdot \mathbf{x}) \qquad (2)$$

where the summation is over all lattice points over the infinite cubic lattice of spacing Δ and the integration over wave space ranges over all vectors $\mathbf{k} \in \mathcal{B}$. The following useful identity is readily derived by taking the limit of infinite box size:

$$\frac{\Delta^3}{8\pi^3} \sum_{\mathbf{x}} \exp(i\mathbf{K} \cdot \mathbf{x}) = \sum_{\mathbf{a} \in \Lambda} \delta(\mathbf{K} - \mathbf{a}) \qquad (3)$$

where 'δ' is the Dirac delta function, Λ is the set of wavevectors of the form $(2pk_m, 2qk_m, 2rk_m)$ where p, q and r are integers (positive, negative or zero), and $\mathbf{K}$ is any vector (not necessarily restricted to $\mathcal{B}$). [This relation is familiar in solid state physics (see e.g. chapter 1, pg. 12 of Jones & March 1973) where the set Λ goes by the name "Reciprocal Lattice".] When the lattice spacing $\Delta \to 0$, the summation over lattice points in (2) becomes an integral over space and the usual continuous Fourier-transform is recovered. In this limit, the right hand side of relation (3) becomes simply $\delta(\mathbf{K})$ and (3) reduces to the familiar expansion of the delta-function in terms of exponentials.

Let us first consider the effect of projecting the exact right-hand side of the Navier-Stokes equation onto the Fourier-basis with wavevector $\mathbf{k}$. The 'ith component' is given by

$$-iP_{imn}(\mathbf{k}) \left[\int_{\mathcal{B}} \int_{\mathcal{B}} d\mathbf{k}' d\mathbf{k}'' \delta(\mathbf{k}' + \mathbf{k}'' - \mathbf{k}) \hat{u}_m(\mathbf{k}') \hat{u}_n(\mathbf{k}'') + \hat{\tau}_{mn}(\mathbf{k}) \right] - \nu k^2 \hat{u}_i(\mathbf{k})$$

where P_{imn} has its usual meaning (see e.g. Lesieur 1987) and $\hat{\tau}_{mn}$ is the exact subgrid stress in Fourier-space. The Einstein summation convention for tensor

indices is implied throughout this report except where otherwise noted. If the exact derivative operator $\partial/\partial x_k$ is replaced by the numerical differentiation $\delta/\delta x_k$, multiplication by wavevectors $\mathbf{k}$ are replaced by multiplication by the corresponding modified wavevectors $\tilde{\mathbf{k}}$. Thus, we obtain

$$
\begin{aligned}
E_i^{(\mathrm{FD})}(\mathbf{k}) =&\, i \left[P_{imn}(\tilde{\mathbf{k}}) - P_{imn}(\mathbf{k}) \right] \int_{\mathcal{B}} \int_{\mathcal{B}} d\mathbf{k}' d\mathbf{k}'' \delta(\mathbf{k}' + \mathbf{k}'' - \mathbf{k}) \hat{u}_m(\mathbf{k}') \hat{u}_n(\mathbf{k}'') \\
&+ i \left[P_{imn}(\tilde{\mathbf{k}}) \hat{T}_{mn}^M(\mathbf{k}) - P_{imn}(\mathbf{k}) \hat{\tau}_{mn}^M(\mathbf{k}) \right] + \nu(\tilde{k}^2 - k^2) \hat{u}_i(\mathbf{k}),
\end{aligned}
\tag{4}
$$

where $\hat{T}_{mn}^M(\mathbf{k})$ is the "modified subgrid model" obtained by replacing all multiplication by wavevectors (if any) in the subgrid model $\hat{\tau}_{mn}^M(\mathbf{k})$ by the corresponding multiplication by modified wavevectors.

To obtain the aliasing error, we consider the effect of evaluating the nonlinear term in physical space:

$$
-i P_{imn}(\tilde{\mathbf{k}}) \left[\widehat{u_m(\mathbf{x}) u_n(\mathbf{x})} + \hat{T}_{mn}^M(\mathbf{k}) \right].
$$

On using the definition (2) of the discrete Fourier transform we have

$$
\widehat{u_m(\mathbf{x}) u_n(\mathbf{x})} = \frac{\Delta^3}{8\pi^3} \sum_{\mathbf{x}} u_m(\mathbf{x}) u_n(\mathbf{x}) \exp(-i\mathbf{k} \cdot \mathbf{x}).
\tag{5}
$$

When $u_m(\mathbf{x})$ and $u_n(\mathbf{x})$ in (5) are expanded in the Fourier-basis we get

$$
\widehat{u_m(\mathbf{x}) u_n(\mathbf{x})} = \frac{\Delta^3}{8\pi^3} \sum_{\mathbf{x}} \int_{\mathcal{B}} \int_{\mathcal{B}} d\mathbf{k}' d\mathbf{k}'' \hat{u}_m(\mathbf{k}') \hat{u}_n(\mathbf{k}'') \exp[i(\mathbf{k}' + \mathbf{k}'' - \mathbf{k}) \cdot \mathbf{x}].
\tag{6}
$$

The summation over lattice points can be performed using (3),

$$
\widehat{u_m(\mathbf{x}) u_n(\mathbf{x})} = \sum_{\mathbf{a} \in \Lambda} \int_{\mathcal{B}} \int_{\mathcal{B}} d\mathbf{k}' d\mathbf{k}'' \hat{u}_m(\mathbf{k}') \hat{u}_n(\mathbf{k}'') \delta(\mathbf{k}' + \mathbf{k}'' - \mathbf{k} - \mathbf{a}).
\tag{7}
$$

All the terms in the sum over $\mathbf{a} \in \Lambda$ with the exception of $\mathbf{a} = 0$ are clearly "spurious contributions" and constitute the 'aliasing error'. Thus, we have

$$
E_i^{(\mathrm{alias})}(\mathbf{k}) = i P_{imn}(\tilde{\mathbf{k}}) \sum_{\mathbf{a} \in \Lambda_0} \int_{\mathcal{B}} \int_{\mathcal{B}} d\mathbf{k}' d\mathbf{k}'' \delta(\mathbf{k}' + \mathbf{k}'' - \mathbf{k} - \mathbf{a}) \hat{u}_m(\mathbf{k}') \hat{u}_n(\mathbf{k}'') + \delta \hat{T}_{mn}^M(\mathbf{k})
\tag{8}
$$

where Λ_0 consists of the vectors $(2pk_m, 2qk_m, 2rk_m)$ where p, q and r can independently take on the values 0 or ± 1 but excluding the case $p = q = r = 0$. The reason integer values of p, q and r with modulus greater than 1 are not included in Λ_0 is that the relation $\mathbf{a} = \mathbf{k}' + \mathbf{k}'' - \mathbf{k}$ cannot be satisfied for such values if $\mathbf{k}, \mathbf{k}', \mathbf{k}'' \in \mathcal{B}$

and hence the delta function ensures that they do not contribute to the sum. The last term $\delta\hat{T}_{mn}^M(\mathbf{k})$ is the contribution to the aliasing error from the subgrid model. Obviously it depends on the nature of the model. For a subgrid model that uses a constant eddy viscosity, this term is linear in the resolved fields, and hence there is no contribution to the aliasing error. For more complicated models such as the Smagorinsky model, it is difficult to evaluate this contribution analytically due to the complicated nature of the nonlinearity.

The expressions (4) and (8) for the finite-differencing and aliasing errors involve the subgrid model τ_{ij}^M. Modeling errors associated with subgrid models are difficult to estimate, and, further, there is no obvious way to single out for this study any one among the wide variety of subgrid models in use. It is therefore advantageous to separate the issue of subgrid modeling from the issue of discretization errors which is the subject of this paper. In order to accomplish this, we introduce the concept of the "ideal subgrid model":

$$\tau_{ij}^M = \tau_{ij}(\mathbf{x}, t) \tag{9}$$

where $\tau_{ij}(\mathbf{x}, t)$ is the exact subgrid stress. One might think of the "ideal subgrid model" (9) in the following way. Imagine a DNS with an infinitely greater resolution running concurrently with the given LES. At every time-step the exact subgrid stress is computed from the DNS fields and supplied to the LES simulation as a function of position. The rest of the analysis in this paper will be presented for such an idealized LES. Since τ_{ij}^M is already given as a function of position and time and involves no computation, it does not contribute to aliasing errors. Thus, for such an idealized LES, $\delta\hat{T}_{mn}^M = 0$ in (8). The contribution from the subgrid model is not, however, zero for the finite-differencing errors even for the ideal model (9). This is because the model is (inaccurately) differentiated for computing the pressure and the subgrid force. The subgrid terms in (4) for the ideal model (9) are given by $\hat{\tau}_{mn}^M = \hat{T}_{mn}^M = \hat{\tau}_{mn}$. Thus,

$$E_i^{\text{(FD)}}(\mathbf{k}) = i\left[P_{imn}(\tilde{\mathbf{k}}) - P_{imn}(\mathbf{k})\right] \int \int dk' dk'' \delta(\mathbf{k}' + \mathbf{k}'' - \mathbf{k})\hat{u}_m(\mathbf{k}')\hat{u}_n(\mathbf{k}'') \\ + \nu(\tilde{k}^2 - k^2)\hat{u}_i(\mathbf{k}). \tag{10}$$

The integration in (10) now ranges over the entire wave-space. Clearly, for this ideal model

$$E_i^{\text{(model)}}(\mathbf{k}) = iP_{imn}(\mathbf{k})\left[\hat{\tau}_{mn}^{(M)}(\mathbf{k}) - \hat{\tau}_{mn}(\mathbf{k})\right] = 0. \tag{11}$$

2.2 Power spectra

In this section, analytical expressions for the power spectra of the finite-differencing error, aliasing error, subgrid and total nonlinear term are derived.

2.2.1 Finite-differencing error

The power spectrum of the finite-differencing error is defined by $\mathcal{E}^{\text{(FD)}}(k)$, where

$$\frac{\mathcal{E}^{\text{(FD)}}(k)}{4\pi k^2} = \lim_{V\to\infty} \frac{8\pi^3}{V}\left\{\langle E_i^{\text{(FD)}}(\mathbf{k})E_i^{\text{(FD)}}(\mathbf{k})^*\rangle\right\}_\Omega, \tag{12}$$

$\{\;\;\}_\Omega$ denotes angular average in wave-number space over the surface of the sphere $|\mathbf{k}| = k$ and V is the volume of the physical box containing the fluid.

From (4), we have,

$$
\begin{aligned}
\langle E_i^{\mathrm{FD}}(\mathbf{k})E_i^{\mathrm{FD}}(\mathbf{k})^* \rangle = {}& \\
\Delta_{imn}(\mathbf{k},\tilde{\mathbf{k}})\Delta_{ipq}^*(\mathbf{k},\tilde{\mathbf{k}}) & \int d\mathbf{k}' d\mathbf{k}'' \langle \hat{u}_m(\mathbf{k}')\hat{u}_n(\mathbf{k}-\mathbf{k}')\hat{u}_p^*(\mathbf{k}'')\hat{u}_q^*(\mathbf{k}-\mathbf{k}'') \rangle \\
+ 2\nu \Im & \left[i\Delta_{imn}^*(\mathbf{k},\tilde{\mathbf{k}})(\tilde{k}^2 - k^2) \int d\mathbf{k}' \langle \hat{u}_m^*(\mathbf{k}')\hat{u}_n^*(\mathbf{k}-\mathbf{k}')\hat{u}_i(\mathbf{k}) \rangle \right] \\
+ \nu^2 |\tilde{k}^2 - k^2|^2 & \langle \hat{u}_i(\mathbf{k})\hat{u}_i^*(\mathbf{k}) \rangle
\end{aligned}
\tag{13}
$$

where $\langle\;\rangle$ denotes ensemble average, $*$ denotes complex conjugate, $\Im$ denotes the imaginary part, and $\Delta_{imn}(\mathbf{k},\tilde{\mathbf{k}}) \equiv P_{imn}(\tilde{\mathbf{k}}) - P_{imn}(\mathbf{k})$. The following two properties of the Δ_{imn} tensors follow immediately from the corresponding properties of P_{imn}; $\Delta_{imm} = 0$, $\Delta_{imn} = \Delta_{inm}$.

In order to make further analytical work possible with (13), we now introduce the "Millionshchikov hypothesis" (see e.g. Monin and Yaglom 1979) that in fully developed turbulence, the joint probability density function of any set of velocity components at arbitrary space-time points can be assumed to be joint-normal. The joint-normal hypothesis was originally evoked in turbulence in an attempt to close the hierarchy of equations for moments (see e.g. Lesieur 1987). Though this did not succeed, the joint-normal hypothesis has been successfully used in other contexts. Thus, Batchelor (Batchelor 1951) used it with success to predict the pressure spectrum of isotropic turbulence. The joint-normal hypothesis implies in particular

$$
\begin{aligned}
\langle u_i(\mathbf{x}_1)u_j(\mathbf{x}_2)u_k(\mathbf{x}_3)u_l(\mathbf{x}_4) \rangle = {}& \langle u_i(\mathbf{x}_1)u_j(\mathbf{x}_2) \rangle \langle u_k(\mathbf{x}_3)u_l(\mathbf{x}_4) \rangle \\
& + \langle u_i(\mathbf{x}_1)u_k(\mathbf{x}_3) \rangle \langle u_j(\mathbf{x}_2)u_l(\mathbf{x}_4) \rangle \\
& + \langle u_i(\mathbf{x}_1)u_l(\mathbf{x}_4) \rangle \langle u_j(\mathbf{x}_2)u_k(\mathbf{x}_3) \rangle
\end{aligned}
\tag{14}
$$

and that all third order moments are zero. Here $\mathbf{u}(\mathbf{x},t)$ is the true velocity field defined at all space time points. On taking the (continuous) Fourier transform of (14) and assuming the turbulence to be homogeneous, we have,

$$
\begin{aligned}
\langle \hat{u}_i(\mathbf{k}_1)\hat{u}_j(\mathbf{k}_2)\hat{u}_k(\mathbf{k}_3)\hat{u}_l(\mathbf{k}_4) \rangle = {}& \delta(\mathbf{k}_1+\mathbf{k}_2)\delta(\mathbf{k}_3+\mathbf{k}_4)\Phi_{ij}(\mathbf{k}_2)\Phi_{kl}(\mathbf{k}_4) \\
& + \delta(\mathbf{k}_1+\mathbf{k}_3)\delta(\mathbf{k}_2+\mathbf{k}_4)\Phi_{ik}(\mathbf{k}_3)\Phi_{jl}(\mathbf{k}_4) \\
& + \delta(\mathbf{k}_1+\mathbf{k}_4)\delta(\mathbf{k}_2+\mathbf{k}_3)\Phi_{il}(\mathbf{k}_4)\Phi_{jk}(\mathbf{k}_3),
\end{aligned}
\tag{15}
$$

where Φ_{ij} is the Fourier transform of the correlation tensor $R_{ij}(\mathbf{x}_2-\mathbf{x}_1) \equiv \langle u_i(\mathbf{x}_1)u_j(\mathbf{x}_2) \rangle$. On substituting (15) into (13) we get after some algebra (see paper 1)

$$
\begin{aligned}
\mathcal{E}^{(\mathrm{FD})}(k) = \Big\{ & 8\pi k^2 \Delta_{imn}(\mathbf{k},\tilde{\mathbf{k}})\Delta_{ipq}{}^*(\mathbf{k},\tilde{\mathbf{k}}) \int \Phi_{mp}^*(\mathbf{k}')\Phi_{nq}^*(\mathbf{k}-\mathbf{k}')\,d^3\mathbf{k}' \\
& + \nu^2 |\tilde{k}^2 - k^2|^2 \Phi_{ii}(\mathbf{k}) \Big\}_\Omega .
\end{aligned}
\tag{16}
$$

Eq. (16) is the general result for homogeneous turbulence. If in addition, the turbulence is isotropic, Φ_{ij} simplifies (Batchelor 1953) to

$$\Phi_{ij}(\mathbf{k}) = \frac{E(k)}{4\pi k^4}(k^2\delta_{ij} - k_i k_j) \tag{17}$$

where $E(k)$ is the three dimensional energy spectrum and δ_{ij} is the Kronecker-delta symbol. The integral in the first term of (16) may be written after substitution of (17) as

$$
\begin{aligned}
J_{mpnq}(\mathbf{k}) &\equiv 8\pi k^2 \int \Phi_{mp}^*(\mathbf{k}')\Phi_{nq}^*(\mathbf{k} - \mathbf{k}')\,d^3\mathbf{k}' \\
&= \frac{k^2}{2\pi} \int \frac{E(P)E(Q)}{P^4 Q^4}\left[P^2 Q^2 \delta_{mp}\delta_{nq} - P_m P_p Q^2 \delta_{nq} - Q_n Q_q P^2 \delta_{mp} + P_m P_p Q_n Q_q\right] \\
&\qquad \times \delta(\mathbf{P} + \mathbf{Q} - \mathbf{k})\,d^3\mathbf{P}d^3\mathbf{Q}.
\end{aligned}
\tag{18}
$$

This integral can be simplified (see paper 1). The result is

$$
\begin{aligned}
J_{mpnq}(\mathbf{k}) = F_1(k)\delta_{mp}\delta_{nq} &+ F_2(k)(\delta_{mn}\delta_{pq} + \delta_{pn}\delta_{mq}) \\
&+ F_3(k)\left[\frac{k_m k_p}{k^2}\delta_{nq} + \frac{k_n k_q}{k^2}\delta_{mp}\right] + F_4(k)\frac{k_m k_p k_n k_q}{k^4} \tag{19}
\end{aligned}
$$

where

$$
\begin{aligned}
F_1(k) &= \frac{1}{16}\left[7I_4 + 6I_3 - 2I_2 + 5I_1\right] \\
F_2(k) &= \frac{1}{16}\left[-3I_4 + 2I_3 + 2I_2 - I_1\right] \\
F_3(k) &= \frac{1}{16}\left[-15I_4 - 6I_3 + 2I_2 + 3I_1\right] \\
F_4(k) &= \frac{1}{16}\left[45I_4 - 30I_3 - 6I_2 + 7I_1\right].
\end{aligned}
\tag{20}
$$

The terms I_m are defined as

$$I_m = k \int_0^\infty d\xi \int_{|\xi-1|}^{\xi+1} d\eta\, E(k\xi)E(k\eta)W_m(\xi,\eta) \tag{21}$$

where the weights W_m are defined as follows:

$$
\begin{aligned}
W_1(\xi,\eta) &= \frac{1}{\xi\eta} \\
W_2(\xi,\eta) &= \frac{(1 - \xi^2 - \eta^2)^2}{4\xi^3\eta^3} \\
W_3(\xi,\eta) &= \frac{(1 + \xi^2 - \eta^2)^2}{4\xi^3\eta} \\
W_4(\xi,\eta) &= \frac{[1 - (\xi^2 - \eta^2)^2]^2}{16\xi^3\eta^3}.
\end{aligned}
\tag{22}
$$

Therefore, after substituting (19) in (16) and using the properties $\Delta_{imm} = 0$ and $\Delta_{imn} = \Delta_{inm}$, the following expression is obtained for the power spectrum of the finite-differencing error (no summation over repeated indices!):

$$\mathcal{E}^{(\mathrm{FD})}(k) =$$

$$[F_1(k) + F_2(k)] \left\{ \sum_{i,m,n} |\Delta_{imn}(\mathbf{k}, \tilde{\mathbf{k}})|^2 \right\}_\Omega + 2F_3(k) \left\{ \sum_{i,m,n,p} \frac{k_m k_p}{k^2} \Delta_{imn}(\mathbf{k}, \tilde{\mathbf{k}}) \Delta^*_{ipn}(\mathbf{k}, \tilde{\mathbf{k}}) \right\}_\Omega$$

$$+ F_4(k) \left\{ \sum_{i,m,n,p,q} \frac{k_m k_p k_n k_q}{k^4} \Delta_{imn}(\mathbf{k}, \tilde{\mathbf{k}}) \Delta^*_{ipq}(\mathbf{k}, \tilde{\mathbf{k}}) \right\}_\Omega + 2\nu^2 E(k) \left\{ |\tilde{k}^2 - k^2|^2 \right\}_\Omega$$

$$(23)$$

In (23), the functions $F_1(k)$, $F_2(k)$, $F_3(k)$ and $F_4(k)$ are known once the energy spectrum is specified. They are not affected by the choice of numerical schemes. On the other hand, the coefficients of these functions in (23) depend *only* on the numerical method (through the dependence of $\tilde{\mathbf{k}}$ on $\mathbf{k}$) and are quite independent of the physical spectrum. Thus, given a specific numerical scheme and energy spectrum, (23) can be used to compute the power spectrum of the finite-differencing error. This is done in §2.3 for various representative numerical schemes.

2.2.2 Aliasing errors

The power spectrum of the aliasing error is defined by

$$\frac{\mathcal{E}^{(\mathrm{alias})}(k)}{4\pi k^2} = \lim_{V \to \infty} \frac{8\pi^3}{V} \left\{ \langle E_i^{(\mathrm{alias})}(\mathbf{k}) E_i^{(\mathrm{alias})}(\mathbf{k})^* \rangle \right\}_\Omega. \qquad (24)$$

From (8) one obtains

$$\langle E_i^{\mathrm{alias}}(\mathbf{k}) E_i^{\mathrm{alias}}(\mathbf{k})^* \rangle = P_{imn}(\tilde{\mathbf{k}}) P^*_{ipq}(\tilde{\mathbf{k}}) \sum_{\mathbf{a}, \mathbf{a}' \in \Lambda_0} \int_B \int_B \int_B \int_B d\mathbf{k}_1 d\mathbf{k}_2 d\mathbf{k}_3 d\mathbf{k}_4 \qquad (25)$$

$$\times \langle \hat{u}_m(\mathbf{k}_1) \hat{u}_n(\mathbf{k}_2) \hat{u}_p^*(\mathbf{k}_3) \hat{u}_q^*(\mathbf{k}_4) \rangle \, \delta(\mathbf{k} + \mathbf{a} - \mathbf{k}_1 - \mathbf{k}_2) \delta(\mathbf{k} + \mathbf{a}' - \mathbf{k}_3 - \mathbf{k}_4).$$

On applying the joint-normal hypothesis, (15), one gets after some algebra (see paper 1)

$$\mathcal{E}^{(\mathrm{alias})}(k) =$$

$$8\pi k^2 \sum_{\mathbf{a} \in \Lambda_0} \left\{ P_{imn}(\tilde{\mathbf{k}}) P^*_{ipq}(\tilde{\mathbf{k}}) \int_B \int_B d\mathbf{k}' d\mathbf{k}'' \Phi^*_{mp}(\mathbf{k}') \Phi^*_{nq}(\mathbf{k}'') \delta(\mathbf{k} + \mathbf{a} - \mathbf{k}' - \mathbf{k}'') \right\}_\Omega.$$

$$(26)$$

The integral in (26) is difficult to handle analytically because integration over the cubical region $\mathcal{B}$ destroys the spherical symmetry of the problem exploited in the computation of $\mathcal{E}^{\mathrm{FD}}(k)$ in the last section. In order to make analytical progress, the following approximation is introduced. The region $\mathcal{B}$, which is a cube in $\mathbf{k}$-space,

is replaced by the largest sphere contained in it. Clearly, this procedure can be implemented simply by removing the suffix '$\mathcal{B}$' from the integral signs in (26) and replacing the energy spectrum $E(k)$ by

$$E^{\min}(k) = \begin{cases} E(k) & \text{if } k < k_m \\ 0 & \text{otherwise.} \end{cases} \tag{27}$$

The superscript 'min' indicates that this procedure underestimates the true aliasing error by failing to take account of the contribution of modes close to the eight corners of the cube. An alternative method that overestimates the error can be provided by replacing the cube by the smallest sphere that contains it. To obtain this estimate one needs to use in place of $E^{\min}$ the following spectrum;

$$E^{\max}(k) = \begin{cases} E(k) & \text{if } k < \sqrt{3}k_m \\ 0 & \text{otherwise.} \end{cases} \tag{28}$$

The true aliasing error is then expected to lie between these two bounds. With the approximation so described, and with the energy spectrum defined as in (27) or (28), the integral in (26) may be extended to the entire wave space. Thus, one obtains

$$\mathcal{E}^{(\text{alias})}(k) = \sum_{\mathbf{a} \in \Lambda_0} \left\{ P_{imn}(\tilde{\mathbf{k}}) P^*_{ipq}(\tilde{\mathbf{k}}) J_{mpnq}(\mathbf{k} + \mathbf{a}) \right\}_{\Omega}. \tag{29}$$

Substitution of the expression for J_{mpnq} gives (no summation over repeated indices!):

$$\mathcal{E}^{(\text{alias})}(k) = \sum_{\mathbf{a} \in \Lambda_0} \left\{ [F_1(K) + F_2(K)] \sum_{i,m,n} |P_{imn}(\tilde{\mathbf{k}})|^2 \right.$$

$$\left. + 2F_3(K) \sum_{i,m,n,p} \frac{K_m K_p}{K^2} P_{imn}(\tilde{\mathbf{k}}) P^*_{ipn}(\tilde{\mathbf{k}}) + F_4(K) \sum_{i,m,n,p,q} \frac{K_m K_p K_n K_q}{K^4} P_{imn}(\tilde{\mathbf{k}}) P^*_{ipq}(\tilde{\mathbf{k}}) \right\}_{\Omega} \tag{30}$$

where $\mathbf{K} = \mathbf{k} + \mathbf{a}$. Note that in this case the $F_i(K)$ does depend on the direction of $\mathbf{k}$ so that the $F_i(K)$ cannot be extracted from the $\{\ \}_{\Omega}$ operation. Though the summation over the set Λ_0 consists of $3^3 - 1 = 26$ terms, for a cubical box one only needs to evaluate 3 terms due to symmetry. Indeed, the full set of "aliasing modes", $\mathbf{a} \in \Lambda_0$, fall into three classes (Rogallo 1981):

$$3D\{(\pm 2k_m, \pm 2k_m, \pm 2k_m) \qquad 2D \begin{cases} (\pm 2k_m, \pm 2k_m, 0) \\ (\pm 2k_m, 0, \pm 2k_m) \\ (0, \pm 2k_m, \pm 2k_m) \end{cases} \qquad 1D \begin{cases} (\pm 2k_m, 0, 0) \\ (0, \pm 2k_m, 0) \\ (0, 0, \pm 2k_m). \end{cases} \tag{31}$$

By symmetry all the contributions within each class are equal. Therefore,

$$\mathcal{E}^{(\text{alias})}(k) = 6\mathcal{E}^{(\text{alias})}_{1D}(k) + 12\mathcal{E}^{(\text{alias})}_{2D}(k) + 8\mathcal{E}^{(\text{alias})}_{3D}(k) \tag{32}$$

where $\mathcal{E}_{1D}^{(\mathrm{alias})}(k)$ is the contribution from any one of the 1D modes, $\mathcal{E}_{2D}^{(\mathrm{alias})}(k)$ is the contribution from any one of the 2D modes, and $\mathcal{E}_{3D}^{(\mathrm{alias})}(k)$ is the contribution from any one of the 3D modes respectively. If the modified wave-number, $\tilde{k}$, of a numerical method and the energy spectrum of the turbulence, $E(k)$, are known, (32) may be evaluated numerically using either $E^{\min}(k)$ or $E^{\max}(k)$ to get the lower and upper estimates for the aliasing error respectively.

2.2.3 Subgrid and total contributions

The total nonlinear term **N** and the (exact) subgrid force **S** can be readily written down in terms of the Fourier-basis:

$$N_i(\mathbf{k}) = -iP_{imn}(\mathbf{k}) \int d\mathbf{k}' \, d\mathbf{k}'' \delta(\mathbf{k}' + \mathbf{k}'' - \mathbf{k})\hat{u}_m(\mathbf{k}')\hat{u}_n(\mathbf{k}''), \qquad (33)$$

and

$$S_i(\mathbf{k}) = -iP_{imn}(\mathbf{k}) \left(\int\int - \int_B\int_B \right) d\mathbf{k}' d\mathbf{k}'' \delta(\mathbf{k}' + \mathbf{k}'' - \mathbf{k})\hat{u}_m(\mathbf{k}')\hat{u}_n(\mathbf{k}''). \quad (34)$$

The power-spectra are defined as

$$\frac{\mathcal{S}(k)}{4\pi k^2} = \lim_{V\to\infty} \frac{8\pi^3}{V} \{\langle S_i(\mathbf{k})S_i(\mathbf{k})^* \rangle\}_\Omega \qquad (35)$$

$$\frac{\mathcal{N}(k)}{4\pi k^2} = \lim_{V\to\infty} \frac{8\pi^3}{V} \{\langle N_i(\mathbf{k})N_i(\mathbf{k})^* \rangle\}_\Omega \qquad (36)$$

where $\{\ \ \}_\Omega$ as usual denotes angular average over the sphere $|\mathbf{k}| = k$.

The evaluation of (36) is similar to the calculation of $\mathcal{E}^{\mathrm{FD}}(k)$ in § 2.2.1. One only needs to replace 'Δ_{imn}' in (16) by '$-P_{imn}$' and drop the last term involving the viscosity. The resulting expressions can be further simplified using the properties of the P_{imn} tensors (see paper 1):

$$\mathcal{N}(k) = k^2[F_1(k) + F_2(k) + F_3(k)]. \qquad (37)$$

where F_1, F_2 and F_3 are as defined in (20).

The computation of $\mathcal{S}(k)$ once again requires us to restrict the **k** space integration to a cubical domain which makes it difficult to handle the integrals analytically. This difficulty is dealt with in precisely the same manner as was done in the computation of the aliasing error. The cubical domain in **k** space is replaced by a spherical region of appropriate size. This is completely equivalent to replacing the energy spectrum $E(k)$ by a pseudo-spectrum $\tilde{E}^{\min}(k)$ or $\tilde{E}^{\max}(k)$ defined as:

$$\tilde{E}^{\min}(k) = \begin{cases} E(k) & \text{if } k > \sqrt{3}k_m \\ 0 & \text{otherwise} \end{cases} \qquad (38)$$

and

$$\tilde{E}^{\max}(k) = \begin{cases} E(k) & \text{if } k > k_m \\ 0 & \text{otherwise.} \end{cases} \qquad (39)$$

With this modification, the calculation is exactly identical to that just presented for the nonlinear term. Thus, one obtains

$$\mathcal{S}(k) = k^2[F_1(k) + F_2(k) + F_3(k)]. \qquad (40)$$

where in the evaluation of the functions F_i, the pseudo-spectrum $\tilde{E}^{\min}(k)$ or $\tilde{E}^{\max}(k)$ should be used in place of $E(k)$ to obtain the lower and upper bounds respectively.
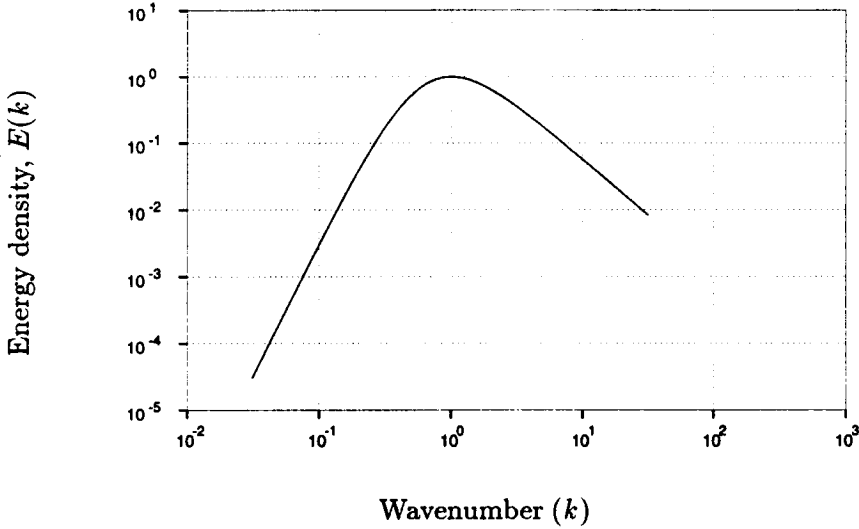
FIGURE 1. The Von-Karman spectrum normalized so that the maximum energy density is at $k = 1$ and $E(1) = 1$.

2.3 Application to LES

The results established in the previous sections will now be applied to establish quantitative measures of errors in LES. In LES, the grid spacing Δ is typically much larger than the Kolmogorov length so that molecular viscosity plays a negligible role. Therefore 'ν' is set to zero throughout this section. For the energy spectrum we assume the "Von-Karman form"

$$E(k) = \frac{ak^4}{(b + k^2)^{17/6}} \tag{41}$$

where the constants $a = 2.682$ and $b = 0.417$ are chosen so that the maximum of $E(k)$ occurs at $k = 1$ and the maximum value $E(1) = 1$. This can always be ensured by a proper choice of length and time-scales. The Von-Karman spectrum has the property $E(k) \sim k^4$ as $k \to 0$ and $E(k) \sim k^{-5/3}$ as $k \to \infty$ and is a fair representation of inertial range turbulence. A plot of this spectrum is shown in Fig. 1.

2.3.1 Spectra

The power spectra $\mathcal{N}(k)$ and $\mathcal{S}(k)$ are evaluated numerically from (37) and (40), respectively, using the Von-Karman spectrum. We assume the LES filter to be equal to the grid spacing Δ. The results are shown in Fig. 2 for $k_m = 8$ and 32, where $k_m \equiv \pi/\Delta$. It is seen that the power spectrum of the total nonlinear term is reasonably flat at high wavenumbers while the subgrid contribution rises monotonically to a maximum (which appears as a "cusp" when plotted on a linear
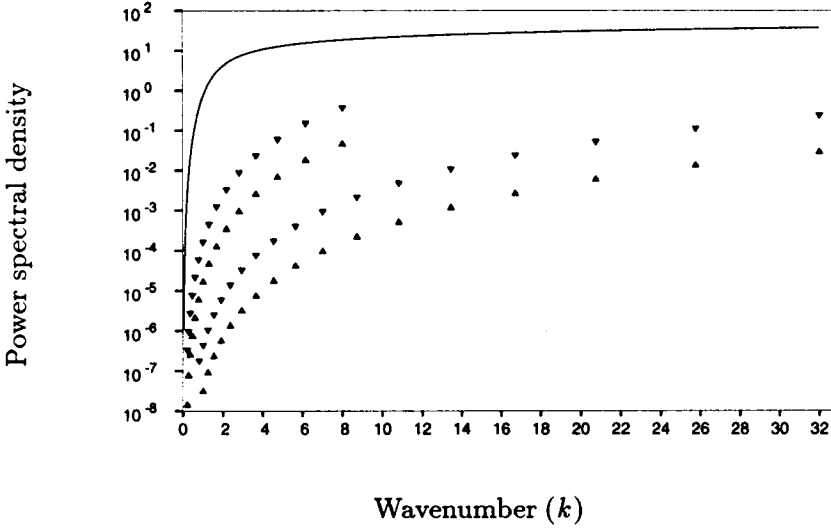
Wavenumber (k)

FIGURE 2. The total nonlinear term (——) compared to the lower (▲) and upper (▼) bound of the true subgrid force for $k_m = 8$ and 32.

scale) at the cut-off wavenumber k_m. The subgrid contribution is seen to be a relatively small part of the total contribution from the nonlinear term.

Subgrid modeling is a very important part of large-eddy simulation. A parametrization of the interaction of the unresolved eddies with the resolved ones is expressed as a subgrid model. It is therefore desirable that the errors inherent in the numerical method be much smaller than the physically motivated subgrid model. We now examine to what extent such an expectation is realized for a second order central-difference method implemented with the nonlinear term in divergence form. A second order central-difference scheme is characterized by the modified wavenumber $\tilde{k}_i = \sin(k_i \Delta)/\Delta$ ($i = 1$, 2 or 3). Eq. (23) is used to compute the power spectra of the finite-differencing error $\mathcal{E}^{(FD)}(k)$ for $k_m = 8$ and 32. These results are compared to the power spectra of the respective subgrid terms in Fig. 3. Only two values of k_m are shown for clarity. The figures have the same qualitative appearance for all values of k_m. The power spectrum of the finite-differencing error rises to a maximum at $k = k_m$ in the same manner as the subgrid contribution. However, for all values of k_m the finite-differencing error is substantially larger than the subgrid contribution over the entire wavenumber range.

Figure 3 indicates that the error in a second order scheme cannot be reduced to a level below the subgrid contribution by sufficiently refining the grid. As the grid is refined (k_m is increased), both the error as well as the subgrid force decrease for all wavenumbers. However, the error continues to dominate the subgrid force throughout the wavenumber range irrespective of the resolution. Let us now examine if this situation can be improved by using higher order central-difference schemes. Figure 4 shows the finite-differencing error evaluated using (23) for a second, fourth,
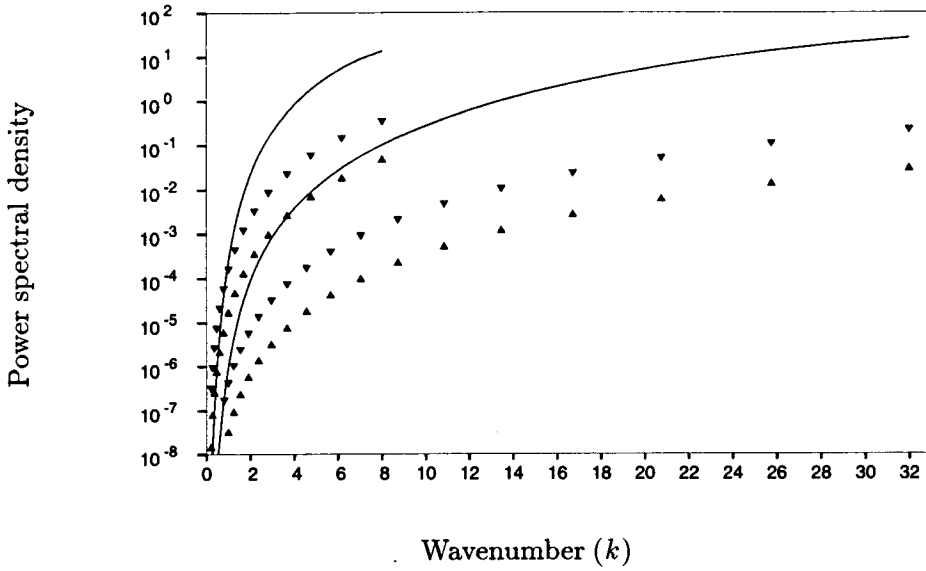
FIGURE 3. Finite-differencing error for the second order central-difference scheme (————) compared to the lower (▲) and upper (▼) bounds of the true subgrid force for $k_m = 8$ and 32.
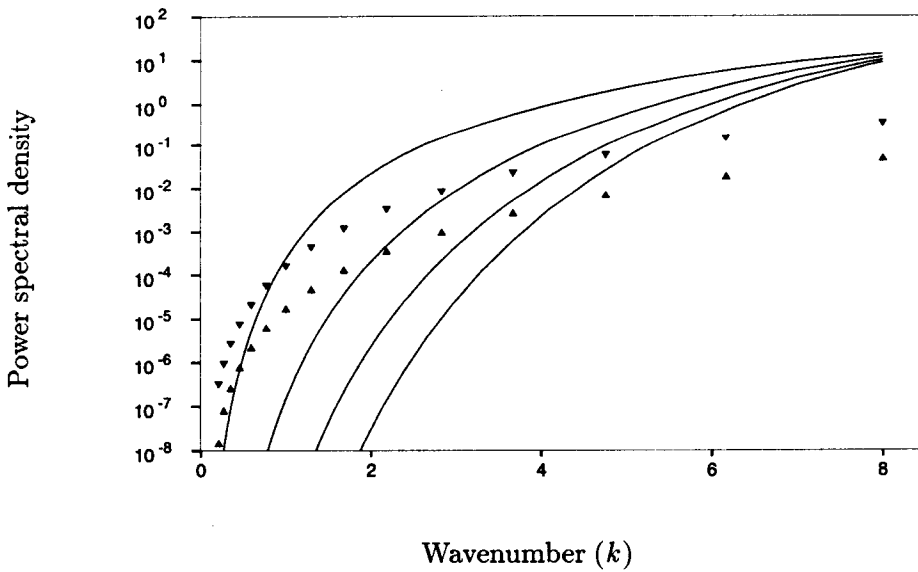
FIGURE 4. Finite-differencing errors (————) compared to the lower (▲) and upper (▼) bounds of the subgrid force for $k_m = 8$. The numerical schemes considered are second (highest curve), fourth, sixth, and eighth (lowest curve) order central-differences.

Wavenumber (k)
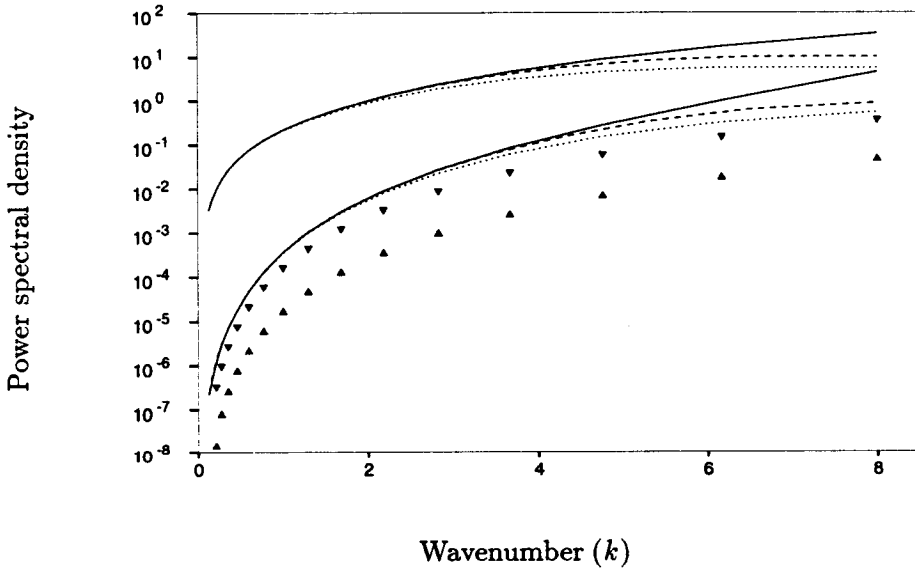
FIGURE 5. The aliasing error for a second-order central-difference method ($\cdots\cdots$), a fourth-order central-difference method ($- \ - \ -$) and an undealiased pseudo-spectral method (———), compared to the lower (▲) and upper (▼) bounds of the subgrid force. Each method is represented by a pair of curves corresponding to the lower and upper bounds of the error.

sixth, and eighth order central-difference scheme together with the subgrid term, computed using (40) for a fixed resolution, $k_m = 8$. It is seen that higher order schemes do lead to reduced levels of error. However, even with an eighth order scheme, the subgrid contribution is dominated by numerical errors in about half of the wavenumber range.

Figure 5 shows the corresponding comparison for the aliasing error computed using (30). In general, increasing the order of a scheme has a relatively weak effect on the aliasing error and the effect is primarily in the high wavenumber region. This effect is in fact in the "reverse" direction compared to the finite-differencing error. That is, the lowest pair of curves which correspond to a second-order scheme have the smallest aliasing error and the highest pair corresponding to an undealiased pseudo-spectral method have the largest. The aliasing errors for sixth and eighth order schemes are intermediate between the fourth and the pseudo-spectral; they have been omitted from Fig. 5 for clarity. The effect is of course quite easy to understand. In the one dimensional problem, the aliasing part of the nonlinear term is multiplied by the modified wavenumber which approaches zero at the cut-off so that the aliasing error is also reduced to zero at k_m. In the three dimensional problem a similar situation applies except that the power spectrum does not actually go to zero on account of the averaging over wavenumber shells. However, the aliasing error is reduced at high wavenumbers for central-difference schemes.

2.3.2 Scaling laws

In this section, the dependence of some measure of "global error" on resolution, k_m, is investigated. An appropriate measure of the kind is

$$\sigma_* = \left[\int_0^{k_m} \mathcal{E}^{(*)}(k)\, dk \right]^{1/2} \tag{42}$$

where '*' stands for 'FD', 'alias', 'nl' or 'sg' corresponding to the global finite-differencing error, aliasing error, total nonlinear term, or subgrid term respectively. σ_* is closely related but not exactly equal to the the rms value, which is given by the integral of the power spectrum over the entire wavenumber range. The correspondence is not exact because the modes at the corners of the cube $[-k_m, k_m] \times [-k_m, k_m] \times [-k_m, k_m]$ outside of the inscribed sphere of radius k_m have not been included in the definition (42). Thus, σ_* is a lower bound of the true rms value. The σ_* can be evaluated as a function of k_m by numerically integrating the power spectra $\mathcal{E}^{(*)}(k)$ presented earlier.

Figure 6 shows the lower and upper bounds (measured by the corresponding σ_*) for the subgrid force σ_{sg} as a function of k_m. The corresponding quantity for the total nonlinear term σ_{nl} is also shown for comparison. The subgrid contributions are seen to obey a power law. A least square fit gives

$$\sigma_{sg} = \begin{cases} 0.36\, k_m^{0.39} & \text{(Lower bound)} \\ 0.62\, k_m^{0.48} & \text{(Upper bound)} \end{cases} \tag{43}$$

The total nonlinear term also appears to follow a power law. A least square fit in this case gives

$$\sigma_{nl} = 1.04\, k_m^{0.97}. \tag{44}$$

The fitted curves (43) and (44) are shown in Fig. 6 as dashed and solid lines respectively. Thus, the relative subgrid contribution is (roughly) $\sigma_{sg}/\sigma_{nl} \sim k_m^{-0.5}$, that is, the role of the subgrid model decreases at higher resolution. As an illustration, for an LES that resolves about a decade of scales beyond the energy peak, the rms value of the subgrid force, according to this formula, should be in the approximate range $11 - 19$ % of the rms value of the total force.

The following heuristic "derivation" (Tennekes & Lumley 1983) is sometimes given for the scaling of the subgrid term. The traceless subgrid stress is $\tau_{ij} = 2\nu_t S_{ij}$ where ν_t is the eddy-viscosity and S_{ij} is the rate of strain. The rate of dissipation $\epsilon = \tau_{ij}S_{ij} = \nu_t |S|^2$ is a constant according to the classical Kolmogorov argument. Therefore, $|\tau_{ij}| \sim \nu_t |S| \sim \sqrt{\epsilon\nu_t}$. Now, it seems reasonable to postulate that ν_t is the product of the grid-spacing, Δ, and the rms velocity of the subgrid eddies, $\sqrt{\langle u'^2 \rangle}$. The latter can be estimated from the Kolmogorov spectrum

$$\sqrt{\langle u'^2 \rangle} \sim \left[\int_{k_m}^{\infty} E(k)\, dk \right]^{1/2} \sim \left[\int_{k_m}^{\infty} k^{-5/3}\, dk \right]^{1/2} \sim (k_m)^{-1/3} \sim \Delta^{1/3}. \tag{45}$$
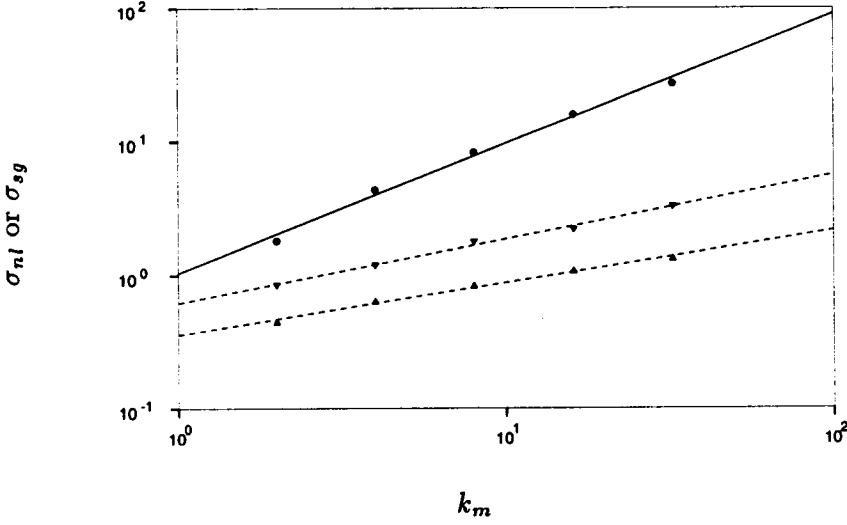
FIGURE 6. Global measure of the total nonlinear term, σ_{nl} (•) and subgrid force, σ_{sg} (lower bound: ▲, upper bound: ▼) plotted as a function of the maximum resolved wavenumber, k_m. The lines represent power law fits obtained by the least-square method.

Thus, $\nu_t \sim \Delta\Delta^{1/3} \sim \Delta^{4/3}$ so that $|\tau_{ij}| \sim \sqrt{\epsilon\nu_t} \sim \Delta^{2/3}$. The subgrid force, which is the derivative of τ_{ij} should then scale as $|\tau_{ij}|/\Delta \sim \Delta^{-1/3} \sim (k_m)^{1/3}$. The scaling exponent (0.4-0.5) in (43) is reasonably close to what this rough argument predicts. It should be noted that, even though the subgrid stress decreases with increasing resolution, its derivative, the subgrid force, actually increases.

Figure 7 shows the integrated finite-differencing error, σ_{FD}, plotted against k_m. There appears to be an asymptotic approach to a power law behavior for large k_m. A least square power law fit to the last three data points gives

$$\sigma_{FD} = k_m^{0.75} \times \begin{cases} 1.03 & \text{(Order 2)} \\ 0.82 & \text{(Order 4)} \\ 0.70 & \text{(Order 6)} \\ 0.5 & \text{(Order 8)} \\ 0 & \text{(Spectral)} \end{cases} \qquad (46)$$

which are shown as solid lines in Fig. 7. The subgrid terms σ_{sg} are also shown for comparison. It is significant that the exponent in the dependence of the integrated error on resolution in (46) turns out to be independent of the order of the scheme. A higher order scheme reduces the error only through a reduced prefactor multiplying the $\sim k_m^{0.75}$ term.

Figure 8 shows the integrated value of the aliasing error σ_{alias} plotted against k_m. The lines are power law fits to the data. Only the second order scheme and the pseudo-spectral scheme without dealiasing is shown. The curves for the fourth,
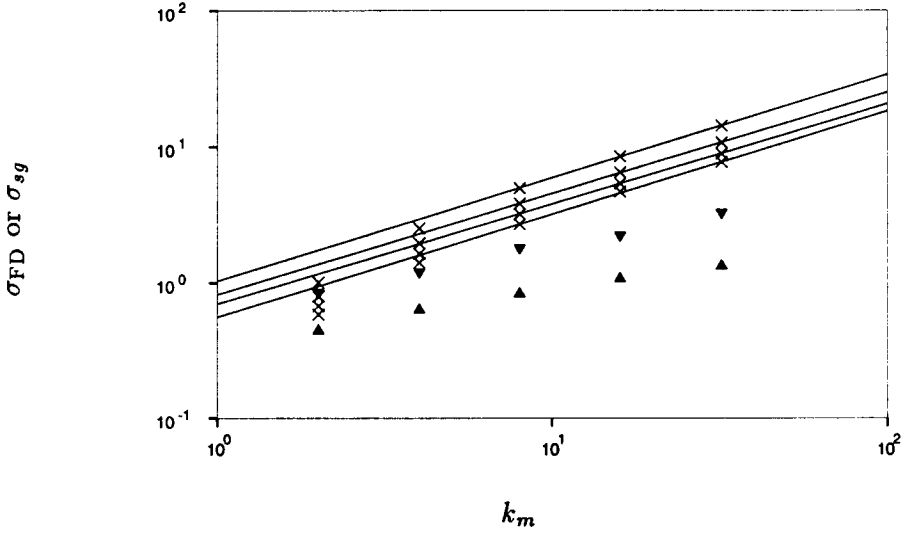
FIGURE 7. Finite-differencing errors, σ_{FD} plotted as a function of the maximum resolved wavenumber k_m ($\times$) for central differencing schemes of order 2 (topmost), 4, 6 and 8 (lowermost). The solid lines are least-square power law fits. Lower ($\blacktriangle$) and upper ($\blacktriangledown$) bounds of the subgrid force σ_{sg} are also shown for comparison.
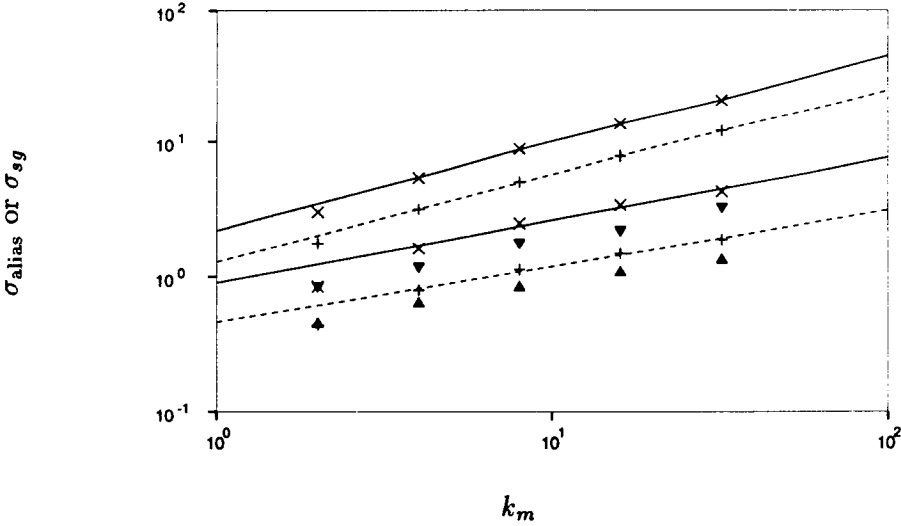
FIGURE 8. Upper and lower bounds of the aliasing error, σ_{alias}, for a second-order (+) and undealiased pseudo-spectral method ($\times$). Solid and dashed lines are least-square power law fits. Upper ($\blacktriangledown$) and lower ($\blacktriangle$) bounds for the subgrid term σ_{sg} are also shown for comparison.

sixth, and eighth order schemes have intermediate positions and have been omitted for clarity. These fits are given by the following analytical expressions;

$$\sigma_{\text{alias}} = \begin{cases} 0.90\,k_m^{0.46} & \text{(Lower bound, Pseudo-spectral)} \\ 2.20\,k_m^{0.66} & \text{(Upper bound, Pseudo-spectral)} \\ 0.46\,k_m^{0.41} & \text{(Lower bound, Second-order)} \\ 1.29\,k_m^{0.65} & \text{(Upper bound, Second-order)} \end{cases} \qquad (47)$$

The important distinction from Fig. 7 is that here the curves are "reversed". Thus, the lowest curve corresponds to the second order scheme and the highest corresponds to an undealiased pseudo-spectral scheme. The subgrid term σ_{sg} is also shown for comparison. Of course, for a spectral scheme properly dealiased with the '3/2-rule' both the aliasing as well as the finite-differencing errors are identically zero.

2.3.3 Discussions

The results of the above analysis may be summarized as follows. In large eddy simulation, the net effect of the unresolved eddies on the resolved ones is represented by a subgrid model. The resulting equations, which are the Navier-Stokes equations augmented by an additional term, the subgrid force, is then solved numerically. In such a procedure the presumption is that the associated numerical errors are small compared to the subgrid model being used. To keep the analysis as simple as possible, isotropic turbulence in a 'box' with periodic boundary conditions was considered together with a simple numerical method: an order n ($n = 2$ to 8) central-difference scheme with the nonlinear term in the divergence form. It was found that the power spectrum of the aliasing error is significantly larger than the subgrid term over most of the resolved wavenumber range. Higher order schemes have the effect of increasing the aliasing error. The finite-differencing error for a second-order scheme also remains significantly larger than the subgrid term over most of the resolved wavenumber range. The situation is improved by going to higher-order schemes. However, even for an eighth-order scheme, the error dominates the subgrid term for almost half of the resolved wavenumber range. An increase in grid resolution makes the errors increase faster than the subgrid force so that the situation cannot be improved by grid refinement as long as the cut-off is in the inertial range.

We now consider a possible remedy for this difficulty. In LES the Navier-Stokes equations are first 'filtered' to remove all scales below some 'filter-width', Δ_f. The resulting equations are then discretized on a grid of spacing Δ_g. In order that the smallest resolved scales be representable on the grid, it is required that $\Delta_g \leq \Delta_f$. In practice one most often assumes $\Delta_g = \Delta_f$, to minimize computational cost and accepts the consequence that the "marginal" eddies may not be well resolved. As a matter of fact, this distinction between Δ_g and Δ_f is often ignored and one speaks of 'filter-width' and 'grid-spacing' interchangeably. However, if one expects to adequately resolve all scales up to 'Δ_f', it is natural to require that 'Δ_g' be several times smaller than 'Δ_f' (Rogallo & Moin 1984). Thus, we are led to consider an LES with a filter-width Δ_f performed on a numerical grid of spacing $\Delta_g < \Delta_f$. Clearly, in any

Wavenumber (k)
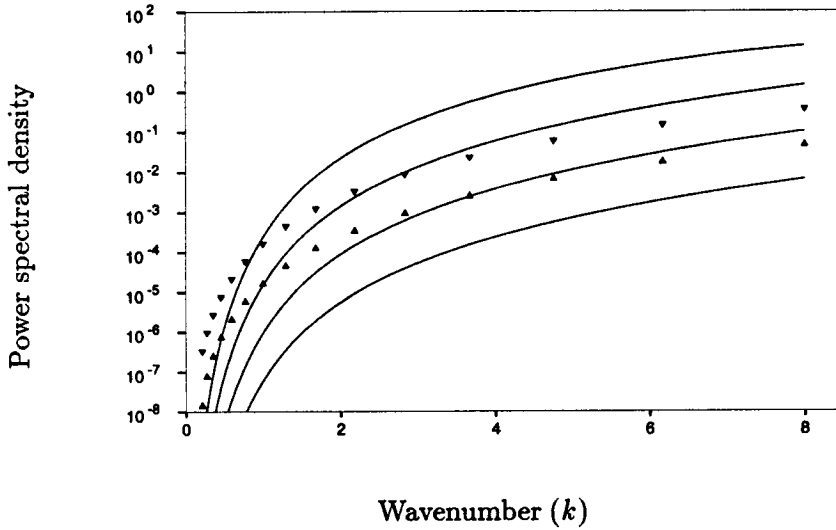
FIGURE 9. The finite-differencing error (———) for a second order central-difference scheme with $\Delta_f = N\Delta_g$ for $N = 1$ (uppermost curve), 2, 4 and 8 (lowermost curve). The lower (▲) and upper (▼) bounds of the subgrid force are shown for comparison. $k_m^f = 8$ is held fixed.

Wavenumber (k)
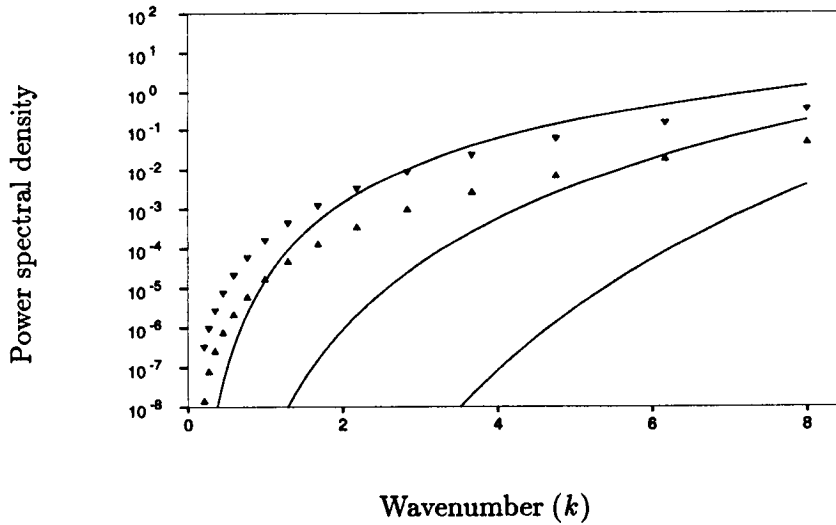
FIGURE 10. The finite-differencing error (———) for $\Delta_f = 2\Delta_g$ for a second (uppermost), fourth and eighth (lowermost) order central-difference scheme. The lower (▲) and upper (▼) bounds of the subgrid force are shown for comparison. $k_m^f = 8$ is held fixed.

such computation all Fourier-modes between $k_m^f = \pi/\Delta_f$ and $k_m^g = \pi/\Delta_g$ must be held at very low amplitudes, for otherwise these "contaminated" modes would soon destroy the accuracy of computation of the modes $(0, k_m^f)$ through nonlinear interactions. This might be achieved naturally by the effective "dissipation range" of the eddy-viscosity. This may also be achieved by replacing the usual discretization of the Navier-Stokes equations by the following alternative (Lund 1995)

$$\frac{\partial u_i}{\partial t} = -\frac{\delta}{\delta x_j} \mathcal{F}[u_i u_j] - \frac{\delta \mathcal{F}[P]}{\delta x_i} - \frac{\delta \mathcal{F}[\tau_{ij}]}{\delta x_j} + \nu \frac{\delta}{\delta x_k} \frac{\delta}{\delta x_k} u_i, \qquad (48)$$

where $\mathcal{F}[\ ]$ represents a suitably designed filtering operation that reduces the amplitudes of all modes in the range (k_m^f, k_m^g) to zero or very small values. [Compact filters for finite-difference schemes that are close to a sharp low pass filter in Fourier space were first considered by Lele (1992). They have been used in the present context by Lund (Lund 1995).] The finite-differencing operator $\delta/\delta x_j$ is on the finer grid Δ_g. The effect of this modification is easy to investigate in the present formalism. Thus, for a second order method, the 'Δ' in the expression for the modified wavenumber need simply be replaced with Δ_g. Figure 9 shows the result of such a computation for a second-order central-difference method with $\Delta_g = \Delta_f/N$ where $N = 1, 2, 4$, and 8 for a fixed $k_m^f = 8$. It is seen that with $N = 8$, the finite-differencing error is about one or two orders of magnitude below the subgrid term throughout the wavenumber range from $k = 0$ to $k_m^f = 8$. However, taking $\Delta_g = \Delta_f/8$ increases the number of grid points by a factor of $8^3 = 512$ and the total computational cost (if the time-step, Δt is limited by the CFL condition so that $\Delta t \sim \Delta$) by a factor of $8^4 = 4096$. It may therefore be advisable to use instead a higher order scheme in conjunction with a grid that is finer than the filter-width. In Fig. 10 Δ_g has been fixed at $\Delta_f/2$ and the spectra of finite-differencing errors is plotted for a second, fourth, and eighth order scheme. It is seen that for an eighth order scheme the finite-differencing error is several orders of magnitude below the subgrid term. The increase in computational cost due to the refined grid is a factor of $2^4 = 16$. Implementation of an eighth order scheme would also carry a penalty in terms of added cost. However, in view of the vastly increased accuracy, the additional cost may be justified. In addition to reducing the finite-differencing error, the filtering scheme (48) completely removes the aliasing error. This is because modes $\mathbf{k}'$ and $\mathbf{k}''$ that 'alias' to a mode $\mathbf{k}$ must satisfy the relation $\mathbf{k}' + \mathbf{k}'' - \mathbf{k} = \mathbf{a}$ where $\mathbf{a}$ is a member of the "reciprocal lattice" Λ. Any component of the vector on the left of this equation can be at most k_m^f so that the left-hand side cannot exceed $3k_m^f$. Since at least one component on the right-hand side is $2k_m^g$ or larger, the equation cannot be satisfied if $3k_m^f < 2k_m^g$, that is, if $\Delta_f > (3/2)\Delta_g$ there cannot be any aliasing errors. This is of course the well known "3/2 dealiasing rule" (see e.g. Canuto *et al.* 1988).

3. Future plans

The analysis presented in this report is kinematic in nature in the sense that the departure of the right-hand side of the Navier-Stokes operator from its ideal

value is investigated. The effect of this error on the dynamics of the solution and ultimately on the prediction of averaged quantities is unknown. However, in the light of the present findings that these errors are comparable in size to the subgrid term, a careful and systematic study is required before finite-difference methods can be considered reliable. Such a program of study should choose a specific flow for which reliable experimental data are available and for which issues such as sensitivity to initial and boundary conditions are reliably known to be unimportant. Numerical simulations should then be performed using both spectral and various finite-difference methods and the results compared to experiments and to each other. The effect of reducing errors using methods described in § 2.3.3 on relevant statistical averages should be studied.

A study of this nature has recently been undertaken by Kravchenko and Moin (Kravchenko and Moin 1995). They used a channel flow spectral code that uses B-splines in the wall normal direction and trigonometric basis functions in the homogeneous directions. By replacing the wavenumbers by the modified wavenumbers in the homogeneous directions they were able to mimic various finite difference schemes. Numerical experiments were run with various forms (divergence, rotational, skew-symmetric) of the nonlinear terms with staggered as well as nonstaggered grids. Aliasing errors in general were found to have a very serious effect on the simulation causing the flow to laminarize in some cases, as might be expected in the light of the present analysis. The effect of aliasing errors on the simulation as well as their size was found to depend strongly on both the form of the nonlinear term as well as the order of the scheme. Aliasing errors had the most serious effect for (undealiased) pseudo-spectral methods, a result also consistent with the present study. The effect of aliasing errors on numerical simulations have also been studied by Blaisdell *et al.* (1995), Zang (1991), Kim *et al.* (1987) and Moser *et al.* (1982) among others using numerical simulations.

Acknowledgments

REFERENCES

BATCHELOR, G. K. 1951 Pressure fluctuations in isotropic turbulence. *Proc. Camb. Phil. Soc.* **47**, 359.

BATCHELOR, G. K., 1953 *The theory of homogeneous turbulence*, Cambridge Univ. Press, Cambridge, England.

BLAISDELL, G. A., SPYROPOULOS, E. T., & QIN, J. H., 1995 The effect of the formulation of nonlinear terms on aliasing errors in spectral methods. *Appl. Num. Math. (submitted).*

CANUTO, C., HUSSAINI, M.Y ., QUARTERONI, A., AND ZANG, T. A. 1988 *Spectral methods in fluid dynamics*, Springer-Verlag, Berlin.

CHU, C. K., 1978 Numerical methods in fluid dynamics. *Advances in applied mechanics.* **18,** 285.

GHOSAL, S. 1996 An analysis of numerical errors in large eddy simulation of turbulence. *J. Comp. Phys. (to appear)*.

HELMBERG, G., 1969 *Introduction to spectral theory in Hilbert space*, North-Holland, Amsterdam, London.

JONES, W., & MARCH, N. H., 1973 *Theoretical solid state physics, Vol I: Perfect lattices in equilibrium*, Wiley-Interscience, London.

KIM, J., MOIN, P. & MOSER, R. 1987 Turbulence statistics in fully developed channel flow at low Reynolds number. *J. Fluid Mech.* **192,** 365.

KRAVCHENKO, A., & MOIN, P. 1995 On the effect of aliasing errors in spectral and finite-difference simulations of turbulent flows. *(preprint)*.

LELE, S. K. 1992 Compact finite difference schemes with spectral-like resolution. *J. Comp. Phys.* **103,** 16.

LESIEUR, M. 1987 *Turbulence in fluids*, Kluwer Academic Publishers, Dordrecht, The Netherlands.

LUND, T. S., 1995 (unpublished).

MONIN, A. S. & YAGLOM, A. M. 1979 *Statistical Fluid Mechanics*, The MIT Press, Cambridge, Massachusetts.

MOSER, R., MOIN, P., & LEONARD, A. 1982 A spectral numerical method for the Navier-Stokes equations with applications to Taylor-Couette flow. *J. Comp. Phys.* **52,** 524.

ROGALLO, R., 1981 Numerical experiments in homogeneous turbulence. *NASA Tech. Memo. TM81315.*

ROGALLO, R. S. & MOIN, P. 1984 Numerical simulation of turbulent flows. *Ann. Rev. Fluid Mech.* **16,** 99.

TENNEKES, H. & LUMLEY, J. L., 1983 *A first course in turbulence*, The MIT Press, Cambridge, Massachusetts, and London, England.

VICHNEVETSKY, R. & BOWLES, J. B. 1982 *Fourier analysis of numerical approximations of hyperbolic equations*, SIAM, Philadelphia.

ZANG, T. A. 1991 On the rotation and skew-symmetric forms for incompressible flow simulations. *Appl. Num. Math.* **7,** 27.

On why dynamic subgrid–scale models work

By J. Jiménez[1]

1. Motivation

Dynamic subgrid models were introduced in (Germano *et al.* 1991) and have proved to be remarkably successful in predicting the behavior of turbulent flows. Part of the reasons for their success are well understood. It is known, for instance, that their behavior as the flow becomes smooth, such as near walls or during transition, is better than that of other "hand-tuned" models. Since they are constructed to generate an effective viscosity which is proportional to some measure of the turbulent energy at the high wavenumber end of the spectrum, their eddy viscosity vanishes as the flow becomes laminar. This alone would justify their use over simpler models.

But beyond this obvious advantage, which is confined to inhomogeneous and evolving flows, the reason why they also work better in simpler homogeneous cases, and how they do it without any obvious adjustable parameter, is not clear. The simplest case, and one of the first to be documented, is the decay of grid turbulence as measured in (Comte–Bellot & Corrsin 1971), which was shown to be well predicted by simple dynamic models in (Moin *et al.* 1991).

This lack of understanding of the internal mechanisms of a useful tool is disturbing, not only as an intellectual challenge, but because it raises the doubt of whether it will work in all cases. This note is an attempt to clarify those mechanisms. We will see why dynamic models are robust and how they can get away with even comparatively gross errors in their formulations. This will suggest that they are only particular cases of a larger family of robust models, all of which would be relatively insensitive to large simplifications in the physics of the flow. We will also construct some such models, although mostly as research tools.

It will turn out, however, that the standard dynamic formulation is not only robust to errors, but also behaves as if it were substantially well formulated. The details of why this is so will still not be clear at the end of this note, specially since it will be shown that the "a priori" testing of the stresses gives, as is usual in most subgrid models, very poor results. But it will be argued that the basic reason is that the dynamic formulation mimics the condition that the total dissipation is approximately equal to the production measured at the test filter level.

2. Accomplishments

2.1 Numerical experiments

We will restrict ourselves to the simple case of the grid turbulence experiments in (Comte–Bellot & Corrsin 1971), reduced to a temporal decay through the usual Galilean transformation, and to the simplest formulation of the dynamic model (Lilly 1992). We establish the notation next.

Consider two filters with characteristic widths δ and $\Delta = 2\delta$. In all our experiments the filters are spectrally sharp, the code is spectral on a triply periodic cubic box (Rogallo 1981) with 32^2 Fourier modes before de-aliasing, and the narrower filter coincides with the grid.

The initial conditions are obtained by filtering a flow field which has been left to decay at a resolution of 64^3 to an energy and spectrum closely resembling those of Comte-Bellot and Corrsin at their first experimental section. The energy transfer, as measured by the skewness of the velocity gradients, is past its maximum value and has begun to decay. The initial skewness of the filtered field is about -0.27 and decays to about -0.21 at the end of the computation. Because the field is disturbed by the initial filtering operation, the cascade is initially perturbed, and it takes a few time steps to recover, but the recovery is fast and the decay proceeds thereafter in an approximately self-similar manner. Both the initial field and the original simulation code were kindly provided by T. Lund.

For the grid- and test-filtered velocity fields we compute Reynolds stresses and rate of strain tensors which we will call τ_{ij}, σ_{ij}, and T_{ij}, S_{ij}, respectively. The test-filtering operation will be denoted by $< \cdot >$, while an overbar will be reserved for averaging over the whole flow field. Because of our choice of the narrow filter, there is no explicit grid-filtering operation, although our numerical velocities should be interpreted as being related to the experimental ones by filtering at width δ

A tensor is denoted by the same letter as its components, and inner products and norms have their usual meaning. In a minor departure from usual LES practice, the symbol $|\cdot|$ is reserved for the L_2 norm, so that $|S|^2 = S_{ij}S_{ij}$, without the extra factor of two used by some authors.

We introduce the Smagorinsky weighted strains

$$M = 2\sqrt{2}\Delta^2|S|S, \qquad m = 2\sqrt{2}\delta^2|\sigma|\sigma, \tag{1}$$

and the differences

$$L = T - <\tau>, \qquad g = M - <m>. \tag{2}$$

The Smagorinsky assumption at both filter levels is that

$$T^* + cM = 0, \qquad \tau^* + cm = 0, \tag{3}$$

where the star stands for traceless projection, $T^* = T - \frac{1}{3}\text{tr}(T)I$. Subtracting and neglecting the spatial variability of the proportionality constant c leads to the tensor equation

$$\lambda \equiv L^* + cg = 0, \tag{4}$$
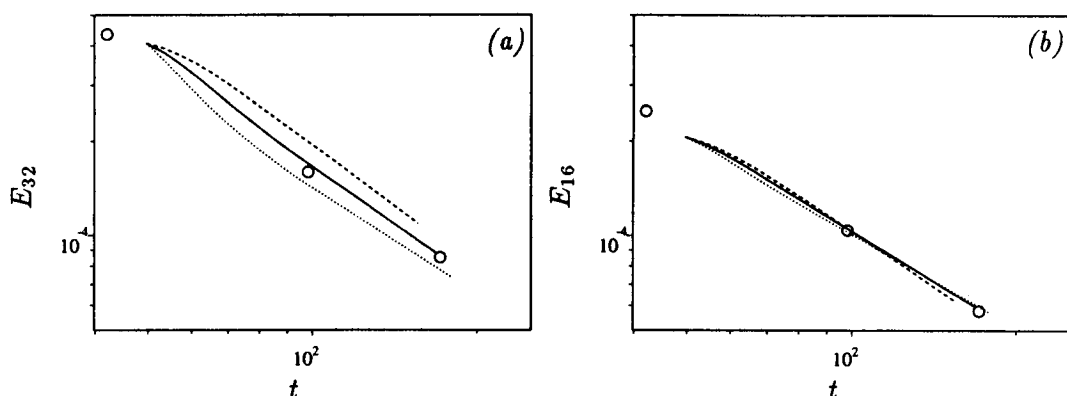
FIGURE 1. Decay of filtered energy for modified dynamic models. ———— : $f = 1$; ---- : $f = 0.5$; ········ : $f = 2$. Symbols are experiment in (Comte–Bellot & Corrsin 1971). (a) Filtered at grid level. (b) Filtered at test level.
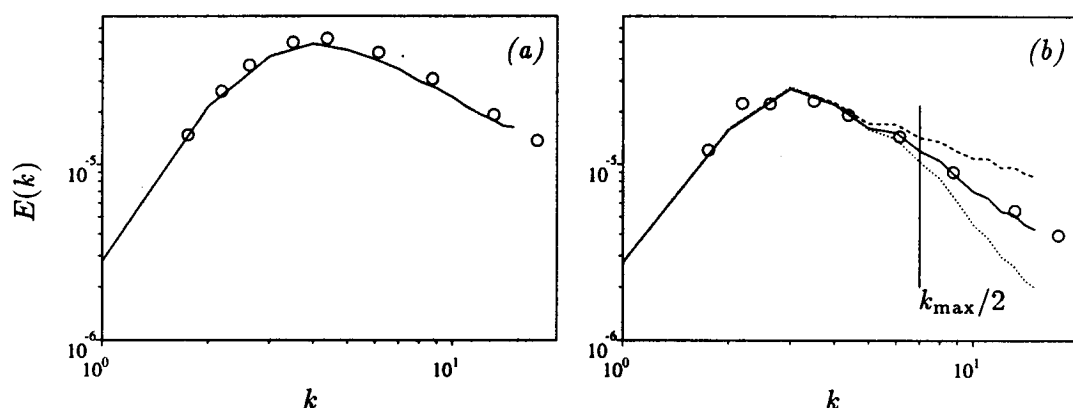
FIGURE 2. Energy spectra of modified dynamic LES runs. Symbols as in Fig. 1. (a) Initial numerical spectrum and $t = 42$ for the experiments. (b) $t \approx 98$.

The constant c is chosen so as to satisfy some contraction of (4), and it has become standard to use g as the contracting tensor (Lilly 1992), on the grounds that it minimizes the L_2 norm of (4). It is well known that when this is done locally numerical instabilities arise because of artificially high back-scatter in those points in which c becomes negative, but that this is cured by averaging over large volumes of the flow. In this note we always average over the whole flow field,

$$c = -f \frac{\overline{L^* \cdot g}}{\overline{|g|^2}}, \qquad f = 1, \tag{5}$$

where the unit factor f is introduced for later convenience. This choice minimizes the norm of (4) when its definition is taken to include integration over the whole volume. Other strategies have been proposed, and in particular the original formulation used S as the contracting tensor (Germano *et al.* 1991). We will not

present here results for that formulation, but experience, including ours during the preparation of this note, indicates that its performance is similar to that of (5).

The final step of the model is to apply (3) for the calculation of τ in the equations of motion.

2.2 Robustness

One way to understand a phenomenon is to observe its response to artificial perturbations, and to study (5) we undertook a series of numerical experiments in which errors were purposefully introduced into it by changing the arbitrary factor f.

As expected, the initial rates of decay are changed proportionally to the change of f, somewhat surprisingly, the effect is only temporary and the logarithmic rate of decay soon recovers the same value as in the undisturbed case, which is very close to the experimental one. The only lasting effect of the prefactor is an offset in the initial conditions (Fig. 1a).

The reason for this is clear once the spectra of the decaying turbulence are examined (Fig. 2b). The one computed with $f = 0.5$ has too much energy in the small scales, while the one computed with $f = 2$ is damped in that region. The large scales, on the other hand, are very similar in the three cases, even if the total energy in the flow has decayed from the initial condition (Fig. 2a) by more than a factor of two. The energy differences seen in Fig. 1a are almost totally due to the differences in the high wavenumbers of the spectra, while the large scales are unaffected by the change of the subgrid model.

In fact, if the energy of the flow is measured by filtering at the test level, which could be argued to be a more natural measure of performance, the three runs are indistinguishable (Fig. 1b), although they are separated by a factor of four in the definition of the model.

This is consistent with the classical idea that the rate of energy decay is fixed by the large scales of the flow (the production), while the small scales adjust themselves to dissipate whichever energy is fed to them by the cascade.

The way in which the adjustment occurs in this particular case is also clear. Consider first the classical Smagorinsky model in which c is a predetermined constant. The dissipation of the model is then $\tau \cdot \sigma \sim c|\sigma|^3$. If c is chosen too low, not enough energy is dissipated at the small scales to compensate for production at the large ones, and energy accumulates in the high wavenumbers. This in turn raises $|\sigma|$ and increases the dissipation, until both rates are again in equilibrium. For a $k^{-5/3}$ spectrum the strain depends mainly on the high wavenumbers, which contain little energy. As a result the adjustment can be accomplished with relatively little effect on the total energy of the flow, and the model is robust to mistuning of the constant c. The Smagorinsky model is in this sense slightly superior to regular viscosity because it makes the dissipation proportional to the cube of $|\sigma|$, rather than to the square, and it is therefore able to adjust itself with milder effects in the total energy.

If, in addition, we accept the last octave of the spectrum as a "sacrificial" range of scales available as a buffer for the model, the effect of the errors in c is minimal, as is the case in Fig. 1b.

2.3 Hyper-Smagorinsky models

This analysis suggests that subgrid-models could be made more robust than Smagorinsky by making their dissipation dependent on measures that are more concentrated towards the high wavenumber end of the spectrum, in such a way that they can adjust with still smaller effects on the total energy.

Consider for example, a "hyper-Smagorinsky" model,

$$\tau^* = -c_n|\sigma_n|\sigma, \tag{6}$$

based on a hyper-strain

$$|\sigma_n|^2 = \int k^{2n}E(k)dk, \tag{7}$$

Note that the case $n = 1$ is a "global" Smagorinsky, in which $|\sigma|$ is computed over the whole field rather than locally. Because of the higher powers of k inside the integral (7), the hyper-strain depends more locally on the tail of the spectrum when $n > 1$, and the models should be able to adjust the dissipation with less effects on the total energy. This is confirmed by the experiments in Fig. 3, where the prefactor technique is applied to the hyper-Smagorinsky models. For each value of n the optimal constant c_n is determined empirically to make the energy decay approximately as in the experiment, and is then modified by substituting it by fc_n.

There are three groups of curves in the figure. The central one corresponds to E_{32} with $f = 1$, while the upper group corresponds to $f = 0.5$ and the lower one to $f = 2$. It is clear that as n increases the sensitivity of the model to errors in the constant decreases, and this is confirmed in Fig. 4, in which the ratio between the energies computed with $f = 0.5$ and 2 is plotted as a function of decay time.

An ideal model would be completely insensitive to the prefactor and would maintain this ratio equal to one. The hyper-Smagorinsky models approach this behavior as n increases, but they never reach the optimum limit because they use an eddy viscosity, which cannot change the total dissipation without affecting broad ranges of the spectrum. A still better family of models would have a hyperviscosity component, but such models are numerically inconvenient and are not explored here. The dynamic model is also included in the figure and is shown to behave best of all, with a sensitivity that is roughly half that of Smagorinsky. This is easy to understand since the effect of large n's is to concentrate the model feedback "sensor" near the end of the spectrum, while the dynamic model computes its constant exclusively from the last octave through the effect of the two filters. Because of that, the dynamic formulation should be nearly optimal among eddy viscosity models with respect to robustness.

Note that in all these cases the initial jump of the energy ratio corresponds to a transient in which the spectrum has not had time to adjust to the incorrect dissipation and is accumulating or losing energy at the small scales.

2.4 Why does it work?

Even if we have shown above one of the reasons why a dynamic model should work reasonably well, even if its formulation is considerably in error with respect to
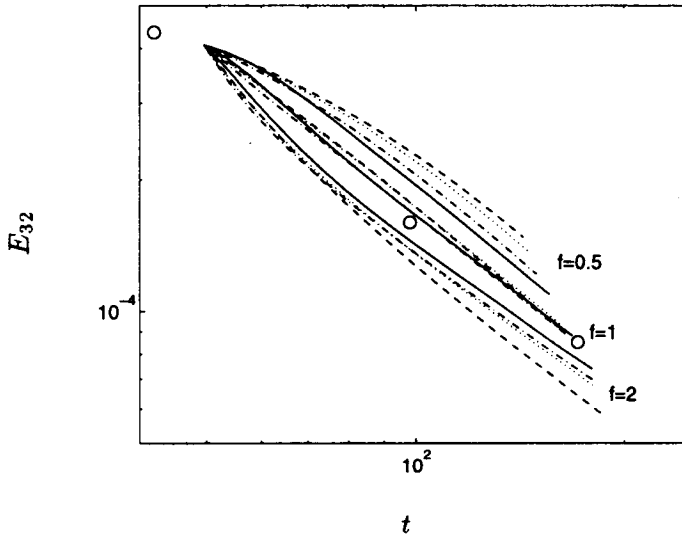
FIGURE 3. Sensitivity of energy decay to mistuning of the proportionality constant, for different "hyper-Smagorinsky" models. The central group of lines uses optimally tuned constants; the top group is modified by $f = 0.5$; the bottom one, by $f = 2$. ———— : dynamic model; — — — — : $n = 0$; ········ : $n = 1$; —·— : $n = 3$; Symbols are from the experiment of (Comte–Bellot & Corrsin 1971).
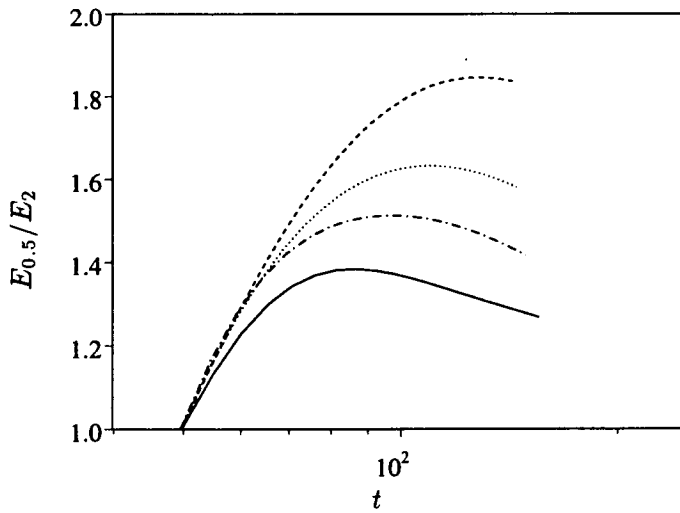
FIGURE 4. Ratio of energy obtained for different "hyper-Smagorinsky" models with $f = 0.5$ and $f = 2$. Symbols as in Fig. 3.

the true dynamics of turbulence, a simple inspection of the spectra in Fig. 2b shows that the standard formulation (5), with $f = 1$, must be very close to the "truth". The tail of its spectrum matches the experimental measurements much better than any of the modified models.

The classical explanation is, first, that the two Smagorinsky assumptions in (3) enforce a scale similarity between the two filter levels, which mimics the scale invariance in the inertial range (Germano *et al.* 1991) and, second, that the least squares approximation of (4–5) ensures that the original Smagorinsky assumptions are reasonably well satisfied (Lilly 1992).

We will argue now that this explanation is unlikely. In the first place, the Reynolds numbers in the (Comte–Bellot & Corrsin 1971) experiment are fairly low ($Re_\lambda \approx 70 - 60$), and the experimental spectra do not contain an inertial range. Their slopes are close to $k^{-4/3}$, and obtaining a computed $k^{-5/3}$ inertial range would require choosing a prefactor $f \approx 1.5$.

Next, the original stress similarity argument requires that the constant c obtained from (5) satisfies the tensor Eq. (4) in some approximate way. An approximation can be optimum and still be so bad that it makes no sense to consider that the model represents the data. This is unfortunately the case in (4). A good approximation would require that $|\lambda|^2/|L^*|^2 \ll 1$, which in turn would imply a high correlation between the tensors $-cg$ and L^*. This can be tested from the results of the calculation, and the correlation coefficient

$$\gamma = -\frac{\overline{L^* \cdot g}}{\left(\overline{|g|^2} \, \overline{|L^*|^2}\right)^{\frac{1}{2}}}, \tag{8}$$

is represented in Fig. 5. After an initial transient, it saturates around 20% and, since

$$\overline{|\lambda|^2/|L^*|^2} = 1 - \gamma^2, \tag{9}$$

this implies that 95% of the magnitude of the stresses remain unexplained by their dynamic Smagorinsky approximation. That the optimal Smagorinsky approximation of the subgrid stresses only explains a small fraction of their magnitude was already noted by Bardina, Ferziger and Reynolds (1983).

This result shows that the Leonard stress L^* and the Germano strain g are far from being coaxial, and that there is little point in trying to model one as proportional to the other. On the other hand, the fact that the method works proves that something is being modeled. Bardina *et al.*, in the same work, noted that the correlation between the model prediction and the true dissipation is much higher than that for the stresses, and it is easy to see that (5) is actually a dissipation formula. The least square approximation results in an exact cancellation of the projection of the tensor over one of its summands, and the projection of the stress on the strain is the dissipation. In fact (5) can be rewritten as

$$\tau_g = -cg, \qquad L \cdot g = \tau_g \cdot g, \tag{10}$$
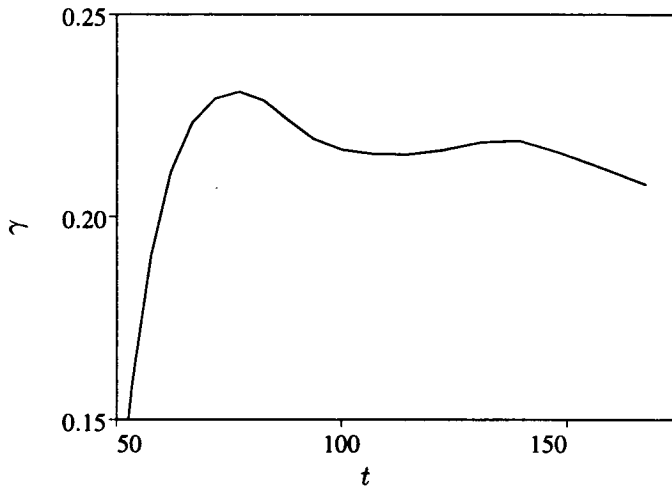
FIGURE 5. Correlation coefficient between the two tensors in (4), computed from a calculation using the dynamic model.

which says that the "dissipation" generated by the Smagorinsky stresses τ_g, is the same as the "production" of the Leonard stresses. Since, in any numerical flow without an explicit grid filter, the grid Reynolds stresses are identically zero and $L = T$, the Leonard production can be used as a surrogate for the production at the test level.

While this argument is suggestive, it is difficult to go much further. Direct computation shows that none of the actual productions and dissipations really match in the dynamic approximation. The numerical production $-T \cdot S$ remains about twice smaller than the dissipation of the Smagorinsky stresses, mainly because a substantial amount of energy is dissipated by the subgrid model on the flow scales between the test and grid filters. Other combinations can be tested with similar lack of success. While there is qualitative agreement in all the obvious balances, the quantitative details are always masked by the broad support of the second order dissipation. Equation (10), while indicative, does not seem to correspond directly to any physical property of the flow.

3. Conclusions and future work

We have shown that a large part of the good behavior of dynamical subgrid models is probably due to their robustness to approximations in the physics. This is shared by other models, with the main requirement being that the formula for the eddy viscosity contains a sensor which responds to the accumulation of energy in the high wavenumber part of the spectrum before it contaminates the energy containing range. The regular Smagorinsky model derives this property from the $|\sigma|$ factor in the eddy viscosity. The classical dynamic model is about twice less sensitive because its constant is computed exclusively from the part of the spectrum between the two filters. Any model with this feedback property, and which contains a reasonable approximation to the flow physics, is likely to represent the energy containing scales

essentially correctly. The quality of the modeling improves substantially if the last octave of the turbulent spectrum is filtered when evaluating the results, and only the large scales are kept.

All this is in addition to the main advantage of the dynamic models, which remains their ability to generate vanishing eddy viscosities in smooth flows, and their resulting good behavior near walls.

From this point of view, the use of the Smagorinsky model as the basis for the dynamic formulation is probably nonessential, and simpler formulations must exist in which the eddy viscosity is computed directly instead of through the Smagorinsky constant.

The classical justification of the dynamic model in terms of scale similarity and optimal approximation of the stresses has been examined and found weak. The approximation provided by the least square formula is so poor in practice as to make any argument based on the stresses meaningless. The least square formulation is a dissipation formula, and Lilly's formulation of the dynamic model can be understood as making the dissipation approximately equal to the measured production. The connection is, however, only approximate, and both quantities agree only qualitatively in computed flows (to within a factor of two). It should be noted that the poor prediction of the stresses, although worrying at first sight for the application to shear flows, in which the stresses are the main results of the computation, is probably not serious. The *mean* Reynolds stresses, in the same way as the total flow energy, are contained in the large flow scales and, if the latter are reasonably well predicted, the former should also be.

Further experiments are needed in cases different from the (Comte–Bellot & Corrsin 1971) decay to make sure that the specially good behavior of the spectrum for the standard model is not accidental. In the same way, tests should be undertaken with other model formulations. The main result of this note should be the realization that the present form of the dynamic model is not unique and probably not optimum, and that other formulations can be developed in terms of considerations such as numerical expedience, not necessarily fully based on strict inertial range physics.

REFERENCES

BARDINA, J., FERZIGER,J. H. & REYNOLDS, W. C. 1983 Improved subgrid-scale models based on large eddy simulation of homogeneous, incompressible, turbulent flows. *Rep.* TF-19, *Dept. Mech. Engng, Stanford, CA.*

COMTE-BELLOT, G. & CORRSIN,S. 1971 Simple Eulerian time correlation of full and narrow-band velocity signals in grid-generated 'isotropic' turbulence. *J. Fluid Mech.* **48**, 273-337.

GERMANO, M., PIOMELLI, U., MOIN, P. & CABOT, W. H. 1991 A dynamic subgrid-scale eddy viscosity model. *Phys. Fluids.* **A 3,** 1760-1765.

LILLY, D. 1992 A proposed modification of the Germano subgrid-scale closure method. *Phys. Fluids.* **A 4,** 633-635.

MOIN, P., SQUIRES, K., CABOT, W. & LEE, S. 1991 A dynamic subgrid-scale model for compressible turbulence and scalar transport. *Phys.Fluids.* **A 3,** 2746-2757.

ROGALLO, R. S. 1981 Numerical experiments in homogeneous turbulence. *NASA Tech. Mem..* **81315,** See also Canuto, C., Hussaini, M. Y., Quarteroni, A. & Zang, T. A., *Spectral methods in fluid dynamics.* Springer (1981), 85-86.

A family of dynamic models
for large-eddy simulation

By D. Carati[1], K. Jansen, AND T. Lund

1. Motivation and objectives

Since its first application, the dynamic procedure has been recognized as an effective means to compute rather than prescribe the unknown coefficients that appear in a subgrid-scale model for Large-Eddy Simulation (LES). The dynamic procedure (Germano *et al.* 1991; Ghosal *et al.* 1995) is usually used to determine the non-dimensional coefficient in the Smagorinsky (1963) model. In reality the procedure is quite general and it is not limited to the Smagorinsky model by any theoretical or practical constraints. The purpose of this note is to consider a generalized family of dynamic eddy viscosity models that do not necessarily rely on the local equilibrium assumption built into the Smagorinsky model. By invoking an inertial range assumption, it will be shown that the coefficients in the new models need not be non-dimensional. This additional degree of freedom allows the use of models that are scaled on traditionally unknown quantities such as the dissipation rate. In certain cases, the dynamic models with dimensional coefficients are simpler to implement, and allow for a 30% reduction in the number of required filtering operations.

2. Accomplishments

2.1 A new family of dynamic eddy viscosity models

The LES equations are obtained from the Navier-Stokes equations by applying a filter, denoted by an overline, which is assumed to damp scales smaller than Δ. In the context of eddy viscosity models, the unknown subgrid-scale stress generated by this operation, $\tau_{ij} = \overline{u_i\,u_j} - \overline{u}_i\,\overline{u}_j$, is assumed to be proportional to the strain tensor $\overline{S}_{ij} = (\partial_i\overline{u}_j + \partial_j\overline{u}_i)/2$:

$$\tau_{ij} = -2\nu_e\overline{S}_{ij}. \tag{1}$$

The eddy viscosity, ν_e, has dimensions L^2/T, where L is length and T is time. The characteristic length in the problem is obviously $L_c = \Delta$. Following the Kolmogorov (1941) dimensional analysis, the characteristic time may be expressed as a function of the rate of energy transfer within the inertial range $\mathcal{E}$: $T_c = (\Delta^2/\mathcal{E})^{1/3}$. The "Kolmogorov expression" for the eddy viscosity is thus:

$$\nu_e = c_k\mathcal{E}^{1/3}\Delta^{4/3}, \tag{2}$$

1 Université Libre de Bruxelles, B-1050 Brussels, Belgium

where c_k is a non-dimensional constant. The rate of energy transfer is usually not directly accessible in LES, and thus Smagorinsky proposed to identify the rate energy transfer within the inertial range with the subgrid-scale dissipation:

$$\mathcal{E} \approx -\tau_{ij}\overline{S}_{ij} = \nu_e|\overline{S}|^2, \tag{3}$$

where $|\overline{S}|^2 = 2\overline{S}_{ij}\overline{S}_{ij}$. When integrated over the volume, the above relation becomes a good approximation since nearly all the dissipation will be carried by the subgrid-scale model when the cutoff is in the inertial range. In the Smagorinsky model, this equality is assumed to be valid at every point in space by invoking a local-equilibrium assumption between production and dissipation of energy. Inserting relation (3) into the Kolmogorov scaling for the eddy viscosity (2) gives the Smagorinsky model

$$\nu_e = c_s|\overline{S}|\Delta^2, \tag{4}$$

where $c_s = c_k^{(3/2)}$ is the non-dimensional Smagorinsky constant. In the Smagorinsky model, the time scale is seen to be $|\overline{S}|^{-1}$. Thus, if local equilibrium is assumed, two expressions are available for the time scale in the eddy viscosity. By dimensional analysis, the eddy viscosity can depend on the ratio of these two time scales as well as on the fundamental scaling in Eq. (2). The most general model can therefore be written as

$$\nu_e = F\left(\frac{|\overline{S}|^3\Delta^2}{\mathcal{E}}\right)\mathcal{E}^{1/3}\Delta^{4/3}, \tag{5}$$

where F is an arbitrary function. In particular, we may focus on a series representation for F:

$$\nu_e = \sum_{l=1}^{n} c_l\,|\overline{S}|^{\zeta_l}\,\mathcal{E}^{(1-\zeta_l)/3}\,\Delta^{(4+2\zeta_l)/3}. \tag{6}$$

Here ζ_l are a sequence of numbers that define the exponents for the various terms in the series. They need not be integers. The parameters c_l are non-dimensional coefficients. As important special cases, note that $n = 1, \zeta_1 = 0$ leads to the Kolmogorov scaling with $c_1 = c_k$, whereas $n = 1, \zeta_1 = 1$ leads to the Smagorinsky model with $c_1 = c_s$.

While Eq. (6) is rather general, it has the apparent drawback that the unknown dissipation rate, $\mathcal{E}$, appears as a model parameter for $\zeta_l \neq 1$. Historically this defect has effectively excluded all models encompassed by Eq. (6) except for the Smagorinsky model. The situation has changed with the introduction of the dynamic procedure, however, and it is possible to use Eq. (6) generally if it is recast in a slightly different form. If we assume that the test and grid filters are in the inertial range, then the dissipation rate as well as each of the model coefficients, c_l, should be the same at two filtering levels. The product of the dissipation rate (raised to some power) and a model coefficient should also be invariant with filtering

scale, and thus the dynamic procedure may be used to determine the *dimensional* parameters $\tilde{c}_l = c_l \mathcal{E}^{(1-\zeta_l)/3}$. Thus when Eq. (6) is recast in terms of $\tilde{c}_l$, we can make use of Eq. (1) and write the subgrid-scale models at the grid and test level as

$$\tau_{ij} = -2 \sum_{l=1}^{n} \tilde{c}_l |\overline{S}|^{\zeta_l} \Delta^{(4+2\zeta_l)/3} \, \overline{S}_{ij}, \tag{7a}$$

$$T_{ij} = -2 \sum_{l=1}^{n} \tilde{c}_l |\widehat{\overline{S}}|^{\zeta_l} \hat{\Delta}^{(4+2\zeta_l)/3} \, \widehat{\overline{S}}_{ij}, \tag{7b}$$

where $\hat{\Delta}$ is the test-filter width and $\widehat{\overline{S}}_{ij}$ is the test-filtered strain rate. When Eqs. (7a) and (7b) are substituted into the Germano identity (Germano *et al.* 1991), a set of integral equations for the $\tilde{c}_l$ are obtained. Following Ghosal *et al.* (1995) we can reduce the integral equations to algebraic relations if we constrain the coefficients to have no spatial variation over the directions in which the test filter is applied. The end result is

$$\langle \dot{M}_{lk} \rangle \tilde{c}_k = -\langle L_{ij} m_{ij}^{(l)} \rangle, \tag{8}$$

where the Leonard tensor is given by $L_{ij} = \widehat{\overline{u}_i \overline{u}_j} - \widehat{\overline{u}}_i \widehat{\overline{u}}_j$. The lth model tensor is defined as

$$m_{ij}^{(l)} = -2 \left(\Delta^{(4+2\zeta_l)/3} \, \widehat{|\overline{S}|^{\zeta_l} \overline{S}_{ij}} - \hat{\Delta}^{(4+2\zeta_l)/3} \, |\widehat{\overline{S}}|^{\zeta_l} \, \widehat{\overline{S}}_{ij} \right). \tag{9}$$

The left hand side of Eq. (8) is a matrix of products of these tensors: $M_{lk} = m_{ij}^{(l)} m_{ij}^{(k)}$. Finally, $\langle \rangle$ denotes a spatial average taken over the directions in which the test filter is applied*. Note that when $n \neq 1$, a linear system must be solved in order to determine the dynamic model coefficients. When the pure Kolmogorov scaling ($n = 1, \zeta_1 = 0$) is used, the dynamic estimation for the eddy viscosity reduces to:

$$\nu_e \approx -\frac{1}{2(\alpha^{4/3} - 1)} \frac{\langle L_{ij} \widehat{\overline{S}}_{ij} \rangle}{\langle \widehat{\overline{S}}_{ij} \widehat{\overline{S}}_{ij} \rangle}, \tag{10}$$

where $\alpha = \hat{\Delta}/\Delta$. This relation was derived earlier by Wong & Lilly, (1994). This model has the advantage that knowledge of the Smagorinsky time scale $|\overline{S}|$ is not required, and thus the model is independent of the local equilibrium assumption. The Kolmogorov model also has the practical advantage that fewer filtering operations are required as compared with the Smagorinsky model. This is true since the term $\widehat{|\overline{S}|\overline{S}_{ij}}$ does not appear in the Kolmogorov model. Finally, it should

---

* In practice averaging is usually not performed in inhomogeneous directions even if these are included in the test filter. This inconsistency introduces an error that has been found to have a negligible impact on the simulation results (Ghosal *et al.*, 1995).
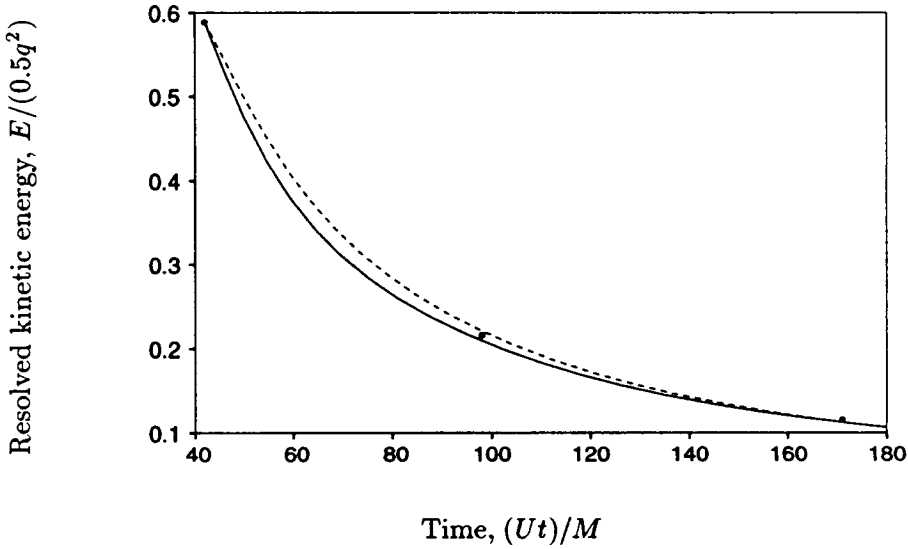
FIGURE 1. Decay of resolved turbulent kinetic energy. ——— : Dynamic Smagorinsky model; - - - - : Dynamic Kolmogorov model; ● : filtered experimental data of Comte-Bellot and Corrsin (1971). U is the mean advection speed in the wind tunnel experiments, M is the spacing between the bars in the turbulence-generating grid, and $0.5q^2$ is the total turbulent kinetic energy at the first measurement station.
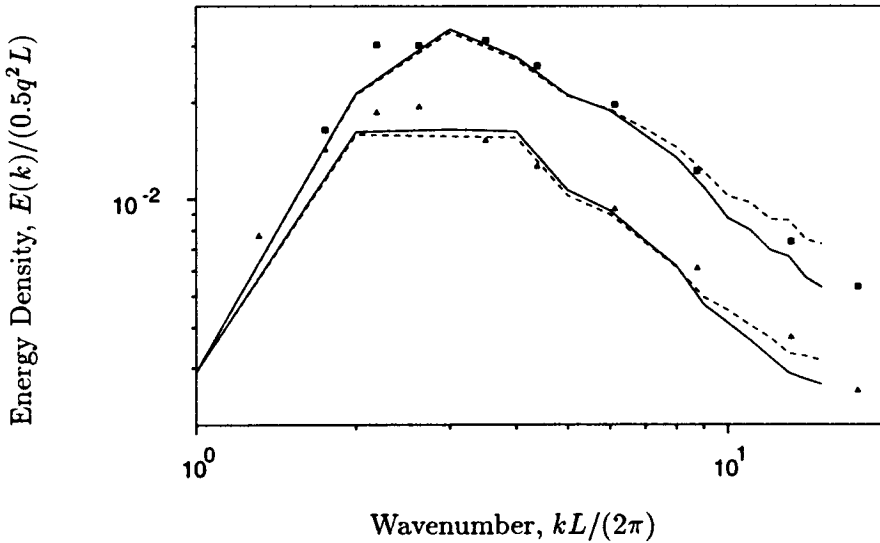

FIGURE 2. Velocity spectra. ——— : Dynamic Smagorinsky model; - - - - : Dynamic Kolmogorov model; ■ , ▲ : experimental data of Comte-Bellot and Corrsin (1971) for $Ut/M = 98$ and 171 respectively. $L = 10.8M$ is the length of a side of the computational box. The other scaling parameters are defined in Fig. 1.

be mentioned that models mixing the Kolmogorov and the Smagorinsky scalings ($n \geq 2, \zeta_1 = 0, \zeta_2 = 1$) could be investigated for situations with poorly developed inertial ranges. Indeed, in that case both Kolmogorov and Smagorinsky time scales might play independent roles and the dynamic procedure could determine the relative weighting of these two scalings.

2.2 Numerical tests

As a first step in evaluating the new class of models, the Kolmogorov model (Eq. (10)) is tested in simulations of decaying isotropic turbulence. The simulations target the experimental measurements of Comte-Bellot and Corrsin (1971) and are performed with a pseudo-spectral code (Rogallo, 1981) using 32^3 mesh points. The equation for the model coefficient is averaged over the volume so that the coefficient is a function of time only. The simulations are initialized so that the 3-D energy spectrum agrees with the experimental data (up to the mesh wavenumber) at the first measuring station. The initial field is obtained by simulating the decay from an earlier time where the velocity phases are set at random. By iteratively adjusting the energy spectrum at the earlier time, it is possible to construct a field that has the desired energy spectrum as well as realistic phase information. The objective of the simulation is to predict the energy decay rate and the 3-D spectrum at the two subsequent experimental measurement stations.

Figure 1 shows the kinetic energy decay history for the dynamic Kolmogorov and Smagorinsky models. There is little difference between the results of the two models and both agree quite well with the experimental data. Near the starting point, the Kolmogorov model is seen to be slightly less dissipative than the Smagorinsky model. This could have to do with the fact that the initial field is generated with the Smagorinsky model and thus a transient is introduced when the model is suddenly switched to the Kolmogorov scaling. Three-dimensional velocity spectra are shown in Fig. 2. Again there is very little difference between the two models. The spectra are seen to be slightly less damped at high wavenumbers in the case of the Kolmogorov model. This difference actually makes the Kolmogorov model agree slightly better with the experimental data at the final measurement station.

The results of these tests suggest that the dynamic Kolmogorov model may work just as well as the Smagorinsky model. This is significant since comparable accuracy can be expected with 30% fewer filtering operations. The fact that the Kolmogorov scaling works also suggests that other terms in Eq. (6) may be useful as well.

3. Future plans

The Kolmogorov model will be tested next in turbulent channel flow. If is proves successful there it will be incorporated in the CTR complex geometry codes. Once these results are interpreted, we will study models that include more terms with the obvious first choice being a blend of Smagorinsky and Kolmogorov scaling ($n = 2, \zeta_1 = 0, \zeta_2 = 1$).

REFERENCES

COMTE-BELLOT, G., & CORRSIN, S. 1971 Simple Eulerian time-correlation full

and narrow-band velocity signals in grid-generated 'isotropic' turbulence. *J. Fluid Mech.* **48,** 273-337.

GERMANO, M., PIOMELLI, U., MOIN, P. & CABOT, W. 1991 A dynamic subgrid-scale eddy-viscosity model. *Phys. Fluids A.* **3,** 1760-1765.

GHOSAL, S., LUND, T., MOIN, P. & AKSELVOLL, K. 1995 The dynamic localization model for large eddy simulation of turbulent flows. *J. Fluid Mech.* **286,** 229-255.

KOLMOGOROV, A. N. 1941 Local Structure of Turbulence in an Incompressible Fluid at Very High Reynolds Numbers. *Dokl. AN SSSR.* **30,** 299.

ROGALLO, R. S. 1981 Numerical experiments in homogeneous turbulence. NASA Tech. Mem. 81315.

SMAGORINSKY, J. 1963 General Circulation Experiments with the Primitive Equations. *Month. Weather Rev..* **91,** 99-164.

WONG, V. C. & LILLY, D. 1994 A comparison of two subgrid closure methods for turbulent thermal convection. *Phys. Fluids.* **6,** 1016-1023.

Large-eddy simulations with wall models

By W. Cabot

1. Motivation and objectives

The near-wall viscous and buffer regions of wall-bounded flows generally require a large expenditure of computational resources to be resolved adequately, even in large-eddy simulation (LES). Often as much as 50% of the grid points in a computational domain are devoted to these regions. The dense grids that this implies also generally require small time steps for numerical stability and/or accuracy. It is commonly assumed that the inner wall layers are near equilibrium, so that the standard logarithmic law can be applied as the boundary condition for the wall stress well away from the wall, for example, in the logarithmic region, obviating the need to expend large amounts of grid points and computational time in this region. This approach is commonly employed in LES of planetary boundary layers (e.g., Mason, 1989; Schmidt & Schumann, 1989), and it has also been used for some simple engineering flows (e.g., Piomelli *et al.*, 1989; Arnal & Friedrich, 1993).

In order to calculate accurately a wall-bounded flow with coarse wall resolution, one requires the wall stress as a boundary condition. The incompressible Navier-Stokes equation is

$$\frac{\partial \mathbf{u}}{\partial t} = -\nabla p + \nabla \cdot \boldsymbol{\tau}, \quad \boldsymbol{\tau} = -\mathbf{u}\mathbf{u} + \nu \nabla \mathbf{u}, \tag{1}$$

in which $\mathbf{u}$ is the velocity, p is the pressure, $\boldsymbol{\tau}$ is the stress, and ν is the molecular viscosity. In a simulation with an unresolved wall, the wall-normal (y) derivative of the stress for tangential (x, z) velocity components,

$$\frac{\partial}{\partial y}\left(-u_i v + \nu \frac{\partial u_i}{\partial y}\right), \quad i = 1, 3, \tag{2}$$

cannot be accurately calculated by applying the usual no-slip condition, $\mathbf{u} = 0$, instead requiring the specification of the wall stress

$$\tau_{i2w} = \nu \left.\frac{\partial u_i}{\partial y}\right|_{y=0}, \quad i = 1, 3. \tag{3}$$

Thus, an adequate model of τ_{i2w} based on outer flow quantities is desired. Asymptotic matching of inner and outer regions in steady, ensemble-averaged, equilibrium flow yields the log-law relation between wall stress and outer mean velocity. However, for the purposes of LES, wall stress models are needed with some degree of time and space dependence. Because the near-wall layer is typically very thin with respect to horizontal scales, boundary layer assumptions may be valid, perhaps even

on horizontal grid scales used in LES, and it may be possible to use simpler boundary layer equations to model the near-wall region and at the same time retain more flexibility in handling flows with widely varying pressure gradients.

The goal of this work is to determine the extent to which equilibrium and boundary layer assumptions are valid in the near-wall regions, to develop models for the inner layer based on such assumptions, and to test these modeling ideas in some relatively simple flows with different pressure gradients, such as channel flow and flow over a backward-facing step. Ultimately, models that perform adequately in these situations will be applied to more complex flow configurations, such as an airfoil.

2. Accomplishments

An examination of momentum balance at different horizontal scales, and correlations between the measured wall stress and some outer flow quantities, have been performed from a direct numerical simulation (DNS) database for channel flow. Because wall stresses need to be predicted in flows with different pressure gradients and in separated flow, models based on the log law and boundary layer equations have been tested both in channel and backward-facing step flows.

2.1 Momentum balance in channel flow

Near-wall data has been examined from a channel flow DNS (J. Kim, personal communication; Kim, Moin & Moser, 1987) with a friction Reynolds number $Re_\tau = 395$ ($Re_\tau \equiv u_\tau \delta/\nu$, where δ is the channel half-width, $u_\tau \equiv |\nu dU/dy|^{1/2}$ is the friction speed, and U is the mean streamwise velocity). Horizontal averages of flow quantities were taken over different scales, from the scale of the entire plane down to scales comparable to expected LES resolutions (a factor of 16 smaller in each direction, or $\Delta x^+ \times \Delta z^+ \approx 160 \times 80$ in wall units scaled by ν/u_τ). The streamwise momentum balance was constructed by integration over volumes with these horizontal dimensions from the wall to a height $y^+ \approx 80$:

$$\left\langle \frac{\partial u}{\partial t} + \frac{\partial u^2}{\partial x} + \frac{\partial uw}{\partial z} + \frac{\partial p'}{\partial x} \right\rangle = -\frac{dP}{dx} + \left\langle \nabla \cdot (\nu \nabla u) - \frac{\partial uv}{\partial y} \right\rangle , \qquad (4)$$

where $\langle \cdots \rangle$ denotes a volume average, and dP/dx is the mean pressure gradient. The results shows that the advection and fluctuating pressure gradient terms on the left-hand side of (4), while small compared to the other terms when averaged over the entire plane, are more than an order of magnitude larger at LES scales. This suggests that momentum balance is dominated by a nearly inviscid balance between advection and pressure gradients at LES scales, casting doubt on the local validity of models, such as the log law, based on a balance between terms on the right-hand side of (4) (J. Jiménez, personal communication).

Correlations between the wall stress τ_{12w} and the mean streamwise velocity at $y^+ \approx 40$ are small but significant (50% at LES scales). Figure 1 shows a scatter plot of the deviation from the mean of actual wall stress versus that predicted from a logarithmic law with the (nearly zero) mean pressure gradient in the channel at
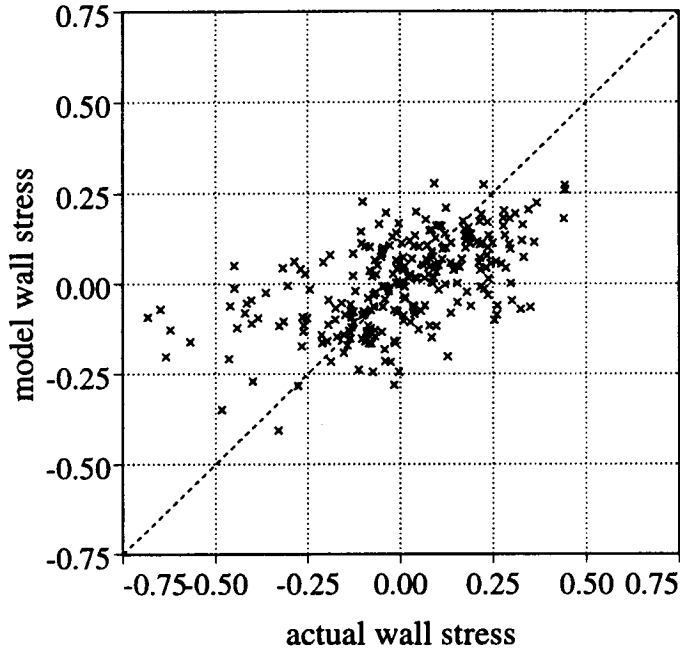
FIGURE 1. Deviation from the mean of actual wall stress from DNS channel flow data ($Re_\tau = 395$) compared with that predicted from the log law model applied at $y^+ \approx 40$. The flow is averaged horizontally on typical LES scales ($\Delta x^+ \times \Delta z^+ \approx 160 \times 80$). The linear diagonal denotes a perfect local correlation.

$y^+ \approx 40$. There is a noticeable linear correlation for values of wall stress near the mean, with larger deviations in high-stress regions. (The nature of the high-stress events has yet to be explored.) On the other hand, the correlation of wall stress to the large, instantaneous, fluctuating pressure gradients is found to be practically nil (only a few percent). Corresponding analyses need to be performed with DNS and LES databases for flow over a backward-facing step (Le & Moin, 1993; Akselvoll & Moin, 1995), which contain a large adverse pressure gradient and separated flow.

2.2 Boundary layer wall models in channel flow

Wall models have been tested in a second-order, central finite difference (FD2) channel code on a staggered mesh with a third-order Runge-Kutta (RK3) time advancement (Akselvoll & Moin, 1995), in which the wall stress boundary conditions are easily implemented. These wall models have been based on the Johnson-King (1985) boundary layer model, which is fairly simple and has had good success in Reynolds-averaged Navier-Stokes (RANS) models of separated flow (Menter, 1991).

A channel flow with a target $Re_\tau = 1030$ was simulated using an outer mesh with the near-wall points for horizontal velocity placed at a matching height $y_m^+ = 32$ or 64. Embedded in the outer mesh is a fine sublayer mesh from the wall to the matching height. The outer mesh technically extends to the walls, but only the

$v = 0$ and $\partial p/\partial y = 0$ boundary conditions are used. Both outer and inner meshes are usually stretched with a hyperbolic tangent mapping. The outer mesh uses 33 wall-normal nodes, and the sublayers uses 21 nodes at each wall. The horizontal domain size is $\Delta x \times \Delta z = 2\pi\delta \times \pi\delta$. Initially, a horizontal mesh of 32×32 was used for both outer and sublayer regions, but it was found that much better results were obtained with a finer 64×64 mesh for the outer region; on the other hand, the mean velocity and rms statistics were found to be insensitive to whether the sublayer mesh was 32×32 or 64×64 ($\Delta x^+ \times \Delta z^+ \approx 200 \times 100$ or 100×50). It was also found that results from the FD2-RK3 code were sensitive to the time step for convective CFL numbers exceeding about 0.5, perhaps due to inaccuracies in implicit terms (cf. Choi & Moin, 1994). In the results presented here, the convective CFL number was kept around 0.6.

Model JK0. The lowest level model for the wall stress is obtained at each horizontal position in the near-wall sublayer (independent of other horizontal locations) from the solution of the ordinary differential equation

$$\frac{d}{dy}(\nu + \nu_t)\frac{dU_i}{dy} = \frac{dP}{dx_i}, \quad i = 1,3, \tag{5}$$

where U_i are the horizontal velocity components in the sublayer, dP/dx_i is the constant mean pressure gradient, and

$$\nu_t = \kappa u_s y_w D^2, \quad D = 1 - \exp(-u_d y_w/A\nu), \tag{6}$$

resembles the eddy viscosity in the Johnson-King (JK) model for the inner regions. Here, though, the scale speeds u_s and u_d are replaced by the friction speed u_τ; y_w is the distance from the wall, κ is the von Kármán constant, and A is a damping-function constant taken to be 19, which gives the best fit to the standard log law in this case (lower values were used by Johnson & King and Menter). The boundary conditions for (5) are $U_i = 0$ at the walls and U_i equal to the horizontal velocity in the outer mesh at the first grid point above the wall. The wall-normal derivative of U_i at the wall yields the wall stress τ_{i2w} used in the outer flow. Eq. (5) is solved by using the same FD2 discretization used in the main code and performing an inversion of the resulting tridiagonal matrix. The solution of (5) is just a smooth blend of the viscous and logarithmic functions and, for the channel, is generally equivalent an instantaneous log law. Because one can consider expressions like (5) to be valid only in some average sense, both in space and time, a running time-average of the matching velocity over about an eddy turnover time is employed.

Model JK0a. The next level of model tests the influence of large advective and instantaneous pressure gradient terms:

$$\frac{\partial}{\partial y}(\nu + \nu_t)\frac{\partial U_i}{\partial y} = \frac{\partial U_i}{\partial t} + \nabla\cdot(U_i\mathbf{U}) + \frac{\partial p}{\partial x_i}, \quad i = 1,3, \tag{7}$$

where U_i are the horizontal velocity components in the sublayer, as in (5). The eddy viscosity is given by (6) and, as in the JK0 model above, uses $u_s = u_d = u_\tau$.

The solutions of (7) at different horizontal locations are now coupled through the divergence term, which is calculated from differences of velocity components on the sublayer mesh. The wall normal velocity $V \equiv U_2$ is calculated locally at each sublayer grid point from differences of the horizontal velocity components using the continuity equation,

$$V = - \int_0^y \frac{\partial U_i}{\partial x_i} dy \ . \tag{8}$$

The usual boundary layer assumption that $\partial p / \partial y = 0$ is used; hence the pressure gradient in (7) for a given horizontal location is set to be constant at all wall-normal locations in the sublayer, using the value in the outer flow at the matching point. A running time average of the pressure gradient is actually used to smooth the wall model. Eq. (7) is discretized and integrated with the same FD2-RK3 scheme used in the main code.

Model JK1. The actual JK model for the inner regions uses velocity scales (u_s and u_d) in the eddy viscosity expression (6) that are melds of u_τ and u_m, where u_m is the square root of the maximum Reynolds stress ($-\overline{uv}$) that occurs at a distance $y_{\max}$ above the wall:

$$u_s = (1 - \gamma) u_\tau + \gamma u_m \ , \quad \gamma = \tanh(y_w / \ell) \ , \quad \ell = u_\tau y_{\max} / (u_\tau + u_m) \ , \tag{9a}$$

$$u_d = \max(u_m, u_\tau) \ . \tag{9b}$$

Model JK1 calculates U_i from (5), but uses (9) to compute the eddy viscosity in (6). In RANS models, u_m and $y_{\max}$ are determined from the solution of an ODE. In LES, the maximum of the stress can in principle be found on the fly at a given horizontal position from values of the Reynolds stress in the sublayer and overlying outer layer. In practice, this is much more difficult to accomplish with any great accuracy, because instantaneous values of the stress along a vertical line fluctuate wildly in space and time. Again, a running time average must be used, along with some local spatial filtering, in order to smooth the signal to a useful level; then a search routine is employed to find the first local maximum of averaged stress moving away from the wall at a given horizontal location. Because this is a rather costly and cumbersome procedure to employ in LES, its benefits must be shown to be substantial to justify its use.

The computational overheads of the above wall models were about 10, 20, and 30% of total cost, respectively; however, the number of interior points was halved and the time step used was 3 times larger than in a regular, resolved LES, so that a savings factor of about 5 was realized.

The mean streamwise velocities that are obtained using these wall models for channel flow are shown in Fig. 2a in comparison with the experimental data (Hussain & Reynolds, 1975) and with a LES (Cabot, 1994) for the same parameters with the same code without wall models (using 65 wall-normal nodes with about the same interior resolution as the LES with wall models and a 64×64 horizontal mesh). It is seen that there is little difference between the results for different wall models in channel flow, suggesting that a simple instantaneous log law provides
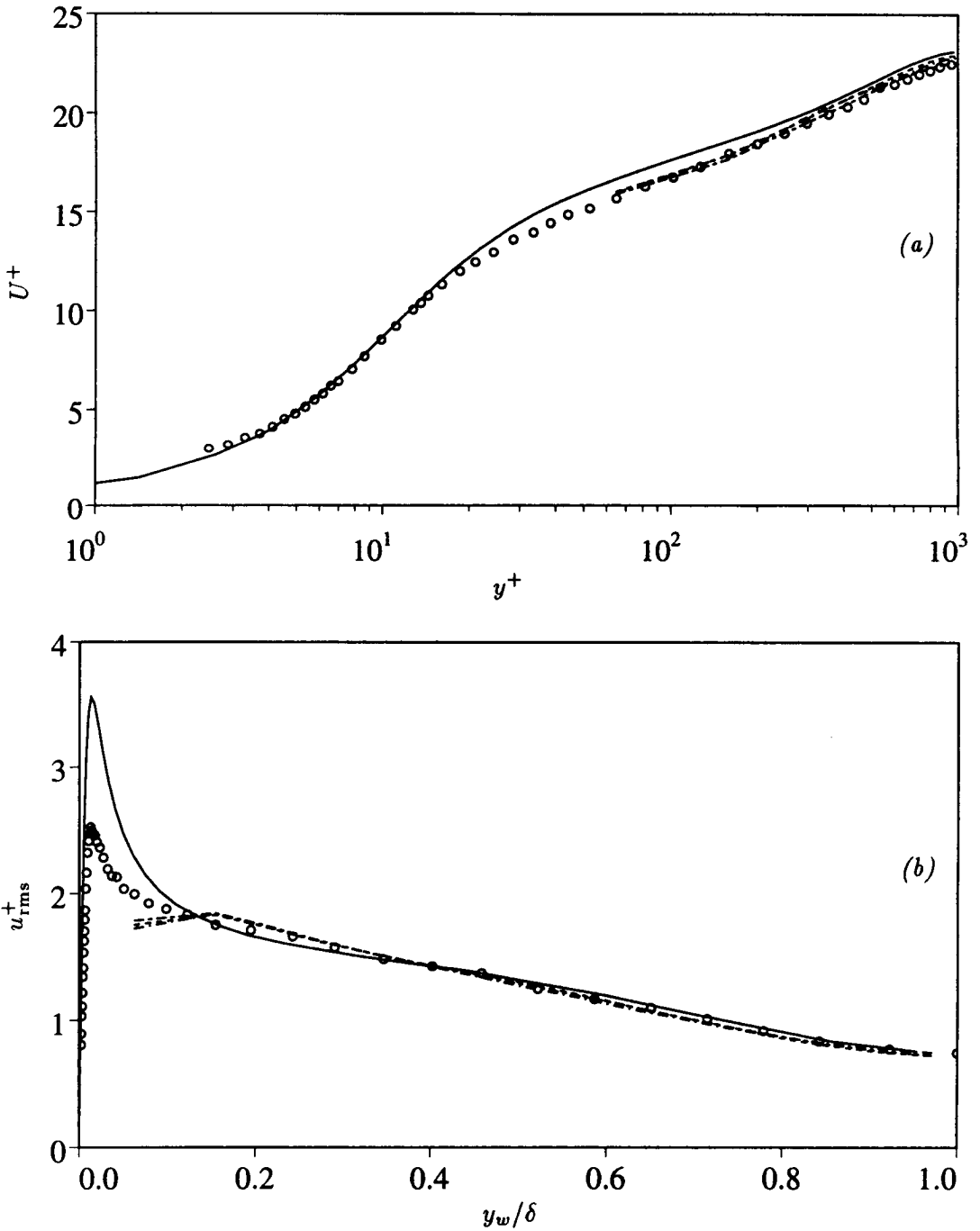
FIGURE 2.   Mean streamwise (a) velocity and (b) velocity fluctuation intensities in channel flow for LES with different wall models (---- JK0, —·— JK0a, —·— JK1), compared with a full LES (——— , Cabot, 1994) and experimental data (○ ○ ○ , Hussain & Reynolds, 1975).

an adequate, cost-effective wall model in this case. The results for U in the outer region are in generally fair agreement with the experimental data and full LES. The streamwise velocity fluctuation intensities (u_{rms}) are shown in Fig. 2b and also show fair agreement with experimental and full LES results, with some discrepancies near the matching point. Note that there is a large disagreement between the full LES results and experimental data in the near-wall region where u_{rms} peaks ($y^+ \leq 50$). The results were insensitive to whether the matching point was at $y^+ = 32$ or 64.

2.3 Boundary layer wall models behind a backward-facing step

Wall models JK0 and JK0a have also been implemented in the LES of flow over a backward-facing step using the same FD2-RK3 scheme used for the channel (Akselvoll & Moin, 1995). The flow has a Reynolds number of 28,000 based on the centerline velocity of the inlet flow and the step height h. There is a long inlet section $10h$ long, $4h$ high, and $2h$ wide on a $100 \times 65 \times 96$ mesh followed by a $20h \times 5h \times 2h$ outlet section on a $146 \times 97 \times 96$ mesh; both x and y coordinates are stretched. The wall model is implemented only along the bottom wall behind the step for test purposes, with a $74 \times 33 \times 48$ sublayer mesh embedded below $y \approx 0.073$ or $y^+ \approx 60$ at the outlet. No account is taken of the geometry of the corner behind the backstep, where there is a weak recirculation zone, but this inaccuracy is not expected to affect the bulk of the flow very much. Because only about 10% of the grid points are removed from the main calculation and time steps can only be increased by about 30%, little computational saving is gained from the wall model in this case.

There is a strong adverse pressure gradient between about $3h$ and $7h$ behind the step and a concomitant separation bubble in this region. Figure 3 shows the near-wall ($y/h \approx 0.10$) streamwise pressure gradient from Akselvoll & Moin's (1995) LES, averaged over time and span; the mean wall-normal gradient of streamwise velocity (proportional to the wall stress) is also shown. The assumption that there is no wall-normal variation in pressure gradient is found to be good for the most part, except in a few regions associated with relatively rapid wall-normal velocities in the reattachment region around $x/h = 5$–8. Preliminary results from the application of the JK0 wall model (which includes no pressure gradient or advection terms) show an underprediction of the level of reversed wall flow (Fig. 3); the recovery region around $x/h = 10$ is also not predicted very well, nor is the recirculation region near the step. The level of the post-recovery region near the outlet is predicted better; but this region is in fact similar to channel flow or a zero-pressure-gradient boundary layer, in which this model was seen to give good results (§2.2). Longer runs (currently in progress) are needed to see how the flow adjusts itself further, and if the resulting statistically steady flow is predicted adequately.

The large pressure gradient and advection terms in Eq. (7) are probably required to obtain better agreement. For instance, if the streamwise pressure gradient integrated over the thickness of the sublayer y_m, which is about $y_m \partial p / \partial x$, is comparable to $\tau_{12w} = \nu \partial U / \partial y |_w$, then it can be expected to significantly modify the structure of the boundary layer and the wall stress itself. In Fig. 3 the streamwise pressure
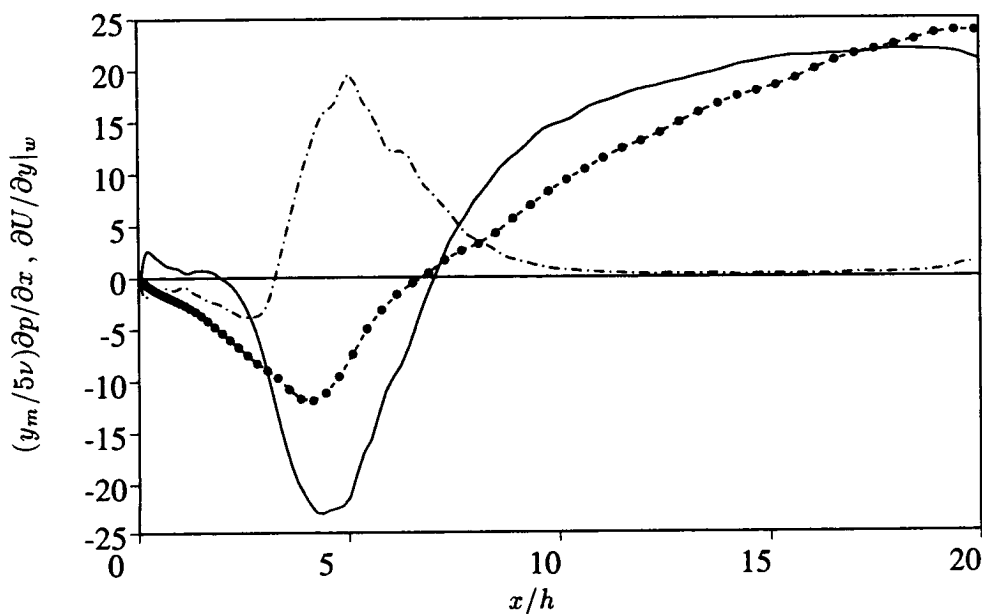
FIGURE 3.   Mean wall-normal gradient of the streamwise velocity at the bottom
wall $\partial U / \partial y|_w$ (————) and mean streamwise pressure gradient near the bottom
wall $\partial p / \partial x$ (—·—) behind a backward-facing step from the LES of Akselvoll &
Moin (1995). The pressure gradient is scaled by $y_m/5\nu$, where y_m is the thickness of
the sublayer used in wall model calculations. Preliminary values of mean $\partial U / \partial y|_w$
predicted with the JK0 wall model are also shown (• • •).

gradient multiplied by $y_m/5\nu$ is seen to be comparable to $\partial U / \partial y|_w$ in the separa-
tion and recirculation regions, and it is likely to have an important effect there. Of
course, the effect of pressure gradient term will be mitigated to a large degree by
the advection terms (mostly $\partial U^2 / \partial x$) in the outer part of the sublayer, but these
terms vanish very near the wall, while the pressure gradient does not.

Application of the JK0a model, with the addition of large pressure gradient and
advection terms, shows a much better initial agreement in the reverse flow region,
although the recovery region around $x/h = 10$ is still not well predicted. The
region around $x/h = 5$ near the head of the separation bubble in the reattachment
zone, characterized by downflows that are strong in comparison with horizontal
flow, has led to numerical instability in the sublayer calculation. The cause of
this is still not known, but it appears to be associated with very large advection
terms $\partial(U_i V)/\partial y$ at locations of rapid downflow. These are also regions where the
assumption of constant horizontal pressure gradients breaks down and the boundary
layer equations are known to be invalid.

3. Future plans

Some fundamental tests need to be performed on backward-facing step flow fields
near the bottom wall, such as the momentum balance at different scales that was

performed for channel flow (§2.1). DNS and LES fields will be studied to attempt to determine, for example, how the changes in pressure gradient affect in detail the wall stress and what terms in the momentum equation are most important in the regions of strong downflow at the head of the separation bubble.

LES with the simple JK0 wall model (essentially the smooth meld of the log law and viscous law) will be run over long times to statistical equilibrium to get a fair assessment of that model's performance. The same model with advection and running time-averaged pressure terms (JK0a) will also be run to longer times if the present numerical instability can be cured. An attempt will also be made to implement the JK1 wall model in the backward-facing step flow, which requires a determination of the maximal shear stress (averaged in some sense) above the wall in order to determine a model velocity scale. Search routines like that used in channel flow, and perhaps a curve fitting scheme applied to the shear stress profiles, will be tried; however, there is always some arbitrariness in these approaches. Alternative, more easily determined, and better quantified velocity scales will also be considered.

REFERENCES

AKSELVOLL, K., & MOIN, P. 1995 Large eddy simulation of turbulent confined coannular jets and turbulent flow over a backward facing step. Dept. of Mech. Eng. Tech. Rep. **TF-63**, Stanford Univ.

ARNAL, M., & FRIEDRICH, R. 1993 Large-eddy simulation of a turbulent flow with separation. In *Turbulent Shear Flows 8*, ed. by F. Durst *et al.*, Springer-Verlag (Berlin), pp. 169–187.

CABOT, W. 1994 Local dynamic models in channel flow. In *Annual Research Briefs 1994*, Center for Turbulence Research, NASA Ames/Stanford Univ., 143–159.

CHOI, H., & MOIN, P. 1994 Effects of the computational time step on numerical solutions of turbulent flow. *J. Comp. Phys.* **113**, 1–4.

HUSSAIN, A. K. M. F., & REYNOLDS, W. C. 1970 The mechanics of a perturbation wave in turbulent shear flow. Dept. of Mech. Eng. Tech. Rep. **FM-6**, Stanford Univ.

JOHNSON, D. A., & KING, L. S. 1985 A mathematically simple turbulence closure model for attached and separated turbulent boundary layers. *AIAA J.* **23**, 1684–1692.

KIM, J., MOIN, P., & MOSER, R. 1987 Turbulence statistics in fully developed channel flow at low Reynolds number. *J. Fluid Mech.* **177**, 133–166.

LE, H., & MOIN, P. 1993 Direct numerical simulation of turbulent flow over a backward-facing step. In *Annual Research Briefs 1992*, Center for Turbulence Research, NASA Ames/Stanford Univ., 161–173.

MASON, P. J. 1989 Large-eddy simulation of the convective atmospheric boundary layer. *J. Atmos. Sci.* **46**, 1492–1516.

MENTER, F. R. 1991 Performance of popular turbulence models for attached and separated adverse pressure gradient flows. *AIAA Paper.* **91-1784.**

PIOMELLI, U., FERZIGER, J., MOIN, P., & KIM, J. 1989 New approximate boundary conditions for large eddy simulations of wall-bounded flows. *Phys. Fluids A.* **1,** 1061–1068.

SCHMIDT, H., & SCHUMANN, U. 1989 Coherent structure of the convective boundary layer derived from large-eddy simulations. *J. Fluid Mech.* **200,** 511–562.

Large-eddy simulation of flow around an airfoil on a structured mesh

By Hans-Jakob Kaltenbach AND Haecheon Choi

1. Motivation and objectives

The diversity of flow characteristics encountered in a flow over an airfoil near maximum lift taxes the presently available statistical turbulence models. This work describes our first attempt to apply the technique of large-eddy simulation to a flow of aeronautical interest. The challenge for this simulation comes from the high Reynolds number of the flow as well as the variety of flow regimes encountered, including a thin laminar boundary layer at the nose, transition, boundary layer growth under adverse pressure gradient, incipient separation near the trailing edge, and merging of two shear layers at the trailing edge.

The flow configuration chosen is a NACA 4412 airfoil near maximum lift. The corresponding angle of attack was determined independently by Wadcock (1987) and Hastings & Williams (1984, 1987) to be close to 12°. The simulation matches the chord Reynolds number $U_\infty c/\nu = 1.64 \times 10^6$ of Wadcock's experiment.

2. Accomplishments

2.1 Numerical method and SGS model

The numerical method for solving the unsteady, incompressible Navier-Stokes equations is described in Choi *et al.* (1993). Second-order spatial central differences on a staggered mesh are combined with a semi-implicit time integration scheme. Formulation of the problem in terms of contravariant velocity components, weighted with the Jacobian, in conjunction with the staggered variable configuration leads to discretized equations that can be solved with the classical splitting approach. The resulting pressure Poisson equation is solved using FFT for the spanwise (periodic) direction and iterative methods for the remaining two-dimensional problems. The computational cost is about equally distributed between computation of the right-hand side and solving the Poisson equation at every substep of a third order Runge Kutta time integration.

The implementation of the dynamic subgrid-scale model (Germano *et al.* 1991) with least-square contraction (Lilly 1992) uses the spanwise homogeneity of the flow to obtain a model coefficient that is a function of streamwise and wall-normal coordinate only. We found that the dynamic procedure occasionally renders unrealistic negative coefficients in regions where the flow is laminar such as at the nose or in the potential flow region. In these regions, the negative values are the result of the dynamic model becoming ill-conditioned and have no physical significance. In the present simulations we prevented any form of backscatter by constraining the model coefficient to be always positive.

x/c	δ_{99}/c	$\Delta x/c$	Δx^+	Δz^+	$\Delta x/\Delta z$	δ_{99}/L_z
0.1	0.004	0.0031	405	137	2.96	0.08
0.2	0.006	0.0033	378	118	3.2	0.12
0.4	0.016	0.0033	274	86	3.2	0.32
0.6	0.030	0.0050	235	49	4.8	0.6
0.8	0.060	0.0088	110	13	8.5	1.2

Table 1. Spacing along upper surface of airfoil. The last two columns show cell aspect ratio and ratio of boundary layer thickness to domain width for case A.

On the present mesh, the CFL limit of 1.5 results in an average timestep of $2 \times 10^{-4} c/U_\infty$. About 80 CPU-seconds on a Cray-C90 are needed to advance the solution over one timestep on a mesh of $638 \times 79 \times 48 = 2.4 \times 10^6$ cells. Therefore, simulation of one time unit c/U_∞ requires 90 CPU-hours. In order to obtain smooth statistics the results have to be averaged over several time units.

2.2 Computational domain and mesh layout

The computational domain is a C-mesh with the outer boundary about three chord lengths away from the surface. At the outer boundary we specify the freestream velocity U_∞. As a consequence, the vertical velocity component (in a coordinate system aligned with the chord at 0° angle of attack) will be zero at the outer boundary. Therefore, the chosen configuration resembles more the flow around an airfoil inside of a wind tunnel with parallel walls than an airfoil in free air. Jansen (1995) has shown that, even with the walls located much closer, the presence of wind tunnel walls mainly affects the flow in the nose region by increasing the suction peak. The pressure distribution in the rear part and the size of the backflow zone, however, are only weakly dependent on whether the wind tunnel walls are included or not. A no-slip condition is enforced at the airfoil surface, and we use a convective (radiative) boundary condition at the outflow plane.

Results from two simulations will be presented. The two cases differ only with respect to the spanwise domain width which is $0.05c$ in case A and $0.025c$ in case B. The spanwise spacing Δz is the same with 48 cells in case A and 24 cells in case B, respectively. Main criterion for the choice of the spanwise domain size is the ratio of boundary layer thickness to domain width, which is tabulated in Table 1. As a consequence of the rapid growth of the boundary layer thickness on the suction side, this ratio, which is initially sufficiently small to capture several structures in the spanwise direction, exceeds one near the trailing edge. It is likely that the development of flow structures in the outer part of the boundary layer will be affected by the limited domain size. Comparison of cases A and B gives insight in the sensitivity of the simulation with respect to this parameter.

The design of an adequate mesh involves several aspects. The most energetic eddies of the boundary layer have to be resolved. More or less general criteria have been developed for the mesh spacing in the case of wall bounded shear flows under zero pressure gradient. However, these criteria depend on the numerical method employed (Lund *et al.*, 1995). Cabot (1994) found that for LES of turbulent channel flow based on second-order finite differences a spacing of $\Delta x^+ = 60$ and
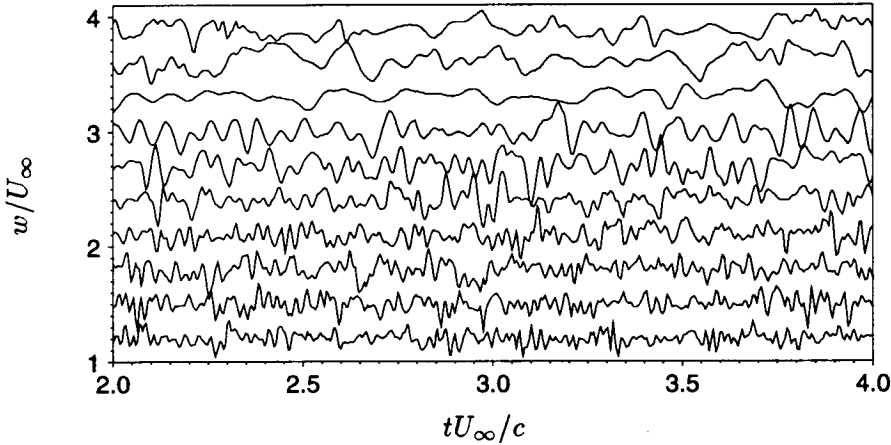
FIGURE 1. Time series of spanwise velocity fluctuation between stations $x/c = 0.24$ (bottom) and $x/c = 0.98$ (top) at about 5% of the local boundary layer height. Individual curves are separated by a vertical offset of 0.3 with the corresponding zero-lines located at 1.2, 1.5, ... 3.9.

$\Delta z^+ = 15 - 20$ is needed to adequately resolve the near wall structures.

Little is known about the minimum spacing requirements for boundary layers which are close to separation. The mesh size in terms of wall units probably becomes less relevant in this case. About half of the 640 streamwise points were distributed over the upper surface, which guaranteed that the streamwise spacing was between 1/3 and 1/5 of the local boundary layer thickness for most of the upper surface, see Table 1. The streamwise spacing varies considerably along the surface due to the boundary layer growth. Near the trailing edge, the grid was refined in x in order to resolve the merging of the two shear layers. No attempt was made to resolve the turbulence on the lower side of the airfoil. Spacings in terms of wall units based on the local skin friction as given in Wadcock's experiment are given in Table 1. It is evident that the spacing in the present simulation is considerably coarser than what has been found to be necessary for channel flow simulations. However, as the boundary layer develops along the surface, the resolution criteria become less restrictive so that the flow in the rear part is much better resolved than in the front section.

In the wall-normal direction we used a hyperbolic mesh generator (Chan, 1993) to distribute 79 layers of cells. The first line away from the wall was at about $y^+ = 1$, and over most of the surface there were between 20 and 30 points inside the boundary layer.

2.3 Difficulties arising from the high Reynolds number

Centered difference schemes suffer from the emergence of grid-to-grid oscillations (2-Δ-waves, wiggles) when used for high Reynolds number simulations. Usually, the viscosity provided by the subgrid-scale model is sufficient to dampen these grid-to-grid oscillations. Several sources for 2-Δ-waves have been identified in the past (Gresho, 1981). They include high cell Peclet numbers in conjunction with large
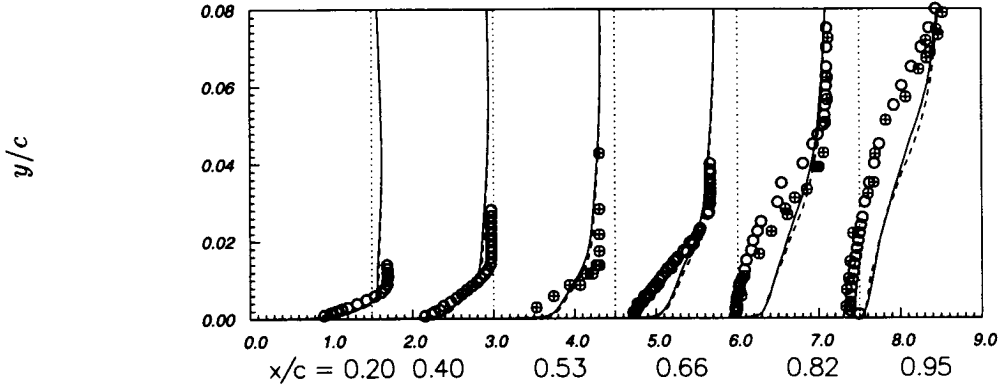
FIGURE 2. Mean velocity profiles, normalized by U_∞, along upper surface. Symbols: case A ——— , B - - - - , measurements by Hastings o and Wadcock + .

streamwise gradients of the advected variable. This situation is typically encountered near the nose and the trailing edge of the airfoil. Other sources are the outflow boundary (an artificial boundary layer is generated in the streamwise direction) and mesh stretching. As shown by Cain & Bush (1994), waves propagating into an increasingly coarse (fine) mesh are amplified (dampened) in a centered scheme. In our simulation we find that strong 2-Δ-waves appear near the nose and near the trailing edge. The wiggles appear almost exclusively in the streamwise coordinate direction. Part of these waves travel with different phase speed and cancellation occurs. However, other parts are steady and accumulate in time. These standing waves contaminate the potential flow region after long integration times. It is difficult to assess to what degree the solution is contaminated by the presence of 2-Δ-waves. On a staggered mesh, velocity components are averaged in order to obtain fluxes at cell faces. This averaging on a scale of the mesh cell can sometimes completely hide the 2-Δ-wave. For example, the convective term $\partial(uu)/\partial x$ in the streamwise momentum balance is evaluated as

$$\frac{1}{\Delta x}\left[\left(\frac{u_{i+1}+u_i}{2}\right)^2 - \left(\frac{u_i+u_{i-1}}{2}\right)^2\right] \quad .$$

The finite difference expression renders the same value independently whether an oscillatory part in the i-direction $\tilde{u}_i = (-1)^i u_a$ with zero mean and arbitrary amplitude u_a is added or not. Similarly, if a 2-Δ-wave in the i-direction is present in the v velocity component, it will not appear in the discrete approximation for $\partial(uv)/\partial y$. However, it will contaminate the term $\partial(uv)/\partial x$. Time averaged fields of velocity components show 2-Δ-waves in the potential flow region, but the pressure field is virtually free of wiggles. This indicates that the presence of 2-Δ-waves in the potential flow region may be tolerated to a certain degree since wiggle free streamlines in accordance with the pressure field can be reconstructed.
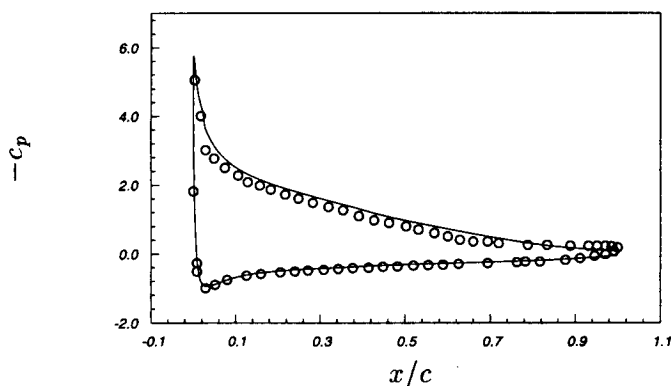
FIGURE 3. Pressure distribution around the airfoil. Symbols: LES ——— , Wadcock ∘ .

The strongest effect of 2-Δ-waves comes from the associated limitations for the computational timestep. Large amplitude wiggles in the wall normal velocity component in conjunction with rather fine wallnormal spacing cause high CFL numbers near the nose. The resulting timestep limitations are so severe that the simulation can not be carried out at an affordable cost. We therefore resorted to an *ad hoc* modification of the numerical scheme. In a small region near the nose (less than 2% of the chord) we applied a 1:2:1-filter in the streamwise and spanwise direction which efficiently eliminates all 2-Δ-waves. Filtering is equivalent to adding a direction dependent diffusion term to the equations. Justification for this procedure comes from the fact that the flow near the nose is laminar and filtering on a scale of the grid cell does not affect the flow physics. Additionally, the boundary layer in the experiments was tripped at a location around $x/c = 0.02$, thereby fixing the region of laminar-turbulent transition. We find that the flow spontaneously transitions as soon as the filter ends. In this sense, we control the location of transition by setting the streamwise extent of the region where the solution is filtered. The filter extended about 40 layers away from the wall and faded to zero over another 15 layers. Unfortunately, this procedure changes the potential flow significantly. Because the mesh cells are rather large in the outer part of the domain, filtering on the grid scale is no longer negligible on the scale where the potential flow changes near the nose. Future simulations can easily avoid this problem by limiting the filter to the vicinity of the surface, i.e. it should end near the boundary layer edge. No attempt was made to dampen 2-Δ-waves in the trailing edge region where the flow is fully turbulent. Any filtering there would probably affect the flow physics.

2.4 Simulation results and discussion

Figure 1 shows time series of the spanwise velocity fluctuation w recorded at several stations along the upper surface of the airfoil. We observe a shift in the frequency which corresponds to the most energetic motions towards lower values as the recording station moves closer to the trailing edge. This is consistent with the
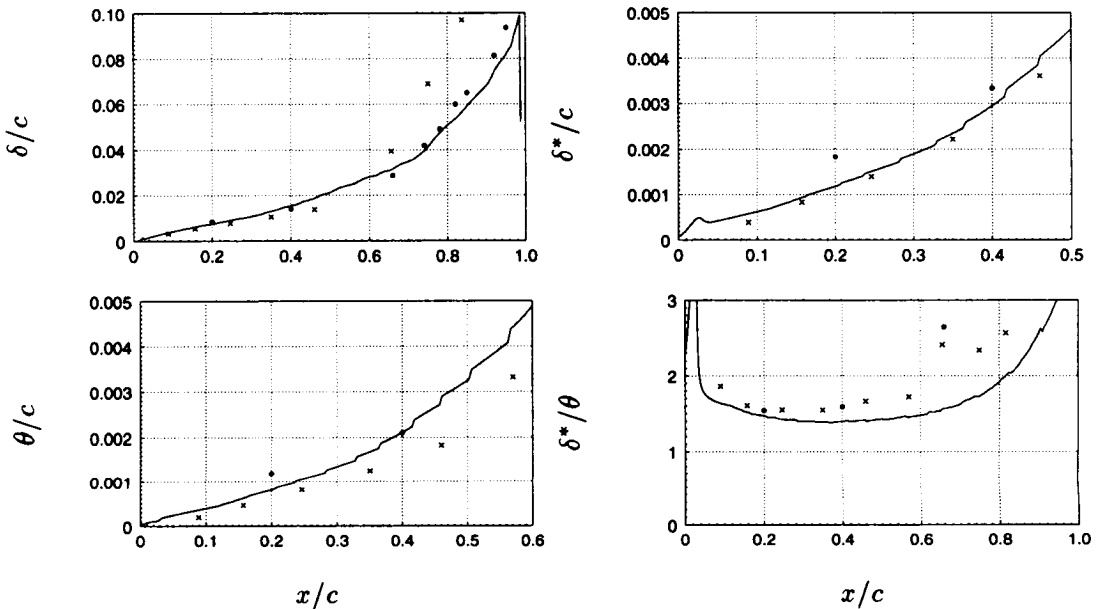
FIGURE 4.   Boundary layer thickness δ, displacement thickness δ^*, momentum thickness θ and shape factor $H = \delta^*/\theta$ along the upper surface of the airfoil. Symbols: ——— LES, • Hastings, × Wadcock.

increase of an inertial timescale (ratio of the boundary layer thickness to the edge velocity) as the boundary layer grows under the influence of the adverse pressure gradient. It becomes evident that the solution has to be sampled over several time units c/U_∞ in order to obtain representative turbulence statistics for the rear part of the airfoil.

Statistics were obtained by averaging the instantaneous flow fields in the spanwise homogeneous direction and in time over more than $2c/U_\infty$. Profiles of the mean velocity in a surface normal coordinate system are shown in Fig. 2. At the first two stations, the edge velocity is about 12% smaller than measured by Hastings. As mentioned earlier, this is a side effect from the filter which was applied in the nose region in order to eliminate 2-Δ-waves. Since filtering was limited to a region close to the surface, simulated and measured mean flow agree much better for distances greater than $y/c = 0.06$. Although a better match between simulated and measured edge velocity is desirable (and can easily be obtained by further reducing the distance from the surface over which the filter is applied), we don't expect turbulence statistics to be significantly affected. One reason is the observation that the simulated adverse pressure gradient matches the measured one over most of the upper surface, see Fig. 3. Filtering affects mainly the magnitude of the suction peak and is partially responsible for the offset in the simulated pressure distribution. Additionally, since wind tunnel walls were not properly considered in this simulation, the pressure distribution near the nose will deviate from the measured one, see Jansen (1995). The goal of the present study is to predict the boundary layer growth and
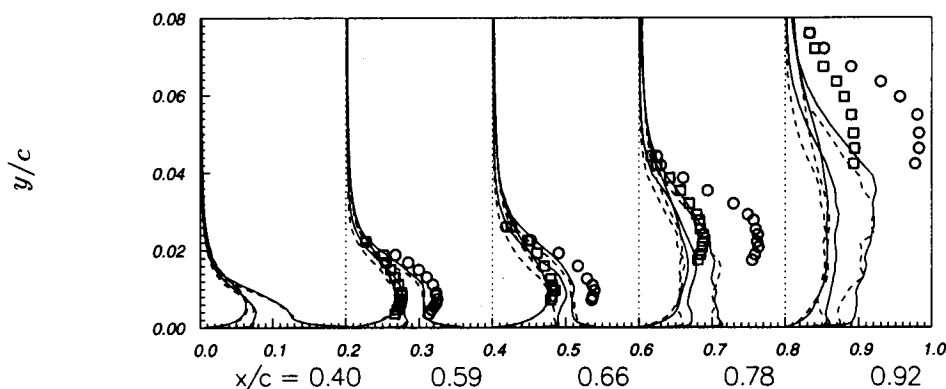
FIGURE 5.   RMS of velocity fluctuations u', v' and w', normalized with U_∞. Symbols: case A ———— , B - - - - , u' o and v' □ from Hastings. In terms of relative magnitude, the three curves for each simulation are v', w', and u' respectively.

the amount of separation near the trailing edge. Accurate prediction of the suction peak is of secondary interest.

Displacement and momentum thickness from the simulation lie in between the measurements of Hastings & Williams (1984) and Wadcock (1987) upstream of $x/c = 0.4$, see Fig. 4. The experimental values differ by up to 40% as a result of differences in boundary layer tripping and Reynolds number. However, the measured shape factor $H \approx 1.55$ is similar in both experiments in the region $x/c = 0.2...0.4$. Contrary to the experiment, H drops gradually in the simulation in the region $x/c = 0.2...0.4$ and reaches values as low as 1.4.

Since both experiments measure similar boundary layer growth and flow retardation near the trailing edge, the flow development does not seem to be very sensitive with respect to the exact values of δ^* and θ of the turbulent boundary that develops behind the transition strip. Although the thickness of the simulated boundary layer is close to the measured ones in the front part of the airfoil, the underprediction of the shape factor in the simulation and the initially opposite trend (decline as opposed to a growth) indicates insufficiencies in the simulated boundary layer for a considerable part of the upper surface. This is not surprising since the resolution is so coarse that the near wall structures can hardly be resolved properly. Examination of instantaneous flow fields close to the surface reveals a very streaky structure with typical spacings in the order of a few mesh cells. Similarly, spanwise two point correlations show a zero-crossing within 2-3 spanwise grid points for all near-wall locations upstream of $x/c = 0.5$, see Fig. 6. This indicates that the simulation has marginal resolution near the wall. Further evidence comes from the comparison of the present case with an earlier simulation which was a factor of 2 coarser in the streamwise direction and a factor of 1.5 coarser in the spanwise direction. The flow
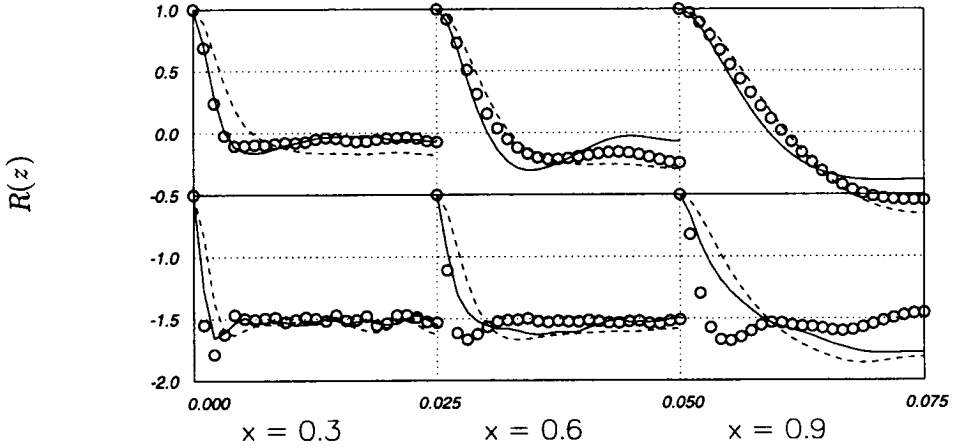
FIGURE 6.   Spanwise two-point correlations R_{uu} (——), R_{vv} ($\circ$) and R_{ww} (– – – –) versus distance z/c for three stations along the upper surface. Bottom figures correspond to the near wall region, top figures to $y/\delta \approx 0.3$. The y coordinate of the lower figures is shifted, i.e. $y = -1.5$ corresponds to a zero correlation.

retardation and the boundary layer growth was significantly improved on the finer mesh. Therefore, further grid refinement and, subsequently, a better prediction of the boundary layer in the front region might lead to better agreement between simulation and measurements over the entire airfoil.

The shear stress provided by the SGS model is an indicator for the role of the SGS model. The maximum contribution is about 15% of the resolved stress $\overline{uv}$ and is found in the front part of the airfoil where the resolution is coarse. Near the trailing edge, the SGS stress is negligible compared to the resolved Reynolds shear stress. The ratio of SGS eddy viscosity to molecular viscosity is about 20, which emphasizes the important role of the model for the kinetic energy budget.

RMS values of the velocity fluctuations are shown in Fig. 5. Agreement between simulation and experiment is reasonable in the middle section of the airfoil. In a characteristic manner for an adverse pressure gradient boundary layer, the location of maximum rms values (and Reynolds shear stress) moves towards the outer part of the boundary layer. Also, the anisotropy of the fluctuations in the outer part of the boundary layer is greatly reduced. Substantial differences between simulation and experiment are indicated by the large discrepancy in simulated and measured rms values (and shear stress) near the trailing edge. It is unclear whether this mismatch is a local effect or rather a result of differences in (spatial) flow history between experiment and simulation.

Results from cases A and B, which only differ with respect to the spanwise domain size, are surprisingly similar. Two-point correlations from the outer part of the boundary layer of case A do not drop to zero within half the spanwise width for locations downstream of $x/c = 0.6$, see Fig. 6. This means that the large scales

of motion are affected by the presence of artificial periodic boundaries. Since the limitations are much more severe in case B as compared to A, one would expect that both cases deviate in the rear part. Presently, it is not clear why the simulation is rather insensitive with regard to the domain width. Kaltenbach (1994) made a similar observation for a flow in a diffuser where the aspect ratio of the outlet duct was smaller than 0.5. Doubling the aspect ratio had only a small effect on the flow evolution. The cost for case B is about half that of case A. Further studies on the effect of grid refinement would be much cheaper if the domain width of case B turns out to be sufficient.

3. Conclusions and future goals

Wall resolving LES of flow around an airfoil has been demonstrated to be feasible with present computers and standard numerical schemes for LES. Qualitatively, the simulation captures typical features of separating flows such as boundary layer retardation and drastic increase in Reynolds stresses. This demonstrates the capability of the LES concept to deal with flows in complex configurations of immediate technical interest. However, the resolution provided was probably too coarse to adequately simulate the boundary layer in the first half of the airfoil. Although the resolution might have been adequate for the rear part, the overall agreement with measurements with respect to prediction of backflow is not satisfactory. History effects might play a role, and further studies should attempt to match better the integral boundary layer parameters of the experiment at an early station. Because of conservation properties, the use of centered difference schemes is very desirable in the context of LES. However, the emergence of 2-Δ-waves is a serious problem for the present high Reynolds number flow and needs further consideration, for example, usage of explicit filters as explored by Lund & Kaltenbach in this volume. Comparison of two cases with different domain width did not show significant sensitivity with respect to this parameter in the range considered. Future simulations should consider the effect of wind tunnel (top and bottom) walls by a corresponding modification of domain size and boundary conditions.

REFERENCES

CABOT, W. 1994 Local dynamic subgrid-scale models in channel flow. In *Annual Research Briefs 1994*, Center for Turbulence Research, Stanford Univ./NASA Ames Research Center, 143-159.

CAIN, A. B. & BUSH, R. H. 1994 Numerical wave propagation analysis for stretched grids. *AIAA-94-0172*, 32nd Aerospace sciences meeting, Jan. 10-13, 1994, Reno, NV.

CHAN, W. M. 1993 User's Manual for the HYPGEN hyperbolic grid generator. *NASA Technical Memorandum 108791*.

CHOI, H., MOIN, P. & KIM, J. 1993 Direct numerical simulation of turbulent flow over riblets . *J. Fluid Mech.* **255,** 503-539.

GERMANO, M., PIOMELLI, U., MOIN, P. & CABOT, W. H. 1991 A dynamic subgrid-scale eddy viscosity model. *Phys. Fluids A.* **3,** 1760-1765.

GRESHO, P. M. & LEE, R. L. 1981 Don't suppress wiggles - they're telling you something. *Computers & Fluids.* **9,** 223-253.

HASTINGS, R. C. & WILLIAMS, B. R. 1984 Studies of the flow field near an NACA 4412 aerofoil at nearly maximum lift. *Royal Aircraft Establishment, Technical Memorandum Aero 2026.*

HASTINGS, R. C. & WILLIAMS, B. R. 1987 Studies of the flow field near an NACA 4412 aerofoil at nearly maximum lift. *Aeronautical Journal.* **91,** 29-44.

JANSEN, K. 1995 Preliminary large-eddy simulations of flow around a NACA 4412 airfoil using unstructured grids. *Article in this volume.*

KALTENBACH, H.-J. 1994 Large eddy simulation of flow through a plane, asymmetric diffuser. In *Annual Research Briefs 1994,* Center for Turbulence Research, Stanford Univ./NASA Ames Research Center, 175-184.

LILLY, D. K. 1992 A proposed modification of the Germano subgrid scale closure method. *Phys. Fluids A.* **3,** 2746-2757.

LUND, T. S., KALTENBACH, H.-J. & AKSELVOLL, K. 1995 On the behavior of centered finite difference schemes for large eddy simulation. In *Proceedings of the sixth International Symposium on Computational Fluid Dynamics,* Lake Tahoe, NV, 4-8 September, 1995.

WADCOCK, A. J. 1987 Investigation of low-speed turbulent separated flow around airfoils. *NASA contractor report 177450.*

Preliminary large-eddy simulations of flow around a NACA 4412 airfoil using unstructured grids

By Kenneth Jansen

1. Motivation and objectives

Large-eddy simulation (LES) has matured to the point where application to complex flows is desirable. The extension to higher Reynolds numbers leads to an impractical number of grid points with existing structured-grid methods. Furthermore, most real world flows are rather difficult to represent geometrically with structured grids. Unstructured-grid methods offer a release from both of these constraints. However, just as it took many years for structured-grid methods to be well understood and reliable tools for LES, unstructured-grid methods must be carefully studied before we can expect them to attain their full potential.

In the past two years, important building blocks have been put into place making possible a careful study of LES on unstructured grids. The first building block was an efficient mesh generator which allowed the placement of points according to smooth variation of physical length scales. This variation of length scales is in all three directions independently, which allows a large reduction in points when compared to structured-grid methods, which can only vary length scales in one direction at a time. The second building block was the development of a dynamic model appropriate for unstructured grids. The principle obstacle was the development of an unstructured-grid filtering operator. New filtering operators were developed in Jansen (1994). In the past year, some of these filters have been implemented into a highly parallelized finite element code based on the Galerkin/least-squares finite element method (see Jansen *et al.* (1993) and Johan *et al.* (1992)).

We have chosen the NACA 4412 airfoil at maximum lift as the first simulation for a variety of reasons. First, it is a problem of significant interest since it would be the first LES of an aircraft component. Second, this flow has been the subject of three experimental studies (Coles and Wadcock (1979), Hasting and Williams (1987), and Wadcock (1987)). The first study found the maximum lift angle to be 13.87°. The later studies found the angle to be 12°. Wadcock reports in the later study that the early data agree very well with his new data at 12°, suggesting that the early experiment suffered from a non-parallel mean flow in the Caltech wind tunnel. It should be pointed out that the Reynolds-averaged simulations are usually run at 13.87° and do not agree with the data when run at 12° as will be shown later in this study. It is hoped that LES can clarify this controversy. The third reason for considering this flow is the variety of flow features which provide an important test of the dynamic model. Starting from the nose where the flow stagnates, thin laminar boundary layers are formed in a very favorable pressure gradient. This pressure gradient soon turns adverse, driving the flow toward a leading edge separation. Only the onset of turbulence can cause the flow to remain attached or to reattach

if it did separate. The persistent adverse pressure gradient eventually drives the turbulent flow to separate in the last 20 percent of chord. The separation bubble is closed near the trailing edge as the retarded upper surface boundary layer interacts with the very thin lower surface boundary layer. The large difference in boundary layers creates a challenging wake to simulate. Only the dynamic model can be expected to perform satisfactorily in this variety of situations: from the laminar regions where it must not modify the flow at all to the turbulent boundary layers and wake where it must represent a wide variety of subgrid-scale structures.

The flow configuration we have chosen is that of Wadcock (1987) at Reynolds number based on chord $Re_c = u_\infty c / \nu = 1.64 \times 10^6$, Mach number $M = 0.2$, and 12° angle of attack.

2. Accomplishments

2.1 Dynamic model implemented and tested

The only obstacle to implementing a dynamic model on unstructured grids is extension of the filtering operator. Four filtering operators were proposed in Jansen (1994). Two of these models were implemented and compared using a simple analytic velocity field for which the filtered values can be determined exactly. From this test, the generalized top-hat was found to be the most accurate, and all subsequent calculations have been carried out using this filter.

2.2 Simulations

A series of simulations has been performed in the last year to develop experience with this new approach. The first simulation was intentionally very coarse as we hoped to improve the mesh selectively and develop an understanding of the sensitivity of the solution to the grid improvements.

2.2.1 First simulation

The first simulation was performed on a very coarse mesh. The near-wall grid did not attempt to resolve the near-wall layer accurately in the first 20 percent of chord and only marginally resolved the remaining flow ($\Delta_x^+ = 300$, $\Delta_z^+ = 80$) at the wall. The grid was coarsened in the streamwise and spanwise directions coming off the wall as suggested by Chapman (1979). The resulting coefficient of pressure distribution was reasonably well predicted on this mesh (see Fig. 1), but the velocity profiles showed poor agreement with the experiment.

2.2.2 Improvement of outer layer

Careful scrutiny of the mesh revealed that the strategy of coarsening in the streamwise direction coming off the wall was inappropriate at this Reynolds number. The inner-layer spacing, Δ, scales on wall units.

$$\frac{\Delta}{c} \propto \frac{\nu}{u_\tau c} = \frac{\sqrt{2}}{Re_c \sqrt{C_f}}$$

Here, ν, is the kinematic viscosity, c is the chord length, and u_τ is the friction velocity defined to be the square root of the coefficient of friction, C_f, over two.
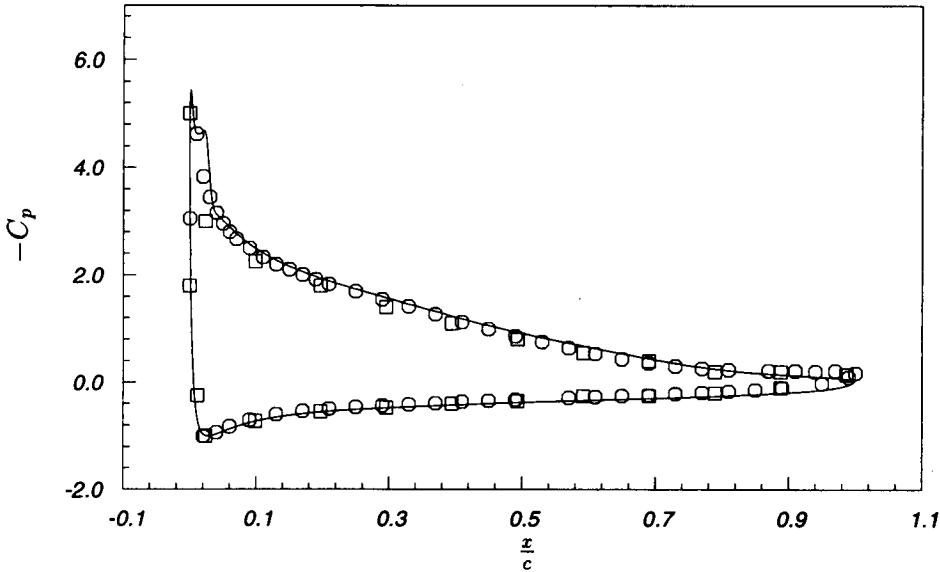
FIGURE 1. Coefficient of pressure along the airfoil surface. LES ——— , Hastings and Williams o , Wadcock (1987) □ .

The outer-layer spacing scales on the boundary layer thickness, δ_{99}. It is reasonable to expect the large eddies in the outer part of the boundary layer to be of order δ_{99}, and therefore the outer-layer spacing, in all directions, should never exceed

$$\Delta = \frac{\delta_{99}}{5}$$

By using Wadcock's experimental data for the C_f and δ_{99}, one can compare these two resolution restrictions as is done in Fig. 2. This figure contains three curves. The solid curve describes the variation of a 200 wall-unit spacing (which can be associated with the streamwise spacing near the wall) over the upper surface where the boundary layer is attached. The dashed curve describes the same variation of 50 wall units (which can be associated with spanwise spacing near the wall). The chain dash curve is the outer-layer spacing as described above. Several points can be made in this figure. First, all three curves change by over an order of magnitude from the tip to the tail region. This illustrates how an unstructured grid saves points by matching resolution to the local changes in the length scales in the streamwise direction. For example, a structured grid would be forced to carry the fine spanwise resolution required near the nose through the entire domain. Second, when comparing the near-wall spanwise resolution to the outer-layer resolution, it is clear that coarsening the spanwise resolution as the distance from the wall increases is justified. The final point, apparent from this figure, is that coarsening of the streamwise resolution in the outer layer is not justified. In fact, over much of the airfoil surface the outer-layer grid resolution is more restrictive than the
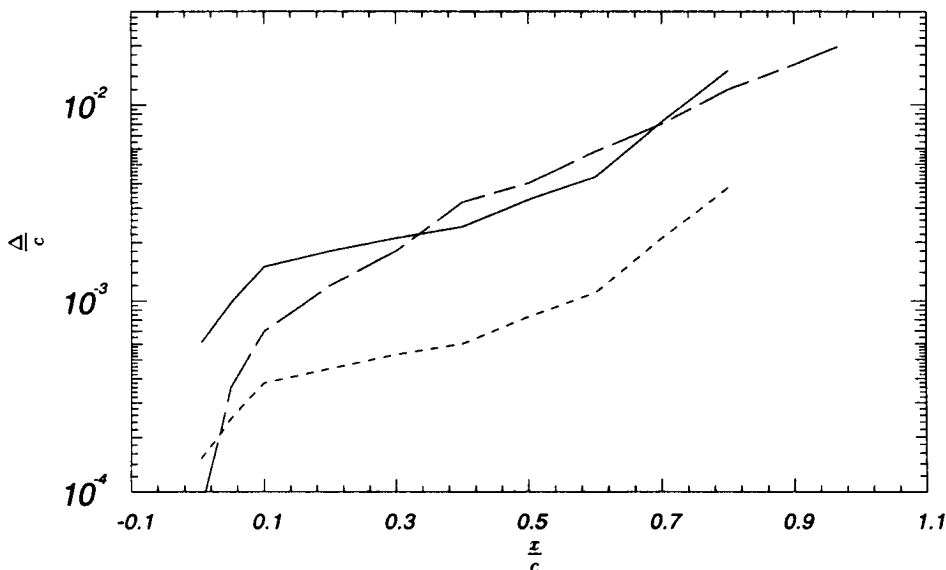
FIGURE 2.   Comparison of length scales over the airfoil surface. 200 wall units (streamwise near-wall spacing) ——— , $\delta_{99}/5$ (outer-layer spacing) ——·— , 50 wall units (spanwise near-wall spacing) ---- .

inner-layer resolution. The choices of 200 wall units and 5 points per boundary layer thickness are somewhat arbitrary, but they are believed to be comparable in their degree of coarseness. It is interesting to observe that the crossover between these two curves corresponds to $Re_\tau = (u_\tau \delta_{99}/\nu) = 1000$. Therefore, when above 1000, the inner-layer resolution is the most restrictive. Otherwise, the outer-layer resolution is the most restrictive. Only at higher Reynolds numbers will coarsening in the streamwise direction be justified.

Considering the above discussion, a new mesh was made where the coarsening of the streamwise spacing was delayed until outside of the boundary layer. This resulted in a mesh with nearly twice as many points as the previous simulation. It also resulted in a rather dramatic change in the early boundary layer structure. It seems that the improved resolution of the outer layer allowed a better resolution of the leading edge separation. The new simulation led to a train of spanwise coherent vortices. These vortices broke down into turbulence at about 10 percent of chord.

The persistence of the spanwise coherent vortices was not in line with the experiments which were all tripped. Some evidence as to the importance of the tripping can be seen in Fig. 3 where we compare the surface coefficient of pressure distribution from the free transition simulation to two experimental data sets from Hastings and Williams (1987). The square data set was taken without a transition strip while the circle data set was taken with a transition strip. Our simulation shows rather good agreement with the free transition. Unfortunately, all velocity and Reynolds stress data were taken with the transition strip in place and agreement with these
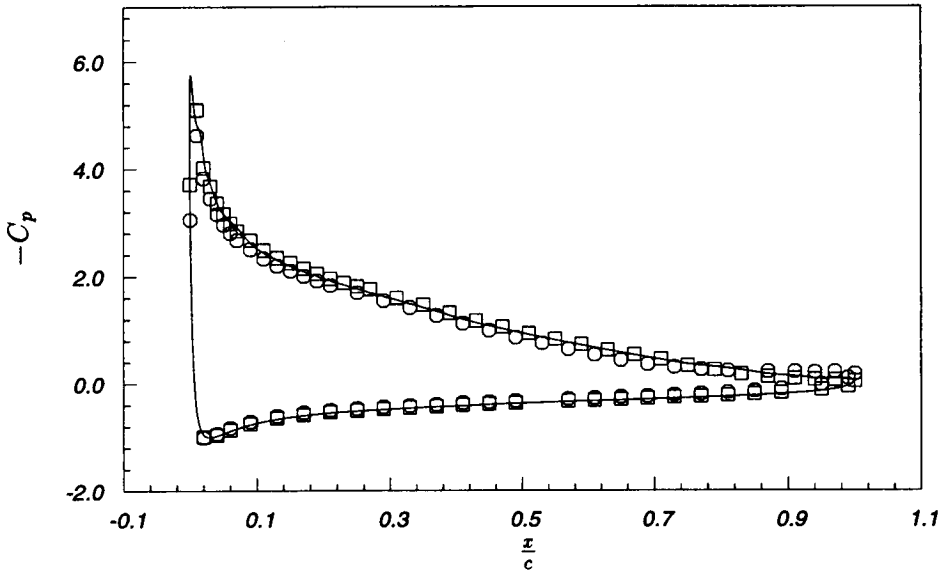
FIGURE 3. Coefficient of pressure along the airfoil surface. LES ———— , Hastings and Williams without trip □ , Hastings and Williams tripped ○ .

quantities is substantially worse than with C_p.

2.2.3 Grid refinement study of the nose

The dramatic change of the flow with changed resolution indicated a need for further refinement in the nose region. At the same time we also hoped to model the transition through a steady blowing pattern as shown in Fig. 4. A shape that could be easily resolved was chosen. Therefore, we could be certain that any sensitivity to grid refinement would be associated with the turbulence structures responding to the blowing and not the resolution of the blowing itself.

A new mesh was generated where the streamwise and spanwise resolution were improved by a factor of two everywhere on the upper surface. The normal spacing was improved at the wall by a factor of two as well, but this did not lead to a doubling of points in this direction due to the stretching. The spanwise domain was cut in half (from $0.05c$ to $0.025c$) for this simulation. Therefore, the number of points approximately doubled rather than a quadrupling.

There was again a rather dramatic change in the solution and so another mesh was generated. This mesh again improved the streamwise and spanwise resolution by a factor of two, although, this time, only in the first 5 percent of chord. The three surface meshes of the first 10 percent of chord are shown in Fig. 5. The velocity profiles in the first 5 percent of chord are shown in Fig. 6. For this forcing pattern, the flow is nearly spanwise- and streamwise-resolution independent.
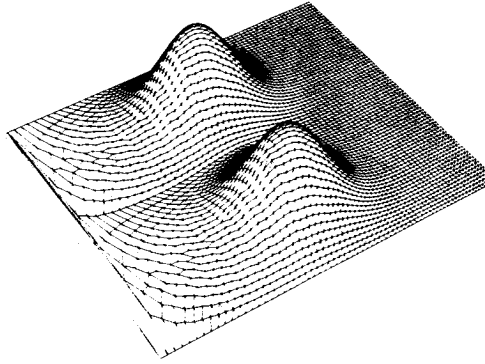
FIGURE 4. Elevation plot of the steady jet normal to the airfoil surface. The actual grid is shown to confirm resolution.

(a)

(b)

(c)
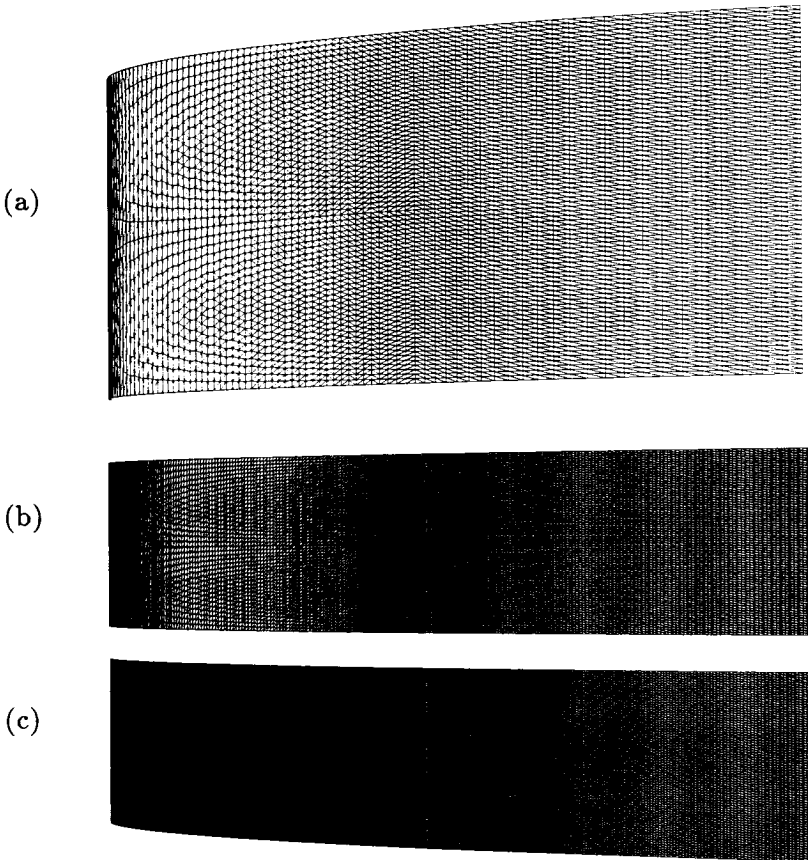
FIGURE 5. Surface meshes near the leading edge $(0.0 < x/c < 0.1)$. Mesh (b) has been refined by a factor of 2, both spanwise and streamwise, from mesh (a). The spanwise domain is also halved. Mesh (c) has been refined by a factor of 2, both spanwise and streamwise, from mesh (b) in the first 5 percent of chord.
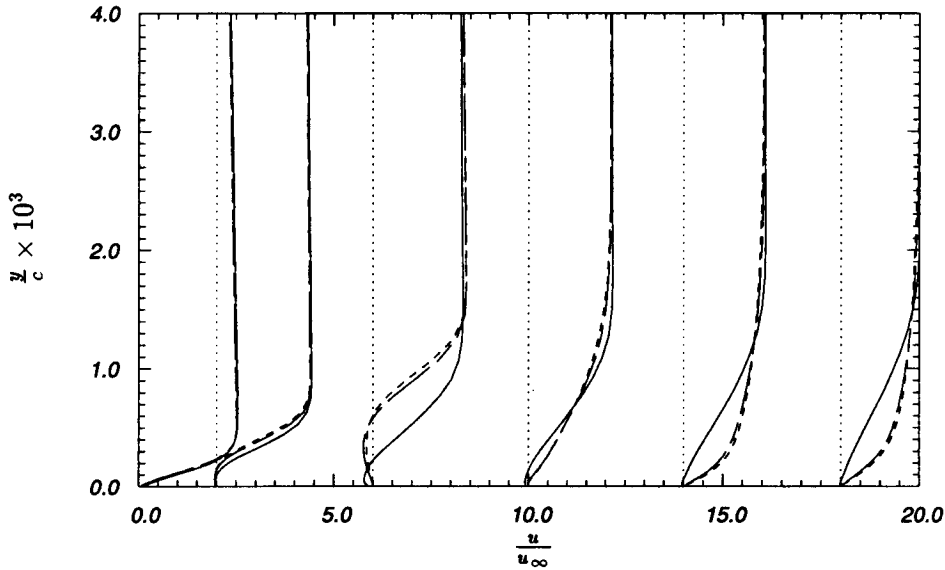
FIGURE 6. Profiles of tangential velocity component at various positions along the airfoil surface ($x/c = 0.005, 0.01, 0.02, 0.03, 0.04, 0.05$). Solutions correspond to grids from previous figure; mesh (a) ——— , mesh (b) ——— , mesh (c) ---- .
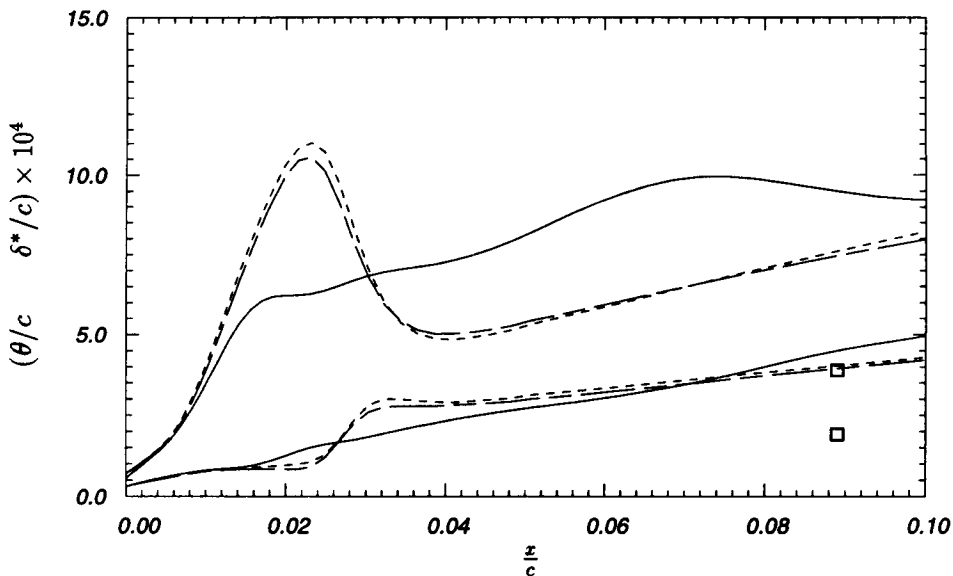
FIGURE 7. Boundary layer parameters (lower curves and data are momentum thickness (θ), higher curves and data are displacement thickness (δ^*)) along the airfoil surface. Solutions correspond to meshes from Fig. 5; mesh (a) ——— , mesh (b) ——— , mesh (c) ---- , Wadcock (1987) ($\square$).

2.3 More accurate transition

While it was useful to obtain a grid-independent solution at the forcing prescribed, the final solution does not agree with experiment, as can be seen in Fig. 7. Here, the momentum and displacement thickness of the grid-independent calculations can be seen to be substantially greater than the experiments at the first available datum point. The discrepancy seems to be associated with the laminar separation at 1 percent of chord. The simulation suggests a transition in the free shear layer, followed by a turbulent reattachment. This mode of transition seems to give the flow a large jump in momentum and displacement thickness. The experiment did not seem take this route to transition. For this reason a more careful study of transition is currently underway.

Wadcock used a strip of tape with serrations cut into the edge on the upstream side. The serrated tape can be modeled in a coarse fashion by our current simulation as can be seen in Fig. 8. The tape is effectively a forward facing step (with serrations) of height $\delta_{99}/4$, followed by a backward facing step. Calculations are underway with this modification.
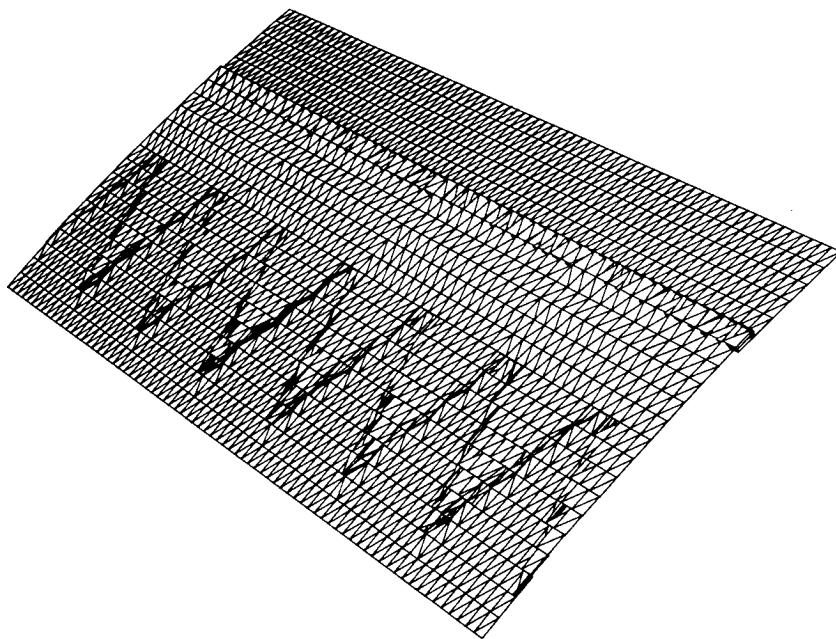
FIGURE 8. A transition strip is modeled geometrically by applying a no-slip boundary condition to the nodes which form a surface of height, shape, and position equivalent to Wadcock's serrated tape which was applied to the airfoil surface.

2.4 Reynolds-averaged simulations

Reynolds-averaged Navier-Stokes simulations (RANS) have not shown good agreement with the experimental data. However, given the cost of LES, they can be a

helpful tool for suggesting sensitivity to changes of basic flow parameters since they require so little computational time. While the results are not expected to be quantitatively correct, trends can at least be suggested by RANS and later confirmed by LES.

A series of RANS calculations was performed to chart various trends in this flow. The RANS calculations used the commonly accepted NASA code (INS2D) of Rogers (1991) and employed a $k - \omega$ model from Menter (1994). First, the effect of angle-of-attack and wind tunnel walls are compared in Figures 9 and 10. The boundary condition on the wind tunnel walls is a slip condition. This accounts for the blockage of the walls without requiring resolution of the boundary layers on them. The effects are compared together because it is common among the RANS modeling community to adjust the angle-of-attack of free air calculations to account for the walls. Figure 10 suggests that the flattening of the C_p near the trailing edge (which is associated with the large separation there) is affected strongly by angle-of-attack and only weakly by the wind tunnel walls. The 13.87° angle-of-attack cannot be justified with the hope of accounting for the effects of the wind tunnel walls in free air calculations.

The second trend studied with the RANS code was the effect of transition position. When the RANS code was run with the transition point fixed at the position of Wadcock's strip, a leading edge separation developed on sufficiently fine meshes. Once beyond the transition point, the flow reattaches. This provides an independent verification of the results observed in the LES.

3. Future plans

3.1 Grid-independent solution of flow with a transition strip

The calculation using the transition strip described above will be continued and checked for grid dependence. It should be noted that grid independence can only be achieved beyond a short distance downstream of the transition strip. True grid independence of the strip and transition itself is probably too expensive to be practical, even with an unstructured grid. It may be necessary to provide small disturbances upstream of the strip to mimic the interaction of freestream turbulence with the strip. This capability has been implemented and tested in the code using a wall jet with spatial and temporal variation.

3.2 Inclusion of the wind tunnel walls

The RANS studies indicated a moderate effect of the wind tunnel walls on the solution. Future simulations will be done with a slip boundary conditions on the wind tunnel walls. Meshes have already been generated for this purpose as can be seen in Fig. 11.

3.3 Higher order methods

Given the number of points that are required to get a grid-independent solution, it seems clear that higher order methods should be explored. This is relatively easy, but non-trivial, to do with the finite element method. There are two benefits to higher order methods besides the obvious one of higher accuracy. First, the higher
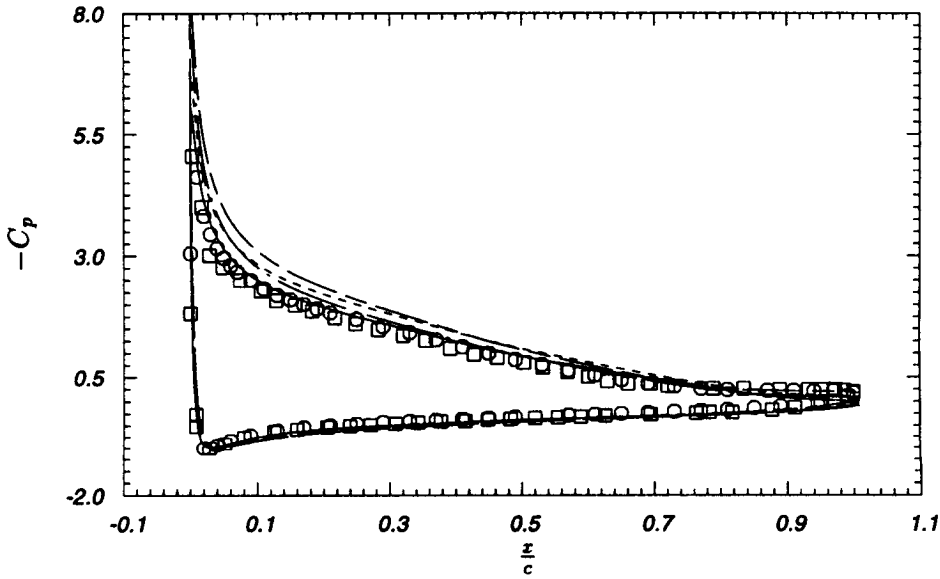
FIGURE 9. Coefficient of pressure along the airfoil surface from RANS simulations. 12° in free air ——— , 12° with walls ---- , 13.87° in free air —·— , 13.87° with walls —--— , Hastings and Williams (1987) ○ , Wadcock (1987) □ .
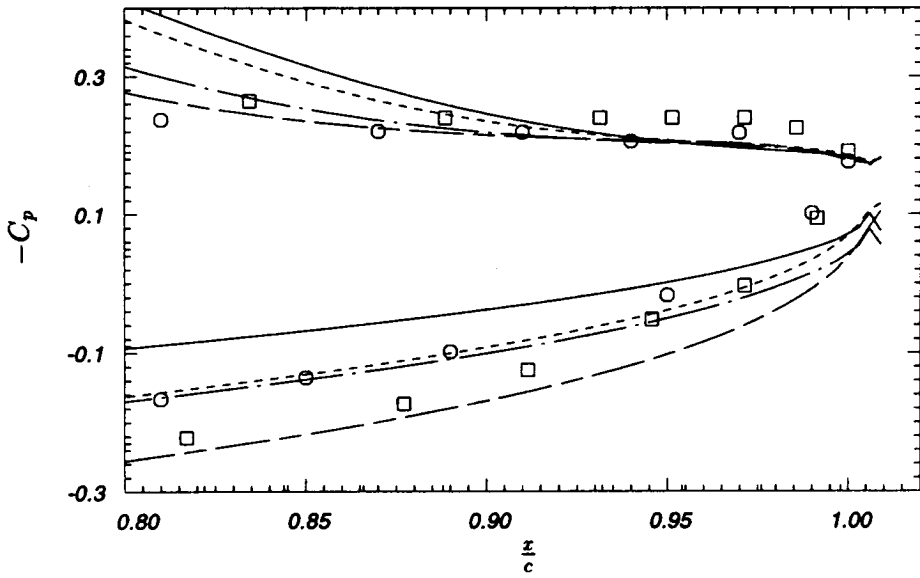
FIGURE 10. Closeup of the trailing-edge region (same legend as above).
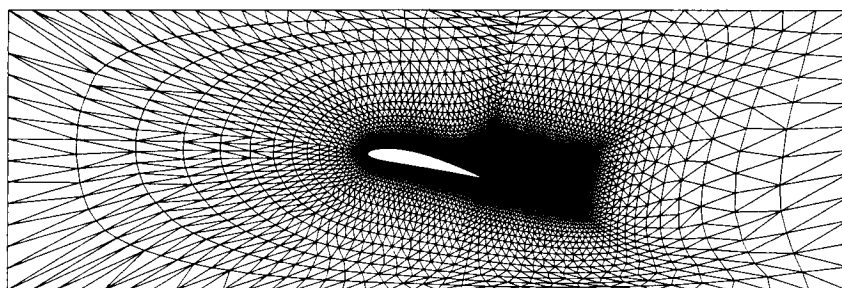
FIGURE 11. The crosssectional plane of an unstructured mesh which accounts for the inviscid effects of the wind tunnel walls.

order methods will have a more complete representation of the residual error of the discrete approximation and, therefore, the scheme will be less dissipative. Second, alternative filters, described in Jansen (1994), can be implemented and tested. It is difficult to predict at this time if the method will lose computational efficiency when extended to higher order.

3.4 Expanded spanwise domain

Once we are satisfied with the solution in the region of the nose, we will have to consider carefully the effect of the narrow spanwise domain on our solution. It is likely that as we predict a larger separation at the trailing edge, the effect of the narrow domain will become more acute. Strategies are being developed to expand only the portion of the domain suffering from a narrow box. If these strategies work a large number of points can be saved.

REFERENCES

CHAPMAN, D. R. 1979 Computational aerodynamics development and outlook. *AIAA J.* **17**, 1293.

COLES, D., & WADCOCK, A. J. 1979 A flying-hot-wire study of two-dimensional mean flow past an NACA 4412 airfoil at maximum lift. *AIAA J.* **17**, 321.

HASTINGS, R. C.& WILLIAMS, B. R. 1987 Studies of the flow field near a NACA 4412 aerofoil at nearly maximum lift. *Aero. J.* **91**, 29.

JANSEN, K. 1994 Unstructured grid large eddy simulation of flow over an airfoil. *Annual Research Briefs 1994.* Center for Turbulence Research, NASA Ames/Stanford Univ.

JANSEN, K., JOHAN, Z., & HUGHES, T. J. R. 1993 Implementation of a one-equation turbulence model within a stabilized finite element formulation of a symmetric advective-diffusive system. *Comp Meth Appl Mech Eng.* **105**, 405.

JOHAN, Z., HUGHES, T. J. R., MATHUR, K. K., & JOHNSSON, S. L. 1992 A data parallel finite element method for computational fluid dynamics on the Connection Machine system. *Comp. Meth. Appl. Mech. Eng.* **99**, 113.

MENTER, F. R. 1994 Two-equation eddy-viscosity turbulence models for engineering applications. *AIAA J.* **32-8,** 1598-1605.

ROGERS, S. E., & KWAK, D. 1991 An upwind differencing scheme for the steady-state incompressible Navier-Stokes equations. *J. Appl. Num. Math.* **8,** 43-64.

WADCOCK, A. J. 1987 Investigation of low-speed turbulent separated flow around airfoils. *NACA CR 177450.*

A new non-eddy viscosity subgrid-scale model and its application to channel flow

By K. B. Shah AND J. H. Ferziger

1. Motivation and objectives

To date, most large-eddy simulations (LES) have been carried out with eddy viscosity subgrid scale (SGS) models, with only a few exceptions that used the mixed model. Even though the assumptions behind Smagorinsky's model are rather stringent, it has been applied successfully to a variety of turbulent flows. This success is attributed to the ability of eddy viscosity models to drain energy from large scales, thus simulating the dissipative nature of turbulence. Most SGS models are absolutely dissipative i.e. they remove energy from the large scales at every instant. However, SGS stresses may transfer energy back to the large scales intermittently; this reverse transfer or backscatter is especially important in geophysical flows and in transition. In a fully developed channel flow, there is reverse flow of energy from small to large scales near the walls (Härtel & Kleiser 1993), but eddy viscosity models are unable to account for this important feature. The dynamic localization eddy viscosity model of Ghosal *et al.* (1995) allows backscatter by co-evolving an auxiliary equation for the SGS energy; however, the computational cost is considerably larger than for conventional SGS models (Cabot 1994). In this report, a new non-eddy viscosity model based on local approximation of total quantities in terms of filtered ones is introduced; the scale similarity model of Bardina (1983) is a special case of this model. This procedure does not require the assumption of homogeneity, permits backscatter of energy from small to large scales, and is readily implemented in finite difference codes.

The results of applying the proposed model to second order finite volume simulation of plane channel flow at high Reynolds numbers ($Re_b = 38000$) is described in this report. Greater emphasis is placed on the high Reynolds number flow since it provides a more rigorous test of the SGS model and its potential application. The results are compared to ones produced by the conventional and dynamic Smagorinsky models and the spectral LES of Piomelli (1993).

2. Accomplishments

2.1 Numerical method

A second order staggered finite volume formulation is used to discretize the Navier-Stokes equations. Uniform meshes are used in the streamwise and the spanwise directions, and hyperbolic tangent stretching is used in the wall-normal direction. A fractional step method is used to decouple the pressure from the momentum equation. The momentum equations are first advanced without satisfying continuity, then the velocity field is adjusted to satisfy continuity. The time advancement

of the momentum equation is semi-implicit, explicit third order Runge-Kutta for the non-linear (convective) terms and implicit second order Crank-Nicolson for the diffusive (viscous) terms. Continuity is enforced by solving a Poisson equation for a pressure-like variable; a fast Fourier transform (FFT) procedure solves this problem efficiently. A full description of this numerical method can be found in Yang *et al.* (1993)

2.2 Computational domain and boundary conditions

The computational domain parameters are listed in table (1). The x, y, and z axes are along the streamwise, wall-normal, and spanwise directions, respectively. The simulations were carried out by fixing the mass flow (or Re_b) rather than the pressure gradient (or skin friction). The physical domain size and grid size are similar to that of Piomelli (1993); however, since Re_τ in present simulation (≈ 1800) is slightly lower than Piomelli's value ($Re_\tau = 1995$), the domain and grid sizes in wall units are slightly different. Reynolds numbers are based on the half channel height δ, bulk velocity U_b for Re_b, and the friction velocity u_τ for Re_τ.

Re_b	Re_τ	(Nx, Ny, Nz)	(Lx, Ly, Lz)	$(\Delta x^+, \Delta z^+)$	$(\Delta y^+_{min}, \Delta y^+_{max})$
38000	≈ 1800	$(64, 80, 80)$	$(2.5\pi, 2.0, 0.5\pi)$	$\approx (221, 35)$	$\approx (1.5, 150)$

TABLE 1: Simulation parameters

2.3 The proposed model

In LES, the effect of unresolved scales of motions on large scales appears through the SGS stress:

$$\tau_{ij} = \overline{u_i u_j} - \overline{u}_i \, \overline{u}_j \tag{1}$$

which must be modeled. Most SGS models employ eddy viscosities, which assume a linear relationship between the anisotropic part of SGS stress tensor and the large scale strain rate tensor. The isotropic part is absorbed into the large scale pressure field. Thus

$$\tau_{ij}^a = \tau_{ij} - \frac{\delta_{ij}}{3}\tau_{ii} = -2\nu_t \overline{S}_{ij} = -\nu_t \left(\frac{\partial \overline{u}_i}{\partial x_j} + \frac{\partial \overline{u}_j}{\partial x_i} \right)$$

The eddy viscosity ν_t is usually taken to be:

$$\nu_t = (C_s \Delta)^2 |\overline{S}|$$

where Δ is the length scale of a typical SGS eddy and C_s is the model parameter which depends on the flow. The dynamic model proposed by Germano *et al.* (1991) computes this parameter in tandem with the calculation. This procedure has been used with remarkable success for a variety of flows, but the model coefficient has large fluctuations with positive and negative values nearly as likely (Lund *et al.* 1993). Numerical instability due to large negative viscosity can be eliminated by averaging in homogeneous directions (Lilly 1992), but this is not very satisfactory.

Recently, a dynamic localization model (Ghosal *et al.* 1995) has been developed which permits negative eddy viscosities by limiting the time that eddy viscosities remain negative by co-evolving the SGS kinetic energy. The equation for SGS energy contains additional model coefficients. The advantage of this method remains to be established in light of its complexity and additional cost.

The scale similarity model of Bardina (1983), a non-eddy viscosity model, is appealing in this respect. It permits backscatter and provides a good representation of instantaneous energy transfer between the large and small scales; however, it fails to provide enough mean dissipation. The scale similarity model can be easily derived by substituting $u_i \approx \overline{u}_i$ in the expression for the exact SGS stress $\tau_{ij} = \overline{u_i\,u_j} - \overline{u}_i\,\overline{u}_j$ which yields a Galilean invariant version of this model:

$$\tau_{ij} = \overline{\overline{u}_i\,\overline{u}_j} - \overline{\overline{u}}_i\,\overline{\overline{u}}_j$$

The mean dissipation is small because forward and backward transfer of energy are nearly balanced. It is plausible that if higher order terms are included in the approximation for u_i instead of $u_i \approx \overline{u}_i$, this model might provide sufficient mean dissipation yet retain the favorable characteristics. Thus, the following form for the SGS stress is proposed:

$$\tau_{ij} = \widehat{u_i^\star\,u_j^\star} - \widehat{u_i^\star}\,\widehat{u_j^\star} \tag{2}$$

where $u_i^\star$ is defined implicitly in terms of the filtered velocity $\overline{u}_i$:

$$\mathcal{L}(u_i^\star) = \overline{u}_i \qquad \mathcal{L} = \mathcal{L}_x \mathcal{L}_y \mathcal{L}_z$$

where $\mathcal{L}_x$ is of the form:

$$\mathcal{L}_x = \left(1 + C_1^\star(\Delta_x)\frac{\partial}{\partial x} + C_2^\star(\Delta_x)\frac{\partial^2}{\partial x^2}\right)$$

$\mathcal{L}_y$ and $\mathcal{L}_z$ are of the similar form. The $\widehat{\ }$ operation is also defined in a similar manner:

$$\widehat{u_i^\star} = \mathcal{V}(u_i^\star) \qquad \mathcal{V} = \mathcal{V}_x \mathcal{V}_y \mathcal{V}_z$$

where $\mathcal{V}$ is similar to the $\mathcal{L}$ operator:

$$\mathcal{V}_x = \left(1 + \widehat{C_1}(\Delta_x)\frac{\partial}{\partial x} + \widehat{C_2}(\Delta_x)\frac{\partial^2}{\partial x^2}\right)$$

$C_1^\star, C_2^\star, \widehat{C_1}$, and $\widehat{C_2}$ are given functions of the local filter width Δ.

This approximation is an extension of the filtering operation. To understand this procedure, consider the expression for $u_i^\star$ in one dimension:

$$\overline{u}_i \approx u_i^\star + C_1^\star(\Delta)\,\frac{du_i^\star}{dx} + C_2^\star(\Delta)\,\frac{d^2 u_i^\star}{dx^2} \tag{3}$$
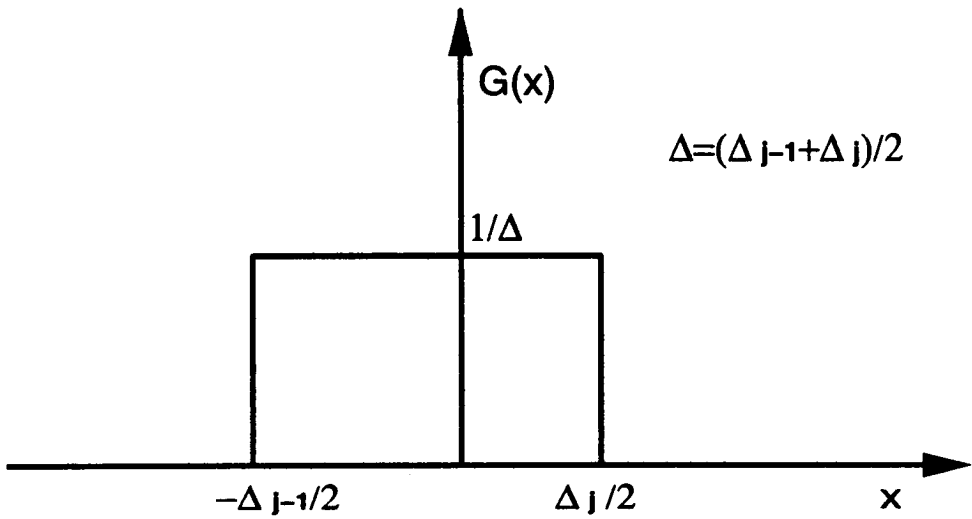
FIGURE 1. A non-symmetrical Box filter.

This is a local Taylor series approximation of the filtered quantity in terms of the unfiltered quantity. For the non-symmetrical box filter defined by Fig. 1:

$$G_j = G(x - x_j) = \begin{cases} 1/\Delta, & \text{if} \quad -\Delta_{j-1}/2 < x - x_j < \Delta_j/2; \\ 1/(2\Delta), & \text{if} \quad x - x_j = -\Delta_{j-1}/2 \text{ or } x - x_j = \Delta_j/2; \\ 0, & \text{if} \quad x - x_j < -\Delta_{j-1}/2 \text{ or } x - x_j > \Delta_j/2. \end{cases}$$

where $\Delta = (\Delta_j + \Delta_{j-1})/2$ is the filter width, the filtering operation defined by:

$$\overline{u(x)} = \int_{-\infty}^{\infty} G(x - x') \, u(x') \, dx'$$

reduces to:

$$\overline{u(x_j)}^{\Delta} = \frac{2}{(\Delta_j + \Delta_{j-1})} \int_{x_j - \frac{\Delta_{j-1}}{2}}^{x_j + \frac{\Delta_j}{2}} u(x') \, dx'$$

Taylor series expansion of $u(x')$ around x_j leads to

$$\overline{u(x_j)}^{\Delta} = u(x_j) + \frac{(\Delta_j - \Delta_{j-1})}{4} u'(x_j) + \frac{(\Delta_j^2 - \Delta_j \Delta_{j-1} + \Delta_{j-1}^2)}{24} u''(x_j) + O(\Delta^3) \quad (4)$$

Equation (3) is a second order approximation to Eq. (4). Extension to three dimensions consists of sequential application of $\mathcal{L}$ operators in each direction, but u^* is no longer a second order approximation u. The coefficients are functions of the local filter widths, which depend on the choice of the filter-grid ratio (FGR) i.e.

the ratio of local filter width Δ to the mesh size. A finite difference approximation to Eq. (3) is:

$$\overline{u_i} = a\ u_{i-1}^\star + b\ u_i^\star + c\ u_{i+1}^\star \tag{5}$$

where a, b, and c can be expressed in terms of the filter width Δ and the grid size h. For filter width equal to the local mesh size $\Delta = (h_j + h_{j-1})/2$, the coefficients a, b, and c can be expressed using the Taylor series:

$$
\begin{aligned}
a &= \frac{h_{j-1}^2 + 2h_{j-1}h_j - 2h_j^2}{12h_{j-1}(h_{j-1} + h_j)} \\
c &= \frac{h_j^2 + 2h_{j-1}h_j - 2h_{j-1}^2}{12h_j(h_{j-1} + h_j)} \\
b &= 1 - (a + c)
\end{aligned}
\tag{6}
$$

where $h_j = x_{j+1} - x_j$. The extension to three dimensions involves sequential application of Eq. (5) in each direction. The solution procedure requires inversion of tridiagonal systems. Details of the implementation of this model are presented in Shah (1996).

Even though the forms of $\mathcal{L}$ and $\mathcal{V}$ are the same, it is not necessary to use the same coefficients in the $\mathcal{L}$ and $\mathcal{V}$ operators. Bardina's scale similarity model is a special case of this model; for $\mathcal{L} = 1$ and the $\hat{\ }$ filter corresponding to the grid filter. Bardina's model may be viewed as a zeroth order approximation ($u_i \approx \overline{u}_i$) of the total quantity. Strictly speaking, it is not a model because it is the Leonard term of the Galilean invariant decomposition of the exact SGS stress (Germano, 1986). The proposed model uses a higher order approximation of the total quantity, and the Leonard term is automatically incorporated. The SGS stress is constructed from the field $u_i^\star$ which is obtained from the filtered field $\overline{u}_i$ by approximating the high wavenumber spectrum in a prescribed manner (as in Eq. (3)) dependent on the choice of filter-grid ratio.

Even though Taylor series expansion cannot be used for Fourier cutoff filters, the model equations (for $\mathcal{L}$ and $\mathcal{V}$) are still valid. The fundamental idea is to construct the SGS stress from the filtered velocity field. The high wavenumber region is expected to be representative of the SGS as most of the interaction between the resolved field and the SGS field take place at these scales. Finally, it must be pointed out that the coefficients $C_1^\star$ and $C_2^\star$ need not be the same as the coefficients in the one dimensional expansion Eq. (4). Two major approximations have been made to the filtering operation; the cross derivative terms that arise in three dimensions and the higher order terms are ignored. The effect of these terms are accounted for by the two coefficients $C_1^\star$ and $C_2^\star$. However, in the present work, we have taken them to be what one gets from a truncated expansion of the box filtering in one dimension (Eq. (4)).

This procedure does not require an assumption of homogeneity. Since it is not an eddy viscosity model, it does not suffer from instability due to negative eddy viscosity. Backscatter of energy from small to large scales, if it exists, is a natural part of the simulation. This procedure has the added advantage of providing an

estimate of the total turbulence quantities. For high Reynolds numbers at which the SGS energy may be significant, this can lead to improved comparisons with physical quantities.

2.4 Results for high Reynolds number ($Re_b = 38000$) plane channel flow

Results from high Re simulations are compared to the spectral LES of Piomelli (1993), which is in good agreement with experimental results. Several simulations were carried out to assess the accuracy of the SGS model and the effect of parameters such as the type of filter employed in the dynamic model and filter-grid ratios (FGR) in the new model. First, we present comparison of mean and turbulent quantities for four cases: no model (CDNS1), Smagorinsky's model with Van Driest (1956) wall damping (SMAG1), dynamic Smagorinsky model with filtering in the homogeneous directions (DSMAG1), and the proposed model with filter-grid ratio = 2.0 (NEWM3). Other results will be presented later to show the effect of filters on the dynamic model and the effect of filter-grid ratio on the new model.

The profile of the mean velocity normalized by skin friction velocity (u_τ) is shown in Figs. 2 & 3 along with Piomelli's spectral LES data and the log law $U^+ = (1/\kappa)\log y^+ + A$ with $\kappa = 0.4$ and $A = 5.5$. The profiles obtained from current LES are characterized by a bulge in the region $10 < y^+ < 200$, and the slope in the log law region is smaller than $1/\kappa = 2.5$. The coarse grid DNS shows a smaller bulge, but there is no improvement in the slope of the profile. The mean velocity profile for the new model is in better agreement with Piomelli's LES and the log law, but the bulge is still present. Interestingly, the new model profile falls below the log law for $300 < y^+ < 800$, in contrast to other models including the coarse DNS which over-predicts the mean velocity through out the channel. Both coarse DNS and the new model fall on the log law and Piomelli's LES for $y^+ > 1000$. Table (2) show a comparison of the skin friction coefficient $c_f = \tau_w / \frac{1}{2}\rho U_b^2$ and the ratio of centerline velocity (U_c) to the bulk velocity (U_b) with the experimental correlations proposed by Dean (1978):

	Re_b	$\dfrac{c_f - c_f^{Dean}}{c_f^{Dean}} \times 100$	U_c/U_b
Dean (1978)	38000		1.124
Smagorinsky (SMAG1)	38000	-5.77	1.086
Dynamic Smag. (DSMAG1)	38000	-8.31	1.090
New Model (DNEWM3)	38000	+2.30	1.110
No model (CDNS1)	38000	+0.25	1.094
Piomelli	42598	+1.75	1.105

TABLE 2: Comparison of the skin friction and centerline velocity with experimental correlations of Dean (1978)

Both the skin friction and the centerline velocity predicted by the new model and the coarse DNS are within 2.5% of Dean's correlation. The conventional Smagorinsky and the dynamic model under-predict the skin friction, which causes the mean velocity profile to rise above the log law.

The rms of *filtered* streamwise velocity normalized by the skin friction velocity is shown in Fig. 4 along with Piomelli's result. The effect of SGS models is now quite pronounced. The Smagorinsky, dynamic, and coarse DNS over-predict the peak in streamwise fluctuations by 40%, but the new model results compare well with Piomelli's. Fig. 5 shows the streamwise fluctuations in global units. All the models under-predict it far from the wall. The SGS contribution, which can be significant, has not been added, but this addition will worsen the results near the wall, which are already too high. Figs. 6, 7, 8, and 9 show the spanwise and wall-normal fluctuations in wall and global units. The predictions of the new model lie below those of other models. Since the streamwise energy is redistributed to the other two components via the pressure-strain interaction, which acts as a sink for the streamwise component and as a source for the spanwise and wall-normal components, larger streamwise fluctuations lead to larger fluctuations in the other two directions.

Figure 10 shows the SGS shear stress τ_{12}^{SGS} for various models; clearly the new model produces the largest SGS stress by far. The SGS stress accounts for 28% of the total stress ($\overline{u}\,\overline{v} + \tau_{12}^{SGS}$) in the new model as opposed to 2% for the Smagorinsky and dynamic models. Far from the walls, the new model produces a significant SGS contribution. It is desirable to compare the total fluctuations (resolved+SGS); however, for Smagorinsky models it is difficult to compute the SGS contribution. Bardina (1983) proposed the following expression for the total turbulent intensity $Q^2 = <u_i\,u_i>$ from the turbulent intensity of the filtered field $Q_f^2 = <\overline{u}_i\,\overline{u}_i>$ and the SGS dissipation rate ϵ:

$$Q^2 = \frac{Q_f^4}{Q_f^2 - c(2\Delta_f \epsilon_f)^{2/3}}$$

where Δ_f is the filter width and $c = 1.04$. Bardina used this estimate to determine the total kinetic energy in various types of homogeneous turbulence and found good agreement with experiments. Figs. 11 & 12 show the total turbulent kinetic energy $Q^2/2$ for the various models. Bardina's estimate was applied to all models except the new model, which evaluates the SGS contribution directly. From Fig. 11 it is evident that SGS models do poorly near the walls. Figs. 11 & 12 show Piomelli's *filtered* fluctuation since it is in good agreement with the experiments, but it too will deteriorate near the wall if the SGS contribution is included. All models except the new model over-predict the peak by almost 70%; the new model does better but over-predicts it by 20%. Table (3) shows the fraction of total turbulent kinetic energy η in the subgrid scales:

$$\eta = \frac{\int_0^{2\delta}(Q^2 - Q_f^2)dy}{\int_0^{2\delta} Q^2 dy}$$
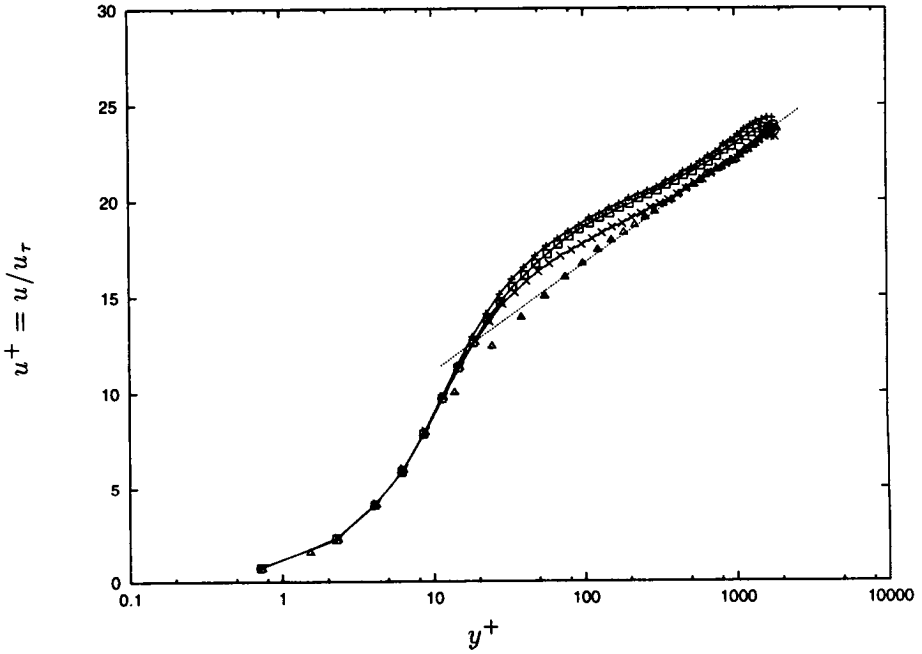
FIGURE 2.   Mean velocity profiles at $Re_b = 38000$. ········ log law; —□— Smagorinsky (SMAG1); -+- dynamic (DSMAG1); —×— no model (CDNS1); △ spectral LES of Piomelli (1993).
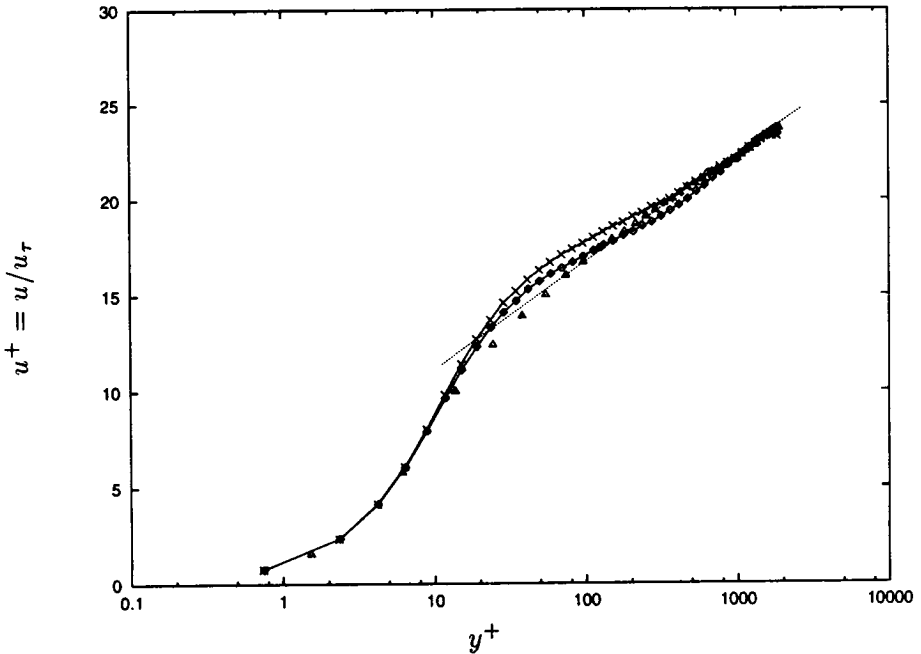
FIGURE 3.   Mean velocity profiles at $Re_b = 38000$. ········ log law; —×— no model (CDNS1); —◇— proposed model; △ spectral LES of Piomelli (1993).
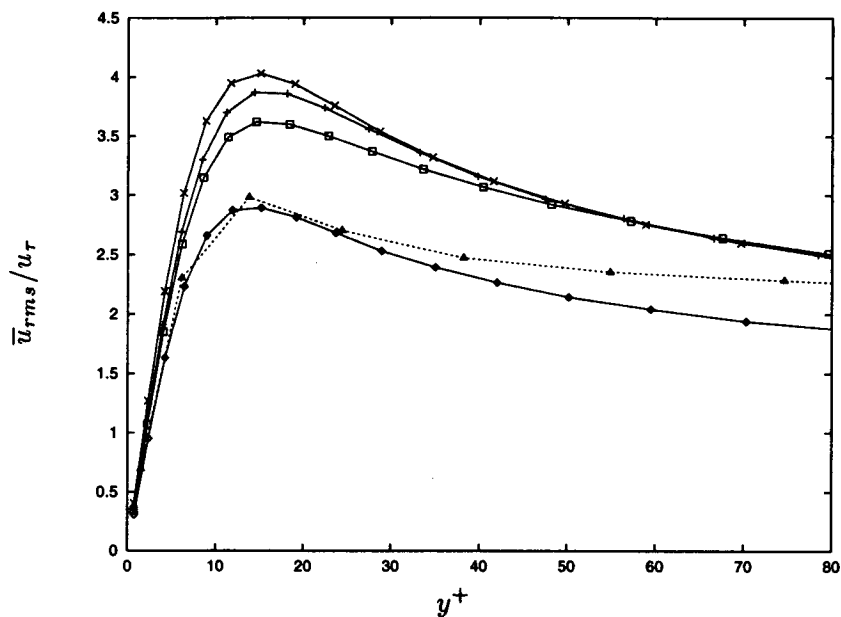
FIGURE 4.   RMS of the *resolved* streamwise velocity at $Re_b = 38000$ in wall units. —□— Smagorinsky (SMAG1); - + -   dynamic (DSMAG1); —×—   no model (CDNS1); —◇—   proposed model (NEWM3); △   spectral LES of Piomelli (1993).
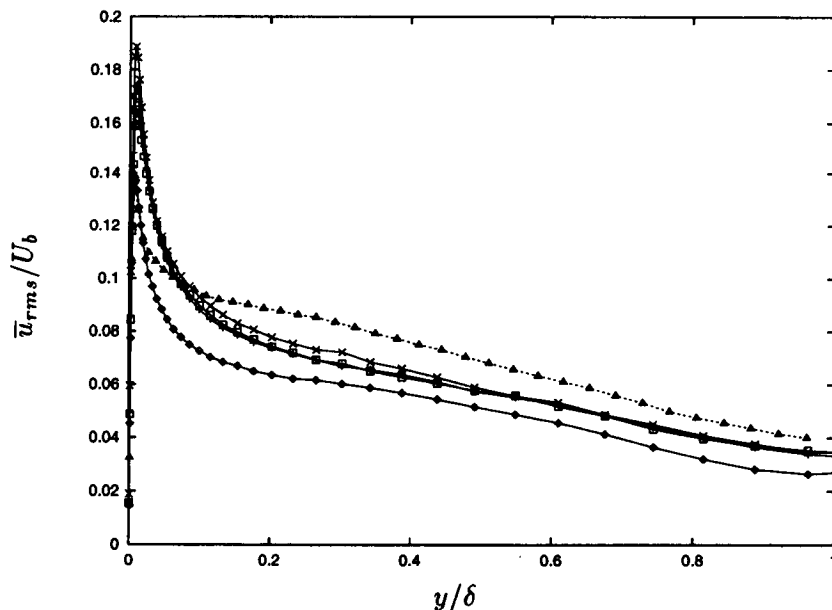
FIGURE 5.   RMS of the *resolved* streamwise velocity at $Re_b = 38000$ in global units. —□— Smagorinsky (SMAG1); - + -   dynamic (DSMAG1); —×—   no model (CDNS1); —◇—   proposed model (NEWM3); △   spectral LES of Piomelli (1993).
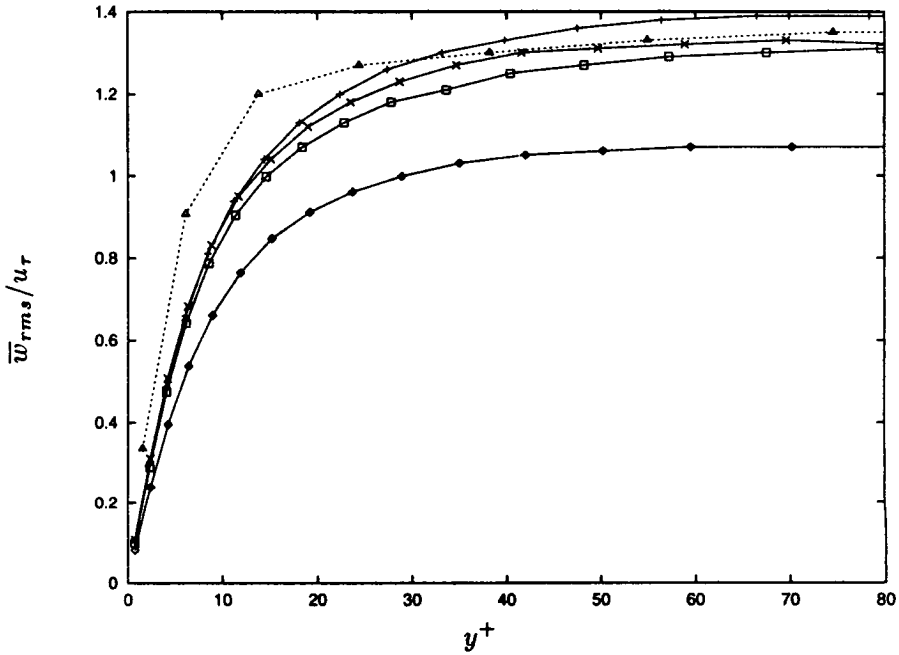
FIGURE 6.   RMS of *resolved* spanwise velocity at $Re_b = 38000$ in wall units.
—□— Smagorinsky (SMAG1); - + -   dynamic (DSMAG1); —×—   no model
(CDNS1); —◇—   proposed model (NEWM3); △   spectral LES of Piomelli (1993).
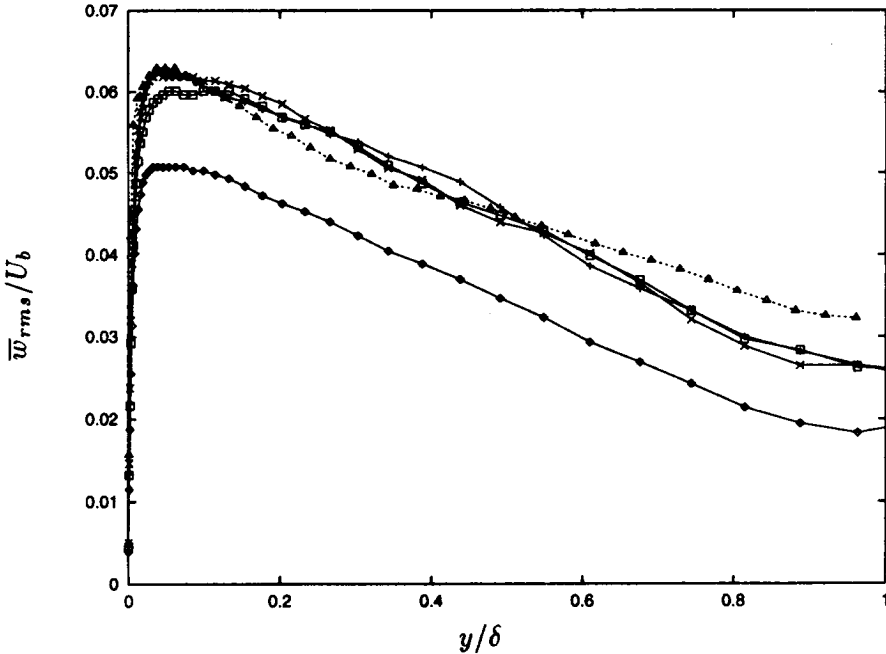
FIGURE 7.   RMS of the *resolved* spanwise velocity at $Re_b = 38000$ in global
units. —□—   Smagorinsky (SMAG1); - + -   dynamic (DSMAG1); —×—   no
model (CDNS1); —◇—   proposed model (NEWM3); △   spectral LES of Piomelli
(1993).
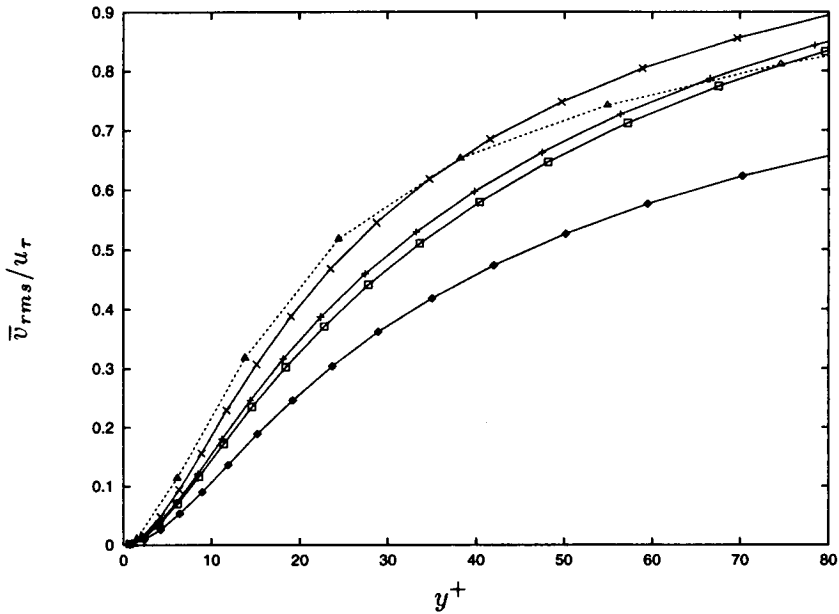
FIGURE 8. RMS of the *resolved* wall-normal velocity at $Re_b = 38000$ in wall units. ──□── Smagorinsky (SMAG1); – + – dynamic (DSMAG1); ──×── no model (CDNS1); ──◇── proposed model (NEWM3); △ spectral LES of Piomelli (1993).
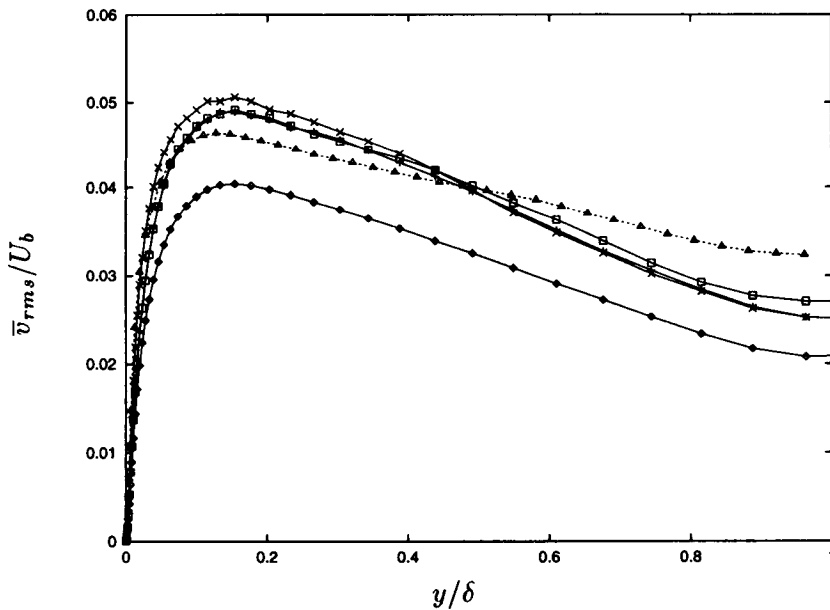
FIGURE 9. RMS of the *resolved* wall-normal velocity at $Re_b = 38000$ in global units. ──□── Smagorinsky (SMAG1); – + – dynamic (DSMAG1); ──×── no model (CDNS1); ──◇── proposed model (NEWM3); △ spectral LES of Piomelli (1993).

A significant portion of the energy resides in SGS in the proposed model (44%). The new model extracts considerable energy from the large scales, creating energetic subgrid scales. But in the Smagorinsky and dynamic models, the energy piles up in the large scales because the SGS stress is unable to drain enough energy from the large scales. As a result, the skin friction is under-predicted since the dissipation and skin friction are directly related.

	η
Smagorinsky (SMAG1)	0.08
Dynamic Smag. (DSMAG1)	0.07
New Model (DNEWM3)	0.44

TABLE 3: Fraction of turbulent kinetic energy in the subgrid scales.

Figure 13 shows the mean SGS dissipation rate $< \epsilon_{SGS} > = < \tau_{ij}\overline{S}_{ij} >$ near the wall for various models. The dissipation rate is normalized by U_b instead of u_τ, which is different for each model. The dynamic model has the smallest peak and the smallest overall SGS dissipation rate. For fully developed channel flow the total dissipation rate (viscous+SGS) is proportional to the pressure drop. Since the dynamic model has the lowest skin friction, the total dissipation is also the smallest. Also, the total dissipation rate from the Smagorinsky and dynamic models are smaller than the coarse DNS (since skin friction is smaller), but the total dissipation rate of the new model is larger. Figures 14 & 15 show the time series of dissipation rate at $x = 1.25\pi$, $z = 0.25\pi$ and $y^+ = 2$, and 12. Significant backscatter of energy is seen in the buffer region and beyond. In the region close to the wall, $y^+ = 2$, the dissipation rate is mostly negative. Away from the walls, backscatter is highly intermittent and, interestingly, a large backscatter follows a large forward scatter. The backscatter in the new model is an integral part of the model and not modeled separately as in stochastic backscatter models. Backscatter is approximately 50% of the net SGS dissipation and 40% of the volume exhibits backscatter.

In the previous discussion of the dynamic model (DSMAG1), the box filter with $\overline{\Delta} = 2h$ was used in the homogeneous directions. Piomelli used a Fourier cutoff test filter in which the energy in the upper half of the wavenumbers in the homogeneous directions was set to zero. The ratio of length scales (test/grid) $\widetilde{\overline{\Delta}}/\overline{\Delta}$ was 2, which was found optimal by Germano *et al.* (1991). However, there was no explicit use of test filter length scale $\widetilde{\overline{\Delta}}$. If the grid filter in LES is a box filter then $\overline{\Delta} = h$, and the optimal ratio implies $\widetilde{\overline{\Delta}} = 2h$. On the other hand, the grid cannot resolve wavelength smaller than $2h$, so the filter width ought to be $\overline{\Delta} = 2h$, thus $\widetilde{\overline{\Delta}} = 4h$. To address these issues, three filters were considered, including a five point filter in the homogeneous directions with $\widetilde{\overline{\Delta}} = 4h$, a filter with $\widetilde{\overline{\Delta}} = 2h$ in all directions (volume filter), and a Fourier filter in the homogeneous directions. The differences in the
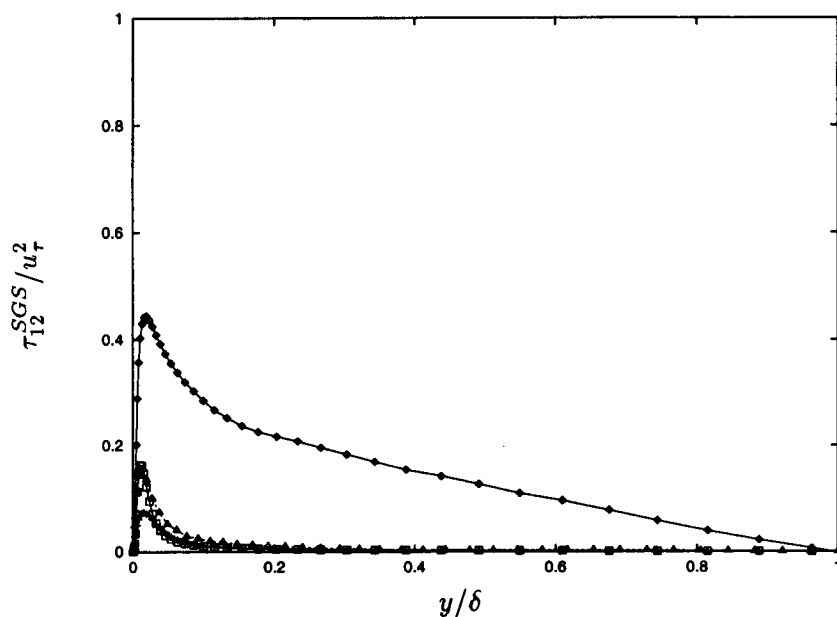
FIGURE 10. SGS shear stress at $Re_b = 38000$. —▫— Smagorinsky (SMAG1); -+- dynamic (DSMAG1); —◇— proposed model (NEWM3); △ spectral LES of Piomelli (1993).
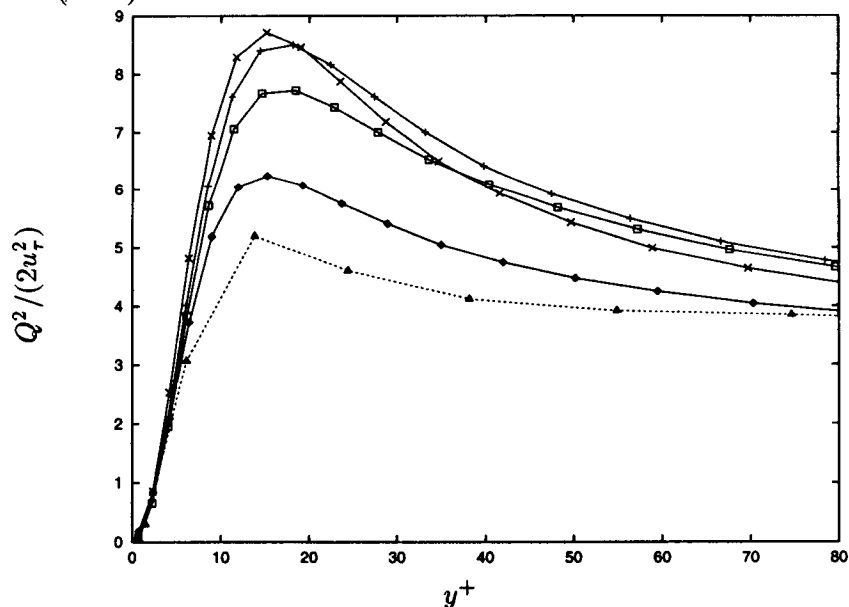

FIGURE 11. Total (resolved+SGS) turbulent kinetic energy (TKE) at $Re_b = 38000$ in wall units. Bardina's (1983) procedure has been used to estimate SGS contribution in the Smagorinsky and the dynamic model. —▫— Smagorinsky (SMAG1); -+- dynamic (DSMAG1); —×— no model (CDNS1); —◇— proposed model (NEWM3); △ *resolved* TKE of Piomelli's spectral LES (1993).
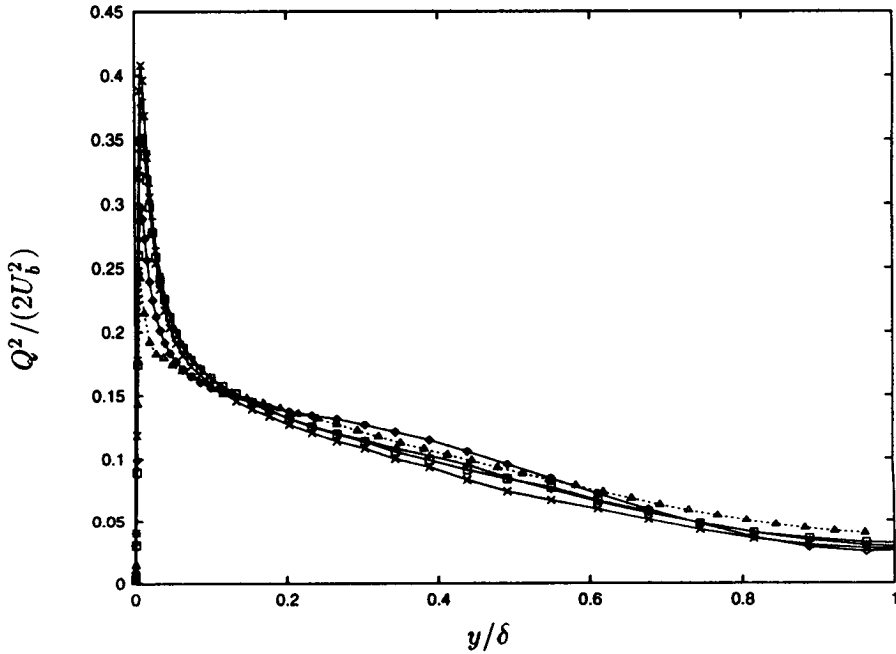
FIGURE 12. Total (resolved+SGS) turbulent kinetic energy (TKE) at $Re_b = 38000$ in global units. Bardina's (1983) procedure has been used to estimate SGS contribution in the Smagorinsky and the dynamic model. ―□― Smagorinsky (SMAG1); ‑+‑ dynamic (DSMAG1); ―×― no model (CDNS1); ―◇― proposed model (NEWM3); △ *resolved* TKE of Piomelli's spectral LES (1993).
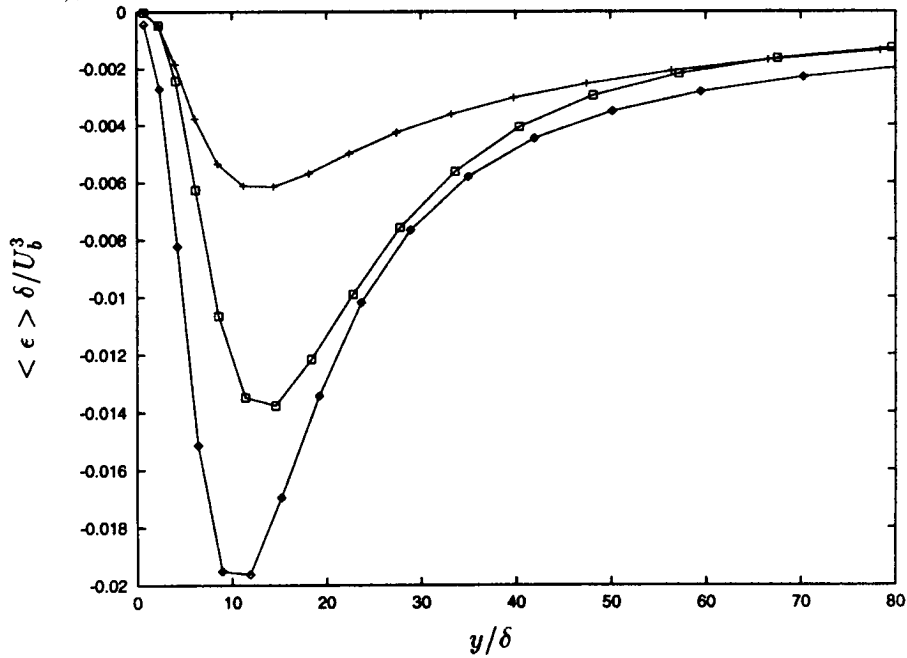
FIGURE 13. SGS dissipation rate at $Re_b = 38000$ in global units. ―□― Smagorinsky (SMAG1); ‑+‑ dynamic (DSMAG1); ―◇― proposed model (NEWM3).
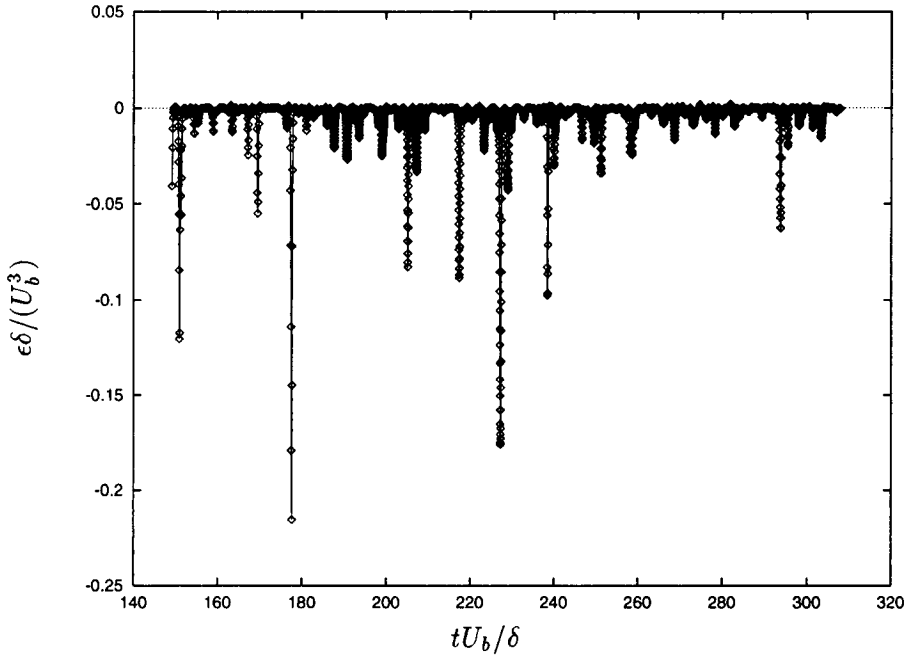
FIGURE 14. Time series of SGS dissipation rate at $Re_b = 38000$ for the proposed model (NEWM3) at $x = 1.25\pi, z = 0.25\pi$ and $y^+ = 2.3$. Positive values signify backscatter.
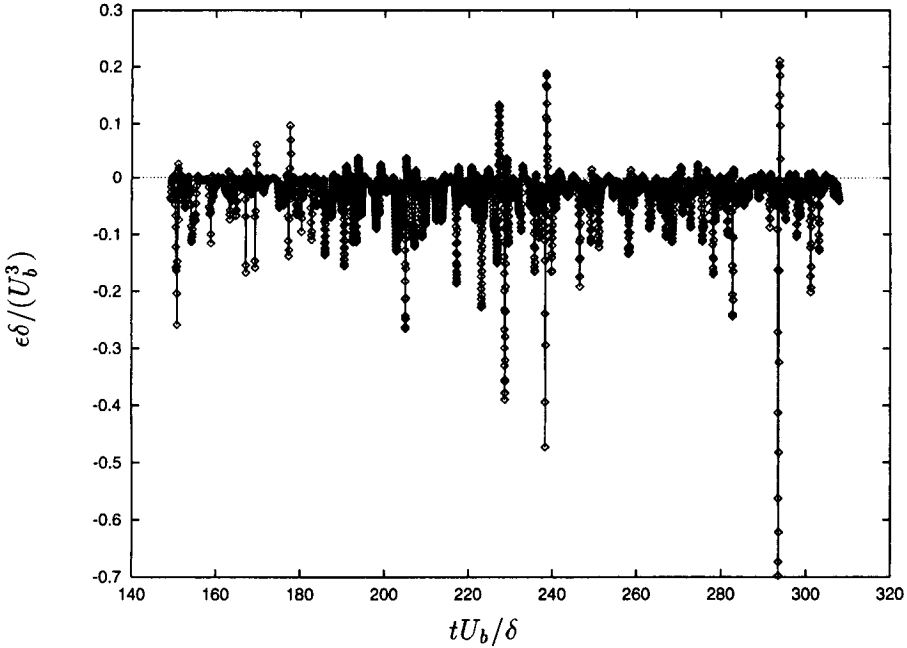
FIGURE 15. Time series of SGS dissipation rate at $Re_b = 38000$ for the proposed model (NEWM3) at $x = 1.25\pi, z = 0.25\pi$ and $y^+ = 12.0$. Positive values signify backscatter.

mean velocity profile and fluctuations were negligible. This apparent insensitivity of the dynamic model to the type of test filter suggests that most of the contribution to the dynamic coefficient C_s comes from wavenumbers in the vicinity of the grid cutoff.

The only parameter in the proposed model is the filter-grid ratio. $FGR = 0$ gives coarse DNS. If three neighboring points in each direction are employed to construct the filter, the maximum filter width is $2h$. In the current simulations same filter-grid ratio was used in defining the * and $^\frown$ operations. The dissipation is reduced considerably if the filter-grid ratio in the definitions of the * and $^\frown$ operations do not match. As shown earlier, if * corresponds to $FGR = 0$ and $^\frown$ corresponds to the grid filter, then Bardina's scale similarity model is recovered. For homogeneous turbulence the optimal FGR should be ≈ 1.0 if a box filter is used. For general inhomogeneous flows there is no clear optimal FGR, although it depends on the mesh size h. As mentioned earlier, the coefficients need not be based on the FGR, and the filter width can have directional dependence. In the present cases, the filter-grid ratio is taken to be a constant and same in all three directions. Three simulations were carried out using $FGR = 1.0$, $\sqrt{3}$, and 2.0. Increasing FGR corresponds to a larger filter width so the subgrid scales are more energetic. The mean velocity and skin friction are insensitive to variation in FGR. The effect of FGR is more pronounced in SGS stress and dissipation rate near the wall. As expected, an increase in FGR leads to larger SGS stresses and dissipation, thus smaller fluctuations in the filtered field. As far as total fluctuations are considered, $FGR = 2.0$ gives the best results. Figure 16 presents a plot of the fraction of turbulent kinetic energy in SGS versus FGR; the fraction of TKE in the SGS increases as $FGR^{0.3}$. For high Reynolds number homogeneous isotropic turbulence with a Kolmogorov energy spectrum, it is possible to estimate the turbulent kinetic energy in the subgrid scales.

$$TKE^{SGS} = \int_k^\infty E(k)\, dk \sim \epsilon^{2/3}\, k^{-2/3} \sim \epsilon^{2/3}\, \Delta^{2/3}$$

where the Kolmogorov spectrum $E(k) \sim \epsilon^{2/3}\, k^{-5/3}$ was used. The 2/3 slope is not obtained in the present LES; the subgrid-scales in the new model are highly anisotropic and the Reynolds number is too low.

3. Conclusion and future plan

A new non-eddy viscosity model has been presented in which the SGS stress is constructed by exciting the high wavenumbers of the filtered field. Its utility was demonstrated for plane channel flow with second order finite differences. The model provides a good representation of the SGS dissipation and predicts total stresses more accurately, especially at high Reynolds numbers in which a significant portion of the energy resides in the unresolved scales. The skin friction and centerline velocity are predicted accurately. The Smagorinsky and dynamic models produce lower net dissipation than the new model, leading to under-prediction of skin friction. At the mid-channel, all models produce similar fluctuations. Overall, the dynamic
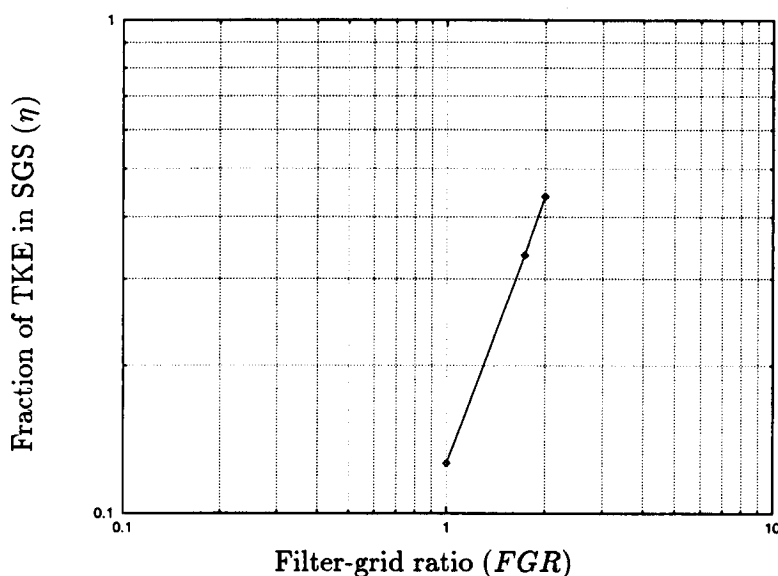
FIGURE 16. Fraction of turbulent kinetic energy in the subgrid-scales for various values of filter-grid ratio (FGR) in the proposed model.

model gives the worst results and is insensitive to the test filter. Piomelli (1993) obtained good results with a similar dynamic model but with a spectral method, so the present results suggest that the second order central differences contaminate the high wavenumber information used by the dynamic procedure. Fluctuations spectra were examined for aliasing errors but the effects were small.

A constant filter-grid ratio was used in the proposed model; however, more tests should be performed to study the effect of this parameter. Also, since backscatter is a prominent feature of this model, it should be tested in situations where backscatter is important such as transitional and geophysical flows. It could also be applied to the plane asymmetric diffuser problem for which other models under-predict separation (Kaltenbach 1994).

Finite difference simulations with better resolution need to be performed to investigate the effect of truncation errors. Also since the dynamic model seems to be sensitive to high wavenumber content, finite difference schemes with better spectral accuracy may be more successful.

The new model is efficient and easy to implement. In the present implementation, the new model takes 7% more CPU time than coarse DNS (same as Smagorinsky), whereas the dynamic model takes 30% more CPU time than coarse grid DNS, on a CRAY C90.

4. Acknowledgments

REFERENCES

BARDINA, J. 1983 Improved turbulence models based on large eddy simulation of homogeneous, incompressible, turbulent flows, *Ph. D. dissertation*, Dept. Mech. Engr., Stanford University, Stanford, California, USA.

CABOT, W. 1994 Local dynamic subgrid-scale models in channel flow. *Annual Research Briefs - 1994.* Center for Turbulence Research, NASA Ames/Stanford Univ. 43-159.

DEAN, R. B. 1978 Reynolds number dependence of skin friction and other bulk flow variables in two-dimensional rectangular duct flow. *J. Fluids Eng.* **100**, 215-223.

GERMANO, M. 1986 A proposal for a redefinition of the turbulent stresses in the filtered Navier-Stokes equations. *Phys. Fluids.* **29** (7), 2323-2324.

GERMANO, M., PIOMELLI, U., MOIN, P., & CABOT, W. H. 1991 A dynamic subgrid-scale eddy viscosity model. *Phys. Fluids.* A **3** (7), 1760-1765.

GHOSAL, S., LUND, T. S., MOIN, P., & AKSELVOLL, K. 1995 A dynamic localization model for large-eddy simulation of turbulent flows. *J. Fluid Mech.* **286**, 229-255.

HÄRTEL, C.& KLEISER, L. 1993 Energy Transfer between large and small scales in wall-bounded turbulent flows. *Engineering Applications of Large Eddy Simulations FED ASME.* **162**, 21-28.

KALTENBACH, H.-J. 1994 Large-eddy simulation of flow through a plane, asymmetric diffuser. *Annual Research Briefs - 1994.* Center for Turbulence Research, NASA Ames/Stanford Univ. 175-184.

KIM, J., MOIN, P., & MOSER, R. 1987 Turbulence statistics in fully developed channel flow at low Reynolds number. *J. Fluid Mech.* **177**, 133-166.

LILLY, D. K. 1992 A proposed modification of Germano subgrid-scale closure method. *Phys. Fluids.* A **4 (3)**, 633-635.

LUND, T. S., GHOSAL, S., & MOIN, P. 1993 Numerical experiments with highly-variable eddy viscosity models. *Engineering Applications of Large Eddy Simulations FED ASME.* **162**, 7-11.

PIOMELLI, U. 1993 High Reynolds number calculations using the dynamic subgrid-scale stress model. *Phys. Fluids.* A 5(6), 1484-1490.

SHAH, K. 1996 Large eddy simulation of flow past a cubic obstacle, *Ph. D. dissertation*, under preparation, Dept. Mech. Engr., Stanford University, Stanford, California, USA.

VAN DRIEST E. R. 1956 On the turbulent flow near a wall. *J. Aerospace Sci.* **23**, 1007-1011.

YANG, K.-S., & FERZIGER, J. H. 1993 Large eddy simulation of turbulent flow in a channel with a surface-mounted two-dimensional obstacle using a dynamic subgrid-scale model. *AIAA Journal.* **31**, 1-8.

Experiments with explicit filtering for LES using a finite-difference method

By T. S. Lund & H.-J. Kaltenbach

1. Motivation and objectives

The equations for large-eddy simulation (LES) are derived formally by applying a spatial filter to the Navier-Stokes equations. The filter width as well as the details of the filter shape are free parameters in LES, and these can be used both to control the effective resolution of the simulation and to establish the relative importance of different portions of the resolved spectrum. In spectral simulations, the natural choice for the LES filter is the truncation associated with the use of a finite number of modes. This choice is "automatic" in the sense that no explicit filtering operations need to be performed during the course of the simulation. In other words, selection of the number of modes dictates the range of scales that can be resolved, and the usual numerical procedures ensure that the higher frequencies generated by nonlinear interactions are excluded from the simulation.

An analogous, but less well justified, approach to filtering is more or less universally used in conjunction with LES using finite-difference methods. In this approach, the finite support provided by the computational mesh as well as the wavenumber-dependent truncation errors associated with the finite-difference operators are assumed to define the filter operation. This approach has the advantage that it is also "automatic" in the sense that no explicit filtering operations need to be performed.

While it is certainly convenient to avoid the explicit filtering operation, there are some practical considerations associated with finite-difference methods that favor the use of an explicit filter. Foremost among these considerations is the issue of truncation error. All finite-difference approximations have an associated truncation error that increases with increasing wavenumber. These errors can be quite severe for the smallest resolved scales, and these errors will interfere with the dynamics of the small eddies if no corrective action is taken. Years of experience at CTR with a second-order finite-difference scheme for high Reynolds number LES has repeatedly indicated that truncation errors must be minimized in order to obtain acceptable simulation results.

Explicit filtering can be used as a means of controlling truncation error by simply removing from the simulation the smallest motions that would otherwise be affected by the error. To implement this approach, an LES filter with a characteristic width greater than the mesh spacing is applied explicitly at the conclusion of each time step during the course of the simulation. The filter operation insures that the error-prone high-frequency solution components are either removed entirely or diminished in amplitude. The ratio of the filter width to the mesh spacing provides a useful measure of the degree to which the truncation error is reduced. As the filter width ratio becomes large the finite-difference approximations can be reasonably accurate over the entire range of scales passed by the filter.

Explicit filtering can also be used to control aliasing, interpolation, and subgrid-scale modeling errors. Aliasing errors arise from the nonlinear generation of frequencies higher than the maximum which the mesh can support. These unresolvable high frequencies "alias" to lower, resolved frequencies. It turns out that for bilinear products, one of the interaction partners must be in the upper third of the wavenumber range in order for the product to alias. Thus aliasing error can be reduced or eliminated by reducing the energy in the upper wavenumber portion of the spectrum. In particular, aliasing error will be eliminated entirely for a filter width ratio greater than or equal to 1.5 when a sharp cutoff filter is used (i.e., the usual 3/2 rule). Interpolation errors are analogous to finite-difference truncation errors in that their magnitude increases with increasing wavenumber. These errors will be reduced in much the same way as the finite-difference truncation error when the solution is filtered. Finally, explicit filtering can be used to control subgrid-scale modeling errors that arise in the implementation of the dynamic subgrid-scale model (Germano *et al.* 1991). In order to compute the subgrid-scale model coefficient, the dynamic model samples turbulent stresses generated by a band of the smallest motions resolved in the simulation. This is also the region of the spectrum where the truncation, interpolation, and aliasing errors are the most severe. If no explicit filtering is performed, the stresses sampled in the dynamic model will be contaminated with the various sources of numerical error, which could lead to erroneous estimates for the subgrid-scale model coefficient.

While the potential advantages of explicit filtering are rather clear, there is a significant cost associated with its implementation. In particular, explicit filtering reduces the effective resolution of the simulation compared with that afforded by the mesh. The resolution requirements for LES are usually set by the need to capture most of the energy-containing eddies, and if explicit filtering is used, the mesh must be enlarged so that these motions are passed by the filter. In simpler terms, the mesh must be expanded in each direction by a factor equal to the filter width ratio in order to retain the effective resolution of an unfiltered simulation. This is a significant overhead for a three-dimensional simulation; a filter width ratio of 2 increases the cost of the simulation by a factor of 8, whereas a filter ration of 3 increases the cost by a factor of 27!

Given the high cost of explicit filtering, the following interesting question arises. Since the mesh must be expanded in order to perform the explicit filter, might it be better to take advantage of the increased resolution and simply perform an unfiltered simulation on the larger mesh? The cost of the two approaches is roughly the same, but the philosophy is rather different. In the filtered simulation, resolution is sacrificed in order to minimize the various forms of numerical error. In the unfiltered simulation, the errors are left intact, but they are concentrated at very small scales that could be dynamically unimportant from a LES perspective. Very little is known about this tradeoff and the objective of this work is to study this relationship in high Reynolds number channel flow simulations using a second-order finite-difference method.

2. Accomplishments

2.1 Numerical method

The second-order staggered mesh scheme of Harlow and Welch (1965) was chosen for this work due to its popularity for contemporary LES. This scheme has a number of practical advantages including mass, momentum, and kinetic energy conservation, coupled pressure and velocity fields, ease of implementation, and straightforward extension to generalized coordinate systems. On the down side, the scheme is of low accuracy and is susceptible to point-to-point oscillations. In an attempt to assess the role of truncation error, the scheme was tested for direct numerical simulation of low Reynolds number turbulent channel flow by Choi *et al.* (1992) and Choi and Moin (1994). They found good agreement in mean and rms velocity profiles when compared with pseudo spectral simulation results on the same mesh. However, they needed to double the mesh in all three directions in order to obtain a good comparison of the vorticity fluctuation profiles. Rai and Moin (1991) performed similar tests but used a much coarser grid for the finite-difference calculation (factor of 14 fewer points than the spectral simulation). They were primarily interested in testing higher-order upwind schemes and found these to be superior to the second-order scheme on the coarse mesh.

Recent experience with the second-order scheme at CTR for high Reynolds number LES has lead to a different conclusion. The scheme has been found to produce acceptable results, but only when rather fine meshes are used (Akselvoll and Moin, 1995; Kaltenbach, 1994, Lund and Moin, 1995). The difference in behavior for LES is probably due to the increased energy level in the smallest resolved scales. These scales make a non-negligible contribution to the low-order statistics in LES, and thus the effects of numerical error are more apparent in this case.

It is hypothesized that explicit filtering should improve the second-order simulation results by removing a portion of the numerical error. It is already known that the simulation results improve as the mesh is refined, and thus the relevant question is whether a greater benefit can be realized through explicit filtering.

2.2 High Reynolds number channel flow test case

The test case for this study is turbulent channel flow at a Reynolds number of 47100 based on centerline velocity and channel half-width (a friction velocity Reynolds number of 2000). This particular Reynolds number was chosen due to the availability of pseudo spectral results (Piomelli, 1993) that are used as a basis for comparison. Piomelli used a computational domain of height 2δ, length $(5\pi/2)\delta$, and width $(\pi/2)\delta$. Fourier expansions were used in the homogeneous direction, whereas a Chebychev expansion was used in the normal direction. The advective terms were cast in skew-symmetric form and no explicit de-aliasing was performed. 64 Fourier modes were used in the streamwise direction, 80 were used in the spanwise direction, and 80 Chebychev modes were used in the normal direction.

The finite-difference mesh is identical to that used in the pseudo spectral simulation with the exception of the distribution of points in the normal direction. The

pseudo spectral simulation uses a cosine mapping function to distribute the colloca-
tion points in the normal direction. While this distribution is necessary in order to
make use of the fast Fourier transform, it leads to a mesh that is strongly stretched
in the near-wall region. Experience with this type of mesh for finite-difference cal-
culations indicates that the grid spacing becomes too coarse within a short distance
from the wall. In order to avoid this problem, the standard hyperbolic tangent
mapping is used. The hyperbolic tangent mesh is designed so that the spacing of
the first mesh cell away from the wall as well as the spacing at the channel centerline
are very close to those of the cosine mesh. It turns out that these constraints can
be met only by increasing the number of points in the normal direction from 81 to
141.

The mesh spacings in wall units are $\Delta x^+ = 250$, $\Delta y^+_{\min} = 1.6$, $\Delta y^+_{\max} = 150$, and
$\Delta z^+ = 40$. In terms of channel half-heights the mesh spacings are $\Delta x/\delta = 0.12$,
$\Delta y_{\min}/\delta = 8.0 \times 10^{-4}$, $\Delta y_{\max}/\delta = 0.075$, and $\Delta z/\delta = 0.02$.

Both the spectral and finite-difference simulations make use of the dynamic
subgrid-scale model (Germano *et al.* 1991) with both test filtering and averag-
ing of the equations for the model coefficient performed in planes parallel to the
wall. The ratio of the test filter to LES filter is fixed at 2 in all simulations. In cases
where an explicit LES filter is used, the test filter is simply adjusted to be twice as
wide as the LES filter. The test filter operation is applied in physical space and the
stencil width is varied to accommodate filters of various widths.

The simulations are performed with a fixed mean pressure gradient. The mass
flow is not constrained and, therefore, will differ from simulation to simulation.

2.3 Explicit filtering strategy

Explicit filtering is restricted to the streamwise and spanwise directions. Several
factors dictate this choice. Foremost of these is that the mesh in the wall-normal
direction is non-uniform and, therefore, the filtering and derivative operation do
not commute. Corrections can be applied in this case (Ghosal and Moin, 1994),
but the effectiveness of these has not yet been established. Second, the cost of
performing simulations with large filter width ratios is not as severe if the mesh is
only expanded in two directions. Finally, except for the core region, the wall-normal
mesh is substantially finer than the other two directions. It is therefore plausible
that the dominant sources of error arise from the streamwise and spanwise directions
and not the normal direction. Indeed in a related study (Lund *et al.* 1995), it was
found that refining the wall-normal mesh while leaving the other two directions
unchanged resulted in very little improvement in the computed statistics. The
same experiment applied to the other two directions, however, lead to a marked
improvement in the results.

A sharp spectral cutoff is used for the explicit filter. This choice is dictated
primarily by the desire to maintain kinetic energy conservation. The sharp cutoff
filter does not alter the non-linear energy transfer since this term is the convolution
of the velocity with the advective terms. If the velocity has no energy beyond
the cutoff wavenumber, then the energy transfer is the same whether or not the
advective terms are filtered with the sharp cutoff. Smooth filters do not share

Case	Mesh			Filter	Effective resolution		
	N_x	N_y	N_z	ratio	N_x	N_y	N_z
A	64	141	80	1.0	64	141	80
B	96	141	120	1.5	64	141	80
C	192	141	240	3.0	64	141	80
D	96	141	120	1.0	96	141	120
E	192	141	240	1.0	192	141	240

Table 1. Mesh and effective resolution for the various simulations.

this property and a non-physical energy drain will result if they are used. Energy conservation for simulations filtered with the sharp cutoff was verified in filtered simulations of isotropic turbulence.

Cutoff filtering is performed with fast Fourier transforms. The current flow solver uses a third-order Runge-Kutta time stepping algorithm and the velocity field is explicitly filtered at the conclusion of each of the three substeps. The computational overhead for the filtering operation is roughly 30%.

2.4 Results from the explicitly filtered simulations

Simulations were run with filter width ratios of 1.0, 1.5, and 3.0 (refer to Table 1.) The mesh was enlarged in the streamwise and spanwise directions by a factor equal to the filter width ratio in each case so that the effective resolution was constant. The modified wavenumber diagram for these simulations are shown in Fig. 1. The chain-dashed vertical line denotes the fixed effective resolution, while the solid curves to the left of this line show the modified wavenumber distributions for the various levels of filtering. When no filter is applied (lowest solid curve in Fig. 1) considerable truncation error is evident for the upper half of the wavenumber range. As the filter width ratio is increased, the situation improves. The error might seem to be acceptable for a filter width ratio of 3.

Figure 2 shows a comparison of the mean velocity profiles from the explicitly filtered simulations, plotted in wall coordinates. The pseudo spectral results of Piomelli (1993) are also included for reference. Starting with the unfiltered simulation, it is seen that the velocity profile deviates strongly from the accepted log-law. Although a logarithmic region is present, the slope is too low and intercept is overpredicted by more than 100%. The mass flow is also overpredicted by 6.3% compared with the correlations of Dean (1978).

A comparison of the unfiltered case with the pseudo spectral simulation provides some insight regarding the role of truncation errors when the second-order scheme is used for high Reynolds number LES. From Fig. 2 it is clear that the second-order scheme is not able to reproduce even the lowest order statistics when compared with a pseudo spectral simulation at the same resolution. Although this might be
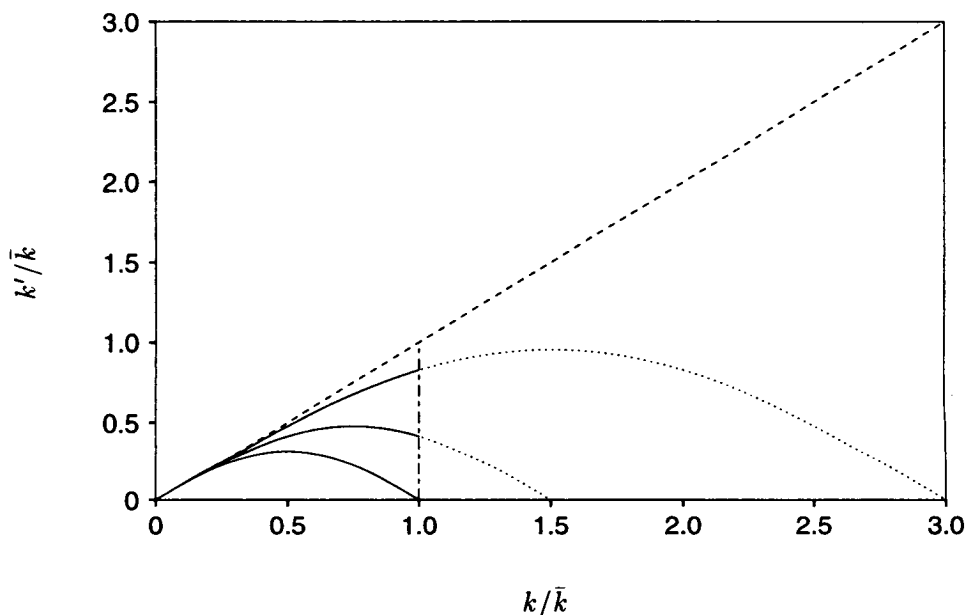
FIGURE 1. Modified wavenumber diagram for the various simulations. From bottom to top the solid lines are for filtered simulations using filter width ratios of 1.0, 1.5, and 3.0, respectively. The vertical chain-dashed line represents the effective resolution of the filtered simulations which was held fixed by expanding the mesh by factor equal to the filter width ratio in each case. From bottom to top, the dotted curves show the modified wavenumber distributions for the unfiltered simulations performed on the meshes expanded by factors of 1.5 and 3.0, respectively. The dashed line is the exact distribution that is achieved with a pseudo spectral method.

expected, it is in contrast to the findings of Choi *et al.* (1992) who obtained a good match with pseudo spectral results for low Reynolds number direct numerical simulations (DNS) of channel flow. As discussed in the introduction, the shift in behavior is suspected to result from a relative increase in numerical error in the LES resulting from the substantial increase in energy in the smallest resolved length scales. The relatively good performance of the second-order scheme in the DNS of Choi *et al.* (1992) was probably aided further by the fact that the DNS was very well resolved. Kim, Moin and Moser (1987) reported no significant change of their spectral DNS results when they coarsened the resolution in the streamwise and spanwise directions by approximately 30%.

Returning to the curves in Fig. 2, it is clear that filtering improves the mean velocity profile. In particular, the log-law intercept decreases toward the usual value and the slope improves. A noticeable wake develops in the outer region of the velocity profile for the case with a filter width ratio of 3. This wake is somewhat larger than the one observed in the pseudo spectral results, and it could be a spurious effect resulting from truncation errors associated with differentiation in
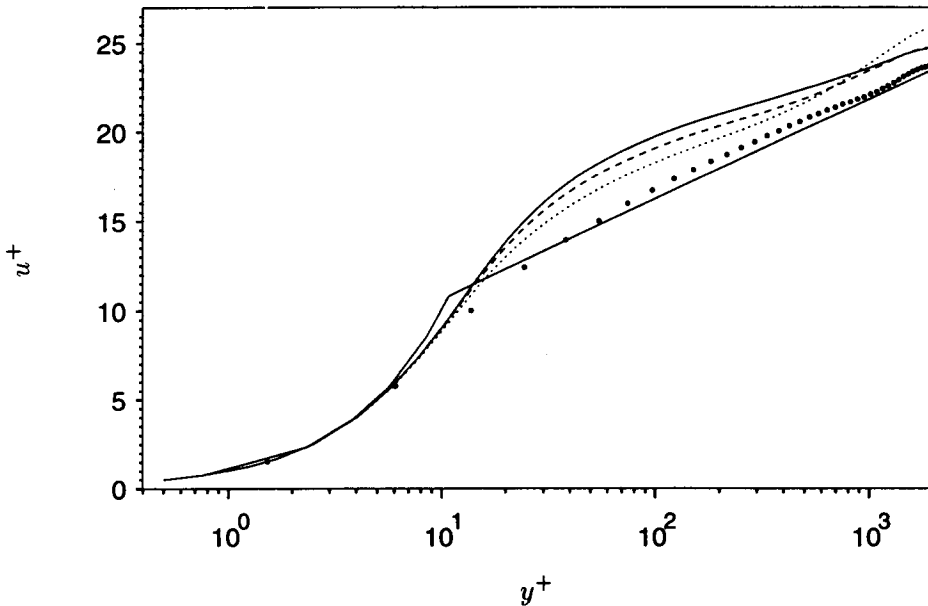
FIGURE 2. Mean velocity profiles from the explicitly filtered simulations. ——— : filter width ratio 1.0; ———— : 1.5; ········ : 3.0; • : pseudo spectral results of Piomelli (1993). The viscous sublayer ($u^+ = y^+$) and log-law ($u^+ = 2.44\ln(y^+) + 5.0$) solutions are also shown for reference.

the wall-normal direction. Explicit filtering is not performed in this direction, and the wall-normal mesh is somewhat coarse in the vicinity of the channel centerline. A simulation with a 25% refinement of the wall-normal mesh spacing was found to give a slightly smaller wake.

Although explicit filtering clearly improves the mean velocity profile, the rate of convergence to the pseudo spectral results appears to be rather slow. Significant errors still exist for a filter width ratio of 3, and a simple extrapolation of these results would seem to indicate that a filter width ratio as large as 6 would be required to recover the standard log-law.

Figure 3 shows the velocity fluctuation profiles plotted in wall coordinates. Starting with the unfiltered case, it is apparent that the second-order scheme is unable to reproduce the pseudo spectral results at high Reynolds number. The streamwise fluctuation is overpredicted, and the other two components are underpredicted. This exaggerated near-wall anisotropy is characteristic of the second-order scheme when the mesh is too coarse. When explicit filtering is used, the results are seen to improve. The streamwise velocity fluctuation is reduced and the anisotropy is improved. Once again, the rate of convergence to the pseudo spectral results is slow, and it appears that a filter width ratio in excess of 3 is required to recover spectral-like accuracy.

As discussed in the introduction, explicit filtering can improve the dynamic model
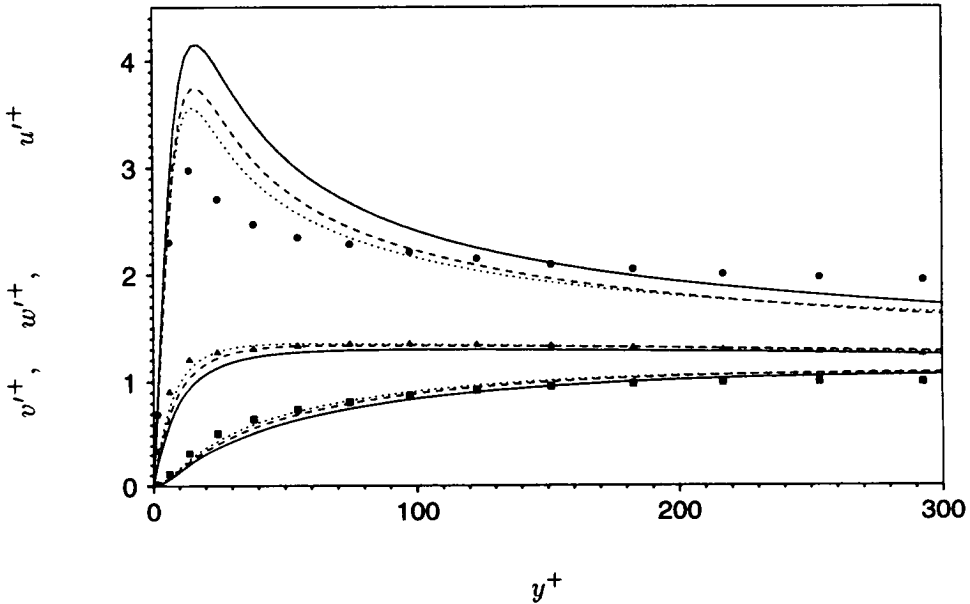
FIGURE 3.   Velocity fluctuation profiles from the explicitly filtered simulations.
———— : filter width ratio 1.0; —— —— : 1.5; ········ : 3.0; •, ▪, and ▴ : u'^+, v'^+, and w'^+ from the pseudo spectral calculation of Piomelli (1993).

calculation of the subgrid-scale model constant since the scales that it samples will be better resolved. This effect is demonstrated in Fig. 4 (a) where the subgrid-scale shear stress is plotted in the near-wall region. When no explicit filter is used, the subgrid-scale shear stress is underpredicted by about a factor of 2 when compared with the value from the pseudo spectral simulation. Although it can not be seen from Fig. 4 (a), the stress is too low over the entire channel. Filtering improves this situation by increasing the stress level throughout the channel. When a filter width ratio of 3 is used, the stress is still about 20% low at the maximum but is very close to the pseudo spectral prediction over much of the rest of the channel.

One interesting feature of the subgrid-scale shear stress distributions is the discrepancy in the location of the maximum value between the finite-difference and pseudo spectral calculations. The peak value from the pseudo spectral simulation is at roughly 12 wall units, whereas a maximum does not occur until about 30 wall units in the finite-difference simulation. The position of the maximum in the finite-difference simulation is insensitive to filter width ratio, which seems to indicate that the discrepancy is not a result of truncation error from the streamwise or spanwise directions. The discrepancy could result from wall-normal truncation error in the finite-difference calculation although this would seem unlikely given the very fine mesh in the near-wall region. At the same time, the collocation points near the wall are much more coarsely spaced in the pseudo spectral simulation and this may affect the prediction of the stress maximum.
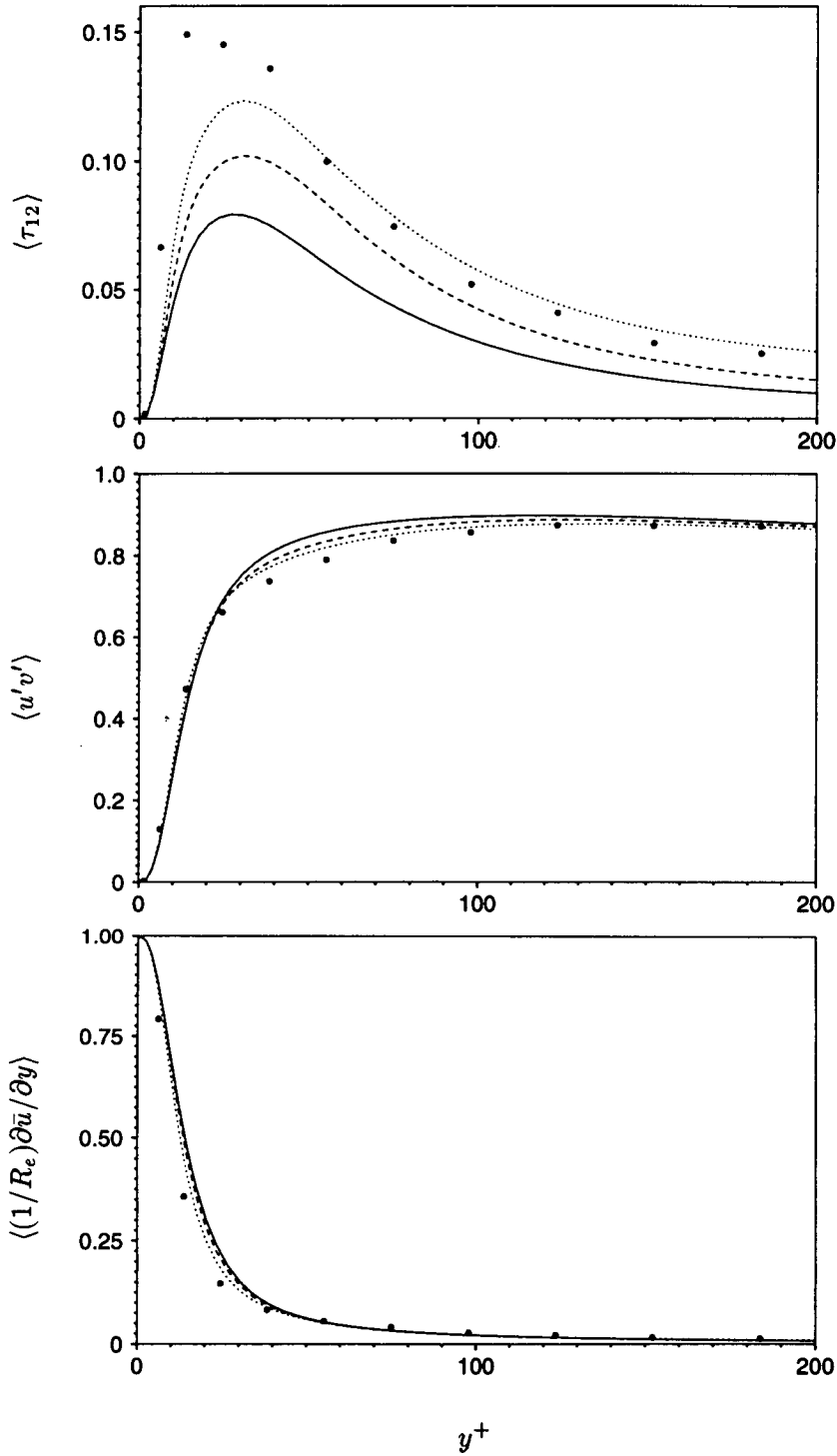
FIGURE 4.   Shear stress profiles from the explicitly filtered simulations. (a): subgrid-scale shear stress; (b): resolved shear stress; (c): viscous shear stress. In each case ——— : filter width ratio 1.0; - - - - : 1.5; ········ : 3.0; • : pseudo spectral results of Piomelli (1993).

The resolved and viscous shear stress profiles are shown in Figs. 4 (b) and (c). Both these stress components are generally over-predicted when no explicit filter is used. The results improve when the simulation is filtered, and the stresses from the case using a filter width ratio of 3 are in reasonable agreement with the pseudo spectral results.

2.5 Results from mesh refinement without explicit filtering

As discussed in the introduction, it is of interest to compare the effectiveness of explicit filtering against straightforward mesh refinement. The explicitly filtered simulations make use of a fine mesh but discard the high-frequency, error-prone scales. Simulations performed on the same fine mesh but without explicit filtering cost roughly the same but include a broader range of motions. The smallest of these are certainly polluted by numerical error, but they may be far enough removed from the energy-containing scales that the errors do not significantly effect the low-order statistics.

The tradeoff between explicit filtering and straightforward mesh refinement was studied by performing two additional simulations on the same meshes used in the explicit filter study, but without application of the filter. The parameters for these simulations are summarized in Table 1 and the corresponding modified wavenumber diagrams are shown in Fig. 1. Note that the modified wavenumber distributions for the refined simulations are identical to the filtered cases up to the cutoff wavenumber. Thus this portion of the spectrum is subject to the same numerical errors in both the filtered and refined cases. The difference between the two series is that the refined simulations include the motions intermediate between the LES filter and the mesh resolution limit. The additional scales are subject to considerable numerical error, but these errors are concentrated at increasing wavenumber as the level of refinement is increased. In particular, note that when the mesh is refined by a factor of 3, the modified wavenumber does not begin to decrease until 1.5 times the cutoff wavenumber (for the filtered simulations). The error increases appreciably only after this point and it is plausible that the useful resolution of this simulation is roughly 50% higher than in the corresponding filtered case.

Figure 5 shows a comparison of the mean velocity profile from the simulations with mesh refinement. The most noticeable change is a decrease in the mean velocity for the fixed wall shear as the mesh is refined. The quality of the logarithmic region is essentially unchanged, however, and its extent decreases with increasing resolution. If a straight line is fit through the "logarithmic" region, the log law intercept is found to improve as the resolution is increased and is roughly correct for a factor of 3 mesh refinement. The slope of the "logarithmic" region does not improve with mesh refinement, however, and the profile for the factor of 3 refinement displays an unusual oscillation about the expected logarithmic distribution. In comparing the profiles from the filtered and unfilter simulations performed on the same mesh (Figs. 2 and 5), it is clear that the log-law intercept is better predicted by the refined simulations without filtering, whereas the slope and extent of the log region is better predicted when the simulation is filtered. Thus it appears that a rough prediction of the correct profile shape can be achieved more efficiently via mesh refinement,

FIGURE 5. Mean velocity profiles from the refined simulations. ——— : no refinement; – – – – : 1.5 increase in resolution; ········ : 3.0 times increase in resolution; ● : pseudo spectral results of Piomelli (1993). The viscous sublayer $(u^+ = y^+)$ and log-law $(u^+ = 2.44 \ln(y^+) + 5.0)$ solutions are also shown for reference.

whereas the finer details of the velocity distribution may require the removal of at least some of the numerical error. It is also interesting to note that the profiles from the filtered simulations (Fig. 2) have evidently not saturated due to numerical error arising from the wall-normal direction. Figure 5 for the unfiltered simulations shows that it is possible to achieve roughly the correct log-law intercept without improving the wall-normal resolution. Thus it might be expected that the filtered simulation profiles shown in Fig. 2 would continue to improve if the filter width ratio were increased further.

Velocity fluctuation profiles from the mesh refinement series are shown in Fig. 6. The velocity fluctuations are seen to respond strongly to increased resolution with the streamwise component showing the greatest improvement. For a factor of 3 increase in resolution, the streamwise velocity fluctuation agrees very well with the pseudo spectral results in the vicinity of the maximum but appears to be somewhat low as the distance from the wall is increased. Both the wall-normal and spanwise velocity fluctuations increase in the near-wall region as the mesh is refined and appear to exceed the values from the pseudo spectral simulation. Part of this effect is due to increased variance coming from the additional small-scale motions supported by the refined meshes in the finite-difference simulations. In order to make an exact comparison, the finite-difference data in Fig. 6 should really have been filtered back to the resolution of the pseudo spectral simulation as the statistics
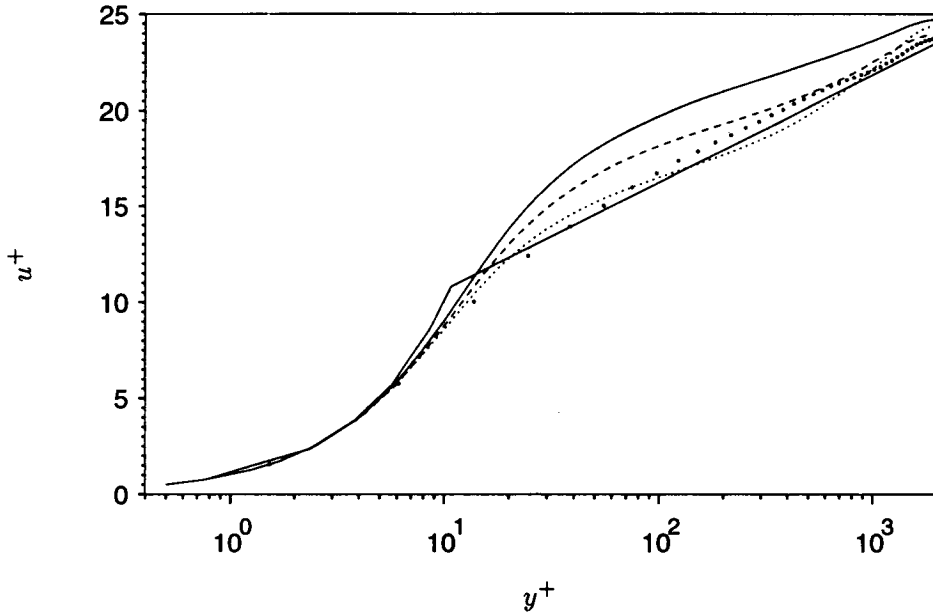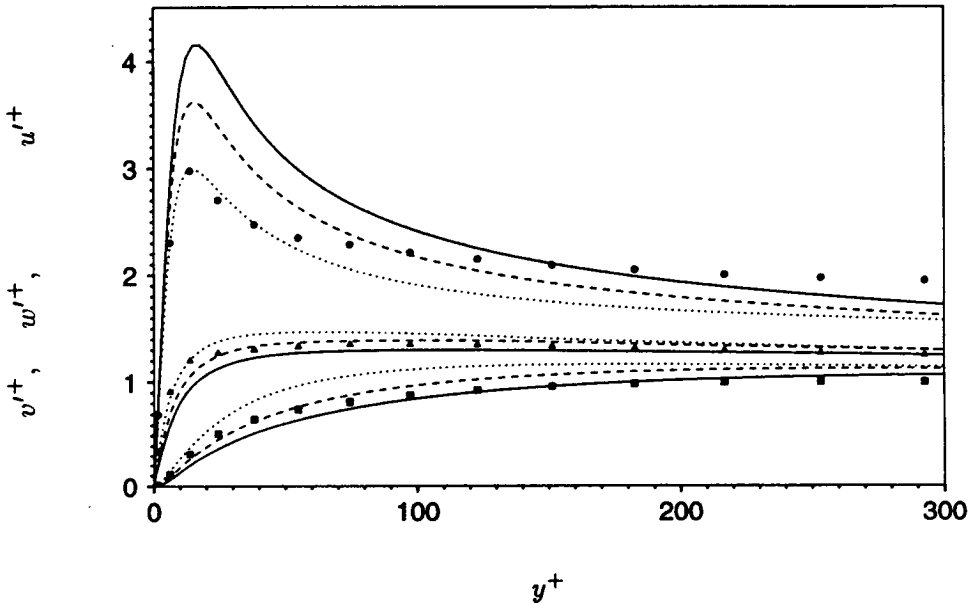
FIGURE 6.   Velocity fluctuation profiles from the refined simulations. ——— : no refinement; ---- : 1.5 times increase in resolution; ······· : 3.0 times increase in resolution; ●, ■, and ▲ : u'^{+}, v'^{+}, and w'^{+} from the pseudo spectral calculation of Piomelli (1993).

were accumulated. Such a filtering of the statistics might also lower the streamwise fluctuation and could affect the apparent agreement with the pseudo spectral results.

In comparing the filtered and unfiltered simulations run on the same mesh (Figs. 3 and 6), it is again apparent that the statistics improve faster when the mesh is simply refined. Unlike the mean velocity profile, however, there do not appear to be any anomalous features associated with the velocity fluctuations when the numerical error is not removed from the simulation.

2.6 Conclusions

The forgoing results have shown that explicit filtering can improve the accuracy of LES performed with a second-order accurate finite-difference scheme. In particular, the quality of the logarithmic region of the mean velocity profile for turbulent channel flow is improved as is the near-wall anisotropy of the velocity fluctuations. The dynamic subgrid-scale model estimation of the shear stress component is also improved. While the statistics clearly benefit from explicit filtering, the rate at which the solution improves is rather slow. Even a filter width ratio of 3 is evidently insufficient to produce results that compare well with a pseudo spectral simulation at the same effective resolution. Based on this result, it appears that a filter width ratio as great as 6 may be required to recover pseudo spectral accuracy if the same effective resolution is used. This is clearly impractical as the cost of performing

such a simulation with filtering in all three directions would be 216 times greater than would be dictated by the basic resolution requirements.

Mesh refinement without explicit filtering was found to improve the statistics at a greater rate when compared with the filtered simulations. This result seems to indicate that there is some benefit from including additional smaller scales in the simulations even if they are contaminated by numerical error. This is probably due to the fact that the error is pushed out to higher wavenumber where it has a relatively weak impact on the low-order statistics. Signs of the residual error are evident in the mean velocity profile, however, and it may not be possible to obtain highly accurate statistics without at least some level of numerical error removal.

The basic message from both the explicit filtering and mesh refinement simulations is that, while the results are clearly improved when numerical error is reduced, the cost of doing so via either mechanism is considerable. Although a factor of 3 refinement of the mesh gives acceptable agreement with pseudo spectral simulation results, this represents a factor of 27 increase in cost for a simulation that is refined in all three directions. Even in the present case of two-dimensional refinement, the cost is increased by nearly an order of magnitude. It is possible that a slight gain may be realized by combining some level of mesh refinement and explicit filtering. For example, it is possible that even better results could be obtained using a mesh that is expanded by a factor of three and then filtered using a filter width ratio of 1.5 so that the effective resolution is doubled. It is doubtful that this strategy would lead to a significant reduction in cost, however.

The results of the present study also hint that a higher-order scheme may be a more cost-effective means at achieving acceptable accuracy. For example, the relative truncation error in a fourth-order scheme can be reduced by the same amount as in the second-order simulation using a mesh expanded by a factor of 1.7 as opposed to a factor of 3. By the same token, the use of an explicit filter may be more effective at moderate filter width ratios when applied to a fourth-order scheme.

Until very recently, there did not exist a fourth-order fully-conservative finite-difference scheme for the three-dimensional Navier-Stokes equations that was applicable in generalized coordinates. Such a scheme has been developed by Y. Morinishi during the past several months and the details are reported in this volume. This scheme has not yet been tested for high Reynolds number LES, but tests in coarse DNS show that it is considerably more accurate than the second-order scheme. The fourth-order scheme will be used to repeat some of the present high Reynolds number channel flow simulations in the coming months. Depending on the outcome of these tests, it may be useful to investigate the use of explicit filtering in conjunction with the fourth-order scheme.

3. Future plans

The main focus during the coming year will be to incorporate the results of the present numerical experiments (and the work of Y. Morinishi) into the CTR complex flow LES program. At this point it looks as if the most promising avenue will be to

convert our existing second-order codes to Morinishi's fourth-order scheme. As more experience is gained with the fourth-order scheme, it will be determined whether or not explicit filtering is a cost-effective means of improving the simulation results. If so, methods will be perfected for explicit filtering in generalized coordinates. Filtering in such a situation is not straightforward since the filter must approximate a spectral cut-off in order to minimize errors in kinetic energy conservation. Filters based on Pade approximates have been suggested by Lele (1992) for this purpose. These ideas were used by Akselvoll (1995) to explicitly filter a LES simulation in a single coordinate direction. While the filter appeared to be effective, there were some ambiguities associated with the boundary conditions necessary to perform the operation. This issue will be addressed if explicit filtering is decided to be used in conjunction with the fourth-order scheme.

REFERENCES

AKSELVOLL, K., & MOIN, P. 1995 Large eddy simulation of turbulent confined coannular jets and turbulent flow over a backward facing step. Rep. TF-63, Thermosciences Div., Dept. Mech. Eng., Stanford University, Stanford, CA.

AKSELVOLL, K. 1995 Private communication

CHOI, H., MOIN, P. & KIM J. 1992 Turbulent drag reduction: studies of feedback control and flow over riblets. Rep. TF-55, Thermosciences Div., Dept. Mech. Eng., Stanford University, Stanford, CA.

CHOI, H. & MOIN, P. 1994 Effects of the computational time step on numerical simulation of turbulent flow. *J. Comp. Phys.* **113,** 1-4.

DEAN, R. B. 1978 Reynolds number dependence of skin friction and other bulk flow variables in two-dimensional rectangular duct flow. *Trans.* ASME I: *J Fluids Engng.* **100,** 215.

GERMANO, M., PIOMELLI, U., MOIN, P., & CABOT, W. H. 1991 A dynamic subgrid-scale eddy viscosity model. *Phys. Fluids A.* **3,** 1760-1765.

GHOSAL, S., LUND, T. S., MOIN, P. & AKSELVOLL, K. 1994 A dynamic localization model for large-eddy simulation of turbulent flows. *J. Fluid Mech.* **282,** 1-27.

HARLOW, F. H. & WELCH, J. E. 1965 Numerical calculation of time-dependent viscous incompressible flow of fluid with a free surface. *Phys. Fluids.* **8,** 2182-2189.

KALTENBACH, H.-J. 1994 Large eddy simulation of flow through a plane, asymmetric diffuser. In *Annual Research Briefs 1994*, Center for Turbulence Research, NASA Ames/Stanford Univ., 175-184.

KIM, J., MOIN, P. & MOSER, R. 1987 Turbulent statistics in fully developed channel flow at low Reynolds number. *J. Fluid Mech.* **177,** 133-166.

LELE, S. K. 1992 Compact finite difference schemes with spectral-like resolution. *J. Comp. Phys.* **103,** 16-42.

LUND, T. S. & MOIN, P. 1995 Large eddy simulation of a boundary layer on a concave surface. In *Proceedings of the tenth Symposium on Turbulent Shear Flows*, Penn. State Univ., 14-16 Aug. 1995, pp. 2.25-2.30.

LUND, T. S., KALTENBACH, H.-J., & AKSELVOLL, K. 1995 On the behavior of centered finite difference schemes for large eddy simulation, in *Proceedings of the sixth International Symposium on Computational Fluid Dynamics*, Lake Tahoe, NV, 4-8 September, 1995.

PIOMELLI, U. 1993 High Reynolds number calculations using the dynamic subgrid-scale stress model. *Phys. Fluids A.* **5**, 1484-1490.

RAI, M. M. & MOIN, P. 1991 Direct simulation of turbulent flow using finite-difference schemes. *J. Comp. Phys.* **96**, 15-53.

Large-eddy simulation of
flow past a circular cylinder

By R. Mittal

1. Motivation and objectives

Some of the most challenging applications of large-eddy simulation are those in complex geometries where spectral methods are of limited use. For such applications more conventional methods such as finite difference or finite element have to be used. However, it has become clear in recent years that dissipative numerical schemes which are routinely used in viscous flow simulations are not good candidates for use in LES of turbulent flows. Except in cases where the flow is extremely well resolved, it has been found that upwind schemes tend to damp out a significant portion of the small scales that can be resolved on the grid. Furthermore, it has been found that even specially designed higher-order upwind schemes that have been used successfully in the direct numerical simulation of turbulent flows produce too much dissipation when used in conjunction with large-eddy simulation.

A case in point is the LES of flow past a circular cylinder performed by Beaudan & Moin (1994) at a Reynolds number of 3900. One of the objectives of this investigation was to study the suitability of higher order upwind-biased schemes for LES of complex flows and to validate the methodology against experimental results of Ong & Wallace (1994) and Lourenco & Shih (1993). In particular, 5th- and 7th-order schemes were used for these simulations. The 5th-order scheme has been successfully used for DNS of transition and turbulence in flow over a flat plate by Rai & Moin (1993) and it was thought that these schemes would be useful in LES of flows in complex geometries. However, the conclusion of the study by Beaudan & Moin (1994) was that except in regions where the mesh was fine enough to resolve a significant portion of the small scales, numerical dissipation overwhelmed the contributions from the subgrid-scale eddy-viscosity model.

In contrast to upwind-biased schemes which control aliasing through numerical dissipation, aliasing is controlled in central schemes by an energy conservation principle. Such schemes do not exhibit numerical dissipation and, therefore, there is no spurious damping of the smaller scales. This feature makes the schemes attractive for use in LES of complex flows. The downside of using such schemes is the dominance of dispersive error, which makes these schemes extremely sensitive to aspects such as the grid stretching factors (Cain & Bush, 1994) and outflow boundary conditions (Gresho & Lee 1981). Thus, even though the central schemes might have a clear advantage over upwind biased schemes in simple geometries, in more complex geometries where complicated grids are used, the superiority of central schemes needs to be established and this is the motivation of the current study.

The objective of the current study is to perform a LES of incompressible flow past a circular cylinder at a Reynolds number of 3900 using a solver which employs an

energy- conservative second-order central difference scheme for spatial discretization and compare the results obtained with those of Beaudan & Moin (1994) and with the experiments in order to assess the performance of the central scheme for this relatively complex geometry.

Salient features of the simulation of Beaudan & Moin (1994):

Beaudan & Moin (1994), henceforth refered to as BM, simulated the flow past a circular cylinder on an O-mesh using a compressible flow solver. One point upwind-biased 5th- and 7th-order schemes were used for the spatial discretization of the convective terms. The simulations were carried out on a $144 \times 136 \times 48$ ($r \times \theta \times z$) grid and good resolution was provided near the cylinder surface and in the near wake region ($x/D < 2.0$). Beyond this region, the grid was stretched geometrically in the streamwise direction such that the streamwise grid spacing at $x/D = 10.0$ was about $0.13D$. The mesh near the outflow boundary was made extremely coarse in order to damp out disturbances and a convective outflow boundary condition was used. Grid stretching ratios in excess of 10% were used to obtain the desired grid spacing in the wake.

Simulations were carried out with no subgrid-scale model, with a fixed coefficient Smagorinsky model and with the spanwise averaged version of the dynamic model (Ghosal *et al.*, 1995, Moin *et al.* 1991). It was observed that mean wall statistics such as drag, pressure coefficients, wall shear stress and separation angles were not significantly different in the three simulations and all showed reasonable agreement with experimental data. In the vortex formation region ($x/D < 4.0$), it was found that the dynamic model predicted mean velocities and Reynolds stresses which were in better agreement with the experimental results than the other two simulations. Beyond this region the difference between the three computed solutions diminished such that the solutions were virtually indistinguishable beyond $x/D > 7.0$. It was found that in this region where the mesh was relatively coarse, numerical dissipation overwhelmed the contribution of the SGS model. The simulation with the 7th-order scheme showed evidence of increased energy in the high wavenumbers, but here too it was found that a substantial portion of the resolvable wavenumber range was damped due to numerical dissipation. It was concluded that these high order upwind-biased schemes were unsuitable for use in LES.

2. Accomplishments

2.1 Numerical method

The solver used in the current work is based on the solver developed by Choi *et al.* (1992) and employs a second-order central-difference method written in generalized coordinates in a spanwise periodic domain. Velocity components and pressure are fully staggered in order to strictly conserve mass in the generalized coordinates. It should be pointed out that strict conservation of momentum and energy is not guaranteed on a non-equispaced mesh. The solution is advanced in time using a fractional step scheme wherein a third-order Runge-Kutta scheme and a Crank-Nicolson scheme is used for the nonlinear convection terms and viscous terms respectively. A multigrid solver is used in conjunction with a Gauss-Siedel line-zebra scheme
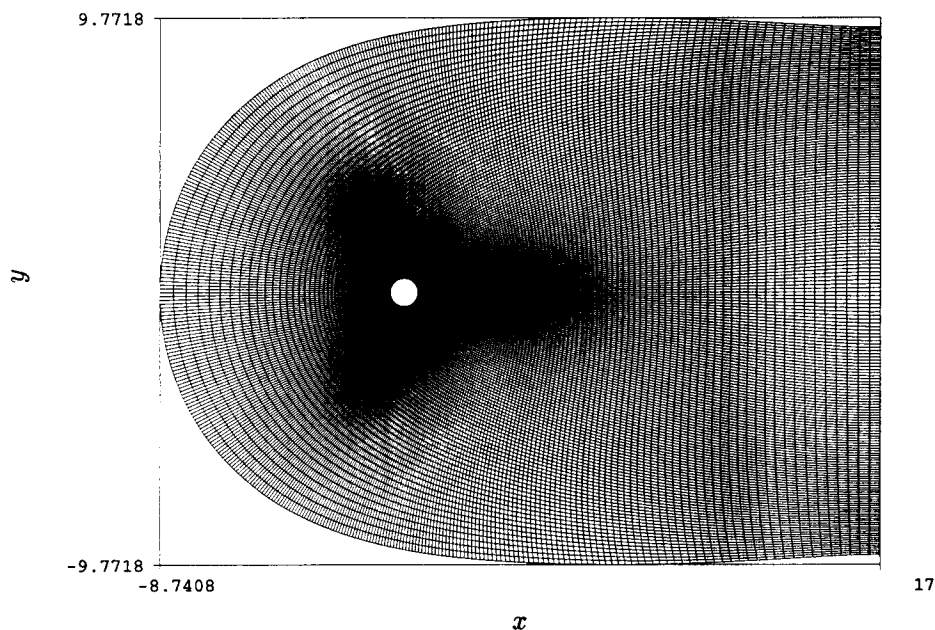
FIGURE 1.   *C*-mesh used for Run-II.

for solving the pressure Poisson equation. The solver employs a spanwise-averaged version of the dynamic model where the total viscosity is constrained to be greater than zero (Ghosal *et al.*, 1995). The spanwise length of the cylinder is chosen to be πD which is the same as BM.

A *C*-mesh is used for the present simulations (Fig. 1). This type of mesh is ideally suited for simulating wake flows since better streamwise resolution can be selectively provided in the wake region. The use of a *C*-mesh also simplifies the application of outflow boundary conditions. Furthermore, another advantage of using a *C*-mesh is that as the flow separates from the cylinder, it remains roughly aligned with one family of grid lines, and thus good control over the streamwise stretching ratio can be maintained in this region. It has been found that in LES, where the resolution is at best marginal, central schemes can tolerate only a small streamwise stretching factor ($< 3\%$). Higher stretching factors can leads to the amplification of grid-to-grid oscillations ($2 - \Delta$ waves). If an *O*-type mesh were to be used for the present simulations, the flow in the region of the separated shear layer would experience large strething ratios as it would go from being aligned with one family of grid lines to being aligned with the other, and solution in this region would be contaminated by $2 - \Delta$ waves. Thus, the use of a *C*-mesh is necessary for obtaining a good solution with the current solver. This brings in the important point that the grid has to be designed keeping in mind the underlying spatial discretization.

2.2 Simulation results and discussion

The first simulation (Run I) was carried out on a 329×100×48 mesh with 80 points on the cylinder surface, 125 streamwise points along the wake centerline, 100 points in the wall normal direction, and 48 points along the spanwise direction. Since this was the first simulation, a relatively coarse mesh was chosen with the objective that results from this simulation would provide an estimate of the resolution requirements. The results from this simulation are summarized in Table 1. Also tabulated for direct comparison are the corresponding results from the 2-D simulation and 3-D LES of BM and experimental results from various studies. This simulation predicted a higher mean drag, rms lift, and base suction pressure coefficient than the corresponding LES of BM and experiments. Furthermore, it was observed that the computed in-plane Reynolds stresses ($\overline{u'^2}$, $\overline{v'^2}$ and $\overline{u'v'}$) in the near wake were significantly higher than the corresponding LES of BM and experiments of Lourenco & Shih (1993). On the other hand, spanwise Reynolds normal stress ($\overline{w'^2}$) in the near wake was under-predicted. All indications were that the flow was not developing enough three-dimensionality.

To get a realistic evolution of the three-dimensionality in the near wake, one requires adequate resolution of the underlying two-dimensional flow in addition to good spanwise resolution of the three-dimensional structures. It was clear that the azimuthal resolution of the attached boundary layer and separation region was much less than in the LES of BM. This could possibly lead to an incorrect location of the separation point and subsequent evolution of the separated shear layer. Therefore, it was decided to continue the simulation on a mesh with increased azimuthal resolution on the cylinder surface.

The second simulation (Run-II) was carried out on a 399×100×48 mesh where the number of points on the cylinder surface was increased from 80 to 150. In order to maintain a smooth streamwise distribution of grid points at the concave corner in the base of the cylinder, streamwise resolution had be improved marginally (by about 10%) in the near wake. The grid was kept roughly the same in all other regions. Some of the results of this simulation are summarized in Table 1. It was observed that overall there was no substantial improvement in the results. The mean drag coefficient, rms lift coefficient, and base pressure coefficient all show a small change towards the correct values but the results are still significantly different from BM and experiments.

In Fig. 2 is shown the variation of lift and drag coefficient with time after the flow has reached a statistically stationary state. All the data presented for this simulation has been averaged over the time period shown in this figure. Figure 3 shows the distribution of the surface pressure coefficient obtained from the present simulations. Results of BM have also been plotted for comparison. It is clear that the current simulations predict a significantly higher suction pressure in the wake region and that increasing the azimuthal resolution on the cylinder surface has only a marginal effect on the surface pressure distribution.

Figures 4a and 4b show the streamwise and cross-stream mean velocity profiles in the near wake ($x/D = 1.54$) obtained from the current simulations. Figure 4a

Table 1. Wall Statistics

	Run − I	*Run − II*	*Beaudan&Moin* (3 − D)	*Beaudan&Moin* (2 − D)	*Lourenco &Shih*
$\overline{C_{pb}}$	−1.28	−1.15	−0.95	−2.16	−0.9±0.05
$\overline{C_D}$	1.2	1.1	1.0	1.74	0.98±0.05
$\overline{\theta_s}$	89°	88°	85.8°	108.1°	85°±2°
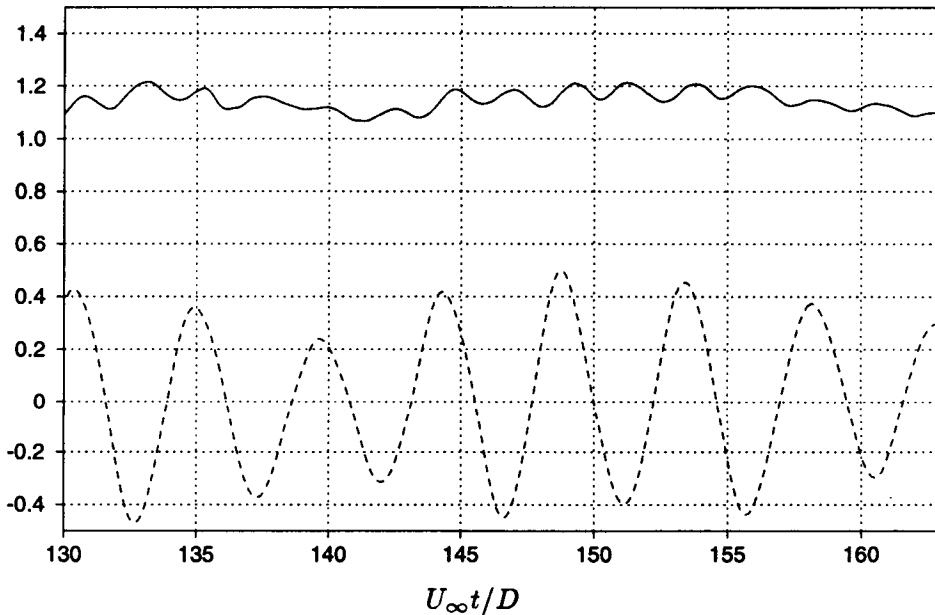
FIGURE 2.   Variation of lift and drag coefficient with time obtained from Run-II.
——— C_D; − − − − C_L.

shows that the current simulations underpredict the momentum deficit in the near wake, and consequently the wake bubble length is also underpredicted (see Table 1). In contrast to the streamwise velocity, the mean cross-stream velocity (Fig. 4b) matches well with the results of BM. Furthermore, it is observed that the experimental data does not match with any of the simulation results. This is consistent with the fact that Beaudan & Moin (1994) indicated that large errors might be present in the experimental measurements (Lourenco & Shih, 1993) of cross-stream velocity in the near wake.
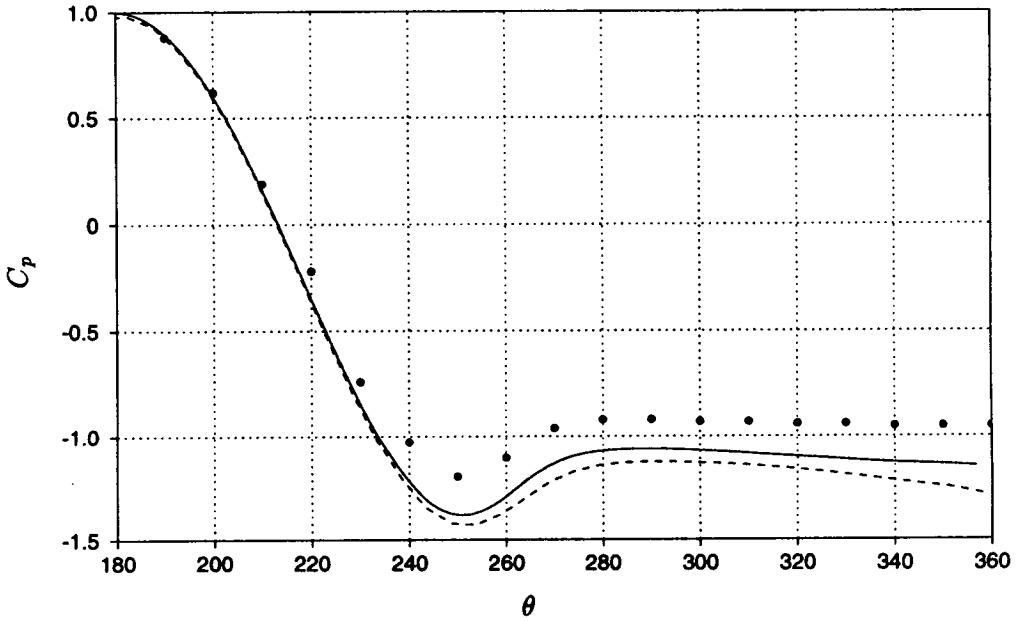
FIGURE 3.   Variation of pressure coefficient on the surface of the cylinder.
———— Run-II; ———— Run-I; ● Beaudan & Moin.
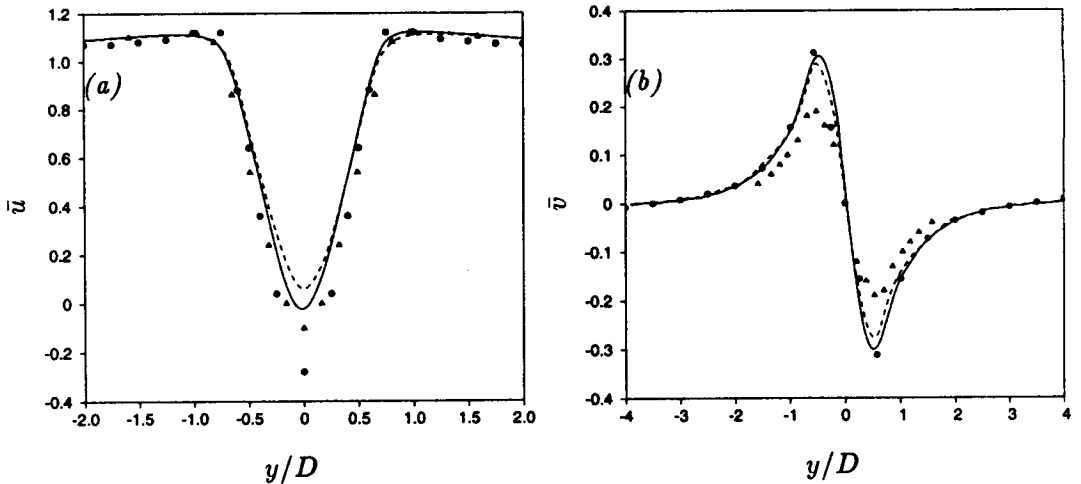
FIGURE 4.   Mean velocity profiles at $x/D = 1.54$. (a) Streamwise velocity. (b)
Cross-stream velocity. ———— : Run-II; ———— : Run-I; ● : Beaudan & Moin; ▲ :
Lourenco & Shih.

In Fig. 5 are shown Reynolds stress profiles at this streamwise location. It can
be observed from Fig. 5a that the current simulations over-predict the streamwise
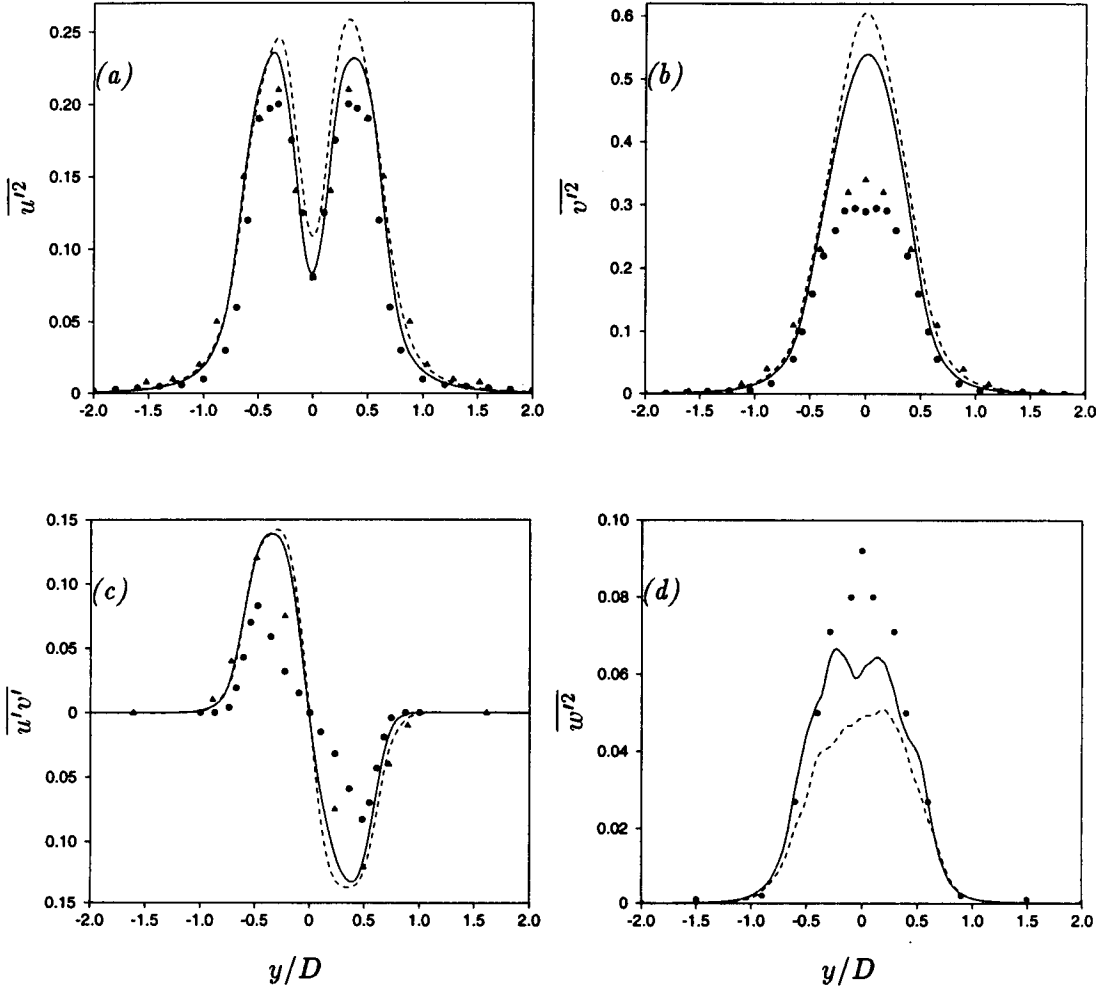
FIGURE 5. Reynolds stress profiles at $x/D = 1.54$. (a) $\overline{u'^2}$ (b) $\overline{v'^2}$ (c) $\overline{u'v'^2}$ (d) $\overline{w'^2}$
——— : Run-II; ---- : Run-I; • : Beaudan & Moin; ▲ : Lourenco & Shih.

Reynolds stress $(\overline{u'^2})$. However, overall, the stress profile is better predicted in Run-II. The noticeable asymmetry of the profile about the wake ceneterline obtained from Run I also suggests that more than six shedding cycles might be needed for averaging the statistics. Figure 5b shows the corresponding profiles of cross-stream normal Reynolds stress $(\overline{v'^2})$, and here large differences between the results of the current simulations and the results of BM can be seen. Run-I and Run-II over-predict the peak stress by about 100% and 80% respectively. A similar trend is observed in Fig. 5c, in which profiles of $(\overline{u'v'})$ are plotted.

Figure 5d shows profiles of the spanwise Reynolds normal stress, and we observe that the current simulation under-predicts this stress component. There is however,
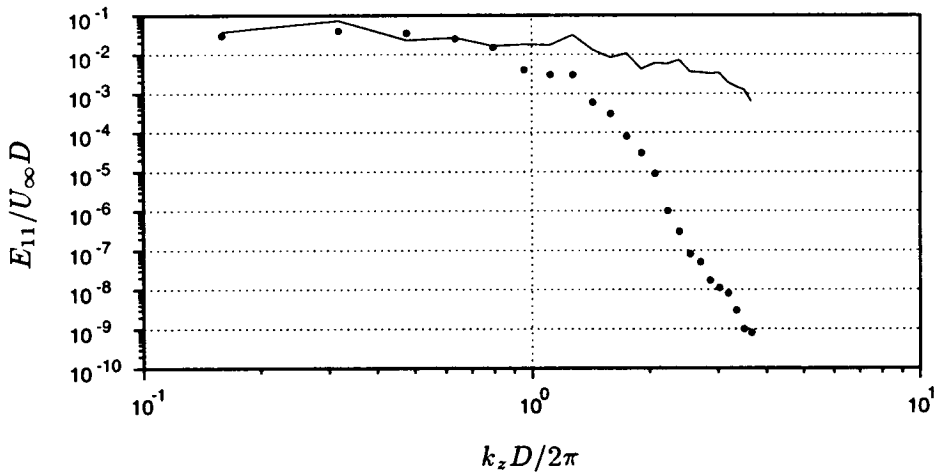
FIGURE 6. One-dimensional spectra at $x/D = 0.7$, $y = 0$. ——— :Run-II; • : Beaudan & Moin.

a noticeable effect of increasing the azimuthal surface resolution on this stress component. First the peak stress obtained from Run-II is about 17% higher than that obtained from Run-I. A more noticeable effect is that in Run-II a 'fuller' profile is obtained in the region $y/D > 0.25$ and this is in much better agreement with BM. This is most likely due to improved streamwise resolution in the near wake which leads to increase in the growth of three-dimensional instability in this region.

Figure 5 shows clear evidence that in the current simulations, the flow is not developing enough three-dimensionality in the near wake. As a result of this, in-plane stresses are over-predicted and spanwise stresses are under-predicted. It has been shown that the in-plane Reynolds stresses play a significant role in determining the base suction pressure (Mittal & Balachandar, 1995). Thus the higher in-plane Reynolds stresses lead to a higher base suction pressure and drag in the current simulations.

Figure 6 shows the spanwise one-dimensional spectra of the streamwise velocity in the near wake obtained from Run-II and the simulation of BM. Direct comparison of the spectra can be made since both simulations employ the same resolution in the spanwise direction. It can be observed that the two spectra match well only for the low wavenumbers (approximately 20% of the wavenumber range). Beyond this range, the spectra obtained by BM exhibits significant damping and the energy shows a decay of about seven orders of magnitude. In contrast, the spectra obtained from the current simulation is relatively flat with about one order of magnitude decay in the high wavenumber range. It should be pointed out that comparison of spanwise spectra at other wake locations shows a similar trend. Thus, it is clear that the higher-order upwind scheme used in the simulation of BM damps out a significant portion of the wavenumbers that can be resolved on the grid.

3. Summary and future plans

The results indicate that the evolution of the secondary instability that is responsible for the generation of three-dimensionality in the near wake is not captured well in the current simulations. This discrepancy could result from inadequate resolution of the underlying two-dimensional flow and/or spanwise resolution of the three-dimensional structures. The current simulations have the same number of grid points in the spanwise direction as Beaudan & Moin (1994). However, given that the current simulations use only a 2nd-order accurate spatial discretization, more spanwise grid points might be needed to match the resolution power of the 5th-order scheme. Comparison of the modified wavenumber for the schemes suggests that the 2nd-order scheme might need up to twice the number of grid points to match the resolution of the 5th-order scheme.

It is also clear from the present study that the restriction imposed on the streamwise grid stretching factor when using central schemes represents a severe constraint on mesh design for complex geometries. In this respect, the higher-order upwind biased schemes are more flexible since they allow the use of higer stretching factors and increased resolution can be provided selectively at desired locations. However, it is also evident that even these higher order upwind schemes exhibit significant dissipation, and the scales corresponding to the top half of the wavenumber range, which are crucial for determining the subgrid-scale dissipation, are effectively damped out due to the numerical dissipation. The second-order central difference scheme, on the other hand, preserves the energy in the small scales and allows the subgrid-scale dissipation to have a more significant impact on the resolvable flow field.

Doubling the number of grid points on the cylinder surface improves the results only marginally. Therefore, it is unlikely that the disagreement in results is due to lack of resolution on the cylinder surface. In-plane resolution in the near wake region could also be one cause of the discrepancy. In particular, the restriction on the streamwise stretching ratio and the presence of the concave corner at base of the cylinder result in the near wake having poorer streamwise resolution than the simulation of BM. A systematic spanwise resolution study would require doubling the spanwise grid points which would effectively double the computational resources required. In contrast, doubling the streamwise resolution in the near wake can be accomplished with about a 30% increase in computational resources and is thus the more viable next step.

The near-term objective then is to obtain wall and near wake statistics which are independent of the near wake in-plane resolution. 2-D simulations, which are relatively cheap, can be used to give a rough estimate of the in-plane resolution requirement. Once statistics which are independent of the in-plane resolution in the near wake are obtained, these will be compared with the results of BM. If the wall and near wake statistics match reasonably well with BM, this will imply that the spanwise resolution is adequate and the next step will then be to obtain and compare the statistics in the downstream wake region. On the other hand, if the wall and near wake statistics do not match with BM, this will be an indication that increased spanwise resolution might be required. The code is in the process of

being ported to the IBM SP2 parallel computer where the turnaround time will be significantly reduced and it will be possible to use larger meshes.

REFERENCES

BEAUDAN, P. & MOIN, P. 1994 Numerical Experiments on the Flow Past a Circular Cylinders at Sub-Critical Reynolds Numbers. *Report No. TF-62, Thermosciences Div., Dept. of Mech. Engr., Stanford Univ.*

CAIN, A. B. & BUSH, R. H. 1994 Numerical Wave Propagation Analysis for Stretched Grids. *AIAA-paper 94- 0172.*

CHOI, H., MOIN, P. & KIM, J. 1992 Turbulent Drag Reduction: Studies of Feedback Control and Flow Over Riblets. *Report No. TF-55, Thermosciences Div., Dept. of Mech. Engr., Stanford Univ.*

GHOSAL, S., LUND, T. S., MOIN, P. & AKSELVOLL, K. 1995 A Dynamic Localization Model for Large-Eddy Simulation of Turbulent Flows. *J. Fluid Mech.* **286**, 229-255.

GRESHO, P. M. & LEE, R. L. 1981 Don't Suppress the Wiggles-They're Telling You Something!. *Comput. Fluids.* **9**, 223-253.

LOURENCO, L. M. & SHIH, C. 1993 Characteristics of the Plane Turbulent Near Wake of a Circular Cylinder. A Particle Image Velocimetry Study. *Private Communication.*

MITTAL, R. & BALACHANDAR, S. 1995 Effect of Three- Dimensionality on the Lift and Drag of Nominally Two- Dimensional Cylinders. *Phys. Fluids.* **7**, (8), 1841-1865.

MOIN, P., SQUIRES, K., CABOT, W. & LEE, S. 1991 A Dynamic Subgrid-Scale Model for Compressible Turbulence and Scalar Transport. *Phys. Fluids A.* **3**, 2746-2757.

ONG, L., & WALLACE, J. 1994 Private Communication.

RAI, M. M. & MOIN, P. 1993 Direct Numerical Simulation of Transition and Turbulence in a Spatially Evolving Boundary Layer. *J. Comp. Phys.* **109**, No. 2, 169-192.

Experimental investigation of flow through an asymmetric plane diffuser

By Carl U. Buice AND John K. Eaton[1]

1. Motivation and objectives

There is a need for experimental measurements in complex turbulent flows that originate from very well-defined initial conditions. Testing of large-eddy simulations and other higher-order computation schemes requires inlet boundary condition data that are not normally measured. The use of fully developed upstream conditions offers a solution to this dilemma in that the upstream conditions can be adequately computed at any level of sophistication. Unfortunately, experimenters have only recently been sensitized to this issue and there are relatively few appropriate data sets.

The plane diffuser experiment by Obi *et al.* (1993) has received a lot of attention because it has fully-developed inlet conditions and it includes separation from a smooth wall, subsequent reattachment, and redevelopment of the downstream boundary layer. Each of these features offers challenges for modern turbulence models. In particular, Durbin and Kaltenbach of CTR have devoted considerable effort in developing several different computations of the flow. Unfortunately, they found that the experiment had several deficiencies as they began careful comparison to the data. The most glaring problem is the fact that the data set does not appear to satisfy mass conservation, a problem that is most likely due to three-dimensional effects in the diffuser.

The objective of this study is to provide careful qualification and detailed measurements in a re-creation of the Obi experiment. The work will include extensive documentation of the flow two-dimensionality and detailed measurements required for testing of flow computations.

2. Accomplishments

The diffuser geometry as specified by Obi *et al.* is shown in Fig. 1. The expected flow includes flow separation approximately midway along the diffuser followed by reattachment in the tailpipe. The problem with this flow is that separation is likely to occur on the end-walls, causing an acceleration of the mid-plane flow. Our approach has been to modify an existing blower wind-tunnel to accommodate a very high aspect ratio version of the diffuser in hopes of minimizing end-wall effects. Unfortunately, the separated regions on the end-wall can be quite large and have a significant effect on the mid-plane flow. After construction, the majority of our efforts have been in controlling the end-wall boundary layer separation.

1 Mechanical Engineering Department, Stanford University
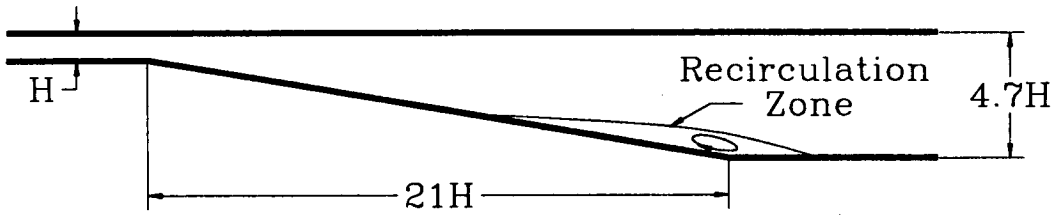
FIGURE 1.   Plane diffuser.

2.1. The experimental apparatus

We have constructed an experimental facility, shown in Fig. 2, in the HTTM laboratory at Stanford. The facility has an upstream channel width (H) of 1.5cm and a depth of 60cm, giving an aspect ratio of 40. The diffuser replicates the geometry of Obi *et al.*, including the 10 degree asymmetric expansion to a total area ratio of 4.7. The blower tunnel can supply well-controlled flow sufficient to provide a channel Reynolds number ($U_{cl}H/\nu$) ranging from approximately 10,000 to 30,000. Two splitter plates have been installed 7cm from the end-walls starting $6H$ upstream of the beginning of the diffuser in order to remove the end-wall boundary layers. Holes have been drilled in the splitter plates within the first 5 channel heights of the diffuser to allow for the removal of the end-wall boundary layer through suction in the region of greatest adverse pressure gradient. Suction is developed by partial obstruction of the exit of the main section of the tunnel by a steel grid and by the presence of an adjustable obstruction located before the diffuser in the isolated end-wall sections.
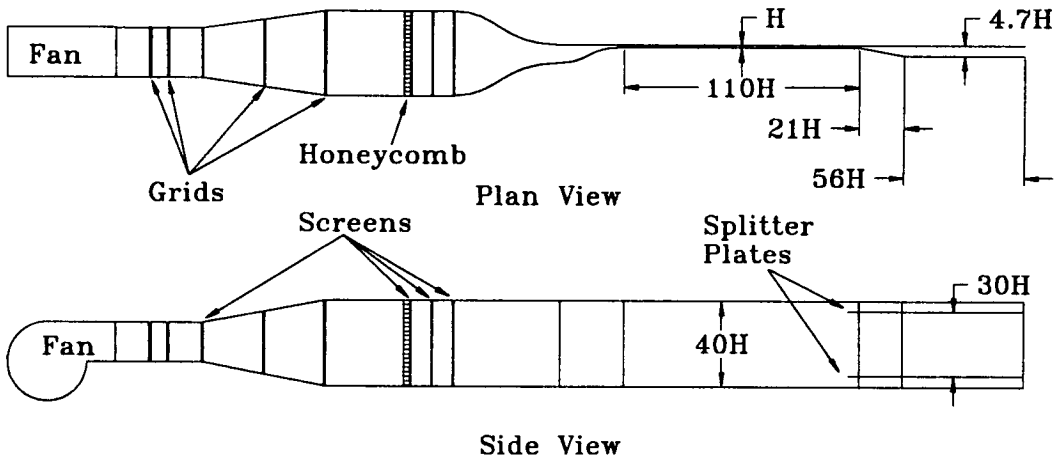
FIGURE 2.   The experimental facility in HTTM.

2.2. Preliminary results

The first step in the qualification of the experimental facility included the removal of the diffuser section, leaving only the full development length of the channel. Wall pressure measurements and hot-wire mean velocity and turbulence profiles showed that the flow near the end of the channel was fully developed and spanwise
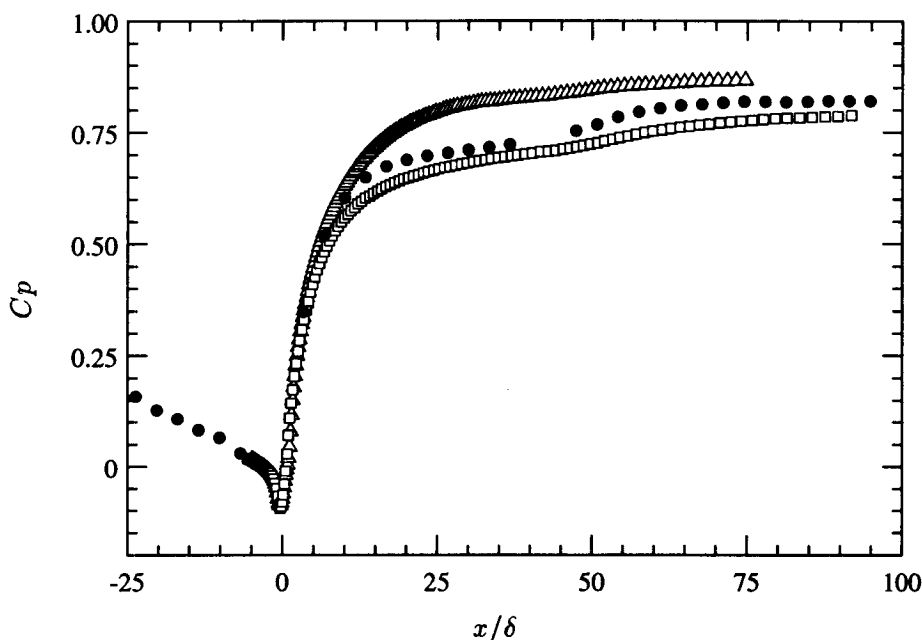
FIGURE 3.   Comparison of static pressure distribution normalized by the inlet bulk velocity. Symbols: $\bullet$, Experimental; $\triangle$, LES; $\square$, $k - \varepsilon - \nu^2$.

homogeneous over 85% of the channel width. The streamwise pressure gradient was measured and verified against the value calculated from the velocity profile.

   The diffuser section was then reinstalled and it became immediately obvious, through tuft flow visualization, that the end-wall boundary layers were severely separated in the outlet region of the diffuser. We choose splitter plates as the best approach for removal of the end-wall boundary layer that developed in the upstream channel flow. The splitter plates also provided a method for passive removal of the end-wall boundary layer in the diffuser. Using just the splitter plates, we were able to produce the correct pressure gradient in the inlet channel flow, which resulted in a pressure distribution that closely resembles the distribution calculated by Durbin, see Fig. 3. Unfortunately, integration of the velocity profiles upstream and downstream of the diffuser still showed a large discrepancy in the mass flow rates, indicating the continuing presence of secondary flow due to the influence of the end-wall region.

3. Future work

   As soon as the tunnel qualification process is complete, hot-wire, wall pressure, and pressure probe measurements will be made in unseparated regions of the flow. These data will be augmented by thermal tuft measurements of the separation and reattachment locations. The final stage of the experiment will include taking detailed measurements of the flow using laser-Doppler anemometry for the velocity field measurements and pulsed-wall probes for the skin friction measurement.

REFERENCES

KALTENBACH, H.-J. 1994 Large-eddy simulation of flow through a plane, asymmetric diffuser, *Annual Research Briefs-1994*, Center for Turbulence Research, NASA Ames/Stanford Univ. 175-184.

OBI, S., AOKI, K. & MASUDA, S. 1993 Experimental and computational study of turbulent separating flow in an asymmetric plane diffuser; in: *Ninth Symposium on Turbulent Shear Flows*, Kyoto, Japan, August 16-19, 1993. p 305.

Conservative properties of finite difference schemes for incompressible flow

By Youhei Morinishi[1]

1. Motivation and objectives

The purpose of this research is to construct accurate finite difference schemes for incompressible unsteady flow simulations such as LES (large-eddy simulation) or DNS (direct numerical simulation).

Experience has shown that kinetic energy conservation of the convective terms is required for stable incompressible unsteady flow simulations. Arakawa (1966) showed that a finite difference scheme that conserves the enstrophy in the absence of viscous dissipation is required for long-time integration in the two-dimensional vorticity-streamfunction formulation. The corresponding conserved variable is kinetic energy in velocity-pressure formulation, and some energy conservative finite difference schemes have been developed for the Navier-Stokes equations in three dimensions. Staggered grid systems are usually required to obtain physically correct pressure fields. The standard second order accurate finite difference scheme (Harlow & Welch 1965) in a staggered grid system conserves kinetic energy and this scheme has proven useful for LES and DNS. However, the accuracy of the second order finite difference scheme is low and fine meshes are required (Ghosal 1995). Spectral methods (Canuto *et al.* 1988) offer supreme accuracy, but these methods are limited to simple flow geometries. Existing fourth order accurate convective schemes (A-Domis 1981, Kajishima 1994) for staggered grid systems do not conserve kinetic energy. Higher order staggered grid schemes that conserve kinetic energy have not been presented in the literature.

The conservation of kinetic energy is a consequence of the Navier-Stokes equations for incompressible flow in the inviscid limit. In contrast, energy conservation in a discrete sense is not a consequence of momentum and mass conservation. It is possible to derive numerical schemes that conserve both mass and momentum but do not conserve kinetic energy. It is also possible to derive schemes that conserve kinetic energy even though mass or momentum conservation are violated.

In this report, conservation properties of the continuity, momentum, and kinetic energy equations for incompressible flow are specified as analytical requirements for a proper set of discretized equations. Existing finite difference schemes in staggered grid systems are checked for satisfaction of the requirements. Proper higher order accurate finite difference schemes in a staggered grid system are then proposed. Plane channel flow is simulated using the proposed fourth order accurate finite difference scheme and the results compared with those of the second order accurate Harlow and Welch (1965) algorithm.

---

1   Permanent address: Nagoya Institute of Technology, Japan

2. Accomplishments

2.1 Analytical requirements

The continuity and momentum equations describe the motion of incompressible flow. For convenience later in the analysis, these equations are written symbolically as

$$(Cont.) = 0 \tag{1}$$

$$\frac{\partial v_i}{\partial t} + (Conv.)_i + (Pres.)_i + (Visc.)_i = 0 \tag{2}$$

where

$$(Cont.) \equiv \frac{\partial v_i}{\partial x_i}, \quad (Pres.)_i \equiv \frac{\partial p}{\partial x_i}, \quad (Visc.)_i \equiv \frac{\partial \tau_{ij}}{\partial x_j} \tag{3},(4),(5)$$

Here, v_i is velocity component, p is pressure divided by density, and τ_{ij} is viscous stress. Henceforth, p will be referred to as pressure.

The conservation properties of Eqs. (1) and (2) will now be established. Note that Eq. (2) is in the following form.

$$\frac{\partial \phi}{\partial t} +^1 Q^\phi +^2 Q^\phi +^3 Q^\phi + \cdots = 0 \tag{6}$$

The term $^k Q^\phi$ is *conservative* if it can be written in divergence form

$$^k Q^\phi = \nabla \cdot (^k F^\phi) = \frac{\partial (^k F_j{}^\phi)}{\partial x_j} \tag{7}$$

To see that the divergence form is conservative, integrate Eq. (6) over the volume and make use of Gauss's theorem for the flux terms $k = 1, 2, \cdots$, all of which are assumed to satisfy Eq. (7)

$$\frac{\partial}{\partial t} \int \int \int_V \phi \, dV = - \int \int_S (^1 F^\phi +^2 F^\phi +^3 F^\phi + \cdots) \cdot dS \tag{8}$$

From Eq. (8), we notice that the time derivative of the sum of ϕ in a volume V equals the sum of the flux $^k F^\phi$ on the surface S of the volume. In particular, the sum of ϕ never changes in periodic field if $^k Q^\phi$ is conservative for all k.

Note that the pressure $(Pres.)_i$ and viscous terms $(Visc.)_i$ are conservative *a priori* in the momentum equation since they appear in divergence form. The convective term is also conservative *a priori* if it is cast in divergence form. This is not always the case, however, and we shall investigate alternative formulations. To perform the analysis, we regard $(Conv.)_i$ as a generic form of the convective term in the momentum equation. At least four types of convective forms have been used traditionally in analytical or numerical studies. These forms are defined as follows.

$$(Div.)_i \equiv \frac{\partial v_j v_i}{\partial x_j} \tag{9}$$

$$(Adv.)_i \equiv v_j \frac{\partial v_i}{\partial x_j} \tag{10}$$

$$(Skew.)_i \equiv \frac{1}{2}\frac{\partial v_j v_i}{\partial x_j} + \frac{1}{2}v_j\frac{\partial v_i}{\partial x_j} \tag{11}$$

$$(Rot.)_i \equiv v_j\left(\frac{\partial v_i}{\partial x_j} - \frac{\partial v_j}{\partial x_i}\right) + \frac{1}{2}\frac{\partial v_j v_j}{\partial x_i} \tag{12}$$

As mentioned above, the *divergence* form, $(Div.)$, is conservative *a priori*. $(Adv.)_i$, $(Skew.)_i$, and $(Rot.)_i$ are referred to as *advective*, *skew-symmetric*, and *rotational* forms respectively. The four forms are connected with each other through following relations.

$$(Adv.)_i = (Div.)_i - v_i \cdot (Cont.) \tag{13}$$

$$(Skew.)_i = \frac{1}{2}(Div.)_i + \frac{1}{2}(Adv.)_i \tag{14}$$

$$(Rot.)_i = (Adv.)_i \tag{15}$$

We notice that there are only two independent convective forms, and the two are equivalent if $(Cont.) = 0$ is satisfied. It is also apparent that the advective, skew-symmetric, and rotational forms are conservative as long as the continuity equation is satisfied.

The transport equation of the square of a velocity component, $v_1{}^2/2$, is v_1 times $i = 1$ component of Eq. (2).

$$\frac{\partial v_1{}^2/2}{\partial t} + v_1 \cdot (Conv.)_1 + v_1 \cdot (Pres.)_1 + v_1 \cdot (Visc.)_1 = 0 \tag{16}$$

In the above equation, the convective term can be modified into the following forms corresponding to those in the momentum equation.

$$v_1 \cdot (Div.)_1 = \frac{\partial v_j v_1{}^2/2}{\partial x_j} + \frac{1}{2}v_1{}^2 \cdot (Cont.) \tag{17}$$

$$v_1 \cdot (Adv.)_1 = \frac{\partial v_j v_1{}^2/2}{\partial x_j} - \frac{1}{2}v_1{}^2 \cdot (Cont.) \tag{18}$$

$$v_1 \cdot (Skew.)_1 = \frac{\partial v_j v_1{}^2/2}{\partial x_j} \tag{19}$$

Note that the skew-symmetric form is conservative *a priori* in the velocity square equation. Since the rotational form is equivalent to advective form, the four convective forms are conservative if $(Cont.) = 0$ is satisfied.

The terms involving pressure and viscous stress in Eq. (16) can be modified into following forms.

$$v_1 \cdot (Pres.)_1 = \frac{\partial p v_1}{\partial x_1} - p\frac{\partial v_1}{\partial x_1} \tag{20}$$

Terms	*Transport Equations*		
in Momentum Eq.	v_i	$v_1^2/2$	K
(*Div.*)	⊙	◯	◯
(*Adv.*) = (*Rot.*)	◯	◯	◯
(*Skew.*)	◯	⊙	⊙
(*Pres.*)	⊙	×	◯
(*Visc.*)	⊙	×	×

Table 1. Conservative properties of convective, pressure, and viscous terms in the v_i, $v_1^2/2$, and K equations. ⊙ is conservative *a priori*, ◯ is conservative if (*Cont.*) = 0 is satisfied, and × is not conservative.

$$v_1 \cdot (Visc.)_1 = \frac{\partial \tau_{1j} v_1}{\partial x_j} - \tau_{1j} \frac{\partial v_1}{\partial x_j} \tag{21}$$

These terms are not conservative since they involve the pressure-strain and the viscous dissipation.

We can determine the conservative properties of $v_2^2/2$ and $v_3^2/2$ in the same manner as for $v_1^2/2$.

The transport equation of kinetic energy, $K \equiv v_i v_i/2$, is v_i times i component of Eq. (2) with summation over i.

$$\frac{\partial K}{\partial t} + v_i \cdot (Conv.)_i + v_i \cdot (Pres.)_i + v_i \cdot (Visc.)_i = 0 \tag{22}$$

In Eq. (22), the conservation property of the convective term is determined in the same manner as for $v_1^2/2$. In addition, the terms involving pressure and viscous stress in Eq. (22) can be modified into following forms.

$$v_i \cdot (Pres.)_i = \frac{\partial p v_i}{\partial x_i} - p \cdot (Cont.) \tag{23}$$

$$v_i \cdot (Visc.)_i = \frac{\partial \tau_{ij} v_i}{\partial x_j} - \tau_{ij} \frac{\partial v_i}{\partial x_j} \tag{24}$$

The pressure term in Eq. (22) is conservative if (*Cont.*) = 0 is satisfied. The viscous stress term in Eq. (22) is not conservative because the second term on the right-hand side of Eq. (24) is the energy dissipation.

Table 1 provides a summary of conservative properties of convective, pressure and viscous terms in the transport equations of v_i, $v_1^2/2$ and K for incompressible flow. The final goal of this work is to derive higher order accurate finite difference schemes that satisfy these conservative properties in a discretized sense.

2.2 Discretized operators

Before starting the main discussion, discretized operators need to be defined. In this report, the discussion of the discretized equations will be limited to uniform
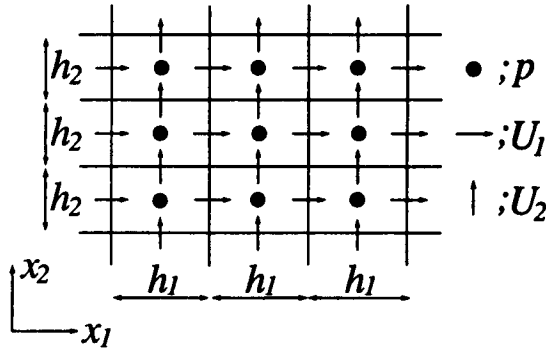
FIGURE 1. Staggered grid system in $x_1 - x_2$ plane.

grid systems. The widths of the numerical grid in each direction, h_1, h_2, h_3, are constant. The grid system shown in Fig. 1 will be referred to as a *staggered* grid system. In the staggered grid system, the velocity components U_i ($i = 1, 2, 3$) are distributed around the pressure points. The continuity equation is discretized centered at pressure points. The momentum equation corresponding to each velocity component is centered at the respective velocity point.

Let the finite difference operator acting on ϕ with respect to x_1 and with stencil n be defined as follows.

$$\left.\frac{\delta_n \phi}{\delta_n x_1}\right|_{x_1,\, x_2,\, x_3} \equiv \frac{\phi(x_1 + nh_1/2,\ x_2,\ x_3) - \phi(x_1 - nh_1/2,\ x_2,\ x_3)}{nh_1} \quad (25)$$

Also, define an interpolation operator acting on ϕ in the x_1 direction with stencil n as follows.

$$\left.\overline{\phi}^{nx_1}\right|_{x_1,\, x_2,\, x_3} \equiv \frac{\phi(x_1 + nh_1/2,\ x_2,\ x_3) + \phi(x_1 - nh_1/2,\ x_2,\ x_3)}{2} \quad (26)$$

In addition, define a special interpolation operator of the product between ϕ and ψ in the x_1 direction with stencil n.

$$\begin{aligned}
\left.\widetilde{\phi\psi}^{nx_1}\right|_{x_1,\, x_2,\, x_3} &\equiv \frac{1}{2}\phi(x_1 + nh_1/2,\ x_2,\ x_3)\,\psi(x_1 - nh_1/2,\ x_2,\ x_3) \\
&\quad + \frac{1}{2}\psi(x_1 + nh_1/2,\ x_2,\ x_3)\,\phi(x_1 - nh_1/2,\ x_2,\ x_3)
\end{aligned} \quad (27)$$

Equations (25) and (26) are second order accurate approximations to first derivative and interpolation, respectively. Combinations of the discretized operators can be used to make higher order accurate approximations to the first derivative and interpolation. For example, fourth order accurate approximations are as follows.

$$\frac{9}{8}\frac{\delta_1 \phi}{\delta_1 x_1} - \frac{1}{8}\frac{\delta_3 \phi}{\delta_3 x_1} \simeq \frac{\partial \phi}{\partial x_1} - \frac{3}{640}\frac{\partial^5 \phi}{\partial x_1{}^5}h_1{}^4 + \cdots \quad (28)$$

$$\frac{9}{8}\overline{\phi}^{1x_1} - \frac{1}{8}\overline{\phi}^{3x_1} \simeq \phi - \frac{3}{128}\frac{\partial^4\phi}{\partial x_1^4}h_1^4 + \cdots \tag{29}$$

Discretized operators in the x_2 and x_3 directions are defined in the same way as for the x_1 direction.

We define two types of conservative forms in the discretized systems. $^kQ^\phi$ in Eq. (6) is (*locally*) *conservative* if the term can be written as

$$^kQ^\phi = \frac{\delta_1(^kF_j^{1\phi})}{\delta_1 x_j} + \frac{\delta_2(^kF_j^{2\phi})}{\delta_2 x_j} + \frac{\delta_3(^kF_j^{3\phi})}{\delta_3 x_j} + \cdots. \tag{30}$$

This definition corresponds to the analytical conservative form of Eq. (7). $^kQ^\phi$ is *globally conservative* if the following relation holds in a periodic field.

$$\sum_{x_1}\sum_{x_2}\sum_{x_3} {}^kQ^\phi\, \Delta V = 0 \tag{31}$$

The sum that appears in Eq. (31) is taken over the period of respective direction. ΔV ($\equiv h_1 h_2 h_3$) is a constant in a uniform grid system. The definition of global conservation corresponds to the conservation property of Eq. (8) in a periodic field. The condition for (local) conservation satisfies the condition for global conservation.

2.3 Continuity and pressure term in a staggered grid system

Now we are ready to consider our main problem. First of all, let's examine the conservative property of the pressure term. As we have observed, the pressure term should be conservative in the transport equations of momentum and kinetic energy.

In the staggered grid system, define the discretized continuity and pressure term as follows.

$$(Cont. - S2) \equiv \frac{\delta_1 U_i}{\delta_1 x_i} = 0 \tag{32}$$

$$(Pres. - S2)_i \equiv \frac{\delta_1 p}{\delta_1 x_i} \tag{33}$$

The $-S2$ denotes that the above approximations are second order accurate in space. Fourth order approximations for the continuity and pressure term in the staggered grid system are

$$(Cont. - S4) \equiv \frac{9}{8}\frac{\delta_1 U_i}{\delta_1 x_i} - \frac{1}{8}\frac{\delta_3 U_i}{\delta_3 x_i} = 0, \tag{34}$$

$$(Pres. - S4)_i \equiv \frac{9}{8}\frac{\delta_1 p}{\delta_1 x_i} - \frac{1}{8}\frac{\delta_3 p}{\delta_3 x_i}. \tag{35}$$

Local kinetic energy can not be defined uniquely in staggered grid systems since the velocity components are defined on staggered grid points. Some sort of interpolation must be used in order to obtain the three components of the kinetic energy at the same point. The required interpolations for the pressure terms in the v_1^2 and K equations are

$$\overline{U_i\frac{\delta_1 p}{\delta_1 x_i}}^{1x_i} = \frac{\delta_1 U_i \overline{p}^{1x_i}}{\delta_1 x_i} - p\cdot(Cont - S2), \tag{36}$$

FD Schemes	*Transport Equations*		
for Momentum Eq.	U_i	$U_1^2/2$	K
$(Pres. - S2)$	$\odot$	$\times$	$\bigcirc_1$
$(Pres. - S4)$	$\odot$	$\times$	$\bigcirc_2$

Table 2. Conservative properties of finite difference schemes for the pressure term in a staggered grid system. $\odot$ is conservative *a priori*, $\bigcirc_1$ is globally conservative if $(Cont. - S2) = 0$ is satisfied, $\bigcirc_2$ is globally conservative if $(Cont. - S4) = 0$ is satisfied, and $\times$ is not conservative.

$$\frac{9}{8}\overline{U_i\frac{\delta_1 p}{\delta_1 x_i}}^{1x_i} - \frac{1}{8}\overline{U_i\frac{\delta_3 p}{\delta_3 x_i}}^{3x_i} = \frac{9}{8}\frac{\delta_1 U_i \overline{p}^{1x_i}}{\delta_1 x_i} - \frac{1}{8}\frac{\delta_3 U_i \overline{p}^{3x_i}}{\delta_3 x_i} - p \cdot (Cont - S4). \quad (37)$$

The following relations can be used to show global conservation unambiguously.

$$\sum_{x_1}\sum_{x_2}\sum_{x_3}\overline{U_i\frac{\delta_1 p}{\delta_1 x_i}}^{1x_i} = \sum_{x_1}\sum_{x_2}\sum_{x_3} U_i \cdot (Pres. - S2)_i \quad (38)$$

$$\sum_{x_1}\sum_{x_2}\sum_{x_3}\left(\frac{9}{8}\overline{U_i\frac{\delta_1 p}{\delta_1 x_i}}^{1x_i} - \frac{1}{8}\overline{U_i\frac{\delta_3 p}{\delta_3 x_i}}^{3x_i}\right) = \sum_{x_1}\sum_{x_2}\sum_{x_3} U_i \cdot (Pres. - S4)_i \quad (39)$$

Therefore, Eqs. (33) and (35) are globally conservative if the corresponding discretized continuity equations are satisfied.

Table 2 shows the summary of the conservative property of the discretized pressure terms in a staggered grid system.

2.4 Convective schemes in a staggered grid system

As we have already mentioned, local kinetic energy K ($\equiv U_i U_i/2$) can not be defined uniquely in a staggered grid system. Let us assume that a term is (locally) conservative in the transport equation of K if the term is (locally) conservative in the transport equations of $U_1^2/2$, $U_2^2/2$ and $U_3^2/2$. Since the conservative properties of $U_2^2/2$ and $U_3^2/2$ are estimated in the same manner as for $U_1^1/2$, only conservative properties of convective schemes in the momentum and $U_1^2/2$ equations need to be considered.

2.4.1 Proper second order accurate convective schemes

Define second order accurate convective schemes in a staggered grid system as follows.

$$(Div. - S2)_i \equiv \frac{\delta_1 \overline{U_j}^{1x_i} \overline{U_i}^{1x_j}}{\delta_1 x_j} \quad (40)$$

$$(Adv. - S2)_i \equiv \overline{U_j}^{1x_i}\frac{\overline{\delta_1 U_i}}{\delta_1 x_j}^{1x_j} \quad (41)$$

$$(Skew. - S2)_i \equiv \frac{1}{2}(Div. - S2)_i + \frac{1}{2}(Adv. - S2)_i \quad (42)$$

FD Schemes	Transport Equations		
for Momentum Eq.	U_i	$U_1^2/2$	K
$(Div. - S2)$	⊙	◯	◯
$(Adv. - S2)$	◯	◯	◯
$(Skew. - S2)$	◯	⊙	⊙

Table 3. Conservative properties of proper second order accurate convective schemes in a staggered grid system. ⊙ is conservative *a priori* and ◯ is conservative if $(Cont. - S2) = 0$ is satisfied.

$(Adv. - S2)_i$ is connected with $(Div. - S2)_i$ through the following relation.

$$(Adv. - S2)_i = (Div - S2)_i - U_i \cdot \overline{(Cont. - S2)}^{1x_i} \tag{43}$$

$(Div. - S2)_i$ is the standard divergence form in a staggered grid system (Harlow & Welch 1965). $(Adv. - S2)_i$ was proposed by Kajishima (1994). $(Skew. - S2)_i$ is equivalent to the scheme that was proposed by Piacsek & Williams (1970). $(Div. - S2)_i$ is conservative *a priori* in the momentum equation. The product between U_1 and $(Skew. - S2)_1$ can be rewritten as

$$U_1 \cdot (Skew. - S2)_1 = \frac{\delta_1 \overline{\overline{U_j}^{1x_1} \widetilde{U_1 U_1}}^{1x_j}/2}{\delta_1 x_j}. \tag{44}$$

Therefore, $(Skew. - S2)_1$ is conservative *a priori* in the transport equation of $U_1{}^2/2$. By using Eq. (43), conservative properties of the various schemes are determined. Table 3 shows the conservative properties of $(Div. - S2)_i$, $(Adv. - S2)_i$ and $(Skew. - S2)_i$. These schemes are seen to be conservative provided continuity is satisfied. In addition, the rotational form is also conservative in light of Eq. (15).

2.4.2 Proposal of proper higher order accurate convective schemes

It is of interest to derive a proper fourth order accurate convective scheme for a staggered grid system. Existing fourth order accurate convective schemes for staggered grid systems (A-Domis 1981, Kajishima 1994) do not conserve kinetic energy. Here, we propose the following set of fourth order accurate convective schemes in a staggered grid system.

$$\begin{aligned}
(Div. - S4)_i &\equiv \frac{9}{8} \frac{\delta_1}{\delta_1 x_j} \left[\left(\frac{9}{8} \overline{U_j}^{1x_i} - \frac{1}{8} \overline{U_j}^{3x_i} \right) \overline{U_i}^{1x_j} \right] \\
&\quad - \frac{1}{8} \frac{\delta_3}{\delta_3 x_j} \left[\left(\frac{9}{8} \overline{U_j}^{1x_i} - \frac{1}{8} \overline{U_j}^{3x_i} \right) \overline{U_i}^{3x_j} \right]
\end{aligned} \tag{45}$$

$$\begin{aligned}
(Adv. - S4)_i &\equiv \frac{9}{8} \overline{\left(\frac{9}{8} \overline{U_j}^{1x_i} - \frac{1}{8} \overline{U_j}^{3x_i} \right) \frac{\delta_1 U_i}{\delta_1 x_j}}^{1x_j} \\
&\quad - \frac{1}{8} \overline{\left(\frac{9}{8} \overline{U_j}^{1x_i} - \frac{1}{8} \overline{U_j}^{3x_i} \right) \frac{\delta_3 U_i}{\delta_3 x_j}}^{3x_j}
\end{aligned} \tag{46}$$

FD Schemes	*Transport Equations*		
for Momentum Eq.	U_i	$U_1^2/2$	K
$(Div. - S4)$	$\odot$	$\bigcirc$	$\bigcirc$
$(Adv. - S4)$	$\bigcirc$	$\bigcirc$	$\bigcirc$
$(Skew. - S4)$	$\bigcirc$	$\odot$	$\odot$

Table 4. Conservative properties of proper fourth order accurate convective schemes in a staggered grid system. $\odot$ is conservative *a priori* and $\bigcirc$ is conservative if $(Cont. - S4) = 0$ is satisfied.

$$(Skew. - S4)_i \equiv \frac{1}{2}(Div. - S4)_i + \frac{1}{2}(Adv. - S4)_i \qquad (47)$$

$(Div. - S4)_i$ is conservative *a priori* in the momentum equation. The product between U_1 and $(Skew. - S4)_1$ can be rewritten as follows.

$$U_1 \cdot (Skew. - S4)_1 = \frac{9}{8}\frac{\delta_1}{\delta_1 x_j}\left[\left(\frac{9}{8}\overline{U_j}^{1x_1} - \frac{1}{8}\overline{U_j}^{3x_1}\right)\overline{\frac{\widetilde{U_1U_1}}{2}}^{1x_j}\right]$$
$$- \frac{1}{8}\frac{\delta_3}{\delta_3 x_j}\left[\left(\frac{9}{8}\overline{U_j}^{1x_1} - \frac{1}{8}\overline{U_j}^{3x_1}\right)\overline{\frac{\widetilde{U_1U_1}}{2}}^{3x_j}\right] \qquad (48)$$

Thus, $(Skew. - S4)_i$ is conservative *a priori* in the transport equation of $U_1{}^2/2$. The relation between $(Adv. - S4)_i$ and $(Div. - S4)_i$ is the following.

$$(Adv. - S4)_i = (Div. - S4)_i - U_i \cdot \left[\frac{9}{8}\overline{(Cont. - S4)}^{1x_i} - \frac{1}{8}\overline{(Cont. - S4)}^{3x_i}\right] \qquad (49)$$

This equation is a proper discrete analog Eq. (13), and $(Adv. - S4)_i$, $(Div. - S4)_i$, and $(Skew. - S4)_i$ are equivalent if $(Cont. - S4) = 0$ is satisfied. Using this relation, the conservative properties of the present schemes are determined. Table 4 shows the conservative properties of the present schemes. Comparing Table 4 with Table 1, we see that the present schemes are a proper set of convective schemes provided that the continuity equation is satisfied.

Proper higher order accurate finite difference schemes in a staggered grid system can be constructed in the same way as for the fourth order schemes.

2.5 Channel flow simulation

Numerical tests of the schemes described above are performed using plane channel flow. The continuity and momentum equations for incompressible viscous flow are solved using the proper second and fourth order accurate finite difference schemes in a staggered grid system using the dynamic subgrid scale model (Germano *et al.* 1991). The flow is drived by a streamwise pressure gradient. A semi-implicit time marching algorithm is used where the diffusion terms in the wall normal direction
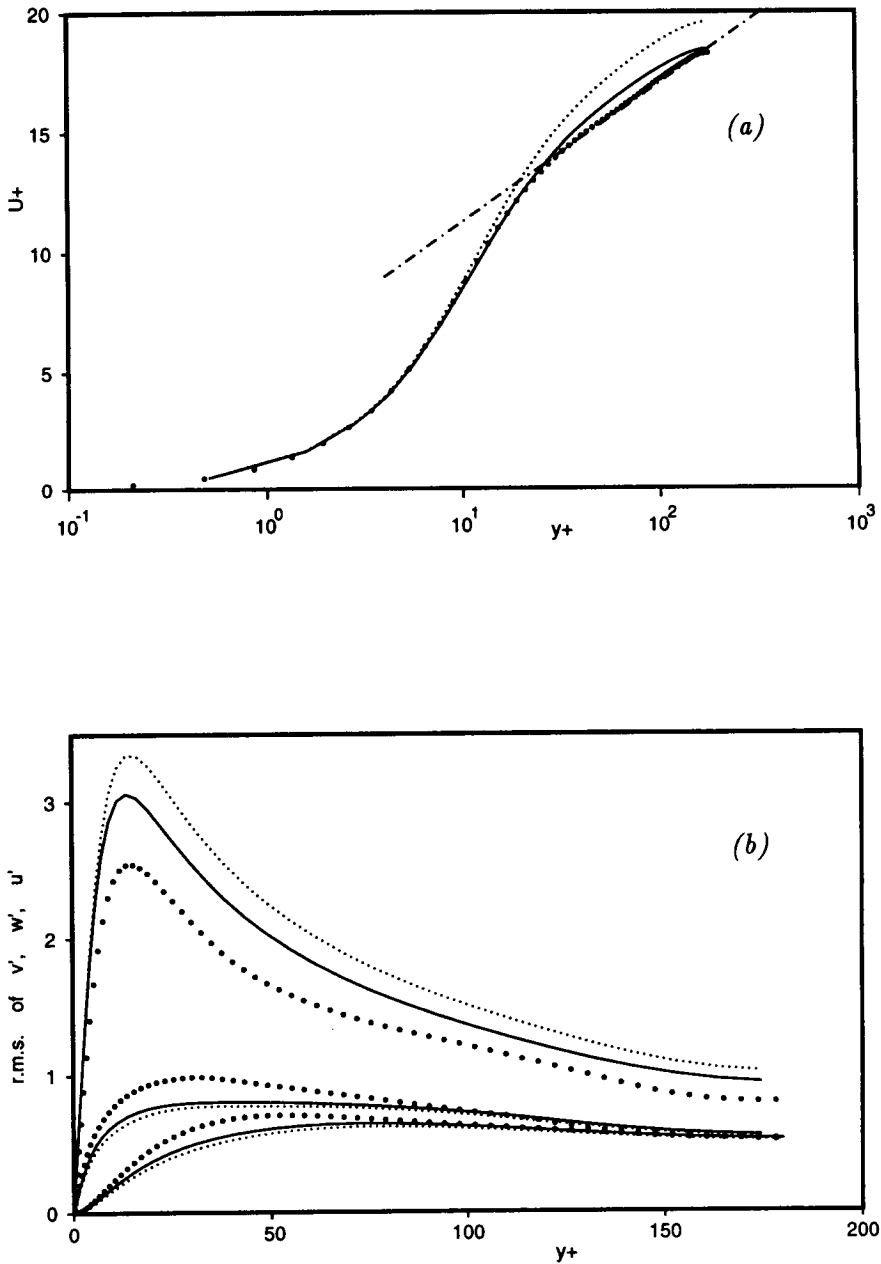
FIGURE 2.   LES of plane channel flow at Re=180 by proper second and fourth order accurate finite difference. (a) Mean streamwise velocity; (b) Velocity fluctuations. Symbols: ········ : 2nd order scheme; ——— : 4th order scheme; ● : DNS, Kim, *et al.* (1987); —·— ; $U+ = 5.5 = 2.5 \log y+$.

are treated implicitly with the Crank-Nicolson scheme and a third order Runge-Kutta scheme (Wray 1986) is used for all other terms. The fractional step method (Dukowicz & Dvinsky 1992) is used in conjunction with the Van Kan (1986) type of pressure term and wall boundary treatment. Periodic boundary conditions are imposed in the streamwise and spanwise directions.

The subgrid-scale model is the dynamic model (Germano *et al.* 1991) with the least square technique (Lilly 1992). Averaging in homogeneous directions is used. Filtering is performed in the spanwise and streamwise directions.

The spatial discretization of the second order scheme is a usual one: $(Div. - S2)$ for the convective term, $(Pres. - S2)$ for the pressure term, and $(Cont. - S2)$ for the continuity. The corresponding Poisson's equation of pressure is solved using a tri-diagonal matrix algorithm in wall normal direction with fast Fourier transforms (FFT) in the periodic directions. The second order accurate control volume type discretization is used for the viscous term.

The spacial discretization of the fourth order scheme is as follows. The convective term, the pressure term, and the continuity are discretized by $(Div. - S4)$, $(Pres. - S4)$, and $(Cont. - S4)$, respectively. The corresponding Poisson's equation of pressure is solved using a septa-diagonal matrix algorithm in wall normal direction with FFT in the periodic directions. A fourth order accurate control volume type discretization is used for the viscous term. The subgrid scale terms are estimated with second order finite differences. The wall boundary condition of the fourth order scheme is designed to conserve mass and momentum in the wall normal direction in a discretized sense.

The Reynolds number based on channel half width and wall friction velocity, Re, is 180. The computational box is $4\pi \times 2 \times \frac{4}{3}\pi$, and the mesh contains $32 \times 65 \times 32$ points (streamwise, wall-normal, and spanwise respectively).

Figure 2 shows the profiles of mean streamwise velocity and velocity fluctuations from the proper second and fourth order schemes. Filtered DNS data (Kim *et al.* 1987) are plotted as a reference in the figures. The mean streamwise velocity profile from the second order scheme is shifted up in the logarithmic region. This defect of the second order scheme is usually observed in coarse LES (Cabot 1994). Another defect of the second order scheme in coarse LES is the peak value of streamwise velocity fluctuation is too high (Cabot 1994). These defects are improved by using the fourth order scheme. The computational cost of the fourth order method is about 1.9 times that for the second order method.

3. Future plans

The fourth order scheme will be tested in high Reynolds number channel flow to see if it has a greater advantage when the velocity fluctuations have a relatively larger fraction of energy near the cutoff wavenumber.

Acknowledgments

REFERENCES

A-DOMIS, M. 1981 Large-eddy simulation of a passive scalar in isotropic turbulence. *J. Fluid Mech.* **104**, 55.

ARAKAWA, A. 1966 Computational design for long-term numerical integration of the equations of fluid motion: Two-dimensional incompressible flow. Part I. *J. Comp. Phys.* **1**, 119.

CABOT, W. 1994 Local dynamic subgrid-scale models in channel flow. *Annual Research Briefs 1994,* Center for Turbulence Research, Stanford Univ./NASA Ames Research Center. 143.

CANUTO, C., HUSSAINI, M. Y., QUARTERONI, A., & ZANG, S. A. 1988 *Spectral Methods in Fluid Dynamics.* Springer-Verlag.

DUKOWICZ, J. K., & DVINSKY, A. S. 1992 Approximation as a high order splitting for the implicit incompressible flow equations. *J. Comp. Phys.* **102**, 336.

GERMANO, M., PIOMELLI, U., MOIN, P., & CABOT, W. H. 1991 A dynamic subgrid-scale eddy viscosity model. *Phys. Fluids A.* **3**, 1760.

GHOSAL, S. 1995 Analysis of discretization errors in LES *(in this briefs)*.

KAJISHIMA, T. 1994 Conservation properties of finite difference method for convection *(in Japanese)*. *Trans. of JSME.* **60-574B**, 2058.

KIM, J., & MOIN, P. 1985 Application of a fractional step method to incompressible Navier-Stokes equations. *J. Comp. Phys.* **59**, 308.

KIM, J., MOIN, P., & MOSER, R. 1987 Turbulence statistics in fully developed channel flow at low Reynolds number. *J. Fluid Mech.* **177**, 133.

LILLY, D. 1992 A proposed modification of the Germano subgrid-scale closure method. *Phys. Fluids A.* **4**, 633.

HARLOW, F. H., & WELCH, J. E. 1965 Numerical calculation of time-dependent viscous incompressible flow of fluid with free surface. *Phys. of Fluids.* **8**, 2182.

PIACSEK, S. A., & WILLIAMS, G. P. 1970 Conservation properties of convection difference schemes. *J. Comp. Phys.* **6**, 392.

VAN KAN, J. 1986 A second-order accurate pressure-correction scheme for viscous incompressible flow. *SIAM J. Sci. Stat. Comp.* **7**(3), 870.

WRAY, A. A. 1986 NASA-Ames Research Center, Moffett Field, CA, Private communication.

An extended structure-based model based on a stochastic eddy-axis evolution equation

By S. C. Kassinos AND W. C. Reynolds

1. Motivation and objectives

Engineering analysis of complex turbulent flows relies heavily on turbulence models. A good model should have a viscoelastic character, predicting turbulent stresses proportional to the mean strain rate for slow deformations and stresses determined by the amount of strain for rapid distortions. Current turbulence models work well only in near-equilibrium situations where the turbulent stresses can be predicted adequately using eddy viscosity representations. They do not perform well when the turbulence is subjected to strong or rapid deformations, which is the case in many engineering systems. More elaborate schemes in which the Reynolds Stress Transport (RST) equations are included in the PDE system have been used in an effort to rectify these problems. While RST models have enjoyed some success, they are not yet widely used in industry because they have not proven reliably better than simpler models in dealing with the more challenging types of complex flows.

We have shown that the Reynolds stresses do not always provide a complete description of the turbulence state and that this poses a fundamental problem for standard RST models that use the Reynolds stress tensor (along perhaps with the mean velocity gradient) as the unique tensorial base for the modeling of the unknown terms. The inadequacy of componentality information is more pronounced in flows with strong mean rotation. These ideas are described in detail by Kassinos and Reynolds (1994), hereafter denoted by KR.

Proper characterization of the state of the turbulence in non-equilibrium flows requires the inclusion of *structure* information to complement the *componentality* carried by the turbulent stresses. We have introduced a number of one-point turbulent tensors carrying non-local information about the turbulence structure and demonstrated how they could be used for the construction of one-point models. However, this approach would require the addition of one second-rank and one fully symmetric third-rank tensor in the PDE system, a considerable overhead for an engineering model.

These considerations motivated the *structure-based* model which incorporates the key structure information in a simple phenomenological approach. The goal is to construct an engineering model with proper viscoelastic character that will reduce to the form of a k-ϵ model when the mean deformation is weak, and will match rapid distortion theory (RDT) when the mean deformation is strong.

The backbone of the structure-based model is a one-point, structure-based model of RDT for homogeneous turbulence. The development of this RDT model has been completed successfully and reported in great in detail in KR, and for that reason is not discussed here. This preliminary report focuses on the extensions of

the structure-based to flows with weak mean deformation rates. If the structure of the turbulence is assumed to be in equilibrium with the mean field and weakly anisotropic, the structure-based model reduces to the form of a k-ϵ model. Hence, we should be able to extend the model so that it spans between an eddy viscosity model, appropriate for weak mean strain rates, and RDT appropriate for high mean strain rates.

2. Accomplishments

2.1 Overview of the structure-based model

2.1.1 Algebraic equations

In a standard k-ϵ model, the turbulent stress tensor R_{ij} is related to the mean strain rate tensor S_{ij} through an eddy viscosity

$$R_{ij} = \frac{1}{3}q^2\delta_{ij} - 2\nu_T S_{ij} \qquad \nu_T = C_\mu k^2/\epsilon \qquad (1)$$

where $R_{ii} = q^2 = 2k$. Transport equations are used for k and ϵ but not for R_{ij} itself. In the structure-based model, we also determine the Reynolds stresses through an algebraic constitutive equation. The difference is that we relate the turbulent stresses to parameters of the turbulence structure instead of the mean strain rate:

$$R_{ij} = q^2[(1-\phi)\frac{1}{2}(\delta_{ij} - a_{ij}) + \phi a_{ij} + \gamma\frac{1}{2}\frac{\Omega_k}{\Omega}(\epsilon_{iky}a_{yj} + \epsilon_{jky}a_{yi})]. \qquad (2)$$

Here Ω_i is the mean vorticity vector and $\Omega^2 = \Omega_i\Omega_i$. The eddy-axis tensor a_{ij} carries information on the orientation and shape of large-scale eddies. The two scalar parameters (ϕ and γ) determine the character of the turbulence structure: ϕ is the fraction of the energy in the *jetal mode* (motion along the eddy axes), $1 - \phi$ is the fraction of the energy in the *vortical mode* (motion in the plane normal to the eddy axes), and γ is the jet-vortex correlation parameter. In the RDT model, we only carry the transport equations for the structure parameters. For weak mean deformations (small Sk/ϵ), we need to add the transport equations for the turbulence scales k and ϵ.

The derivation of the algebraic constitutive Eq. (2) for r_{ij} is based on a representation the turbulence as a superposition of two-dimensional eddy fields. The motivation is to account for the effects of the mean deformation on the energy-containing eddies. The normalized eddy-axis tensor a_{ij} represents an energy-weighted direction cosine tensor of the large eddies,

$$A_{ij} \equiv \langle V^2 a_i a_j \rangle = A_{kk} a_{ij}, \qquad (3)$$

where $\langle \ \rangle$ denotes an averaging, V^2 is twice the kinetic energy of the basis field, and a_i is a unit vector aligned with the axis of independence of the field of 2D eddies. Note that $A_{ii} = \langle V^2 \rangle = q^2$, and so the eddy-axis tensor scales on the

turbulent kinetic energy, as does R_{ij}. When the turbulence structure is isotropic, all the eddies are randomly distributed and $a_{ij} = \delta_{ij}/3$. For turbulence consisting of 2D vortices aligned with the x_1 direction, $a_{11} = 1$ and all other components vanish. Hence, the eddy-axis tensor carries the dimensionality information needed by a turbulence model. In fact, a_{ij} is related to the structure *dimensionality* tensor (see KR) through the model algebraic equation

$$D_{ij} = \tfrac{1}{2}q^2(\delta_{ij} - a_{ij}). \tag{4}$$

2.1.2 Transport equations

We use PDE for the structure parameters but not for the turbulent stresses themselves. The evolution equation for the normalized eddy-axis tensor a_{ij} is determined from definition (3) and the kinematics of the eddy axis vector a_i. In the RDT limit a_i satisfies the simple equation

$$\frac{da_i}{dt} = G_{ik}a_k - G_{nm}a_m a_n a_i \tag{5}$$

where $G_{ij} = U_{i,j}$ is mean gradient tensor. Using (5), definition (3) and some analysis, one can show that in the RDT limit the evolution of a_{ij} is given by

$$\begin{aligned}
\frac{da_{ij}}{dt} =& G^*_{ik}a_{kj} + G^*_{jk}a_{ki} - [3\phi + 1]G^*_{km}Z_{kmij} + (3\phi - 1)G^*_{nm}a_{nm}a_{ij} \\
& - 2\gamma S^*_{nm}\frac{\Omega_k}{\Omega}\epsilon_{nkt}(Z_{tmij} - a_{tm}a_{ij})
\end{aligned} \tag{6}$$

where $G^*_{ij} = G_{ij} - G_{kk}\delta_{ij}/3$ and $S^*_{ij} = S_{ij} - S_{kk}\delta_{ij}/3$. Closure of (6) requires modeling of the energy weighted fourth-moment

$$Z_{ijnm} = \langle V^2 a_i a_j a_n a_m \rangle / q^2 \tag{7}$$

in terms of the second moments a_{ij}. A fully realizable accurate model for **Z** has been developed (see KR).

The evolution equations for the two scalar parameters

$$\frac{d\phi}{dt} = \dots \qquad \frac{d\gamma}{dt} = \dots \tag{8}$$

are derived from the Navier-Stokes equations with some modeling to account for information lost in conditionally averaging over the eddies. The exact form of these equations is given in KR (see Eqs. 5.10.4 and 5.10.5 therein).

2.2 Blending of RDT and k-ε modeling for homogeneous turbulence

The simplest approach in extending the RDT structure-based model to slow deformations is the addition of terms in the evolution equations for a_{ij} that model the restoration of isotropy as a result of turbulence-turbulence interactions. Similar

terms in the evolution equations for ϕ and γ will restore the vortical turbulence ($\phi = 0, \gamma = 0$) appropriate for isotropy.

For slow deformations we must add equations for the turbulence scales. We are currently investigating the use of the familiar k and ϵ equations, with minor modifications to take advantage of the structure information provided by the eddy-axis tensor. An algebraic relationship is used to obtain the turbulence time scale τ in terms of k and ϵ.

The modeling of the return to isotropy terms in the eddy-axis tensor Eq. (6) is perhaps the most sensitive step in implementing these extensions since the simple kinematic basis of this equation is critical for full realizability in the RDT limit. The added return-to-isotropy terms must capture the key physics without disturbing the realizability of the model. For this reason, we next discuss in detail a method of extending the a_{ij} equation that guarantees maintaining realizability.

2.3 A stochastic eddy-axis evolution equation

In the RDT limit, the eddy axis vector a_i evolves according to the simple kinematic Eq. (5). When the mean deformation is weak, this equation must also involve return to isotropy terms accounting for the eddy-eddy (or turbulence-turbulence) interactions. Guidance on the form of these isotropization terms can be obtained by considering a generalization of the eddy-axis kinematic equation that includes stochastic forcing terms, in analogy to the Langevin equation (Arnold, 1974). This approach offers the advantage that the realizability of the resulting eddy-axis transport equation is guaranteed (Durbin and Speziale, 1994). We work with the energy-scaled eddy-axis vector

$$A_i = V a_i \tag{9}$$

where $V = \sqrt{V_k V_k}$ and a_i is the unit eddy-axis vector. The RDT evolution equation for A_i is simply [see (5) and (9)]:

$$\frac{dA_i}{dt} = G_{ik} A_k - G_{nm} a_n a_m A_i - G_{nm} v_n v_m A_i \tag{10}$$

where $v_i = V_i / V$. Next we consider a stochastic generalization of (10) given by

$$
\begin{aligned}
dA_i =& [G_{ik} A_k - G_{nm} a_n a_m A_i - G_{nm} v_n v_m A_i] dt \\
&+ C_1 A_i dt + C_2 d\mathcal{W}_i + C_3 d\mathcal{W}_p \Gamma_p A_i + C_4 \epsilon_{ipq} d\mathcal{W}_p A_q.
\end{aligned} \tag{11}
$$

The stochastic forcing in (11) is provided by the Wiener process $d\mathcal{W}_i(t)$, which has increments that are steps of the random walk and provide Guassian white-noise forcing (Arnold 1974). The properties of these increments are

$$\overline{d\mathcal{W}_i} = 0 \qquad \overline{d\mathcal{W}_i d\mathcal{W}_j} = dt \delta_{ij} \qquad \overline{d\mathcal{W}_i} = 0. \tag{12}$$

The second property in (12) shows that the Wiener process has magnitude $d\mathcal{W} = O(dt)^{1/2}$; therefore, $d\mathcal{W}_i/dt$ is not defined as $dt \to 0$. Hence, in order to evaluate $dA_{ij}/dt = \overline{dA_i A_j}/dt$, we first form the product

$$d(A_i A_j) = (A_i + dA_i)(A_j + dA_j) - A_i A_j \tag{13}$$

retaining terms to $O(dt)$, then average over all eddies, and finally divide by dt. Note that the coefficients in (11) are not necessarily constants and are assumed to have the appropriate functional forms (in terms of deterministic functions like k, ϵ, etc.) that give the correct dimensions in each term. The C_1 term is introduced by analogy to the Langevin equation and, as will be shown, is needed in order to ensure realizability. The C_2 term provides isotropic stochastic forcing that tends to randomize the orientation of the eddy axes. The deterministic vector Γ_i acts as an organizing vector for the stochastic forcing in the C_3 term; for example, Γ_i could represent an organizing effect for the non-linear interactions provided by the structure of the larger scales or the mean field. Finally, the C_4 term assumes that the non-linear turbulence-turbulence interactions can provide an effective random rotation acting on an individual eddy axis. Substituting (11) in (13), one obtains

$$
\begin{aligned}
d(A_i A_j) = {}& [G_{ik}A_k A_j + G_{jk}A_k A_i - 2G_{nm}(a_n a_m + v_n v_m)A_i A_j + 2C_1 A_i A_j]dt \\
& + C_2^2 dW_i dW_j + C_2 C_3 (dW_i dW_q \Gamma_q A_j + dW_p \Gamma_p A_i dW_j) \\
& + C_2 C_4 (dW_i \epsilon_{jqr} dW_q A_r + \epsilon_{ipt} dW_p A_t dW_j) \\
& + C_3^2 dW_p \Gamma_p A_i dW_q \Gamma_q A_j + C_3 C_4 (\epsilon_{jqr} A_r A_i + \epsilon_{iqt} A_t A_j) dW_q dW_p \Gamma_p \\
& + C_4^2 \epsilon_{ipt} dW_p A_t \epsilon_{jqr} dW_q A_r \, .
\end{aligned}
\tag{14}
$$

Averaging over the ensemble of eddies and simplifying, one obtains

$$
\begin{aligned}
\frac{dA_{ij}}{dt} = {}& G_{ik}A_{kj} + G_{jk}A_{ki} - 2G_{nm}q^2 Z_{nmij} - 2G_{nm}\langle v_n v_m A_i A_j \rangle + 2C_1 A_{ij} \\
& + C_2^2 \delta_{ij} + C_3^2 \Gamma^2 A_{ij} + C_3 C_4 \Gamma_p (\epsilon_{jpt} A_{ti} + \epsilon_{ipt} A_{tj}) + C_4^2 (q^2 \delta_{ij} - A_{ij}) \, .
\end{aligned}
\tag{15}
$$

Note that we have no control over the sign of the terms involving C_2^2, C_3^2 and C_4^2, which must be positive for realizability, but we have a choice over the sign of the terms involving C_1 and $C_3 C_4$. Taking the trace of (15), one finds

$$
\frac{dA_{ii}}{dt} = \frac{dq^2}{dt} = 2P - 2\epsilon = -2G_{nm}R_{nm} + 2C_1 q^2 + 3C_2^2 + C_3^2 \Gamma^2 q^2 + 2C_4^2 q^2 \, .
\tag{16}
$$

Therefore we must have

$$
2C_1 q^2 + 3C_2^2 + C_3^2 \Gamma^2 q^2 + 2C_4^2 q^2 = -2\epsilon \, .
\tag{17}
$$

Based on dimensional considerations, we let

$$
C_1 = \tilde{C}_1/\tau \qquad C_2 = \tilde{C}_2\sqrt{\epsilon} \qquad C_3 = \tilde{C}_3/\sqrt{\tau} \qquad C_4 = \tilde{C}_4/\sqrt{\tau} \, .
\tag{18}
$$

Then condition (17) becomes

$$
2\tilde{C}_1 q^2/\tau + 3\tilde{C}_2 \epsilon + \tilde{C}_3 \Gamma^2 q^2/\tau + 2\tilde{C}_4^2 q^2/\tau = -2\epsilon \, ,
\tag{19}
$$

and if we assume $\tau = q^2/2\epsilon$ then

$$2\tilde{C}_1 + \frac{3}{2}\tilde{C}_2^2 + \tilde{C}_3^2\Gamma^2 + 2\tilde{C}_4^2 = -1 \,. \tag{20}$$

Note that realizability requires $\tilde{C}_1 \leq -1/2$. Using (3), (15), and (18), one finds that the evolution equation for a_{ij} is given by

$$\frac{da_{ij}}{dt} = G_{ik}a_{kj} + G_{jk}a_{ki} - 2G_{nm}Z_{nmij} - 2G_{nm}\langle v_n v_m A_i A_j\rangle/q^2 + 2S_{nm}r_{nm}a_{ij}$$
$$+ \frac{1}{\tau}\Big[(1 + 2\tilde{C}_1 + \tilde{C}_3^2\Gamma^2 - \tilde{C}_4^2)a_{ij} + \frac{1}{2}(\tilde{C}_2^2 + 2\tilde{C}_4^2)\delta_{ij} + \tilde{C}_3\tilde{C}_4\Gamma_p(\epsilon_{jpt}a_{ti} + \epsilon_{ipt}a_{tj})\Big] \,. \tag{21}$$

Note that the trace condition $da_{ii}/dt = 0$ is satisfied if (20) is assumed. Next we require that the terms involving $\tilde{C}_1$, $\tilde{C}_2^2$, $\tilde{C}_3^2$, and $\tilde{C}_4^2$ in (21) combine to produce a return to anisotropy term of the form $C_*^2(\frac{1}{3}\delta_{ij} - a_{ij})$. This can be accomplished if

$$-1 = 2\tilde{C}_1 + \frac{3}{2}\tilde{C}_2^2 + \tilde{C}_3^2\Gamma^2 + 2\tilde{C}_4^2 \,. \tag{22}$$

Note that (22) is identical to (20), and hence this additional requirement is automatically satisfied if the trace condition (20) is imposed. Solving (20) for $\tilde{C}_1$ and substituting back into (21), one finds

$$\frac{da_{ij}}{dt} = G_{ik}a_{kj} + G_{jk}a_{ki} - 2G_{nm}Z_{nmij} - 2G_{nm}\langle v_n v_m A_i A_j\rangle/q^2 + 2S_{nm}r_{nm}a_{ij}$$
$$+ \frac{1}{\tau}\Big[\frac{3}{2}(\tilde{C}_2^2 + 2\tilde{C}_4^2)(\frac{1}{3}\delta_{ij} - a_{ij}) + \tilde{C}_3\tilde{C}_4\Gamma_p(\epsilon_{jpt}a_{ti} + \epsilon_{ipt}a_{tj})\Big] \,. \tag{23}$$

The fourth term on the RHS of (23) can be evaluated using the conditional averaging procedure described in KR (see pp. 85-95). Substituting the resulting expression in (23) produces

$$\frac{da_{ij}}{dt} = G_{ik}^*a_{kj} + G_{jk}^*a_{ki} - [3\phi + 1]G_{km}^*Z_{kmij} + (3\phi - 1)G_{nm}^*a_{nm}a_{ij}$$
$$- 2\gamma S_{nm}^*\frac{\Omega_k}{\Omega}\epsilon_{nkt}(Z_{tmij} - a_{tm}a_{ij}) \tag{24}$$
$$+ \frac{1}{\tau}\Big[\frac{3}{2}(\tilde{C}_2^2 + 2\tilde{C}_4^2)(\frac{1}{3}\delta_{ij} - a_{ij}) + \tilde{C}_3\tilde{C}_4\Gamma_p(\epsilon_{jpt}a_{ti} + \epsilon_{ipt}a_{tj})\Big] \,.$$

The algebraic k-ϵ Eq. (1), expressed in terms of the Reynolds stress anisotropy $\tilde{r}_{ij} = r_{ij} - \delta_{ij}/3$, is given by

$$\tilde{r}_{ij} = -\frac{2\nu_T}{q^2}S_{ij}^* = -2C_\mu\frac{q^2}{4\epsilon}S_{ij}^* = -C_\mu\frac{q^2}{2\epsilon}S_{ij}^* \tag{25}$$

where $\nu_T = C_\mu k^2/\epsilon = C_\mu(q^2)^2/(4\epsilon)$ is the turbulent viscosity. For irrotational mean strain, the algebraic constitutive Eq. (2) for the structure-based model produces (with $\phi = \gamma = 0$)

$$\tilde{r}_{ij} = -\frac{1}{2}\tilde{a}_{ij} \tag{26}$$

where $\tilde{a}_{ij} = a_{ij} - \frac{1}{3}\delta_{ij}$ is the anisotropy of a_{ij}. From (25) and (26) we see that consistency with k-ϵ modeling (in the weak strain limit) would require

$$\tilde{a}_{ij} = C_\mu \frac{q^2}{\epsilon} S_{ij}^* . \tag{27}$$

Now if we assume equilibrium under weak strain rates in (23), we obtain

$$\frac{1}{\tau}[\frac{3}{2}(\tilde{C}_2^2 + 2\tilde{C}_4^2)\tilde{a}_{ij}] = \frac{4}{15}S_{ij}^* . \tag{28}$$

Substituting (27) in (28), one finds that consistency between the structure-based model and k-ϵ modeling in the limit of equilibrium structure under weak deformation requires

$$\frac{3}{2}(\tilde{C}_2^2 + 2\tilde{C}_4^2) = \frac{4}{15C_\mu} . \tag{29}$$

Next we consider two limiting cases where there are no non-linear eddy-eddy interactions, and hence the coefficient $\frac{3}{2}(\tilde{C}_2^2 + 2\tilde{C}_4^2)$ should vanish. The first case is that of a 2C-field of jets having $a_{22} = 0$ and $\phi = 1$, corresponding to the type of structure one might expect to find at the wall in a boundary layer. The jets in this 2C field have no way of re-orienting each other towards a more isotropic distribution. The second limiting case is that of a 2D-field of vortices with $a_{11} = 1$ and $\phi = 0$, corresponding to the RDT limiting state in the irrotational axisymmetric contraction flow. Again these vortices have no means of re-orienting each other, and the return to isotropy must shut off. Both of these limiting cases can be accounted for by the postulating the functional form

$$\frac{3}{2}(\tilde{C}_2^2 + 2\tilde{C}_4^2) = \alpha(1 - \phi)(1 - a^2) \tag{30}$$

where $a^2 = a_{ik}a_{ki}$. Then the k-ϵ consistency requirement (29) for equilibrium under weak strain rates produces

$$\alpha = \frac{2}{5C_\mu} . \tag{31}$$

Based on this analysis, we propose using

$$\frac{da_{ij}}{dt} = G_{ik}^* a_{kj} + G_{jk}^* a_{ki} - [3\phi + 1]G_{km}^* Z_{kmij} + (3\phi - 1)G_{nm}^* a_{nm}a_{ij}$$

$$- 2\gamma S_{nm}^* \frac{\Omega_k}{\Omega}\epsilon_{nkt}(Z_{tmij} - a_{tm}a_{ij}) \tag{32}$$

$$+ \frac{1}{\tau}\left[\alpha(1 - \phi)(1 - a^2)(\frac{1}{3}\delta_{ij} - a_{ij}) + C_e\frac{\Omega_p}{\Omega}(\epsilon_{jpt}a_{ti} + \epsilon_{ipt}a_{tj})\right] .$$

Considering equilibrium in homogeneous shear suggests the values using $\alpha \approx 1.8$ and $C_e \approx -0.35$, which we have adopted. Note that we have taken the deterministic vector Γ_i to be a unit vector aligned with the mean vorticity vector Ω_i; this choice was suggested by looking at a number of homogeneous flows, including homogeneous shear, irrotational axisymmetric strain, and plane stain.

2.4 Extension of the scalar transport equations

We are currently using one simple term in each of the two scalar equations that tend to restore vortical turbulence ($\phi = 0, \gamma = 0$), appropriate for isotropy. The form of the extended equations is as follows:

$$\frac{d\phi}{dt} = \dots \text{RDT} \dots - C_\phi \phi / \tau \qquad \text{with} \qquad C_\phi = 1.3 \qquad (33)$$

$$\frac{d\gamma}{dt} = \dots \text{RDT} \dots - C_\gamma \gamma / \tau \qquad \text{with} \qquad C_\gamma = 2.8 \, . \qquad (34)$$

The numerical values for the model constants were calibrated for homogeneous shear. Here RDT stands for the RHS of these equations in the RDT limit as given in KR [see Eqs. (5.10.4) and (5.10.5)].

2.5 Evolution of the turbulence scales

The choice of turbulence scales to be used in a turbulence model is not unique. For example, standard k-ϵ models use transport equations for k and ϵ, and determine the turbulence time scale through an algebraic equation. Another possibility is to use the evolution equation for the time scale τ (or the reciprocal time scale ω) along with the equation for k, and then evaluate ϵ from an algebraic equation. Each of these approaches has some problems. We are currently investigating the use of the k and ϵ equations in the form shown below.

$$\frac{dk}{dt} = P - \epsilon \qquad (35)$$

$$\frac{d\epsilon}{dt} = [-C_d S_{kk} - C_s S_{ij} r_{ij} - C_0 / \tau - C_\Omega \sqrt{\Omega_{ij} \Omega_{jk} a_{ik}}] \epsilon \qquad (36)$$

with

$$C_d = \frac{4}{3} \qquad C_s = 3.0 \qquad C_0 = \frac{11}{6} \qquad C_\Omega = 0.01 \, . \qquad (37)$$

Note that the ϵ equation has the standard form except for the last term involving C_Ω. This term takes advantage of the structure information in a_{ij} and allows for a decrease in the dissipation rate in the presence of mean rotation, except when the turbulence becomes two-dimensional, as observed in direct numerical simulations.

3. Evaluation of the proposed extensions

In this section, the extended structure-model given by (2), (4), and (32)-(37) is tested for four independent homogeneous flows. First we summarize the values

of the constants that we will be using. For clarity we also include the values for the constants in the RDT model [Eqs. (5.9.6)-(5.9.11) in KR] for which we use the notation of KR:

- Rapid model: $C_1 = 5.9$ $C_2 = 2.0$ $C_3 = 7.0$ $C_4 = 2.5$ (38)

- Slow model: $\alpha = 1.8$ $C_e = -0.35$ $C_\phi = 1.3$ $C_\gamma = 2.8$

$$C_d = \frac{4}{3}   C_s = 3.0   C_0 = \frac{11}{6}   C_\Omega = 0.01.$$ (39)

3.1 Homogeneous shear in a rotating frame

We first consider the problem of homogeneous shear in a rotating frame. The mean velocity gradient tensor G_{ij}, the frame vorticity Ω_i^f, and frame rotation rate Ω_i are defined by

$$G_{ij} = \begin{pmatrix} 0 & S & 0 \\ 0 & 0 & 0 \\ 0 & 0 & 0 \end{pmatrix}, \qquad 2\Omega_i = \Omega_i^f = (0, 0, \Omega^f).$$ (40)

We consider initially isotropic turbulence

$$r_{ij} = \tfrac{1}{3}\delta_{ij}, \qquad k = k_0, \qquad \epsilon = \epsilon_0.$$ (41)

First, we consider the case of homogeneous shear in a stationary frame ($\Omega^f = 0$) with an initial $Sk_0/\epsilon_0 = 2.36$. Figure 1 shows the model predictions for the components of the normalized Reynolds stress tensor $r_{ij} = R_{ij}/q^2$. The symbols are from the direct numerical simulation of Rogers *et. al.* (1986), which also had $Sk_0/\epsilon_0 = 2.36$. The agreement between the model predictions and the direct numerical simulation is good. As shown in Table 1, the equilibrium state predicted by the model is in good agreement with the experiments of Tavoularis & Karnik (1989).
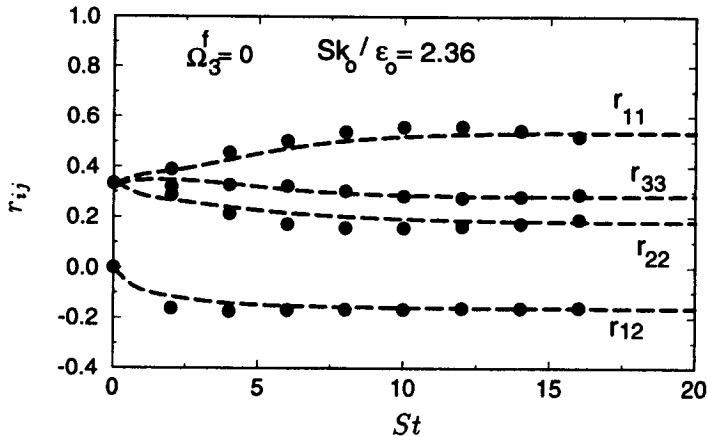

FIGURE 1.   Time evolution of the normalized Reynolds stress tensor in homogeneous shear for $Sk_0/\epsilon_0 = 2.36$. Comparison of the predictions of the structure-based model (– – – –) with the direct numerical simulations of Rogers *et. al.* (1986) (•).

The solution in the case of homogeneous shear in a rotating frame depends on the initial conditions only through the dimensionless parameter Sk_0/ϵ_0, and on the frame vorticity through the dimensionless parameter Ω^f/S (Speziale *et. al*, 1991). The value of Ω^f/S determines whether the flow is stable, in which case k and ϵ decay in time, or unstable, in which case both k and ϵ grow exponentially in time. In the stable regime $(\epsilon/Sk)_\infty = 0$, and in the unstable regime $(\epsilon/Sk)_\infty > 0$.

Equilibrium Values	Structure Model	Experiments
r_{11}	0.53	0.51 ± 0.04
r_{22}	0.18	0.22 ± 0.02
r_{33}	0.29	0.27 ± 0.03
r_{12}	-0.16	-0.16 ± 0.01
Sk/ϵ	5.30	4.60 ± 0.50
P/ϵ	1.70	1.47 ± 0.14

TABLE 1. Equilibrium results for homogeneous shear: comparison with the experiments of Tavoularis & Karnik (1989).
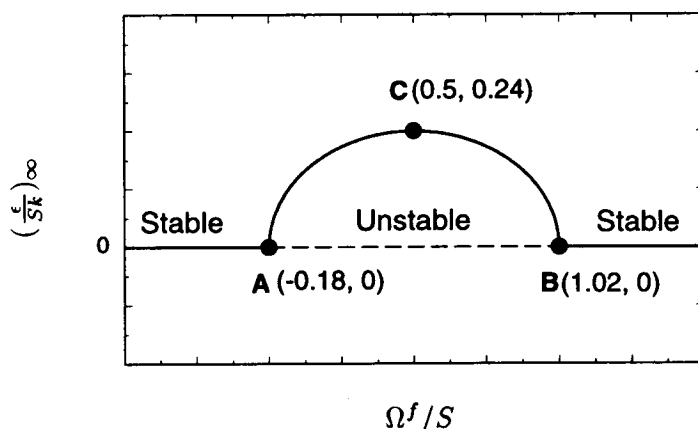
FIGURE 2. Bifurcation diagram of the structure-based model for homogeneous shear in a rotating frame.

Linear analysis and LES show that the flow is unstable for $-0.21 \lesssim \Omega^f/S \le 1$ and stable outside these bounds. The most unstable case, having the highest growth rate for k and ϵ and the largest $(\epsilon/Sk)_\infty$, corresponds to $\Omega^f/S = 0.5$. Figure 2 shows the bifurcation diagram for the structure-based model. The structure-based model does an excellent job predicting the location of the bifurcation points A and B, and that of the most energetic state C (largest growth rate for k).

In the absence of DNS or experimental data, we evaluate the model performance using the large-eddy simulations of Bardina *et. al* (1983). Figure 3 shows the evolution of the normalized kinetic energy k/k_0 with non-dimensional time St. Note
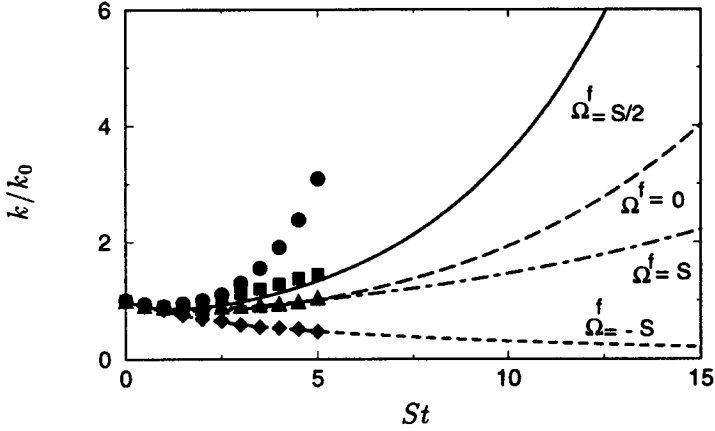
FIGURE 3. Time evolution of the turbulent kinetic energy in rotating shear flows. Comparison of the predictions of the structure-based model (lines) with the large-eddy simulations of Bardina *et. al* (1983) shown as symbols: $\Omega^f = 0$, (- - - - , ■); $\Omega^f = 0.5S$, (——— , ●); $\Omega^f = S$, (— · — , ▲); $\Omega^f = -S$, (· · · · · · · , ◆).

that the model captures the general trends correctly. For example, it correctly predicts that the highest rate of growth (for both k and ϵ) should occur for $\Omega^f = S/2$, which RDT shows is the most unstable case. It also predicts a weak rate of growth for the case $\Omega^f = S$ and a decay (relaminarization) for $\Omega^f = -S$. The numerical agreement with the LES is reasonable, but the model tends to predict somewhat lower rates of growth, particularly so in the case $\Omega^f = 0.5S$. This problem is common to all the currently available second-order closures as noted by Speziale *et. al.* (1989).

3.2 Axisymmetric strain

Next, we consider the performance of the extended structure-based model for the cases of axisymmetric contraction and expansion in homogeneous turbulence. The mean velocity gradient tensor is given by

$$S_{ij} = \begin{pmatrix} S & 0 & 0 \\ 0 & -S/2 & 0 \\ 0 & 0 & -S/2 \end{pmatrix} \tag{42}$$

with $S > 0$ for contraction and $S < 0$ for expansion. We consider an initially isotropic state as specified in (41). The solution depends on these conditions through the non-dimensional parameter Sk_0/ϵ_o. Comparisons are made with the DNS of Lee & Reynolds (1985). In both cases, we compare with the slowest runs from these simulations, which correspond to $Sk_0/\epsilon_0 = 0.56$ (contraction case AXK) and $Sk_0/\epsilon_0 = 0.41$ (expansion case EXO).

In Fig. 4(a), we consider the time evolution of the components of the Reynolds stress anisotropy $\tilde{r}_{ij}$. The total strain

$$C^* = \exp\left(\int_0^t |S_{\max}(t')| \, dt' \right) \tag{43}$$

FIGURE 4.   Comparison of the model predictions (———) with the direct numerical simulations of Lee & Reynolds (1985) (•) for irrotational axisymmetric contraction with $Sk_0/\epsilon_0 = 0.56$. (a) Evolution of the Reynolds stress anisotropy tensor $\tilde{r}_{ij}$. (b) Evolution of the normalized turbulent kinetic energy k/k_0.
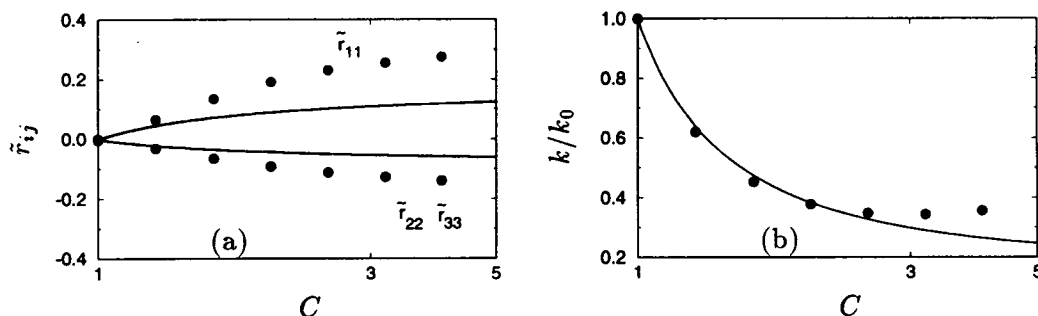
FIGURE 5.   Comparison of the model predictions (———) with the direct numerical simulations of Lee & Reynolds (1985) (•) for irrotational axisymmetric expansion with $Sk_0/\epsilon_0 = 0.41$. (a) Evolution of the Reynolds stress anisotropy tensor $\tilde{r}_{ij}$. (b) Evolution of the normalized turbulent kinetic energy k/k_0.
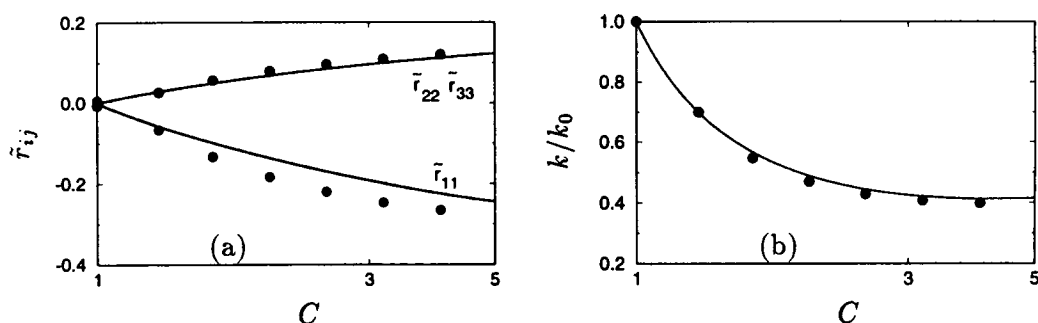

FIGURE 6.   Comparison of the model predictions (———) with the direct numerical simulations of Lee & Reynolds (1985) (•) for irrotational plane strain with $Sk_0/\epsilon_0 = 0.50$. (a) Evolution of the Reynolds stress anisotropy tensor $\tilde{r}_{ij}$. (b) Evolution of the normalized turbulent kinetic energy k/k_0.
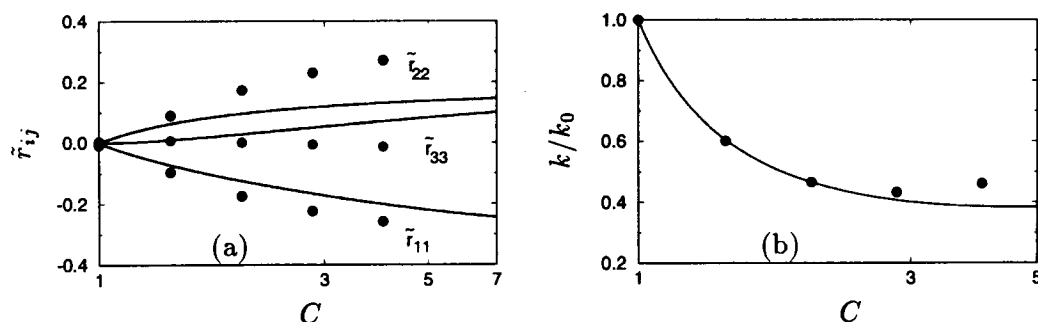
serves as the time coordinate in this plot. The model predictions, shown in solid lines, are in very good agreement with the DNS of Lee & Reynolds (1985) shown in symbols. The same good agreement between model and DNS is obtained in Fig. 4(b), where we consider the time evolution of the normalized turbulent kinetic energy k/k_0.

The evolution of the Reynolds stress anisotropy in the case of axisymmetric expansion is considered in Fig. 5(a). Note that the model underpredicts significantly the level of anisotropy as compared to the DNS of Lee & Reynolds (1985). The model prediction for the evolution of the normalized turbulent kinetic energy [shown in Fig. 5(b)] is accurate up to $C \approx 2.6$, but eventually it also degrades. This deficiency of structure-based model is discussed shortly.

3.3 Plane strain

We now turn to the case of homogeneous turbulence subjected to plane strain. The mean velocity gradient tensor is given by

$$S_{ij} = \begin{pmatrix} S & 0 & 0 \\ 0 & -S & 0 \\ 0 & 0 & 0 \end{pmatrix}. \tag{44}$$

We consider initially isotropic conditions corresponding to (41) with $Sk_0/\epsilon_o = 0.5$. These conditions correspond to the slowest run (case PXA) reported by Lee & Reynolds (1985).

Figure 6(a) shows the time evolution of the Reynolds stress anisotropy. Note that the model predictions are accurate only for very small total strain and quickly degrade, particularly for $\tilde{r}_{11}$ and $\tilde{r}_{33}$. As in the axisymmetric expansion case, the model prediction for the rate of decay of k/k_0 remains accurate for a somewhat larger total strain, but eventually it degrades also [see Fig. 6(b)].

3.4 Some problems with the current approach

The relatively poor performance of the structure-based model in the axisymmetric expansion and plane strain flows prompted us to take a closer look at both the physics of these flows and at our model. What we have learned helped us understand better these flows and also provided us with a solution to the problems faced by the structure-based model in these flows.

Rapid distortion analysis (RDT) shows that under irrotational mean strain $\tilde{r}_{ij} = \tilde{d}_{ij}$. This result is clearly exhibited in the most rapid runs from the DNS of Lee & Reynolds (1985), including the rapid expansion and plane strain runs corresponding to $Sk_0/\epsilon_0 = 41.0$ and $Sk_0/\epsilon_0 = 50.0$ respectively. However, when the slowest runs for these two flows are considered, corresponding to cases EXO and PXA discussed above, one finds that $\tilde{\mathbf{r}} \gg \tilde{\mathbf{d}}$ (see Fig. 7). These observations become even more interesting if one notices that the level of stress anisotropy $\tilde{r}_{ij}$ in the slow axisymmetric expansion and plane strain runs exceeds the level of stress anisotropy in the corresponding rapid runs! This effect is demonstrated in Fig. 8, where we show plots of $|II_r| = \tilde{r}_{ij}\tilde{r}_{ji}/2$ versus $|II_d| = \tilde{d}_{ij}\tilde{d}_{ji}/2$. The open symbols correspond
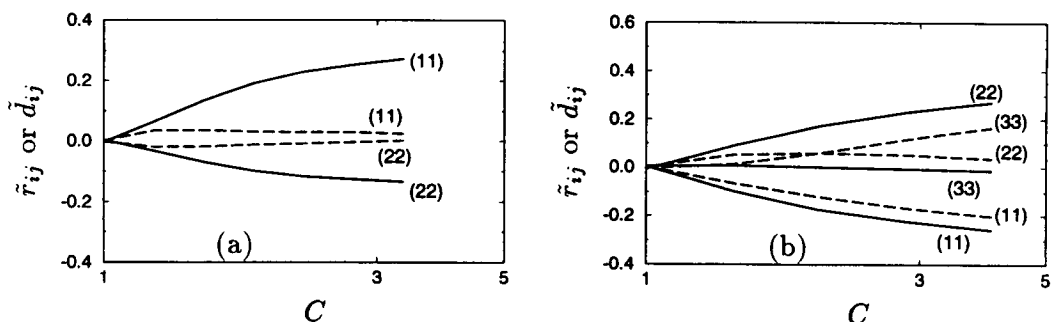
FIGURE 7.   Comparison of the Reynolds stress anisotropy $\tilde{r}_{ij}$ (———) with the dimensionality anisotropy $\tilde{d}_{ij}$ (- - - -) from the direct numerical simulations of Lee & Reynolds (1985). (a) Irrotational axisymmetric expansion with $Sk_0/\epsilon_0 = 0.41$. (b) Plane strain with $Sk_0/\epsilon_0 = 0.50$.
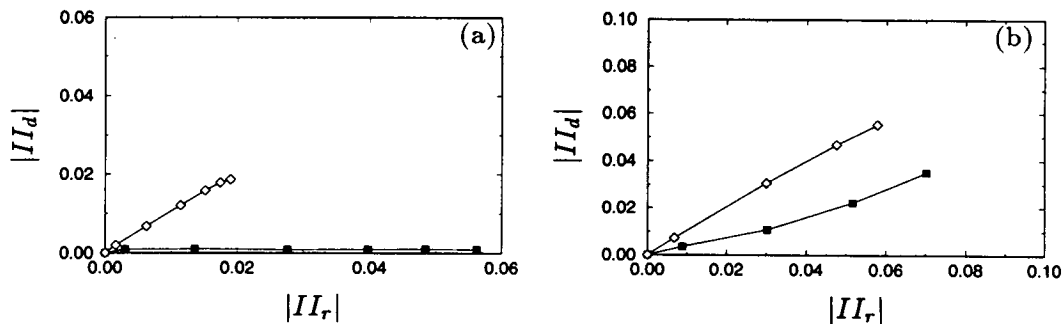
FIGURE 8.   The second invariants of the stress anisotropy $-II_r$ vs. the second invariant of the dimensionality anisotropy $-II_d$. (a) Axisymmetric expansion at $Sk_0/\epsilon_0 = 0.41$ (■) and at $Sk_0/\epsilon_0 = 41.0$ (◊). (b) Plane strain at $Sk_0/\epsilon_0 = 0.50$ (■) and at $Sk_0/\epsilon_0 = 50.0$ (◊).

to the most rapid run and the closed symbols to the slowest run of Lee & Reynolds (1985) for each flow. Note that in the rapid runs $|II_d| \approx |II_r|$ whereas in the slow runs $|II_d| \ll |II_r|$. What is more, in each flow, the maximum level reached by $|II_r|$ is higher in the slow run that it is the rapid run.

By using a linearized version of the RDT evolution equations for $\tilde{r}_{ij}$ and $\tilde{d}_{ij}$, valid for small anisotropies, we have been able to show that these intriguing effects are primarily controlled by the rapid terms in the two evolution equations. In other words, RDT will maintain $\tilde{\mathbf{r}} = \tilde{\mathbf{d}}$ if it is initially true, but an arbitrarily small deviation $\tilde{\boldsymbol{\Delta}} = \tilde{\mathbf{r}} - \tilde{\mathbf{d}}$ will be amplified by the rapid terms. The initial conditions of the simulations of Lee & Reynolds imposed a very small initial $\tilde{\boldsymbol{\Delta}}_0 = \tilde{\mathbf{r}}(0) - \tilde{\mathbf{d}}(0)$. However, even in the absence of any initial $\tilde{\boldsymbol{\Delta}}_0$, such a deviation could be triggered by unequal rates of return to isotropy for the two tensors.

The fact that these unexpected effects (once triggered by the initial conditions or non-linear effects) seem to be dominated by the rapid terms prompted us to take

a closer look at our rapid model. We believe that the difficulties encountered in these flows are related not to the slow model developed above, but rather to the form of the basic constitutive Eq. (2), which relates the Reynolds stresses to the eddy-axis tensor. The reason for this failure lies in the fact the current version of the structure model assumes that, in absence of mean rotation, $\phi = \gamma = 0$. This means that the principal axes of r_{ij} remain locked onto the principal axes of a_{ij}. This is appropriate for the RDT of initially isotropic turbulence, when the eddies do not have time to interact with each other. The cases examined above show that this is not appropriate for slower mean strain rates where the non-linear eddy-eddy interactions are important. These non-linear eddy-eddy interactions provide an effective eddy rotation acting on an individual eddy due to the circulation associated with the background sea of eddies. The effective eddy rotation tends to rotate the principal axes of the stresses associated with an individual eddy so that these become misaligned with the eddy axis, and some ϕ and γ are produced. But in order to capture these effects it is not enough to allow for non-zero ϕ and γ under irrotational strain; we also need to replace the mean vorticity Ω_i in (2) with the effective eddy rotation rate Ω_i^*; this will produce a contribution in the jet-vortex correlation term even in the absence of mean rotation. Simple kinematic analysis (see Appendix I in KR) shows that Ω_i^* is given by

$$\Omega_i^* = \epsilon_{irp} a_p \dot{a}_r \qquad \dot{a}_i = \frac{da_i}{dt} \, . \tag{45}$$

Note that because of (45) the effective eddy rotation rate will be sensitive to the slow model adopted in the a_i (or A_i) evolution equation. Some preliminary analysis suggests that these changes in the constitutive Eq. (2), coupled with an appropriate slow model in the A_i (and hence a_{ij}) equations, will allow the structure-based model to access states above the RDT limit on the axisymmetric expansion line of the anisotropy invariant map.

4. Summary and future plans

We have proposed and implemented an extension of the structure-based model for weak deformations. It was shown that the extended model will correctly reduce to the form of standard k-ϵ models for the case of equilibrium under weak mean strain. The realizability of the extended model is guaranteed by the method of its construction. The predictions of the proposed model were very good for rotating homogeneous shear flows and for irrotational axisymmetric contraction, but were seriously deficient in the case of plane strain and axisymmetric expansion.

We have concluded that the problem behind these difficulties lies in the algebraic constitutive equation relating the Reynolds stresses to the structure parameters rather than in the slow model developed here. In its present form, this equation assumes that under irrotational strain the principal axes of the Reynolds stresses remain locked onto those of the eddy-axis tensor. This is correct in the RDT limit, but inappropriate under weaker mean strains, when the non-linear eddy-eddy interactions tend to misalign the two sets of principal axes and create some non-zero ϕ and γ.

We plan to modify the constitutive equation and the evolution equation for the eddy-axis tensor a_{ij} as necessary to reflect these effects. This will require replacing the mean vorticity vector Ω_i in the constitutive equation by an effective eddy rotation rate $\Omega_i^* = \epsilon_{irp} a_p \dot{a}_r$ that correctly accounts for the non-linear effects described above. The slow model in the eddy-axis equation may have to be adjusted accordingly since the effective eddy rotation rate Ω_i^* will be sensitive to it.

Once these modifications have been implemented and evaluated, we will focus in extending the structure-based model for inhomogeneous flows. This extension will require the addition of diffusion terms in the transport equations for the structure parameters and the turbulence scales. Some preliminary work in determining the form of the diffusion terms and appropriate boundary conditions for these equations has been carried out.

REFERENCES

ARNOLD, L. 1974 *Stochastic Differential Equations*. John Wiley and Sons.

BARDINA, J, FERZIGER, J. H., & REYNOLDS, W. C. 1983 *Improved turbulence models based on large eddy simulation of homogeneous, incompressible, turbulent flows*. Report TF-19, Thermosciences Division, Department of Mechanical Engineering, Stanford University.

DURBIN, P. A. & SPEZIALE, C. G. 1994 Realizability of second-moment closures via stochastic analysis. *J. Fluid Mech.* **280,** 395-407.

KASSINOS, S. C. & REYNOLDS, W. C. 1994 *A structure-based model for the rapid distortion of homogeneous turbulence*. Report TF-61, Thermosciences Division, Department of Mechanical Engineering, Stanford University.

LEE, M. J. & REYNOLDS, W. C. 1985 *Numerical experiments on the structure of homogeneous turbulence*. Report TF-24, Thermosciences Division, Department of Mechanical Engineering, Stanford University.

ROGERS, M. M., MOIN, P., & REYNOLDS, W. C. 1986 *The structure and modeling of the hydrodynamic and passive scalar fields in homogeneous turbulent shear flow*. Report TF-25, Thermosciences Division, Department of Mechanical Engineering, Stanford University.

SPEZIALE, C. G., & MAC GIOLLA MHUIRIS, N. 1989 On the prediction of equilibrium states in homogeneous turbulence. *J. Fluid Mech.* **209,** 591-615.

SPEZIALE, C. G., SARKAR, S., & GATSKI, T. B. 1991 Modelling the pressure-strain correlation of turbulence: an invariant dynamical systems approach. *J. Fluid Mech.* **227,** 245-272.

TAVOULARIS, S. & KARNIK, U. 1989 Further experiments on the evolution of turbulent stresses and scales in uniformly sheared turbulence. *J. Fluid Mech.* **204,** 457-478.

Turbulence modeling for non-equilibrium flow

By P. A. Durbin

1. Motivation and objectives

The work performed during this year has involved further assessment and extension of the $k - \varepsilon - v^2$ model, and initiation of work on scalar transport. The latter is introduced by the contribution of Y. Shabany to this volume.

Flexible, computationally tractable models are needed for engineering CFD. As computational technology has progressed, the ability and need to use elaborate turbulence closure models has increased. The objective of our work is to explore and develop new analytical frameworks that might extend the applicability of the modeling techniques. In past years the development of a method for near-wall modeling was described. The method has been implemented into a CFD code and its viability has been demonstrated by various test cases. Further tests are reported herein.

Non-equilibrium near-wall models are needed for some heat transfer applications. Scalar transport seems generally to be more sensitive to non-equilibrium effects than is momentum transport. For some applications turbulence anisotropy plays a role and an estimate of the full Reynolds stress tensor is needed. We have begun work on scalar transport *per se*, but in this brief I will only report on an extension of the $k - \varepsilon - v^2$ model to predict the Reynolds stress tensor. The $k - \varepsilon - v^2$ model contains a representation of anisotropy via the k and $\overline{v^2}$ velocity scales. By invoking an algebraic stress approximation a formula can be derived to relate the stress tensor $\overline{u_i u_j}$ to k, $\overline{v^2}$ and $\partial_j U_i$.

2. Accomplishments

The governing equations of the $k - \varepsilon - v^2$ model will not be presented here. They can be found in Durbin (1995a). The mean flow satisfies the incompressible Navier-Stokes equations with an eddy viscosity. The turbulence model uses the standard $k - \varepsilon$ equations, a $\overline{v^2}$ transport equation, and an elliptic relaxation equation for the source term (f_{22}) in the $\overline{v^2}$-equation.

Subroutines were written to extend the INS-2D code of Rogers and Kwak (1990) to axisymmetric flow, including swirl. The flows computed with this extended code are a confined coaxial jet, with and without swirl, and an impinging circular jet. The former is a test case for certain combustor flows; the latter is relevant to impingement cooling.

2.1 Confined coaxial jets

The geometry is illustrated by Fig. 1. The upstream section is a coaxial pipe that dumps into a larger cylinder. Inlet profiles were created by computing fully developed pipe flow. This is the correct condition for the non-swirling experiment of

Habib and Whitelaw (1979). The swirling flow experiment of Roback and Johnson (1983) was not fully developed at the inlet. Indeed, it was necessary to contrive a swirl distribution within the pipe that would reproduce the swirl measured at the first measurement station in the experiment.

Figure 2 shows the computational and experimental results for the centerline velocity for 1:1 and 3:1 peak velocity ratios of the coaxial jets. This illustrates that the model predicts reasonable entrainment rates for the axisymmetric jet.

Swirling flow computations are contained in Fig. 3. It is possible to derive a swirl contribution to the turbulence model by regarding $\overline{v^2}$ as the radial component of the Reynolds normal stress. The solid line has this correction, the dashed line does not. It can be seen that the swirl effect on the turbulence is not important. As plotted, the experimental data do not conserve mass flux—they probably should be rescaled. However, the second profile shows that there is considerable scatter in the measurements.

The streamwise extent and radial height of the backflow region is well predicted by the model. Of course, the existence of the backflow bubble is a product of the Navier-Stokes equations; but the size of the bubble is controlled by how the turbulent entrainment is modeled. Also the model is responsible for the existence of a (statistically) steady, stable solution to the equations.

2.2 Impinging jet

The stagnation point jet is a flow in which some standard turbulence models have failed dramatically. The key features of this flow are both the large total strain along the stagnation streamline and the mean flow being perpendicular to the surface. A virtue of the elliptic relaxation method is that the governing equations and boundary conditions automatically distinguish the normal component of turbulent intensity. Damping functions for Reynolds stress models have failed in this flow because they assumed the mean flow to be tangent to the surface.

The large strain produces a 'stagnation point anomaly' (Durbin 1996) in the $k - \varepsilon$ and $k - \omega$ types of model. We did not experience that difficulty with the $k - \varepsilon - v^2$ model, but the underlying use of the standard $k - \varepsilon$ system will produce anomalous behavior in more strongly strained flows. Figure 5 shows the anomalously high heat transfer coefficient obtained with the $k - \varepsilon$ model and the more reasonable results with $k - \varepsilon - v^2$. The data are from Cooper *et al.* (1993).

The origin of the different behaviors of these models is explained by Fig. 6. This shows hot wire data for the streamwise intensity along the stagnation point streamline along with predictions of k and $\overline{v^2}$. The overprediction of St by $k - \varepsilon$ is due to using k, instead of the normal component, for the transport velocity scale, coupled to an overprediction of k.

2.4 Algebraic stress model

In applications of eddy diffusion to passive scalar transport, it is sometimes necessary to represent the anisotropy of the turbulence. For instance, near a wall, the turbulent diffusivity tangential to the surface can be an order of magnitude larger than that in the normal direction. The $k - \varepsilon - v^2$ eddy viscosity, $C_\mu \overline{v^2} T$
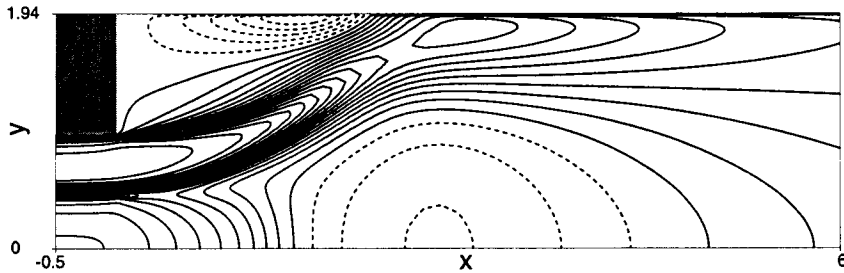
FIGURE 1. Contours of constant u-velocity for swirling, confined coaxial jet, showing a backflow bubble on the axis: S=0.47 corresponding to the Johnson and Roback experiment.
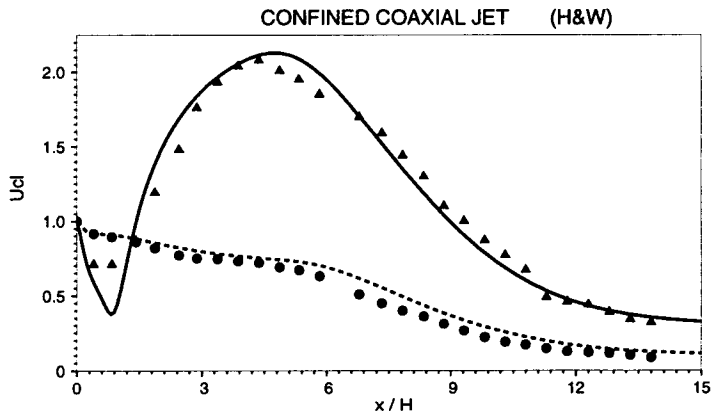
FIGURE 2. Centerline velocities for non-swirling coaxial jets. Data from Habib and Whitelaw. ● , jet velocity ratio=1; ▲ , jet velocity ratio=3; curves=model.

(T is the turbulence time-scale, k/ε at high Reynolds number), describes transport in the normal direction, which is usually suitable for solving the mean momentum equation. However, if there is a concentrated heat source on the surface, then heat transport in the streamwise direction can be important. This type of application requires that the full Reynolds stress tensor be estimated, using the more limited information predicted by the model.

A potential advantage of the $k - \varepsilon - v^2$ over the $k - \varepsilon$ model is that $\overline{v^2}/k$ provides a measure of anisotropy. Of course, the crucial role of anisotropy near walls was the original motivation for $k - \varepsilon - v^2$: the $\overline{v^2}$-equation enables the model to be integrated to the wall without damping functions because it acknowledges this important property of the turbulence. Here the anisotropic nature of this model will be exploited further: an algebraic formula to predict the other components of the Reynolds stress tensor from knowledge of k, ε, and $\overline{v^2}$ will be proposed.
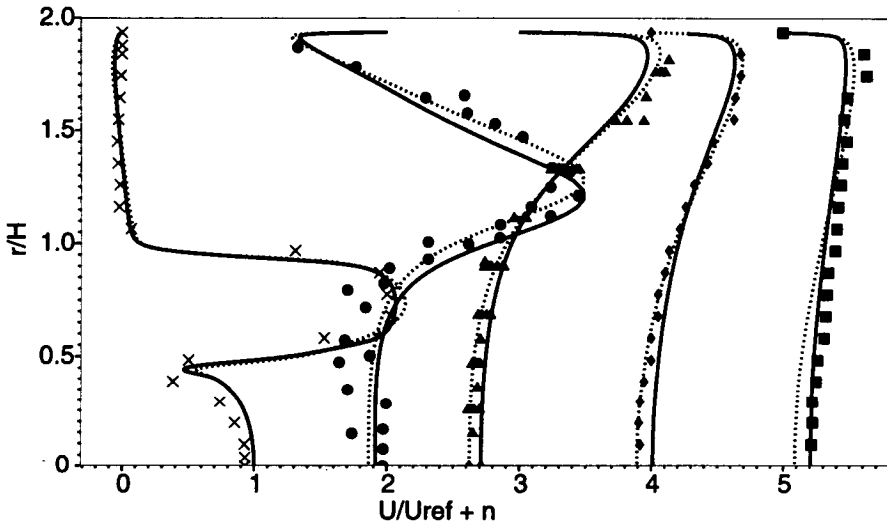
FIGURE 3.   Mean velocity profiles for the swirling jet with experimental data. The origin of the first velocity profile is at 0, the others are displaced to 2,3,4,5. Hence the second, third and fourth profiles show backflow on the axis, in agreement with the experiment. Data from Johnson and Roback. The dashed lines were computed with the basic model, the solid lines have a swirl term added to the v^2-equation.
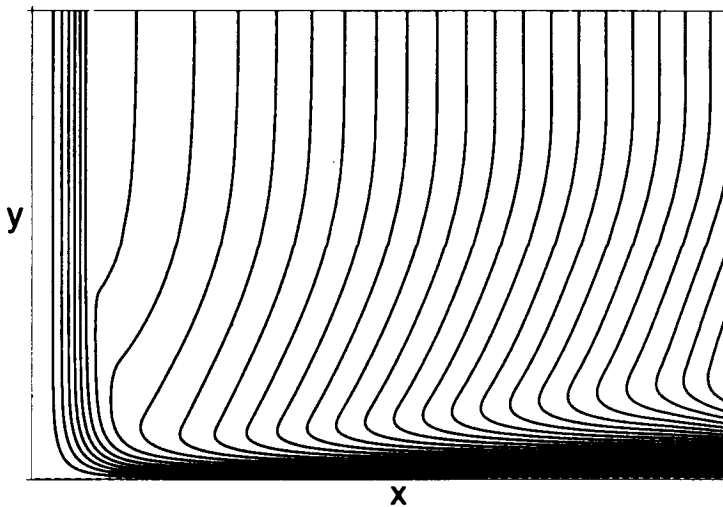
FIGURE 4.   Streamlines for an axisymmetric jet impinging on a plane wall.

IMPINGING JET
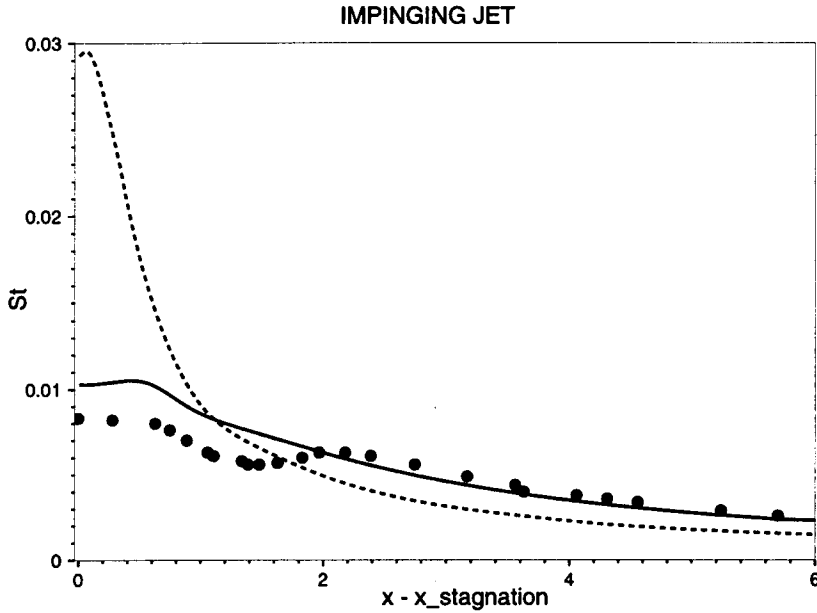
FIGURE 5. Stanton number versus radial distance along the impingement wall. The dashed line illustrates the stagnation point anomaly observed with the standard $k - \varepsilon$ model + wall damping function. The $k - \varepsilon - v^2$ model does not show that anomaly in this flow.

IMPINGING JET (Re=23,000; H/D=2)
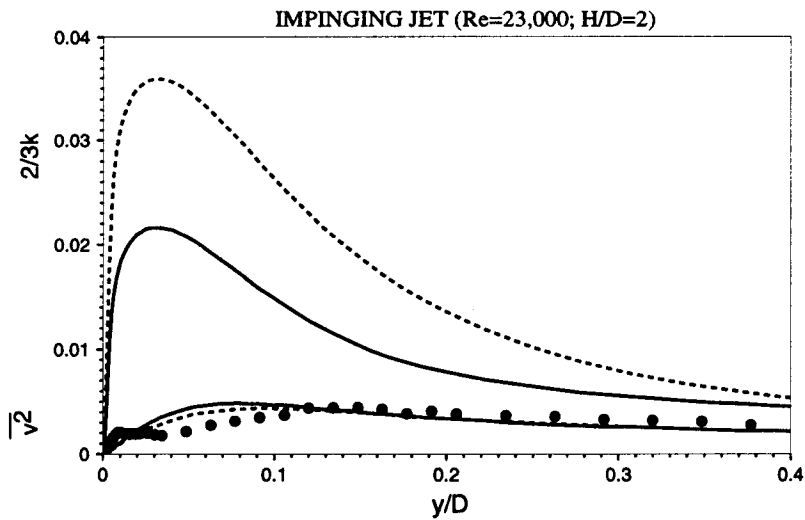
FIGURE 6. Single wire measurements of streamwise velocity fluctuations on the stagnation streamline with model prediction of $\overline{v^2}$ shown by the lower curves. The upper curves show k. The solid curves impose the bound discussed in Durbin (1996).
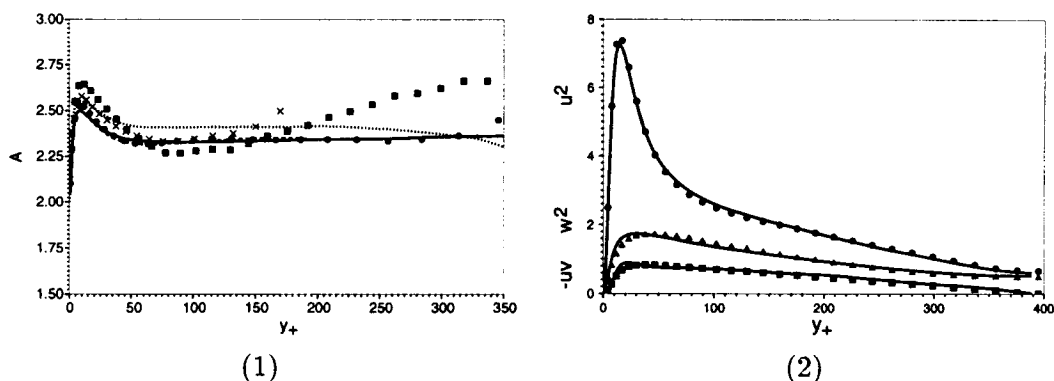
FIGURE 7. (1) Symbols: $A = (\overline{u_1^2} - \overline{u_2^2})/(\,^2/_3\ k - \overline{u_2^2})$ from DNS data; Curves: $A = 2 + 6S^*/(15 + 10S^*)$. (2) Reynolds stresses in channel flow, $R_\tau = 395$.
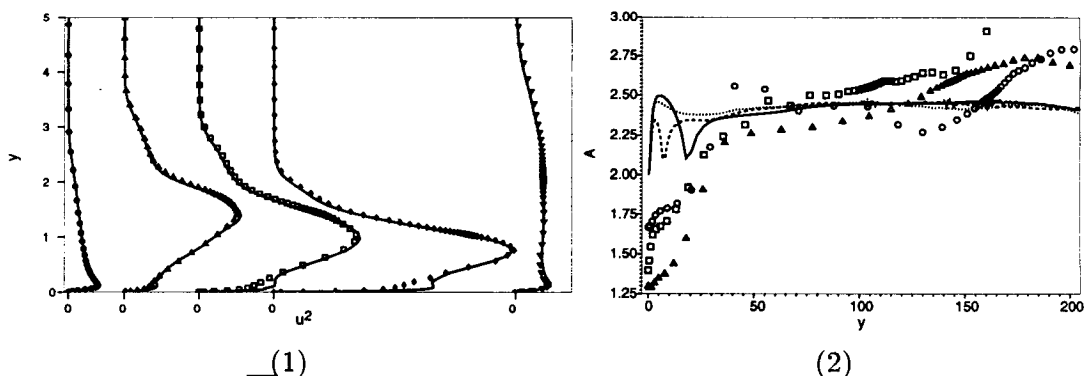
FIGURE 8. (1) $\overline{u^2}$ in flow over a backstep at various downstream positions. (2) Backstep: Symbols: $A = (\overline{u_1^2} - \overline{u_2^2})/(\,^2/_3\ k - \overline{u_2^2})$; Curves: $A = 2 + 6S^*/(15 + 10S^*)$

A general constitutive relation that depends additionally on the mean flow gradients is of the form

$$\overline{u_i u_j} = kF_{ij}(\mathbf{I}, \mathbf{S}, \mathbf{\Omega}, \overline{v^2}, k, T) \tag{1}$$

where $S_{ij} = \,^1/_2\,(\partial_j U_i + \partial_i U_j)$; $\Omega_{ij} = \,^1/_2\,(\partial_j U_i - \partial_i U_j)$ and $\mathbf{I}$ is the identity tensor. For two-dimensional incompressible flow, the most general tensor function of $\mathbf{\Omega}$ and $\mathbf{S}$ can be tailored to present purposes. This leads to the form

$$\overline{u_i u_j} = -2\nu_T S_{ij} + \,^2/_3\ k\delta_{ij}$$
$$+ \left(\,^2/_3\ k - \overline{v^2}\right)\left[A\left(\frac{\Omega_{ik}S_{kj} - S_{ik}\Omega_{kj}}{|S^2| + |\Omega^2|}\right) + (A - 2)\left(\frac{3S_{ik}S_{kj}}{|S^2|} - \delta_{ij}\right)\right] \tag{2}$$

where A is a coefficient that can be a function of the invariants $|S^2| = S_{ij}S_{ji}$ and $|\Omega^2| = -\Omega_{ij}\Omega_{ji}$. This is a type of quasi-equilibrium assumption; Durbin (1995b) describes a method to derive this constitutive relation by an equilibrium approximation.

In two-dimensional incompressible, parallel shear flow, $\overline{u_2^2} = \overline{v^2}$ and (2) becomes

$$\overline{u_1^2} = \overline{v^2} + \left(\,^2/_3\ k - \overline{v^2}\right) A. \tag{3}$$

An assumption commonly made to infer k from cross-wire measurements of $\overline{u_1^2}$ and $\overline{u_2^2}$ is $k = \sqrt[3]{4} \, (\overline{u_1^2} + \overline{u_2^2})$: this gives $A = 2$. Equation (3) permits A to be evaluated from DNS data as $A = (\overline{u_1^2} - \overline{u_2^2})/(\sqrt[2]{3} \, k - \overline{u_2^2})$. Figure 7(1) evaluates A from boundary-layer and channel-flow DNS data. A is greater than 2 over the entire flow: a rather better approximation is $A = 2.4$. Correspondingly, a more accurate estimate of k from cross-wire data would be $k \approx (\overline{u_1^2} + 1.4\overline{u_2^2})/1.6$. The function

$$A = 2 + \frac{6S^*}{15 + 10S^*} \tag{4}$$

where $S^* = Sk/\varepsilon$, gives a slightly better approximation to the data. In Fig. 7(2) the algebraic model (2) is evaluated for channel flow; DNS data for $\overline{u_1^2}$ in flow over a backward facing step (provided by H. Le) is shown in Fig. 8(1), along with curves obtained from the algebraic model; x-derivatives have been ignored and (4) used. The step is located at $x = 0$ and the reattachment point is at $x = 6$. In the separated shear layer, the algebraic relation between k, $\overline{v^2}$, and $\overline{u_1^2}$ is quite accurate. Near the wall, in the the neighborhood of reattachment, the model (4) produces a spurious maximum: this is due to a peak in the anisotropy measure $\sqrt[2]{3}k - \overline{v^2}$; neither k or $\overline{v^2}$ themselves show this peak. This illustrates a limitation to the present method of representing anisotropy. Figure 8(2) shows evaluations of A using backstep data. Comparison of the curves and symbols shows how the anisotropic contribution to $\overline{u_1^2}$ is overpredicted near the wall by (4).

REFERENCES

COOPER, D., JACKSON, D. C., LAUNDER, B. E. & LIAO, G. X. 1993 Impinging jet studies for turbulence model assessment. *Int. J. Heat Mass Transfer.* **36**, 2675–2684

DURBIN, P. A. 1995a Separated flow computations with the $k - \varepsilon - v^2$ model. *AIAA Journal.* **44**, 659–664

DURBIN, P. A. 1995b Constitutive equation for the $k - \varepsilon - v^2$ model. *6^{t}h Int. Symp. on CFD,* 258–262

DURBIN, P. A. 1996 On the $k - \varepsilon$ stagnation point anomaly. *Int. J. Heat and Mass Transf.* to appear

ROGERS, S. E. & KWAK, D. 1990 Upwind differencing scheme for the time-accurate incompressible Navier-Stokes equations. *AIAA Journal.* **28**, 253–262

HABIB, M. A. & WHITELAW, J. H. 1979 Velocity characteristics of a confined coaxial jet. *ASME J. Fluids Eng.* **101**, 521–529

ROBACK, R. & JOHNSON, B. V. 1983 Mass and momentum turbulent transport experiments with confined swirling coaxial jets. *NASA CR-168252*

A new approach to the formulation of scalar flux closure

By Y. Shabany AND P. Durbin

1. Motivation and objectives

The solution of fluid dynamics equations for a turbulent flow requires the modeling of turbulence statistics if the averaged form of the equations are used. This is usually the case except in direct numerical solution methods which are limited to low Reynolds numbers. The major effort of the researchers in this field is to develop closure models that improve the accuracy of turbulent flow predictions. However, it is understood that the more accurate the models are, the more complex they will be. The second order closure models seemed to provide a compromise between complexity and accuracy. In this class of models the exact equations for Reynolds stresses and scalar fluxes are derived and the unknown terms are modeled in terms of the other known parameters.

The modeling of Reynolds stress and scalar flux transport equations is done separately, although the same approaches are used in most cases. It must be mentioned that the area of scalar transport has received less attention than momentum transport (Reynolds stress). Therefore, turbulence models for scalar fluxes are rather less well developed than models for Reynolds stresses. This may be in part because prediction of the mean flow and Reynolds stress is often a prerequisite to prediction of convective scalar transport. But, conversely, because of this intimate coupling between momentum and scalar flux, models of scalar transport may provide constraints on the momentum model.

This report shows that if a stochastic differential equation (Langevin equation) for velocity fluctuation vector is known, it is possible to derive the equations for scalar flux transport. Durbin and Speziale (1994) showed that the second moment of this stochastic differential equation gives an equation for the evolution of Reynolds stress tensor. Similarly, the stochastic equation will give an equation for scalar flux. Therefore, a coupling between these two is present. The basis for the present work is that there should be Langevin equations that can produce acceptable models for both the Reynolds stress tensor and the scalar flux vector. Having found this basic Langevin equation, the amount of work needed to model the second order closure problems is reduced; using the well developed models for Reynolds stress equations, it will be possible to derive corresponding models for scalar flux equation.

2. Accomplishments

2.1 Langevin equation and scalar flux closure

The simplest Langevin equation for a random velocity vector is

$$du_i = -\frac{c_1}{2T}u_i dt + \sqrt{c_0 \epsilon}\, d\mathcal{W}_i(t), \tag{1}$$

where u_i is the velocity fluctuation vector, t is the independent variable time, T is the turbulent time scale (k/ϵ) where k is the turbulent kinetic energy per unit mass and ϵ is the rate of dissipation of k, and $W_i(t)$ is the Wiener stochastic process (Arnolds, 1974). c_1 and c_0 are constants which are determined later. It was shown by Durbin and Speziale (1994) that the second moment of this equation,

$$\frac{d\overline{u_i u_j}}{dt} = -\frac{c_1}{T}\overline{u_i u_j} + c_0 \epsilon \delta_{ij}, \tag{2}$$

is an equation for the evolution of Reynolds stresses in the absence of mean velocity gradient provided that $c_1 = 2$ and $c_0 = 2/3$.

In homogeneous turbulent flow the position of a fluid particle is determined by the following equation.

$$\frac{dX_i}{dt} = u_i + X_j U_{i,j} \tag{3}$$

Here, X_i is the Lagrangian position vector of the particle and U_i is the velocity of the fluid particle, which is at position X_i at time t; $U_{i,j}$ is constant in homogeneous turbulence. The dispersion tensor K_{ij} is defined as

$$K_{ij} = \overline{u_i X_j}. \tag{4}$$

It can be shown that if the molecular diffusion of the scalar contaminant Θ is neglected (high Peclet number), the turbulent scalar flux is related to the dispersion tensor by

$$\overline{u_i \theta} = -K_{ij} \Theta_{,j}. \tag{5}$$

Therefore, if a transport equation for K_{ij} is known, the equation for the transport of scalar contaminant can be derived using Eq. 5.

The transport equation for K_{ij} is simply obtained by substituting Eqs. 1 and 3 in

$$\begin{aligned} d(u_i X_j) &= (u_i + du_i)(X_j + dX_j) - u_i X_j \\ &= u_i dX_j + X_j du_i + du_i dX_j, \end{aligned} \tag{6}$$

and averaging. This is the same method used by Durbin and Speziale (1994) to derive the transport equation for Reynolds stresses. The result is:

$$\frac{dK_{ij}}{dt} = \overline{u_i u_j} - \frac{c_1}{2T} K_{ij}. \tag{7}$$

Note that the mean velocity gradient and therefore the second term of Eq. 3 is zero for the case considered here. The coefficient of the second term of Eq. 7 $(c_1/2)$ does not agree with the empirical values which are about $2c_1$ where $c_1 = 1.8$ (Launder, 1978). Therefore, Eq. 1 can not be used as a base Langevin equation for both Reynolds stress and scalar flux closure models. However, a modified form of this equation given as

$$du_i = -\frac{c_M}{T} u_i dt + \sqrt{(2c_M - 1)\epsilon}\, p_{ik} dW'_{t_k} + \sqrt{c_0 \epsilon}\, dW_{t_i} \tag{8}$$

provides a consistent Langevin equation for both momentum and scalar flux transport. In Eq. 8 p_{ij} is the generalized square root of b_{ij} defined by $p_{ij}^2 - \frac{1}{3}p_{kk}^2\delta_{ij} = b_{ij}$ and $c_0 = \frac{2}{3}\left[2c_M - 1 - (c_M - \frac{c_1}{2})p_{kk}^2\right]$. Note that $\mathcal{W}_t$ and $\mathcal{W}_t'$ are independent Wiener processes and $\overline{d\mathcal{W}_t d\mathcal{W}_t'} = 0$. It can be shown that the second moment of Eq. 8 is Eq. 2 and the evolution equation for K_{ij} is

$$\frac{dK_{ij}}{dt} = -\frac{c_M}{T}K_{ij} + \overline{u_i u_j} \tag{9}$$

The scalar gradient evolves by $d(\Theta_{,j})/dt = -U_{k,j}\Theta_k$ (which is zero in this case but not in general). Hence the transport equation of the scalar flux, $\overline{u_i\theta}$, is simply obtained by taking d/dt of Eq. 5, substituting Eq. 9 for dK_{ij}/dt, and using the above mentioned evolution equation for $\Theta_{,j}$. The final result is

$$\frac{d\overline{u_i\theta}}{dt} = -\overline{u_i u_j}\Theta_{,j} - \frac{c_M}{T}\overline{u_i\theta}. \tag{10}$$

This is the equation for the transport of scalar flux in the absence of mean velocity gradient. The first and second terms are the production by mean scalar gradient and the slow part of the pressure-scalar gradient correlation respectively.

The importance of this method is that there is no need to develop a separate closure model for the equation of scalar transport if there is already a closure model for the transport of Reynolds stresses. It was shown (Durbin and Speziale, 1994) that for any Reynolds stress closure model there is a Langevin equation, the second moment of which is that model equation. Having this Langevin equation, it is possible to derive a transport equation for the scalar flux by the method outlined above.

2.2 Results

The general linear model for the evolution of Reynolds stress tensor is

$$\begin{aligned}
\frac{d\overline{u_i u_j}}{dt} = &-\frac{c_1}{T}(\overline{u_i u_j} - \frac{2}{3}k\delta_{ij}) - c_2(P_{ij} - \frac{2}{3}P\delta_{ij}) - c_3(D_{ij} - \frac{2}{3}P\delta_{ij}) \\
&- c_s k S_{ij} + P_{ij} - \frac{2}{3}\epsilon\delta_{ij}
\end{aligned} \tag{11}$$

where

$$P_{ij} = -\overline{u_i u_k}U_{j,k} - \overline{u_j u_k}U_{i,k},$$

$$D_{ij} = -\overline{u_i u_k}U_{k,j} - \overline{u_j u_k}U_{k,i},$$

$$P = \frac{1}{2}P_{ii}.$$

A special case of this model is the IP model where $c_3 = C_s = 0$. It can be shown that the second moment of Langevin equation

$$du_i = -\frac{c_M}{T}u_i dt + \sqrt{(2c_M - c_1)\epsilon}\, p_{ik}d\mathcal{W}_{t_k}' + (c_2 - 1)u_k\partial_k U_i dt + \sqrt{c_0\epsilon}\, d\mathcal{W}_{t_i} \tag{12}$$

is the special case of Eq. 11 corresponding to the IP model, provided that

$$c_0 = \frac{2}{3} \left[2c_M - 1 - c_2 \frac{P}{\epsilon} - (c_M - \frac{c_1}{2})p_{kk}^2 \right] .$$

Following the procedure mentioned in Section 2, it can be shown that the evolution equation for K_{ij} is

$$\frac{dK_{ij}}{dt} = \overline{u_i u_j} - \frac{c_M}{T} K_{ij} + K_{ik} U_{j,k} + (c_2 - 1)K_{kj} U_{i,k}. \tag{13}$$

Note that K_{ij} is not a symmetric tensor. The scalar flux equation is

$$\frac{d\overline{u_i \theta}}{dt} = -\frac{c_M}{T} \overline{u_i \theta} - \overline{u_i u_j} \Theta_{,j} + (c_2 - 1)\overline{u_k \theta} U_{i,k}. \tag{14}$$

The significance of this result is that the coefficients of the scalar flux model are not independent of those in the Reynolds stress equations (Eq. 11).

The dimensionless dispersion tensor is defined as

$$D_{ij} = \frac{\epsilon}{k^2} K_{ij}.$$

An evolution equation for D_{ij} can be obtained. However, in equilibrium, the rate of change of D_{ij} is zero. Therefore, the following algebraic equation is obtained.

$$\frac{D_{ij}}{g_k} = \tau_{ij} + D_{ik}(S_{kj}^* - \omega_{kj}^*) + (c_2 - 1)(S_{ik}^* + \omega_{ik}^*)D_{kj} \tag{15}$$

where $\tau_{ij} = \overline{u_i u_j}/k$, $S_{ij}^* = T S_{ij}$, $\omega_{ij}^* = T \omega_{ij}$ and

$$g_k = \left[c_M + c_{\epsilon 2} - c_{\epsilon 1} \frac{P}{\epsilon} + 2 \frac{P}{\epsilon} - 2 \right]^{-1} .$$

In a two-dimensional uniform shear flow:

$$S_{ij} = \frac{1}{2} \begin{pmatrix} 0 & S \\ S & 0 \end{pmatrix} \quad \text{and} \quad \omega_{ij} = \frac{1}{2} \begin{pmatrix} 0 & S \\ -S & 0 \end{pmatrix}$$

It can be shown that in this case

$$\begin{aligned}
D_{11} &= g_k \left[\tau_{11} + c_2 g_k S^* \tau_{12} - 2(1 - c_2)(g_k S^*)^2 \tau_{22} \right] , \\
D_{12} &= g_k \left[\tau_{12} + (c_2 - 1)g_k S^* \tau_{22} \right] , \\
D_{21} &= g_k \left[\tau_{12} + g_k S^* \tau_{22} \right] , \\
D_{22} &= g_k \tau_{22}.
\end{aligned} \tag{14}$$
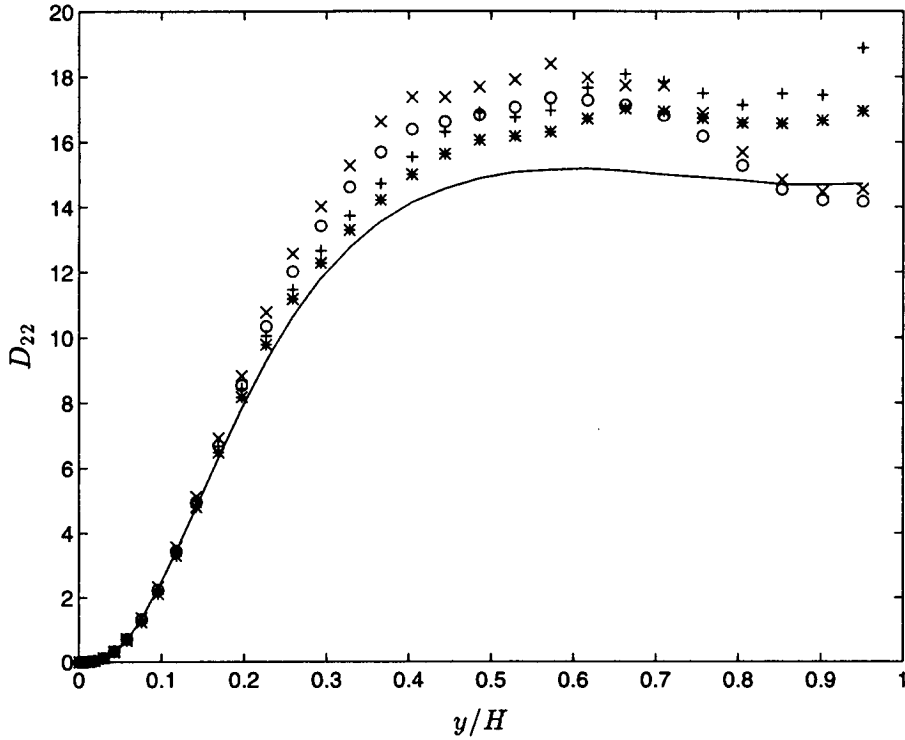
FIGURE 1. Eddy diffusivity profiles according to the IP model; ———— , model prediction; *, DNS(HS) Pr=0.71; +, DNS(HS) Pr=2.0; o, DNS(HW) Pr=0.71; ×, DNS(HW) Pr=2.0.

Evaluation of D_{22} with $c_M = 3.4$ is compared to the numerical data of Kim and Moin (1989) in Fig. 1. The DNS data are for heat source (HS) and heated wall (HW) cases. With $c_M = 3.4$ the value calculated for D_{12} is not in good agreement with the numerical data; a value close to 0.85 gives more reasonable results. However, this value of c_M is preferred in order to predict the transverse scalar flux, $\overline{v\theta}$, as accurate as possible. This component of scalar flux has the main contribution in channel flow and boundary layer heat transfer.

The same calculations were done for the general linear model and the results are

$$D_{11} = \frac{g_k}{\Delta} \left[\tau_{11} + (\frac{2}{\Delta} + c_2 - 2)g_k S^* \tau_{12} - 2(1 - c_2)\frac{(g_k S^*)^2}{\Delta}\tau_{22} \right],$$

$$D_{12} = \frac{g_k}{\Delta} \left[\tau_{12} - (1 - c_2)g_k S^* \tau_{22} \right],$$

$$D_{21} = \frac{g_k}{\Delta} \left[\tau_{12} + c_3 g_k S^* \tau_{11} + (\frac{2}{\Delta} - 1)g_k S^* \tau_{22} + 2c_3 \frac{(g_k S^*)^2}{\Delta}\tau_{12} \right], \qquad (15)$$

$$D_{22} = \frac{g_k}{\Delta} \left[\tau_{22} + c_3 g_k S^* \tau_{12} \right],$$

where $\Delta = 1 + (1 - c_2)c_3(g_k S^*)^2$ and $g_k = \left[c_M + (2 - c_{\epsilon 1})\frac{P}{\epsilon} + c_{\epsilon 2} - 2 \right]^{-1}$. The

expression for D_{22} given by Eq. 15 shows that for high enough values of S^* there is a possibility for D_{22} to become negative if c_3 is not equal to zero; for the channel flow case this happens in the near wall region. The negative value of D_{22} does not have any physical interpretation and is not supported by DNS data of Kim and Moin (1989). However, a non-zero value of c_3 is necessary to predict different values for b_{22} and b_{33} in homogeneous shear flow.

4. Future work

The main purpose of this research is to obtain a consistent way of deriving both Reynolds stress tensor and scalar flux vector closures from same Langevin equation for velocity fluctuation vector. The following main problems must be resolved before this goal is achieved:

1. The coefficient of the slow term (c_M) in the evolution equation of different components of scalar flux must be different in order to get a good agreement with experimental or DNS data for all the components of scalar flux. Therefore, a simple constant value does not seem to solve the problem.

2. As mentioned at the end of Section 3 a non-zero value of c_3 is necessary to differentiate the values of b_{22} and b_{33} in a homogeneous shear flow. On the other hand, a non-zero value of this constant causes the model to predict negative values of D_{22} for high enough S^* which seems unreasonable.

The solution of these two problems is the main focus of this research.

REFERENCES

ARNOLDS, L. 1974 *Stochastic Differential Equations: Theory and Application.* John Wiley and Sons.

DURBIN, P. A. & SPEZIALE, C. G. 1994 Realizability of Second-Moment Closure via Stochastic Analysis. *J. Fluid Mech.* **280**, 395-407

KIM, J. & MOIN, P. 1989 *Turbulent Shear Flows 6.* Springer-Verlag. 85-91

A similarity hypothesis for the two-point correlation tensor in a temporally evolving plane wake

By D. W. Ewing[1], W. K. George[2], R. D. Moser[3], AND M. M. Rogers[4]

1. Motivation and objectives

It has long been known that the equations that govern the evolution of the single-point moments, such as the mean velocity or the turbulent Reynolds stresses, admit similarity solutions for many of the basic shear flows (*e.g.* George 1989 or Tennekes and Lumley 1972). In this approach, it is argued that the flow evolves such that all of the terms in the governing equations make the the same relative contribution so the flow reaches an 'equilibrium' or similarity state. In many cases the initial conditions of the flow are inconsistent with the hypothesized similarity solutions so these solutions are, at most, an approximation of the flows asymptotic state. However, the agreement between the predictions of the theory and experimental data (*e.g.*, Wygnanski *et al.* 1989) suggests that flows do approach such an asymptotic state.

Traditionally (*e.g.*, Tennekes and Lumley 1972), it was argued that this asymptotic state is universal for all flows of a particular type (*e.g.*, all plane wakes). However, this argument is not consistent with the measurements in the far field of plane wakes reported by Wygnanski *et al.* (1989), who found that the similarity profiles of the normal Reynolds stresses (particularly the streamwise component) differed for different types of wake generators. George (1989) argued that this occurred because the governing equation for the similarity profile of the turbulent kinetic energy contained a constant that depended on the growth rate of the flow. Consequently, George (1989) concluded that the similarity profiles for the normal stresses would not be universal unless the growth rates of all wakes were the same, which was not the case for the wakes studied by Wygnanski *et al.* (1986). (A similar conclusion was reached from a later analysis of the governing equations for the individual normal stresses; *e.g.*, George 1994 or Ewing and George 1994.) George (1989) attributed the differences in the growth rates of the wakes (and hence the asymptotic states) to differences in the coherent structures produced by the bodies generating the wake.

1 Department of Mechanical Engineering, Queen's University, Kingston, Canada, K7L 3N6.

2 Department of Mechanical and Aerospace Engineering, State University of New York at Buffalo, Amherst, NY, 14260.

3 Department of Theoretical and Applied Mechanics, University of Illinois at Urbana-Champaign, Urbana, IL 61801.

4 NASA Ames Research Center.

It is now widely recognized that coherent structures play an integral role in many of the processes that determine the growth rate of a turbulent flow, including the entrainment of irrotational flow and the gross mixing of the fluid across the layer. A question that has not yet been resolved is whether the structures in the flow themselves (or more properly the coherent structures and the probability density functions describing their occurrences) approach an 'equilibrium' or similarity state when the single-point moments measured in the flow agree with the predictions of the similarity hypothesis. That is, can all of the statistical measures of the structures (the single-point moments being the simplest) at different points in a flow's evolution be related by a similarity transformation.

The primary objective of this research is to examine whether the governing equations for more complex statistical measures of the structures in the temporally evolving plane wake admit similarity solutions. (In the initial stage of this research it was established that the governing equations for the mean momentum and the Reynolds stresses admit similarity solutions, *v.* Moser *et al.* 1995). The two-point velocity correlation tensor was chosen because it contains more information about the turbulent structure than the single-point moments and it is often used in attempts to educe coherent structures from the flow (*e.g.*, Grant 1958 or Payne and Lumley 1967). There have been few previous attempts to demonstrate that the governing equations for these two-point correlations admit similarity solutions in non-homogeneous flows. Ewing and George (1994) and Ewing (1995) demonstrated that the governing equations for the two-point velocity correlation tensor in the far fields of the spatially evolving axisymmetric and plane jets admit similarity solutions. However, in both of these cases the predictions of the similarity hypotheses were not tested using experimental data, so it was not determined if these similarity solutions are accurate descriptions of real shear flows. This question is addressed in this research using data from Direct Numerical Simulations of the temporally evolving wake computed by Moser and Rogers (1994).

2. Accomplishments

2.1 Theoretical analysis

In the temporally evolving wake, shown in Fig. 1, a momentum deficit spreads in one non-homogeneous direction, x_2, as the flow evolves in time. The other two directions, including the direction of the mean flow, x_1, are homogeneous. Consequently, the governing equations for the two-point velocity correlations in this flow can be written as

$$\frac{\partial \overline{u_i u_j'}}{\partial t} + (U_1 - U_1') \frac{\partial \overline{u_i u_j'}}{\partial \varsigma} =$$

$$-\frac{1}{\rho} \left[\frac{\partial}{\partial \varsigma} \left(\overline{pu_j'} \delta_{i1} - \overline{p'u_i} \delta_{j1} \right) + \frac{\partial \overline{pu_j'}}{\partial x_2} \delta_{i2} + \frac{\partial \overline{p'u_i}}{\partial x_2'} \delta_{j2} + \frac{\partial}{\partial \gamma} \left(\overline{pu_j'} \delta_{i3} - \overline{p'u_i} \delta_{j3} \right) \right]$$

$$-\frac{\partial}{\partial \varsigma} \left(\overline{u_1 u_i u_j'} - \overline{u_1' u_i u_j'} \right) - \frac{\partial \overline{u_2 u_i u_j'}}{\partial x_2} - \frac{\partial \overline{u_2' u_i u_j'}}{\partial x_2'} - \frac{\partial}{\partial \gamma} \left(\overline{u_3 u_i u_j'} - \overline{u_3' u_i u_j'} \right)$$
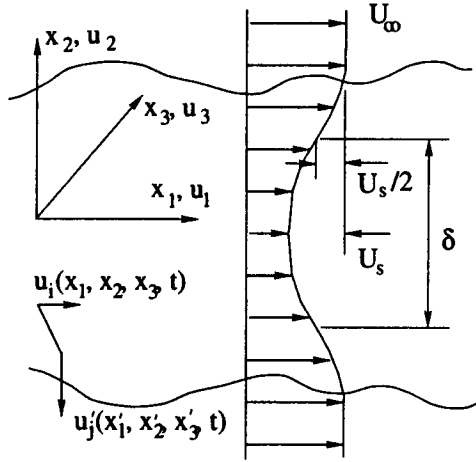
FIGURE 1. Geometry of the temporally evolving wake

$$-\overline{u'_j u_2}\frac{\partial U_1}{\partial x_2}\delta_{i1} \ - \ \overline{u_i u'_2}\frac{\partial U'_1}{\partial x'_2}\delta_{j1} + \nu\left(2\frac{\partial^2}{\partial \varsigma^2} + \frac{\partial^2}{\partial x_2^2} + \frac{\partial^2}{\partial x_2'^2} + 2\frac{\partial^2}{\partial \gamma^2}\right)\overline{u_i u'_j}, \quad (1)$$

where $\varsigma = x_1 - x'_1$, $\gamma = x_3 - x'_3$, U_1 is the mean velocity in the x_1-direction, and u_i are the fluctuating velocity components in the x_i directions. In these equations, the primed variables are evaluated at one arbitrary point in space while the unprimed variables are evaluated at a second arbitrary point. The two-point velocity correlations must also satisfy initial conditions and a number of boundary conditions; *i.e.*,

$$\lim_{x_2,x'_2,\varsigma,\gamma\to\pm\infty}\overline{u_i u'_j} = 0, \quad (2)$$

assuming the turbulence in the free stream is negligible.

Following the approach outlined by George (1989), it is hypothesized that the governing equations for the two-point correlation tensor admit similarity solutions given by

$$\overline{u_i(x_1,x_2,x_3,t)u'_j(x'_1,x'_2,x'_3,t)} = Q^{i,j}(t)q_{i,j}(\xi,\eta,\eta',\zeta,*), \quad (3a)$$

$$\overline{p(x_1,x_2,x_3,t)u'_j(x'_1,x'_2,x'_3,t)} = P_1^{j}(t)p_{,j}^1(\xi,\eta,\eta',\zeta,*), \quad (3b)$$

$$\overline{p'(x'_1,x'_2,x'_3,t)u_i(x_1,x_2,x_3,t)} = P_2^{i}(t)p_{i,}^2(\xi,\eta,\eta',\zeta,*), \quad (3c)$$

$$\overline{u_k u_i u'_j} = T_1^{ki,j}(t)tt_{ki,j}^1(\xi,\eta,\eta',\zeta,*), \quad (3d)$$

$$\overline{u_i u'_k u'_j} = T_2^{i,kj}(t)tt_{i,kj}^2(\xi,\eta,\eta',\zeta,*), \quad (3e)$$

where

$$\xi = \frac{\varsigma}{\delta_1(t)} = \frac{x_1 - x'_1}{\delta_1(t)}, \quad \eta = \frac{x_2}{\delta(t)}, \quad \eta' = \frac{x'_2}{\delta(t)}, \quad \zeta = \frac{\gamma}{\delta_3(t)} = \frac{x_3 - x'_3}{\delta_3(t)}, \quad (3f)$$

and the $*$ in Eqs. 3a -3e indicate that the solutions may depend on the source conditions of the flow. At this point the length scales δ_1 and δ_3 are arbitrary.

The allowable choices for these scales are determined by examining the equations of motion. The length scale used to scale the x_2 is equal to the scale used in the single-point analysis, $\delta(t) \propto (t - t_o)^{1/2}$ (Moser *et al.* 1995), since the similarity solutions for the single- and two-point correlations must be consistent in the limit when the separation distance between the two points is zero. Here, t_o is the location of the virtual origin of the wake.

Substituting these hypothesized solutions for the two point correlations and the similarity solution for the mean velocity given by (Moser *et al.* 1995)

$$U_{1\infty} - U_1(x_2, t) = U_s(t) f(\eta) \tag{4}$$

into Eq. 1 yields

$$
\left[\frac{dQ^{i,j}}{dt}\right] q_{i,j} - \left[\frac{Q^{i,j}}{\delta_1} \frac{d\delta_1}{dt}\right] \xi \frac{\partial q_{i,j}}{\partial \xi} - \left[\frac{Q^{i,j}}{\delta} \frac{d\delta}{dt}\right] \left(\eta \frac{\partial}{\partial \eta} + \eta' \frac{\partial}{\partial \eta'}\right) q_{i,j} - \left[\frac{Q^{i,j}}{\delta_3} \frac{d\delta_3}{dt}\right] \zeta \frac{\partial q_{i,j}}{\partial \zeta}
$$

$$
+ \left[\frac{U_s(t) Q^{i,j}}{\delta_1}\right] \{f(\eta') - f(\eta)\} \frac{\partial q_{i,j}}{\partial \xi} = -\frac{1}{\rho} \left(\left[\frac{P_1^{,j}}{\delta_1}\right] \frac{\partial p_{,j}^1}{\partial \xi} \delta_{i1} - \left[\frac{P_2^{i,}}{\delta_1}\right] \frac{\partial p_{i,}^2}{\partial \xi} \delta_{j1}\right.
$$

$$
+ \left[\frac{P_1^{,j}}{\delta}\right] \frac{\partial p_{,j}^1}{\partial \eta} \delta_{i2} + \left[\frac{P_2^{i,}}{\delta}\right] \frac{\partial p_{i,}^2}{\partial \eta'} \delta_{j2} + \left[\frac{P_1^{,j}}{\delta_3}\right] \frac{\partial p_{,j}^1}{\partial \zeta} \delta_{i3} - \left[\frac{P_2^{i,}}{\delta_3}\right] \frac{\partial p_{i,}^2}{\partial \zeta} \delta_{j3}\right)
$$

$$
- \left[\frac{T_1^{1i,j}}{\delta_1}\right] \frac{\partial tt_{1i,j}^1}{\partial \xi} + \left[\frac{T_2^{i,1j}}{\delta_1}\right] \frac{\partial tt_{i,1j}^2}{\partial \xi} - \left[\frac{T_1^{2i,j}}{\delta}\right] \frac{\partial tt_{2i,j}^1}{\partial \eta} - \left[\frac{T_2^{i,2j}}{\delta}\right] \frac{\partial tt_{i,2j}^2}{\partial \eta'}
$$

$$
- \left[\frac{T_1^{3i,j}}{\delta_3}\right] \frac{\partial tt_{3i,j}^1}{\partial \zeta} + \left[\frac{T_2^{i,3j}}{\delta_3}\right] \frac{\partial tt_{i,3j}^2}{\partial \zeta} + \left[\frac{Q^{2,j} U_s}{\delta}\right] q_{2,j} \frac{df}{d\tilde{\eta}}\Big|_{\tilde{\eta}=\eta} \delta_{i1} + \left[\frac{Q^{i,2} U_s}{\delta}\right] q_{i,2} \frac{df}{d\tilde{\eta}}\Big|_{\tilde{\eta}=\eta'} \delta_{j1}
$$

$$
+ \nu \left(2 \left[\frac{Q^{i,j}}{\delta_1^2}\right] \frac{\partial^2}{\partial \xi^2} + \left[\frac{Q^{i,j}}{\delta^2}\right] \frac{\partial^2}{\partial \eta^2} + \left[\frac{Q^{i,j}}{\delta^2}\right] \frac{\partial^2}{\partial \eta'^2} + 2 \left[\frac{Q^{i,j}}{\delta_3^2}\right] \frac{\partial^2}{\partial \zeta^2}\right) q_{i,j}, \tag{5}
$$

where the time-dependent portion of each term is contained in square brackets. It is possible to remove the time dependence from these equations if the time-dependent portion of the all terms in each equation are proportional, leaving a set of equations for the similarity solutions in terms of the similarity variables and the constants whose values depend on the ratios of the time-dependent terms. In this case, the similarity solutions again represent an 'equilibrium' solution for the governing equations since all of the terms make the same relative contribution as the flow evolves.

It is straightforward to demonstrate that the time dependent portions of the four viscous terms in Eq. 5 are only proportional if

$$\delta_1 \propto \delta \propto \delta_3 \propto (t - t_o)^{1/2}. \tag{6}$$

This implies that all three length scales must have the same virtual origin.

Further, the time-dependent portions of the convective and the unsteady terms in Eq. 5 are only proportional to the time-dependent portions of these viscous terms if

$$\left[\frac{Q^{i,j}}{\delta}\frac{d\delta}{dt}\right] \propto \left[\frac{U_s Q^{i,j}}{\delta}\right] \Rightarrow \left[\frac{1}{\delta}\frac{d\delta}{dt}\right] \propto \left[\frac{U_s}{\delta}\right] \tag{7a}$$

and

$$\left[\frac{U_s Q^{i,j}}{\delta}\right] \propto \left[\frac{\nu Q^{i,j}}{\delta^2}\right] \Rightarrow \left[\frac{U_s}{\delta}\right] \propto \left[\frac{\nu}{\delta^2}\right]. \tag{7b}$$

These constraints are satisfied if the three time scales δ/U_s (a characteristic time scale of the mean strain rate), δ^2/ν (a viscous time scale), and $(1/\delta \; d\delta/dt)^{-1}$ (a charteristic time scale of the spreading of the flow) are proportional. Thus, the ratio of these time scales are constant; *i.e.*,

$$\beta = \frac{1}{U_s}\frac{d\delta}{dt} \propto const \tag{8a}$$

and

$$Re_\delta = \frac{U_s \delta}{\nu} \propto const, \tag{8b}$$

which are the constraints derived in the analysis of the single-point equations.

The constraint that the Reynolds number is a constant is a gratifying result since a single length scale was used to define each of the similarity coordinates in Eq. 3f. Thus, it was implicitly assumed that all of the physically relevant length scales in the flow grow in proportion as the flow evolves; an assumption that is generally thought to be valid in a constant-Reynolds-number flow (Batchelor 1953). The functional form of the solutions will, of course, depend on the ratios of the physically relevant length scales (or the Reynolds number).

The constant β that appears in the equations is analogous to the constant that George (1989) found in the governing equation for the turbulent kinetic energy in the spatially evolving wake. It is very likely that the value of this ratio depends on the coherent structures in the flow, and it is through this constant that their influence is incorporated into the equations for the similarity solutions.

The time-dependent portions of the rest of the terms in Eq. 5 are proportional if

$$P_1^{i,} \propto U_s Q^{i,k}, P_1^{,j} \propto U_s Q^{k,j}, \tag{9a}$$

and

$$T_1^{ki,j} \propto T_2^{i,kj} \propto U_s Q^{i,j}. \tag{9b}$$

These expressions must be satisfied for any choice of k. The choice for $Q^{i,j}$ is not uniquely determined from Eq. 5; however, $Q^{i,j}$ is not arbitrary since the similarity solution for the two-point velocity correlation tensor must be consistent with the similarity solution derived for the single-point moments (Moser *et al.* 1995). Thus, it follows that

$$Q^{i,j} \propto U_s^2. \tag{10}$$

Of course, these constants of proportionality may be functions of β or Re_δ.

Thus, the governing equations for the two-point velocity correlation tensor in the temporally evolving wake admit similarity solutions, of which the similarity solution for the single-point Reynolds stresses are a special case. It is straightforward to demonstrate that the governing equations for the similarity solutions include the constants Re_δ and β. Thus, in general, the similarity solutions are functions of these two ratios whose values depend on the source conditions of the flow. In many flows, the initial conditions are not consistent with the hypothesized similarity solution so these solutions are, at most, an approximation of the asymptotic state of the flow (as with the single-point similarity solutions).

2.2 Implications of the similarity hypothesis

When a similarity solution exists for the two-point velocity tensor, other statistical measures that can be determined directly from this two-point correlation also have similarity solutions. In many cases, these results provide useful predictions to compare with data in order to test the similarity hypothesis.

For example, when a similarity solution exists for the two-point velocity correlation tensor, the one-dimensional spectra in the x_1-direction given by

$$F_{ij}^1(k_1, x_2, x_2', \gamma) = \frac{1}{2\pi} \int_{-\infty}^{\infty} R_{i,j}(\varsigma, x_2, x_2', \gamma) e^{-ik_1\varsigma} d\varsigma$$

(where $R_{i,j} = \overline{u_i u_j'}$) can be written as

$$F_{ij}^1(k_1, x_2, x_2', \gamma) = [Q_{i,j}\delta] \, \tilde{F}_{ij}^1(\tilde{k}_1, \eta, \eta', \zeta), \tag{11a}$$

where the similarity solution for the one-dimensional spectra is given by

$$\tilde{F}_{ij}^1(\tilde{k}_1, \eta, \eta', \zeta) = \frac{1}{2\pi} \int_{-\infty}^{\infty} q_{i,j}(\xi, \eta, \eta', \zeta) e^{-i\tilde{k}_1\xi} d\xi \tag{11c}$$

and $\tilde{k}_1$ is the given by

$$\tilde{k}_1 = k_1 \delta. \tag{11b}$$

A similar relationship can be derived for the one-dimensional spectra in the x_3-direction. Thus, when a similarity solution exists for the two-point velocity correlation tensor, the one-dimensional spectra of the field maintain the same shape while continuously shifting downward and to lower wavenumbers as the flow spreads.

It is also straightforward to demonstrate that many of the classically defined turbulent length scales are proportional to the similarity length scale. For example, the Taylor microscales given by

$$\lambda_{\alpha,\beta}^k = \left\{ -2\overline{u_\alpha u_\beta} \left(\frac{\partial^2 R_{\alpha,\beta}}{\partial \tilde{x}_k^2} \bigg|_{\tilde{x}_k = x_k - x_k' = 0} \right)^{-1} \right\}^{1/2} \tag{12}$$

can be written as (Ewing 1995)

$$\lambda^k_{\alpha,\beta} = [\delta]\, \tilde{\lambda}^k_{\alpha,\beta}(\eta, Re_\delta, \beta), \tag{13}$$

It is also straightforward to show that the integral length scales and the Kolmogorov length scale are proportion to the similarity length scale (Ewing 1995).

A number of other interesting implications of the two-point similarity hypothesis, such as similarity solutions for the moments related to the two-point velocity-gradient correlation tensor (*e.g.*, the two-point vorticity correlation or the dissipation of the turbulent kinetic energy in the flow), are discussed in Ewing (1995) and Ewing *et al.* (1995).

2.3 Comparison with simulation data

Although the previous analysis demonstrated that the hypothesized similarity solutions are consistent with the equations of motion, this does not ensure that these solutions are an accurate description of real flows. In this case the predictions of the similarity hypothesis for the two-point velocity correlation tensor are compared to the data from two Direct Numerical Simulations of the temporally evolving wake computed by Moser and Rogers (1994). These simulations were carried out in finite boxes with periodic boundary conditions in the homogeneous directions in contrast to the theory, which was developed for a wake in an infinite domain. Consequently, the theory cannot exactly approximate the flow in these simulations. However, it is generally argued that the evolution of the scales of motion that are 'much' smaller than the dimension of the boxes in the periodic directions should be similar to the evolution of those in an infinite wake. Thus, a comparison between the predictions of the similarity hypothesis and the data from the simulations is essentially a test of both the similarity hypothesis and this idea. Agreement between the predictions of the theory and the data lends support to both. (Experimentalists experience the very same problem when data from finite experimental rigs, such as wind tunnels, are used to test hypotheses developed for infinite flow; *e.g.*, George and Gibson 1992).

The initial conditions for the wake simulations were generated using two realizations from a turbulent boundary layer simulation yielding a wake with a Reynolds number, given by

$$Re_{\delta_d} = \frac{\int_{-\infty}^{\infty}(U_1 - U_{1\infty})dx_2}{\nu}, \tag{14}$$

of 2000. In the first (unforced) wake simulation the base initial conditions were used to initiate the flow while in the second (forced) wake simulation the u_1 and u_2 velocity components of the spanwise two-dimensional modes were amplified by a factor of 5. These simulations are computed in periodic boxes of length $50\delta_d$ in the x_1-direction and $12.5\delta_d$ in the x_3-direction, where δ_d is the initial displacement thickness of the wake. Moser and Rogers (1994) found that the data from both simulations were approximately in agreement with the predictions of the similarity hypothesis for a period of the flow's evolution. For example, it is evident from Figs. 2a and 2b that the Reynolds number of both flows is approximately constant
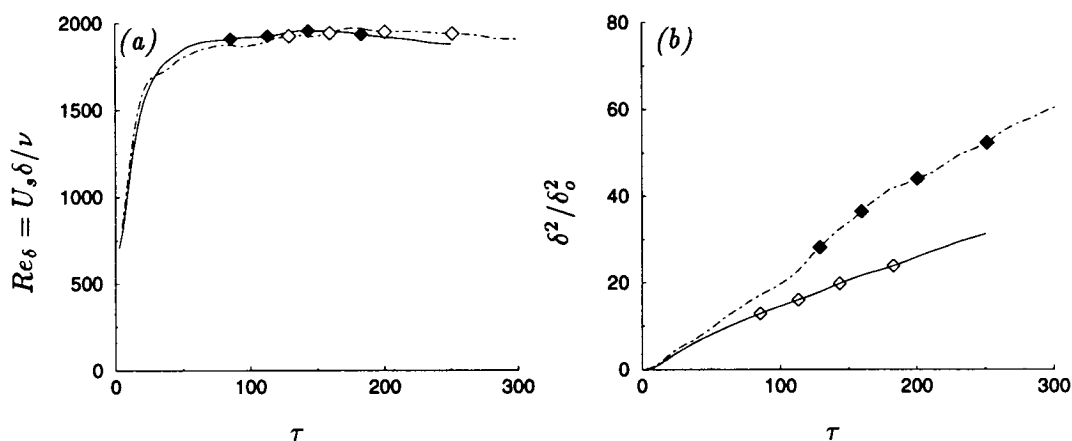
FIGURE 2. Evolution of the Reynolds number and similarity length scale: ——— : unforced wake simulation; - - - - : forced wake simulation; ◇ : location of points used to examine the two-point similarity hypothesis.

and the square of the similarity length scales in the flows grow approximately linearly, as predicted in the similarity analysis, for a significant time period. The two-point similarity hypothesis is tested using data from four points in this range, indicated by the diamonds in Figs. 2a and 2b.

The unscaled one-dimensional spectra F_{11}^1 and F_{22}^1 at the centerline of the two wakes (spatially averaged in the x_3-direction) are illustrated in Figs. 3a and 3b. The spectra exhibit peaks in the low-wavenumber region that are inconsistent with the similarity hypothesis since they occur at the same wavenumber in physical variables. However, it is not anticipated that the similarity hypothesis should collapse the spectra in this region because it is likely that these motions are affected by the periodic boundary conditions or, conversely, the coarse discretization of wave space at these scales. In contrast, the spectra in the high-wavenumber region shift downward and to the left as the flow evolves, in agreement with the predictions of the similarity hypothesis. The amplitude of the spectra in this high-wavenumber region differ by a factor of approximately $3 - 4$ so they should provide a good test of the similarity hypothesis.

The scaled one-dimensional spectra $\tilde{F}_{11}^1$ at the centerline and the half-deficit point, $\eta = 0.5$, in the unforced wake are illustrated in Fig. 4, while the scaled one-dimensional spectra $\tilde{F}_{22}^1$ at the same points in the forced wake simulation are illustrated in Fig. 5. In both of these figures the data from the half-deficit point in the wake are shifted up by a order of magnitude. Overall there is excellent collapse of the data for the region where $\tilde{k}_1 \geq 15\Delta\tilde{k}_1$, indicating that the statistical measures of all but the largest motions evolve as predicted by the similarity hypothesis. There is some discrepancy between the predictions and the data at the largest wavenumbers; however, these variations occur because the effective resolution of the simulations varies as the flow evolves (Ewing 1995). The one-dimensional spectra of the correlations in the x_3-direction (Ewing 1995) exhibit better collapse than the
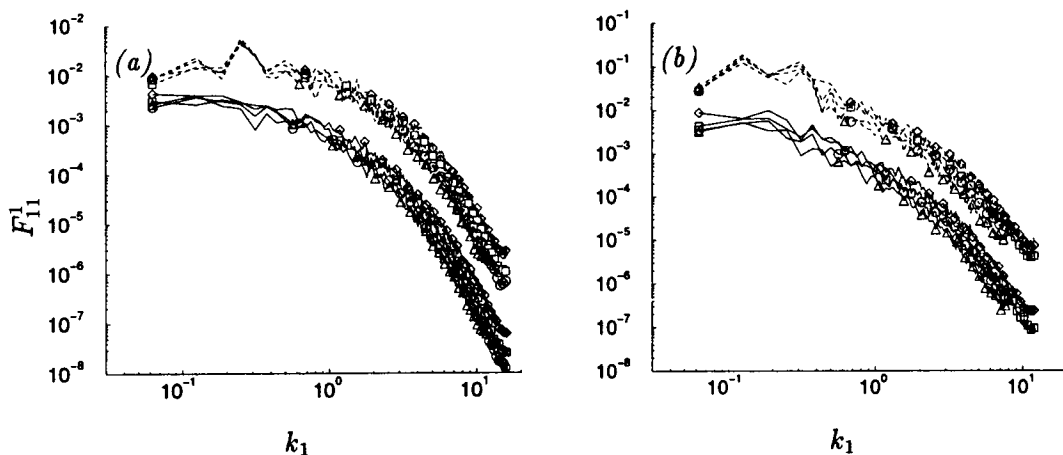
FIGURE 3. Unscaled one-dimensional spectra in *(a)* the unforced wake, *(b)* the forced wake: ——— : F_{11}^1, - - - - : F_{22}^1. In *(a)* δ/δ_d is equal to: 3.494 ◇ , 4.008 □ , 4.446 ○ , and 4.884 △ . In *(b)* δ/δ_d is equal to: 5.306 ◇ , 6.037 □ , 6.636 ○ , and 7.235 △ .
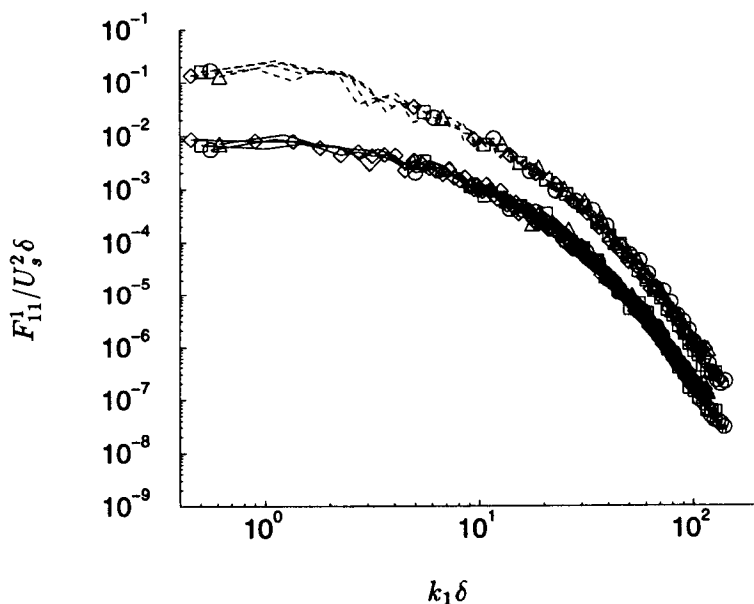
FIGURE 4. Scaled one-dimensional spectra, $\tilde{F}_{11}^1$ in the unforced wake at ——— $\eta = 0.0$ and - - - - $\eta = 0.5$. δ/δ_d is equal to; 3.494 ◇ , 4.008 □ , 4.446 ○ , and 4.884 △ .

spectra in the x_1-direction (partially because these spectra are spatially averaged in the x_1-direction, which is 4 times longer than the x_3-direction used to average $\tilde{F}_{\alpha\alpha}^1$).

The large-scale motions make a contribution to the two-point velocity correlation tensor for all separation distances. Consequently, the structure functions in the
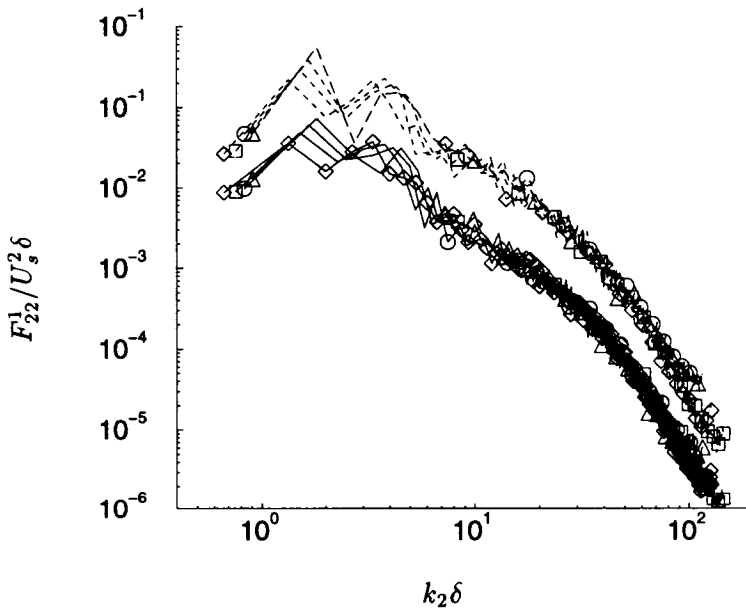
FIGURE 5.   Scaled one-dimensional spectra, $\tilde{F}_{22}^1$ in the forced wake at ——— $\eta = 0.0$ and - - - - $\eta = 0.5$. δ/δ_d is equal to; 5.306 $\diamond$, 6.037 $\square$, 6.636 $\circ$, and 7.235 $\triangle$.

x_2-direction, given by

$$\overline{(u_\alpha - u'_\alpha)^2} = \overline{u_\alpha^2} + \overline{u_\alpha'^2} - 2R_{\alpha,\alpha}(x_2, x'_2) \tag{15}$$

are used to compare the prediction of the similarity hypothesis and the data, since they are more measures of the motions whose sizes are on the order of the separation distance between the points. The structure functions for $\alpha = 1$ centered around the centerline and the half-deficit point in the unforced wake, scaled with appropriate similarity variables, are shown in Figs. 6a and 6b. In both cases the profiles from the four different times collapse for small and intermediate separation distances, suggesting again that the statistical measures of all but the largest scales of motion in the flow are evolving as predicted by the similarity hypothesis. The structure functions from the forced wake simulation also collapse for small and intermediate separation distances when they are scaled using similarity variables (Ewing 1995).

2.4 Scalar fields

The similarity analysis was also extended to the governing equations for a passive scalar field. It was demonstrated that these equations admit similarity solutions for both a scalar field with a mean deficit in the wake region and a scalar field where the mean value in the two free streams differ. The predictions of the similarity hypothesis were compared to data from the simulations, which were computed with this second type of scalar field. However, the variations of the two-point scalar correlation in the simulations were much smaller than the variations of the two-point velocity correlation tensor (as predicted by the similarity hypothesis). As

FIGURE 6. Scaled structure functions about *(a)* $\eta = 0$ *(b)* $\eta = 0.5$. δ/δ_d is equal to: 3.494 $\diamond$, 4.008 $\square$, 4.446 $\circ$, and 4.884 $\triangle$.

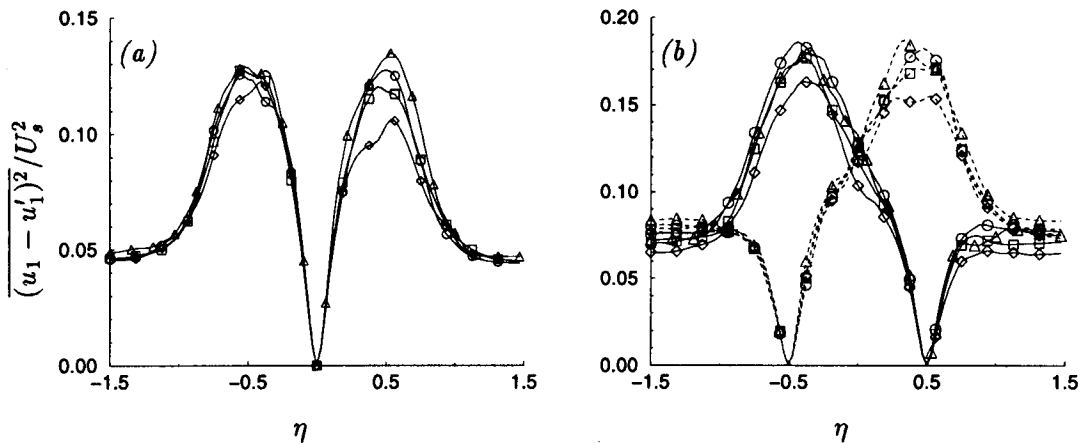a result, the data from the period where the simulations were approximately self-similar did not vary sufficiently to rigorously test the predictions of the similarity hypothesis for the scalar field. Further details of this comparison can be found in Ewing (1995).

3. Conclusions

The analysis demonstrated that the governing equations for the two-point velocity correlation tensor in the temporally evolving wake admit similarity solutions, which include the similarity solutions for the single-point moment as a special case. The resulting equations for the similarity solutions include two constants, β and Re_δ, that are ratios of three characteristic time scales of processes in the flow: a viscous time scale, a time scale characteristic of the spread rate of the flow, and a characteristic time scale of the mean strain rate. The values of these ratios depend on the initial conditions of the flow and are most likely measures of the coherent structures in the initial conditions. The occurrences of these constants in the governing equations for the similarity solutions indicates that these solutions, in general, will only be the same for two flows if these two constants are equal (and hence the coherent structures in the flows are related).

The comparisons between the predictions of the similarity hypothesis and the data presented here and elsewhere (Ewing 1995) indicate that the similarity solutions for the two-point correlation tensors provide a good approximation of the measures of those motions that are not significantly affected by the boundary conditions caused by the finite extent of real flows. Thus, the two-point similarity hypothesis provides a useful tool for both numerical and physical experimentalist that can be used to examine how the finite extent of real flows affect the evolution of the different scales of motion in the flow. The similarity analysis of the governing equations for the multi-point correlations can be extended to a wide range of spatially and temporally evolving flows using the methodology outlined by Ewing (1995), so this technique

can be used to examine the effect of finite boundaries on the evolution of a number of different flows.

REFERENCES

EWING, D. & GEORGE, W. K. 1994 Applications of a similarity hypothesis to the proper orthogonal decomposition for spatially evolving flows. In *Proc. of the Int. Symp. on Turb. Heat and Mass Trans.*, Lisbon, Portugal.

EWING, D. 1995 On multi-point similarity solutions in turbulent free-shear flows. *Ph.D.* Dissertation, State University of New York at Buffalo.

EWING, D., GEORGE, W. K., ROGERS, M. M.& MOSER, R. D. A similarity hypothesis for the two-point correlations in a temporally evolving, plane wake *J. Fluid Mech. in preparation.*

GEORGE, W. K. 1989 The self-similarity of turbulent flows and its relation to initial conditions and coherent structures. In *Advances in Turbulence.* edit. W. K. George and R. E. Arndt, Hemisphere Publishing.

GEORGE, W. K. & GIBSON, M. M. 1992 The self-preservation of homogeneous turbulence. *Expt. in Fluids.* **13,** 229.

GEORGE, W. K. 1994 Some new idea for similarity of turbulent shear flows. In *Proc. of the Int. Symp. on Turb. Heat and Mass Trans.*, Lisbon, Portugal.

GRANT, H. L. 1958 The large eddies of turbulent motion. *J. Fluid Mech.* **3,** 149.

MOSER, R. D. & ROGERS M. M. 1994 Direct simulation of a self-similar plane wake. NASA Tech. Memo, TM 108815.

MOSER, R. D., ROGERS, M. M., & EWING, D. 1995 *J. Fluid Mech. in preparation.*

PAYNE, F. R. & LUMLEY, J. L. 1967 Large eddy structure of the turbulent wake behind a circular cylinder. *Phys. Fluids Supp.* **10,** 194.

TENNEKES, H. & LUMLEY, J. L. 1972 *A First Course in Turbulence.* MIT Press.

WYGNANSKI, I., CHAMPAGNE, F., & MARASLI, B. 1986 On the large-scale structures in two-dimensional, small-deficit, turbulent wakes. *J. Fluid Mech.* **168,** 31.

Distorted turbulence submitted to frame rotation: RDT and LES results

By Fabien S. Godeferd[1]

1. Motivation and objectives

The stability analysis of homogeneous turbulence submitted to mean velocity gradients can be investigated from a pure mathematical point of view by examining the growth of a single Fourier mode as a perturbation to a background flow. The engineering method of studying the same flow is to use Rapid Distortion Theory (RDT) applied to a group of Fourier modes that represent a more "physical" turbulent flow. However, both approaches deal with the amplification or damping coefficients that arise from the linearized equations. Comparison of simple RDT approximation to the more costly Direct Numerical Simulation (DNS) has led to good agreement, at least qualitatively, in terms of structure between predictions of sheared homogeneous turbulent flow through RDT and results of simulations of a stationary channel flow (Lee, Kim & Moin, 1990). They find that the shear induced by the mean velocity profile close to the walls is the main factor for this agreement. Starting from a purely isotropic flow, streak-like structures appear in sheared homogeneous flows, even in the linear approximation. The objective of this effort is to carry the analysis of Lee *et al.* (1990) to the case of shear with rotation. We apply the RDT approximation to turbulence submitted to frame rotation for the case of a uniformly sheared flow and compare its mean statistics to results of high resolution DNS of a rotating plane channel flow. In the latter, the mean velocity profile is modified by the Coriolis force, and accordingly, different regions in the channel can be identified. The properties of the plane pure strain turbulence submitted to frame rotation are, in addition, investigated in spectral space, which shows the usefulness of the spectral RDT approach. This latter case is investigated here. Among the general class of quadratic flows, this case does not follow the same stability properties as the others since the related mean vorticity is zero.

2. RDT equations in spectral space

2.1 Basic equations

We consider here incompressible homogeneous turbulence with total velocity field $U(x,t) = \overline{U}(x) + u(x,t)$, where u is the fluctuating velocity and $\overline{U}$ is the mean velocity. The mean velocity is taken to be independent of time with uniform uniform gradient in space. Therefore, only the mean velocity gradients $\overline{U}_{i,j} = \overline{G}_{ij}$ appear in the equations. The flow is set in a rotating frame with angular velocity vector

1 LMFA/URA CNRS 263 – École Centrale de Lyon – France

Ω^f, and the classical symmetric/skew symmetric decomposition is performed on the mean velocity gradients tensor

$$S_{ij} = \left(\overline{U}_{i,j} + \overline{U}_{j,i}\right)/2$$

and

$$W_{ij} = \left(\overline{U}_{i,j} - \overline{U}_{j,i}\right)/2 \ .$$

The rotation tensor is related to the vorticity through $W_{ij}1/2\epsilon_{ijk}\Omega_k$. The rapid distortion approximation is obtained by dropping the nonlinear terms in the Navier-Stokes equations. Using the previously introduced decomposition for the mean velocity gradients, we get the corresponding linearized equation, which, for a non viscous fluid, reads

$$\dot{\boldsymbol{u}} = \partial_t \boldsymbol{u} + \overline{U}_j \partial_j u_i = -\boldsymbol{S} \cdot \boldsymbol{u} - (\Omega + 2\Omega^f) \times \boldsymbol{u} - \nabla p \qquad (1)$$

where the equations are written in the rotating frame Ω_k. In this frame, a general method of decomposition for homogeneous sheared flows is used by considering the expansion of the fluctuating fields in terms of time-dependent Fourier modes $\exp(i\boldsymbol{k}(t) \cdot \boldsymbol{x})$, where the wave vectors evolve in time according to $\partial_t k_i = -\overline{U}_{j,i} k_j$. The Lagrangian wave vectors $\boldsymbol{K}$, which are associated with the Lagrangian physical coordinates $\boldsymbol{X}$ that follow the distortion of the flow, are related to the Eulerian ones by the relation

$$\boldsymbol{k} \cdot \boldsymbol{x} = \boldsymbol{K} \cdot \boldsymbol{X} \ .$$

These variables, $(\boldsymbol{X}, \boldsymbol{K})$, which follow the deformation of the space, have been used by Cambon *et al.* (1985) and are exactly the same as the Rogallo space variables (Rogallo, 1981).

2.2 Solutions in the Craya-Herring local frame

In the following, we shall take advantage of the Craya-Herring decomposition of the fluctuating velocity $\hat{\boldsymbol{u}}$ (Craya, 1958, Herring, 1974) by choosing a given direction in the flow along a vector $\boldsymbol{n}$. This decomposition uses a local frame of reference in the plane perpendicular to the wave vector $\boldsymbol{k}$. The Fourier transformed velocity $\hat{\boldsymbol{u}}$ is such that $\boldsymbol{k} \perp \hat{\boldsymbol{u}}$ from the continuity equation $\boldsymbol{k} \cdot \hat{\boldsymbol{u}} = 0$. The first component of $\hat{\boldsymbol{u}}$ in this frame is its projection $\hat{\varphi}^1$ onto the "equatorial" vector $\boldsymbol{e}_1 = \boldsymbol{k} \times \boldsymbol{n}/|\boldsymbol{k} \times \boldsymbol{n}|$, and its second component is the remaining part $\hat{\varphi}^2$, along $\boldsymbol{e}_2 = \boldsymbol{e}_1 \times \boldsymbol{k}/|\boldsymbol{e}_1 \times \boldsymbol{k}|$. We refer to $\boldsymbol{n}$ as the *polar* direction and to the plane orthogonal to $\boldsymbol{n}$ as the *equator*, since the $(\boldsymbol{e}_1, \boldsymbol{e}_2)$ frame is also the set of axes associated with spherical coordinates. The Foureir transformed fluctuating velocity can then be written as

$$\hat{u}_i(\boldsymbol{k}, t) = \hat{\varphi}_1(\boldsymbol{k}, t)e_i^1 + \hat{\varphi}_2(\boldsymbol{k}, t)e_i^2 \ .$$

Using these variables, the linearized evolution Eq. (1) can be rewritten, and one obtains the equations for each component of $\hat{\boldsymbol{u}}$ in the Craya-Herring frame

$$\dot{\hat{\varphi}}_n(\boldsymbol{k}, t) + m_{nl}(\boldsymbol{k})\hat{\varphi}_l(\boldsymbol{k}, t) = 0 \qquad (2)$$

where $k, l = 1, 2$ and the linear operator matrix

$$m_{nl} = S_{ij} \left(e_i^k e_j^l - \epsilon_{nl3} e_i^2 e_j^1 \right) + \epsilon_{nl3} \left(\Omega_l + 2\Omega_l^f \right) \frac{k_l}{k} .$$

Note that m does not depend on the modulus of the wave vector, but only on its orientation. Therefore, the time evolution factors of the different modes of velocity $\hat{\varphi}_n(k, t)$ are identical for all the wave vectors with the same orientation. The advantage of this procedure is to save computing time since the values of the amplification factors need be computed only for different orientations of a unit wave vector (*i.e.* a discretization of a sphere of radius unity) (Cambon, 1982, Benoit, 1992). These coefficients allow one to evaluate the time variation for all vectors in wave space. Once Eq. (2) is solved for a given set of initial conditions by way of a matrix exponential rather than inverting the linear system, the complete statistics in the flow can be computed easily without further computations. All of the statistics such as spectra of two-point correlations and, of course, one-point quantities are entirely known through the knowledge of the amplification coefficients and statistical quantities at the initial time. The whole method has been implemented in a code named MITHRA at the LMFA (Benoit, 1992).

Alternatively, Eq. (2) holds for all discretization of the spectral space, and we have been able to apply this method of resolution for wave vectors that are spread on a classical spectral cubic distribution, as for direct numerical simulations (see Section 4.3). The independence of the amplification of the different velocity modes with the modulus of the wave vector is no more valid when one considers a *viscous* fluids for which, of course, a dissipation term proportional to νk^2 appears in the equations.

Note that the distortion of the computing mesh in RDT and in DNS are the same but have a different impact on the accuracy of the computation. In the former approach, there is no flux of energy through the boundary of the resolved space. Therefore, no problem of resolving the different scales in the flow arises since the different scales are as well represented by the distorted mesh as they were in the initial one, at $t = 0$. If one now considers the DNS approach, there is a flux of energy through the boundaries of the resolution mesh, and a remeshing at given periodic intervals in time is necessary if one wants to keep as much resolved energy containing scales in the computational box as possible.

2.3 Linear stability results

We consider here a general type of deformation in the plane (1,2) with mean velocity gradients such that (quadratic flow),

$$\overline{G} = \begin{pmatrix} D & -\Omega \\ \Omega & D \end{pmatrix} ,$$

or equivalently

$$\overline{G} = \begin{pmatrix} 0 & D - \Omega \\ D + \Omega & 0 \end{pmatrix}$$

if the principal axes of the associated pure strain tensor S are chosen. Cambon *et al.* (1994) have confirmed that linear stability analysis gives a maximum destabilization for zero tilting vorticity $2\Omega^f + \Omega = 0$, whereas stability is found for zero absolute vorticity $2\Omega + 2\Omega^f = 0$.

In the case of simple uniform shear with rotation, the pressureless analysis by Bradshaw concluded with a stability governed by the Bradshaw-Richardson number $B = R(R+1) > 0$, with $R = 2\Omega^f/S$ or $B = 2\Omega^f(2\Omega^f - S)/S^2 > 0$. The maximum growth rate of the unstable case is obtained for $B = -1/4$ (or equivalently $R = -1/2$. In the general case for given Ω^f and D, Salhi & Cambon (1995b) have shown the validity of the extended criterion $B = D^2 - (2\Omega^f - \Omega)^2$.

Now that we have stated the stability criteria for the general case of distortions, we shall use it for studying the behavior of two specific cases, a purely strained and a sheared turbulence.

3. Purely strained homogeneous turbulence in a rotating frame

The case of a plane pure strain applied to the flow is one of the simplest, with a deformation tensor written as

$$G = \begin{pmatrix} D & 0 \\ 0 & D \end{pmatrix}$$

and $\Omega = 0$. No stability result can be obtained through the classic Bradshaw criterion for pure shear, for here Ω is zero. We expect the stability of the flow to depend upon the ratio of the two controlling parameters, namely $2\Omega^f/D$, the rotation number. The symmetry of the deformation implies independence of the results with the sign of the rotation rate Ω^f. Indeed, the pressureless analysis gives $B = D^2 - (2\Omega^f)^2$ (Salhi & Cambon, 1995b, Speziale *et al.*, 1995).

3.1 Stability analysis

We have computed the time evolution of the kinetic energy for different values of the rotation rate, which leads to the following simple linear stability result (Fig. 1): q^2 grows exponentially for $2\Omega^f/D < 1$ and is damped otherwise; the rotation of the frame applied to a plane pure strained flow is stabilizing only for high rotation rate. However, at very large values of the cumulative distortion Dt, even the latter cases may exhibit a growth of kinetic energy. In this case, the time scale is probably large enough so that the nonlinear terms can no longer be neglected.

The evolution of the enstrophy $\omega^2 = < \omega_i \omega_i >$ (ω is the vorticity of the fluctuating flow) with the non-dimensional time t/T is shown in Fig. 2. $T = (2\pi/\Omega^f)$ is the characteristic time of the frame rotation. We find that the exponential growth occurs *for all values* of the rotation rate. But there is a clear separation in the growth rates of ω^2 between the stabilized cases and the destabilized ones (with respect to the kinetic energy).

For such a deformation, the growth rate of the kinetic energy should *a priori* be independent of the sign of the rotation applied to the flow. This symmetry condition is a good test of the accuracy of the numerical resolution method. Indeed, we see

in Fig. 1 that the q^2 evolutions for $2\Omega^f/D = 1$ and $2\Omega^f/D = -1$ begin to depart slightly around the value $Dt = 5$ for the cumulative distortion rate. Therefore, if we need to reach higher values, *e.g.* $Dt > 10$, with sufficient precision, a very large number of discretized points is necessary. This condition would be much more strenuous if we used a classical cubic discretization of the space rather than spreading the resolution points on a sphere of unit radius.

3.2 Production of kinetic energy

The behavior of the production term in the equation for kinetic energy depends on the value of the ratio $2\Omega^f/D$, reflecting the stabilizing or destabilizing role of the solid body rotation on the strained turbulent flow. We can compute the evolution in time of the only non-zero term $- < u_1 u_2 >$, and investigate its proportion at a given instant t with respect to the kinetic energy at this instant. This *relative* value is a clue for understanding how the rotation modifies the production of kinetic energy. We can see from Fig. 3 that $- < u_1 u_2 >$ is positive when the stability criterion $2\Omega^f/D > 1$ is not met, but also that the transition from this unstable regime to the stable one where $- < u_1 u_2 > < 0$ is not smooth. This effect, possibly due to round-off errors, shows the degree of sensitiveness of the flow to the resolution method even though our numerical scheme here is of very high order and our resolution grid is very fine.

3.3 Full spectral distribution

The instability of the plane strained homogeneous turbulence under rotation is well reflected through the one-point quantity q^2. However, the exponential growth of kinetic energy is the consequence of the amplification of an unstable region of wave vector orientations in spectral space. Accordingly, we have plotted in Figs. 5 and 6 the distribution of kinetic energy, and similarly in Fig. 4 that of the enstrophy, on a sphere of given radius. One can therefore identify the zone of maximum destabilization, or maximum amplification, of kinetic energy as being the wave vector orientations mainly responsible for the destabilization of the flow. The surface is initially a sphere, but is distorted when time evolves. However, our representation is Lagrangian, and therefore all the distributions are represented on a sphere. This kind of representation has been successfully used by Cambon *et al.* (1994) for concluding that only a very narrow band of wave vectors is destabilized in the case of the elliptical flow submitted to frame rotation. Figure 6 shows that no such peculiar orientation is present in the case of the strained turbulence. However, it shows that the most destabilized wave vectors are those orthogonal to the frame rotation vector, *i.e.* those that lie in the equatorial region of the sphere, since there is no explicit effect of the Coriolis force on these wave vectors. Equivalently, in physical space there is no influence of the Coriolis force on fluid motion that is parallel to the rotation vector. The unstable modes are all located in a band at an angle $\pi/4$ radians, where the longer the evolution time the thinner the band, along with the above mentioned concentration in the equatorial plane. The difference between Figs. 5 and 6 shows how the rotation tends to reduce the thinning of the instability band. The enstrophy, shown in Fig. 4, exhibits the same pattern as the
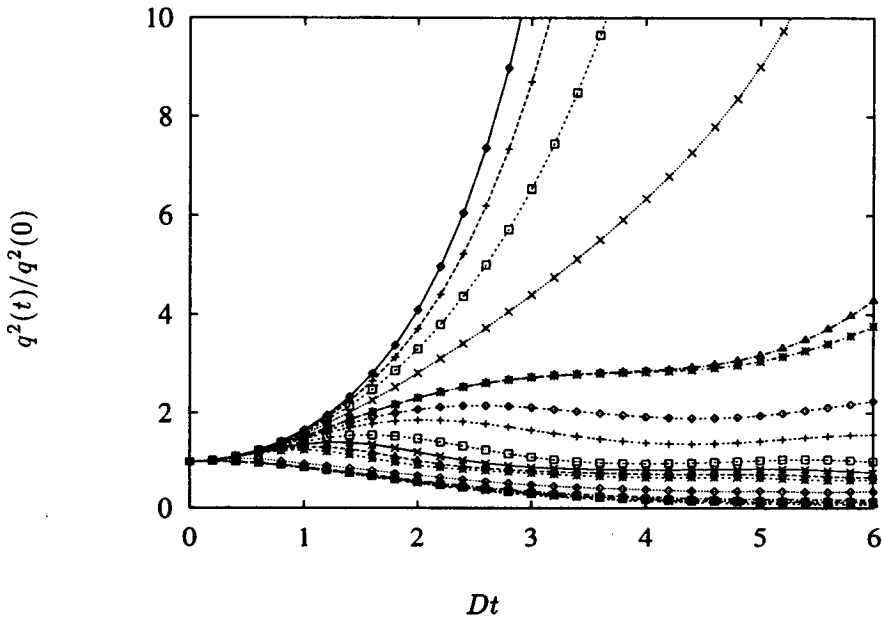
FIGURE 1. Normalized kinetic energy $q^2(t)/q^2(0)$ for different values of the rotation rate Ω^f, as a function of the non-dimensional time Dt. Curves clockwise from top of figure: $\Omega^f = 0,\ 0.2,\ 0.3,\ 0.4,\ -0.5,\ 0.5,\ 0.55,\ 0.6,\ 0.7,\ 0.8,\ 0.9,\ 1,\ 2,\ 5,\ 8,\ 10,\ 20$.

FIGURE 2. Normalized enstrophy $\omega^2(t)/\omega^2(0)$ for different values of the rotation rate Ω^f, as a function of the non-dimensional time $t/(2\pi/\Omega)$. The case at $\Omega^f = 0$ is non dimensionalized using $\Omega^f = 1$. Curves as in Fig. 1.
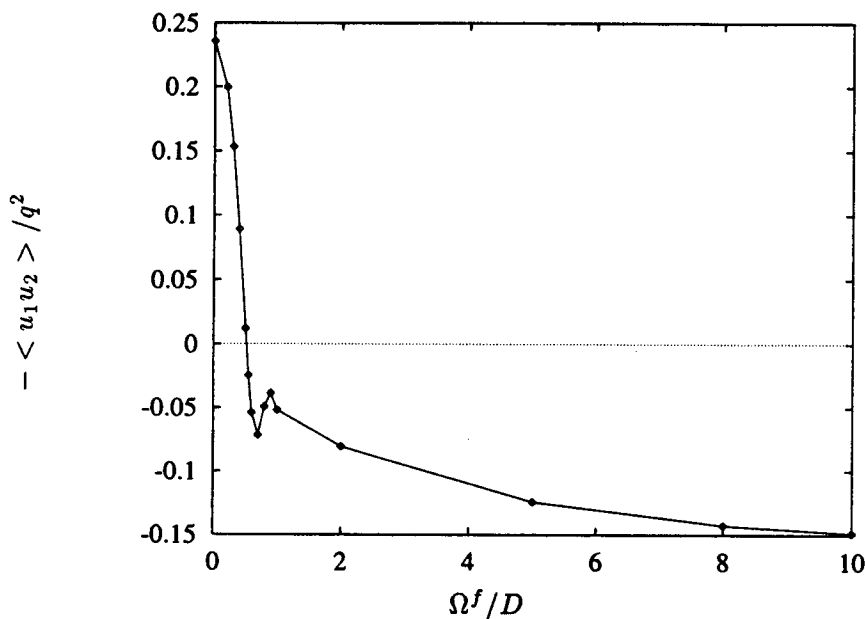
FIGURE 3. Normalized production of kinetic energy $- < u_1 u_2 > /q^2$ at time $t = 3$ for different values of the ratio Ω^f/D.

kinetic energy distribution.

4. Sheared homogeneous turbulence in a rotating frame

We now go on to the case of sheared homogeneous turbulence for which the mean velocity gradients lead to the decomposition:

$$\mathbf{S} = \begin{pmatrix} 0 & D \\ D & 0 \end{pmatrix}$$

and

$$\mathbf{W} = \begin{pmatrix} 0 & -\Omega \\ \Omega & 0 \end{pmatrix}$$

with the particular choice $\Omega = D$. The resulting mean velocity gradient is $d\overline{U}_1/dy = 2D = S$.

4.1 Stability analysis

The general stability results have been briefly reviewed in Section 2.3 (see also Salhi & Cambon, 1995a). Accordingly, the evolution of the kinetic energy shows an exponential growth when the rotation of the frame does not compensate the vorticity induced by the shear, namely $2\Omega^f/S < 1$, as shown in Fig. 7.

But, looking only at the enstrophy growth rates (Fig. 8), it is not possible to distinguish the destabilized cases and the stabilized ones, as can be done in the case of the plane strain. The mechanism of enstrophy production is different in the two cases and is less affected by the rotation in a homogeneous shear flow.
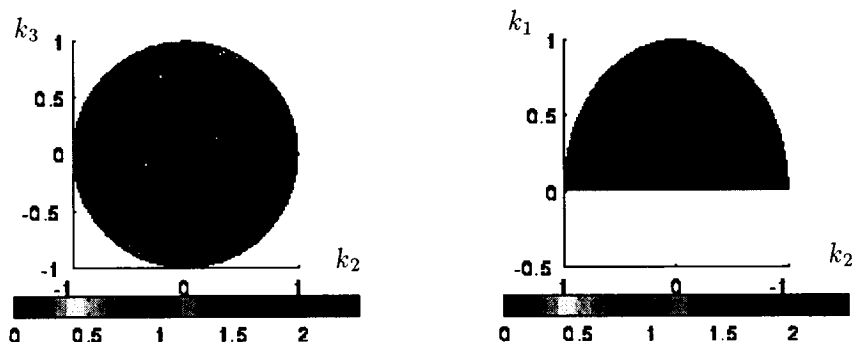
FIGURE 4.   Full spectral distribution of the enstrophy ω^2 for a plane strained homogeneous turbulence with frame rotation $\Omega^f = 10$. Left figure: top view of the spectral sphere; right figure: side view. Snapshot taken at $Dt = 1.5$.
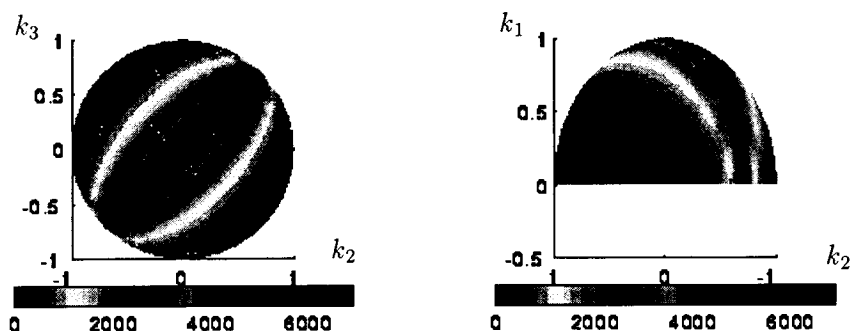
FIGURE 5.   Full spectral distribution of the kinetic energy for a plane strained homogeneous turbulence with a rotation rate $\Omega^f = 0.2$. Left figure: top view of the spectral sphere; right figure: side view. Snapshot taken at $Dt = 1.5$.
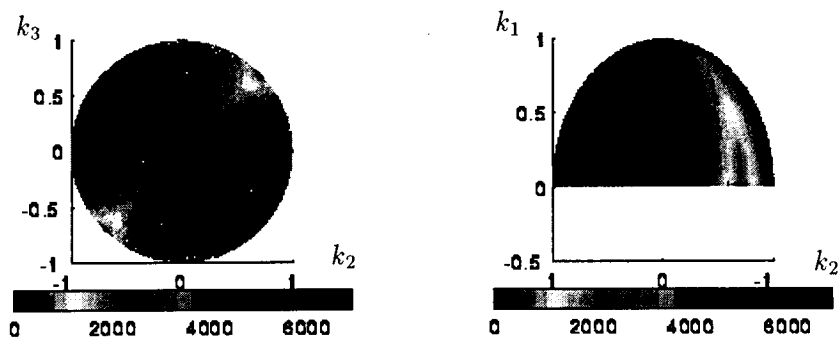
FIGURE 6.   Full spectral distribution of the kinetic energy for a plane strained homogeneous turbulence with $\Omega^f = 10$. Left figure: top view of the spectral sphere; right figure: side view. Snapshot taken at $Dt = 1.5$.
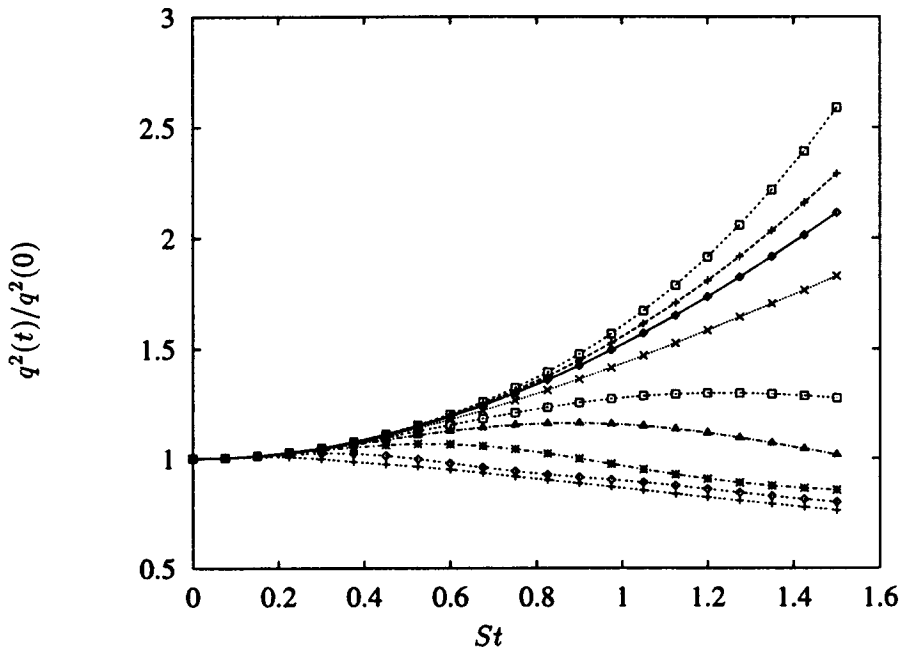
FIGURE 7. Normalized kinetic energy $q^2(t)/q^2(0)$ for different values of the rotation number $2\Omega^f/S$, as a function of the non-dimensional time St. Curves clockwise from top of figure: $2\Omega^f/S = -0.5, 0.1, 0, 1, 0.5, 1.5, 2, 3, 5$.
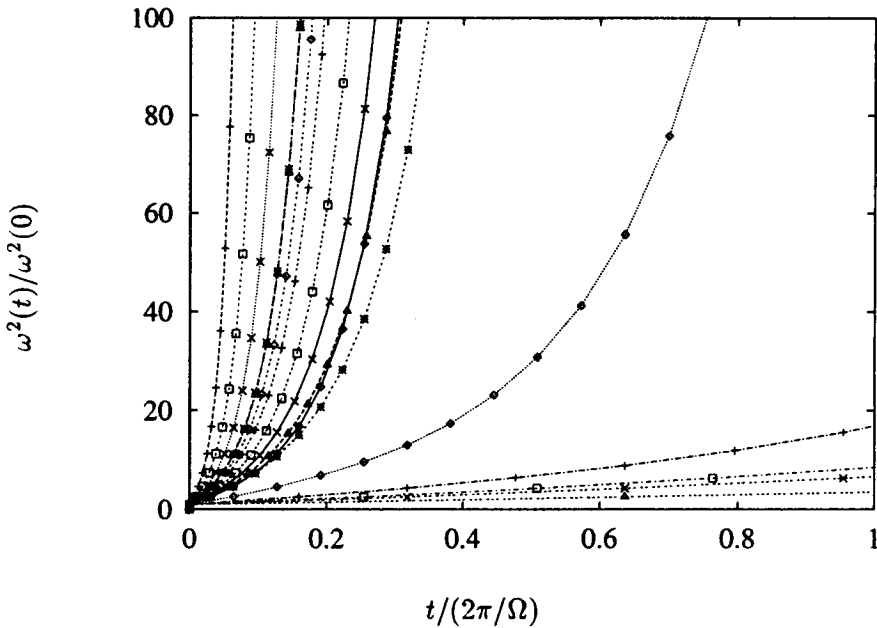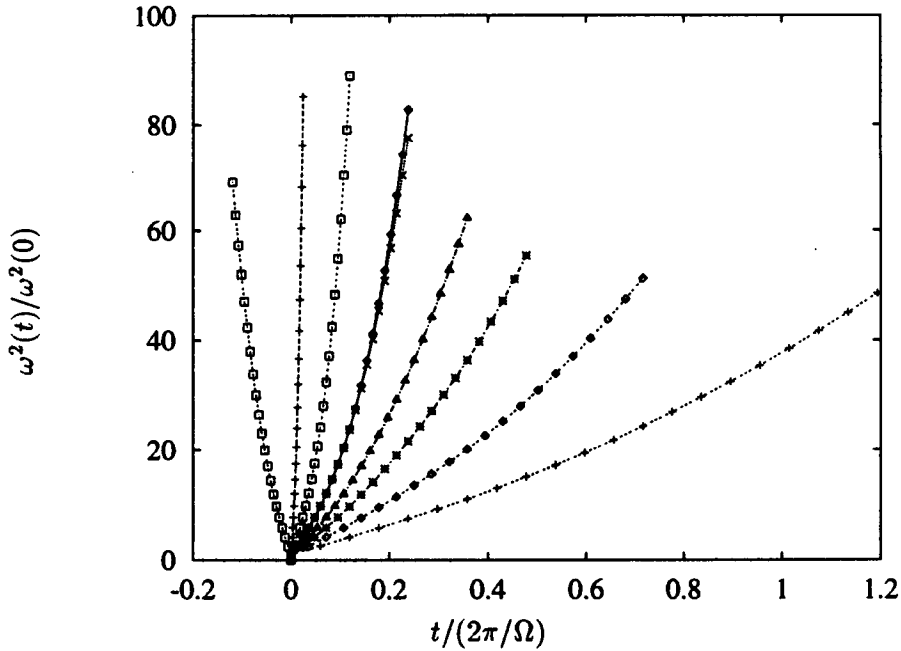

FIGURE 8. Normalized enstrophy $\omega^2(t)/\omega^2(0)$ for different values of the rotation number $2\Omega^f/S$, as a function of the non-dimensional time $t/(2\pi/\Omega^f)$ (and of t for the case $\Omega^f = 0$). Curves as in Fig. 7.
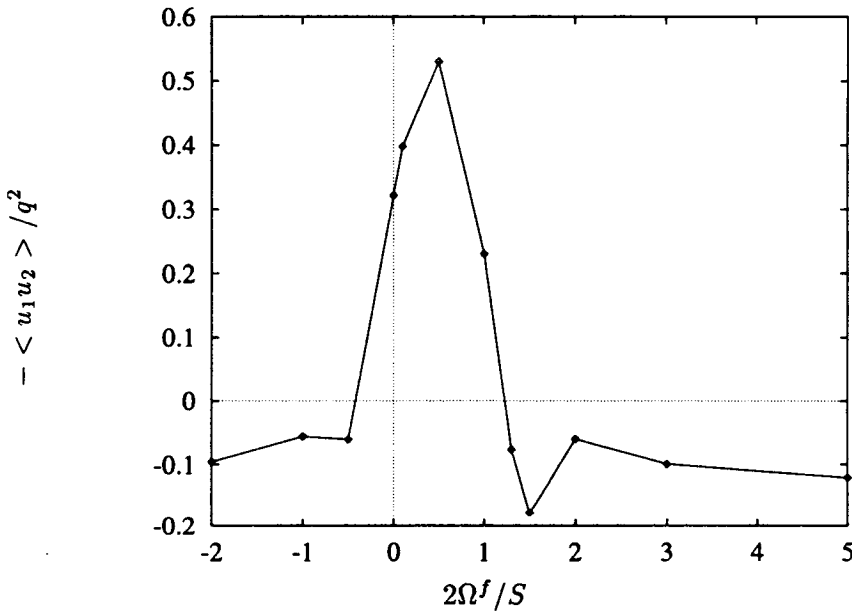
FIGURE 9.   Normalized production of kinetic energy $- < u_1 u_2 > /q^2$ at time $t = 3$ for different values of the ratio $2\Omega^f/S$.

4.2 Production of kinetic energy

Figure 9 shows the negative of the Reynolds shear stress, $- < u_1 u_2 >$, normalized by the kinetic energy $q^2(t)$ at time t. We find that the transition zone, in terms of Ω, does not evolve smoothly in the crucial transition zone, in terms of the rotation number. The distribution of the production is not symmetric around $R = 2\Omega^f/S = 0$, since, in this case, maximum destabilization is obtained for $R = -1/2$.

4.3 Structure of rotating homogeneous shear flow

As mentioned in Section 2.2, the equations for the RDT approximation can be solved for wave vectors evenly distributed on a cube in spectral space. A resolution of 32^3 points has been chosen, and an initial isotropic fluctuating velocity field has been built using random Fourier modes (see Rogallo, 1981). By computing the time evolution of this velocity field, submitted to the mean shear, and to different values of the rotation rate, one can see qualitatively the structure of the flow. Figures 10, 11, and 12 show the isolines of the streamwise component of the velocity in a given plane of constant mean velocity and at different times, *i.e.* different cumulative distortions.

It can be seen that the case at maximum *destabilizing* rotation rate $\Omega^f = 5$ in Fig. 12 has rapidly elongating structures that align with the streamwise direction. For the intermediate destabilizing value of the rotation, $\Omega^f = 2$, the structures still align in this direction, but elongate somehow less, and more slowly, even at the quite high cumulative distortion rate $St = 2D = 10$. We notice by comparing the plots at the intermediate value $St = 5$ that one has to wait for the full deformation

(symmetric *and* anti-symmetric parts) to play a role before having a full characterization of the most destabilizing case (Fig. 12). Finally, the stabilizing case at $\Omega^f = -2$ presents a different pattern at the same last value of $St = 10$, and the intermediate states at $St = 2.5$ and $St = 5$ are clearly closer to the isotropic case than those in Fig. 12. For identifying the different cases, which is *a priori* not obvious, one has to look at the characteristic length of the black patches on the iso-contours plots. Figure 12 presents almost no such region, whereas Fig. 10 exhibits longer "structures" in darker regions than the stabilized case in Fig. 11. Nevertheless, the — still subjective — interpretation of such a representation has to be completed with statistical indicators of the anisotropy.

For this purpose, we can also introduce here the 2D energy components $\mathcal{E}_{ij}^l = <u_i u_j > L_{ij}^l$, as the product of the Reynolds stress tensor components with a corresponding integral length scale (Salhi & Cambon, 1995b). These quantities may be a better indicator for looking at the anisotropy in the flow than each of the Reynolds stress or the integral length separately, since both the anisotropy of $< u_i u_j >$ and L_{ij}^l play a role in $\mathcal{E}_{ij}^l$. For example, in the inviscid case, it is possible to get *analytical* solutions for the evolution of most of these energy components in the case of a homogeneous shear flow, but not for L_{ij}^l separately. The "eddy elongation parameter", *i.e.* the ratio $\kappa = L_{11}^1 / L_{11}^3$ can be computed from these since it is also $\kappa = < u_1 u_1 > L_{11}^1 / (< u_1 u_1 > L_{11}^3) = \mathcal{E}_{11}^1 / \mathcal{E}_{11}^3$. A large value of κ indicates the stretching of the structures. For instance, for $R = 2\Omega^f/S = 2$, a stabilized case, $\kappa \simeq 0.7$, whereas for $R = -2$, the destabilized case, $\kappa \simeq 1.3$, both at the same given instant $St = 10$. And for the case of zero absolute vorticity $R = 1$, the ratio *remains constant*. These three cases are close to the situations presented in three planes in a rotating channel flow (see Section 5), where the destabilized, stabilized, and middle regions are represented. (Of course, when comparing different energy components, one has to be aware that different components of the Reynolds stress tensor can be involved, as well as that opposite tendencies on $< u_i u_j >$ and L_{ij}^l could leave E_{ij}^l almost unchanged.)

Finally, it is interesting to notice that the *symmetric* part of the deformation tensor $\overline{G}$ has its eigenvectors oriented at an angle of $\pi/4$ radians to the streamwise direction. Accordingly, at the first stage of the evolution, the flow structures tend to be aligned with this orientation. Of course, for later stages in time, the full role of the deformation is a stretching in the direction of the mean flow.

5. LES of a rotating channel flow

In this section, we consider results from 128^3 direct numerical simulations performed at NASA Ames Research Center by Kim. The reader is referred to Lee *et al.* (1990) for all the details of the numerical method. A stationary velocity field is obtained in a channel between two parallel plane walls, which is located in a frame rotating around the spanwise direction. The streamwise direction is x, the spanwise direction is z, and the (inhomogeneous) vertical direction is y. The mean velocity profile (shown in Fig. 13) induces a shear that depends on the transverse coordinate (perpendicular to the walls). Therefore, the previous homogeneous stability
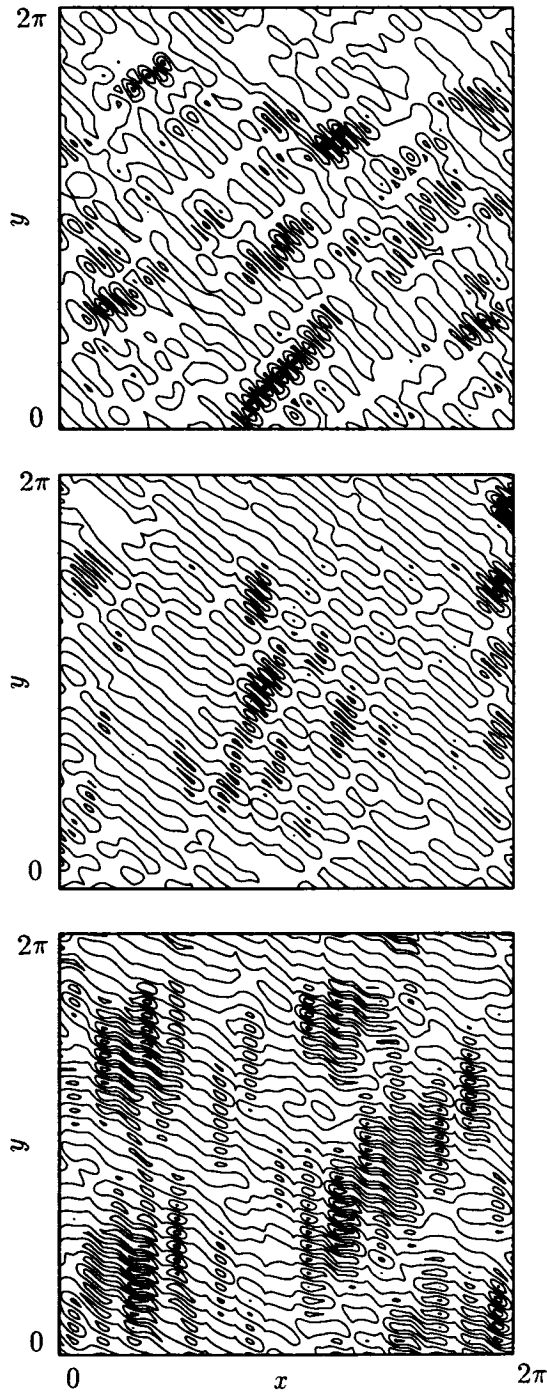
FIGURE 10.   Isolines of u_x component of fluctuating velocity at $Dt = 2.5$, 5, 10 from top to bottom at mid-height in the periodic computational box of homogeneous isotropic turbulence. The rotation number is $2\Omega^f/S = 2$.
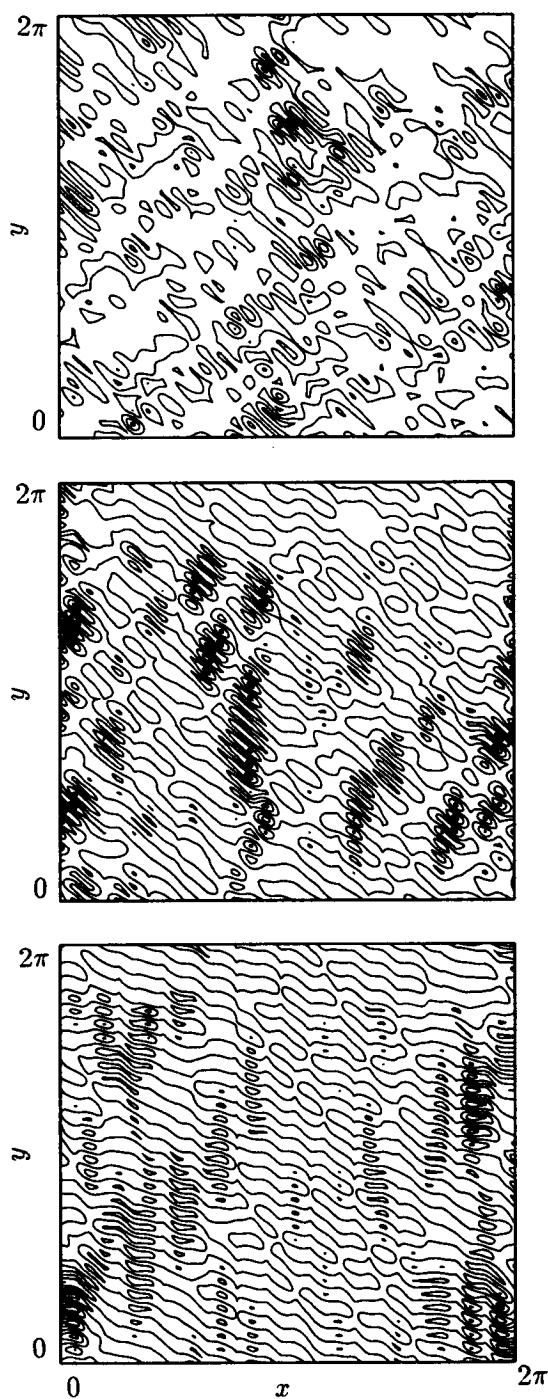
FIGURE 11.   Same as Fig. 10 with $2\Omega^f/S = -2$.
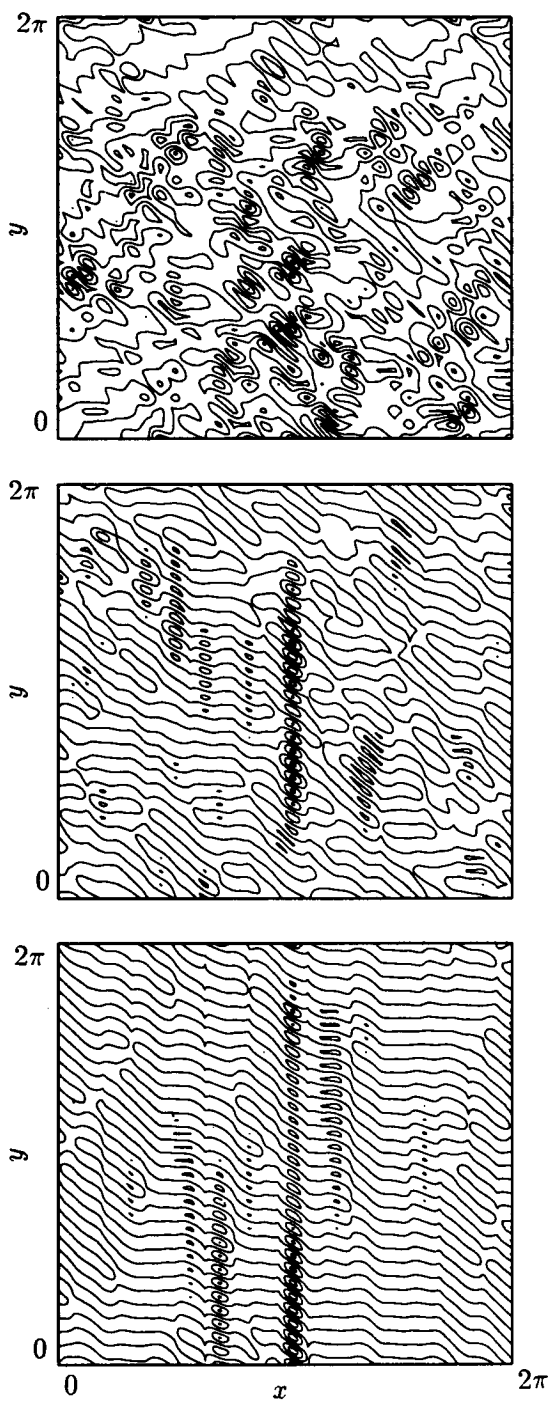
FIGURE 12.　Same as Fig. 10 with $2\Omega^f/S = 5$.
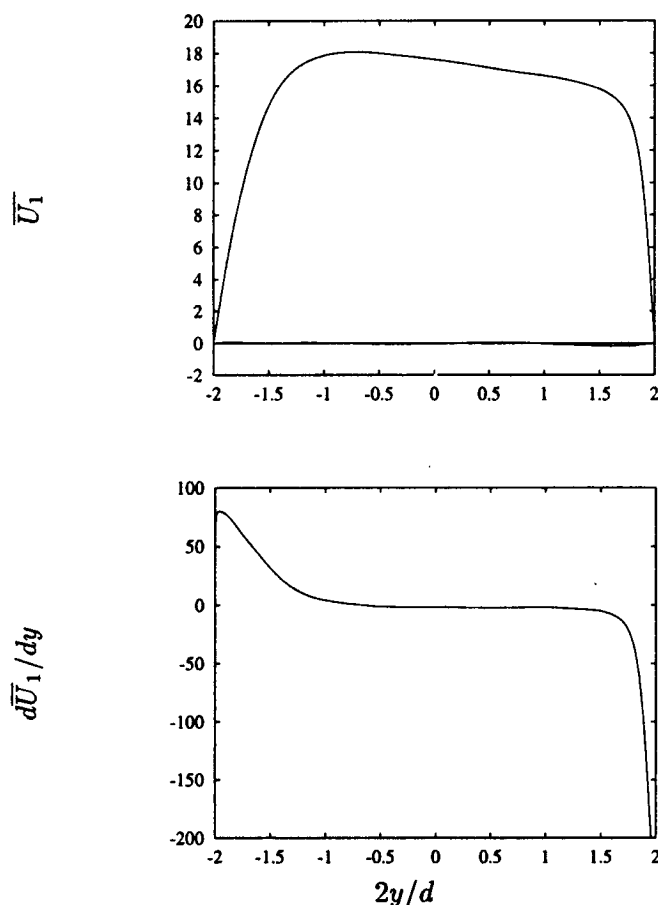
FIGURE 13. Mean velocity profile of $\overline{U}_1$ in the rotating channel (top figure), and corresponding shear $d\overline{U}_1/dy$ (bottom figure). On top figure the other components $\overline{U}_2$ and $\overline{U}_3$ are almost zero.

analysis of rotating shear flows can be compared, in terms of anisotropy, to the turbulence in different planes in the rotating channel flow where the mean shear is constant. Experimental and numerical investigations (Johnston *et al.*, 1972, Watmuff *et al.*, 1985, Kristoffersen & Andersson, 1993) have shown the particular role of the rotation onto different regions in the channel, namely the modification of the mean velocity profile, with a destabilization of the flow close to the pressure wall (negative shear), and a stabilization near the suction wall (positive shear). The latter effect eventually leads to a *relaminarization* of the flow in the corresponding region.

Figure 14 gathers the distribution of the Reynolds stress tensor components. The lack of symmetry is evident, with enhanced components of the fluctuating velocity towards the destabilized wall; the production $- < u_1 u_2 >$ of kinetic energy changes sign when moving from one wall to the other. This can be related to a similar effect shown in Fig. 9, where the production for the homogeneous case is plotted versus
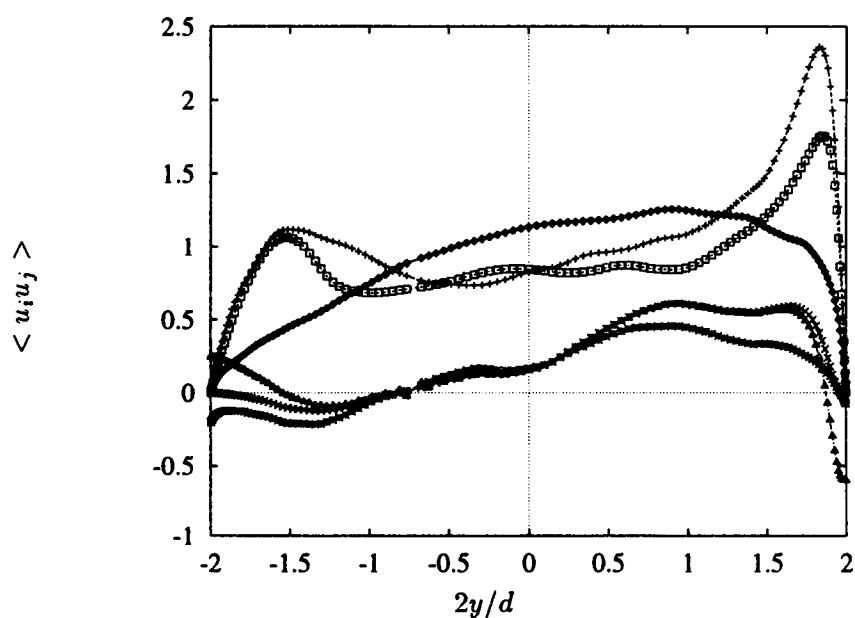
FIGURE 14.   Variation of the components of the Reynolds stress tensor with the distance to the wall. $< u_1^2 >$: +, $< u_2^2 >$: ◊, $< u_3^2 >$: □ , $< u_1 u_2 >$: ×, $< u_1 u_2 >$: *, $< u_2 u_3 >$:△ .
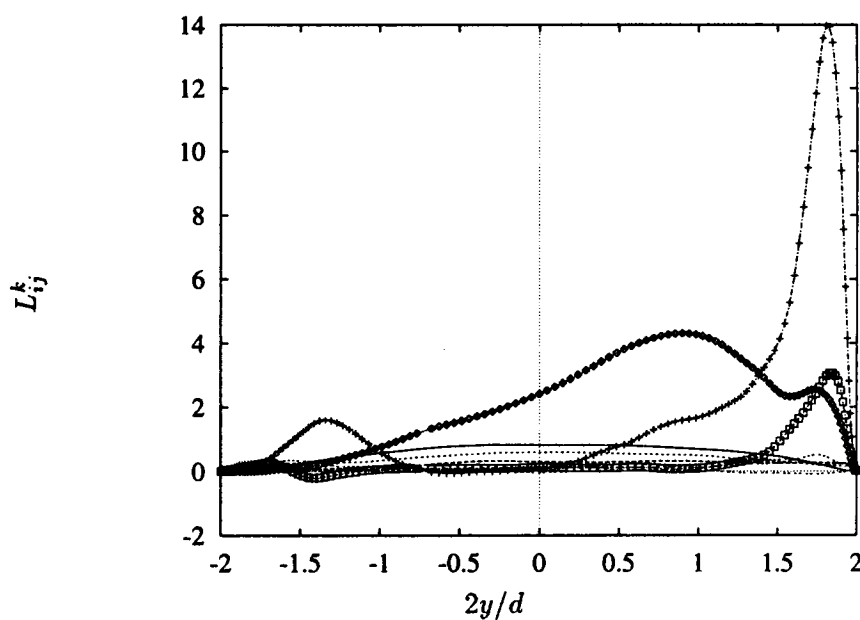
FIGURE 15.   Variation of the integral length scales with the distance to the wall. L_{22}^x: ◊, L_{11}^x: +, L_{33}^x: □ , L_{22}^y: ——— , L_{33}^y: ‑‑‑‑ .
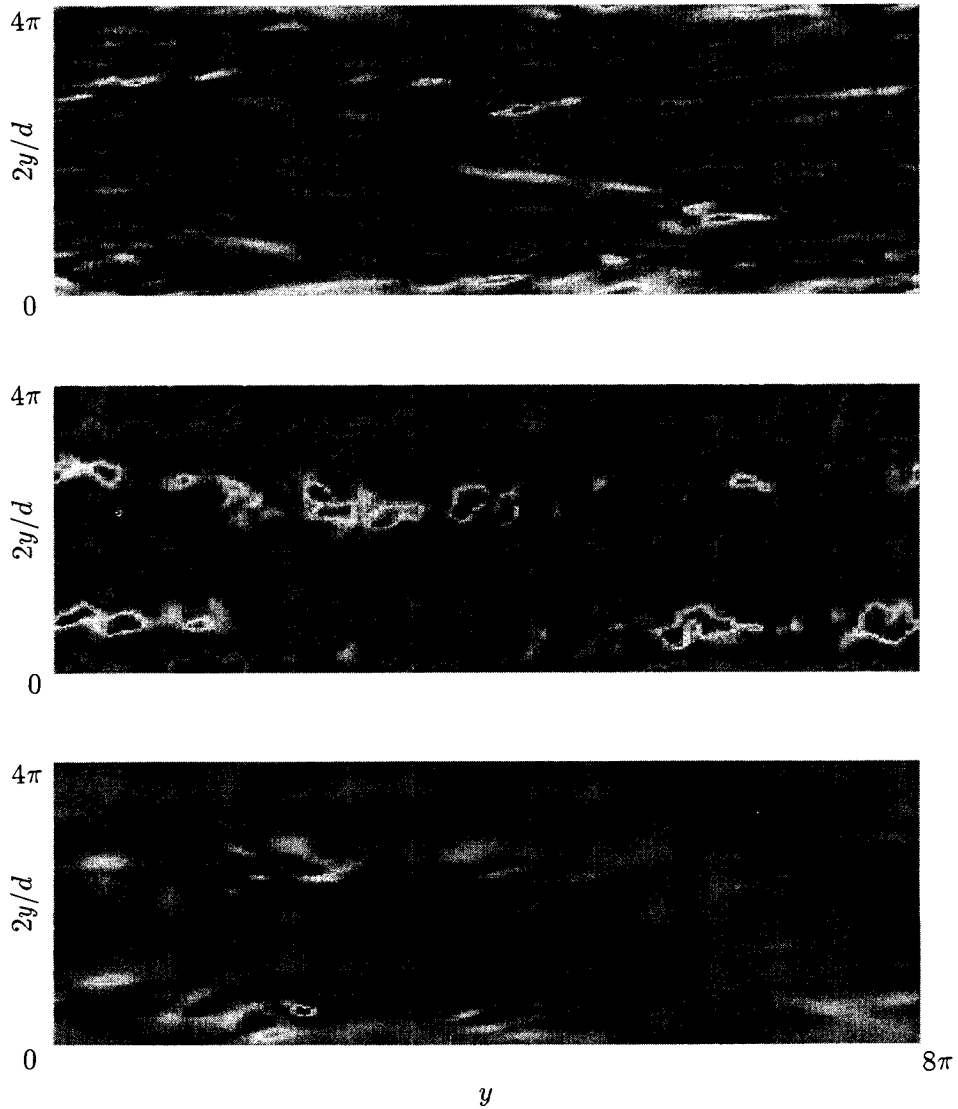
FIGURE 16. Iso-surfaces of the streamwise component of the velocity in the planes $2y/d = 1.95$, 0, -1.95, figures from top to bottom, in the rotating channel.

$2\Omega^f/S$. In the DNS channel, the modification of this ratio results from the variation of S with the distance to the walls.

Distributions of the fluctuating velocity field exhibit different patterns depending on the distance to the wall. Figure 16 shows the iso-surfaces of the streamwise component u_x in planes parallel to the walls, in the stabilized, middle and destabilized regions. One sees immediately that the level of turbulence in the destabilized region is much higher than that in the other ones (see also the variance of the components u_i in Fig. 14). Moreover, the destabilized region presents structures clearly

elongated in the streamwise direction, *as in the homogeneous case.* It is interesting to compute the corresponding integral length scales to evaluate quantitatively the anisotropy of these structures and how much they are stretched in the different planes. Figure 15 shows the integral length scales

$$L_{ij}^k = \int_0^\infty dx_k <u_i u_j>(x_k)/<u_i u_j>(0) ,$$

where ij shows which components of the fluctuating velocity are taken into account, and k shows the direction of separation. Obviously, the most striking feature of this figure is the very large increase of L_{11}^x that confirms the elongation of the structures, maximum at $x = 1.8$, in the region of maximum mean shear. The tendency is somewhat smaller for the transverse correlation L_{33}^x, but an interesting fact is that the transverse correlation length for u_y has its maximum displaced towards the center of the channel. The quite large value of the mean shear close to the stabilized wall is also responsible for the (small) peak of L_{11}^x, no matter the stabilizing effect of the rotation in this particular case. Here, we notice that the qualitative predictions of RDT applied to the homogeneous shear flow with rotation agree with the distributions of the integral length scales in the channel flow. Indeed, the general streak-like structures appear in the homogeneous RDT results, and the rotation affects the different regions in the same way equivalent regions of homogeneous rotating turbulence with the same value of R (as in Section 4.3) are affected.

6. Future plans

In light of the results presented in this summary, it will be interesting to refine the study by investigating quantitatively the different parameters of both the homogeneous rotating shear flow and the rotating channel flow. DNS computations with different rotation rates, if available, would be a valuable database for comparison, at the level of one-point statistics, with the equivalent RDT approach. The modeling of the anisotropy in the flow, especially through the evolution of the integral length scales as well as the anisotropy tensors, will probably benefit from such studies. Finally, one can investigate if the Coriolis force, due to the rotation of the frame, could be an analog of the centrifugal acceleration in curved flows. Since the RDT approximation can be closely related to stability analyses, we can try to see if and how the streak-like structures in the rotating channel can be matched to Görtler vortices due to curvature.

REFERENCES

BENOIT, J. P. 1992 Étude expérimentale et théorique d'une turbulence homogène soumise à des effets couplés de rotation et de déformation plane. Ph.D. Thesis.

BRADSHAW, P. 1969 The analogy between streamline curvature and buoyancy in turbulent shear flow. *J. Fluid Mech.* **36**, 177–191.

CAMBON, C. 1982 Étude spectrale d'un champ turbulent incompressible soumis à des effets couplés de déformation et de rotation imposés extérieurement. *Thèse de doctorat détat, Université Claude Bernard-Lyon I.*

CAMBON, C., BENOIT, J. P., SHAO, L. & JACQUIN, L. 1994 Stability Analysis and large-eddy simulation of rotating turbulence with organized eddies. *J. Fluid Mech.* **278**, 175–200.

CAMBON, C., TEISSÈDRE, C. & JEANDEL, D. 1985 Etude d'effets couplés de déformation et de rotation sur une turbulence homogène. *J. Méc. Théor. Appl.* **4**, 629–657

CRAYA, A. 1958 Contribution à l'analyse de la turbulence associée à des vitesses moyennes. *P.S.T. Ministère de l'Air, no. 345.*

HERRING, J. R. 1974 Approach of axisymmetric turbulence to isotropy. *Phys. Fluids.* **17**, 859–872.

JOHNSTON, J. P., HALLEEN, R.M. & LEZIUS, D.K. 1972 Effects of spanwise rotation on the structure of two-dimensional fully developed turbulent channel flow. *J. Fluid Mech.* **56**, 533.

KRISTOFFERSEN, R. & ANDERSSON, H. I. 1993 Direct simulations of low-Reynolds-number turbulent flow in a rotating channel. *J. Fluid Mech.* **256**, 163–197.

LEE, M. J., KIM, J. & MOIN, P. 1990 Structure of turbulence at high shear rate. *J. Fluid Mech.* **216**, 561–583.

ROGALLO, R.S. 1981 Numerical experiments in homogeneous turbulence. *NASA Technical Memorandum.* **81315.**

SALHI, A. & CAMBON, C. 1995a Revisiting rotating shear flow at high shear rate. Submitted to J. Fluid Mech.

SALHI, A. & CAMBON, C. 1995b Stability of a plane quadratic flow in a rotating frame. Submitted to Phys. Rev. Letters.

SPEZIALE, C. G., ABID R. & BLAISDELL, G. 1995 On the consistency of Reynolds stress turbulence closures with hydrodynamic stability theory. Submitted to Phys. Fluids.

WATMUFF, J. H., WITT, H. T. & JOUBERT, P. N. 1985 Developing turbulent boundary layers with system rotation. *J. Fluid Mech.* **157**, 405–448.

Helicity fluctuations and turbulent energy production in rotating and non-rotating pipes

By P. Orlandi[1]

1. Motivation and objectives

In this paper finite-difference second-order accurate direct simulations have been used to investigate how the helicity density fluctuations change when a turbulent pipe rotates about its axis. In this case the rotation axis is in the direction of the near wall vortical structures, which play a fundamental role on the wall friction and turbulence production. The helicity density is the trace of the tensor $\gamma'_{ij} = < v'_i \omega'_j >$ whose elements form the components of $\mathbf{v}' \times \boldsymbol{\omega}'$. When the momentum equations are written in rotational form, the turbulence energy production splits into two parts, one related to the convection of the large scales and the other related to the energy cascade to the small scales. From data of direct simulations the modifications of the turbulent energy production in different regions of the pipe have been analyzed by finding the *pdf* of the components of $\mathbf{v}' \times \boldsymbol{\omega}'$ and by their connection to the modifications of the vortical structures. The joint *pdf* of the dissipation with the helicity density has shown that the dissipation is highly correlated with regions of very low helicity density in the non-rotating pipe. When the pipe rotates the helicity density increases and the dissipation decreases, since in this case there is a drag reduction. It has been speculated that the alignment between velocity and vorticity could be a common feature in drag reducing flows.

The turbulent pipe rotating about its axis is important for many engineering applications such as rotating heat exchangers and cooling systems of rotors, but it is also interesting since it is a configuration where the external rotation is oriented in the same direction as the near wall vortical structures. Recently there is a wide consensus that the streamwise vortical structures are responsible for the wall friction and for the turbulence production. Therefore the control of wall turbulence by acting on these structures should be further pursued. A possible action could be the imposition of a background rotation. Bardina *et al.* (1985) observed that in isotropic turbulence the background rotation reduced the energy transfer to the small scales. In inhomogeneous flows the rotation was applied in the same direction as the main vorticity, e.g. Kim (1983) performed the direct simulation of a plain channel rotating about the streamwise direction and Metais *et al.* (1995) of a mixing layer with the rotation parallel to the vorticity of the rolls. In planar flows, with periodicity in the spanwise direction, it is difficult to imagine an experiment with the rotation axis parallel to the direction of the secondary vortical structures. On

the contrary, in a turbulent pipe or in a round jet the application of the background rotation with the same orientation as the secondary vortical structures is feasible in a numerical as well as in a real experiment. In the present paper we are thus studying a pipe rotating around its axis.

The most important outcome of the rotating pipe is a drag reduction that increases with the rotation rate, as it was experimentally observed by Nishibori *et al.* (1987) and Reich & Beer (1989) and numerically by Orlandi & Fatica (1995). In the numerical simulation it was shown that the drag reduction is caused by a change in the structure of the near wall vorticity. In the direct simulation, instead of a rotating wall, a reference frame moving with the wall has been used and a Coriolis body force appears. This choice allows us to see from the equation of motion how each component of the turbulent stress is affected by the rotation. In the present paper as well as in the previous one (Orlandi & Fatica 1995) the aim is to reach a clear comprehension of the causes of drag reduction in a rotating pipe that could be useful in finding the most effective way to achieve wall turbulence control. In previous simulations in a straight channel, for example, it was observed that spanwise pressure gradients (Sendstadt & Moin, 1993) produced drag reduction. The rotating pipe presents analogies with this configuration.

In the present paper we analyze the tensor $\gamma_{ij} = < v_i \omega_j >$ which appears in the vorticity as well as in the momentum equation. The averages $<>$ are performed in the two homogeneous directions over a large number of fields separated by three non-dimensional time units. Often it is objected that the γ_{ij} tensor of the instantaneous fields is not Galilean invariant. To overcome this criticism we considered only the tensor γ'_{ij} of the fluctuating quantities. The trace of the tensor is the helicity density, and the other elements give the three components of the $\mathbf{v}' \times \boldsymbol{\omega}'$ vector. Hussain (1986) as well as Rogers and Moin (1987) observed from the identity $|\mathbf{v}' \times \boldsymbol{\omega}'|^2 + |\mathbf{v}' \cdot \boldsymbol{\omega}'|^2 = |\mathbf{v}'|^2 |\boldsymbol{\omega}'|^2$ that since the term $|\mathbf{v}' \times \boldsymbol{\omega}'|^2$ indicates a high rate of energy cascade to smaller scales, it might be expected that regions of high helicity density are regions where the energy cascade is inhibited. Rogers & Moin (1987) focused their attention on isotropic, homogeneous turbulence as well as on the channel. For the channel they got different results from those of Pelz *et al.* (1985) and they affirmed that it is questionable whether helicity fluctuations play an important role in three-dimensional incompressible turbulence in complete disagreement with the Pelz *et al.* conclusions. Since a similar pseudospectral numerical method was used in the two studies but with different resolution, we have made a further study of the turbulent pipe to provide a further check on the importance of the helicity density in turbulent wall flows. The same calculations have been performed recently by Tsinober *et al.* (1995) through a data base generated by a numerical method with a resolution similar to the present one. As expected, the pipe results agree with those of Rogers & Moin (1987) for the channel. Tsinober *et al.* (1995) further focused the study on the alignment between vorticity and vortex stretching and the vorticity and the rate of strain tensor. However, they did not investigate the properties of $\mathbf{v}' \times \boldsymbol{\omega}'$, which have been analyzed here.

The comparative analysis performed in this study between the helicity fluctuations in the non-rotating and rotating pipe show that this quantity could have a relevance in the detection of conditions leading to drag reduction.

2. Accomplishments

Orlandi & Fatica (1995) have shown that the second and higher order statistics of the velocity field for the non-rotating pipe agreed with those obtained in other simulations (Eggels *et al.* (1994)) as well as in experiments at the same low Reynolds number. In the rotating case $N = V_{\theta 0}/U_b$ indicates the ratio between the bulk velocity U_b and the rotation velocity of the wall $V_{\theta 0}$. The dimensionless number N is the inverse of the Rossby number $Ro = U_P/2\Omega R$, usually used in geophysical flows, where Ω is the background rotation, U_P is the laminar pipe Poiseuille centerline velocity, and R is the radius of the pipe (R=1). The Reynolds number based on the radius R and U_P in the present simulation was set equal to 4900, which gives a Reynolds number based on the friction velocity, $Re_\tau = 172.4$ for $N = 0$ and $Re_\tau = 156.9$ for $N = 2$. In a previous paper of Orlandi & Fatica (1995), a comparison was made for $N = 0, 0.5, 1, 2$, with the mean velocity profiles of Reich & Beer (1989) since Nishibori *et al.* (1987) showed that the turbulence profiles largely depend on the inlet conditions. However, the grid independence for the *rms* velocity was checked by increasing the number of points in the radial and axial directions. Since here the interest is directed to investigate quantities related to the vorticity field, the present *rms* vorticity has been compared with that by Kim *et al.* (1987) in the channel. Fig. 1a shows that the present numerical method predicts profiles very similar to those in the channel. By grid refinement it has been checked that the differences in Fig. 1a are not related to insufficient grid resolution. From Fig. 1a we see the numerical method is accurate, in agreement with Choi *et al.* (1991), who claim that the vorticity *rms* is a good indicator of the accuracy of a numerical scheme. In the pseudospectral simulations the velocity and the vorticity are evaluated at the same physical positions. On the contrary in the present scheme, velocity and vorticity components are evaluated at different points of the cell, leading to further truncation errors in the evaluation of the statistics at the cell center.

At the rotation rate $N = 2$ Fig. 1b shows that in the wall region there are substantial modifications of the *rms* vorticity profiles. Orlandi & Fatica (1995) through numerical flow visualizations have shown that the substantial reduction of ω'_r is responsible for the reduction in intensity of the low and high speed streaks. Contour plots emphasized that in the non-rotating case contour levels of ω'_r are directed in the streamwise direction, whereas in the rotating pipe these are inclined and their magnitude is reduced. A similar effect was observed by Sendstadt & Moin (1992) in the simulation of a three-dimensional boundary layer.

In the non-rotating case the mean profiles of the fluctuating helicity components $< h_\theta >, < h_r >, < h_x >$ defined as $< v_\theta \omega'_\theta >, < v'_r \omega'_r >, < v'_x \omega'_x >$ have very small amplitudes (Fig. 2b), and this indicates that there is an equal probability of right- or left-handed helical motions within the turbulent field. When the mean rotation is
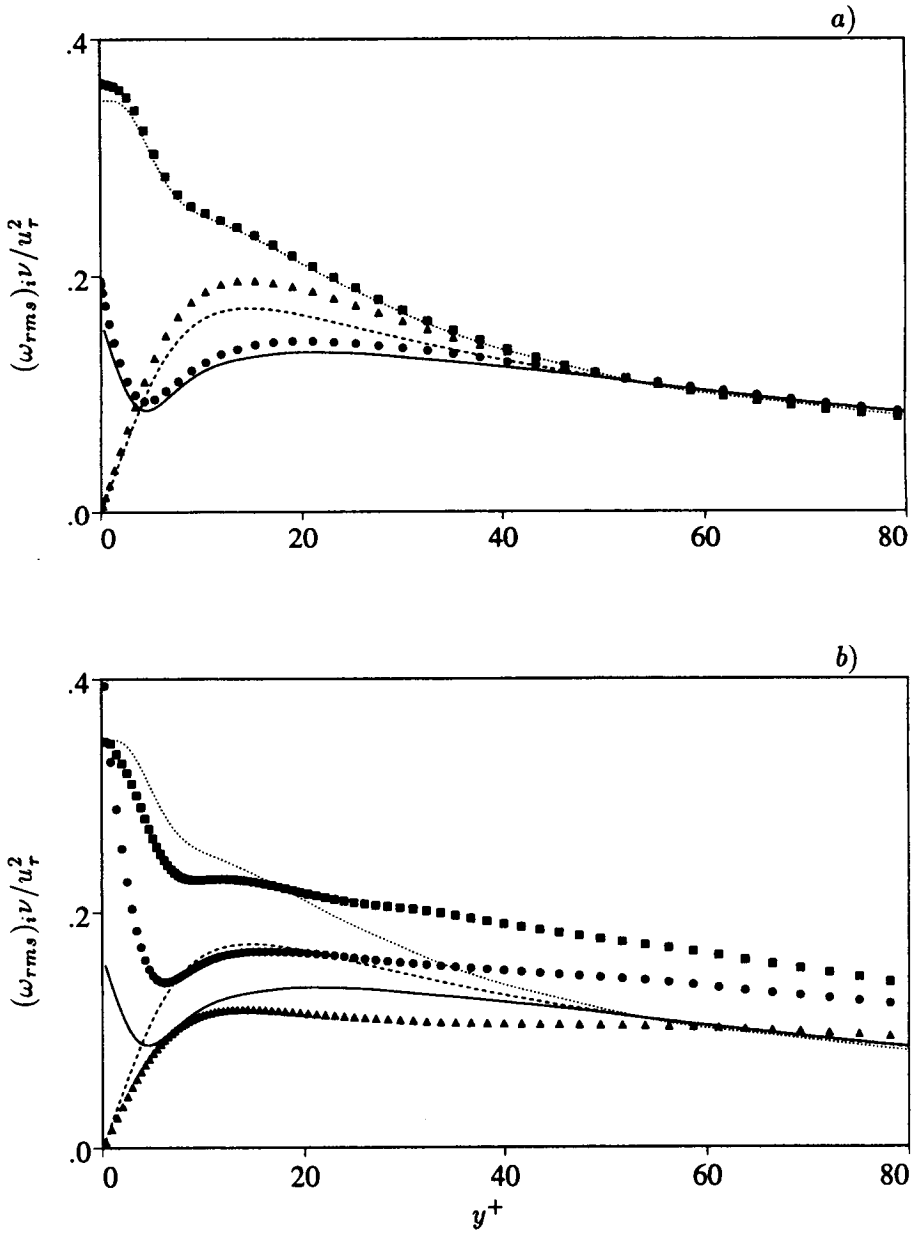
FIGURE 1. Profiles of *rms* vorticity fluctuations, a) lines, pipe. Symbols, channel by Kim *et al.*, b) lines $N = 0$, symbols $N = 2$; (———— and ● ω'_x), (- - - - and △ ω'_r), (········· and ■ ω'_θ).
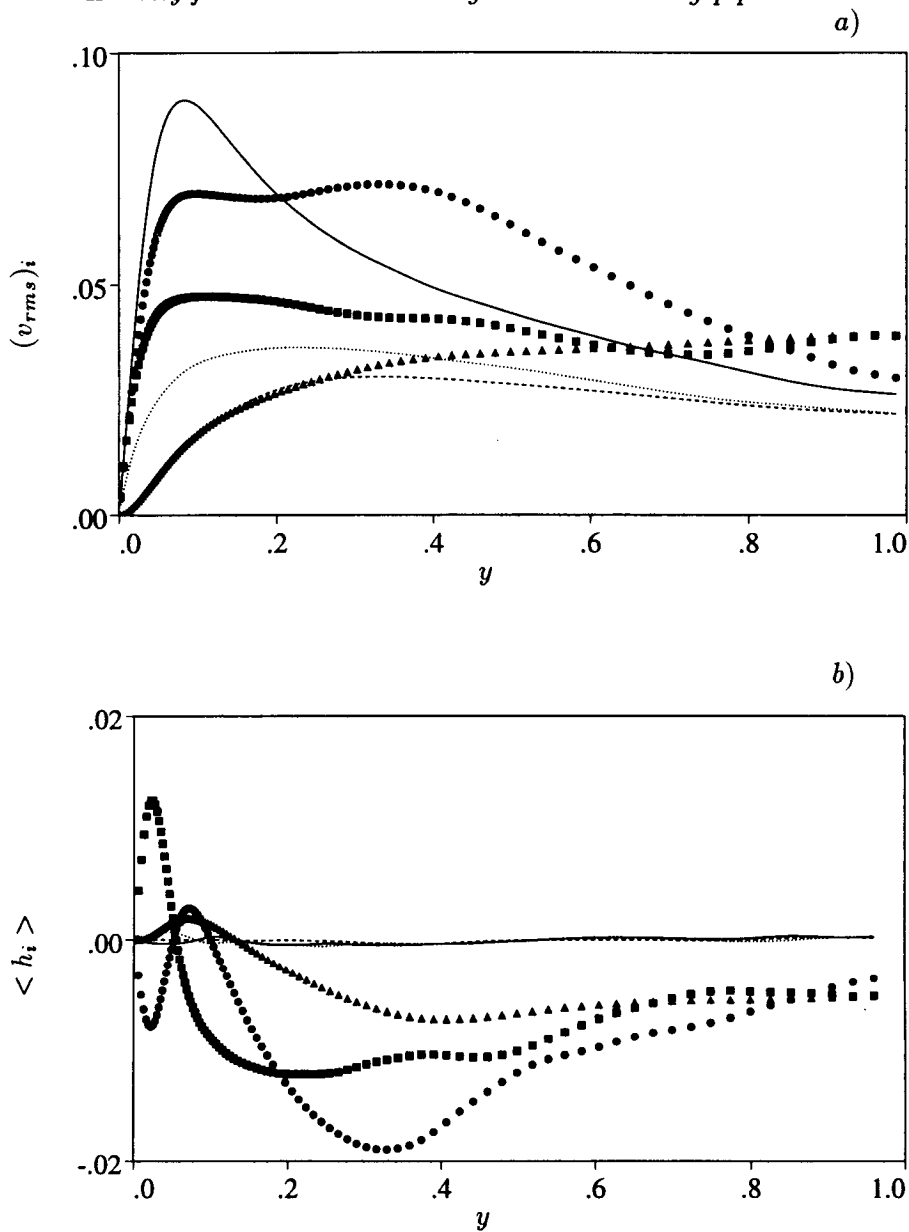
FIGURE 2. Profiles of a) rms velocity fluctuations, (——— and $\bullet$ v_x'), (- - - - and $\triangle$ v_r'), ($\cdots\cdots$ and $\blacksquare$ v_θ'), b) helicity density, (——— and $\bullet$ $\omega_x' v_x'$), (- - - - and $\triangle$ $\omega_r' v_r'$), ($\cdots\cdots$ and $\blacksquare$ $\omega_\theta' v_\theta'$); lines $N = 0$, symbols $N = 2$.
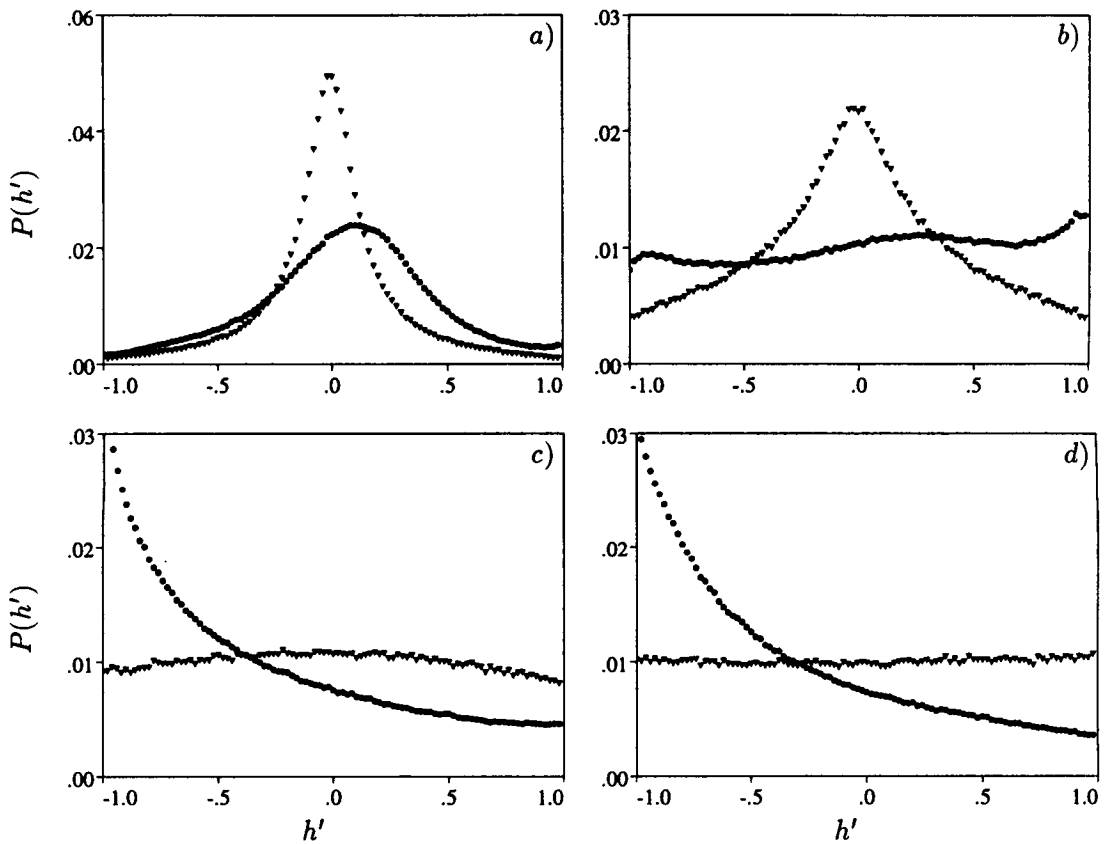
FIGURE 3.   Probability density function of the helicity density, a) $y^+ = 4$, b) $y^+ = 10$, c) $y^+ = 50$, d) $y^+ = 120$; $\triangle$ $N = 0$, $\bullet$ $N = 2$.

applied, the profiles changes everywhere in the pipe. Since the rotation is breaking the symmetry between right- and left-handed helical structures, the *pdf* of the angle between the velocity and vorticity fluctuations ($h' = \mathbf{v}' \cdot \boldsymbol{\omega}'/\sqrt{|\mathbf{v}|^2|\omega|^2}$) is a useful tool to understand the changes in Fig. 2b.

Fig. 3b shows, as found by Rogers & Moin (1987) in the channel, that at $y^+ = 10$, the position of maximum energy production, the vorticity and the velocity fluctuations are not aligned. This poor alignment is due to the fact that in the wall region, as shown in Fig. 1a, ω'_θ is the greatest component and from Fig. 2a that v'_x is greater than the other two components. The nonalignment increases as the wall is approached, see Fig. 3a, and in the log region the *pdf* is relatively flat as in isotropic turbulence (see Figs. 3c-d). When the rotation is imposed the nonalignment persists in the viscous region (Fig. 3a), but the loss of symmetry causes the large variations of the helicity density shown in Fig. 2b. From the *pdf* of each component, not shown here, we find that the rotation produces a positive angle between the azimuthal components. In the streamwise direction, on the contrary, there is a large probability that the low speed streaks ($v'_x < 0$) are correlated
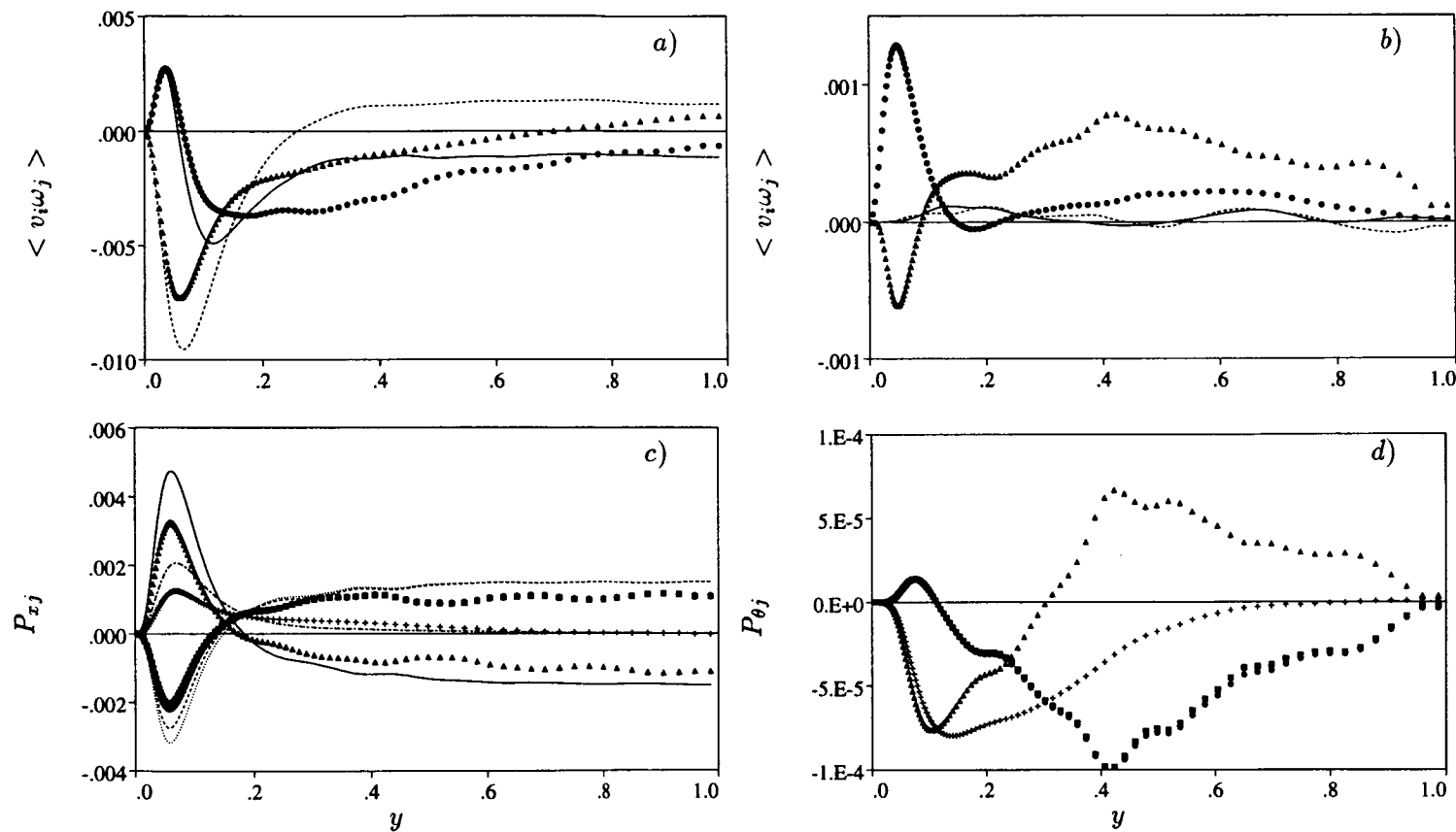
FIGURE 4. Profiles of a) (——— and $\bullet$ $< \omega'_\theta v'_r >$), (- - - - and $\vartriangle$ $< \omega'_r v'_\theta >$); b) (——— and $\bullet$ $< \omega'_r v'_x >$), (- - - - and $\vartriangle$ $< \omega'_x v'_r >$); c) (——— and $\vartriangle$ P_{xC}), (- - - - and $\bullet$ P_{xR}), ($\cdots\cdots$ and $\blacksquare$ P_{xI}), (—$\cdot$—$\cdot$ $+$ $P_{xR} - P_{xC}$);d) (——— and $\vartriangle$ $P_{\theta C}$), (- - - - and $\bullet$ $P_{\theta R}$), ($\cdots\cdots$ and $\blacksquare$ $P_{\theta I}$), (—$\cdot$—$\cdot$ $+$ $P_{\theta R} - P_{\theta C}$); lines $N = 0$, symbols $N = 2$.

Helicity fluctuations in rotating and non-rotating pipes

with positive ω_x' and vice-versa. Fig. 3b shows that in the region of maximum turbulent energy production, the rotation produces a strong alignment between the fluctuating velocity and vorticity. This increase of the alignment with rotation is due to the increase of ω_x' and of v_θ'. However the almost equal probability of alignment and counteralignment explains why in Fig. 2b at $y \approx 0.5$ two helicity components intersect the axis. For $y < 0.5$ there is an alignment, and it produces positive values of the helicity density in Fig. 2b; on the other hand in the central region of the pipe, the counteralignment explains the negative values in Fig. 2b. This alignment between velocity and vorticity fluctuations in the near wall region can then be considered as an indication of the drag reduction. In the central region the non zero helicity density is an indication of the energy transfer reduction leading to the increase of the turbulent energy as shown in Fig. 2a. From the *pdf* of each of the helicity components, not reported here, it is shown that the alignment and the counteralignment at $y^+ = 10$ (Fig. 3b) are due to the θ and x components with the θ contribution being the more important. This condition is caused by the increase of the *rms* values of v_θ' and decrease of v_x'. The total kinetic energy in the rotating case decreases near the wall and increases in the central region. It is therefore interesting to investigate the reasons for the changes in the turbulent energy production and dissipation.

Since the production of turbulent energy can be linked to $\mathbf{v}' \times \boldsymbol{\omega}'$, it is interesting to look at the distribution of each term across the pipe. When the convective terms of the Navier-Stokes equations are written in the rotational form, the production terms of turbulent kinetic energy are

$$
\begin{aligned}
&-U_x[< v_\theta' \omega_r' > - < \omega_\theta' v_r' >] + \frac{1}{r}\frac{\partial r U_x < v_x' v_r' >}{\partial r} + \\
&-U_\theta[< v_r' \omega_x' > - < \omega_r' v_x' >] + \frac{1}{r}\frac{\partial r U_\theta < v_\theta' v_r' >}{\partial r} + \\
&-U_r[< v_x' \omega_\theta' > - < \omega_x' v_\theta' >] + \frac{1}{r}\frac{\partial r U_r < v_r' v_r' >}{\partial r}.
\end{aligned}
\tag{1}
$$

These six terms for brevity can be indicated respectively by P_{xR}, P_{xC}, $P_{\theta R}$, $P_{\theta C}$, P_{rR}, P_{rC}; the terms P_{rR} and P_{rC} have been left in Eq. (1) although both in the rotating and in the non-rotating case $U_r = 0$. The other observation is that in the rotating case, at least at this intermediate rotation rate ($N = 2$), U_θ is much smaller than U_x. To understand the effect of the external rotation in the wall region, the plots of the radial profiles of axial and azimuthal components of $< \mathbf{v}' \times \boldsymbol{\omega}' >$ are shown in Figs. 4a-b. Since the following identities hold:

$$
\begin{aligned}
U_x[< v_\theta' \omega_r' > - < \omega_\theta' v_r' >] &= \frac{U_x}{r}\frac{\partial r < v_x' v_r' >}{\partial r} = P_{xI}, \\
U_\theta[< v_r' \omega_x' > - < \omega_r' v_x' >] &= \frac{U_\theta}{r^2}\frac{\partial r^2 < v_\theta' v_r' >}{\partial r} = P_{\theta I}.
\end{aligned}
\tag{2}
$$

the right-hand sides have been also plotted in Fig. 4c, where, as found by Tsinober *et al.* (1995), in the simulation the identities do not hold. The reason for the unbalance

is related to the interpolations needed to evaluate each term of $< \mathbf{v}' \times \boldsymbol{\omega}' >$. In our scheme we were not able to find a discretization scheme preserving exactly the identity. In the rotating case the unbalance is reduced, and this circumstance confirms that the distributions of fluctuating velocity and vorticity components are smoother and that interpolation errors are reduced.

Before describing the effects of the external rotation on the $\mathbf{v}' \times \boldsymbol{\omega}'$ terms, and the *pdf* of the components of the vector $\mathbf{p}' = \mathbf{v}' \times \boldsymbol{\omega}'/\sqrt{|\mathbf{v}'|^2 |\boldsymbol{\omega}'|^2})$, it is interesting to analyze the meaning of the terms in Eq. (1). For $N = 0$ the turbulent energy production is given only by the first two terms in Eq. (1). The first term is related, as asserted by Rogers & Moin (1987), to the cascade of energy from large to small scales, showing energy is lost or gained depending on the radial position. Near the wall energy is lost; in contrast, in the central region energy is gained. The difference between the first and the second term in Eq. (1) gives the turbulent energy production, which is positive everywhere. Both in the rotating and in the non-rotating case the first two terms give the major contribution to the turbulence energy production as shown in Fig. 4c-d. The radial component of $\mathbf{v}' \times \boldsymbol{\omega}'$ (not shown here) is the greatest, but since it is multiplied by U_r in both cases, it gives a null contribution to the turbulence production. On the contrary, when the external rotation is applied, the θ component increases (Fig. 4b), and since it is multiplied by U_θ, it gives a contribution smaller (Fig. 4d) than that in the x direction, which is multiplied by U_x (Fig. 4c). In the rotating case, the axial component is reduced at $y^+ = 10$ (Fig. 4c) with $< v'_\theta \omega'_r >$ decreasing more than $< v'_r \omega'_\theta >$. Since v'_θ does not have a large variation, the reduction is mainly due to the *rms* value of ω'_r. This reduction, as before mentioned, is due to the changes of orientation, spacing, and size of the vortical structures near the wall.

Figs. 5a-d show the *pdf* of the three components of $\mathbf{v}' \times \boldsymbol{\omega}'$ at the same positions where the *pdf* of the helicity density were given in Fig. 3. The first consideration is that near the wall the vector $\mathbf{v}' \times \boldsymbol{\omega}'$ is counteraligned with the r direction; that is, it is pointing out from the wall. This orientation is maintained also when the pipe rotates. Near the wall, Fig. 4a shows that $| < v'_r \omega'_\theta > | > | < v'_\theta \omega'_r > |$, and from Figs. 5a-b the positive contribution of $< v'_r \omega'_\theta > - < v'_\theta \omega'_r >$ is due to the ejection and sweep events producing the higher correlations of v'_θ and ω'_r of same sign. Figs. 5a-b, moreover, confirm that near the wall the radial component of $\mathbf{v}' \times \boldsymbol{\omega}'$ is the greatest and that it is weakly influenced by the rotation. However, even if the vortex dynamics could change the radial distribution of $< v'_x \omega'_\theta > - < v'_\theta \omega'_x >$, its contribution to the energy production is null. Near the wall the rotation breaks the symmetry of the $< v'_x \omega'_r > - < v'_r \omega'_x >$, and this term becomes negative as shown in Figs. 5a-b where the contribution to the θ component is due to the correlation of opposite sign between v'_r and ω'_x. In the inner part of the pipe there is no preferred orientation between fluctuating velocity and vorticity, which is the condition characteristic of weak turbulence production. In this region Fig. 4c shows in the non-rotating case that the amount of turbulent energy production due to $\mathbf{v}' \times \boldsymbol{\omega}'$ is positive and it is balanced by the energy convected from the large scales. Fig. 5c shows that this positive contribution is due to the greater probability of
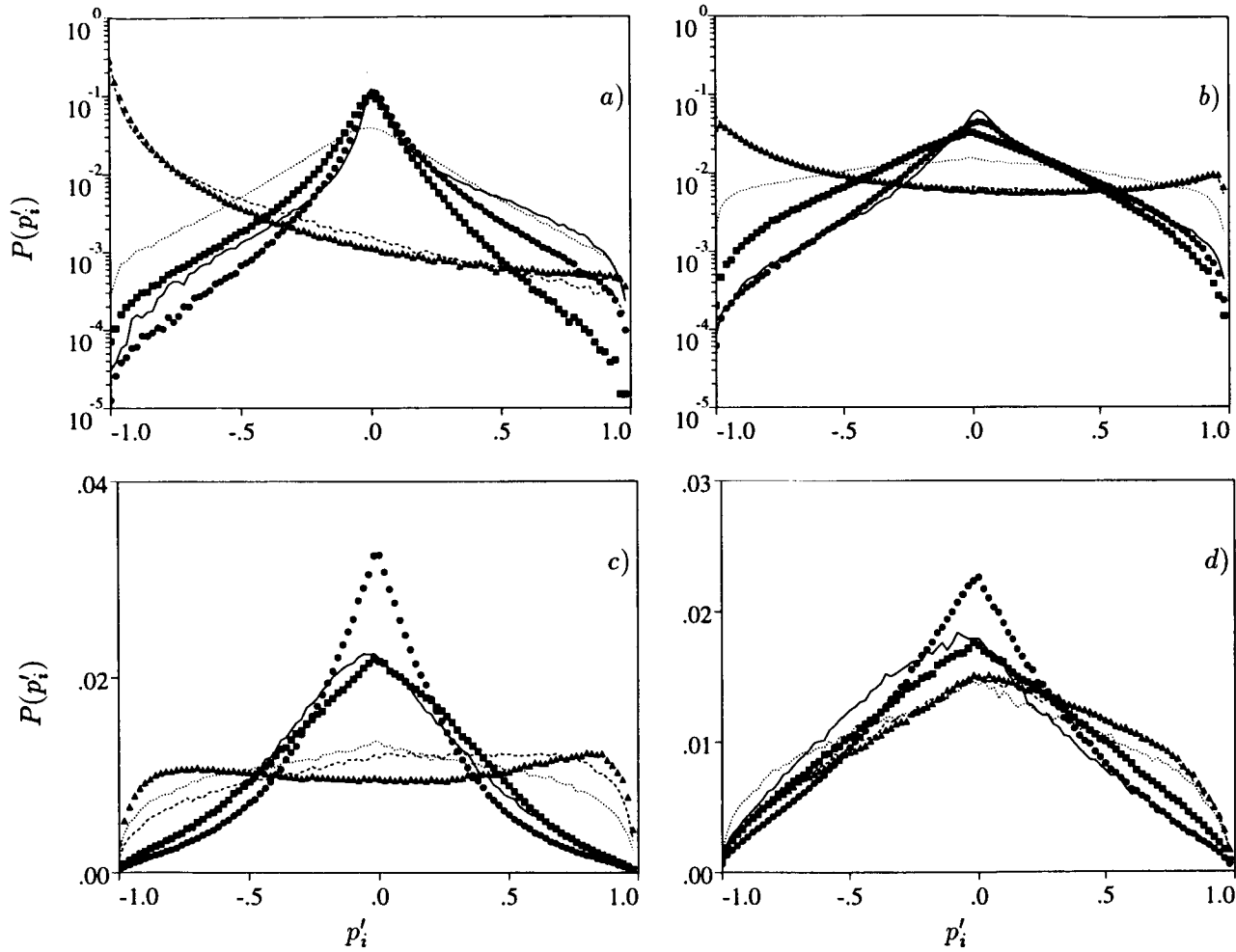
FIGURE 5. Probability density function of (——— and $\bullet$ p'_x), (- - - - and $\blacktriangle$ p'_r) (········ and $\blacksquare$ p'_θ) at a) $y^+ = 4$, b) $y^+ = 10$, c) $y^+ = 50$, d) $y^+ = 120$; lines $N = 0$, symbols $N = 2$.
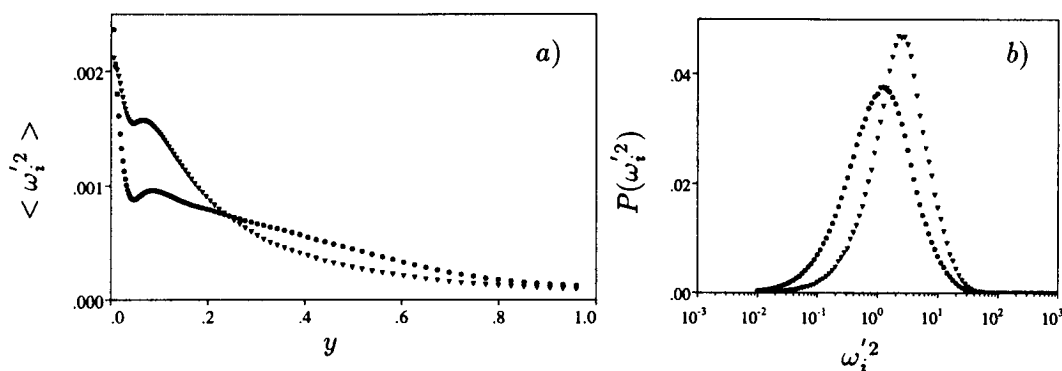
FIGURE 6.   a) Dissipation radial profile, b) Probability density function of the local dissipation at $y^+ = 10$; $\triangle\ N = 0$, $\bullet\ N = 2$.

having positive rather than negative values of p'_i. This occurrence is related to the high correlation of negative azimuthal gradients of axial velocity (negative tilting rotation) with positive v'_r and the high correlation of events with same sign of v'_r and ω'_θ. Fig. 5c also shows that in the non-rotating case positive and negative correlations for the azimuthal components of $\mathbf{v}' \times \boldsymbol{\omega}'$ are equally distributed. When the rotation is imposed the tendency towards the symmetry for the axial component occurs, in agreement with the decrease of difference between the two terms in Fig. 4a. The rotation produces bigger changes in the θ component that goes from theoretical zero values to positive value as shown in Fig. 4b. Fig. 5c emphasizes that the positive values are given by the major number of points where v'_r and ω'_x have equal sign. Ejections of fluid from the wall ($v'_r < 0$ in this case) are thus correlated with clockwise axial fluctuating vorticity. As mentioned above $< v'_x\omega'_r > - < v'_r\omega'_x >$, although it is of the same order as the axial component when $N = 2$, it gives a much smaller contribution to the energy production because it is multiplied by U_θ.

The local energy dissipation can be related to the helicity density in the sense that where there is an elevated helicity density the dissipation is reduced; thus we expect that since in the rotating pipe the helicity density increases the dissipation diminishes. In fact, Fig. 6a shows that in the wall region, mainly around $y^+ = 10$, there is a large reduction when the rotation is imposed. At $y^+ = 10$ the *pdf* of the dissipation $\epsilon' \approx \omega_l'^2$ in Fig. 6b shows that for $N = 0$ the maximum is shifted towards higher values and that the distribution is more peaked than for $N = 2$. The joint probability density distribution between local dissipation and helicity density was calculated and, as shown in Fig. 7a in the non-rotating case, the high levels of dissipation are correlated to low levels of h'. On the contrary, when the pipe rotates, Fig. 7b shows that the dissipation is reduced, increasing the probability of low dissipation and positive helicity density.

3. Conclusions

In this paper, the direct simulation of a turbulent pipe has been used to investigate how the turbulence production and dissipation change when a solid body rotation

P. Orlandi

$a)$ $\qquad\qquad\qquad\qquad\qquad\qquad$ $b)$
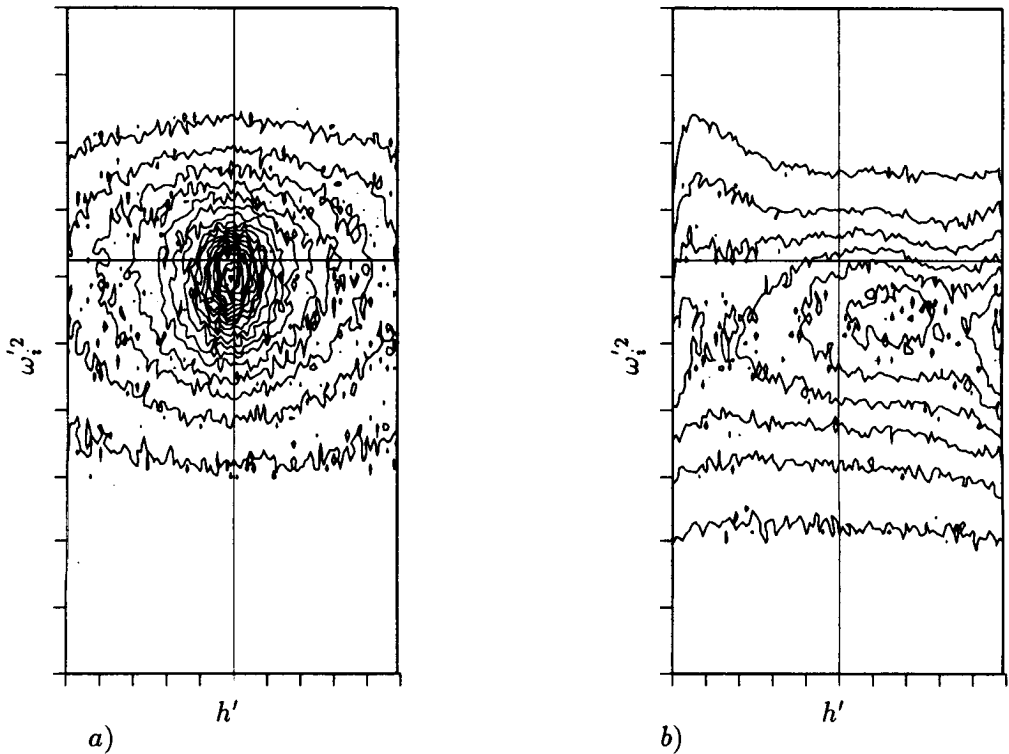
FIGURE 7.   The joint *pdf* $P(\omega_i'^2, h')$ at $y^+ = 10$ for a) $N = 0$, b) $N = 2$. The horizontal scale goes from -1 to 1. The vertical scales goes from 10^{-2} to 10^{+2}. Two marks are separated by $10^{0.4}$.

is applied. The effect of background rotation on turbulent flows has a wide range of applications related e.g. to sound level reduction or combustion control and deserves further study. The pipe rotating about its axis is a very interesting case since the background rotation is parallel to the direction of the secondary vortical structures that play a fundamental role on wall friction and turbulence production. The global results of the imposed rotation on the turbulent pipe is drag reduction and a reduction of the turbulent kinetic energy near the wall. In the past, several studies were devoted to understanding whether the helicity density could be an indicator of dissipation levels. In the previous studies flows with zero mean helicity were considered, whereas in the rotating pipe the symmetry is disrupted by the rotation and a mean helicity is present. This study has shown that when the helicity increases, the dissipation is reduced. As a conclusion, which could be useful to achieve drag reduction, it can be asserted that to have a drag reduction the external action should be such as to disrupt the symmetry of right- and left-handed helical structures. It would then be interesting to use the direct simulation of three-dimensional boundary layers (Sendstadt & Moin 1991) to investigate whether this condition is verified. Of more practical interest will be to verify this occurrence in turbulent flows over riblets or dilute polymers solutions where a higher drag

reduction is achieved.

In this study the Navier Stokes equations in rotational form permit the turbulent energy production to be split into a part related to the energy cascade from large to small scales and into a part related to the convection by large scales. The full simulation data have shown the latter is greater than the former in the wall region and that, on the contrary, these two terms balance each other in the central region. From the *pdf* of the former, it has been shown how the vortical structures are changed in the wall region by the background rotation and how they are related to the changes in the energy production.

4. Future plans

The current study is limited to intermediate rotation rates $N \leq 2$. Of greater interest will be the increase in the rotation rate to reach the condition of complete laminarization. In this case, according to the Taylor-Proudman theorem, it is necessary to perform the simulations on a very long pipe, which would require a large number of grid points in the axial direction. This study is affordable and it will be done in the near future, using a parallel version of the code developed by our group in Rome that can run efficiently on parallel computers.

Acknowledgments

REFERENCES

BARDINA, J., FERZIGER, J. H. & ROGALLO, R. S. 1985 Effect of rotation on isotropic turbulence, Computation and modelling. *J. Fluid Mech.* **154.**

CHOI, H. & MOIN, P. 1994 Effects of the computational time step on numerical solutions of turbulent flow. *J. of Comp. Phys.* **113,** 1-4.

EGGELS, J. G. M., UNGER, F., WEISS, M. H., WESTERWEEL, J., ADRIAN, R. J., FRIEDRICH, R. & NIEUWSTADT, F. T. M. 1994 Fully developed turbulent pipe flow: a comparison between direct numerical simulation and experiment. *J.Fluid Mech.* **268,** 175-209.

HUSSAIN, A. K. M. F. 1986 Coherent structures and turbulence. *J. Fluid Mech.* **173,** 303-356.

KIM, J. 1939 The effect of rotation on turbulence structure. *Proc. 4th Intl. Symp. on Turb. Flows, U. Karlsruhe.* (6.1-6.4.)

KIM, J., MOIN, P. & MOSER, R. 1987 Turbulence statistics in fully developed channel flow at low Reynolds number. *J. Fluid Mech.* **177,** 133-166.

METAIS, O., FLORES, C., YANASE, S., RILEY, J. J., & LESIEUR, M. 1995 Rotating free-shear flows. Part.2 Numerical simulations. *J. Fluid Mech.* **293**, 47-80.

NISHIBORI, K., KIKUYAMA, K., & MURAKAMI, M. 1987 Laminarization of turbulent flow in the inlet region of an axially rotating pipe. *JSME International Journal.* **30**, 255-262.

ORLANDI, P. & FATICA, M. 1995 Direct simulations of a turbulent pipe rotating along the axis. *Submitted to J. Fluid Mech.*

PELTZ, R. B., YAKHOT, V., ORSZAG, S. A., SHTILMAN, L. & LEVICH, E. 1985 Velocity-vorticity patterns in turbulent flows. *Phy. Rev. Lett.*. **54**, 2505-2508.

REICH, G. & BEER, H. 1989 Fluid flow and heat transfer in axially rotating pipe 1. Effect of rotation on turbulent pipe flow. *Int. J. Heat Mass Transfer.* **32**, 551-561.

ROGERS, M. M., & MOIN, P. 1987 Helicity fluctuation in incompressible turbulent flows. *Phys. Fluids.* **30**, 2662-2671.

SENDSTAD, O. & MOIN P. 1991 On the mechanism of 3-D turbulent boundary layers. *8th Symposium on turbulent shear flows, Munich 20-3.*

TSINOBER, A., EGGELS, J. G. M., & NIEUWSTADT, F. T. M. 1995 On alignments and small scale structures in turbulent pipe flow. *Fluid Dynamics Research.* **16**, 297-310.

Analysis of the two-point velocity correlations in turbulent boundary layer flows

By M. Oberlack

1. Motivation and objectives

Two-point *Rapid Distortion Theory* (RDT) has become an important tool in the theory of homogeneous turbulence. Modelers try to implement appropriate results from RDT in their statistical turbulence models, for example in the structure based model developed by Kassinos and Reynolds (1994).

On the other hand, in non-homogeneous equilibrium flows the logarithmic law is one of the cornerstones in statistical turbulence theory. Experimentalists have found the log-law in a broad variety of different turbulent wall shear flows, and statistical models have been made to be consistent with the log-law.

The logarithmic law was first derived by von Kármán (1930a, 1930b) using dimensional arguments. Later Millikan (1939) derived the law-of-the-wall more formally using the so called "velocity defect law", also first introduced by von Kármán (1930b). Even though the derivation was much more comprehensive from a physical point of view, the velocity defect law is essentially an empirical observation. A first derivation of the law-of-the-wall using asymptotic methods in the Navier-Stokes equations was given by Mellor (1972). Mellor needed the viscous sub-layer to obtain the log-region, and his scaling of the inertial range in the log-region is in error because it does not give the one-point limit of production equals dissipation.

The general objective of the present work is to explore the use of RDT in analysis of the two-point statistics of the log-layer. RDT is applicable only to unsteady flows where the non-linear turbulence-turbulence interaction can be neglected in comparison to linear turbulence-mean interactions. Here we propose to use RDT to examine the structure of the large energy-containing scales and their interaction with the mean flow in the log-region.

The contents of the work are twofold: First, two-point analysis methods will be used to derive the law-of-the-wall for the special case of zero mean pressure gradient. The basic assumptions needed are one-dimensionality in the mean flow and homogeneity of the fluctuations. It will be shown that a formal solution of the two-point correlation equation can be obtained as a power series in the von Kármán constant, known to be on the order of 0.4.

In the second part, a detailed analysis of the two-point correlation function in the log-layer will be given. The fundamental set of equations and a functional relation for the two-point correlation function will be derived. An asymptotic expansion procedure will be used in the log-layer to match Kolmogorov's universal range and the one-point correlations to the inviscid outer region valid for large correlation distances.

2. Governing equations of the two-point velocity correlation function

Using the standard Reynolds decomposition $U_i = \bar{u}_i + u_i$ and $P = \bar{p} + p$, the Reynolds averaged Navier Stokes (RANS) equations read

$$\frac{\partial \bar{u}_i}{\partial t} + \bar{u}_k \frac{\partial \bar{u}_i}{\partial x_k} = -\frac{1}{\rho}\frac{\partial \bar{p}}{\partial x_i} + \nu \frac{\partial^2 \bar{u}_i}{\partial x_k^2} - \frac{\partial \overline{u_i u_k}}{\partial x_k} \tag{1}$$

and the fluctuation equation, later on referred to as $\mathcal{N}$-equation, is

$$\mathcal{N}_i(\boldsymbol{x}) = \frac{\partial u_i}{\partial t} + \bar{u}_k \frac{\partial u_i}{\partial x_k} + u_k \frac{\partial \bar{u}_i}{\partial x_k} - \frac{\partial \overline{u_i u_k}}{\partial x_k} + \frac{\partial u_i u_k}{\partial x_k} + \frac{1}{\rho}\frac{\partial p}{\partial x_i} - \nu \frac{\partial^2 u_i}{\partial x_k^2} = 0 \ . \tag{2}$$

The corresponding continuity equations are

$$\frac{\partial \bar{u}_k}{\partial x_k} = 0 \quad \text{and} \quad \frac{\partial u_k}{\partial x_k} = 0 \ . \tag{3}$$

The five two-point correlation tensor functions that appear in the two-point correlation equation (5), further below, are defined as

$$\begin{aligned}
R_{ij}(\boldsymbol{x}, \boldsymbol{r}; t) &= \overline{u_i(\boldsymbol{x}, t)\, u_j(\boldsymbol{x}^{(1)}, t)} \ , \\
\overline{pu_j}(\boldsymbol{x}, \boldsymbol{r}; t) &= \overline{p(\boldsymbol{x}, t)\, u_j(\boldsymbol{x}^{(1)}, t)} \ , \\
\overline{u_j p}(\boldsymbol{x}, \boldsymbol{r}; t) &= \overline{u_j(\boldsymbol{x}, t)\, p(\boldsymbol{x}^{(1)}, t)} \ , \\
R_{(ik)j}(\boldsymbol{x}, \boldsymbol{r}; t) &= \overline{u_i(\boldsymbol{x}, t)\, u_k(\boldsymbol{x}, t)\, u_j(\boldsymbol{x}^{(1)}, t)} \ , \\
R_{i(jk)}(\boldsymbol{x}, \boldsymbol{r}; t) &= \overline{u_i(\boldsymbol{x}, t)\, u_j(\boldsymbol{x}^{(1)}, t)\, u_k(\boldsymbol{x}^{(1)}, t)} \ .
\end{aligned} \tag{4}$$

All tensors in (4) are functions of the physical and the correlation space coordinates $\boldsymbol{x}$ and $\boldsymbol{r} = \boldsymbol{x}^{(1)} - \boldsymbol{x}$ respectively. The double two-point correlation R_{ij}, later on simply referred to as two-point correlation, converges to the Reynolds stress tensor $\overline{u_i u_j}$ in the limit of zero separation $\boldsymbol{r}$.

The well known two-point correlation equation (Rotta (1972)) can be written as

$$\begin{aligned}
\frac{DR_{ij}}{Dt} &= -R_{kj}\frac{\partial \bar{u}_i(\boldsymbol{x}, t)}{\partial x_k} - R_{ik}\left.\frac{\partial \bar{u}_j(\boldsymbol{x}, t)}{\partial x_k}\right|_{\boldsymbol{x}+\boldsymbol{r}} - [\bar{u}_k(\boldsymbol{x}+\boldsymbol{r}, t) - \bar{u}_k(\boldsymbol{x}, t)]\frac{\partial R_{ij}}{\partial r_k} \\
&\quad - \frac{1}{\rho}\left[\frac{\partial \overline{pu_j}}{\partial x_i} - \frac{\partial \overline{pu_j}}{\partial r_i} + \frac{\partial \overline{u_i p}}{\partial r_j}\right] + \nu\left[\frac{\partial^2 R_{ij}}{\partial x_k \partial x_k} - 2\frac{\partial^2 R_{ij}}{\partial x_k \partial r_k} + 2\frac{\partial^2 R_{ij}}{\partial r_k \partial r_k}\right] \\
&\quad - \frac{\partial R_{(ik)j}}{\partial x_k} + \frac{\partial}{\partial r_k}\left[R_{(ik)j} - R_{i(jk)}\right]
\end{aligned} \tag{5}$$

For both two-point velocity-pressure correlations, $\overline{u_i p}$ and $\overline{pu_j}$ a Poisson equation can be derived. The divergence $\partial/\partial x_i - \partial/\partial r_i$ of equation (5) leads to a Poisson equation for $\overline{pu_j}$,
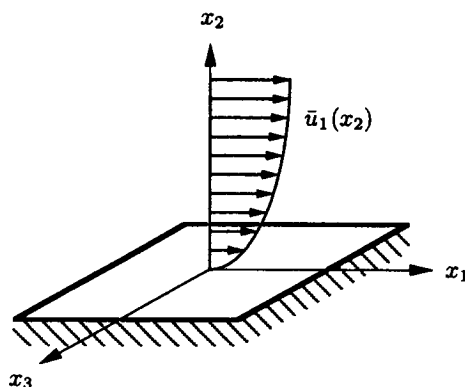
FIGURE 1. Sketch of the coordinate system and the mean velocity field

$$\frac{1}{\rho}\left[\frac{\partial^2 \overline{pu_j}}{\partial x_k \partial x_k} - 2\frac{\partial^2 \overline{pu_j}}{\partial r_k \partial x_k} + \frac{\partial^2 \overline{pu_j}}{\partial r_k \partial r_k}\right] = -2\frac{\partial \bar{u}_k(\boldsymbol{x},t)}{\partial x_l}\left[\frac{\partial R_{lj}}{\partial x_k} - \frac{\partial R_{lj}}{\partial r_k}\right]$$
$$- \left[\frac{\partial^2 R_{(kl)j}}{\partial x_k \partial x_l} - 2\frac{\partial^2 R_{(kl)j}}{\partial x_k \partial r_l} + \frac{\partial^2 R_{(kl)j}}{\partial r_k \partial r_l}\right] \tag{6}$$

and the divergence $\partial/\partial r_j$ leads to the corresponding Poisson equation for $\overline{u_i p}$,

$$\frac{1}{\rho}\frac{\partial^2 \overline{u_i p}}{\partial r_k \partial r_k} = -2\left.\frac{\partial \bar{u}_k(\boldsymbol{x},t)}{\partial x_l}\right|_{\boldsymbol{x}+\boldsymbol{r}}\frac{\partial R_{il}}{\partial r_k} - \frac{\partial^2 R_{i(kl)}}{\partial r_k \partial r_l} \tag{7}$$

where the vertical line means that the derivative is taken with respect to $\boldsymbol{x}$ but will be evaluated at $\boldsymbol{x} + \boldsymbol{r}$. All of the dependent variables in (5)–(7) have to satisfy the continuity conditions

$$\frac{\partial R_{ij}}{\partial x_i} - \frac{\partial R_{ij}}{\partial r_i} = 0 \ , \qquad \frac{\partial R_{ij}}{\partial r_j} = 0 \tag{8}$$

$$\frac{\partial \overline{pu_j}}{\partial r_j} = 0 \quad \text{and} \quad \frac{\partial \overline{u_i p}}{\partial x_i} - \frac{\partial \overline{u_i p}}{\partial r_i} = 0 \ . \tag{9}$$

For the analysis of the self-similar, two-point correlation equation further below, two identities are important. They can easily be derived from a geometrical consideration by interchanging the two points $\boldsymbol{x}$ and $\boldsymbol{x}^{(1)} = \boldsymbol{x} + \boldsymbol{r}$

$$R_{ij}(\boldsymbol{x},\boldsymbol{r}) = R_{ji}(\boldsymbol{x}+\boldsymbol{r},-\boldsymbol{r}) \ , \quad \overline{u_i p}(\boldsymbol{x},\boldsymbol{r}) = \overline{pu_i}(\boldsymbol{x}+\boldsymbol{r},-\boldsymbol{r}) \ . \tag{10}$$

The latter identities are the key elements for the derivation of some boundary conditions and for the deeper understanding of the self-similar two-point correlations. There exists a similar identity for the triple correlation which will not be used here.

3. The log-law – a self-similar form of the two-point correlation equation

A sketch of the coordinate system and the mean velocity field adopted in the proceeding paper is given in Fig. 1. Within this subsection it will be shown that the logarithmic part of the law-of-the-wall mean velocity profile can be derived from the two-point correlation equation and hence from the Navier-Stokes equation if there exists a regime where the following assumptions hold:

- the mean velocity is parallel to the wall;
- the statistics in that domain are independent of viscosity and time;
- the Reynolds number is high;
- no mean pressure acts on the flow field.

The last assumption can be eliminated, but in this approach it will be focused on the zero pressure gradient case. Beside the above assumptions no other conditions are needed in order to determine the log-law mean velocity profile and the self-similarity of the correlation functions.

Inferring the above assumption in the Reynolds averaged Navier-Stokes equations (1), it is easy to confirm that the gradient of the Reynolds stress tensor on the right hand side is the only remaining term. Integrated one time we obtain that $\overline{u_i u_j}$ is independent of x. However, this is not necessarily true for the two-point correlation tensor R_{ij}. It could depend on x if the dependence vanishes in the zero separation limit. This can only be achieved by having the following dependence on a new variable

$$\tilde{r} = r g(x) \tag{11}$$

where $g(x)$ has to be determined later and no other hidden dependence on x can be in the correlation functions. Of course, the latter definition of $\tilde{r}$ can be generalized to different unknown scaling functions for every component of r, but from equation (5) it can be verified that only a single scaling function exists. With the above given assumptions, defining $x = \tilde{x}$ and using the transformation rules

$$\frac{\partial}{\partial x_i} = \frac{\partial}{\partial \tilde{x}_i} + \frac{1}{g} \frac{\partial g}{\partial \tilde{x}_i} \tilde{r}_k \frac{\partial}{\partial \tilde{r}_k} \ , \qquad \frac{\partial}{\partial r_k} = g \frac{\partial}{\partial \tilde{r}_k} \tag{12}$$

the R_{ij}-equation (5) reduces to

$$
\begin{aligned}
0 = {}& -R_{2j}\,\delta_{i1}\,\frac{d\bar{u}_1(x_2)}{dx_2} - R_{i2}\,\delta_{j1}\,\frac{d\bar{u}_1(x_2)}{dx_2}\bigg|_{x_2+r_2} \\
& - \left[\bar{u}_1\left(x_2 + r_2\right) - \bar{u}_1\left(x_2\right)\right] g\,\frac{\partial R_{ij}}{\partial \tilde{r}_1} \\
& - \frac{1}{\rho}\left[\frac{1}{g}\frac{\partial g}{\partial \tilde{x}_i}\,\tilde{r}_k\,\frac{\partial \overline{pu_j}}{\partial \tilde{r}_k} - g\,\frac{\partial \overline{pu_j}}{\partial \tilde{r}_i} + g\,\frac{\partial \overline{u_i p}}{\partial \tilde{r}_j}\right] \\
& - \frac{1}{g}\frac{\partial g}{\partial \tilde{x}_k}\,\tilde{r}_l\,\frac{\partial R_{(ik)j}}{\partial \tilde{r}_l} + g\,\frac{\partial}{\partial \tilde{r}_k}\left[R_{(ik)j} - R_{i(jk)}\right] \ .
\end{aligned}
\tag{13}
$$

As mentioned above, there is no hidden x dependence in the correlation function and therefore all $\tilde{x}$ derivatives coming from (12a) have been omitted. Obviously, equation (13) can only have a non-trivial solution, and thus be independent of x, if all the coefficients have the same functional dependence on x. Hence, the following set of differential equations determine the $\bar{u}_1$ and g dependence on x

$$\frac{1}{g}\frac{\partial g}{\partial x_i} \sim g \quad \text{for } i = 1,2,3 \ , \quad \frac{d\bar{u}_1(x_2)}{dx_2} \sim g \tag{14}$$

and

$$\frac{1}{g}\left.\frac{d\bar{u}_1(x_2)}{dx_2}\right|_{x+r} = f_1(\tilde{r}) \neq f_2(x) \ , \quad \bar{u}_1(x_2+r_2) - \bar{u}_1(x_2) = f_3(\tilde{r}) \neq f_4(x) \ . \tag{15}$$

are additional consistency conditions for $\bar{u}_1$ and g. The last equation in (14) determines g to depend only on x_2. Hence, the equations (14) have two independent sets of solutions given by

$$g(x_2) = \frac{1}{c_2^{(1)}(x_2 - c_1^{(1)})} \ , \quad \bar{u}_1(x_2) = \frac{c_3^{(1)}}{c_2^{(1)}}\ln(x_2 - c_1^{(1)}) + c_4^{(1)} \tag{16}$$

and

$$g(x_2) = c_1^{(2)} \ , \quad \bar{u}_1(x_2) = c_2^{(2)}c_1^{(2)}x_2 + c_3^{(2)} \tag{17}$$

where the $c_q^{(p)}$'s are integration constants or proportionality factors. Obviously, only the first set of equations correspond to a boundary layer flow because the solutions (17) define homogeneous shear turbulence which contradicts the assumption to be independent of time. Both equations (15) require $c_1^{(1)} = 0$ and $c_2^{(1)}$ can be absorbed in the correlation functions. In common notation we finally obtain

$$\bar{u}_i = u_\tau\, \delta_{i1}\left[\frac{1}{\kappa}\ln(x_2) + \mathcal{C}\right] \tag{18}$$

and

$$\tilde{r} = \frac{r}{x_2} \tag{19}$$

where u_τ is defined as

$$u_\tau = \sqrt{\frac{\nu}{\rho}\left.\frac{d\bar{u}}{dx_2}\right|_{x_2=0}} \ . \tag{20}$$

Inserting (18) and (19) into equation (13) and multiplying by the von Kármán constant κ the final form of the R_{ij}-equation results:

$$0 = -R_{2j}^* \, \delta_{i1} - R_{i2}^* \, \delta_{j1} \frac{1}{1+\tilde{r}_2} - \ln(1+\tilde{r}_2) \frac{\partial R_{ij}^*}{\partial \tilde{r}_1}$$

$$+ \frac{\kappa}{\rho} \left[\delta_{i2}\tilde{r}_k \frac{\partial \overline{pu_j}^*}{\partial \tilde{r}_k} + \frac{\partial \overline{pu_j}^*}{\partial \tilde{r}_i} - \frac{\partial \overline{u_i p}^*}{\partial \tilde{r}_j} \right]$$

$$+ \kappa \left[\tilde{r}_l \frac{\partial R_{(i2)j}^*}{\partial \tilde{r}_l} + \frac{\partial}{\partial \tilde{r}_k} \left(R_{(ik)j}^* - R_{i(jk)}^* \right) \right] \tag{21}$$

where

$$R_{ij}^* = \frac{R_{ij}}{u_\tau^2} \;\; , \;\; R_{(ik)j}^* = \frac{R_{(ik)j}}{u_\tau^3} \;\; , \;\; R_{i(jk)}^* = \frac{R_{i(jk)}}{u_\tau^3} \;\; , \;\; \overline{pu_j}^* = \frac{\overline{pu_j}}{u_\tau^3} \;\; \text{and} \;\; \overline{u_i p}^* = \frac{\overline{u_i p}}{u_\tau^3} \;\; . \tag{22}$$

The procedure described above can be extended to the three-point triple-correlation equation and any higher order correlation equation if an additional spatial point is introduced for each additional tensor order. As a result it is easy to verify that the whole set of equations define an *infinite* set of *linear* tensor equations but which are far too complex to be solved in general. Nevertheless, it is worthwhile to analyze some features of the solution.

In principle this infinite set of equations could be solved by the following procedure. Beginning with the two-point correlation equation, the triple correlation can be considered as an inhomogeneous part of the R_{ij} equation. Once the homogeneous solution is obtained, the inhomogeneous solution can be computed by standard methods. In the next step, the triple-correlation equation has to be tackled and its solution will be substituted in the solution for R_{ij}, and so forth for higher correlations. In each equation the von Kármán constant κ only appears as a factor of the highest order tensor and hence the final solution for R_{ij} is a power series in κ

$$R_{ij}^* = \sum_{m=0}^{\infty} a_{ij}^{(m)} \kappa^m \;\; . \tag{23}$$

$a_{ij}^{(0)}$ represents the solution of the two-point correlation equation after neglecting the triple-correlations and all higher order terms.

The structure of the formal solution in equation (23) admits the hope that a truncated series may provide some insight in the log-law statistics. Hence, in the following the triple-correlations will be neglected. Using the similarity variable in the poisson and the continuity equations, the $\overline{pu_j}$ equation (6) becomes

$$\tilde{r}_k\tilde{r}_l \frac{\partial^2 \overline{pu_j}^*}{\partial \tilde{r}_k\tilde{r}_l} + \frac{\partial^2 \overline{pu_j}^*}{\partial \tilde{r}_k\tilde{r}_k} + 2\tilde{r}_k \frac{\partial^2 \overline{pu_j}^*}{\partial \tilde{r}_k\tilde{r}_2} + 2\tilde{r}_k \frac{\partial \overline{pu_j}^*}{\partial \tilde{r}_k} + 2\frac{\partial \overline{pu_j}^*}{\partial \tilde{r}_2} = \frac{2\rho}{\kappa} \frac{\partial R_{2j}^*}{\partial \tilde{r}_1} \;\; , \tag{24}$$

the $\overline{u_i p}$ equation (7) becomes

$$\frac{\partial^2 \overline{u_i p}^*}{\partial \tilde{r}_k \tilde{r}_k} = -\frac{2\rho}{\kappa} \frac{1}{1 + \tilde{r}_2} \frac{\partial R_{i2}^*}{\partial \tilde{r}_1} \quad, \tag{25}$$

and the continuity equations (8) and (9) yield

$$\tilde{r}_k \frac{\partial R_{2j}^*}{\partial \tilde{r}_k} + \frac{\partial R_{ij}^*}{\partial \tilde{r}_i} = 0 \quad, \qquad \frac{\partial R_{ij}^*}{\partial \tilde{r}_j} = 0 \quad, \tag{26}$$

$$\frac{\partial \overline{pu_j}^*}{\partial \tilde{r}_j} = 0 \quad \text{and} \quad \tilde{r}_k \frac{\partial \overline{u_2 p}^*}{\partial \tilde{r}_k} + \frac{\partial \overline{u_i p}^*}{\partial \tilde{r}_i} = 0 \quad. \tag{27}$$

The identities (10) can also be transformed in a similar manner. Introducing the transformation (19) into the equation (10a), we obtain the relation $R_{ij}(x_2, x_2 \tilde{r}) = R_{ji}(x_2(1 + \tilde{r}_2), -x_2 \tilde{r})$. Because it was previously assumed that all two-point correlation functions are solely functions of $\tilde{r}$, only the ratio of the first and the second parameter can appear in R_{ij}. This argumentation can be extended to the pressure velocity correlation. Thus, we finally obtain

$$R_{ij}^*(\tilde{r}) = R_{ji}^* \left(\frac{-\tilde{r}}{1 + \tilde{r}_2} \right) \tag{28}$$

and

$$\overline{u_i p}^*(\tilde{r}) = \overline{pu_i}^* \left(\frac{-\tilde{r}}{1 + \tilde{r}_2} \right) \quad. \tag{29}$$

The latter identity also holds if $\overline{u_i p}^*$ and $\overline{pu_i}^*$ are interchanged.

These two relations give valuable insight into the structure of the solution. Relation (28) connects different $\tilde{r}$ domains to each other and provides boundary conditions in the $\tilde{r}_2$ direction.

One interesting feature of (28) is that it can be considered as a functional equation for each trace element. It is easy to verify that one solution, but probably not the most general solution to equation (28), is given by the following form

$$R_{[\gamma\gamma]}^*(\tilde{r}) = F_\gamma \left[\left(\ln(1 + \tilde{r}_2) \right)^2, \frac{\tilde{r}_1}{\tilde{r}_2}, \frac{\tilde{r}_3}{\tilde{r}_2} \right] \tag{30}$$

where $R_{[\gamma\gamma]}^*$ is one of the three trace elements of R_{ij}^*.

In addition if the solution for any off-diagonal R_{ij}^* element $(i \neq j)$ is known, (28) provides the solution for the R_{ji}^*. A similar feature for $\overline{u_i p}^*$ and $\overline{pu_i}$ is given by relation (29).

If boundary conditions have to be satisfied in infinity, all correlation functions decay to zero. Therefore, any solution of equations (21) and (24)–(27) have to obey the boundary conditions

$$R_{ij}^*(\tilde{r}_k \to \pm\infty) = \overline{pu_i}^*(\tilde{r}_k \to \pm\infty) = \overline{u_i p}^*(\tilde{r}_k \to \pm\infty) = 0 \quad \text{for} \quad k = 1, 3 \tag{31}$$
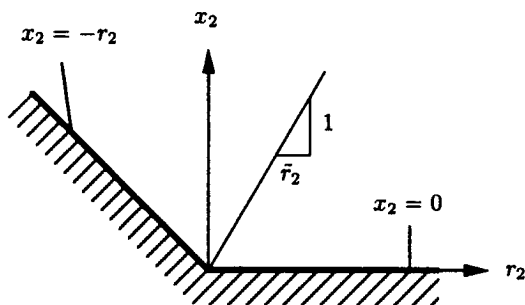
FIGURE 2.   Sketch of the boundary condition in the x_2-r_2 plane.

and

$$R_{ij}^*(\tilde{r}_2 \to \infty) = \overline{pu_i}^*(\tilde{r}_2 \to \infty) = \overline{u_i p}^*(\tilde{r}_2 \to \infty) = 0 \ . \tag{32}$$

To better understand the boundary conditions in the wall-normal direction, a sketch of the x_2-r_2 plane is given in Fig. 2. Picking any value for x_2, the negative part of r_2 can not be smaller than x_2 and hence one bound is on the line $x_2 = -r_2$. The bound for the physical coordinate is at $x_2 = 0$. Using the definition of the scaled non-dimensional coordinate (19), it is clear from Fig. 2 that $\tilde{r}_2$ represents the inverse of the slope given by any straight line through the origin ranging between the two latter bounds. Hence, the domain for $\tilde{r}_2$ is restricted to $-1 \le \tilde{r}_2 < \infty$. Using (28) and (29) together with (32) one obtains

$$R_{ij}^*(\tilde{r}_2 = -1) = 0 \tag{33}$$

and

$$\overline{pu_i}^*(\tilde{r}_2 = -1) = \overline{u_i p}^*(\tilde{r}_2 = -1) = 0 \ . \tag{34}$$

Obviously, the boundary conditions are all homogeneous and one may expect the solution to be zero. In section (5) it will be discussed why the equations might have a non-trivial solution, but a rigorous proof is still outstanding. In the next section an integral relation coming from the one-point equations will be derived, which closes the missing information regarding the scaling of the two-point correlations.

4. Kolmogorov's universal range and one-point correlations

The self-similarity of the correlation functions introduced in section 3 is only valid in the limit of large Reynolds number, based on the wall distance and the friction velocity

$$Re_\tau = \frac{u_\tau x_2}{\nu} \tag{35}$$

This is also the definition of y^+. From experiments it is known that the log region starts at about $y^+ = 40$ and extends to $y^+ = 0.2U\delta/\nu$.

The analysis in the previous chapters is inviscid, and hence is not a regular expansion in Re_τ. It is not applicable for small correlation distances, as will be explained in some detail now. An inner viscous layer in correlation space has to be introduced in order to meet the requirement that viscosity is important for the dissipation tensor ε_{ij} in the one-point limit.

Comparing the two-point correlation equation (5) in its most general form to the inviscid version in the log-layer (21), no viscous term has been retained. In contrast to that, the Reynolds stress transport equation in the log-layer

$$- \left[\overline{u_i u_2} \delta_{j1} + \overline{u_2 u_j} \delta_{i1} \right] \frac{u_\tau}{\kappa x_2} + \Phi_{ij} - \varepsilon_{ij} = 0 \tag{36}$$

contains the viscosity ν in the dissipation tensor, defined by

$$\varepsilon_{ij} = 2\nu \overline{\frac{\partial u_i}{\partial x_k} \frac{\partial u_j}{\partial x_k}} = 2\nu \lim_{r=0} \left[\frac{\partial^2 R_{ij}}{\partial x_k \partial r_k} - \frac{\partial^2 R_{ij}}{\partial r_k \partial r_k} \right] \tag{37}$$

and the pressure-strain tensor is defined by

$$\Phi_{ij} = \overline{\frac{p}{\rho} \left[\frac{\partial u_j}{\partial x_i} + \frac{\partial u_i}{\partial x_j} \right]} = \lim_{r=0} \left[\frac{\partial \overline{p u_j}}{\partial r_i} + \frac{\partial \overline{u_i p}}{\partial x_j} - \frac{\partial \overline{u_i p}}{\partial r_j} \right] \ . \tag{38}$$

The contraction of equation (36) together with $\overline{u_1 u_2} = -u_\tau^2$ determines the scalar dissipation

$$\varepsilon = \frac{\varepsilon_{kk}}{2} = \frac{u_\tau^3}{\kappa x_2} \ . \tag{39}$$

As mentioned above we find from equation (36) that the asymptotic arguments we have used so far are not valid for correlation distances on the order of the Kolmogorov length scale l_η. The Kolmogorov length and velocity scale are given by

$$l_\eta = \left(\frac{\nu^3}{\varepsilon} \right)^{\frac{1}{4}} = x_2 Re_\tau^{-\frac{3}{4}} \kappa^{\frac{1}{4}} \quad \text{and} \quad u_\eta = (\nu \varepsilon)^{\frac{1}{4}} = u_\tau Re_\tau^{-\frac{1}{4}} \kappa^{-\frac{1}{4}} \ . \tag{40}$$

The only scaling of the independent variables with which the correct balance can be achieved in the two-point correlation equation is given by

$$\boldsymbol{\xi} = \frac{\boldsymbol{r}}{l_\eta} = Re_\tau^{\frac{3}{4}} \kappa^{-\frac{1}{4}} \frac{\boldsymbol{r}}{x_2} \ . \tag{41}$$

In line of Kolmogorov's arguments, the scaling of the dependent variables must be

$$R_{ij} = u_\tau^2 \overline{u_i u_j}^* - u_\eta^2 \left[B_{ij}^{(0)}(\boldsymbol{\xi}) + O\left(Re_\tau^{-\frac{1}{4}} \right) \right] \ ,$$

$$R_{(ik)j} = u_\eta^3 \left[D_{(ik)j}^{(0)}(\boldsymbol{\xi}) + O\left(Re_\tau^{-\frac{1}{4}} \right) \right] \ ,$$

$$R_{i(jk)} = u_\eta^3 \left[D_{i(jk)}^{(0)}(\boldsymbol{\xi}) + O\left(Re_\tau^{-\frac{1}{4}} \right) \right] \quad ,$$

$$\overline{pu_j} = \rho u_\eta^3 \left[M_j^{(0)}(\boldsymbol{\xi}) + O\left(Re_\tau^{-\frac{1}{4}} \right) \right] \quad ,$$

$$\overline{u_j p} = \rho u_\eta^3 \left[N_i^{(0)}(\boldsymbol{\xi}) + O\left(Re_\tau^{-\frac{1}{4}} \right) \right] \quad . \tag{42}$$

Putting (41) and (42) into (5), (6) and (7) the leading order terms in each equation are given by

$$-\delta_{i1}\overline{u_2 u_j}^* - \delta_{j1}\overline{u_i u_2}^* + \frac{\partial M_j^{(0)}}{\partial \xi_i} - \frac{\partial N_i^{(0)}}{\partial \xi_j} - 2\frac{\partial^2 B_{ij}^{(0)}}{\partial \xi_k \partial \xi_k} + \frac{\partial D_{(ik)j}^{(0)}}{\partial \xi_k} - \frac{\partial D_{i(jk)}^{(0)}}{\partial \xi_k} \quad , \tag{43}$$

$$\frac{\partial^2 M_j^{(0)}}{\partial \xi_k \partial \xi_k} = -\frac{\partial^2 D_{(kl)j}^{(0)}}{\partial \xi_k \partial \xi_l} \tag{44}$$

and

$$\frac{\partial^2 N_i^{(0)}}{\partial \xi_k \partial \xi_k} = -\frac{\partial^2 D_{i(kl)}^{(0)}}{\partial \xi_k \partial \xi_l} \quad . \tag{45}$$

In order to obtain a uniform solution there must an overlapping region that matches the inner and the outer solution together. From (42a) we see that the limit $\boldsymbol{\xi} \to \infty$ in the inner layer of the two-point correlation converges to the Reynolds stress tensor and the same must be valid for a solution of the equations (21) and (24)–(29) in the outer layer for the limit $\tilde{r} \to 0$. Using the same limits for both regions in the triple- and the pressure-velocity correlations, they both drop to zero as they should do. As a result, the matching between the inertial subrange and obviously specifies the outer solution R_{ij}^* at $r = 0$ to be $\overline{u_i u_j}$, but the actual numerical value of Reynolds stress tensor is still unknown.

Note, that the equation corresponding to (43) in Mellor's paper (1972) (his equation (59)) has a serious error. It does not have the production terms which, of course, are responsible for the energy transfer rate.

As mentioned above the inner layer does not determine the absolute value of the Reynolds stress tensor because the triple correlations can not be neglected in (43)–(45). Thus an additional assumption is needed to determine the values of $\overline{u_i u_j}$.

In Kolmogorov's original hypotheses it was suggested that in the limit of large Reynolds number the dissipation will be isotropic. Saddoughi's (1994) very high Reynolds number experiment of a turbulent boundary layer in a wind tunnel supports this idea of isotropy. Hence, we take

$$\varepsilon_{ij} = \frac{2}{3}\delta_{ij}\varepsilon \quad . \tag{46}$$

Using this, the three trace elements of Φ_{ij} can be obtained from the Reynolds Stress tensor equation which in non-dimensional form can be written as

$$-[\overline{u_i u_2}^* \delta_{j1} + \overline{u_2 u_j}^* \delta_{i1}] + \Phi_{ij}^* - \frac{2}{3}\delta_{ij} = 0 \quad \text{with} \quad \Phi_{ij}^* = \Phi_{ij}\frac{\kappa x_2}{u_\tau^3} \qquad (47)$$

or in component notation

$$\Phi_{11}^* = -\frac{4}{3}, \quad \Phi_{22}^* = \frac{2}{3}, \quad \Phi_{33}^* = \frac{2}{3}. \qquad (48)$$

Note, that the latter result for the pressure-strain correlation holds no matter what is assumed for the triple-correlations. As a result, all high Reynolds number second-moment closure models should be consistent with this result. In most second moment models this could only be ensured by adding wall reflection terms to the pressure-strain model.

Because the system (21) and (24)–(29) has homogeneous boundary conditions on all boundaries, there is nothing that specifies the amplitude of R_{ij}^* or the value of $\overline{u_i u_j}^*$ as mentioned above. In fact, this would also be true if higher correlation functions would have been taken into account. The definition (38) together with the result (48) can be used to calculate the values for the Reynolds stress tensor.

The term on the right-hand side of (38) can be rewritten as an integral of the two-point correlation and some boundary integrals. This was necessary because the limit $r \to 0$ has to be evaluated within the dissipation range where not enough is known about the two-point velocity-pressure correlation. It can be found that the dissipation range, which is of the order of l_η, makes a higher order contribution to the above mentioned integral in the limit of large Reynolds number and thus can be neglected. After neglecting the triple-correlations we find

$$\Phi^* = -\frac{1}{2\pi}\int_{\tilde{V}} \frac{1}{1+\tilde{r}_2}\left[\left(\delta_{j2}\frac{\partial R_{i2}^*}{\partial \tilde{r}_1} + \tilde{r}_l\frac{\partial^2 R_{il}^*}{\partial \tilde{r}_l \partial \tilde{r}_1}\right) + \frac{\partial^2 R_{i2}^*}{\partial \tilde{r}_j \partial \tilde{r}_1}\right]\frac{dV(\tilde{r})}{|\tilde{r}|} + (i \leftrightarrow j) \qquad (49)$$

where $(i \leftrightarrow j)$ abbreviates the addition of the previous term with indices interchanged. No boundary integral has to be kept due to the homogeneous boundary conditions for all variables. Once a solution to the equations (21) and (24)–(27) are computed the scaling of the two-point correlations can be calculated by equating (48) and (49). Using this, the value for $\overline{u_i u_j}^*$ can be taken from R_{ij}^* at $r = 0$ as has been proven by the matching between the Kolmogorov universal range and the outer inviscid solution.

5. Future plans

There are basically two outstanding problems within the whole approach of RDT in the log-layer. The first one is the fact that it has to be proven that the system (21), (24)–(29) has a non-zero solution even though all boundary conditions are homogeneous. A strong hint towards this character of the equation is gained by the analysis of the discretised set of equations which, of course, is linear. To see why the equations may have a non-zero solution, a result from linear algebra may

be recalled. If in a linear system of the form $\boldsymbol{Ax} = 0$ the matrix $\boldsymbol{A}$ has the rank ζ and $\zeta < n$ where n is the number of equations, then the system has nontrivial solutions. In this particular case considering the discretised equations (21), (24)–(27), $\boldsymbol{A}$ is a quadratic matrix and its rank can only be smaller than n if there is some redundancy in the equations. In fact, this redundancy is due to the identities (28) and (29). Even though the structure of the discretised system provides some information, the proof of a corresponding feature in the differential equations is still outstanding. Once the previous problem is solved, a numerical algorithm has to be coded to solve the discretised equations (21) and (24)–(29) because it is very unlikely that an analytical solution can be found. In the next step of post-processing the numerical results, the ability of the asymptotic limits used in the RDT of the log-layer has to be revised and if necessary enhanced by including higher correlations in the analysis. Finally, the results of the theory will be compared with DNS data from the turbulent channel flow (Kim *et al.* 1987).

Acknowledgment

REFERENCES

VON KÁRMÁN, TH. 1930 Mechanische Ähnlichkeit und Turbulenz. *Nachr. Ges. Wiss. Goettingen.* **68.**

VON KÁRMÁN, TH. 1930 Mechanische Ähnlichkeit und Turbulenz. *Proc. 3rd Int. Congr. Appl. Mech., Stockholm.* **1.**

KASSINOS, S. C. & REYNOLDS, W. C. 1994 A structure-based model for rapid distortion of homogeneous turbulence. *Thermosciences Report No.* **TF-61.**

KIM, J., MOIN, P. & MOSER, R. D. 1987 Turbulence statistics in fully developed channel flow at low Reynolds number. *J. Fluid Mech.* **177,** 133-166.

MELLOR, G. L. 1972 The large Reynolds number asymptotic theory of turbulent boundary layers. *Int. J. Engng Sci.* **10,** 851-873.

MILLIKAN, C. B. 1939 A critical discussion of turbulent flows in channels and circular tubes. *Proc. 5rd Int. Congr. Appl. Mech., Cambridge.*

ROTTA, J. C. 1972 *Turbulente Strömungen. Teubner Verlag Stuttgart.*

SADDOUGHI, S. G. & VEERAVALLI, S. V. 1994 Local isotropy in turbulent boundary layers at high Reynolds number. *J. Fluid Mech.* **268,** 333-372.

A preliminary attempt to use neural networks for turbulent eddy classification

By Ron F. Blackwelder

1. Motivation and objectives

This note describes an attempt to use standard neural network tools to fashion a means of detecting eddy patterns in the wall region of a turbulent flow. The research was motivated by the desire to formulate a means to use only flow parameters that can be sensed on the wall to describe the passing eddy structure. If a simple formulation can be obtained, it could conceivably be utilized to control actuators embedded in the wall. Such actuators have been developed by Jacobson and Reynolds(1993a), Blackwelder and Liu (1994), Tung *et al.* (1995), and others. These actuators have the common characteristics that they are small and are typically flush with the wall when not deployed. When they are activated, it is assumed that they will be able to interact constructively with the turbulent eddies near their location to either decrease the wall shear stress, enhance or reduce the mixing, etc. At present, there is only a nascent understanding of the interaction dynamics between the actuators and the eddies in the flow. Nevertheless, for such interaction to succeed, methods to couple the actuators to the oncoming flow must be obtained. General methods must be found that will detect the space and temporal location of the desired structure. In particular, it will be necessary to know when the eddies will arrive at the location of the actuator. This research attempted to use the shear stress measurements on the wall in the vicinity of an actuator location to predict when a particular eddy pattern would arrive and/or occur at the designated location. In this work the eddy pattern to be detected was identified by its velocity signature only.

2. Techniques

Artificial Neural Networks(ANN) have been used rather extensively in control theory for a variety of purposes. They consist of algorithms that, when properly configured, have the ability to "learn" a desired response. In fluid mechanics, Faller *et al.* (1994) utilized an ANN to predict separation pressure on an airfoil after training it with existing unsteady airfoil data obtained at different pitch rates. Jacobson and Reynolds (1993b) used two different ANN controllers to alter the shear stress on the wall of a modeled boundary layer and deduced a skin friction reduction of 8%. Fan, *et al.* (1993) utilized ANN in a transitional boundary layer to reduce the magnitude of the disturbances in the layer.

The approach used in this note is similar to that of Jacobson and Reynolds (1993b). However instead of using a model to generate data, well-resolved direct numerical simulation (DNS) data from a turbulent channel flow was used. The ANN was configured similar to the feed-forward network shown in Fig. 1 adapted
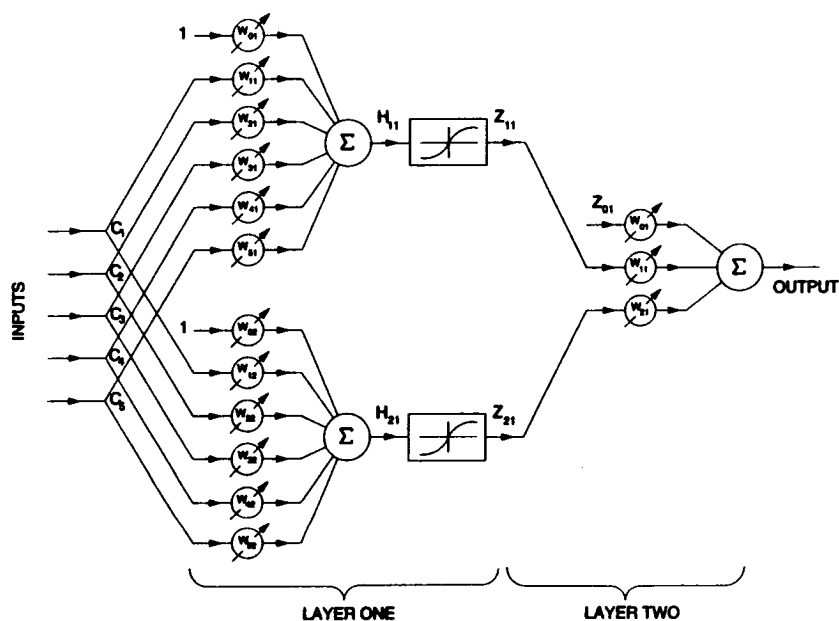
FIGURE 1. Schematic of a two layer ANN with five inputs and one output.

from Jacobson and Reynolds (1993b). This two-layer network consists of five inputs, two internal nodes, and a single output. It is designated as a 5-2-1 network which represents the number of inputs, nodes, and outputs. In a practical device, the inputs would correspond to signals obtained from a series of sensors located on the wall of the flow. Thus only data obtained in the wall region was used as input into the ANN. It was further assumed that for practical application the output from an ANN would be utilized to operate an actuator located at a point, $\mathbf{p}$, on the wall.

For the work presented here, the input to the ANN utilized i_{max} inputs obtained from the two velocity components parallel to the wall. Typically this data was obtained at the first resolved calculation point lying above the wall and hence represented the wall shear, $\partial u/\partial y$ and $\partial w/\partial y$, at the various data points. The choice of these variables and their physical location with respect to the point, $\mathbf{p}$, are crucial because this is one of the primary means by which the physics enter the problem. The number of inputs, i_{max}, varied during the course of the investigation from 5 to 50. The inputs included data obtained from locations upstream, Δx, and spanwise, Δz, from the position $\mathbf{p}$. Usually $\partial u/\partial y$ and $\partial w/\partial y$ were both used from a single spatial location; hence, the number of spatial locations providing data was always less than or equal to the number of inputs, i_{max}.

Neural networks as shown in Fig. 1 are quite flexible and can consist of a large number of inputs and layers. Few rules exist for their design and it is left to the user to develop a network best suited to his application. One of the few guidelines available is that more than one layer must be utilized to adequately model nonlinearities in a problem. In addition, it behooves the user to keep the number of inputs, nodes, and layers to a minimum to reduce the computational effort.

The ANN used in this investigation consisted of two layers with two to five nodes in the second layer and a single output. The weights were designated as w_{ijk}, where the first subscript denotes the node in the previous layer, the second subscript is the output node for the present layer, and the third subscript is the layer number. A bias input is included in each layer and thus i varies from zero to i_{max}. Likewise j and k have values between unity and j_{max} and k_{max} respectively. Thus a total of $(i_{max} + 1)j_{max} + (j_{max} + 1)$ coefficients, w_{ijk}, were used in the ANN. Their initial values were chosen as random numbers and adjusted later by training.

Letting I_i be the ith input, then the linear sum of the outputs from the first layer, $H_{jk} = I_i w_{ijk}$, was scaled to lie between ± 1 by the sigmoid function, F, which was taken to be the hyperbolic tangent function;

$$Z_{jk} = \tanh(H_{jk})$$

Z_{j1} are the outputs from the first layer and the input into the second layer. By convention, the output of the last layer, O, is not passed through the sigmoid; hence, a two layer ANN with a single output is simply $O = H_{12}$.

The value of the weights were found by training which used a back propagation algorithm described by Hertz *et al.* (1991). This requires *a priori* knowledge of a target vector, ϕ, which the ANN attempts to predict. Choi *et al.* (1994) have shown that a 25% drag reduction can be accomplished by using the normal velocity component at $y^+ = 10$ to prescribe suction and blowing at the wall directly below its location. Using this result, the target chosen for the present study was the scalar value of the normal velocity component located at $y^+ = 10$ above the point **p**. The DNS data were used to extract m_{max} training sets; each consisted of the pattern of the u and w data near the wall in the neighborhood of **p** and the value of the target, $\phi = v(p_x, y^+ = 10, p_z)$. As each training set was presented to the ANN algorithm, the standard deviation was computed from the difference between the target and the ANN output over the m sets of data as

$$\epsilon^2 = \frac{1}{2} \sum_{m=1}^{m_{max}} [\phi^m - O^m(w_{ijk})]^2$$

To minimize the standard deviation, the gradient descent algorithm suggests changing w_{ijk} by an amount Δw_{ijk} proportional to the gradient of ϵ^2 given by

$$\Delta w_{ijk} = -\mu \frac{\partial \epsilon^2}{\partial w_{ijk}}$$

where μ is an arbitrary constant of order unity. Thus for the output stage of an i_{max}-2-1 network, the changes for the weight coefficients are given by

$$\Delta w_{i12} = \mu \frac{\partial O^m}{\partial w_{i12}} (\phi^m - O^m)$$
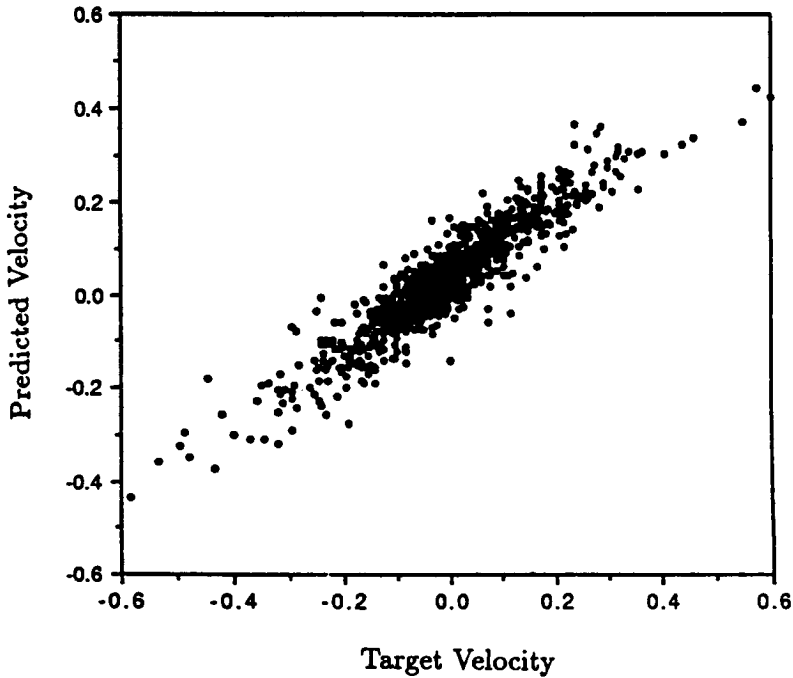
FIGURE 2. Predicted velocity versus the target velocity after one hundred iterations of the test patterns.

where the sum over m is implied. For such a network, the output variable is $O^m = H_{12}^m = w_{k12}Z_{k1}^m$ so that

$$\Delta w_{i12} = \mu Z_{k1}^m \frac{\partial w_{k12}}{\partial w_{i12}} \delta^m$$

or

$$\Delta w_{i12} = \mu \delta^m Z_{i1}^m$$

where $\delta^m = \phi^m - O^m$. This specifies the weights in the second layer. In a similar manner, the back propagation algorithm can determine the weights in the first layer.

3. Results

The main results of this study were obtained by examining the predicted output velocity as a function of the target velocity for the $m_{\max}$ patterns after training. Except where noted, the results are for a 10-4-1 neural network. Typically, 1024 test patterns were taken from one temporal set of data and used in the training. Figure 2 illustrates the output for ten values of $\partial u/\partial y$ and $\partial w/\partial y$ taken at $\Delta x = 0$ and at five spanwise locations, $\Delta z = 0$, ± 13 and ± 26, with respect to **p**. The best results as determined by the standard deviation were obtained when $\Delta x = 0$; e.g. $\epsilon = 0.062$ for the data in Fig. 2 with $\Delta x = 0$. At $\Delta x = \pm 20$, ϵ increased to 0.10 and at $\Delta x = \pm 40$, $\epsilon = 0.14$.

The training algorithm attempted to calculate values of the weights that minimize the difference between the output and the desired target. Hence it is not

unreasonable to assume that the magnitude of the calculated weights would be an indication of the value of that particular input. If so, an examination of the weights could be used to prune those weights that are the least useful. This appeared to be a valid assumption as long as the input parameter was strongly correlated with the target variable. This was tested by letting one of the inputs have the value of the target velocity. The algorithm produced weights in the first layer, w_{ij1}, that were typically smaller than 0.1 except for the weight related to the input containing the target which was of order unity. However, as training continued and more targets were presented to the algorithm, the weights continued to change. This was true even though the targets presented were a repeat of those targets already analyzed by the algorithm. If the weight in the second layer became small, the values of the weights in the first layer were often large since their effect was not propagated through the second layer due to the smaller weight there. This relationship was a result of the non-linearity in the network and will probably be found in any ANN having more than one layer. It was found that the product of the weights along the propagation path was a better indicator of correlated inputs. That is, when the target value was used as an input on one channel, the product of the weights from the first and second layer for that data path was much larger than for the other channels.

On the other hand, when a random valuable was used as one of the inputs, the results were more consistent; namely the value of the weights associated with the random variable ultimately approached zero. However it often took more than 200 iterations through the set of pattern data before this result was achieved, which was deemed to be excessively long. As stated above, the products of the weights from the different layers through the propagation channel was a much better indicator of the lack of correlation with the target value. In general, an examination of the magnitude of the weights after a fixed number of iterations was of little help in choosing appropriate inputs. But if the weights approached zero and remained very small for a large number of iterations, this was considered a good indication that the input on that channel was indeed of little help in predicting the target and could be pruned. In general, it was found that physical insight was a better guide and indicator of appropriate input variables than the magnitude of the weights.

The time taken for the algorithm to converge to a good prediction of the target was of concern. It was found that the value of ϵ decreased rapidly to a nominal value of 0.06 after three to six passes through the test patterns. Further iterations provided very little decrease in the standard deviation. However the values of the weights were not constant and were often changing significantly after one hundred iterations through the set of patterns. In some cases, the values of the weights were not constant after ten thousand iterations. In a couple of cases no convergence was found at all but rather the weights oscillated. When the weights did converge to a constant value, that final value depended upon the initial random values of weights.

The convergence of the weights was studied by adding dither (i.e. random noise) to the weights at each iteration. A dither amplitude of approximately one per cent of the root mean square value of the weights eliminated the oscillatory nature of

the weights, but did not seem to speed their convergence. However, a slightly small value of the standard deviation was found with the dither.

During the iterations, the set of approximately 1024 pattern data and target values was usually presented sequentially; i.e. $m = 1, 2, 3 \ldots$. It was discovered that presenting the patterns in a random fashion had several advantages. First, the weights did not get caught into a cyclical pattern and oscillate. Secondly, the standard deviation decreased slightly to $\epsilon < 0.05$.

4. Conclusions

The artificial neural networks used in this exercise provided a reasonable prediction of the desired results. The standard deviation between the target values and the output value was typically 6% or less. However, the algorithms took a large number of iterations to converge, suggesting that more work needs to be devoted to improving their speed. Possible uses of the conjugate gradient or other tools could provide improvements in the algorithms. The use of temporal data, in addition to the spatial data use in this study, may also speed convergence.

Acknowledgments

REFERENCES

BLACKWELDER, R. F. & LIU, D. 1994 Delay of break-down of streamwise vortices embedded in a boundary layer. ASME Fluids Engineering Division. FED-Vol. 193, *Turbulence Control*, 9, ASME.

CHOI, H., MOIN, P., & KIM. 1994 Active turbulence control for drag reduction in wall-bounded flows. *J. Fluid Mech.* **262**, 75–110.

FALLER, W. E., SCHRECK, S. J., & LUTTGES, M. W. Real-time prediction and control of three-dimensional unsteady separated flow fields using neural networks. AIAA Aerospace Sciences Meeting, Jan 10–13, 1994, AIAA-94-0532.

FAN, X., HOFMANN, L., & HERBERT, T. 1993 Active flow control with neural networks. AIAA Shear Flow Conference, July 6–9, 1993, AIAA-93-3273.

HERTZ, J., ANDERS, K., & PALMER, R. G. 1991 *Introduction to the Theory of Neural Computation*. Addison-Wesley Pub. Co., Redwood City, CA.

JACOBSON, S. A. & REYNOLDS, W. C. 1993a Active boundary layer control using flush-mounted surface actuators. *Bull. Am. Phy. Society.* **38**, 12, 2197.

JACOBSON, S. A. & REYNOLDS, W. C. 1993b Active control of boundary layer wall shear stress using self-learning neural networks. AIAA Shear Flow Conference, July 6–9, 1993, AIAA-93-3272.

TUNG, S., HONG, W., HUANG, J., HO, C.-H., LUI, C., & TAI, Y.-C. 1995 Control of a streamwise vortex by a mechanical actuator. Tenth Symposium on Turbulent Shear Flows, Penn. State University, August 14–16.

Preliminary results of the "on-demand" vortex-generator experiments

By Seyed G. Saddoughi[1]

1. Motivation and background

This is a report on the continuation of our experimental investigations (Saddoughi 1994) of "on-demand" vortex generators. Conventional vortex generators as found on aircraft wings are mainly for suppression of separation during the off-design conditions. In cruise they perform no useful function and exert a significant drag penalty. Therefore, replacement of fixed rectangular or delta-wing generators by devices that could be activated when needed would be of interest.

Also in our previous report, we described one example of an "on-demand" device, which was developed by Jacobson & Reynolds (1995) at Stanford University, suitable for manufacture by micro-electro-mechanical technology. This device consists of a surface cavity elongated in the stream direction and covered with a lid cantilevered at the upstream end. The lid, which is a metal sheet with a sheet of piezoelectric ceramic bonded to it, lies flush with the boundary. On application of a voltage the ceramic expands or contracts; however, adequate amplitude can be obtained only by running at the cantilever resonance frequency and applying amplitude modulation: for 2.5 mm × 20 mm cantilevered lids, they obtained maximum tip displacements of the order of 100 μm. Thus fluid is expelled from the cavity through the gap around the lid on the downstroke. They used an asymmetrical gap configuration and found that periodic emerging jets on the narrow side induced periodic longitudinal vorticity into the boundary layer. Their device was used to modify the inner layer of the boundary layer for skin-friction reduction.

Also in our previous report, we proposed that the same method could be implemented for the replacement of the conventional vortex generators; however, to promote mixing and suppress separation we needed to deposit longitudinal vortices into the outer layer of the boundary layer, which required a larger vortex generator than the device built by Jacobson & Reynolds. Our vortex generator was built with a mechanically-driven cantilevered lid with an adjustable frequency. The device was made about ten times the size of Jacobson & Reynolds', the shape or size of the cavity and lid (28 mm × 250 mm) could be easily changed. The cavity depth, the cantilever-tip displacement, and the maximum lid frequency were 20 mm, 10 mm, and 60 Hz respectively. Our vortex generator was mounted on a turntable so that its yaw angle could be changed. Finally, tests over a range of ratios of vortex-generator size to boundary-layer thickness could be carried out simply by changing the streamwise location of the device.

1 Currently with Department of Mechanical Engineering, McGill University, Montreal, Canada, H3A 2K6.

Our vortex generator was mounted on the top wall of the 76 cm × 76 cm flow-visualization wind tunnel in the Mechanical Engineering Department at Stanford University. We conducted extensive flow-visualization experiments at different free-stream velocities for the vortex generator set at different orientations to the flow direction. Smoke was sucked into the flow by the boundary-layer fluid, through a slot located upstream of the vortex generator. A laser-light sheet was used to visualize the motion in cross-stream planes.

For the first time, we were able to see the vortices that the "on-demand" vortex generator deposited into the boundary layer. Also, we obtained a more efficient vortex generation for the case where the vortex generator was pointed in the upstream direction. However, in all of our experiments we observed that the stronger jet emerged from the wide-gap side rather than the narrow side. This was contrary to the finding of Jacobson & Reynolds.

2. Accomplishments

2.1 Continuation of the flow-visualization experiments

To explain the differences in flow behaviors between our case and the experiment of Jacobson & Reynolds, we investigated the effect of Stokes' parameter, $St \equiv \sqrt{2\pi f d^2/\nu}$, where f is the frequency, d is the diameter of the circular hole for the wall-jet actuators, and ν is the kinematic viscosity. Based on dimensional analysis, Rathnasingham *et al.* (1994) proposed that for this kind of actuator, $St > 1$ is required to prevent the blockage of the exit flow due to the viscous effects.

For the present type of actuator, one may assume d to represent the gap-width size. In our investigations, for the narrow gap at the highest lid-frequency, $St < 1$. Therefore, it appeared that for our narrow gap the exit flow was viscous dominated. However, for the narrow gap of Jacobson & Reynolds' case, $St > 1$ since their experiments were conducted in water, and also in their case the lid frequency was larger than the present studies.

In order to match the Stokes' parameters for our case with those of Jacobson & Reynolds' experiments, we repeated all of our flow-visualization experiments in a water tunnel at Stanford University. In this case dye was introduced inside the cavity when the actuator was off. Photographs were taken after the vortex generator was switched on.

An example of these pictures is presented in Fig. 1. In this case the top view is shown, where the flow is from left to right and the vortex generator is pointing in the downstream direction. In this picture the wide-gap side is located on top of the actuator plate. In this case for both the narrow and wide gaps $St > 1$; however, it can be seen clearly that all the dye is ejected out only from the wide gap. Thus it appears that $St > 1$ is not a sufficient condition to prevent the blockage of the exit flow through a gap.

It does appear that Direct Numerical Simulation (DNS) results are needed to explain the differences between the present case and the experiment by Jacobson & Reynolds. These DNS are being conducted presently by Koumoutsakos (see related report in this volume).

FIGURE 1. Top view of flow-visualization experiment in water tunnel. Flow is from left to right. Vortex generator is pointing in the downstream direction and ejecting the dye only from the wide-gap side.

2.2 Quantitative identification of longitudinal vortices

Vortex generators delay flow separation by increasing the overall skin friction. The presence of longitudinal vortices in a boundary layer can be detected by spanwise skin-friction (C_{fz}) measurements. The C_{fz} values will be high at places where the normal-to-the-wall component of mean velocity near the surface will be negative, bringing high-speed fluid down from above, and low when the flow is away from the surface (for detailed measurements and discussion see Shabaka, Mehta & Bradshaw 1985).

We took spanwise skin-friction measurements in the smoke tunnel by means of Preston tubes. These measurements were conducted at a fixed longitudinal location, which corresponded to a distance of $4W$ downstream of the end of the vortex generator, where W is the width of the actuator plate. The spanwise extent of the data was approximately $10W$. Measurements were conducted for three different vortex generator operating conditions: (1) switched off, (2) switched on, pointing downstream, and (3) switched on, pointing upstream. All the data were normalized by the mean value of the skin-friction coefficient for the vortex-generator switched-off condition, $C_{fz-mean(off)}$. In Figs. 2 and 3 the normalized C_{fz} values for condition (1) are compared with the data for conditions (2) and (3) respectively.

Two well-defined peaks in the spanwise distribution of skin friction for condition (2) can be seen in Fig. 2. This indicates that when the vortex generator points
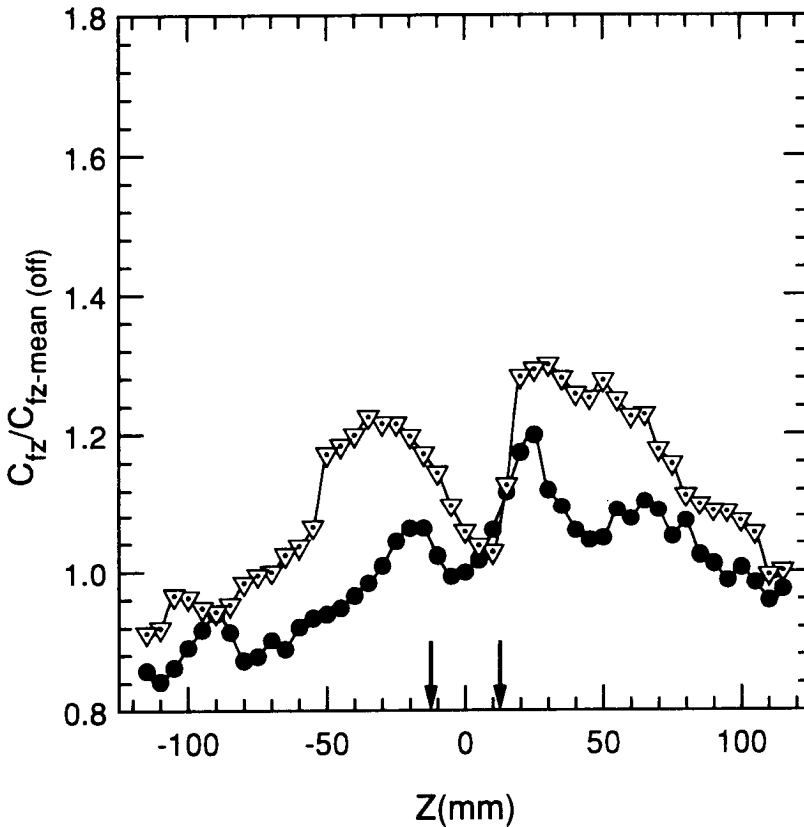
FIGURE 2. Comparison between the distributions of normalized spanwise skin-friction coefficients for vortex generator switched-off (●) and switched-on (pointing downstream) (▽) conditions. Distance between arrows shows the width of the actuator plate.

downstream, two counter-rotating vortices with common flow away from the surface are created. However, in Fig. 3 we can observe that when the actuator points in the upstream direction, a single strong vortex is generated. This is consistent with our wind-tunnel flow-visualization experiments. However, it is important to note that in this respect a definite conclusion cannot be reached, because for the reference-flow condition (i.e. the case where the vortex generator was switched off) the spanwise variation of C_{fz} is fairly large (more than ±10%). Therefore, it is not clear whether the vortex generator would have increased the skin-friction coefficients by such large amounts, if these pre-existing variations were not present in the boundary layer.

3. Future plans

This project will be continued at McGill University. We plan to install the vortex generator in a canonical boundary layer and repeat all the spanwise measurements of skin friction. To obtain a measure of the mean longitudinal vorticity, hot-wire measurements will be conducted. Also, our on-demand vortex generators will be
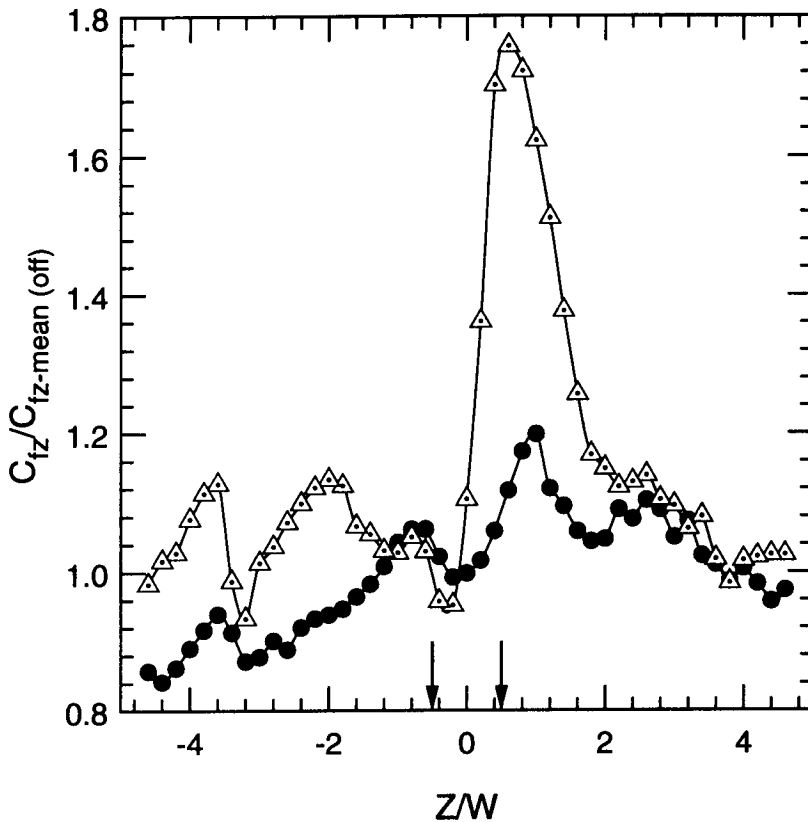
FIGURE 3. Comparison between the distributions of normalized spanwise skin-friction coefficients for vortex generator switched-off (●) and switched-on (pointing upstream) (△) conditions. Distance between arrows shows the width of the actuator plate.

used in laboratory adverse-pressure-gradient boundary layers to suppress separation.

Acknowledgments

This work was carried out in collaborations with Dr. Nagi Mansour and Professor Peter Bradshaw, and with help and advice from Professor Bill Reynolds. We would like to thank Don Bott and Carl Buice for their help during the experiments.

REFERENCES

JACOBSON, S. A. & REYNOLDS, W. C. 1995 An experimental investigation towards the active control of turbulent boundary layers. *Stanford University Thermosciences Division, Rep. TF-64.*

RATHNASINGHAM, R., PIEPSZ, O., GOLDBERG, H. D., SCHMIDT, M. A. & BREUER, K. S. 1994 Performance of sensors and actuators for turbulent flow control. *Bulletin of the American Physical Society*, Vol. 39, No. 9, p-1909.

SADDOUGHI, S. G. 1994 Experimental investigations of "on-demand" vortex generators. *Annual Research Briefs-1994*, Center for Turbulence Research, Stanford University/NASA Ames. 197-203.

SHABAKA, I. M. M. A., MEHTA, R. D. & BRADSHAW, P. 1985 Longitudinal vortices imbedded in turbulent boundary layers. Part 1. Single vortex. *J. Fluid Mech.* **155,** 37-57.

Simulations of vortex generators

By   P. Koumoutsakos

1. Motivation and background

We are interested in the study, via direct numerical simulations, of active vortex generators. Vortex generators may be used to modify the inner part of the boundary layer or to control separation thus enhancing the performance and maneuverability of aerodynamic configurations. We consider generators that consist of a surface cavity elongated in the stream direction and partially covered with a moving lid that at rest lies flush with the boundary. Streamwise vorticity is generated and ejected due to the oscillatory motion of the lid. The present simulations complement relevant experimental investigations of active vortex generators at NASA Ames and Stanford University (Saddoughi ,1994, and Jacobson and Reynolds, 1993). Jacobson and Reynolds (1993) used a piezoelectric device in water, allowing for small amplitude high frequency oscillations. They placed the lid asymmetrically on the cavity and observed a strong outward velocity at the small gap of the cavity. Saddoughi used a larger mechanically driven device in air to investigate this flow and he observed a jet emerging from the wide gap of the configuration, contrary to the findings of Jacobson and Reynolds.

Our task is to simulate the flows generated by these devices and to conduct a parametric study that would help us elucidate the physical mechanisms present in the flow. Conventional computational schemes encounter difficulties when simulating flows around complex configurations undergoing arbitrary motions. Here we present a formulation that achieves this task on a purely Lagrangian frame by extending the formulation presented by Koumoutsakos, Leonard and Pepin (1994). The viscous effects are taken into account by modifying the strength of the particles, whereas fast multipole schemes employing hundreds of thousands of particles allow for high resolution simulations. The results of the present simulations would help us assess some of the effects of three-dimensionality in experiments and investigate the role of two-dimensional vortex generation due to an oscillating lid.

2. Accomplishments

An adaptive computational scheme, based on vortex methods, has been developed to investigate flows past the two dimensional configuration shown in Fig. 1.

The configuration consists of a cavity partially covered with an oscillating lid that is placed asymmetrically. In this report we describe our numerical method and present preliminary results of our direct numerical simulations.

2.1 Mathematical formulation

Two-dimensional incompressible unsteady flow of a viscous fluid may be determined by the vorticity transport equation as

$$\frac{\partial \omega}{\partial t} + \mathbf{u} \cdot \nabla \omega = \nu \nabla^2 \omega \tag{1}$$
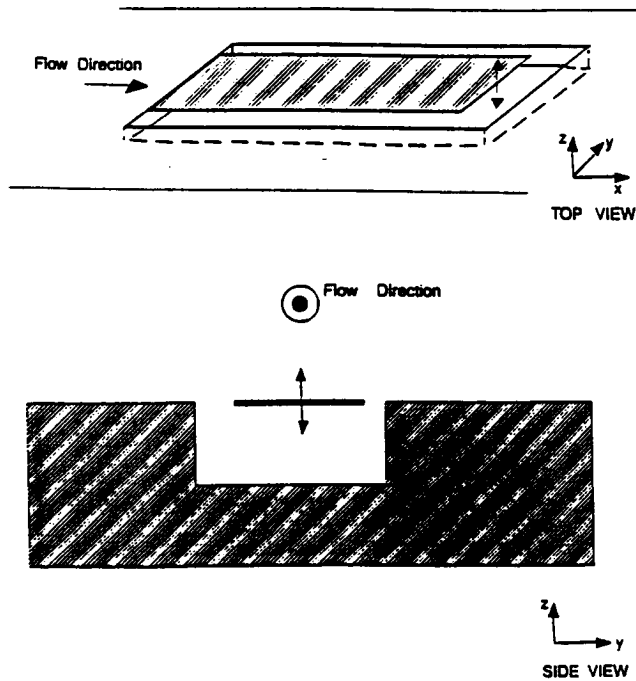
FIGURE 1.   Definition sketch.

where $\mathbf{u}(\mathbf{x},t)$ is the velocity, $\boldsymbol{\omega} = \omega\,\widehat{\mathbf{e}}_z = \nabla \times \mathbf{u}$ the vorticity and ν denotes the kinematic viscosity . Using the definition of the vorticity and the continuity ($\nabla \cdot \mathbf{u} = 0$) it can be shown that $\mathbf{u}$ is related to $\boldsymbol{\omega}$ by a Poisson equation

$$\nabla^2 \mathbf{u} = -\nabla \times \boldsymbol{\omega} \tag{2}$$

The vorticity equation (Eq. 1) may be expressed in a Lagrangian formulation by solving for the vorticity carrying fluid elements ($\mathbf{x_a}$) based on the following set of equations:

$$\begin{aligned} \frac{d\mathbf{x_a}}{dt} &= \mathbf{u}(\mathbf{x_a},t) \\ \frac{d\omega}{dt} &= \nu\,\nabla^2\omega \end{aligned} \tag{3}$$

For flow around a non-rotating body, moving with velocity $\mathbf{U_b}(t)$, the velocity of the fluid ($\mathbf{u}$) on the surface of the body ($\mathbf{x_s}$) is equal to the velocity of the body: $\mathbf{u}(\mathbf{x_s},t) = \mathbf{U_b(t)}$ At infinity we have: $\mathbf{u}(\mathbf{x}) \to \mathbf{U}_\infty$ as $|\mathbf{x}| \to \infty$ where $\mathbf{U}_\infty$ is the free stream velocity.

2.2 Particle (vortex) methods

The present numerical method is based on the discretization of the above equations in a Lagrangian frame using particle (vortex) methods. The vorticity field

is considered as a discrete sum of the individual vorticity fields of the computational particles, having core radius ϵ, strength $\Gamma(t)$, and an individual distribution of vorticity determined by the function η_ϵ, so that:

$$\omega(\mathbf{x}, t) \doteq \sum_{n=1}^{N} \Gamma_n(t) \, \eta_\epsilon(\mathbf{x} - \mathbf{x}_n(t)) \tag{4}$$

In the context of vortex methods the right-hand side of Eq. 3 is replaced by integral operators. The velocity field may be determined from the vorticity field using the Green's function formulation for the solution of Poisson's equation (Eq. 2).

$$\mathbf{u} = = -\frac{1}{2\pi} \int \mathbf{K}(\mathbf{x} - \mathbf{y}) \times \omega \, dy + \mathbf{U}_0(\mathbf{x}, t) \tag{5}$$

where $\mathbf{U}_0(\mathbf{x}, t)$ accounts for the presence of the body and $\mathbf{U}_\infty$, and $\mathbf{K}(\mathbf{z}) = \mathbf{z}/|\mathbf{z}|^2$. The use of the Biot-Savart law to compute the velocity field guarantees the enforcement of the boundary condition at infinity.

The Laplacian operator may be approximated by an integral operator (Mas-Gallic, 1987) as well:

$$\nabla^2 \omega \approx \int G_\epsilon(|\mathbf{x} - \mathbf{y}|) \, [\omega(\mathbf{x}) - \omega(\mathbf{y})] \, dy \tag{6}$$

These integrals are discretized using a quadrature having as quadrature points the locations of the particles. Fast multipole algorithms with a computational cost scaling as $\mathcal{O}(N)$ (Greengard and Rohklin, 1987) have been efficiently implemented, allowing for high resolution simulations using a few millions of particles (grid points).

The no-slip boundary condition is enforced by formulating the physical mechanism it describes. A vorticity flux $(\partial \omega / \partial n)$ may be determined on the boundary in a way that ensures the no-slip condition is satisfied. We implement a fractional step algorithm that allows for the calculation of this vorticity flux by extending the formulation presented (Koumoutsakos, Leonard and Pepin 1994) to account for multiple bodies. It is shown then that this mechanism of vorticity generation can be expressed by an integral operator as well, so that the vorticity field is modified by:

$$\frac{d\omega}{dt} \approx \nu \int H(\mathbf{x}_a, \mathbf{y}) \, \frac{\partial \omega}{\partial n}(\mathbf{y}) \, dy \tag{7}$$

where the kernel $H(\mathbf{x})$ is described in [5].

The accuracy of the method relies on the accuracy of the quadrature rule. The convergence properties of vortex methods with a finite core dictate that the particles must overlap at all times (Beale, 1986). When particles cease to overlap in the present scheme, a procedure is implemented (Koumoutsakos and Leonard, 1995) that restores the particle overlap while conserving the moments of the vorticity field.

2.3 Fractional step algorithm - boundary conditions

A fractional step algorithm is implemented that accommodates the enforcement of the no-slip boundary condition. Let us assume that at the n-th time step (corresponding to time $t - \delta t$) the vorticity field has been computed (respecting the no-slip boundary condition) and we seek to advance the solution to the next time step (time t). The following two-step procedure is implemented:

•Step 1 (kinematics-no through flow):

Particles are advanced via the Biot-Savart law and their strength is modified based on the scheme of particle strength exchange. In order to account for the presence of the body the no-through flow needs to be enforced. This is accomplished by distributing vortex sheets on the surface of the bodies. For a doubly connected domain as that shown in Fig. 1b the potential flow problem is solved using the following set of equations:

$$\int_{-L/2}^{L/2} \frac{\kappa(\xi)}{\mathbf{x}_p - \xi} d\xi \ + \ \int_{-\infty}^{\infty} \gamma_w(\zeta) \frac{\partial}{\partial s(\mathbf{x}_p)} Log|\zeta - \mathbf{x}_p| d\zeta \ = \ \mathbf{u}_n(\mathbf{x}_p) \qquad 8a$$

$$\int_{-L/2}^{L/2} \kappa(\xi, t) d\xi \ = \ -\nu \int_0^t \int_{-L/2}^{L/2} \frac{\partial \omega(\mathbf{x}_p, T)}{\partial n(\mathbf{x}_p)} d\mathbf{x}_p \, dT \qquad (8b)$$

$$\int_{-L/2}^{L/2} \kappa(\xi) \frac{\partial}{\partial n(\zeta)} Log|\zeta - \xi| d\xi \ + \ \int_{-\infty}^{\infty} \gamma_w(\zeta') \frac{\partial}{\partial n(\zeta)} Log|\zeta - \zeta'| d\zeta' \ = \ \mathbf{u}_t(\zeta) \quad (8c)$$

where $\kappa(\xi), \mathbf{x}_p$ and $\gamma_w(\zeta), \zeta$ denote vortex sheets and location of points on the surface of the plate and the cavity respectively.

The above set of equations, when discretized using a panel method, results in a well posed system of equations (Koumoutsakos and Leonard, 1995), which can be solved iteratively. Note that Eq. 8b guarantees the solvability of the equations and the uniqueness of the pressure distribution on the surface of the bodies.

•Step 2 (dynamics - no slip):

The no-slip boundary conditions are enforced in this stage by a vorticity (not particle) creation algorithm. The vortex sheet that is distributed on the surface of the body enters the fluid, thus generating a vorticity flux at the surface of the body. This vorticity flux accounts for the modification of the strength of the particles so as to enforce the no-slip boundary condition. Algorithmically, in this step, the diffusion equation is solved on a Lagrangian frame with Neuman boundary conditions. Please see Koumoutsakos et al. (1994) for further details.

2.4 Results

A series of simulations have been carried out to determine the important parameters of the flow. It has been speculated that the parameters of the flow such as the frequency of oscillation (f), the gap diameter (d_s, d_l for the small and the large
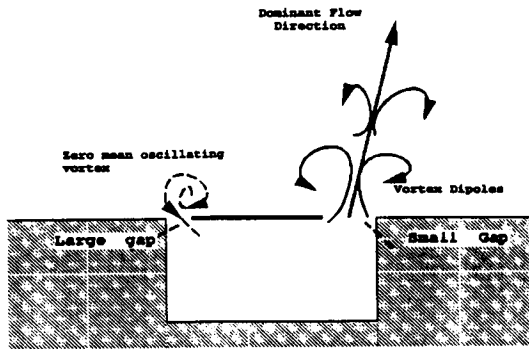
FIGURE 2. Sketch of flow type I.

gap respectively), and the viscosity of the flow may be combined so as to produce a coefficient, called the *Stokes number*:

$$St^{s,l} = \sqrt{\frac{2\pi f d_{s,l}^2}{\nu}}$$

to characterize the different physical phenomena of the flow. We have performed a series of computations by varying the above parameters of the flow along with the amplitude of the oscillations in an attempt to match the respective experimental cases. The simulations have shown a dramatic difference in the flow behavior for various parameters of the configuration. In the following we present the types of flows that are being observed (and described below) computationally and experimentally, along with the respective Stokes numbers.

Large Gap	Small Gap	Flow Type
12.600(Exp.)	2.960 (Exp.)	I
34.010	14.680	I
53.238	14.589	I
4.652 (Exp.)	0.930 (Exp.)	II
15.597	1.794	II
13.870	3.381	II
46.515	9.744	II

In what we call *flow type I*, a positive (inducing an outward velocity) vortex dipole establishes itself in the small gap region just outside the cavity. The pair is produced by the downward motion of the plate. It is continuously fed by the downward motion of the oscillation cycle in such a way as to overcome its erosion by diffusion. The self induced velocity of the dipole, on the other hand, is balanced by the upward motion of the plate, thus establishing a quasi-steady vorticity distribution at the small gap of the configuration. On the large gap side, the distance of the plate from the cavity walls is such that no strong vorticity is being ejected from the cavity walls. The vorticity that is produced at the tip of the plate has a zero mean strength, and diffusion acts to reduce its strength rapidly. Hence as the plate is oscillating no
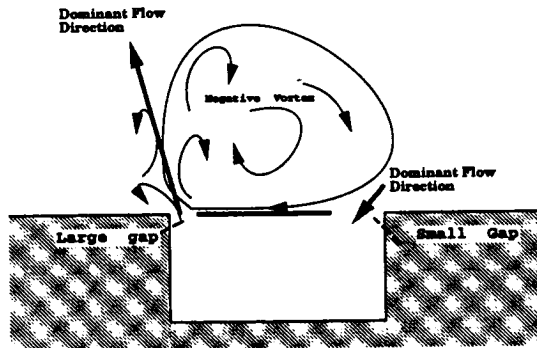
FIGURE 3. Sketch of flow type II.

dominant vortical features are established at this end of the lid. As we reduce the frequency of oscillations, we may observe that dipoles are being ejected from the small gap of the cavity at the downward motion of the plate, while a new pair is being formed at the small gap. However,the dipoles that emerge from the gaps are quickly eroded by diffusion and do not significantly alter the character of the flow.

A strikingly different pattern is observed in *flow type II*. In this configuration, the lid is relatively closer to both edges of the cavity and the amplitude of oscillations is about an order of magnitude in absolute value larger than the previous cases. Hence vortex dipoles are being formed on both gaps of the cavity. The stronger pairs are initially formed in the area of the small gap. Due to the low frequency of the plate oscillations, the upwash motion of the plate does not overcome the self-induced velocity of the vortical pairs and vorticity is ejected from both gaps. However, as the dipoles that are being formed at the large side of the cavity are more asymmetric, with the clockwise vorticity being more dominant, their path arches towards the cavity lid. This establishes, at later times, a large clockwise vortical region over the cavity. This vortex in turn, further modifies the behavior of the flow as it induces an additional downwash velocity on the small side of the gap. The effect of this clockwise (negative) vortex on the flow at the small gap side is twofold: (a) It diverts the positive vortex that is formed at the tip of the lid during the downward motion of the plate in a direction parallel to the lid and (b) it induces an additional downwash velocity. Thus the dipole strength is progressively reduced at the small gap, resulting in a blockage of the vorticity production and fluid ejection from the small gap. The final configuration with the large negative vortex over the cavity lid appears to be stable, thus establishing a flow field with a main jet of fluid emanating form the large gap side of the cavity.

The above described mechanisms may offer an initial tentative 'two-dimensional explanation' to the different behavior exhibited by the flow in the experiments of Jacobson and Reynolds (1995) and Saddoughi (1994). A more systematic study (see below) of the configuration is in order while future three-dimensional simulations would reveal the full mechanism of vorticity generation and flow ejection from the gaps observed in the experiments.
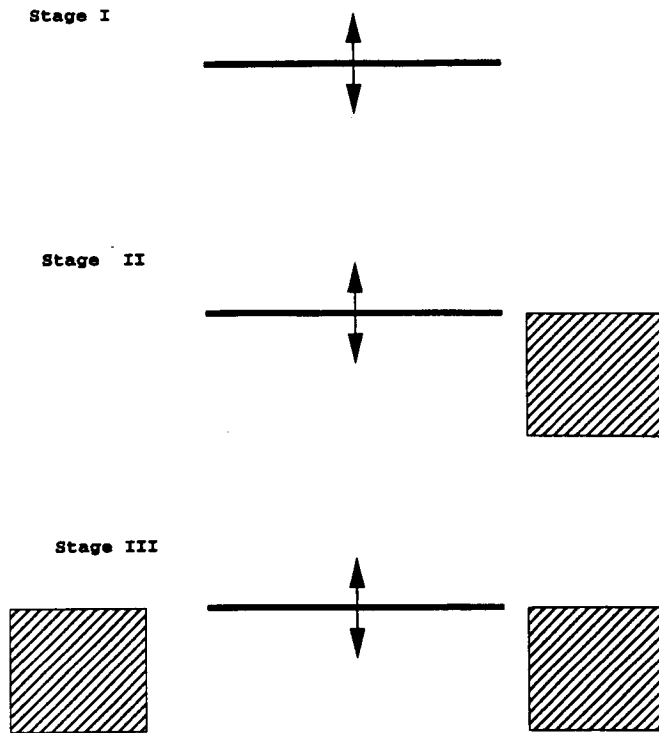
FIGURE 4.   Proposed simulated configurations.

3. Conclusions and future work

We have presented simulation of flows past complex configurations undergoing arbitrary motions using a Lagrangian computational scheme based on high resolution viscous vortex methods. The results of these computations attempt to elucidate some of the intricate behavior that has been observed in related experimental works on flows past active vortex generators.

In order to investigate further the mechanisms of vorticity generation and the observed flow patterns, we are in the process of conducting further detailed simulations. More specifically (Fig. 4) each stage of our study would attempt to isolate and examine a different aspect of vorticity generation and destruction which appear in these vortex generators.

(i) In the first stage we are in the process of conducting simulations of a free oscillating plate. This study would help us establish the generation of vorticity at the cavity lids as well as demonstrate the effect of the frequency of oscillation in the generation of vorticity and the interplay of vorticity generation and destruction due to the plate oscillation and diffusion. A theoretical analysis would be conducted to examine the limit of very high frequency oscillations.

(ii)In the second stage of our study, we would examine the interaction of the plate with a corner. This study would help us understand the vorticity formation

at both gaps of the full configuration. By varying the distance of the plate from the cavity we would be able to determine distances as well as frequencies and amplitudes of oscillation for which a vortex dipole is being formed, and we would be able to determine when the effects of the cavity is negligible.

(iii) In the third stage, the full configuration would be examined in a more careful and systematic manner based on our gained insight from the studies of the more simplified configurations.

We are also in the process of developing three-dimensional codes (Koumoutsakos, 1995) for the study of the full configuration that would elucidate the three-dimensional aspects of the flow.

Acknowledgments

REFERENCES

BEALE, J. T. 1986 On the accuracy of vortex methods at large times. *Proc. Workshop on Comp. Fluid Dyn. and React. Gas Flows.* IMA, Univ. of Minnesota.

GREENGARD, L. & ROHKLIN, V. 1987 A fast algorithm for particle simulations. *J. Comp. Phys.* **73**, 325-348.

JACOBSON, S. & REYNOLDS, W. C. 1993 Active boundary layer control using flush-mounted surface actuators. *Bulletin of the American Physical Society.* **96**, 2197.

KOUMOUTSAKOS, P. & LEONARD, A. 1995 High Resolution simulations of the flow past an impulsively started cylinder. *J. Fluid Mech.* **96**, 1-32.

KOUMOUTSAKOS, P., LEONARD, A. & PEPIN F. 1994 Boundary Conditions for Viscous Vortex Methods. *J. of Comp. Phys.* **113**, 52-61.

KOUMOUTSAKOS, P. 1995 Fast multipole expansion schemes for N-body problems. *Annual Research Briefs.* Center for Turbulence Research, NASA Ames/Stanford Univ., 377-390.

MAS-GALLIC, S. 1987 Contribution à l' analyse numérique des méthodes particulaires. *Thèse d'Etat.* Université Paris VI.

RATHANASINGHAM, R. ,PIEPSZ, O.,GOLDBERG, H. D., SCHMIDT, M., & BREUER, K. S. 994 Performance of sensors and actuators for turbulent flow control. *Bulletin of the American Physical Society.* **39**, 1909.

SADDOUGHI, S. G. 1994 Experimental investigations of "on-demand" vortex generators. *Annual Research Briefs.* Center for Turbulence Research, NASA Ames/Stanford Univ., 197-203.

The radiated noise from isotropic turbulence and heated jets

By G. M. Lilley

1. Motivation and objectives

Our understanding of aerodynamic noise has its foundations in the work of Sir James Lighthill (1952), which was the first major advance in acoustics since the pioneering work of Lord Rayleigh in the last century. The combination of Lighthill's theory of aerodynamic noise as applied to turbulent flows and the experimental growing database from the early 1950's was quickly exploited by various jet propulsion engine designers in reducing the noise of jet engines at takeoff and landing to levels marginally acceptable to communities living in the neighborhoods of airports. The success in this noise containment led to the rapid growth of fast economical subsonic civil transport aircraft worldwide throughout the 1960's and has continued to the present day. One important factor in this success story has been the improvements in the engine cycle that have led to both reductions in specific fuel consumption and noise. The second is the introduction of Noise Certification, which specifies the maximum noise levels at takeoff and landing that all aircraft must meet before they can be entered on the Civil Aircraft Register. The growing interest in the development of a new supersonic civil transport to replace 'Concorde' in the early years of the next century has led to a resurgence of interest in the more challenging problem of predicting the noise of hot supersonic jets and developing means of aircraft noise reduction at takeoff and landing to meet the standards now accepted for subsonic Noise Certification.

The prediction of aircraft noise to the accuracy required to meet Noise Certification requirements has necessitated reliance upon experimental measurements and empirically derived laws based on the available experimental data bases. These laws have their foundation in the results from Lighthill's theory, but in the case of jet noise, where the noise is generated in the turbulent mixing region with the external ambient fluid, the complexity of the turbulent motion has prevented the full deployment of Lighthill's theory from being achieved. However, the growth of the supercomputer and its applications in the study of the structure of turbulent shear flows in both unbounded and wall bounded flows, which complements and in certain cases extends the work of the few dedicated experimental groups working in this field for the past forty years, provides an opportunity and challenge to accurately predict the noise from jets. Moreover a combination of numerical and laboratory experiments offers the hope that in the not too distant future the physics of noise generation and flow interaction will be better understood and it will then be possible to not only improve the accuracy of noise prediction but also to explore and optimize schemes for noise reduction. The present challenge is to provide time and space accurate numerical databases for heated subsonic and supersonic jets to

provide information on the fourth-order space-time covariance of Lighthill's equivalent stress tensor, T_{ij}, which governs the characteristics of the farfield radiated noise and the total acoustic power. Validation with available experimental databases will establish how close Lighthill's theory is to the accurate prediction of the directivity and spectrum of jet noise and the total acoustic power, and the need, in the applications of the theory, to include the effects of flow-acoustic interaction.

2. Accomplishments

2.1 Lighthill's acoustic analogy

Our understanding of the theory of jet noise has its foundations in Lighthill's theory of aerodynamic noise (1952, 1954, 1962, 1963, 1978). Lighthill's theory is based on an acoustic analogy whereby the exact Navier-Stokes equations for fluid flow are rearranged, using an ingeneous technique, to form an inhomogeneous wave equation for the fluctuating fluid density. Since all disturbances created by a turbulent flow result in alternate compressions and expansions of a fluid element as it is convected by the flow, the time rate of change of this fluid element, δV, per unit volume of fluid, following the fluid is

$$\lim_{\delta V \to 0} \frac{1}{\delta V} \frac{D\delta V}{Dt} = -\frac{D\ln\rho}{Dt} = \nabla \cdot v \tag{1}$$

and as a consequence noise is generated and radiated away from the fluid element with a propagation speed equal to the speed of sound. Although the dilatation, $\theta = \nabla \cdot \mathbf{v}$, in Eq. 1 is zero in an incompressible flow it is always finite in compressible flows, and similarly so is $\nabla \cdot \rho\mathbf{v}$. In order to ensure the finiteness of the latter throughout the flow in calculations concerning aerodynamic noise, Lighthill derived the inhomogeneous wave equation for the density fluctuations by eliminating $\nabla \cdot \rho\mathbf{v}$ between the equations of conservation of mass and momentum. The forcing function on its right-hand side represents a distribution of acoustic sources in the ambient flow at rest, replacing the complete unsteady flow. In Lighthill's theory $\partial^2 T_{ij}/\partial x_i \partial x_j$ is the strength of these acoustic sources per unit volume, where

$$T_{ij} = \rho v_i v_j - \tau_{ij} + (p - c_\infty^2 \rho)\delta_{ij} \tag{2}$$

is Lighthill's instantaneous applied acoustic stress tensor. p, ρ, c, and τ_{ij} are respectively the pressure, density, speed of sound, and the viscous stress tensor. In this acoustic analogy the equivalent acoustic sources may move but not the fluid.

Here we follow Lighthill's approach and derive the inhomogeneous wave equation for the fluctuating pressure in the form derived by Lilley (1973), where the only deviation from Lighthill's derivation is in the replacement of $\partial(p - \rho c_\infty^2)/\partial t$ by its equivalent terms from the total enthalpy, h_s, equation together with continuity, giving

$$\frac{\partial(p - c_\infty^2\rho)}{c_\infty^2 \partial t} = -\frac{(\gamma-1)}{2c_\infty^2}\frac{\partial \rho v^2}{\partial t} - \nabla \cdot \frac{\rho v(h_s - h_\infty)}{h_\infty} + \frac{(\gamma-1)}{c_\infty^2}\nabla \cdot (q + v \cdot \tau). \tag{3}$$

where q is the heat flux vector and γ is the ratio of the specific heats. The suffix ∞ denotes ambient conditions. The resultant inhomogeneous wave equation is

$$\frac{\partial^2 p}{c_\infty^2 \partial t^2} - \nabla^2 p = \nabla \cdot (\nabla \cdot \rho vv - \tau) - \frac{(\gamma - 1)}{2c_\infty^2} \frac{\partial^2 \rho v^2}{\partial t^2} - \nabla \cdot \frac{\partial}{\partial t} \frac{\rho v(h_s - h_\infty)}{h_\infty}$$

$$+ \frac{(\gamma - 1)}{c_\infty^2} \nabla \cdot \frac{\partial}{\partial t}(q + v \cdot \tau) \equiv A(x, t) \tag{4}$$

having the unbounded solution

$$(p - p_\infty)(x, t) = \frac{1}{4\pi} \int_V [A(y, t)] \frac{d^3 y}{|x - y|} \tag{5}$$

where the [..] denotes the function is evaluated at the retarded time, $\tau = t - |x - y|/c_\infty$. The far-field approximation, when $|x - y| \approx x$, is

$$(p - p_\infty)(x, t) \approx \frac{1}{4\pi x c_\infty^2} \int_V d^3 y \frac{\partial^2}{\partial t^2} \left(\rho u_x^2 - \tau_{xx} \right.$$

$$\left. - \frac{(\gamma - 1)}{2} \rho v^2 + (\gamma - 1) \frac{\rho u_x (h_s - h_\infty)}{c_\infty} - (\gamma - 1) \frac{(q_x + u_k \tau_{kx})}{c_\infty} \right) \tag{6}$$

where u_x is the component of the velocity in the direction joining the source at y to the far-field observer at x. We find the integrand in Eq. 6 is identical with the component, (xx), of Lighthill's stress tensor, T_{ij}. Apart from the noise generated by the diffusive terms, q and τ, which at high Reynolds numbers is shown to be very small and can be neglected, the major sources of sound in a turbulent flow involve the fluctuations of the momentum flux, ρvv, and the fluctuations of the total enthalpy flux, $\rho v(h_s - h_\infty)$. The fluctuations of the kinetic energy, $\rho v^2/2$, make a small contribution to the radiated noise. (In an inviscid incompressible flow the time gradient of the integral of the kinetic energy would be zero.)

2.1.1 The acoustic power output in isotropic turbulence

The intensity, $I(x)$, of the radiated sound in the far-field is proportional to the square of the fluctuating pressure and is defined by

$$I(x, t) = \frac{< (p - p_\infty)^2 >}{\rho_\infty c_\infty.} \tag{7}$$

Similarly the autocorrelation, $I(x, t^*)$, for a stationary turbulent flow is

$$I(x, t^*) = \frac{1}{16\pi^2 x^2 \rho_\infty c_\infty^5} \int_V d^3 y \int \frac{\partial^4}{\partial \tau^4} P_{xx,xx}(y, r, \tau)) d^3 r \tag{8}$$

where t^* is the far-field time difference and the spectral density, $I(x, \omega)$ is

$$I(\boldsymbol{x},\omega) = \frac{1}{2\pi} \int I(\boldsymbol{x},t^*)\exp(i\omega t^*)dt^*$$

$$= \frac{\pi\omega^4}{2x^2\rho_\infty c_\infty^5} \int_V P_{xx,xx}(\boldsymbol{y},\boldsymbol{k},\omega)d^3\boldsymbol{y} \qquad (9)$$

where $\boldsymbol{r}$ is the spatial separation in fixed coordinates, τ is the retarded time difference defined by $\tau = t^* + \boldsymbol{x}\cdot\boldsymbol{r}/xc_\infty$, ω is the far-field circular frequency, and $P_{xx,xx}$ is the source, $(\boldsymbol{y})$,-observer, $(\boldsymbol{x})$, aligned space-retarded time covariance of T_{ij}, and

$$P_{xx,xx}(\boldsymbol{y},\boldsymbol{k},\omega) = \frac{1}{16\pi^4} \int \exp(i\boldsymbol{k}\cdot\boldsymbol{r})d^3\boldsymbol{r} \int \exp(i\omega\tau)P_{xx,xx}(\boldsymbol{y},\boldsymbol{r},\tau)d\tau \qquad (10)$$

is the four-dimensional wavenumber-frequency spectrum function corresponding to the aligned space-retarded time covariance of T_{ij}. The frequency of the sound, ω, is the same as in the turbulence, and the wavenumber vector of the sound, $\boldsymbol{k} = -\omega\boldsymbol{x}/xc_\infty$, equals the wavenumber vector in the turbulence. In near incompressible flow, where the wavelength of sound is large, $|\boldsymbol{k}| \to 0$. In the turbulence small values of k_x receive contributions from all scales of turbulence.

The total acoustic power per unit volume of turbulence is found by integrating the intensity per unit volume at the given source position, $\boldsymbol{y}$, over a large spherical surface so that for isotropic turbulence

$$p_s = \frac{1}{4\pi\rho_\infty c_\infty^5} \int \frac{\partial^4}{\partial\tau^4} P_{xx,xx}(\boldsymbol{y},\boldsymbol{r},\tau)d^3\boldsymbol{r}. \qquad (11)$$

When the acoustic sources are in uniform motion with the eddy convection speed, V_c, and the space-retarded time covariance of T_{ij} is measured in the moving frame, where the moving coordinates are defined by

$$\boldsymbol{\eta} = \boldsymbol{y} - c_\infty\boldsymbol{M}_c\tau \qquad (12)$$

such that the source emits as it crosses the fixed point $\boldsymbol{y}$ at time $t = \tau$, the spectral density of the sound intensity per unit volume is given from the Lighthill-Ffowcs Williams eddy convection theory (1963) in the form

$$i(\boldsymbol{x},\omega) = \frac{\pi\omega^4}{2x^2\rho_\infty c_\infty^5} P_{xx,xx}(\boldsymbol{y},\boldsymbol{k},\omega_T). \qquad (13)$$

$\boldsymbol{M}_c = \boldsymbol{V}_c/c_\infty$ is the vector convection Mach number. The radiated sound in the far-field at frequency, ω, arises from turbulence in the moving frame with frequency, ω_T, which is the *Döppler* shifted frequency, with $\omega_T = \omega(1 - \boldsymbol{M}_c\cdot\boldsymbol{x}/x)$. The wavenumber in the turbulence, $\boldsymbol{k} = -\omega\boldsymbol{x}/xc_\infty$, and is unaffected by the eddy motion. When the direction to the far-field is near the Mach wave direction, where normal to the

Mach wave ($\boldsymbol{M}_c \cdot \boldsymbol{x}/x = 1$), detailed analysis shows that the relation between the frequencies in the turbulence and that of the radiated sound becomes

$$\omega_T = \omega \left(|1 - \boldsymbol{M}_c \cdot \boldsymbol{x}/x|^2 + S_T^2 M_T^2 \right)^{1/2} \tag{14}$$

where S_T and $M_T = v_T/c_\infty$ are respectively the characteristic Strouhal number and Mach number of the turbulence. The reference Strouhal number of the turbulence, which we assume to be a constant throughout a given turbulent flow and is of order unity, is defined by $S_T = \Omega L/v_T$, where L is the local integral scale of the turbulence and Ω is the reference frequency in the turbulence. The reference turbulent velocity is given as $v_T = \sqrt{2K/3}$, where K is the local kinetic energy of the turbulence. In isotropic turbulence v_T is equal to $\sqrt{<u^2>}$, where u is the velocity component in any direction.

The corresponding result for the intensity per unit volume, found by integrating (13) over all frequencies, is

$$i(\boldsymbol{x}) = \frac{1}{16\pi^2 x^2 \rho_\infty c_\infty^5} \left(|1 - \boldsymbol{M}_c \cdot \boldsymbol{x}/x|^2 + S_T^2 v_T^2/c_\infty^2 \right)^{-5/2} \int \frac{\partial^4}{\partial \tau^4} P_{xx,xx}(\boldsymbol{y},\boldsymbol{\delta},\tau)) d^3\boldsymbol{\delta} \tag{15}$$

where $\boldsymbol{\delta}$ is the separation distance in the moving frame and τ is the corresponding retarded time difference, showing the preferential direction for sound radiation in the downstream direction of the convecting eddies with a sharp peak in the direction normal to the Mach angle when the eddy convection Mach number is supersonic.

2.1.2 The specific noise power in heated isotropic turbulence

We will assume the turbulence has a uniform density, ρ_0, and ratio of specific heats, γ_0, compared with the ambient medium values of ρ_∞, and γ_∞. The mean pressure in the turbulent flow is assumed equal to that of the external medium. We found above there were three dominant source terms in Lighthill's aligned stress tensor, T_{xx}, and if we further assume they are statistically independent, we find their separate contributions to the radiated sound power are in the case of stationary isotropic turbulence at rest

$$p_s^{(1)} = \frac{1}{4\pi} \frac{\rho_0^2 u^8 S_T^4}{\rho_\infty c_\infty^5 L} \int \frac{\partial^4}{\partial \tau^4} \frac{<(u_x)_A^2 (u_x)_B^2> - <u^2>^2}{<u^2>^2} d^3\boldsymbol{r} \tag{16}$$

$$p_s^{(2)} = \frac{1}{4\pi} \frac{\rho_0^2 u^8 S_T^4}{\rho_\infty c_\infty^5 L} \frac{(\gamma_0 - 1)^2}{4} \int \frac{\partial^4}{\partial \tau^4} \frac{<v_A^2 v_B^2> - <v^2>^2}{<u^2>^2} d^3\boldsymbol{r} \tag{17}$$

$$p_s^{(3)} = \frac{1}{4\pi} \frac{\rho_0^2 u^6 S_T^4}{\rho_\infty c_\infty^3 L} \left(\frac{\gamma_0 - 1}{\gamma_\infty - 1} \right)^2 \int \frac{\partial^4}{\partial \tau^4} \frac{<(u_x)_A (h')_A (u_x)_B (h')_B> - <u_x h'>^2}{<u^2> h_\infty^2} d^3\boldsymbol{r} \tag{18}$$

where v and h' are respectively the fluctuation of the velocity and enthalpy, and $< .. >$ denotes a mean value. Suffixes $\boldsymbol{A}$ and $\boldsymbol{B}$ denote the two source positions, distance $\boldsymbol{r}$ apart, forming the respective space-retarded time covariances.

Let us consider the evaluation of the aligned velocity squared space-retarded time covariance that appears in $p_s^{(1)}$ in (16).

$$P_{xx,xx}^{(1)}(\boldsymbol{r}) = <(u_A^2 u_B^2 - <u^2>^2)>.$$ (19)

Now this fourth-order isotropic tensor can be shown to be a function of the longitudinal and lateral velocity squared covariances which are functions of r only. When the turbulence follows Gaussian statistics, as assumed by Proudman (1952), we find according to Millionshtchikov's hypothesis as given by Batchelor (1953) that the velocity squared covariances can be replaced by the sum of the squares of the corresponding second order covariances involving $f(r)$ and $g(r)$ where the second order longitudinal and lateral covariances are respectively

$$\overline{u_p(\boldsymbol{x})u_p(\boldsymbol{x}+\boldsymbol{r})} = u^2 f(r)$$ 20)

and

$$\overline{u_n(\boldsymbol{x})u_n(\boldsymbol{x}+\boldsymbol{r})} = u^2 g(r).$$ (21)

Lighthill (1992) has shown more generally that the fourth- order longitudinal velocity covariance

$$\overline{(u_p(\boldsymbol{x})^2 u_p(\boldsymbol{x}+\boldsymbol{r})^2} - <u^2>^2 = \left(\overline{u_p(\boldsymbol{x})u_p(\boldsymbol{x}+\boldsymbol{r})}\right)^2 \left(\frac{\overline{u^4}}{\overline{u^2}^2} - 1\right),$$ (22)

and a similar relation holds for the fourth-order lateral covariance by replacing the suffix, p, by the suffix, n. The relationship between the respective fourth and second-order covariances holds for the given retarded time difference, τ. The velocity flatness factor, $T_1 = \overline{u^4}/\overline{u^2}^2$ has the value 3 in Gaussian statistics, and is found by Townsend (1956) to be nearly 3 in decaying isotropic turbulence. A similar result was obtained in the (DNS) results of Sarkar and Hussaini (1993) and Dubois (1993).

In weakly compressible flows, the turbulent Mach number is very small, and in this case we may assume that the modulus of the wave-number $\boldsymbol{k}$ in the turbulence is small also. In terms of the longitudinal velocity correlation function, $f(r,\tau)$, the contribution to the acoustic power spectral density is

$$p_s^{(1)}(\omega) = \frac{\rho_\infty \omega^4 <u^2>^2 (T_1 - 1)}{c_\infty^5} \frac{2}{15\pi} \int_0^\infty \cos\omega\tau d\tau \int_0^\infty r^4 \left(\frac{\partial f}{\partial r}\right)^2 dr.$$ (23)

as given by Lilley (1994). The integrals in (23) can only be evaluated when the distribution $f(r,\tau)$ is known.

Lilley (1994) used the (DNS) databases obtained by Sarkar and Hussaini (1993), Dubois (1993) and the (DNS) and (LES) databases obtained by Witkowska (1994) to obtain the spatial and temporal covariances. Thus using the data derived from these database the value of the Proudman constant, $\alpha_P^{(1)}$, in

$$p_s^{(1)} = \alpha_P^{(1)} \frac{\rho_0 u^8}{\rho_\infty c_\infty^5 L}$$ (24)
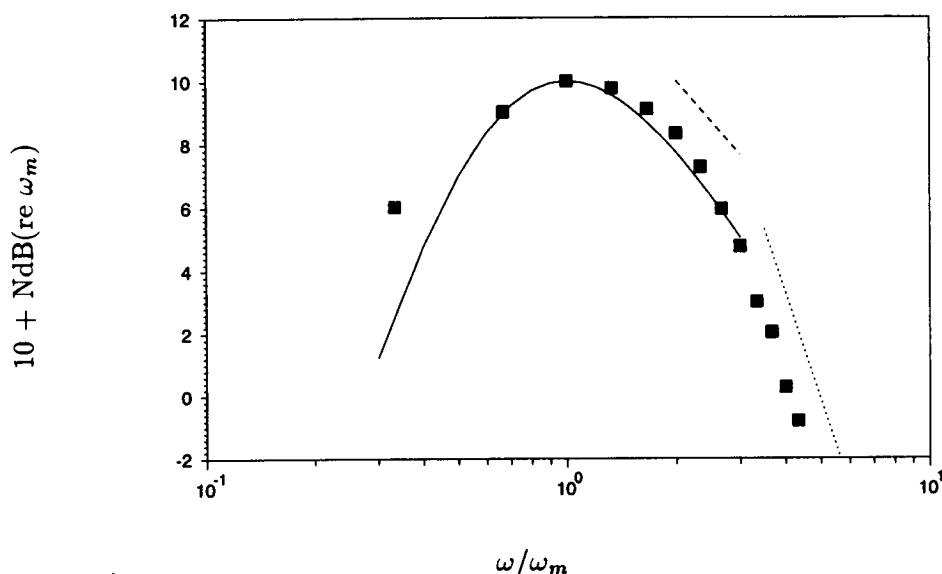
FIGURE 1. Acoustic energy spectrum in isotropic turbulence. Sarkar & Hussaini (1993) ∎ : ———— $(\omega/\omega_m)^4/(1 + 2(\omega/\omega_m)^2)^3$: – – – – $\omega^{-4/3}$: ········ $\omega^{-7/2}$

becomes

$$\alpha_P^{(1)} = 1.80(T_1 - 1)S_T^4. \tag{25}$$

When the flatness factor, $T_1 = 3$, as discussed above, and the reference Strouhal number, $S_T = 1$, we find the Proudman constant, $\alpha_P^{(1)} = 3.6$. The available (DNS) databases gave values of S_T between 1 and 1.25. The temporal covariance was checked between the (DNS) space-time covariance results of Dubois (1993) and the far-field acoustic spectra obtained by Sarkar and Hussaini (1993).

These results are for low Reynolds numbers and low Mach numbers, and there are doubts as to their applicability to higher Reynolds numbers and Mach numbers. The low Reynolds numbers of the (DNS) data precludes the existence of an inertial subrange and there is less than a decade of separation between wavenumbers in the energy-containing and Taylor microscale ranges of eddies. The peak frequency of the radiated noise is at a frequency slightly higher than that of the energy containing eddies. This suggests that the dominant eddies responsible for the generation of sound are slightly smaller than those in the energy containing range. This is consistent with the deductions of Lighthill and Proudman. At high Reynolds numbers all simplified models of turbulence along with dimensional analysis suggest it is the eddies of scales close to the energy containing range which are responsible for the bulk of the sound generation. In a recent paper Zhou and Rubinstein (1995) consider the noise radiated from the turbulent inertial subrange and find that the temporal correlations derived by Lilley (1994) are consistant with the sweeping hypothesis of Kraichnan (1964), and Praskovsky *et al.* (1993), involving a nonlocal property of the energy containing eddies. Zhou *et al.* deduce that the noise power generated

at high Reynolds numbers should have a spectral decay of $\omega^{-4/3}$. The current low Reynolds number database as shown in Fig. 1 suggests the decay law is of order ω^{-2} over a wide range of frequencies before falling exponentially in the dissipation range, although near the energy containing range the spectral decay does follow the $(\omega/\omega_m)^{-4/3}$ law. Zhou *et al.* also show, at high Reynolds numbers, the straining hypothesis would lead to a spectrum of radiated noise, in the inertial subrange of $(\omega/\omega_m)^{-7/2}$. If we compare these results with the output from the DNS data, noting an inertial subrange barely exists at these low Reynolds numbers, we find from Fig. 1 this law could only exist at much higher wavenumbers. However Zhou *et al.* show the assumptions made by Proudman (1952) lead to results for the acoustic power output consistant with the straining hypothesis, whereas the assumptions made by Lilley (1994) are more consistant with the sweeping hypothesis.

In addition Zhou *et al.* (1995) have examined a large databank of high Reynolds number atmospheric and windtunnel turbulence data at around the peak and higher wavenumbers to derive values of the incompressible fourth-order space time covariance and so find values for the Proudman constant using the formulas derived by Lilley (1994) and discussed above. Although this data is largely for anisotropic turbulence it is regarded as a useful guide to the Reynolds number dependence of the integral properties of isotropic turbulence which govern noise generation and its acoustic power. The calculated value of the Proudman constant obtained by Zhou *et al.* (1995) is within the range found by Lilley (1994), based on the databases described above, suggesting there is only a weak dependence on Reynolds number.

The contribution $p_s^{(2)}$ can be combined with $p_s^{(1)}$ and their combined contribution is similar to that when enthalpy fluctuations are absent. In the evaluation of $p_s^{(3)}$ we need the value of the fourth-order covariance $< (u_x h')_A (u_x h')_B >$. If we assume Gaussian statistics and impose Millionshtchikov's hypothesis, and noting that in isotropic turbulence $< u_x h' >$ is zero in incompressible flow,

$$< (u_x h')_A (u_x h')_B - < u_x h' >^2 >\approx< (u_x)_A (u_x)_B >< (h')_A (h')_B > . \qquad (26)$$

On the assumption that the non-dimensional correlation function for the enthalpy fluctuations is equal to $f(r, \tau)$, then the acoustic power spectral density arising from $p_s^{(3)}$, is similar to that arising from $p_s^{(1)}$ and $p_s^{(2)}$. We find that

$$p_s^{(3)} = \frac{4\sqrt{2}}{\pi} \frac{\rho_0^2 u^6 S_T^4}{\rho_\infty c_\infty^3 L} \frac{< (h')^2 >}{h_\infty^2} \frac{(\gamma_0 - 1)^2}{(\gamma_\infty - 1)^2} . \qquad (27)$$

Our final values for the two terms in the contributions to the acoustic power output are

$$p_s = \alpha_P \frac{\rho_0^2}{\rho_\infty} \frac{u^8}{c_\infty^5 L} + \alpha_H \frac{\rho_0^2}{\rho_\infty} \frac{u^6}{c_\infty^3 L} \qquad (28)$$

where

$$\alpha_P = \frac{4\sqrt{2}}{\pi} (T_1 - 1) S_T^4 \left(1 + \frac{3(\gamma_0 - 1)^2}{4} \right) \qquad (29)$$

and

$$\alpha_H = \frac{4\sqrt{2}}{\pi} \left(\frac{\gamma_0 - 1}{\gamma_\infty - 1} \right)^2 S_T^4 \frac{<(h')^2>}{h_\infty^2}. \tag{30}$$

We find that the term involving the enthalpy fluctuations generates acoustic power proportional to u^6 and hence dominates over the u^8 contribution at low Mach numbers. These results show that, typically, the dipole contribution equals the quadrupole contribution when $M_T = 0.28$.

2.2 The acoustic power from a heated jet

The physical process of noise generation in the mixing region of a jet is assumed similar to that in isotropic turbulence. However the turbulence is now anisotropic and inhomogeneous and is dependent on the mean rate of strain. Its Reynolds stress tensor contains both shear and normal stress components. Nevertheless with respect to the principal axes of stress only the direct stresses act. The sum of these enables us to find the local values of the average kinetic energy of the turbulence. The turbulence intensity is assumed proportional to the velocity difference across the shear layer. In the fully developed mixing region of a jet, the turbulent intensity depends on the velocity difference between the center-line velocity of the jet, which decays with downstream distance, and the external velocity. The integral scale of the turbulence is assumed to be proportional to the local width of the mixing region based on the vorticity thickness where the mean flow growth is governed by entrainment and the mean shear. The intense turbulence is found to exist near the center of the mixing region. The turbulence is intermittent, but a useful model is to assume the average properties of the turbulence are approximately uniform over the mean vorticity thickness of the jet and zero outside. The average convection speed, V_c, of the main energy-containing eddies in a turbulent mixing region over a wide range of different gases, velocities, and temperatures can be obtained from the work of Papamoshou and Roshko (1988). For the mixing region of an unheated jet near the nozzle exit, V_c is about $0.58V_j$. With these properties we may assume the turbulence is quasi-isotropic having a mean convection speed, V_c. In the model used here we have neglected the orientation of the principal axes of strain to the mean convection direction and its effect on the noise directivity.

The radiated noise to the far-field of a mixing region is estimated based on the hypothesis that the fourth order space-retarded time covariance has similar properties in shear flow turbulence as in isotropic turbulence, apart from changes in the scales of length and velocity. The local reference turbulent velocity, based on the local kinetic energy, and a local reference integral length scale, corresponding to the scale of the energy containing eddies, are defined at each section of the mixing region or jet. The spectrum of turbulence is assumed to be similar to that of isotropic turbulence but with the frequency of the peak energy, ω_m, proportional to the mean velocity gradient. The turbulent Strouhal number, S_T, in the case of the mixing region, is of order 1.7 when based on the values used for the peak frequency and the reference velocity and length scales.

In the jet mixing region it is assumed that since the turbulent Mach number is small we may neglect the effect of density fluctuations on the noise generated even

in the case of the heated jet. We further assume the mean density to be a constant across the mixing region at any station downstream of the nozzle exit with a value based on the density at the position where the local mean velocity is equal to the mean convection speed. The mean flow is assumed to be self-preserving and the mean density, temperature, stagnation enthalpy, and velocity profiles are calculated throughout the flow using a simple eddy viscosity model. In this model the equations of momentum and total enthalpy are similar and hence the mean velocity is a linear function of the mean total enthalpy. The reference density, compatible with the convection speed, is then determined at each downstream station. The effects of turbulence convection can be applied using the Lighthill-Ffowcs William (1963) theory of convective amplification.

2.2.1 *The noise power from heated jets and comparison with experimental data*

The total acoustic power radiated from a circular heated jet can be evaluated from the results for isotropic turbulence with the modifications discussed above to allow for the effects of anisotropy, mean density variation, and convection. The present theory does not address the acoustic power from supersonic jets when shock waves are present and the 'mixing region' noise is augmented by shock-cell noise and 'screech'.

The contributions to the acoustic power are integrated over the complete volume of the flow. A large number of flow parameters must however be specified. These include the jet exit Mach number and temperature, the flight Mach number, and the corresponding convection Mach number. Also required is the corresponding mean jet exit density and enthalpy ratios, the length of the potential core, the growth of the jet in the initial mixing region and far downstream, the mean turbulent intensity and its law of decay, and the ratio of the integral turbulence scale to the local jet width. All these parameters are functions of the jet exit Mach number and the ratio of the jet to flight Mach numbers. For the hot jet we require the mean square of the enthalpy fluctuations. Due to the near linear increase in the turbulent integral length scales in the jet mixing region with downstream distance, we find the dominant frequency of the noise generation decreases inversely proportional to distance from the nozzle exit. Thus the radiated noise spectrum reflects more the peak energy contributions in the local noise spectra than the contributions from all frequencies in the local spectra. A consequence is the radiated noise spectrum of a jet increases as ω^2 before the peak frequency and then falls as ω^{-2}. The proof of this simplification in the pattern of the noise generation from a jet rests in the detailed comparison between the far-field noise polar correlation measurements made by Fisher *et al.* (1977) on model and full-scale jet engines and the corresponding predictions made by Lilley (1991), using Lighthill's acoustic analogy with a jet noise model similar to that described above.

Comparison of the present results with experimental data is also shown in Figs. 2 and 3. The results show the correct trends for the heated jet at low Mach numbers and the changes in the acoustic power in the upper end of the subsonic jet Mach number range and at supersonic speeds for the fully expanded jet. In these figures A_j and V_j are respectively the jet exit area and speed. $M_j = V_j/c_\infty$ is the so-called
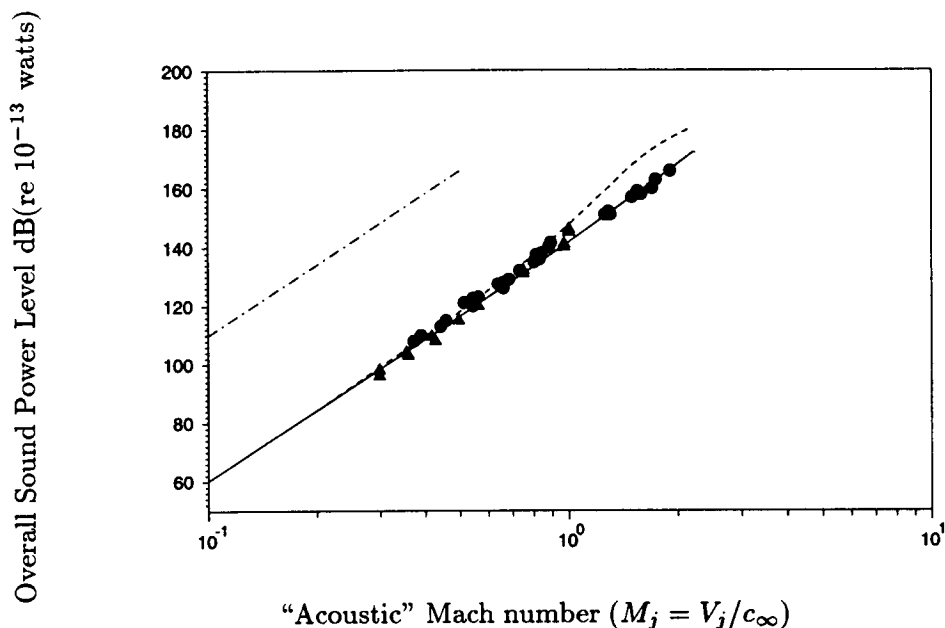
FIGURE 2. Overall noise power for cold jets. $A_j = 0.000507m^2$. ---- neglects refraction: ——— Lighthill-Ffowcs Williams with refraction: —·— V_j^8: ▲ Lush (1971): ● Olsen *et al.* (1973)

"acoustic" Mach number.

An easily observable influence of flow-acoustic interaction occurs at high frequencies, where the sound waves propagating through the flow at small angles to the flow direction are refracted by the flow, resulting in a near zone of silence in the high frequencies close to the jet boundary as shown in Fig. 4. The present results shown in Figs. 2 and 3 include the elementary effects of refraction. The theory of flow-acoustic interaction, which embraces the effects of refraction, is discussed in Goldstein (1978), and in the discussion on the detailed DNS calculations of Colonius *et al.* (1995) on the vortex pairing phenomenon in mixing layers. An important consequence of the phenomenon of flow-acoustic interaction is the result that the far-field observer "hears what is seen".

3. Future plans

The present paper concerns the noise power per unit volume from near incompressible isotropic turbulence based on the fourth-order space-retarded time covariance of T_{ij}. These results are extended analytically to the case of heated turbulence on the assumption that for turbulent Mach numbers, based on the root mean square value of the turbulent velocity and the ambient speed of sound, less than 0.3, the effects of density fluctuations in the turbulence on the noise generated can be neglected. A hypothesis is then introduced whereby the non-dimensional form of the isotropic fourth-order space-retarded time covariance of T_{ij} is used as an input to compute the noise power from a heated circular jet at subsonic and supersonic
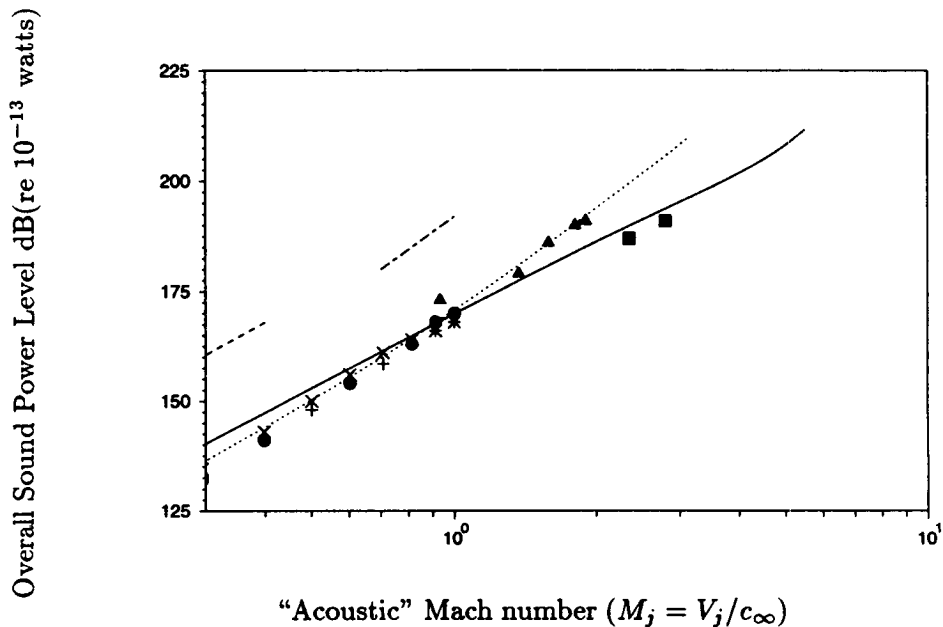
FIGURE 3.   Overall noise power for hot jets of various enthalpy ratios h_{sjet}/h_∞. $A_j = 1.0m^2$.: Exps. Hoch *et al.* (1973): × 1.2: + 1.4: • 1.7: Tanna (1977) ▲ 2.0: ■ 6.25: Theory ········ 2.0: ——— 6.25. ---- V_j^6: —·— V_j^8
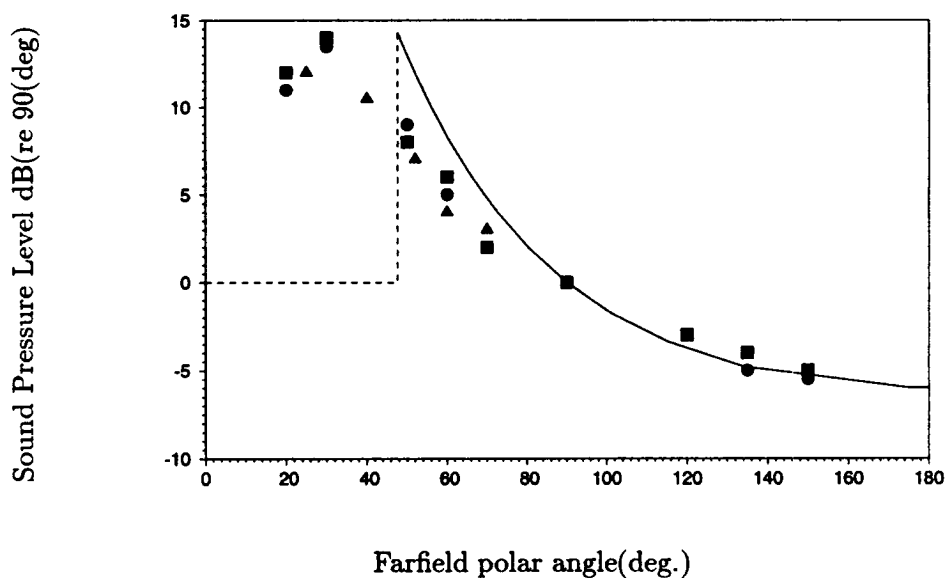
FIGURE 4. Directivity of jet noise. Exps. Lassiter & Hubbard (1952) ■ : Westley & Lilley ○ : Fitzpatrick & Lee ▲ : Lighthill-Ffowcs Williams with refraction ——— : Zone of silence ----

speeds, when the jet is fully expanded and no shocks are present. The results are compared with subsonic and supersonic noise measurements covering a wide range of Mach numbers and jet to ambient temperature ratios. Fair agreement is obtained, but of greater importance is the fact that the trends in noise power prediction for the heated jet based on Lighthill's theory, but including the effects of refraction, is verified by this comparison with experiment. Without the input from the DNS database, this work would not have been possible.

Future work should include new evaluations of the fourth- order space retarded time covariance of T_{ij} in heated isotropic turbulence, in compressible mixing regions, and in jets at subsonic and supersonic speeds. Current DNS and LES mixing region databases could be used as a start for these evaluations, but further work, using LES, is needed to generate the corresponding data for the jet. To find the changes with jet Mach number and temperature on the total volume and amplitude of the noise producing acoustic sources, it will be necessary to use two-equation RANS calculations of the compressible circular jet covering a wide range of velocity and temperature differences between the jet and the uniform external medium. There is also need to extend the present work on flow-acoustic interaction to include its effects at higher Reynolds numbers on the turbulent jet over a range of jet Mach numbers and temperatures.

REFERENCES

BATCHELOR, G. K. 1953 *The theory of homogeneous turbulence.* Cambridge University Press.

COLONIUS, T., LELE, S. K. & MOIN, P. 1995 Sound generation in a mixing layer. Part 1: A comparison of direct numerical simulations with an acoustic analogy, and Part 2: The nature of the acoustic sources and the far field directivity. *To be published in J. Fluid Mech.*

DUBOIS, T. 1993 Private communication. (Also see A.Debussche, T.Dubois and R.Temam, "The nonlinear Galerkin method: A multi-scale method applied to the simulation of homogeneous turbulent flows." ICASE Rep. 93/93.

FFOWCS WILLIAMS, J. E. 1963 The noise from turbulence convected at high speed. *Phil Trans Roy. Soc. (A).* **255**, 469-503.

FISHER, M. J., HARPER-BOURNE, M.& GLEGG, S. A. L. 1977 Jet engine noise source location: The polar correlation technique. *J. Sound Vib.* **51**, 23-54.

FITZPATRICK, H. M. & LEE, R. 1952 Measurements of the noise radiated from subsonic jets. *David W. Taylor Model Basin, Navy Dept.* **835.**

GOLDSTEIN, M. E. 1976 *Aeroacoustics.* McGraw-Hill.

HOCH, R.,DUPONCHEL, J. P.,COCKING,B.J. & BRYCE, W. D. 1973 Studies of the influence of density on jet noise. *J. Sound Vib.* **28**, 649-688.

KRAICHNAN, R. H. 1964 Kolmogorov's hypotheses and Eulerian turbulence theory. *Phys. Fluids.* **7**, 1723-1734.

LASSITER, L. W.& HUBBARD, H. H. 1952 Experimental studies of the noise from subsonic jets in still air. *NACA TN.* **2757.**

LIGHTHILL, M. J. 1952 On sound generated aerodynamically: 1. General theory. *Proc. Roy. Soc. (A).* **211,** 564-587.

LIGHTHILL, M. J. 1954 On sound generated aerodynamically: 2. Turbulence as a source of sound. *Proc. Roy. Soc. (A).* **222,** 1-32.

LIGHTHILL, M. J. 1962 Sound generated aerodynamically. The Bakerian Lecture. *Proc. Roy. Soc. (A).* **267,** 147-182.

LIGHTHILL, M. J. 1963 Jet noise. The Wright Brothers Lecture. *AIAA Journal.* **1,** 1507-1517.

LIGHTHILL, M. J. 1978. *Waves in Fluids.* Cambridge University Press.

LIGHTHILL, M. J. 1992 An estimate of the covariance of T_{xx} without using statistical assumptions, *see Appendix 1 of "On the noise radiated from a turbulent high speed jet," by G. M. Lilley in "Computational aeroacoustics" by J.C . Hardin and M. K. Hussaini.* Springer Verlag.

LILLEY, G. M. 1973 On the noise from air jets, *in Noise Mechanisms. AGARD CP.* **131,** 13.1-13.12.

LILLEY, G. M. 1991 Jet noise: Classical theory and experiments, *in Aeroacoustics of flight vehicles: Theory and Practice. Vol. 1: Noise Sources.* NASA Ref. Pub. **1258,** 211-289.

LILLEY, G. M. 1994 The radiated noise from isotropic turbulence. *Theoretical and Computational Fluid Dynamics.* **6,** 281-301.

LUSH, P. A. 1971 Measurements of subsonic jet noise and comparison with theory. *J. Fluid Mech.* **46,** 477-500.

OLSEN, W. A., GUTIERREZ, O. A. & DORSCH, R. G 1973 Experimental studies of the noise from subsonic jets in still air. *NASA TM X.* **68182.**

PAPAMOSCHOU, D. & ROSHKO, A. 1988 The compressible turbulent shear layer: an experimental study. *J. Fluid Mech.* **197,** 453-477.

PRASKOVSKY, A., GLEDZER, E., KARYAKIN, M.& ZHOU, Y. 1993 Sweeping decorrelation hypothesis and energy- inertial scale interaction in high Reynolds number flows. *J. Fluid Mech.* **248,** 493-571.

PROUDMAN, I. 1952 The generation of noise by isotropic turbulence. *Proc. Roy. Soc. (A).* **214,** 119-132.

SARKAR, S.& HUSSAINI, M. K. 1993 Computation of the sound generated by isotropic turbulence. *ICASE Rep.* **93-74.**

TANNA, H. K. 1977 An experimental study of jet noise Part 1:Turbulent mixing noise. *J.Sound Vib.* **50,** 405-428.

TOWNSEND, A. A. 1956 *The structure of turbulent shear flow.* Cambridge University Press.

WESTLEY, R. & LILLEY, G. M. 1952 An investigation of the noise from a small jet and methods for its reduction. *College of Aeronautics Cranfield.* **53.**

WITKOWSKA, A. 1994 *Estimation numérique du bruit rayonné par une turbulence isotrope.* Thése L'École Centrale de Lyon.

ZHOU, Y. & RUBINSTEIN, R. 1995 Sweeping and straining effects in sound generation by high Reynolds number isotropic turbulence. *To be published.*

ZHOU, Y., PRASKOVSKY, A.& ONCLEY, S. 1995 On the Lighthill relationship and sound generation in isotropic turbulence. *Theor. Comput. Fluid Dyn.* **7,** 355-361.

Aerodynamic sound of flow past an airfoil

By Meng Wang

1. Motivation and objectives

The long term objective of this project is to develop a computational method for predicting the noise of turbulence-airfoil interactions, particularly at the trailing edge. We seek to obtain the energy-containing features of the turbulent boundary layers and the near-wake using Navier-Stokes Simulation (LES or DNS), and then to calculate the far-field acoustic characteristics by means of acoustic analogy theories, using the simulation data as acoustic source functions.

Two distinct types of noise can be emitted from airfoil trailing edges. The first, a tonal or narrowband sound caused by vortex shedding, is normally associated with blunt trailing edges, high angles of attack, or laminar flow airfoils. The second source is of broadband nature arising from the aeroacoustic scattering of turbulent eddies by the trailing edge. Due to its importance to airframe noise, rotor and propeller noise, etc., trailing edge noise has been the subject of extensive theoretical (e.g. Crighton & Leppington 1971; Howe 1978) as well as experimental investigations (e.g. Brooks & Hodgson 1981; Blake & Gershfeld 1988).

A number of challenges exist concerning acoustic analogy based noise computations. These include the elimination of spurious sound caused by vortices crossing permeable computational boundaries in the wake, the treatment of noncompact source regions, and the accurate description of wave reflection by the solid surface and scattering near the edge. In addition, accurate turbulence statistics in the flow field are required for the evaluation of acoustic source functions.

Major efforts to date have been focused on the first two challenges. To this end, a paradigm problem of laminar vortex shedding, generated by a two dimensional, uniform stream past a NACA0012 airfoil, is used to address the relevant numerical issues. Under the low Mach number approximation, the near-field flow quantities are obtained by solving the incompressible Navier-Stokes equations numerically at chord Reynolds number of 10^4. The far-field noise is computed using Curle's extension to the Lighthill analogy (Curle 1955). An effective method for separating the physical noise source from spurious boundary contributions is developed. This allows an accurate evaluation of the Reynolds stress volume quadrupoles, in addition to the more readily computable surface dipoles due to the unsteady lift and drag. The effect of noncompact source distribution on the far-field sound is assessed using an efficient integration scheme for the Curle integral, with full account of retarded-time variations. The numerical results confirm in quantitative terms that the far-field sound is dominated by the surface pressure dipoles at low Mach number. The techniques developed are applicable to a wide range of flows, including jets and mixing layers, where the Reynolds stress quadrupoles play a prominent or even dominant role in the overall sound generation.

2. Accomplishments

2.1 Aeroacoustic theory

The density fluctuations due to acoustic wave propagation from a stationary aerodynamic source region into a uniformly moving medium is governed by, in dimensionless form (Goldstein 1976),

$$\left[\left(\frac{\partial}{\partial t} + \frac{\partial}{\partial x_1} \right)^2 - \frac{1}{M^2} \frac{\partial^2}{\partial x_j \partial x_j} \right] \rho = \frac{\partial^2 T_{ij}}{\partial x_i \partial x_j}, \tag{1}$$

where

$$T_{ij} = \rho v_i v_j + \delta_{ij} \left(p - \frac{\rho}{M^2} \right) - \tau_{ij} \tag{2}$$

is the Lighthill stress tensor defined in terms of the fluctuating velocity relative to the free-stream value, $v_i = u_i - \delta_{i1}$, and

$$\tau_{ij} = \frac{1}{Re} \left(\frac{\partial v_i}{\partial x_j} + \frac{\partial v_j}{\partial x_i} - \frac{2}{3} \delta_{ij} \frac{\partial v_k}{\partial x_k} \right) \tag{3}$$

represents the viscous part of the Stokes stress tensor. The velocity, density, and pressure are nondimensionalized relative to the undisturbed free-stream quantities U'_∞, ρ'_∞, and $\rho'_\infty U'^2_\infty$, respectively. The spatial coordinates are normalized by the airfoil chord (or more generally, the characteristic body size) C'. The time is normalized by C'/U'_∞. Re and M denote respectively the free-stream Reynolds number based on chord and the free-stream Mach number. δ_{ij} is the Kronecker delta, and the usual summation convention applies for repeated subscripts.

Like the Lighthill equation, (1) is an exact restatement of the mass and momentum conservation equations for a compressible fluid. The use of relative velocity in the source function ensures that the Lighthill stress, predominantly the fluctuating Reynolds stress, is quadratically small outside the source region in the free-stream. One notices that, since the radiated acoustic field has a characteristic spatial scale of M^{-1} times the hydrodynamic length scale, the two spatial derivative terms on the left-hand side of (1) are of $O(M)$ and $O(1)$, respectively, relative to the time derivative term.

Ffowcs Williams and Hawkings (1969) derived a general solution for noise produced by a rigid surface moving through a quiescent medium. An exact solution to (1) is most easily obtained by rewriting the Ffowcs Williams-Hawkings equation in terms of the "reception coordinates", i.e., in a reference frame moving with the body. For low Mach number flows, however, the bulk convective effect can be ignored to first approximation, and the simpler solution owing to Curle (1955) prevails. If $\mathbf{x}$ and $\mathbf{y}$ are used to denote the position vectors of an observation point and a source element, respectively, and let $\mathbf{r} = \mathbf{x} - \mathbf{y}$ and $r = |\mathbf{r}|$, Curle shows that

$$\rho(\mathbf{x}, t) - 1 = \frac{M^2}{4\pi} \frac{\partial}{\partial x_i} \int_S \frac{n_j}{r} p_{ij}(\mathbf{y}, t - Mr) d^2\mathbf{y}$$

$$+ \frac{M^2}{4\pi} \frac{\partial^2}{\partial x_i \partial x_j} \int_V \frac{T_{ij}(\mathbf{y}, t - Mr)}{r} d^3\mathbf{y} \tag{4}$$

for a rigid body at rest. In the above equation $p_{ij} = p\delta_{ij} - \tau_{ij}$, and n_i is the directional cosine of the outward unit normal to the rigid surface S over which the surface integration takes place. The volume integral is taken over the entire unsteady flow region V external to the body. In the acoustic far-field defined by $r \gg l_e/M$, where l_e is the typical eddy size, (4) can be simplified to a form most suitable for numerical evaluation,

$$
\rho(\mathbf{x}, t) - 1 \approx \frac{M^3}{4\pi} \frac{\partial}{\partial t} \int_S \frac{r_i}{r^2} n_j p_{ij}(\mathbf{y}, t - Mr) d^2\mathbf{y}
$$
$$
+ \frac{M^4}{4\pi} \frac{\partial^2}{\partial t^2} \int_V \frac{r_i r_j}{r^3} T_{ij}(\mathbf{y}, t - Mr) d^3\mathbf{y}. \tag{5}
$$

Furthermore, if the size of the source region is small compared with one acoustic wavelength $(l_s \ll l_e/M)$, the source region can be considered acoustically compact. The far-field density can be approximated by

$$
\rho(\mathbf{x}, t) - 1 \approx \frac{M^3}{4\pi} \frac{x_i}{|\mathbf{x}|^2} \dot{D}_i(t - M|\mathbf{x}|) + \frac{M^4}{4\pi} \frac{x_i x_j}{|\mathbf{x}|^3} \ddot{Q}_{ij}(t - M|\mathbf{x}|), \tag{6}
$$

where

$$
\dot{D}_i(t) = \frac{\partial}{\partial t} \int_S n_j p_{ij}(\mathbf{y}, t) d^2\mathbf{y}, \tag{7}
$$

$$
\ddot{Q}_{ij}(t) = \frac{\partial^2}{\partial t^2} \int_V T_{ij}(\mathbf{y}, t) d^3\mathbf{y}. \tag{8}
$$

2.2 Exit boundary correction

In the application of Curle's integral solution, the surface integral, taken over the finite airfoil surface, is well defined. The same cannot be said, however, regarding the volume integral, as the unsteady flow region is often truncated in the wake by the artificial computational boundary (cf. Fig. 1). At the outflow boundary the Lighthill stress terms are still significant, and their sudden termination are known to cause strong, spurious acoustic sources (Crighton 1993). The same difficulty has been encountered by Mankbadi *et al.* (1994) and Mitchell *et al.* (1995a) in jet noise calculations. Mitchell *et al.* employed model extensions which allow the Lighthill source terms to decay to zero slowly downstream of the computational domain. In the subsequent analysis we illustrate a simple, more systematic boundary correction procedure in which only the information at the outflow boundary is required.

The rational for outflow boundary correction is based on the observation that, despite the apparently large unsteady region which extends beyond the computational domain, the physical source of sound, associated with specific events such as the vortex generation and shedding process in the present case or the vortex pairing in Mitchell *et al.* (1995a), is captured within the domain. Downstream of the vortex-shedding region, the eddies are convected passively and are thus acoustically

silent. The boundary correction formula is derived most easily by considering compact quadrupoles evaluated in two domains of volume integration, whose boundaries coincide except at the downstream exits. The exit boundaries, normal to the flow direction, are set to be Δy_1 apart. If $\dot{Q}_{ij}^{+}$ and $\dot{Q}_{ij}^{-}$ are used to denote the first time derivative of the Lighthill stress integrals evaluated in the larger and smaller domains, respectively, one can deduce that

$$\dot{Q}_{ij}^{+}(t) \approx \dot{Q}_{ij}(t) + E_{ij}\left(t - \frac{\tau}{2}\right), \tag{9}$$

$$\dot{Q}_{ij}^{-}(t) \approx \dot{Q}_{ij}(t) + E_{ij}\left(t + \frac{\tau}{2}\right). \tag{10}$$

The common term in the two equations, $\dot{Q}_{ij}(t)$, represents the physical noise source situated within both domains, and function E_{ij} represents the boundary error caused by eddies escaping from the respective exit boundary. Since the separation between the two boundaries is very small, an eddy can be considered "frozen" as it traverses the distance Δy_1, and hence the error terms in (9) and (10) differ only by a small phase difference $\tau = \Delta y_1/U_c$, where U_c is the local eddy convection velocity. Phase-shifting (9) and (10) by $\tau/2$ and $-\tau/2$, respectively, and subtracting the latter equation from the former yield

$$\dot{Q}_{ij}\left(t + \frac{\tau}{2}\right) - \dot{Q}_{ij}\left(t - \frac{\tau}{2}\right) = \dot{Q}_{ij}^{+}\left(t + \frac{\tau}{2}\right) - \dot{Q}_{ij}^{-}\left(t - \frac{\tau}{2}\right) \tag{11}$$

or

$$\ddot{Q}_{ij}(t) \approx \frac{1}{2}\left[\ddot{Q}_{ij}^{+}(t) + \ddot{Q}_{ij}^{-}(t)\right] + \frac{1}{\tau}\left[\dot{Q}_{ij}^{+}(t) - \dot{Q}_{ij}^{-}(t)\right] \tag{12}$$

after a Taylor series expansion to $O(\tau^2)$. The first term on the right-hand side of (12) is the algebraic average of the quadrupole sources calculated from the two integration domains, whereas the second term clearly represents the desired correction at the exit boundary. It is interesting to note that the correction term involves only the first time-derivative, in contrast to the second time-derivative in the original source terms. In the numerical implementation, Δy_1 should take the smallest possible value (one mesh spacing) to ensure the validity of the frozen-eddy assumption.

Physical insight can be gained by substituting (8) into the right hand side of (12) and taking the limit as $\Delta y_1 \to 0$, noting that $\tau = \Delta y_1/U_c$. This leads to

$$\ddot{Q}_{ij}(t) = \frac{\partial^2}{\partial t^2}\int_{V_0} T_{ij}(\mathbf{y},t)\,d^3\mathbf{y} + \frac{\partial}{\partial t}\int_{S_0} U_c T_{ij}(\mathbf{y},t)\,d^2\mathbf{y}, \tag{13}$$

which shows clearly that the boundary correction to the quadrupole source calculated in a truncated domain V_0 is equivalent to the time derivative of the Lighthill stress fluxes across the exit boundary S_0, carried by the convecting eddies at velocity U_c. In other words, the net contribution from the missing acoustic source functions outside the integration domain can be approximated by a flux term evaluated on the exit surface. In the above derivation, the eddy convective velocity U_c

is assumed to be parallel to the y_1 axis, and S_0 is a plane surface perpendicular to the flow direction. If S_0 is a curved surface, the projected area normal to y_1 is used. The above formulation can be generalized to the case of noncompact sources. In the far-field, the quadrupole contribution to $\rho - 1$, denoted as ρ_q, takes the form,

$$\rho_q(\mathbf{x}, t) = \frac{M^4}{4\pi} \left\{ \frac{\partial^2}{\partial t^2} \int_{V_0} \frac{r_i r_j}{r^3} T_{ij}(\mathbf{y}, t - Mr) \, d^3\mathbf{y} \right.$$
$$\left. + \frac{\partial}{\partial t} \int_{S_0} \frac{r_i r_j}{r^3} U_c T_{ij}(\mathbf{y}, t - Mr) \, d^2\mathbf{y} \right\}. \tag{14}$$

In aeroacoustic problems whose solutions are known to be time periodic, it is customary to conduct calculations in the frequency domain (e.g., Mankbadi *et al.* 1994; Mitchell et al. 1995a). The corresponding quadrupole noise with a boundary correction can be easily obtained by taking the Fourier time transform of (14),

$$\hat{\rho}_q(\mathbf{x}, \omega) = -\frac{M^4}{4\pi} \left\{ \omega^2 \int_{V_0} \frac{r_i r_j}{r^3} \hat{T}_{ij}(\mathbf{y}, \omega) e^{iM\omega r} d^3\mathbf{y} \right.$$
$$\left. + i\omega \int_{S_0} \frac{r_i r_j}{r^3} U_c \hat{T}_{ij}(\mathbf{y}, \omega) e^{iM\omega r} d^2\mathbf{y} \right\}. \tag{15}$$

Again, the corrective surface term accounting for the effect of escaping eddies is simple and readily computable along with the volume integral. The derivation, on the other hand, would be less straightforward if it were carried out in the frequency domain where the physical significance of the boundary correction is not as obvious.

2.3 Model problem

2.3.1 Near-field simulation

We consider the unsteady flow field and the sound generated by a NACA0012 airfoil placed in a 2-D uniform flow at chord Reynolds number $Re = 10^4$ and two angles of attack: $\alpha = 5°$ and $\alpha = 8°$. In the spirit of Lighthill's analogy, the acoustic source functions can be determined from an incompressible flow approximation, given that the compressibility effect is of $O(M^2)$. A finite-difference code developed by Choi (1993) is used to solve the incompressible Navier-Stokes and continuity equations numerically in a generalized coordinate system. Second-order central difference is used for spatial discretization on a staggered grid. The time advancement is of the fractional-step type, in combination with the Crank-Nicolson method for viscous terms and the third order Range-Kutta method for convective terms. The Poisson equation for pressure is solved using a multi-grid iterative procedure.

Computations are carried out on a C-type mesh configuration with a total of 896 by 104 mesh cells. The simulations are run with a time step $\Delta t = 2.3 \times 10^{-3}$. No-slip velocity conditions are imposed on the airfoil surface. Along the C-shaped outer boundary, approximately three chord lengths away from the airfoil, the velocities are fixed at the free-stream values, $u_i = (1, 0)$. At the downstream boundary the
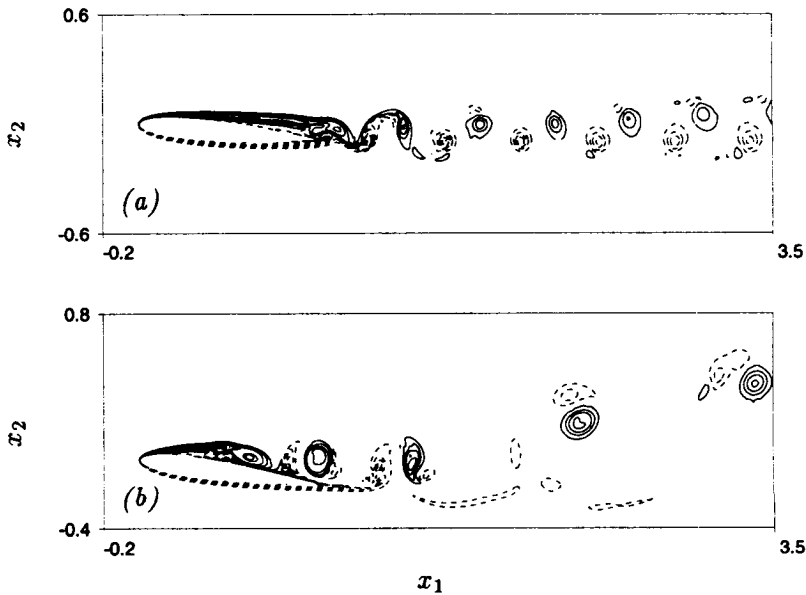
FIGURE 1.   Contours of negative vorticity $-\omega$ for 2-D laminar flows past a NACA0012 airfoil at $Re = 10^4$. (a) $\alpha = 5°$, $t = 24.5$ (contour levels from -308.0 to 804.0, increment 8.0); (b) $\alpha = 8°$, $t = 26.8$ (contour levels from -335.0 to 1175.0, increment 10.0).

convective outflow condition (Pauley *et al.* 1987) is applied to allow the vortical disturbances in the wake to leave the computational domain smoothly.

Simulations start with uniform velocity $u_i(t = 0) = (1, 0)$ everywhere. During the initial transient period, a starting vortex is shed at the trailing edge and boundary layers develop on the upper and lower surfaces. The upper surface boundary layer soon separates. It interacts with the lower boundary layer near the trailing edge to develop a periodic vortex shedding pattern for $\alpha = 5°$, as depicted in Fig. 1a in terms of contours of negative vorticity $-\omega$ at $t = 24.5$. The same vorticity contours for $\alpha = 8°$ at $t = 26.8$ are plotted in Fig. 1b. In this case vortex shedding is initiated by the instability of the separated shear-layer near the mid-chord on the suction side. The calculated unsteady lift and drag coefficients exhibit aperiodic, perhaps chaotic oscillations with time even after an extended time lapse (~ 30 chord flow-through times). Similar behavior has been observed and analyzed in the context of nonlinear dynamics by Pulliam (1989).

2.3.2 Acoustic calculation

The simulated flow-field around the airfoil presented above is two-dimensional, implying constant properties in an infinite span. The acoustic formulation in Sections 2.1 and 2.2, on the other hand, represents three-dimensional solutions to a forced, linear wave equation, and we are interested in the acoustic waves emitted from unit span based on the above formulation. Alternatively, one could consider a strictly 2-D problem by employing a 2-D version of the acoustic analogy, which can
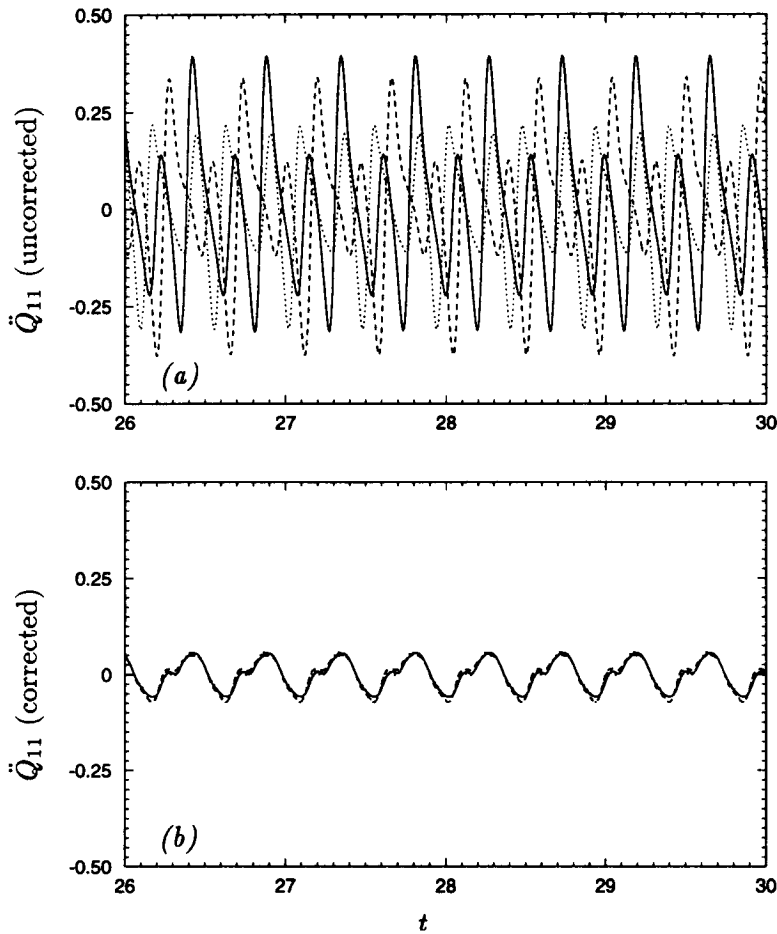
FIGURE 2. The longitudinal quadrupole $\ddot{Q}_{11}$ calculated from three different-sized source domains whose downstream boundaries are located at $x_1 \approx 2.59$ (——), 2.89 (- - - -), and 3.21 (········). The airfoil angle of attack $\alpha = 5°$ (a) Without boundary correction; (b) with boundary correction.

be derived easily by integrating the 3-D formulae along the infinite span (Mitchell *et al.* 1995b; Wang 1993). The results are, however, of less physical relevance since in practical situations involving a long span, the near-field inevitably develops three-dimensionality, and thus the phase difference between the various radiating elements along the span cannot be ignored.

To illustrate the effect of boundary correction, Figs. 2a and 2b compare the time oscillations of the compact longitudinal quadrupole $\ddot{Q}_{11}$ calculated from (13), before and after the boundary correction term is added. In the calculations, it is assumed that $T_{ij} \approx v_i v_j$, an approximation justified by the relatively large Reynolds number and small Mach number. The three curves represent evaluations based on three different sized source domains whose downstream boundaries are 20 grid points
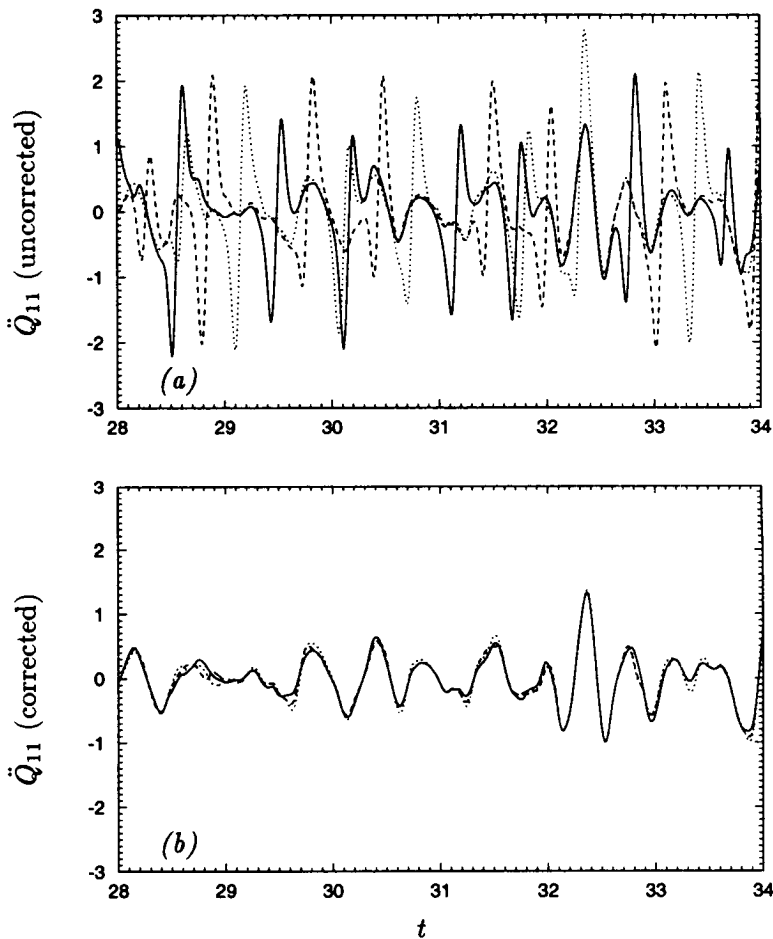
FIGURE 3.   The same as in Fig. 2, except that the airfoil angle of attack $\alpha = 8°$.

apart, located at $y_1 \approx 2.59$, 2.89, and 3.21, respectively. The primitive (uncorrected) Lighthill quadrupole, shown in Fig. 2a, is seen to exhibit a strong dependence on the downstream boundary location. After applying the corrections, the three curves are seen to converge as shown in Fig. 2b, indicating the physical noise source caused by vortex generation near the trailing edge, which is well captured within all the three integration domains. In estimating the boundary Reynolds stress fluxes, a constant convective velocity $U_c = 0.90$ is used for all the three surfaces. The corrective effects are found to be rather insensitive to the value of U_c, although a slight improvement has been observed by fine-tuning the value of U_c based on the local convective velocity on each surface. The other two quadrupole components, $\ddot{Q}_{12}$ and $\ddot{Q}_{22}$, are computed and compared in the same manner, and equally drastic reductions in boundary errors are obtained. The residual boundary error for $\ddot{Q}_{22}$ is, however, larger than those in Fig. 2 due to its larger pre-correction error magnitude.

An example of boundary corrections applied to an aperiodic source is given in

Figs. 3a and 3b. The quadrupole $\ddot{Q}_{11}$ is obtained based on the near-field simulation data for the case of $\alpha = 8°$. Again, three exit boundaries passing the same y_1 stations as in Fig. 2 are used to illustrate the dominant impact of boundary errors in the source calculation, as shown in Fig. 3a. The corrected $\ddot{Q}_{11}$ source terms in Fig. 3b, as well as the other two quadrupole components not shown in the figure, compare well despite the non-harmonic nature of the signals. This is important since the main advantage of solving aeroacoustic problems in the time domain lies in its ability to treat arbitrary, non-periodic signals. In comparison with the $\alpha = 5°$ case (cf. Fig. 2b), Fig. 3b indicates higher amplitude, lower frequency acoustic phenomena corresponding to the stronger vortices shed at a slower rate in the near-field. The eddy convective velocity U_c is found to be best approximated by 1.0.

In the event that the source integration domain is not small in comparison to the dominant acoustic wavelength, retarded-time variations in the source region become significant. The boundary corrections are applied directly to the far-field density according to (14). To examine the efficacy of this more general approach, an efficient integration-interpolation method has been developed for the evaluation of the surface and volume integrals in (5) and (14). The scheme treats each near-field computational cell or boundary element as an individual acoustic source. At each simulation time step t_n, the future time $\sigma_n = t_n + M|\mathbf{x} - \mathbf{y}|$, at which the emitted acoustic signal reaches the far-field position $\mathbf{x}$, is calculated. The scheme then locates in the discretized far-field time series the point straddled by σ_{n-1} and σ_n, and interpolates linearly on the integrands to find their contributions to the far-field density at that time. The total density history at the observation point is obtained by summing up contributions from all the source elements and simulation time steps. This procedure, which is second order accurate, uses the same time step as for the near-field simulation and requires minimal extra computer memory.

Figures 4a and 4b contrast the far-field acoustic pressure signals due to quadrupole radiation for the case of $\alpha = 5°$, evaluated in the same integration domains as in Fig. 2, before and after the boundary corrections. The fluctuating pressure ($p_q \equiv \gamma \rho_q$, renormalized by the mean free-stream value) is calculated directly from (14) with full account of the retarded time, at a given far-field position $|\mathbf{x}| = 50$, $\theta = 30°$, where θ defines the angle measured counter-clockwise from the downstream x_1 axis. The free-stream Mach number $M = 0.2$. The three p_q curves corresponding to the three different exit boundaries compare rather well after corrections are applied. The discrepancy, in the form of higher frequency oscillations, is mainly due to the T_{22} source component whose boundary effect is more difficult to eradicate.

The retarded-time effect is demonstrated in Figs. 5a and 5b for $M = 0.1$ and 0.2, respectively, by comparing the computational results with and without using the compact source approximation. The two figures again plot the quadrupole contribution to the acoustic pressure at $|\mathbf{x}| = 50$ and $\theta = 30°$, for the case of $\alpha = 5°$. The solid lines are obtained using (14), while the dashed lines are based on the compact source formulae (6) and (13). Both have been subjected to the appropriate boundary corrections. The integration domain employed is the smallest among the three used for Fig. 4. As expected, the noncompact formulation produces
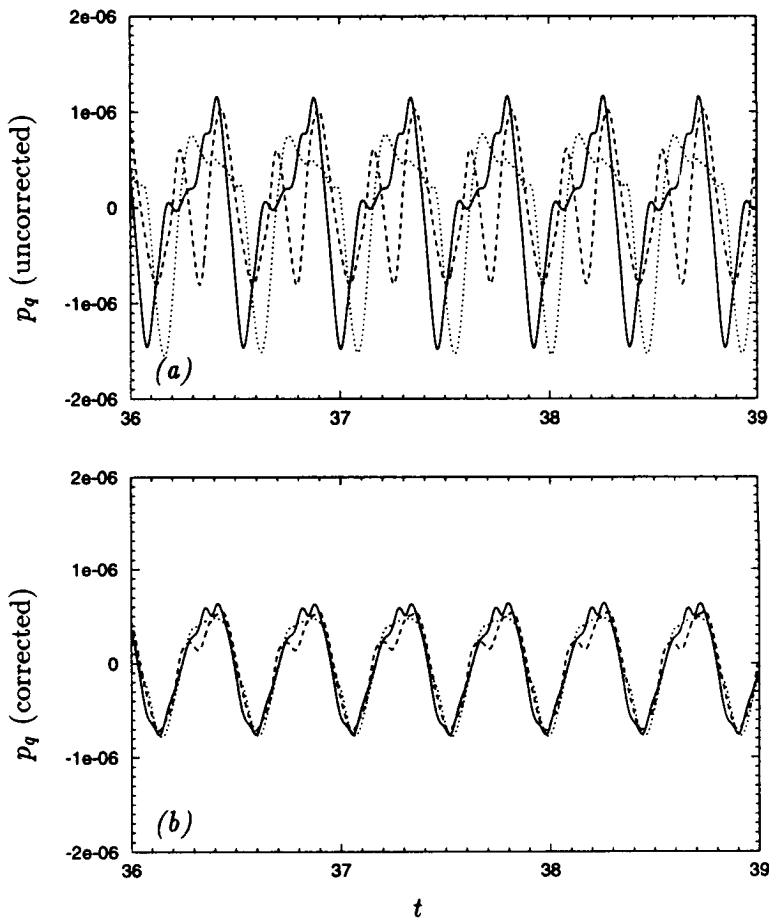
FIGURE 4. The acoustic pressure at $|\mathbf{x}| = 50$, $\theta = 30°$ due to quadrupole radiation, calculated from (14) using the same three integration domains as in Figs. 2 and 3. The airfoil is flying at $M = 0.2$ and $\alpha = 5°$. (a) Without boundary correction; (b) with boundary correction.

stronger radiation because of less cancellation among signals from different source elements. The retarded-time effect is relatively small at $M = 0.1$ and becomes somewhat significant at $M = 0.2$. Furthermore, one observes that there exists little phase difference between the compact and noncompact solutions, suggesting that the acoustic source is centered near the origin of the far-field coordinate $\mathbf{x}$, which in the present calculation is defined at the trailing edge.

It should be pointed out that in the examples described in Figs. 4 and 5, the active source (vortex-shedding region) is only slightly noncompact. On the other hand, the source integration domains, containing 6 to 10 eddies depending on the exit boundary selection, are fairly noncompact, particularly for the case of $M = 0.2$. They thus provide valid tests for the general boundary treatment method (14) as well as the numerical integration scheme with retarded time variations. The good
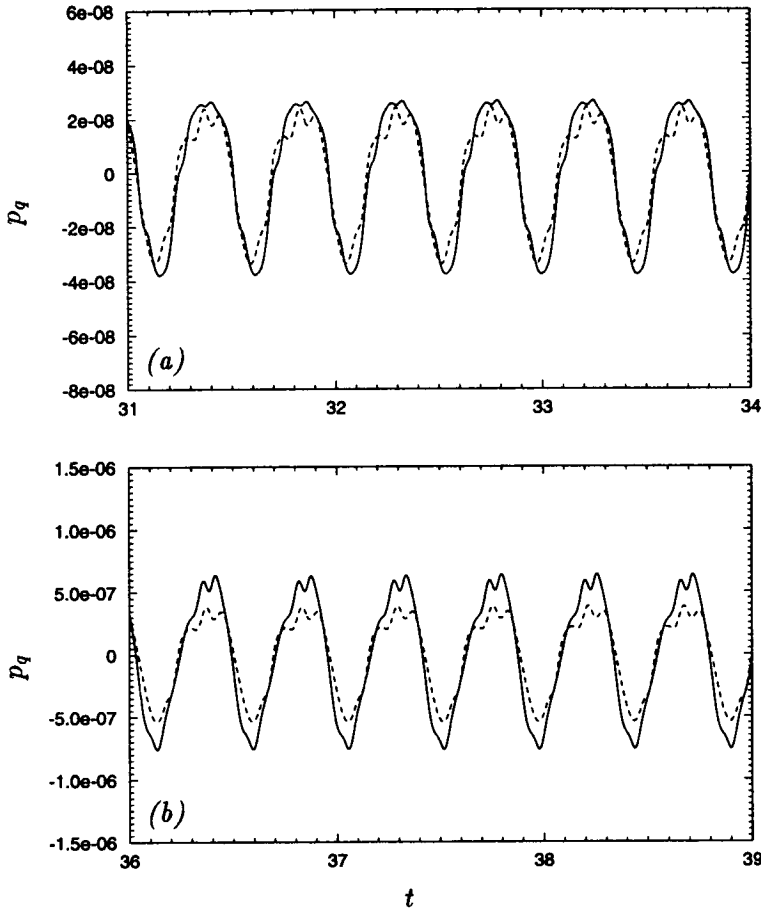
FIGURE 5. The acoustic pressure at $|\mathbf{x}| = 50$, $\theta = 30°$ due to quadrupole radiation, calculated based on noncompact (———) and compact (– – – –) source formulations. The airfoil angle of attack $\alpha = 5°$. (a) $M = 0.1$; (b) $M = 0.2$.

agreement with compact source solution at low Mach number ($M = 0.1$ and below) shows that the integration procedure is capable of providing adequate cancellations among signals from the passive convection region.

A comment is in order concerning the selection of the integration boundary S_0. In principle, S_0 can be placed anywhere so long as the active noise source is enclosed within the source integration domain. From a computational standpoint, however, the velocity field in the vicinity of the outflow boundary for the Navier-Stokes simulation is somewhat distorted due to the application of the convective boundary condition. The non-physical eddy distortion may serve as another source of spurious noise if it is included in the calculation. For this reason, we always choose smaller source integration domains than the actual flow simulation domain by placing S_0 at least 15 grid points upstream from the computational outflow boundary.

Finally, the acoustic dipole sources due to the unsteady compressive stress exerted
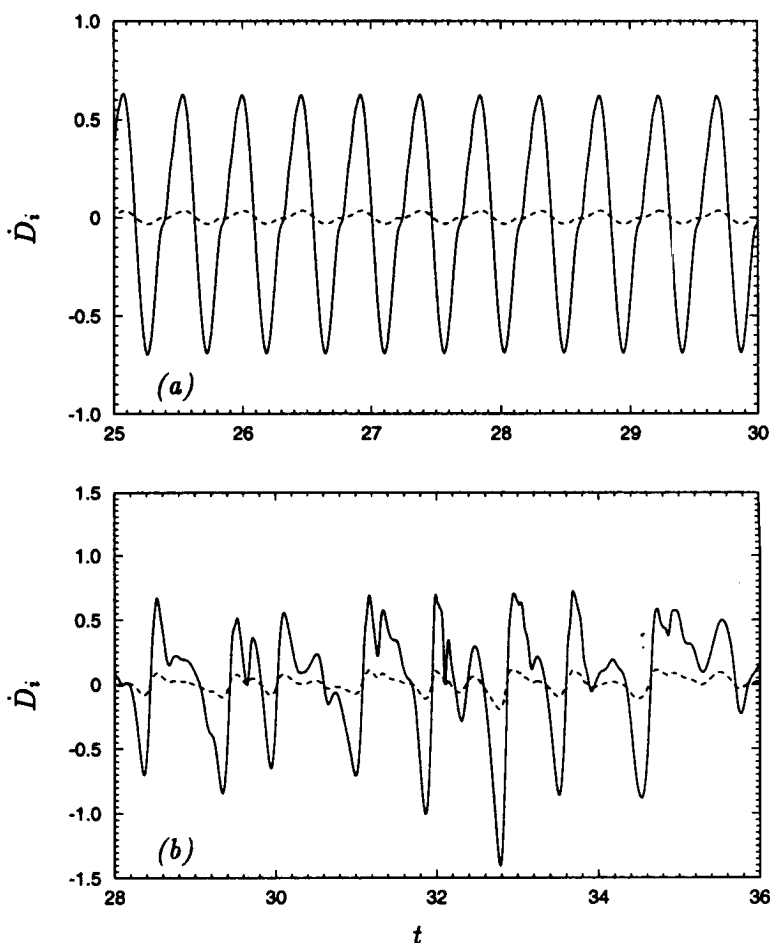
FIGURE 6.   Acoustic dipoles on the airfoil surface, calculated from (8) for (a) $\alpha = 5°$; and (b) $\alpha = 8°$. - - - - $\dot{D}_1$ (drag dipole); —— $\dot{D}_2$ (lift dipole).

by the airfoil surface are evaluated and compared with the volume quadrupoles. Under the condition that the airfoil chord is small relative to the acoustic wavelength, the compact solution form (6)–(8) applies. The calculated dipole components are depicted in Figs. 6a and 6b for the cases of $\alpha = 5°$ and $\alpha = 8°$, respectively. Both the pressure and viscous stress are included in the calculations of p_{ij}. As expected, the viscous contribution to the lift dipole $\dot{D}_2$ is negligibly small. Its effect on the drag dipole $\dot{D}_1$, on the other hand, reaches approximately 27% in magnitude with opposite phase, relative to the pressure contribution, for the case of $\alpha = 5°$. Overall, the lift dipole is much stronger than the drag dipole, and both amplify with increasing angle of attack. Relative to the quadrupole components calculated earlier, $\dot{D}_2$ is of larger or comparable magnitude and thus dominates the far-field radiation, given that its coefficient in (6) is $O(M^{-1})$ larger than that of the quadrupole terms. Along the horizontal (x_1) axis, however, the quadrupole sources may play a limited

role because the magnitude of $\dot{D}_1$ is also small.

3. Conclusions and future directions

In acoustic analogy based calculations of aerodynamic sound, it is important to distinguish the active source region, where production of the unsteady Reynolds stress takes place, from passive regions characterized by the convective motion of eddies. The former should always be enclosed within the domain of source integration, whereas the latter may be truncated provided that an adequate account of the effect of eddies crossing the permeable integration boundary is provided.

This report illustrates the necessity for, and means of, boundary corrections through a paradigm problem of airfoil vortex shedding. It demonstrates that the spurious noise generated by the exit boundary in the airfoil wake is due to the time variation of the unsteady momentum fluxes across the boundary, carried by the escaping eddies. For a class of problems where eddies (organized structures) leave (enter) the source integration domain at a nearly constant speed, the spurious boundary noise can be eliminated or reduced drastically by the correction terms in (12)–(15). This approach allows a quantitative evaluation of the radiated quadrupole noise, which has rarely been done in the past.

In the case of vortex-shedding noise from a small airfoil, studied above, computational results suggest that the volume quadrupole noise is small in the low Mach number limit in comparison to the lift and drag dipole noise emitted from the airfoil surface. The techniques developed in this study are equally applicable to other flow configurations such as jets and mixing layers, where the volume acoustic sources provide the dominant contribution to the far-field noise.

A crucial issue to be addressed next is the aeroacoustic scattering by the airfoil trailing-edge, the major source of broadband noise according to experimental measurements (Brooks & Hodgson 1981; Blake & Gershfeld 1988). Both theory (Crighton & Leppington 1971; Howe 1978) and experimental results indicate a non-multipole character of the sharp-edge noise. In the limiting case of scattering by a half-plane, the far-field intensity exhibits a M^5 dependence and $\sin^2(\theta/2)$ directivity. A computational prediction should capture these fundamental characteristics. While the Curle integral is formally exact, its usefulness as a predictive tool depends upon the precise knowledge about the volume and surface source terms. If the near-field source functions are approximated by the incompressible Navier-Stokes solutions, as in the present case, the Curle-integral prediction is only accurate for compact surfaces relative to the dominant acoustic wavelength, since the exact boundary conditions on the surface are not satisfied by the acoustic field. For acoustically noncompact airfoils where edge scattering noise is generated, the compressible (acoustic) contribution to the surface integral is significant, and proper account of the acoustic-surface interaction must hence be taken.

In order to account for the surface reflection and edge diffraction, the appropriate Green's functions, whose normal derivatives vanish on the solid surface, must be employed in an integral solution to the Lighthill equation. Solution development may be carried out in either the time domain or the frequency domain. In either

case, it is likely that the Green's function has to be determined numerically in the discrete sense, given the relatively complex geometry. An alternative to the Green's function approach would be to solve the Lighthill equation numerically, using the turbulence data generated by the near-field Navier-Stokes simulation as a discretized forcing function. These different approaches will be explored to find the most effective solution technique. In the meantime, we will work closely with the LES group at CTR in an effort to establish reliable turbulence statistics in the near field to be used as source functions for the acoustic analogy based far-field calculations.

REFERENCES

BROOKS, T. F. & HODGSON, T. H. 1981 Trailing edge noise prediction from measured surface pressures. *J. Sound & Vib.* **78,** 69–117.

BLAKE, W. K. & GERSHFELD, J. L. 1988 The aeroacoustics of trailing edges. In *Frontiers in Experimental Fluid Mechanics,* Chapt. 10, (Gad-el-Hak, M. Eds.), Springer-Verlag.

CHOI, H. 1993 Toward large eddy simulation of turbulent flow over an airfoil. *Annual Research Briefs-1993,* Center for Turbulence Research, Stanford University/NASA Ames, 145–149.

CRIGHTON, D. G. 1993 Computational aeroacoustics for low Mach number flows. In *Computational Aeroacoustics.* ICASE/NASA LaRC Series, (Hardin J. C. and Hussaini, M. Y. Eds.), Springer-Verlag.

CRIGHTON, D. G. & LEPPINGTON, F. G. 1971 On the scattering of aerodynamic noise. *J. Fluid Mech.* **46,** 577–597.

CURLE, N. 1955 The influence of solid boundaries upon aerodynamic sound. *Proc. Royal Soc. Lond.* A. **231,** 505–514.

FFOWCS WILLIAMS, J. E. & HAWKINGS, D. L. 1969 Sound generation by turbulence and surfaces in arbitrary motion. *Phil. Tran. Royal Soc. Lond.* A. **264,** 321–342.

GOLDSTEIN, M. E. 1976 *Aeroacoustics,* Chapt. 4, McGraw-Hill.

HOWE, M. S. 1978 A review of the theory of trailing edge noise. *J. Sound & Vib.* **61,** 437–465.

MANKBADI, R. R., HAYDER, M. H. & POVINELLI, L. A. 1994 Structure of supersonic jet flow and its radiated sound. *AIAA J.* **32,** 897–906.

MITCHELL, B. E., LELE, S. K. & MOIN, P. 1995a Direct computation of the sound generated by vortex pairing in an axisymmetric jet. *AIAA Paper* 95-0504.

MITCHELL, B. E., LELE, S. K. & MOIN, P. 1995b Direct computation of the sound from a compressible co-rotating vortex pair. *J. Fluid Mech.* **285**, 181–202.

PAULEY, L. L., MOIN, P. & REYNOLDS, W. C. 1988 *A Numerical Study of Unsteady Laminar Boundary Layer Separation*, Report No. TF-34, Dept. of Mech. Engr., Stanford University.

PULLIAM, T. H. 1989 Low Reynolds number numerical solutions of chaotic flows. *AIAA Paper* 89–0123.

WANG, M. 1993 Sound radiation due to boundary layer transition. *Annual Research Briefs–1993*, Center for Turbulence Research, Stanford University/NASA Ames, 299–312.

Page intentionally left blank

Effects of pressure gradients
on turbulent premixed flames

By D. Veynante[1] AND T. Poinsot[2]

1. Motivations and objectives

Most ducted turbulent flames are subjected to external pressure gradients. Compared to "free" flames, i.e. turbulent flames without externally imposed pressure gradients, the combination of the external pressure gradients with the large density changes found in premixed flames may lead to strong modifications of the flame structure. These modifications are mainly due to the differential buoyancy effects between cold, heavy reactants and hot, light products. They affect turbulent transport along with many characteristics of the flame itself, such as the flame speed, thickness, wrinkling, and local structure. Pressure gradients are also a key mechanism for the counter-gradient turbulent transport described below. Accordingly, studying the effects of pressure gradients on premixed turbulent flames is an important issue both for fundamental understanding of turbulent combustion and for modeling.

Using the assumption of single-step chemistry, the mass fractions of the reactive species are all linearly related (Williams 1985) and may be expressed in terms of a single reduced mass fraction: the reaction progress variable c. The progress variable ranges from zero to unity in the fresh and fully burnt gases, respectively. Using the classical Favre decomposition, a quantity q can be split into a mass-weighted mean, $\widetilde{q} \equiv \overline{\rho q}/\overline{\rho}$, and a turbulent fluctuation, q''. The transport equation for the mean reaction progress variable $\widetilde{c}$ may be written as:

$$\frac{\partial \overline{\rho}\widetilde{c}}{\partial t} + \frac{\partial \overline{\rho}\widetilde{u_i}\widetilde{c}}{\partial x_i} + \frac{\partial \overline{\rho u_i'' c''}}{\partial x_i} = -\frac{\overline{\partial \mathcal{J}_k}}{\partial x_k} + \overline{\dot{\omega}}_c \tag{1}$$

where ρ is the mass density, u_i is the flow velocity, $\mathcal{J}_k$ is the molecular diffusion flux, $\dot{\omega}_c$ is the volumetric production rate of the chemical reaction, and the overbar superscript denotes conventional Reynolds ensemble-averaging. Equation (1) has the form of a standard turbulent transport equation where the rate of change of $\widetilde{c}$ results from a balance between convection by the mean flow, convection by the turbulent flow, molecular diffusion, and chemical reaction. The contribution of molecular diffusion is usually neglected for high Reynolds number flows. In Eq. (1), two terms need to be modeled: the mean reaction rate $\overline{\dot{\omega}}_c$ and the turbulent transport $\overline{\rho u_i'' c''}$ terms. The first term has received considerable attention in recent years

1 Laboratoire EM2C, Ecole Centrale Paris, France
2 Institut de Mecanique des Fluides de Toulouse and CERFACS, France

and various models have been derived and incorporated into practical codes for turbulent combustion. The second term, however, has received considerably less attention and is generally described with a simple classical gradient eddy-viscosity model:

$$\overline{\rho u_i'' c''} = \overline{\rho} \widetilde{u_i'' c''} = -\frac{\mu_t}{\sigma_c} \frac{\partial \widetilde{c}}{\partial x_i} \tag{2}$$

where μ_t denotes the turbulent dynamic viscosity and σ_c a turbulent Schmidt number.

Both theoretical and experimental research (Bray et al., 1981, 1982; Shepherd et al., 1982) have shown the occurrence of counter-gradient transport in some turbulent flames: flames where the turbulent flux $\overline{\rho u_i'' c''}$ and the $\widetilde{c}$ gradient, $\partial \widetilde{c}/\partial x_i$, have the same sign in opposition with the prediction of Eq. (2). This is generally due to the differential effect of pressure gradients on cold reactants and hot products. Recent studies based on direct numerical simulations of turbulent premixed flames without externally imposed pressure gradients (Trouvé et al.,1994; Rutland & Cant, 1994) have confirmed that counter-gradient diffusion was found in simulations, but that classical gradient diffusion was also possible. A criterion indicating the presence of gradient or counter-gradient diffusion in atmospheric flames has been derived by Veynante et al.(1995). This criterion leads to a reduced number called N_B, or the Bray number:

$$N_B = \frac{\tau}{2\alpha(u'/s_l^0)} \tag{3}$$

where s_l^0 is the laminar flame speed, u' is the RMS turbulent velocity, τ is the heat release factor defined as $\tau = T_b/T_u - 1$, with T being the temperature and indices u and b referring to the fresh and burnt gases, respectively. The term α is an efficiency function of order unity, introduced to take into account the reduced ability of small turbulent vortices to affect the flame front. For low values of N_B, typically $N_B \leq 1$, where flames exist in relatively large turbulence intensity, gradient diffusion is obtained. For large values of N_B counter-gradient diffusion occurs. In fact, counter-gradient turbulent diffusion is promoted by heat release and thermal expansion (increasing values of τ) whereas increased turbulence intensity tends to induce gradient transport.

The work of Veynante et al.(1995) was performed for free flames without externally imposed pressure gradients or volume forces, such as gravity. Since turbulent transport in flames appears to be controlled by a dynamic balance between fresh and burnt gases, confined flames subjected to strong pressure gradients should exhibit a large sensitivity to these gradients. For example, we expect that imposing a pressure gradient on a turbulent flame exhibiting counter-gradient diffusion may lead to a gradient-diffusion situation. This change could affect the flame brush thickness, the turbulent flame speed, and finally the complete structure of the turbulent flame brush, as described in a number of papers by Masuya & Libby, 1981; Bray et al., 1982.

Our objective in this study is to explore the effects of pressure gradients on premixed turbulent flames using direct numerical simulations. We will first recall

the physics of this phenomenon and how pressure gradients may be included in a simulation for reacting flows in Section 2. We will also describe the most general theory to treat the problem, i.e. the Bray-Moss-Libby formulation. The simulation used for this work will be described in Section 3. Section 4 will present the structure of laminar flames submitted to pressure gradients. Section 5 will present results for turbulent flames. Finally, Section 6 will describe a model for the turbulent flux incorporating the effects of pressure gradients.

2. Pressure gradients in premixed flames

2.1 The Bray-Moss-Libby approach for turbulent transport in premixed flames

Bray *et al.*(1989) have proposed a simple algebraic closure for the reaction term $\overline{\dot{\omega}_c}$ in Eq. (1), but focus their attention on the turbulent transport term $\overline{\rho u_i'' c''}$. In the Bray-Moss-Libby (BML) approach, the flame is analyzed as a thin flame sheet, or "flamelet," separating fresh reactants ($c = 0$) and fully burnt products ($c = 1$). This assumption leads to a bimodal probability density for the progress variable c, and the turbulent flux is then expressed, according to Bray 1980, as:

$$\overline{\rho u_i'' c''} = \overline{\rho} \widetilde{c}(1 - \widetilde{c})(\overline{u_{ib}} - \overline{u_{iu}}) \tag{4}$$

where $\overline{u_{iu}}$ and $\overline{u_{ib}}$ are the conditional mean velocities within the unburnt and burnt gases, respectively. The occurrence of counter-gradient transport may be easily explained from this expression. Let us consider a left-traveling flame along the x_i-direction ($\partial \widetilde{c}/\partial x_i > 0$). Thermal expansion and the associated flow acceleration through the flame, along with favorable buoyancy and/or pressure gradients, will tend to make $\overline{u_{ib}}$ larger than $\overline{u_{iu}}$, thereby promoting counter-gradient turbulent diffusion of $\widetilde{c}$, resulting in $\overline{\rho u_i'' c''} > 0$. Under the Bray-Moss-Libby approach, the second and third turbulent moments such as $\overline{\rho u_i'' u_j''}$, $\overline{\rho u_i'' u_j'' c''}$, and $\overline{\rho u_i'' u_j'' u_k''}$ may be directly expressed as functions of conditioned quantities in fresh and in burnt gases. Nevertheless, conditional quantities such as $(\overline{u_{ib}} - \overline{u_{iu}})$ are difficult to close and an alternative approach must be pursued for estimating the turbulent transport: $\overline{\rho u_i'' c''}$. A simple algebraic closure based on the eddy viscosity concept cannot be used here. In the Bray-Moss-Libby model, closure is achieved by a transport equation for $\overline{\rho u_i'' c''}$ (Bray 1980, Bray *et al.*1989, Bray 1990). A brief derivation of this equation is provided here, including a constant volume force F_i^v and a constant acceleration Γ_i. We start from the momentum equation:

$$\frac{\partial \rho u_i}{\partial t} + \frac{\partial \rho u_i u_j}{\partial x_j} = -\frac{\partial P}{\partial x_i} + F_i^v + \rho \Gamma_i + \frac{\partial \tau_{ik}}{\partial x_k} \tag{5}$$

and the equation for the progress variable c:

$$\frac{\partial \rho c}{\partial t} + \frac{\partial \rho u_i c}{\partial x_j} = -\frac{\partial \mathcal{J}_k}{\partial x_k} + \dot{\omega}_c \tag{6}$$

where P, τ_{ij} and $\mathcal{J}_k$ are respectively the pressure, the viscous stress tensor and the molecular diffusive flux of c. Multiplying Eq. (5) by c and Eq. (6) by u_i, then

adding and averaging the two resulting equations leads to a transport equation for $\overline{\rho \widetilde{u_i c}}$. In a similar way, adding the averaged version of Eq. (5) multiplied by $\widetilde{c}$ and the averaged form of Eq. (6) multiplied by $\widetilde{u_i}$ leads to a transport equation for $\overline{\rho \widetilde{u_i} \widetilde{c}}$. Subtracting the two resulting equations provides a transport equation for the turbulent flux $\overline{\rho \widetilde{u_i'' c''}}$:

$$
\underbrace{\frac{\partial}{\partial t} \overline{\rho \widetilde{u_i'' c''}}}_{\textbf{(I)}} + \underbrace{\frac{\partial}{\partial x_j} (\overline{\rho \widetilde{U_j} \widetilde{u_i'' c''}})}_{\textbf{(II)}} = \underbrace{-\frac{\partial}{\partial x_j} \left(\overline{\rho \widetilde{u_j'' u_i'' c''}} \right)}_{\textbf{(III)}} \underbrace{- \overline{\rho \widetilde{u_i'' u_j''}} \frac{\partial \widetilde{c}}{\partial x_j}}_{\textbf{(IV)}} \underbrace{- \overline{\rho \widetilde{u_j'' c''}} \frac{\partial \widetilde{U_i}}{\partial x_j}}_{\textbf{(V)}}
$$

$$
\underbrace{- \overline{c'' \frac{\partial \overline{p}}{\partial x_i}}}_{\textbf{(VI)}} \underbrace{- \overline{c'' \frac{\partial p'}{\partial x_i}}}_{\textbf{(VII)}} \underbrace{- \overline{u_i'' \frac{\partial \mathcal{J}_k}{\partial x_k}}}_{\textbf{(VIII)}} + \underbrace{\overline{c'' \frac{\partial \tau_{ik}}{\partial x_k}}}_{\textbf{(IX)}} + \underbrace{\overline{\rho \widetilde{u_i'' \dot{\omega}}}}_{\textbf{(X)}} + \underbrace{\overline{c'' F_i^v}}_{\textbf{(XI)}} \tag{7}
$$

Bray *et al.*(1981) studied each term in Eq. (7) and proposed some approximations. For example, they explored the role of the mean pressure gradient term (VI) assuming that this term is so large that only cross dissipation terms (VIII and IX) can provide a balance, leading to a turbulent flux directly proportional to the pressure gradient. All terms in Eq. (7) may be extracted from our direct numerical simulations (Trouvé *et al.*, 1994; Veynante *et al.*, 1995) to validate these analyses.

Two main comments arise from Eq. (7). First, the mean pressure gradient appears explicitly in the source term (VI) $(\overline{c''} \partial \overline{p}/\partial x_i)$. Under the BML analysis, $\overline{c''}$ may be easily closed (Masuya & Libby, 1981):

$$
\overline{c''} = \overline{c} - \widetilde{c} = \tau \frac{\widetilde{c}(1 - \widetilde{c})}{1 + \tau \widetilde{c}} \tag{8}
$$

which is exact for an infinitely thin flame front. This quantity, being always positive, indicates a pressure decrease from fresh to burnt gases and tends to promote counter-gradient diffusion, or positive values of the turbulent flux $\overline{\rho \widetilde{u_i'' c}}$.

Another important feature concerning the present numerical simulations deals with volume and buoyancy forces. A constant volume force F_i^v leads to a source term in Eq. (7) with a similar form for the pressure gradient term, whereas a constant acceleration force Γ_i does not. However, the introduction of F_i^v or Γ_i has a direct influence on the mean pressure gradient $\partial \overline{P}/\partial x$ (term VI). So, terms (VI) and (XI) should be grouped to describe the effect of F_i^v or Γ_i. We start from the averaged momentum transport equation:

$$
\frac{\partial \overline{\rho} \widetilde{u_i}}{\partial t} + \frac{\partial \overline{\rho} \widetilde{u_i} \widetilde{u_j}}{\partial x_j} + \frac{\partial \overline{\rho \widetilde{u_i'' u_j''}}}{\partial x_j} = -\frac{\partial \overline{P}}{\partial x_i} + F_i^v + \overline{\rho} \Gamma_i + \frac{\partial \overline{\tau}_{ik}}{\partial x_k} \tag{9}
$$

For sufficiently large volume and/or buoyancy forces, an equilibrium between these forces and the mean pressure gradient can be used, which leads to the hydrostatic approximation:

$$
\frac{\partial \overline{P}}{\partial x_i} = F_i^v + \overline{\rho} \Gamma_i \tag{10}
$$

Therefore, to first order, term (VI + XI) becomes:

$$-\overline{c''}\left(\frac{\partial \overline{P}}{\partial x_i} - F_i^v\right) = -\overline{c''}\bar{\rho}\Gamma_i \tag{11}$$

Both F_i^v and Γ_i induce a mean pressure gradient in the flow field (see Eq. 5). However, only Γ_i will directly affect the balance of $\widetilde{\rho u_i'' c''}$ (Eq. 7). * Accordingly, our study of the influence of the mean pressure gradient on turbulent transport will be conducted using a constant acceleration Γ_i.

2.2 Physical and numerical issues related to pressure gradients in flames

Theoretical models indicate that both normal and tangential pressure gradients influence turbulent flames. Masuya & Libby (1981) have studied confined oblique flames and have shown that, for a given pressure gradient, turbulent transport in normal and transverse directions are correlated. As a first step, we will only consider pressure gradients in the mean propagation direction x_1: only $F_1^v = F_v$ and $\Gamma_1 = \Gamma$ may be nonzero. All pressure gradients are scaled by the pressure gradient inside the laminar flame zone given by:

$$|\nabla P_{lam}| \simeq \rho (s_l^0)^2 \tau / \delta_l^0 \tag{12}$$

where δ_l^0 is the unstrained laminar flame thickness that is obtained from the maximum temperature gradient $\delta_l^0 = Max(\frac{dT}{dx})/(T_b - T_u)$.

The pressure gradient ∇P_{lam} is created by dilatation inside the flame zone. It is large, but due to the thinnish flame front, the overall pressure jump between fresh and burnt gases remains small since $\Delta P/P \simeq \tau\gamma(s_l^0/c)^2$ where the ratio of flame to sound speeds is of the order of 0.001. On the contrary, volume forces or external pressure gradients are imposed on distances much larger than the flamelet thickness and will overcome the effect of dilatation in turbulent flame brushes. These effects and their relative importance in various flames may be quantified in terms of two quantities: the reduced external pressure gradient ∇P_{ext}^+, and the reduced mean pressure gradient ∇P_{mean}^+. We consider these gradients positive when the pressure increases when going from the fresh to the burnt gases. Figures 1 and 2 illustrate how these gradients may be estimated in a turbulent flame brush of thickness l_b with and without an external pressure gradient. With no external pressure gradient, corresponding to Fig. 1, the pressure jump across the flame will be conserved but spread over the flame brush thickness l_b so that the mean pressure gradient in the flame brush will be $\nabla P_{mean}^+ \simeq \nabla P_{lam}^+ \delta_l^0/l_b$. In the case of an externally imposed pressure gradient, corresponding to Fig. 2, ∇P_{mean}^+ will be of the order of ∇P_{ext}^+ everywhere in the flow; although the maximum instantaneous pressure gradient may still be found at the flame, ∇P_{ext}^+ will be dominant over the flame brush thickness.

Pressure gradients in real flames are imposed either by flame confinement, as in ducted flows, or by gravity. Typical values of ∇P_{lam}^+, ∇P_{ext}^+, and ∇P_{mean}^+ are

---

* This result is due to the fact that, contrary to a constant acceleration, a constant volume force does not introduce buoyancy phenomena.
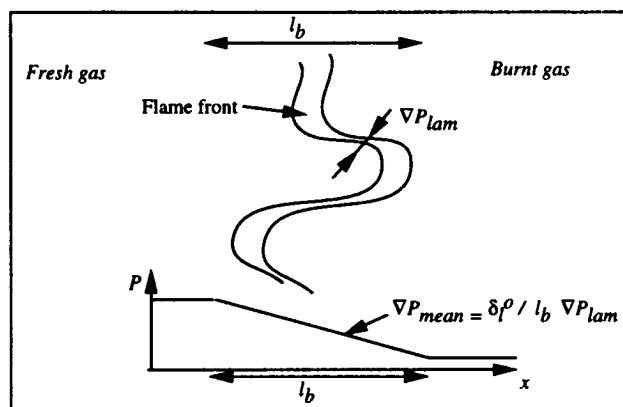
FIGURE 1. Pressure gradients in a free flame ($\nabla P_{ext}^+ = 0$).
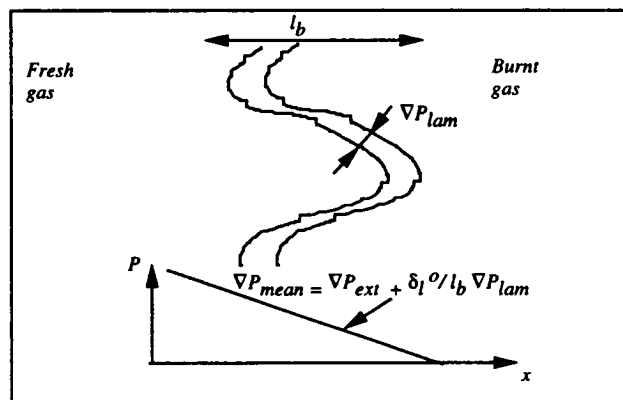
FIGURE 2. Pressure gradients in a flame with imposed pressure gradient.

given in Table I for different turbulent premixed flames along with their dimensional values. In the case of "free" flames, the pressure gradient is imposed by the flame itself. The flame data correspond to the experiment of Schefer *et al.*(1982). The flame brush thickness is of the order of the integral length scale $l_t = 1$ cm.

TABLE I. Typical pressure gradients for a propane/air flame (P=1 atm, $\phi = 1.2$)

	s_l^0 m/s	δ_l^0 m	T_b/T_u	$|\nabla P_{lam}|$ Pa/m	$|\nabla P_{ext}|$ Pa/m	$|\nabla P_{ext}^+|$	$|\nabla P_{mean}^+|$
Free flame	0.32	0.0005	6.5	250	0	0.	0.05
1 g flame	0.32	0.0005	6.5	250	$\simeq 10$	0.5	0.5
Ducted flame	0.32	0.0005	6.5	250	1000	5	5

These estimations indicate that the largest pressure gradients will be obtained in ducted flames where large pressure differences are created. Gravity alone will create smaller effects. At this point, it is worth discussing the differences between flames subjected to a constant acceleration, such as gravity, or to a constant pressure gradient. In the first case, the induced pressure gradient is $\rho\Gamma$, which is different in the fresh and burnt gases, see below. The induced pressure gradient will be constant in the latter case. For both cases, however, the pressure gradient will induce differential acceleration for fresh and burnt gas pockets in both cases thus leading to a modification of turbulent transport. Most authors therefore expect similar effects from constant acceleration or from pressure gradients.

There are at least three ways to introduce pressure gradients in a direct numerical simulation of premixed turbulent flames: impose a constant volume force F_v; impose a pressure gradient through the boundary conditions; or impose a constant acceleration Γ, i.e. a volume force that is a function of the local density $F_g = \rho\Gamma$, where $\Gamma = g$ in the case of gravity. All of these techniques produce an imposed pressure gradient, see Appendix I. However, we have seen that the first solution leads to a flow where the pressure gradient $\frac{\partial P}{\partial x}$ is compensated everywhere by the volume force F_v and has no effect on $\widetilde{\rho u''c''}$. The second solution was investigated, but it is difficult to implement in a simulation if the mean flow remains one-dimensional, which is required for statistical purposes. In this paper, we will use only the third solution with various values of the acceleration Γ.

3. Direct numerical simulation of premixed flames with pressure gradients

The present direct numerical simulations were performed with a two-dimensional version of NTMIX. A complete description of this code may be found in Haworth & Poinsot (1992) or Poinsot & Lele (1992). It solves the fully compressible Navier-Stokes equations with a single irreversible reaction *Fuel → Products*. Variable density as well as viscosity and transport coefficients are taken into account. The conservation equations solved by the simulation are:

$$\frac{\partial \rho}{\partial t} + \frac{\partial}{\partial x_i}(\rho u_i) = 0, \tag{13}$$

$$\frac{\partial \rho u_i}{\partial t} + \frac{\partial}{\partial x_j}(\rho u_i u_j) = -\frac{\partial p}{\partial x_i} + F_i^v + \rho\Gamma_i + \frac{\partial \tau_{ij}}{\partial x_j}, \tag{14}$$

$$\frac{\partial \rho E}{\partial t} + \frac{\partial}{\partial x_i}[(\rho E + p)u_i] = (F_i^v + \rho\Gamma_i)u_i + \frac{\partial}{\partial x_i}(u_j \tau_{ij})$$
$$+ \frac{\partial}{\partial x_i}(\lambda \frac{\partial T}{\partial x_i}) + Q\dot{w}, \tag{15}$$

$$\frac{\partial(\rho\widetilde{Y})}{\partial t} + \frac{\partial}{\partial x_i}(\rho\widetilde{Y}u_i) = \frac{\partial}{\partial x_i}(\rho\mathcal{D}\frac{\partial\widetilde{Y}}{\partial x_i}) - \dot{w}, \tag{16}$$

where

$$\rho E = \frac{1}{2}\rho \sum_{k=1}^{3} u_k^2 + \frac{p}{\gamma - 1}, \tag{17}$$

$$\tau_{ij} = \mu \left(\frac{\partial u_i}{\partial x_j} + \frac{\partial u_j}{\partial x_i} - \frac{2}{3}\delta_{ij}\frac{\partial u_k}{\partial x_k} \right), \tag{18}$$

$$\dot{w} = \dot{w}_R/Y_R^o = \rho\widetilde{Y}B\exp\left(-\beta/\alpha\right)\exp\left(\frac{-\beta(1-\theta)}{1-\alpha(1-\theta)}\right). \tag{19}$$

In these expressions ρ is the mass density, p is the thermodynamic pressure, ρE is the total energy density, Q designates the heat of reaction per unit mass of fresh mixture ($Q = -\Delta h_f^o Y_R^o$ where Δh_f^o is the heat of reaction per unit mass of reactant). F_i^v and Γ_i are the i-component of the constant volume force F^v and the constant acceleration Γ, respectively. The reduced temperature is $\Theta = (T - T_u)/(T_b - T_u)$. The fresh gas temperature is T_u, and T_b is the adiabatic flame temperature for unity Lewis number. The activation temperature is T_a. B is the pre-exponential factor and the coefficients α and β are the temperature factor and the reduced activation energy, respectively:

$$\alpha = (T_b - T_u)/T_b; \qquad \beta = \alpha T_a/T_b. \tag{20}$$

The mass fraction of the reactants Y_R is nondimensionalized by the initial mass fraction of reactants Y_R^o in the fresh gases: $\widetilde{Y} = Y_R/Y_R^o$. This varies from 1 in the fresh gases to 0 in the burnt gases.

We assume that the gas mixture is a perfect gas with constant molar mass and a specific heat ratio $\gamma = 1.4$. The thermal conductivity λ and the diffusion coefficient $\mathcal{D}$ are obtained from the viscosity coefficient μ according to

$$\lambda = \mu C_p/P_r \quad \text{and} \quad \mathcal{D} = \mu/(\rho S_c), \tag{21}$$

where the Prandtl number P_r and the Schmidt number Sc are constant. As a consequence the Lewis number $L_e = S_c/P_r$ is also constant. The viscosity μ is a function of temperature: $\mu = \mu_u(T/T_u)^b$.

The computational domain is L_x by L_y with N_x by N_y grid points. Two box sizes have been used: the small box has $N_x = N_y = 257$. The aspect ratio is $L_y/L_x = 2.5$. The second box, or large box, has $N_x = 257$ and $N_y = 1025$. The aspect ratio for this box is $L_y/L_x = 6.66$. The following parameters have been used for both cases:

TABLE II. Fixed parameters for direct numerical simulations of flames subjected to pressure gradients

$Re = cL_x/\nu$	Le	Pr_o	T_a/T_b	T_b/T_u	b	s_l^0/c	δ_l^0/L_x	Nx
12000.	1.	0.75	8.	4.	0.76	0.0159	0.027	257

where the speed of sound and kinematic viscosity in the fresh gases are denoted by c and ν.
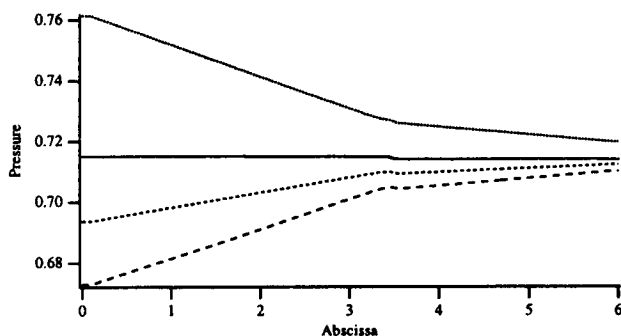
FIGURE 3. Pressure profiles in 1D laminar flames without and with imposed acceleration g^*. $g^* = 0$ (———); $g^* = -6.25$ (········); $g^* = 3.12$ (----) ; $g^* = 6.25$ (— — —)
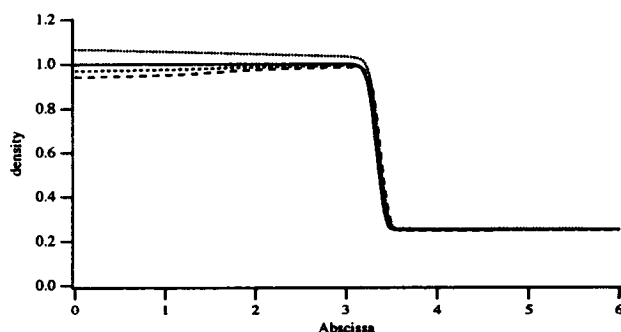
FIGURE 4. Density profiles in 1D laminar flames without and with imposed acceleration g^*. $g^* = 0$ (———); $g^* = -6.25$ (········); $g^* = 3.12$ (----); $g^* = 6.25$ (— — —)

4. Laminar flames submitted to pressure gradients

First, one dimensional laminar flames are computed without and with an imposed constant acceleration Γ. Introducing the reduced acceleration, $g^* = \Gamma \delta_l^0 / (s_l^0)^2$, which may be viewed as the inverse of a Froude number, four values of g^* are considered here: $g^* = 0$ (no imposed acceleration), $g^* = -6.25$ (favorable pressure gradient), $g^* = 3.12$ and $g^* = 6.25$ (adverse pressure gradient). Pressure profiles are plotted as a function of the downstream locations in Fig. 3 for the four g^* values. As expected, pressure gradients are constant for each side of the flame front but decrease by a factor $T_b/T_u = 4$ between fresh and burnt gases due to density changes. The pressure drop due to thermal expansion is apparent for the $g^* = 0$
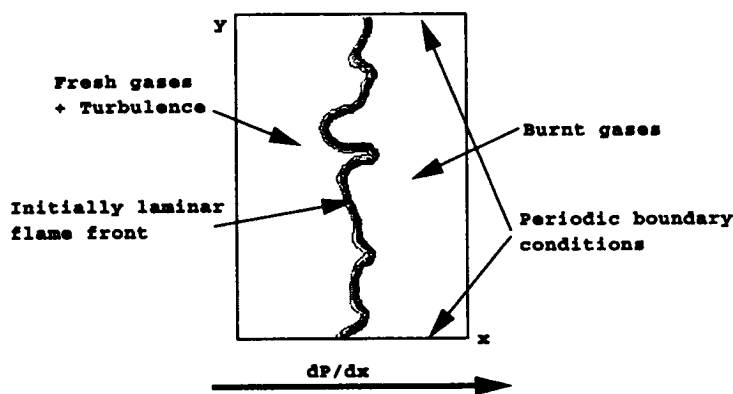
FIGURE 5.   Configuration for the numerical simulations.

case.

For all of the g^* values considered, the laminar flame structure is not affected by the imposed acceleration: flame thickness, reaction rate and mass fraction profiles remain unchanged. Nevertheless, due to the pressure gradient, a weak change in density, similar to the one described in Appendix 1, is observed inside the fresh or burnt gases, see Fig. 4, but remains negligible compared to the one induced by thermal expansion. The same trend is noticed for the flow velocity which is modified by about 3% by the pressure gradient and a factor of 4 by thermal expansion.

TABLE III. Numerical parameters for direct numerical simulations of 2D turbulent flames

$Case$	u_0'/s_l^0	l_t/δ_l^0	g^*	N_x	N_y
A	5.	3.5	0.	257	1025
B	5.	3.5	-6.25	257	1025
C	2.	2.7	0.	257	257
D	2.	2.7	3.12	257	257
E	2.	2.7	6.25	257	257

5. Turbulent flames submitted to pressure gradients

The previously computed 1D laminar flames are used as initial solutions for 2D flame-turbulence interaction simulations (Fig. 5). A Passot-Pouquet turbulence spectrum, with given turbulence intensity u' and integral length scale l_t, is superposed on the combustion field (Haworth & Poinsot, 1992). Two sets of numerical

FIGURE 6. Superimposed instantaneous temperature and vorticity fields. Initial turbulence level $u'_0/s^0_l = 5$. (a) No imposed pressure gradient ($g^* = 0.$ - case A); (b) Favorable imposed pressure gradient ($g^* = -6.25$ - case B).

simulations have been conducted. The first set, consisting of runs A and B, starts from a high turbulence level ($u'_0/s^0_l = 5$) and exhibits a classical gradient turbulence transport. The initial Bray number for this flow is $N_B = 0.6$. A favorable pressure gradient (i.e. $\nabla P^+_{mean} < 0$) is imposed with a positive acceleration ($\Gamma > 0$) to reach a counter gradient diffusion situation. The second set, consisting of runs C-E, starts from a low turbulence level ($u'_0/s^0_l = 2$), counter-gradient situation, with an initial Bray number of $N_B = 1.5$. Under an adverse pressure gradient (i.e. $\nabla P^+_{mean} > 0$), the flow is found to exhibit gradient turbulent transport. Numerical parameters are displayed on Table III where g^* is the reduced imposed acceleration
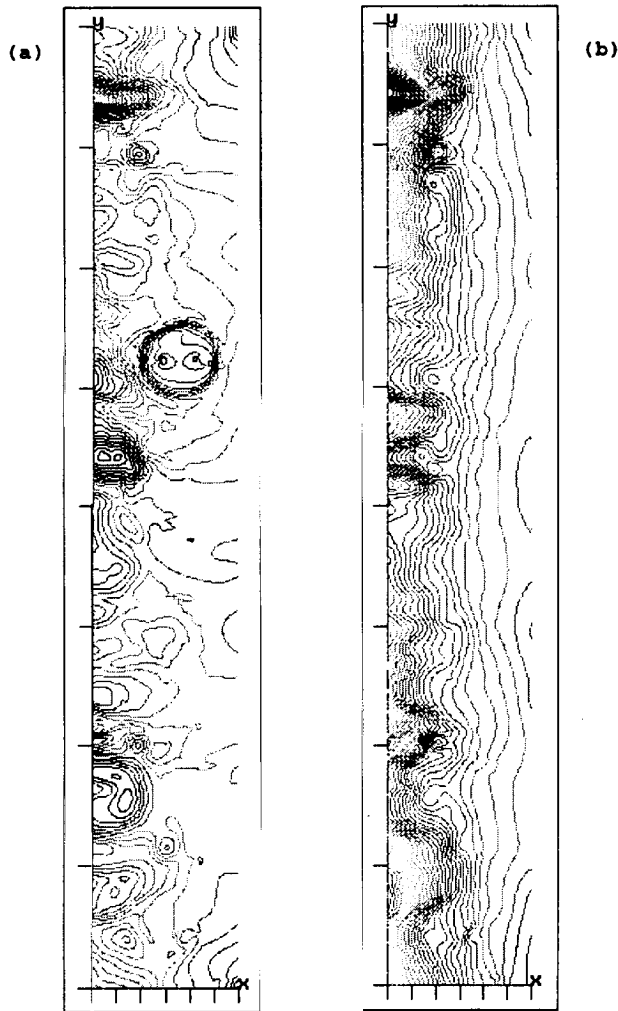
FIGURE 7.   Instantaneous pressure field. Initial turbulence level $u'_0/s^0_l = 5$. (a) No imposed pressure gradient ($g^* = 0.$ - case A); (b) Favorable imposed pressure gradient ($g^* = -6.25$ - case B).

$(g^* = \Gamma \delta^0_l/(s^0_l)^2)$. The values of ∇P^+_{mean} were chosen of the order of the pressure gradient found in the experiment of Shepherd *et al.*(1982).

5.1 Effect of the mean pressure gradient on the turbulent flame structure

Instantaneous temperature and vorticity fields are displayed in Fig. 6 for an initial turbulence level $u'_0/s^0_l = 5$ without (case A) and with (case B) an imposed mean pressure gradient. Corresponding pressure fields are displayed in Fig. 7. The flame structures are quite different. Due to the favorable pressure gradient ($\partial \overline{P}/\partial x < 0$), the wrinkling of the flame front is lower and the turbulent flame brush is thinner.
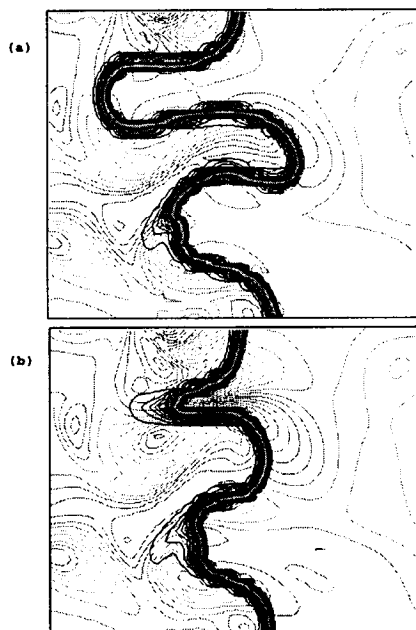
FIGURE 8. Superimposed instantaneous temperature and vorticity fields. Zoom from Fig. 6 Initial turbulence level $u'_0/s^0_l = 5$. (a) No imposed pressure gradient ($g^* = 0.$ - case A); (b) Favorable imposed pressure gradient ($g^* = -6.25$ - case B).
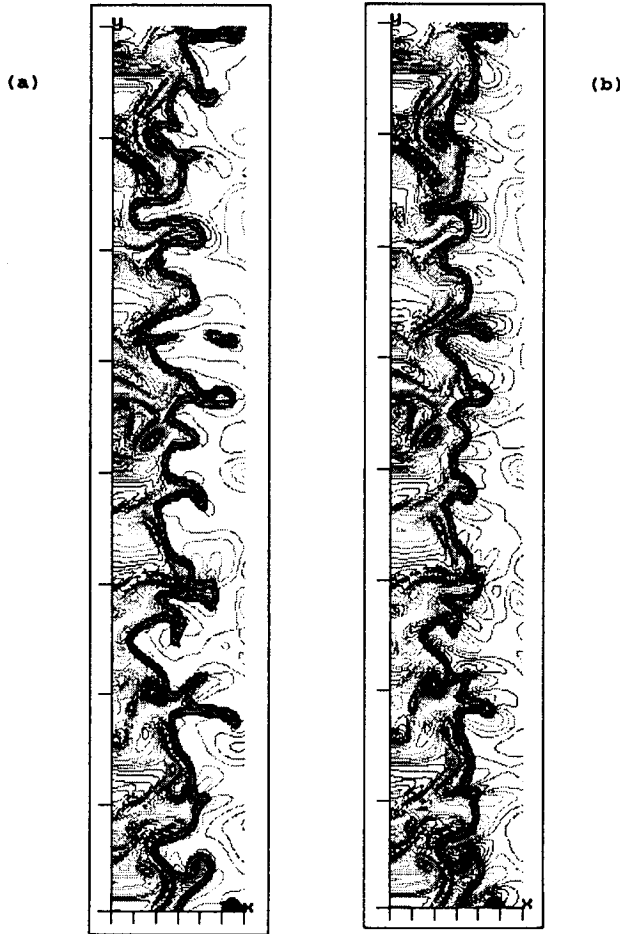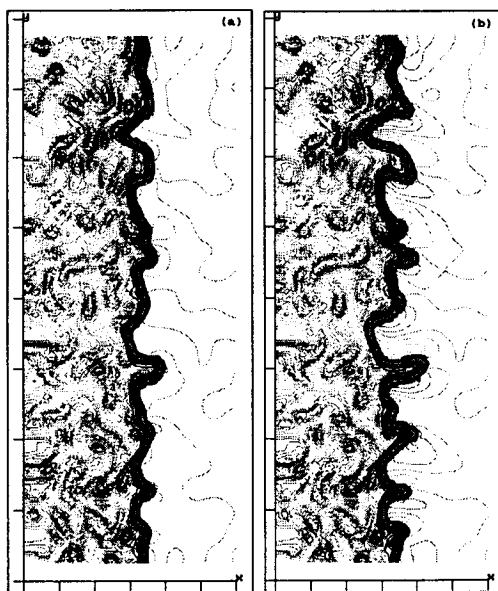

FIGURE 9. Superimposed instantaneous temperature and vorticity fields. Initial turbulence level $u'_0/s^0_l = 2$. (a) No imposed pressure gradient ($g^* = 0.$ - case C); (b) Adverse imposed pressure gradient ($g^* = -6.25$ - case E).
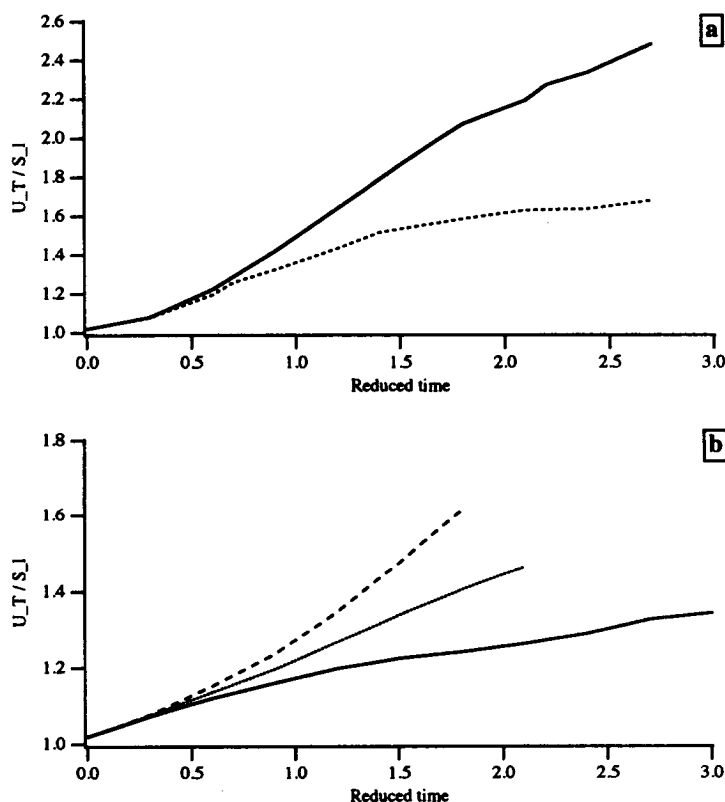
FIGURE 10. Reduced turbulent flame speed S_T/s_l^0 plotted as a function of the reduced time t/t_f, where $t_f = \delta_l^0/s_l^0$ is a flame time, for different values of g^*. (a) initial turbulent level $u_0'/s_l^0 = 5$; cases A (———) and B (————); (b) initial turbulent level $u_0'/s_l^0 = 2$; cases C (———), D (········) and E (————).

Despite similar minimum and maximum values, the pressure field is mainly dominated by vortices in case A whereas the pressure gradient, imposed by the constant acceleration Γ, is clearly apparent for case B.

Close-ups of the temperature and vorticity fields of Fig. 6 are displayed in Fig. 8. As previously described, the flame front is less wrinkled in case C despite a similar turbulence distribution in the fresh gases. The internal flame front structure, however, is strongly modified by the mean pressure gradient and buoyancy effects. Protrusions of high temperature levels are clearly apparent in fresh gases. Accordingly, local flame front characteristics may be strongly affected, which will be investigated in the future.

Instantaneous temperature and vorticity fields are displayed for cases C and E in Fig. 9. The initial turbulence level is lower $(u_0'/s_l^0 = 2)$: without externally imposed pressure gradient, this flow exhibits a counter gradient turbulent transport as predicted by the Bray number criterion $(N_B = 1.5)$. In case E, an adverse pressure gradient is imposed and a transition towards gradient transport is expected.
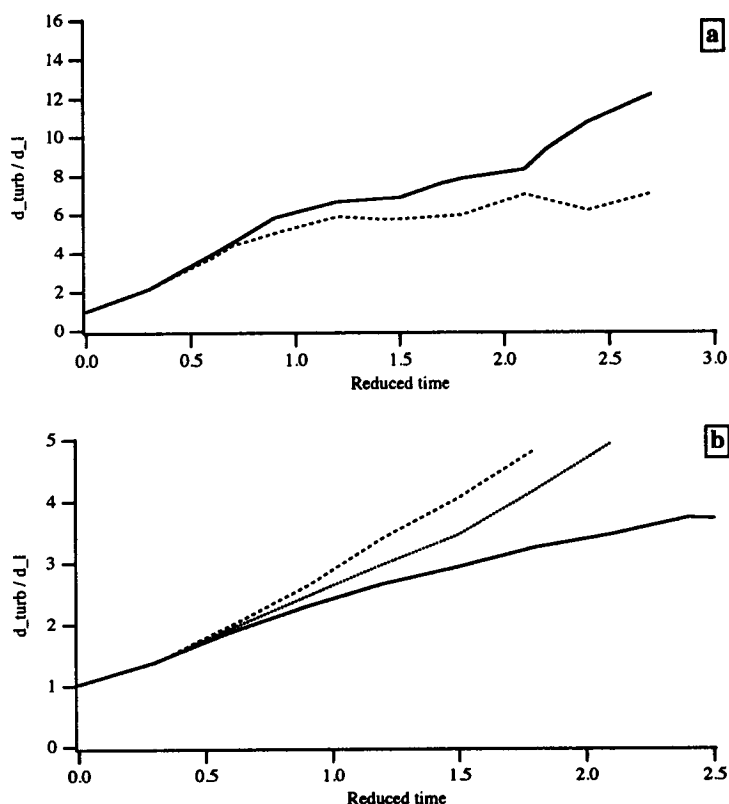
FIGURE 11. Reduced turbulent flame thickness δ_T/δ_l^0 plotted as a function of the reduced time t/t_f, where $t_f = \delta_l^0/s_l^0$ is a flame time, for different values of g^*. (a) initial turbulent level $u_0'/s_l^0 = 5$; cases A (———) and B (————); (b) initial turbulent level $u_0'/s_l^0 = 2$; cases C (———), D (········) and E (————). The turbulent flame brush is determined from the maximum value of the $\bar{c}$ gradient $(\delta_t = 1/Max\,(\partial\bar{c}/\partial x)$

The flame front wrinkling is somewhat increased by the adverse pressure gradient, due to the differential acceleration induced by buoyancy between fresh and burnt gases.

5.2 Effect of the mean pressure gradient on global turbulent flame characteristics

The global turbulent flame characteristics, namely the turbulent flame speed S_T and flame brush thickness δ_T, are plotted in Figs. 10 and 11 as a function of reduced time for different values of g^*. As expected from the previous flow-field visualizations, a favorable pressure gradient, i.e. $\partial\overline{P}/\partial x < 0$, which is generally encountered in practical situations of confined turbulent flames, leads to a thinner turbulent flame brush and a lower turbulent flame speed. The decrease in S_T may reach 30%. On the other hand, an adverse pressure gradient, i.e. $\partial\overline{P}/\partial x > 0$, induces an increase in flame brush thickness and a higher turbulent flame speed. These results are in agreement with the influence of a constant acceleration Γ on
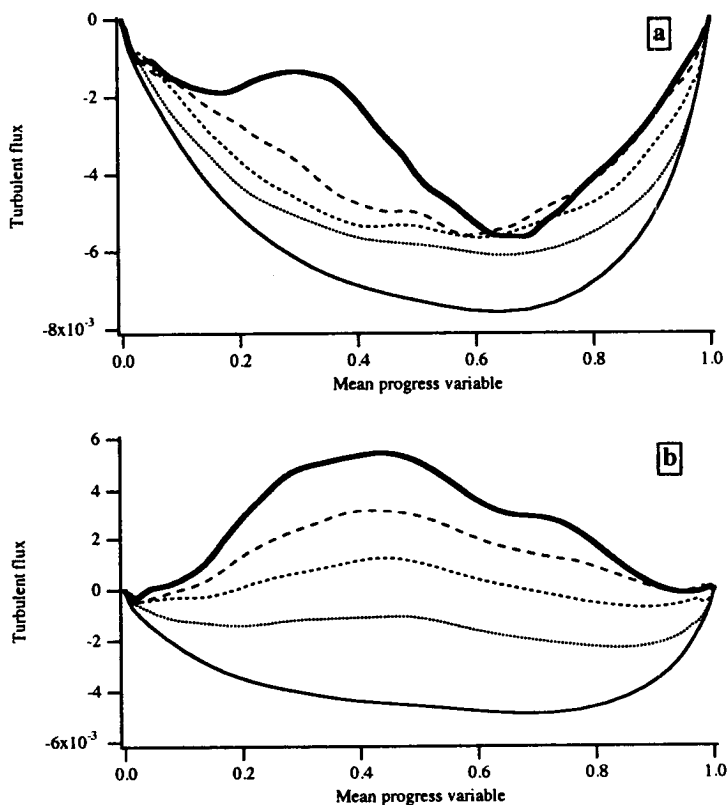
FIGURE 12. Transverse profiles of the turbulent flux $\overline{\rho u_1'' c''}$ plotted as a function of the mean progress variable $\tilde{c}$ for different reduced time step $t^+ = t/t_f$ where $t_f = \delta_l^0/s_l^0$ is a flame time. Initial turbulence level $u_0'/s_l^0 = 5$. $t^+ = 0.6$ (——); 0.9 (········); 1.2 (- - - -); 1.5 (— — —); 1.8 (——). (a) No imposed pressure gradient ($g^* = 0.$ - case A); (b) favorable imposed pressure gradient ($g^* = -6.25$ - case B).

S_T theoretically predicted by Libby (1989).

5.3 Turbulent transport $\overline{\rho u'' c''}$

The transverse profiles of the turbulent flux $\overline{\rho u'' c''}$ as a function of the mean progress variable $\tilde{c}$ for the cases A and B at various times are shown in Fig. 12. Case A, without an imposed mean pressure gradient, is clearly of gradient type, i.e. $\overline{\rho u'' c''} < 0$, whereas the imposed favorable pressure gradient leads to a counter gradient turbulent transport. This finding is in agreement with the work of Bray *et al.*(1982) and is expected from Eq. (7). Even in clearly counter gradient situations, the turbulent flux $\overline{\rho u'' c''}$ is always negative, or of gradient type, at the leading edge of the flame brush, where $\tilde{c} \to 0$. As shown by Bray and his coworkers, these gradient zones allow flame stabilization.

The total turbulent flux, i.e. $\int_{-\infty}^{+\infty} \overline{\rho u_1'' c''} dx$, is plotted as a function of the reduced time for the different simulations in Fig. 13. Favorable pressure gradients promote
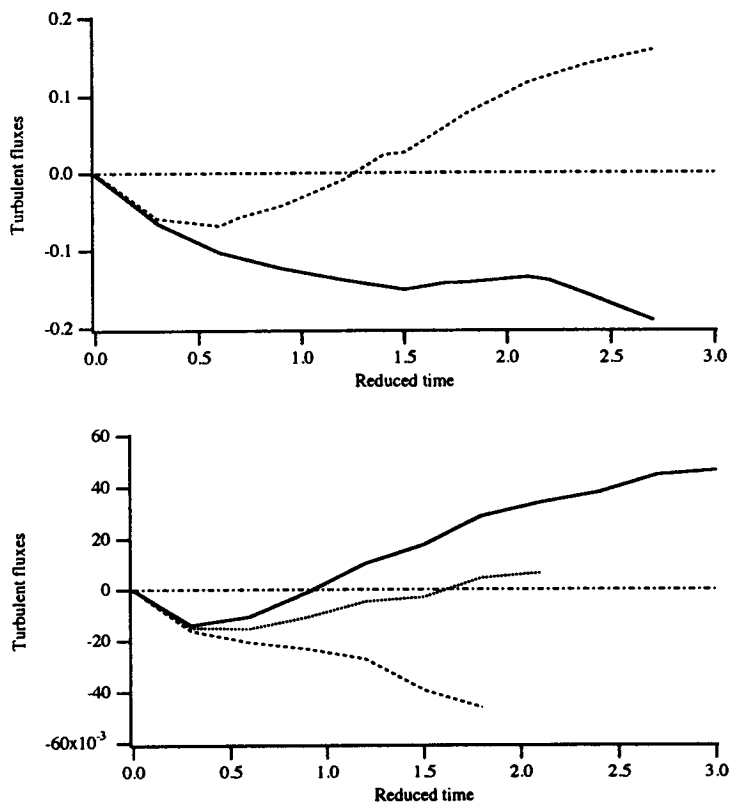
FIGURE 13.   Total turbulent flux $\int_{-\infty}^{+\infty} \widetilde{\rho u_1'' c''}\, dx$ plotted as a function of the reduced time t/t_f where $t_f = \delta_l^0/s_l^0$ is a flame time for the different cases. (a) initial turbulence level $u_0'/s_l^0 = 5$: Cases A (———) and B (– – – –); (b) initial turbulence level $u_0'/s_l^0 = 2$: Cases C (———), D ($\cdots\cdots$) and E (– – – –).

counter-gradient diffusion, corresponding to a reduction of both the turbulent flame speed S_T and the turbulent flame thickness δ_T. On the other hand, adverse pressure gradients lead to an increase in S_T and δ_T and induce gradient turbulent transport.

5.4 Analysis of the $\widetilde{\rho u'' c''}$ transport equation

All terms in Eq. 7 may be obtained from direct numerical simulations. This analysis serves to identify the dominant terms as well as the nature of their contribution. A typical direct numerical simulation evaluation of terms (I)-(X) appearing in the $\tilde{c}$-flux budget of Eq. 7 is presented in Fig. 14 for case C. The figure also displays the imbalance that was found when numerically closing the $\tilde{c}$-flux budget in Eq. 7. This imbalance is due to inherent numerical errors involved in the simulations as well as in the post-processing of the data. Its magnitude remains small, which suggests that the simulations can be used to analyze the variations of second-order moments. For instance, Fig. 14 shows that the dissipation terms (VIII) and (IX), which are generally modeled together, are of the same order and act to promote gradient diffusion.

FIGURE 14. Variations of the different terms appearing in the $\tilde{c}$-flux budget across the turbulent flame brush. Case C: counter-gradient turbulent diffusion and no imposed pressure gradient.

On the other hand, pressure terms (VI) and (VII), and the velocity-reaction rate correlation (X), strongly act to promote counter-gradient diffusion. The two source terms due to mean progress variable gradient (IV) and mean velocity gradient (V) tend to decrease the turbulent fluxes as expected and, accordingly, in the present counter-gradient situation act to promote gradient turbulent diffusion. The mean pressure gradient term corresponds to the pressure jump across the flame brush (see Fig. 17):

$$-\overline{c''}\frac{\partial \overline{p}}{\partial x} = (\overline{c} - \tilde{c})\frac{\partial \overline{p}}{\partial x} \approx \tau \frac{\tilde{c}(1 - \tilde{c})}{1 + \tau\tilde{c}} \frac{\rho_u \tau (s_l^0)^2}{\delta_T} \qquad (22)$$

The fluctuating pressure term (VII) cannot be neglected as generally assumed in the models proposed to close the transport equation (7).

A similar analysis is now performed for case E, where, due to the imposed adverse pressure gradient, the turbulent diffusion becomes gradient type, as indicated in Fig. 15. As expected, the mean pressure gradient term tends to promote gradient turbulent diffusion and corresponds to the imposed pressure gradient. Once again, the fluctuating pressure term (VII) is not negligible and acts to counterbalance the mean pressure gradient term (VI). In fact, the combined term (VI) + (VII) is mainly negative and corresponds to a gradient diffusion. The reaction term acts to promote counter-gradient diffusion.

The budget of the transport equation for $\overline{\rho u_1'' c''}$ for case B is presented in Fig. 16.
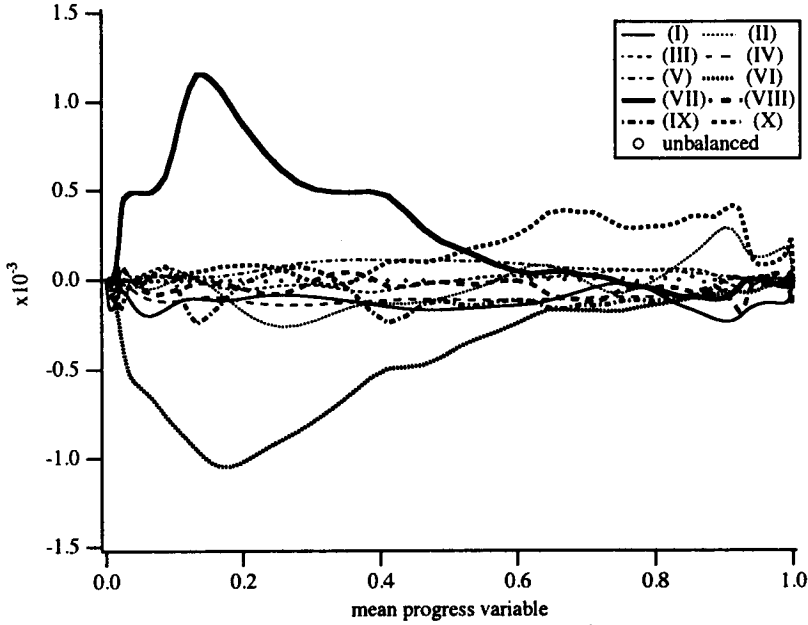
FIGURE 15.   Variations of the different terms appearing in the $\widetilde{c}$-flux budget across the turbulent flame brush. Case E: gradient turbulent diffusion induced by an adverse mean pressure gradient.

The favorable mean pressure gradient acts to promote counter-gradient turbulent diffusion from term (VI). Once again, term (VII) tends to counterbalance term (VI). For such a situation, Bray *et al.*(1982) propose to neglect the pressure fluctuation effects (term VII) and assume that only the cross-dissipation terms (VIII + IX) can provide a balance to the mean pressure term (VI). In fact, from our simulation, the mean pressure term (VI) is balanced by the sum of the three contributions: the cross-dissipation term (VIII + IX), the pressure fluctuation term (VII) that cannot be neglected, and the source term due to gradients of $\widetilde{c}$ (IV).

The mean pressure gradient across the flame brush may be simply modeled as the sum of two contributions: the imposed pressure gradient and the pressure jump due to thermal heat release. As a result, the source term (VI) in $\overline{\rho u'' c''}$ becomes:

$$-\overline{c''}\frac{\partial \overline{p}}{\partial x} = (\overline{c} - \widetilde{c})\frac{\partial \overline{p}}{\partial x} \approx \tau \frac{\widetilde{c}(1 - \widetilde{c})}{1 + \tau\widetilde{c}} \left[\frac{\rho_u \tau (s_l^0)^2}{\delta_T} - \overline{\rho}\Gamma \right] \qquad (23)$$

where $\overline{\rho}\Gamma$ corresponds to the imposed pressure gradient. This expression is verified in the present simulations (Fig. 17).

6. Theoretical analysis and modeling

6.1 Model for turbulent flux without pressure gradient

In this section, we first recall the derivation of a model for the turbulent flux of the mean progress variable $\widetilde{c}$. Details about this modeling may be found in Veynante *et*
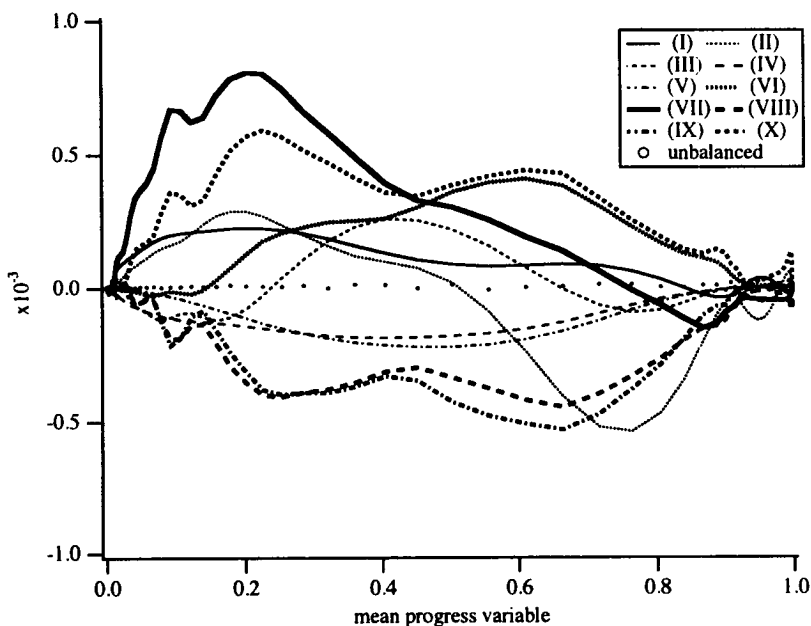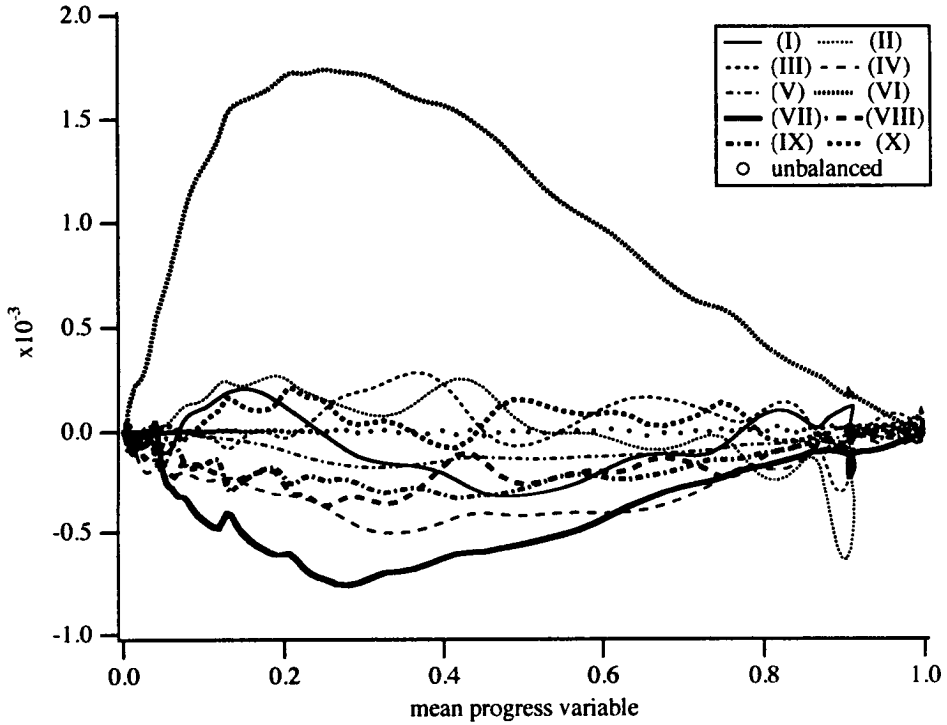
FIGURE 16. Variations of the different terms appearing in the $\widetilde{c}$-flux budget across the turbulent flame brush. Case B: counter-gradient turbulent diffusion induced by a favorable mean pressure gradient.

al.(1995). This derivation starts from a relation proposed by Bidaux & Bray (1994) connecting the flame front averaged fluctuating velocity, $\langle u_i'' \rangle_s$, to the conditioned unburnt and burnt mean velocities:

$$\langle u_i'' \rangle_s = (c^* - \widetilde{c})(\overline{u_{ib}} - \overline{u_{iu}}) \tag{24}$$

where c^* corresponds to the iso-c line used to define the flame location.

From Eq. (4), the previous relation leads to:

$$\langle u_i'' \rangle_s = \frac{(c^* - \widetilde{c})}{\widetilde{c}(1 - \widetilde{c})} \widetilde{u_i'' c''} \tag{25}$$

This expression may be used to derive an estimate of $\widetilde{u_i'' c''}$ via a model for the mean velocity fluctuation $\langle u_i'' \rangle_s$; considering limiting cases of low turbulence levels where flow dynamic is mainly controlled by the thermal expansion across the flame brush, and high turbulence levels where the turbulent velocities dominate the flow induced by thermal expansion, Veynante *et al.*(1995) proposed the following expression for $\langle u_1'' \rangle_s$ where index 1 corresponds to the direction normal to the flame:

$$\langle u_1'' \rangle_s = (c^* - \widetilde{c})(\tau s_L - 2\alpha u') \tag{26}$$
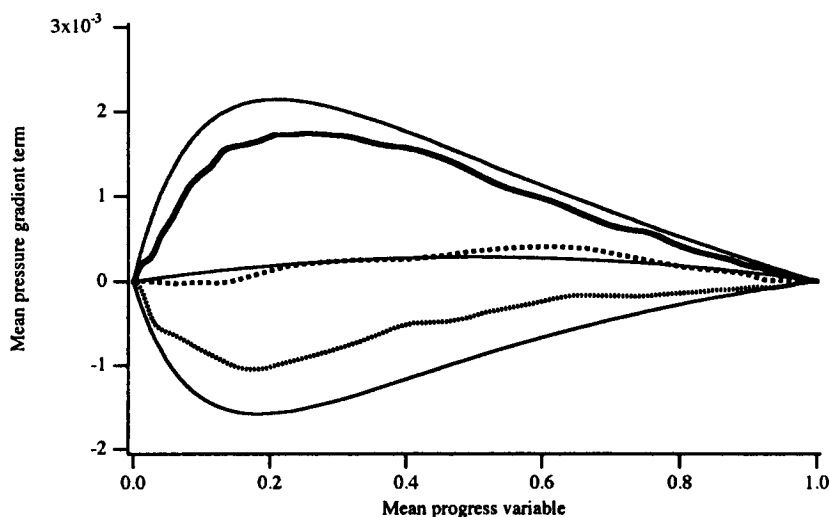
FIGURE 17. Comparison between direct numerical simulation data for cases B (———), C (————) and E (········) and modeled mean pressure gradient source term (———) from Eq. (23) in the the $\widetilde{c}$-flux transport equation (Eq. 7).

leading to:

$$\widetilde{u_1''c''} = \widetilde{c}(1 - \widetilde{c})(\tau s_L - 2\alpha u') \tag{27}$$

and to the Bray number criterion. Here u' denotes the rms velocity fluctuations and α is an efficiency function to take into account the low ability of small turbulent vortices to affect the flame front.

6.2 Model for turbulent flux with pressure gradient

Our objective in this section is to incorporate pressure gradient effects in the previous analysis. Pressure gradients induce differential buoyancy effects between cold heavy reactants and light hot products. We quantify this buoyancy effect through a characteristic velocity $U_B(\widetilde{c})$, which is simply added to the two velocities used in Eq. (26): the velocity induced by the flame, $(c^* - \widetilde{c})\tau s_L$; and the velocity induced by turbulence, $2(c^* - \widetilde{c})\alpha u'$,

$$\langle u_1'' \rangle_s = (c^* - \widetilde{c})(\tau s_L - 2\alpha u') + U_B(\widetilde{c}) \tag{28}$$

The estimation of $U_B(\widetilde{c})$ is done as follows. In the fresh gases, $U_B(0) = U_B^b$ corresponds to the relative speed of a pocket of burnt gas (density ρ_b, diameter l).

Similarly a velocity $U_B(1) = U_B^u$ will be associated to the movement of unburnt gas pockets in the burnt products. Assuming an equilibrium between buoyancy and drag forces and using Stokes law for the drag of the pocket, U_B^b is given by:

$$U_B^b \approx -\frac{1}{12}\frac{\tau}{\tau+1}\frac{l^2}{\nu_u}\Gamma \tag{29}$$

where ν_u is the kinematic viscosity in the fresh gases.

For a pocket of fresh gases with density ρ_u and diameter l, the same analysis leads to a relative displacement speed U_B^u:

$$U_B^u \approx \frac{1}{12}\frac{\tau l^2}{\nu_b}\Gamma \tag{30}$$

where ν_b is the kinematic viscosity in the burnt gases.

Assuming a linear variation of the buoyancy velocity $U_B(\tilde{c})$ with $\tilde{c}$ between the flame leading and trailing edges leads to:

$$U_B(\tilde{c}) \approx \frac{1}{12}\frac{\tau}{\tau+1}\frac{l^2}{\nu_u}\Gamma\left[\left(1+(\tau+1)^{1-n}\right)\tilde{c}-1\right] \tag{31}$$

where the kinematic viscosity ratio has been estimated as: $\frac{\nu_u}{\nu_b} \approx \left(\frac{T_u}{T_b}\right)^n = \left(\frac{1}{\tau+1}\right)^n$ and $n = 1.76$.

For $3 \leq \tau \leq 6$, we have $0.74 \leq 1/\left(1+(\tau+1)^{1-n}\right) \leq 0.8$. In a first step, to achieve simple expressions, the c-level retained to define the flame front may be chosen as $c^* = 1/\left(1+(\tau+1)^{1-n}\right)$, leading to:

$$U_B(\tilde{c}) \approx \frac{1}{12}\frac{\tau}{c^*(\tau+1)}\frac{l^2}{\nu_u}\Gamma(\tilde{c}-c^*) \tag{32}$$

Then, from Eq. (25) and (28), a simple model for the turbulent flux $\widetilde{u_1''c''}$ is:

$$\widetilde{u_1''c''} = \tilde{c}(1-\tilde{c})\left(\tau s_L - 2\alpha u' - \beta\frac{\tau l^2}{12c^*(\tau+1)\nu_u}\Gamma\right) \tag{33}$$

where a model constant β is introduced to take into account the various limitations of the simplified analysis proposed here.

The previous expression needs a characteristic length l corresponding to the typical size of a pocket of fresh gases in a medium of burnt gases, and vice versa. As a first step, the integral length scale l_t, a rough estimate of the flame front wrinkling scale, is used. Predictions from expression (33) are compared with simulation data for the reduced time 1.8 in Fig. 18 using $c^* = 0.8$ and $\beta = 0.12$. The efficiency function, α, is a function of the length scale ratio l_t/δ_l and is obtained from previous direct numerical simulations (Veynante *et al.*, 1995) to be about 0.5 for the length
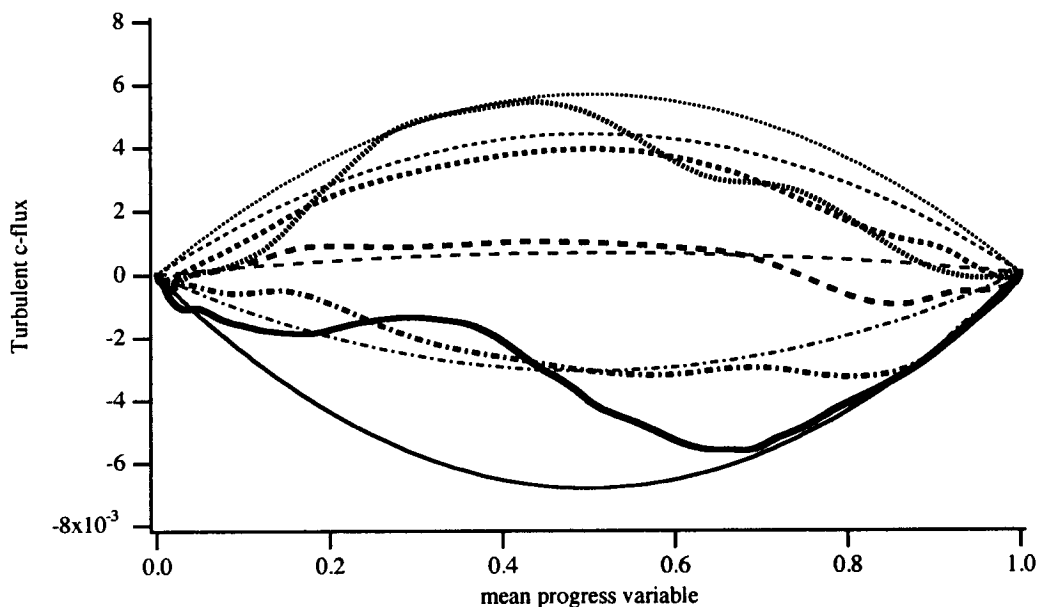
FIGURE 18. Comparison between direct numerical simulation data (Bold curves) and model predictions (thin curves) from Eq. 33 of the turbulent flux $\widetilde{u_1''c''}$ as a function of the mean progress variable $\tilde{c}$ at reduced time 1.8 for cases A (———), B (⋯⋯⋯), C (– – – –), D (— — —), and E (—·—). $\alpha = 0.5$, $\beta = 0.12$ and $c^* = 0.8$. The characteristic length l is taken equal to the integral length scale l_t

scale ratio used here. The agreement between numerical data and model predictions is satisfactory. The influence of the imposed acceleration and the transition between gradient and counter-gradient transport are well predicted from Eq. (33).

A simple criterion may be derived to predict the occurrence of counter-gradient turbulent diffusion, i.e. $\widetilde{u_1''c''} \geq 0$), from Eq. 33:

$$N_B^\Gamma = \frac{\tau}{2\alpha \frac{u'}{s_L}} \left[1 - \beta \frac{l^2 \Gamma}{12c^* (\tau + 1) \nu_u s_L} \right] \geq 1 \tag{34}$$

The effect of the constant acceleration is to introduce a coefficient for the Bray number N_B defined by Veynante *et al.*(1995), see Eq. (3). N_B^Γ may be rewritten as:

$$N_B^\Gamma = \frac{\tau}{2\alpha \frac{u'}{s_L}} \left[1 - \beta \frac{g^* Re_f}{12c^* (\tau + 1)} \left(\frac{l}{\delta_l} \right)^2 \right] \geq 1 \tag{35}$$

where $Re_f = \delta_l s_L / \nu_u$ is a flame Reynolds number.

This modified Bray number may be estimated from our numerical simulation using the initial turbulence values ($l = l_t$, $u' = u'_0$, $s_L = s^0_l$), $\alpha = 0.5$ (from (Veynante *et al.*, 1995), $\beta = 0.12$ and $c^* = 0.8$. Results are summarized and validated in Table IV; it appears that $N^\Gamma_B \geq 1$ flows indeed exhibit counter-gradient diffusion.

The same analysis may be easily extended to the case of an externally imposed pressure gradient $\partial \overline{P}/\partial x$, leading to

$$U_B(\widetilde{c}) \approx \frac{\tau l^2}{12\rho_u \nu_u} \left(\frac{\partial \overline{P}}{\partial x}\right) \left[\left(1 + (\tau + 1)^{1-n}\right)\widetilde{c} - 1\right] \tag{36}$$

and

$$\widetilde{u''_1 c''} = \widetilde{c}(1 - \widetilde{c})\left(\tau s_L - 2\alpha u' - \beta \frac{\tau l^2}{12\rho_u \nu_u c^*}\left(\frac{\partial \overline{P}}{\partial x}\right)\right) \tag{37}$$

This expression leads to the following criterion for counter-gradient turbulent transport:

$$N^p_B = \frac{\tau}{2\alpha\frac{u'}{s_L}}\left[1 - \beta\frac{\tau \nabla p^* Re_f}{12c^*}\left(\frac{l}{\delta_l}\right)^2\right] \geq 1 \tag{38}$$

$$\nabla p^* = \left(\frac{\partial \overline{P}}{\partial x}\right)\frac{\delta_l}{\rho_u \tau s^2_l}$$

which is the reduced pressure gradient (i.e. the pressure gradient made nondimensionalized by the pressure gradient across the corresponding laminar flame). The previous result is based on a simple analysis, assuming an equilibrium between buoyancy and drag forces for a pocket of fresh (burnt) gases in a medium of burnt (fresh) gases. This approach is probably too crude and has to be improved to describe the instability mechanisms of an interface between two gases with different densities. The dependence of $\widetilde{u''c''}$ with the square of the integral length scale l_t needs to be examined and validated, especially for large values of l_t.

TABLE IV. Estimation of N^Γ_B. GD (CGD) refers to gradient (counter-gradient) turbulent diffusion

Case	u'_0/s^0_l	l_t/δ^0_l	g^*	*GD/CGD*	N^Γ_B
A	5.	3.5	0.	GD	0.60
B	5.	3.5	-6.25	CGD	1.3
C	2.	2.7	0.	CGD	1.5
D	2.	2.7	3.12	GD	0.96
E	2.	2.7	6.25	GD	0.43

In the experiment of Shepherd *et al.*(1982), $u' \approx 1$ m/s and $l_t \approx 1$ cm, leading to Bray numbers $N_B \approx 0.9$ and $N^p_B \approx 20$. Due to the large length scale ratio,

$l_t/\delta_l \approx 20$, $\alpha = 1$, (cf. Veynante *et al.*1995). These results are compared in Table V with the experimental estimation of the turbulent flux $\overline{\rho u_1''c''}$. Accordingly, the unconfined case without pressure gradients lies in the transition region between gradient and counter-gradient diffusion. In fact, counter-gradient diffusion is found in the experiment, but the turbulent flux remains quite low. On the other hand, the confined case with an externally imposed pressure gradient, N_B^p measures the intensity and the sign of the turbulent flux $\overline{\rho u_1''c''}$. The large value of N_B^p for the confined experiment is questionable because of the large length scale ratio (l_t/δ_l).

TABLE V. Estimation of N_B^p in the Shepherd *et al.*(1982) experiment for the confined (with pressure gradients) and unconfined (without pressure pressure gradients). Experimental estimations of $\overline{\rho u_1''c''}/\overline{\rho}\widetilde{U}_0$, where $\widetilde{U}_0$ is the reference burner inlet velocity, are provided. $u' \approx 1$ m/s, $l_t \approx 1$ cm.

Case	N_B^p	$\overline{\rho u_1''c''}/\overline{\rho}\widetilde{U}_0$
unconfined	0.9	0.0043
confined	20.	0.051

7. Conclusion

The influence of a constant acceleration Γ on a turbulent premixed flame is studied by direct numerical simulation. This acceleration Γ induces a mean pressure gradient across the flame brush, leading to a modification of the turbulent flame structure due to differential buoyancy mechanisms between heavy cold fresh and light hot burnt gases. Such a pressure gradient may be encountered in practical applications in ducted flames.

A favorable pressure gradient, i.e. the pressure decreases from unburnt to burnt gases, is found to decrease the flame wrinkling, the flame brush thickness, and the turbulent flame speed. A favorable pressure gradient also promotes counter-gradient turbulent transport. On the other hand, adverse pressure gradients tend to increase the flame brush thickness and turbulent flame speed, and promote classical gradient turbulent transport.

The balance equation for the turbulent flux $\overline{\rho u''c''}$ of the Favre averaged progress variable $\bar{c}$ is also analyzed. The first results show that the fluctuating pressure term, $(\overline{c''\partial p'\partial x})$, cannot be neglected as generally assumed in models. Simple models assuming that a high mean pressure gradient may only be balanced by the cross-dissipation term seem too approximate. This analysis has to be continued to compare simulation data and closure schemes proposed for the $\overline{\rho u''c''}$ transport equation.

The analysis developed by Veynante *et al.*(1995) has been extended to imposed acceleration and mean pressure gradients. A simple model for the turbulent flux $\widetilde{u''c''}$ is proposed and validated from simulation data. Then, a modified criterion is derived to delineate between counter-gradient and gradient turbulent diffusion. In

fact, counter-gradient diffusion may occur in most practical applications, especially for ducted flames.

REFERENCES

BRAY, K. N. C. 1980 Turbulent flows with premixed reactants. *in Topics in Applied Physics* **44**. Springer-Verlag.

BRAY, K. N. C., LIBBY, P. A., MASUYA, G. & MOSS, J. B. 1981 Turbulence production in premixed turbulent flames. *Comb. Sci. Tech.* **25**, 127-140.

BRAY, K. N. C., MOSS, J. B. & LIBBY, P. A. 1982 Turbulent transport in premixed flames *in Convective Transport and Instability Phenomena*, J. Zierep and H. Oertel, University of Karlsruhe.

BRAY, K. N. C., CHAMPION, M. & LIBBY, P. A. 1989 The interaction between turbulence and chemistry in premixed turbulent flames. In *Turbulent Reactive Flows, Lecture Notes in Eng.* **40**, Springer-Verlag.

BRAY, K. N. C. 1990 Studies of the turbulent burning velocity. *Proc. R. Soc. Lond. A.* **431**, 315-335.

HAWORTH, D. C. & POINSOT, T. 1992 Numerical simulations of Lewis number effects in turbulent premixed flames. *J. Fluid Mech.* **244**, 405-436.

LIBBY, P. A. & BRAY, K. N. C. 1981 Countergradient diffusion in premixed turbulent flames. *AIAA J.* **19**, 205-213.

LIBBY, P. A. 1989 Theoretical analysis of the effect of gravity on premixed turbulent flames. *Comb. Sci. Tech.* **68**, 15-33.

MASUYA, G. & LIBBY, P. A. 1981 Nongradient theory for oblique turbulent flames with premixed reactants. *A.I.A.A. Journal.* **19**, 1590-1599.

MOSS J. B. 1980 Simultaneous Measurements of Concentration and Velocity in an Open Premixed Turbulent Flame. *Combust. Sci. Tech.* **22**, 119-129.

POINSOT, T, & LELE, S. K. 1992 Boundary conditions for direct numerical simulations of compressible viscous flows. *J. Comp. Phys.* **101**, 104-129.

RUTLAND, C. J. & CANT, R. S. 1994 Turbulent transport in premixed flames. *Proc. of the Summer Program*, Center for Turbulence Research, NASA Ames/-Stanford Univ.

SHEPHERD, I. G., MOSS, J. B. & BRAY, K. N. C. 1982 Turbulent transport in a confined premixed flame. *Nineteenth Symp. (International) on Combust.* 423-431. The Combustion Institute.

TROUVÉ, A., VEYNANTE, D. BRAY, K. N. C. & MANTEL, T. 1994 The coupling between flame surface dynamics and species mass conservation in premixed turbulent combustion. *Proc. of the Summer Program*, Center for Turbulence Research, NASA Ames/Stanford Univ.

VEYNANTE, D., TROUVÉ, A., BRAY, K. N. C. & MANTEL T. 1995 Gradient and counter-gradient scalar transport in turbulent premixed flames. (Submitted to *J. Fluid Mech.*)

WILLIAMS, F. A. 1985 *Combustion theory.* 2nd ed., Benjamin Cummings.

Appendix I: tests of NTMIX with constant force or accelerations

To validate the implementation of volume forces in the simulation, simple examples of one-dimensional flows with constant force or acceleration have been run. We consider an isentropic one-dimensional flow submitted to a force F_v. F_v is either constant or equal to $\rho\gamma$. The governing equations are:

$$\frac{\partial(\rho u)}{\partial x} = 0$$

$$\frac{\partial(\rho u^2 + p)}{\partial x} = F$$

For constant volume force F_v, F is constant and equal to F_v and for constant acceleration, $F = \rho\Gamma$.

This system is integrated once to give:

$$\rho u = \rho_0 u_0$$

$$\frac{\partial u}{\partial x} = -\frac{u_0}{c_o^2 \rho_0} \cdot \frac{F}{(u_0/u)^{\gamma+1}(1. - M^2(u/u_0)^{\gamma+1})}$$

where index 0 designates the inlet condition. $M = u/c$ is the local Mach number and $\gamma = 1.4$.

If the local Mach number M is small, this system may be integrated easily to give:

For constant volume force F_v:

$$u(x) = u_0(1 - \frac{F_v x}{P_0})^{-1/\gamma}$$

$$\rho(x) = \rho_0(1 - \frac{F_v x}{P_0})^{1/\gamma}$$

$$P(x) = P_0 - F_v x$$

Note that $\frac{\partial P}{\partial x} = -F_v$

For constant acceleration Γ:

$$u(x) = u_0(1 + \frac{(\gamma+1)\Gamma x}{c_0^2})^{-1/(\gamma+1)}$$

$$\rho(x) = \rho_0(1 + \frac{(\gamma+1)\Gamma x}{c_0^2})^{1/(\gamma+1)}$$

$$P(x) = P_0(1 + \frac{(\gamma + 1)\Gamma x}{c_0^2})^{\gamma/(\gamma+1)}$$

where c_0 is the inlet sound speed ($c_0 = \gamma P_0/\rho_0$).

For small values of Γ, $\frac{\partial P}{\partial x} = \rho_0 \Gamma$

Fig. 19 shows (for a constant volume force $F_v/\rho_0 c_0^2 = 0.01$) that the simulation results match these analytical expressions well. (A similar agreement is obtained in the case of a constant acceleration)
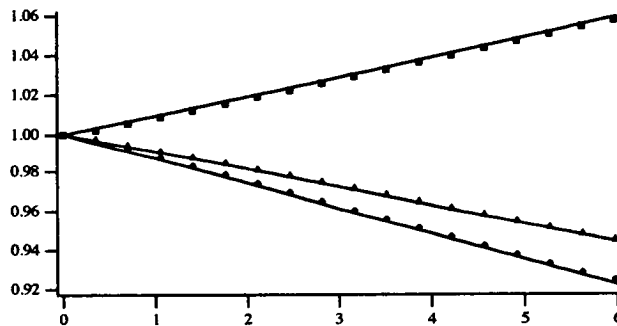

FIGURE 19. Tests of code for one-dimensional flow with constant volume force $F_v/\rho_0 c_0^2 = 0.01$. Comparison between simulation data: velocity (■), pressure (◇), density (▲) and analytical results (——).

Modeling complex chemical effects in turbulent nonpremixed combustion

By Nigel S. A. Smith

1. Motivation

Virtually all of the energy derived from the consumption of combustibles occurs in systems which utilize turbulent fluid motion. Since combustion is largely related to the mixing of fluids and mixing processes are orders of magnitude more rapid when enhanced by turbulent motion, efficiency criteria dictate that chemically powered devices necessarily involve fluid turbulence.

Where combustion occurs concurrently with mixing at an interface between two reactive fluid bodies, this mode of combustion is called *nonpremixed* combustion. This is distinct from *premixed* combustion where flame-fronts propagate into a homogeneous mixture of reactants. These two modes are limiting cases in the range of temporal lag between mixing of reactants and the onset of reaction. Nonpremixed combustion occurs where this lag tends to zero, while premixed combustion occurs where this lag tends to infinity. Many combustion processes are hybrids of these two extremes with finite non-zero lag times.

Turbulent nonpremixed combustion is important from a practical standpoint because it occurs in gas fired boilers, furnaces, waste incinerators, diesel engines, gas turbine combustors, and afterburners etc. To a large extent, past development of these practical systems involved an empirical methodology. Presently, efficiency standards and emission regulations are being further tightened (Correa 1993), and empiricism has had to give way to more fundamental research in order to understand and effectively model practical combustion processes (Pope 1991).

A key element in effective modeling of turbulent combustion is making use of a sufficiently detailed chemical kinetic mechanism. The prediction of pollutant emission such as oxides of nitrogen (NO_x) and sulphur (SO_x), unburned hydrocarbons, and particulates demands the use of detailed chemical mechanisms. It is essential that practical models for turbulent nonpremixed combustion are capable of handling large numbers of 'stiff' chemical species equations.

1.1 Reactive Species Closure problem

A common way of idealizing a turbulent flow field is to decompose it into an averaged flow component and a deviational contribution. The nature of the deviational component depends upon the flow and the averaging scheme, but the object of the decomposition is to be able to understand and predict the development of the average component without detailed knowledge of the deviations present in each realization of the flow.

The classical difficulty faced in modeling turbulent nonpremixed combustion is that of closing the averaged equations for chemically reactive species. The instantaneous equation for the evolution of the mass fraction Y_α of a reactive species α is

the following,

$$\frac{\partial}{\partial t}(\rho Y_\alpha) + \frac{\partial}{\partial x_i}(\rho u_i Y_\alpha) = \frac{\partial}{\partial x_j}(\rho D_\alpha \frac{\partial Y_\alpha}{\partial x_j}) + \rho \dot{w}_\alpha \qquad (1)$$

where $\dot{w}_\alpha$ is the net chemical production rate of the species α, and D_α is the corresponding molecular diffusivity where a simplified Fickian approximation has been made to model molecular transport. Applying a traditional averaging scheme, such as density weighted (Favre) unconditional ensemble averaging, yields the following,

$$\frac{\partial}{\partial t}(\bar{\rho}\tilde{Y}_\alpha) + \frac{\partial}{\partial x_i}(\bar{\rho}\widetilde{u_i Y}_\alpha) = \frac{\partial}{\partial x_j}(\bar{\rho}D_\alpha\widetilde{\frac{\partial Y_\alpha}{\partial x_j}}) + \bar{\rho}\tilde{\dot{w}}_\alpha. \qquad (2)$$

In order to close the averaged species equation a model must be provided for the averaged source term $\tilde{\dot{w}}_\alpha$. First order closures that evaluate the instantaneous chemical rate expressions with averaged species concentrations and temperature,

$$\tilde{\dot{w}}_\alpha(Y_1, Y_2, \ldots, Y_N, T) \approx \dot{w}_\alpha(\tilde{Y}_1, \tilde{Y}_2, \ldots, \tilde{Y}_N, \tilde{T}) \qquad (4)$$

are known to be highly inaccurate in combustion cases of practical interest. The chemical reactions encountered in combustion processes are highly nonlinear, and thus small perturbations in the input parameters can cause very large changes in the computed reaction rate.

1.2 Conditional Moment Closure method

The philosophy underpinning the Conditional Moment Closure (CMC) method, as described by Bilger (1991, 1993), is to minimize the level of perturbations from the mean by averaging the reactive species equations *conditionally* upon a conserved scalar mass fraction. In so doing, the resultant statistical moments account for the variations in fluid concentration which result from turbulent mixing alone. At the expense of adding an additional computational dimension to the modeling problem, conditional averaging allows chemical closure to be achieved for most cases of nonpremixed turbulent combustion.

The average of a fluctuating turbulent quantity A, conditional upon the conserved scalar mixture fraction $\xi(x_i, t)$ being equal to a sample value η, is the following (see Klimenko 1990):

$$< A(x_i,t) \mid \xi(x_i,t) = \eta > \equiv \frac{1}{P_\eta} \int \int A(x_i,t)\delta(\xi(x_i,t) - \eta)dx_i dt \qquad (5)$$

In the above definition, P_η is the probability density function of the conserved scalar at the location x_i and time t, and δ denotes the Dirac delta function. In all that follows, the full conditional averaging operator $< \ldots \mid \xi(x_i,t) = \eta >$ will be abbreviated to $< \ldots \mid \eta >$ for the sake of brevity.

Klimenko (1990, 1992) and Bilger (1991, 1993) independently showed that the evolution of the conditional mean mass fraction $Q_\alpha \equiv\, <Y_\alpha \mid \eta>$ of a reactive species α is governed by the following,

$$<\rho \mid \eta> \frac{\partial Q_\alpha}{\partial t} + <\rho u_i \mid \eta> \frac{\partial Q_\alpha}{\partial x_i} = \frac{1}{2} <\rho\chi \mid \eta> \frac{\partial^2 Q_\alpha}{\partial \eta^2} + <\rho\dot{w}_\alpha \mid \eta> +e_q \quad (6)$$

where the molecular diffusivities of all species are assumed to be uniform. The residual term e_q is a conditional correlation between deviational velocity and mass fraction, which is typically assumed to be small. This assumption is not valid in cases where substantial premixing of the reactants occurs, in which case this term can become very important in the reactive species equation (Bilger 1991).

$$e_q \equiv -\frac{\partial}{\partial x_i}(P_\eta <\rho \mid \eta><u_i' q_\alpha' \mid \eta>)/P_\eta \quad (7)$$

The symbol χ denotes the instantaneous scalar dissipation rate and is defined (below) in terms of the mixture fraction ξ.

$$\chi \equiv 2D_\xi (\frac{\partial \xi}{\partial x_i})^2 \quad (8)$$

In order to close the CMC scalar equation, means of determining $<\chi \mid \eta>$ and $<\dot{w}_\alpha \mid \eta>$ are required.

Klimenko (1992) (see also Klimenko and Bilger 1992) showed that the conditional mean scalar dissipation rate should be determined from the conserved scalar PDF equation to ensure conservation of mass.

$$\frac{\partial}{\partial t}(<\rho \mid \eta> P_\eta) + \frac{\partial}{\partial x_i}(<\rho u_i \mid \eta> P_\eta) = -\frac{1}{2}\frac{\partial^2}{\partial \eta^2}(<\rho\chi \mid \eta> P_\eta) + e_\xi \quad (9)$$

The residual term e_ξ describes molecular diffusion of the PDF in physical space and is negligible at high Reynolds numbers.

Closure of the chemical source term is achieved via a simple first order approximation involving *conditionally* averaged species mass fractions $<\dot{w}_\alpha \mid \eta> \approx \dot{w}_\alpha(Q_1, \ldots, Q_N, <T \mid \eta>)$. This closure approximation is valid in all cases except where the combustion system is close to extinction, since in those cases deviations from the conditional means are large. In such instances doubly conditioned modeling, using conditions upon mixture fraction and a reaction progress variable, is a suitable course of action (Bilger 1991).

The single greatest advantage of the CMC method over other turbulent nonpremixed combustion models is its ability to cope with very detailed chemical descriptions. When contrasted with the Joint Probability Density Function (JPDF) method (see Pope 1985, 1991) the CMC method only adds a new equation to be solved with each new species rather than an additional dimension to the problem. In comparison to laminar flamelet methods, the CMC method does not require there to be a large separation of characteristic scales between mixing and chemical reaction in order to be applicable.

2. Objectives

The objective of this study was to evaluate the CMC method for turbulent non-premixed combustion, verify or debunk current model assumptions, and where possible suggest model refinements.

Direct numerical simulations (DNS) of nonpremixed combustion in isotropic decaying turbulence were carried out as a first step in this study. By studying nonpremixed combustion in isotropic turbulence with an isotropic flame distribution, all of the computational grid points can be used in calculating spatially degenerate statistics. These statistics allow important modeling problems to be examined without interference from the extraneous, though also important, complications introduced by mean gradients.

Of key interest in this study is the effectiveness of the first order chemical closure employed by the current CMC methodology in a system which embodies the essential elements of combustion chemistry. In this study one- and two-step chemical mechanisms were employed to describe $H_2 - N_2$ fuel burning in air. The one-step mechanism is composed of the non-carbon step from the two-step wet-CO mechanism of Chung and Williams (1990), and allows for global reaction termination due to radical consumption even though no radical species are actually carried (see below).

$$2H_2 + O_2 \rightarrow 2H_2O \qquad\qquad (I')$$

The two-step mechanism carries the crucial radical, monatomic hydrogen (H), and contains distinct reactions for radical formation and consumption. The chemical rate constants for reactions I and II (see below) were also taken from the non-carbon steps of Chung and Williams (1990).

$$3H_2 + O_2 \rightleftharpoons 2H_2O + 2H \qquad\qquad (I)$$

$$H + H + M \rightarrow H_2 + M \qquad\qquad (II)$$

In addition to the abundance of evidence in chemical kinetic literature, recent DNS studies conducted at the CTR have demonstrated the importance of the explicit calculation of chemical radical species in combustion simulations (see Mantel 1994, Vervisch 1992).

Differential diffusion of reactive scalars in nonpremixed combustion is left unmodeled by both the CMC (Smith 1994) and JPDF methods (Yeung and Pope 1993). Although it is of diminished importance in highly turbulent combustion, practical cases have been found where differential diffusion is significant (see Chen *et al.* 1990, Smith *et al.* 1993, Smith 1994, Bilger 1982). The secondary objective of this study was to observe differential diffusion phenomena by comparing simulations that are identical save for the specification of uniform or non-uniform species molecular diffusivities. These observations are to be used to develop model refinements for the prediction of differential diffusion behavior.

2.1 Modeling method

The spatially degenerate CMC and PDF equations corresponding to statistically isotropic conditions with uniform molecular diffusivities are given below,

$$\frac{\partial Q_\alpha}{\partial t} = \frac{1}{2} < \chi \mid \eta > \frac{\partial^2 Q_\alpha}{\partial \eta^2} + < \dot{w}_\alpha \mid \eta > \qquad (10)$$

$$\frac{\partial}{\partial t}(< \rho \mid \eta > P_\eta) = -\frac{1}{2}\frac{\partial^2}{\partial \eta^2}(< \rho\chi \mid \eta > P_\eta) \qquad (11)$$

where the conditional averages are taken over the entire domain and residual terms have been neglected.

The CMC equation (Eq. 10) was solved with the conditional mean scalar dissipation rate profile being given by the PDF equation in the following manner:

$$< \chi \mid \eta > = \frac{-2}{< \rho \mid \eta > P_\eta} \int \int \frac{\partial}{\partial t}(< \rho \mid \eta' > P_{\eta'})d\eta' d\eta' \qquad (12)$$

In this study it is possible to use PDF information from the simulation to determine the conditional mean scalar dissipation rate, but in practice this information will not typically be available to the modeler. Following the approximations used in practice, the conserved scalar PDFs were assumed to be clipped Gaussian in form. This assumption reduces the number of degrees of freedom in the PDF to two, namely specification of the conserved scalar mean and variance. Beta functions are an arguably superior assumed form (Girimaji 1991), however Gaussians readily lend themselves to accurate integration (Smith 1994).

In cases where differential diffusion is significant, further terms appear in the CMC and PDF equations. Discussion of differential diffusion modeling is deferred to Section 4.

2.2 Simulation conditions

An upgraded version of the code used by Ruetsch (1994) was employed in the direct numerical simulations. The new code includes a flexible multi-step chemical kinetics module for handling arbitrary thermochemistry. The code retains original features such as the high-order compact finite differencing scheme described by Lele (1992) for spatial differencing, and the third order Runge-Kutta timestepping algorithm of Wray. The Navier-Stokes characteristic boundary conditions described by Poinsot and Lele (1992) are also retained, but this feature was not used in this study due to the periodic nature of the simulation domain.

The simulations performed to date have been two dimensional (129x129) in order to extensively test the new code and simulation conditions, before expending a great deal of computation time on three dimensional simulations.

The turbulent field was initialized using an incompressible phase scrambled kinetic energy spectrum for the velocity components and a conserved scalar. The initialized conserved scalar field can be seen Fig. 1 where black regions denote pure

FIGURE 1. Initial distribution of the conserved scalar. White regions denote $\xi = 1$ while black regions denote $\xi = 0$. Initial conserved scalar unmixedness $\Omega = 0.84$.

oxidizer zones and white regions denote pure fuel zones. Scalar *unmixedness* can be defined as,

$$\Omega \equiv < \xi^2 > /(< \xi > (1- < \xi >)) \tag{14}$$

which can be seen to be a normalized measure of the fluctuation level. Unmixedness varies between zero, where the scalar field is homogeneous, and unity where only pure fuel and pure oxidizer zones exist with no mixing at all. The initial conserved scalar fields used here had initial unmixednesses of $\Omega \approx 0.8$ in all cases.

Reactive species mass fractions and internal energy were mapped onto the conserved scalar field using adiabatic chemical equilibrium relationships between mixture fraction (conserved scalar) and the reactive scalars. The adiabatic equilibrium reactive scalar mass fraction profiles are plotted versus conserved scalar mixture fraction in Fig. 2. Note that the fuel is comprised of almost 97% nitrogen (N_2) by mass, thereby giving a stoichiometric mixture fraction of $\xi_{stoic} = 0.5$. As the mean mixture fraction for the simulations was also 0.5, the overall equivalence ratio was unity in all cases.

The imposition of a 'hot' scalar field onto the initial 'cold' field solution required the adjustment of the density field to minimize the effect on the pressure field. Although the scalar mapping was essentially a constant pressure process, the resultant pressure field had a noticeable acoustic component that arose from the imposed imbalance in the momentum equations. This acoustic adjustment led to an initial root mean square pressure fluctuation that was approximately $5.e - 5$ of the mean pressure. Due to periodicity, the acoustic waves were unable to leave the domain but did slowly decrease with time due to dissipation.
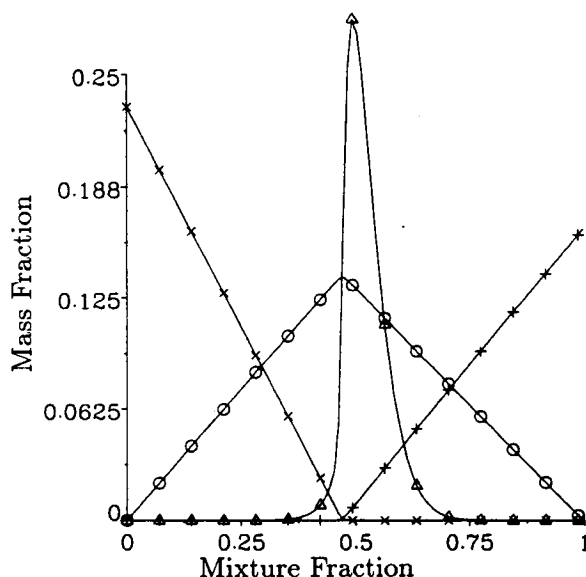
FIGURE 2. Initial conditional mean reactive scalar profiles for two-step chemical description of H_2/N_2-air combustion. Symbol key : $+$ - $H_2(*10)$, $\times$ - O_2, $\circ$ - H_2O, $\triangle$ - $H(*2 \cdot 10^5)$.

3. Results

The general behavior of the numerical simulations can be described as consisting of a brief initial period of chemical and fluid-dynamic adjustment, followed by an extended period of relaxation towards a perfectly mixed quiescent state. The simulations were run over a period of one to two initial turbulent timescales $(\tau_{t,0})$, during which time the conserved scalar unmixedness was found to exponentially decay (see Fig. 3). During the same period the turbulent Reynolds number (determined using the mean viscosity at each time) decreased from ~ 60, to a value of ~ 40.

Due to the chemical reactions taking place between the mixing fluids, the mean temperature and pressure typically rose by a factor of $\sim 4/3$ during the course of each simulation. From Fig. 3, the differences between the one- and two-step chemical calculations can be seen in terms of the mean species yield. It is evident that the one-step chemical description tends to underpredict the overall rate of reaction compared to the two-step case. Despite the fact that both chemical reaction mechanisms cause the system to tend to the same thermodynamic state in the absence of any mixing activity, it is apparent that the global reaction rate predicted by the one-step reduced mechanism is somewhat hindered in the presence of mixing.

In both reaction mechanisms, the chain branching step $H + O_2 \rightleftharpoons OH + O$ is the controlling component in the global rate. The one-step chemical mechanism determines the radical concentration from a quasi-steady state assumption that strictly only holds in the chemical equilibrium limit. Where mixing rates are high, fluid particles do not remain at the same equivalence ratio long enough to allow equilibrium conditions to be reached, and so the quasi-steady state assumption
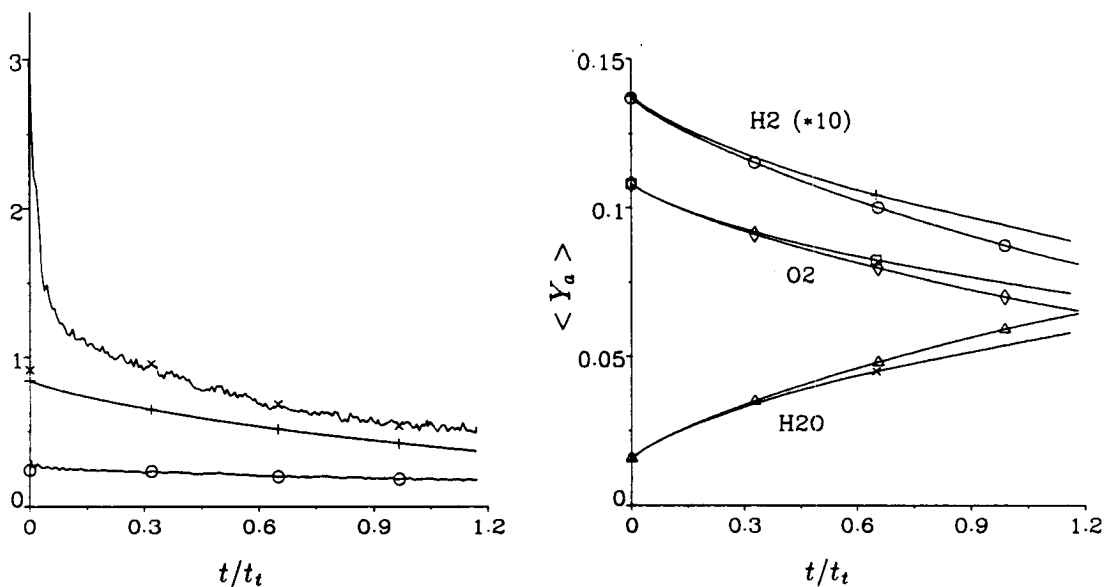
FIGURE 3. Time history of unconditional mean statistics from uniform diffusivity simulations. (Left) Turbulent mixing quantities : $+$ - Ω, $\times$ - $< \epsilon >$ ($*2.5 \cdot 10^{10}$), $\circ$ - $\frac{1}{2} < u_i^2 >$ ($*1 \cdot 10^6$). (Right) Major species mass fractions for each chemical case : $+$ - one step H_2, $\circ$ - two step H_2, $\sqcap$ - one step O_2, $\diamond$ - two step O_2, $\times$ - one step H_2O, $\triangle$ - two step H_2O

breaks down. The two-step mechanism on the other hand carries H as a computed species, and is not subject to this assumption. It would seem that the one-step prediction of H radical levels is lower than it should be under the mixing rates studied here, and this in turn limits the global reaction rate.

The simulations with non-uniform molecular diffusivities displayed slightly different behavior to that discussed above. Discussion of non-uniform diffusivity effects is deferred to Section 3.2.

3.1 Model results for uniform diffusivity cases

The level of mixing intensity in the CMC model equations is described by the conditional mean scalar dissipation rate. It is important to accurately predict this quantity since it often closely balances the chemical production source terms (see Bilger 1989, Smith 1994). The conditional mean scalar dissipation rate profiles predicted by the model and observed in the companion simulations are plotted in Fig. 4 at three time stations $t/\tau_t = 1/3, 2/3$, and 1. The conditional variance profiles of scalar dissipation rate are also plotted from the simulation data as an indication of the scatter in instantaneous dissipation rate from the conditional means. This scatter is not modeled and is a potential source of inaccuracy.

It is apparent that despite the rather crude assumed-form PDF model used in computing the conditional mean scalar dissipation rate, the agreement with the observed profiles is quite reasonable. The most notable difference being the tendency of the predicted profiles to be greater than the observed profiles at very lean and
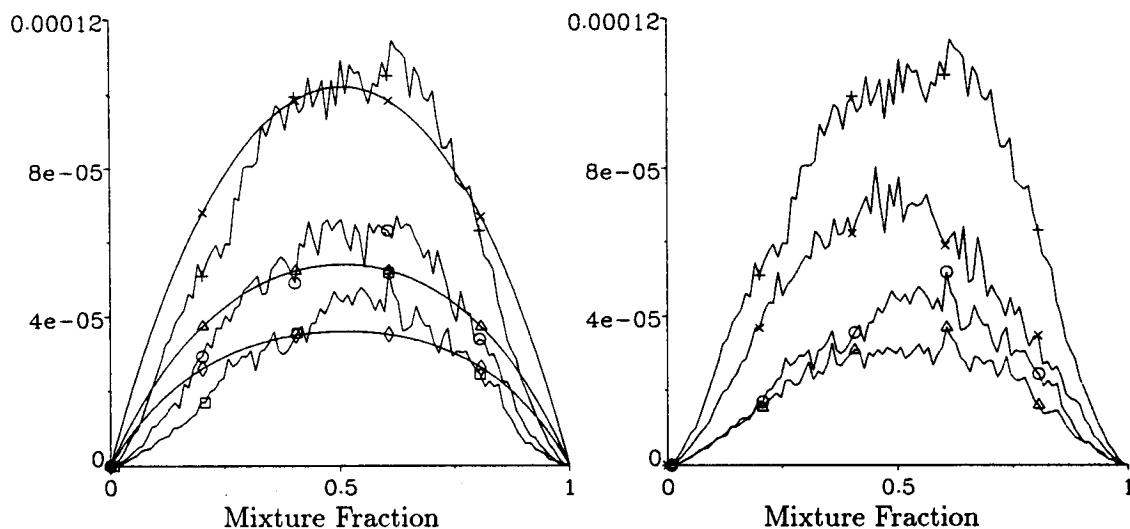
FIGURE 4.   (Left) Comparison of modeled and observed conditional mean scalar dissipation rate $< \chi \mid \eta >$ profiles at different calculation times: $+$ - DNS at $t/\tau_t = 1/3$, $\times$ - CMC at $t/\tau_t = 1/3$, o - DNS at $t/\tau_t = 2/3$, $\triangle$ - CMC at $t/\tau_t = 2/3$, $\sqcap$ - DNS at $t/\tau_t = 1$, and $\diamond$ - CMC at $t/\tau_t = 1$ (Right) Comparison of observed conditional mean and RMS profiles of scalar dissipation rate at two different calculation times: $+$ - mean at $t/\tau_t = 1/3$, $\times$ - rms at $t/\tau_t = 1/3$, o - mean at $t/\tau_t = 1$, and $\triangle$ - rms at $t/\tau_t = 1$.

very rich mixture fractions.

3.1.1 One-step chemical mechanism case

In Fig. 5, conditional mean temperature and H_2O mass fraction profiles are compared between CMC model predictions and simulation data. It is clear that the conditional mean profiles predicted by the model substantially exceed the profiles measured in the DNS. Further, the predicted profiles increase in magnitude with increasing time while the measured conditional mean profiles remain approximately stationary.

The root mean square deviations from the conditional mean profiles, measured in the DNS, increase in magnitude with increasing time. These deviations are not accounted for in the simple first order chemical closure currently used in the CMC model. It seems that these deviations from the conditional mean profiles are sufficient to cause the observed DNS conditional mean reaction rate to be substantially lower than the reaction rate modeled using conditional mean scalar profiles.

Comparing the time histories of the one step chemistry model predictions and simulation results (see Fig. 6), it is apparent that the relative discrepancy between the unconditional mean profiles increases with time. The principal reason for this is that the mixing field slowly tends towards homogeneity, and thus conditional profile discrepancies near the mean mixture fraction become more prominent in the
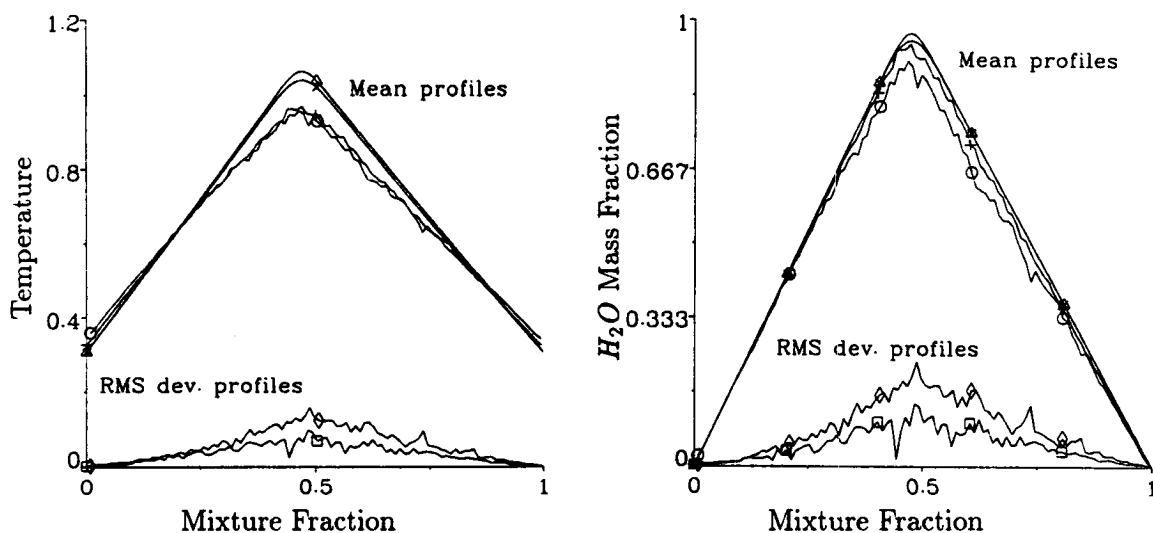
FIGURE 5. Comparison of modeled and observed conditional statistics of temperature (left) and H_2O mass fraction (right) at different calculation times. $+$ - DNS at $t/\tau_t = 1/3$, $\times$ - CMC at $t/\tau_t = 1/3$, $\circ$ - DNS at $t/\tau_t = 1$, $\triangle$ - CMC at $t/\tau_t = 1$, $\sqcap$ - DNS at $t/\tau_t = 1/3$, and $\diamond$ - DNS at $t/\tau_t = 1$
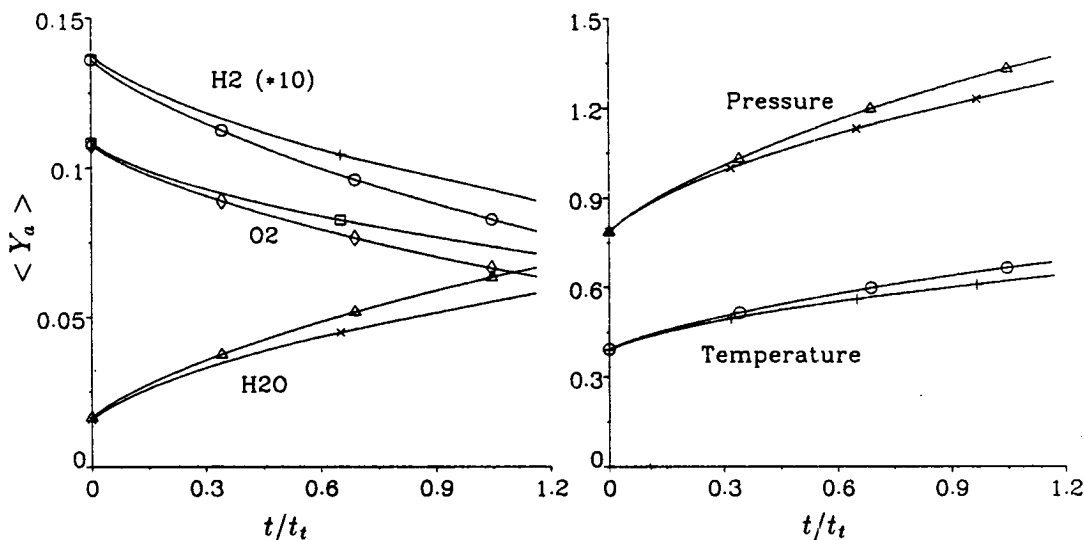
FIGURE 6. Time history of unconditional mean chemical yields from one-step chemistry cases of model and simulation : (Left) $+$ - DNS $H_2(*10)$, $\circ$ - CMC $H_2(*10)$, $\times$ - DNS H_2O, $\triangle$ - CMC H_2O, $\sqcap$ - DNS O_2, $\diamond$ - CMC O_2. (Right) x - DNS pressure, $\triangle$ - CMC pressure, $+$ - DNS temperature, $\circ$ - CMC temperature.
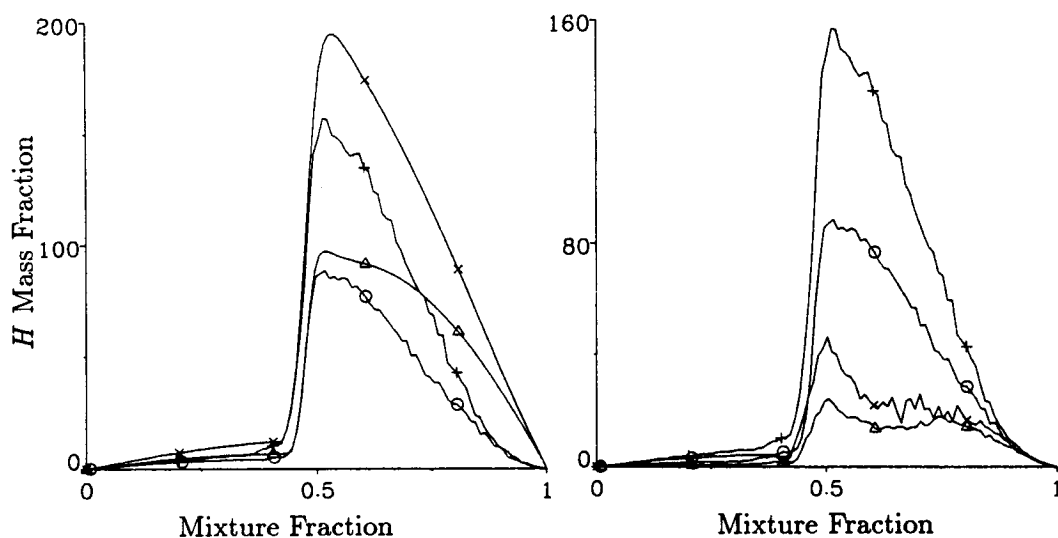
FIGURE 7. Comparison of modeled and observed conditional statistics for H radical mass fraction at different calculation times. (Left) Mean modeled and observed profiles : $+$ - DNS at $t/\tau_t = 1/3$, $\times$ - CMC at $t/\tau_t = 1/3$, o - DNS at $t/\tau_t = 1$, $\triangle$ - CMC at $t/\tau_t = 1$. (Right) Mean and RMS deviations from DNS : $+$ - mean at $t/\tau_t = 1/3$, $\times$ - mean at $t/\tau_t = 1$, o - RMS dev. at $t/\tau_t = 1/3$, $\triangle$ - RMS dev. at $t/\tau_t = 1$.

convolution with the PDF.

Additionally there is a compounding effect of differences in mean pressure and temperature. The model tends to overpredict the heat release rate as a consequence of the first order chemical closure employed, and this in turn leads to overpredictions of temperature and mean pressure. This departure increases because the elevated temperatures and pressures cause even greater predicted heat release rates. It should be pointed out, however, that the model and simulation trends should converge given a sufficiently long time due to the limited amount of fuel and oxidizer present, and the fact that mixing motions will eventually disappear.

3.1.2 Two-step chemical mechanism case

The discrepancies between model and observation are significantly reduced in the cases considered with two-step chemistry. The major species profiles (not plotted) agree so closely as to be almost indistinguishable, save for the small perturbations associated with the DNS data. The only significant differences exist in the comparison of predictions and observations for the radical species (H) and temperature.

A comparison of conditional mean H mass fraction profiles for various calculation times is plotted on the left-hand side of Fig. 7. It is clear that the CMC model overpredicts the level of H present, but the relative degree of overprediction at the peak mass fraction decreases with time as the magnitude of the profiles decreases. It also seems that the overprediction of conditional mean scalar dissipation rate at
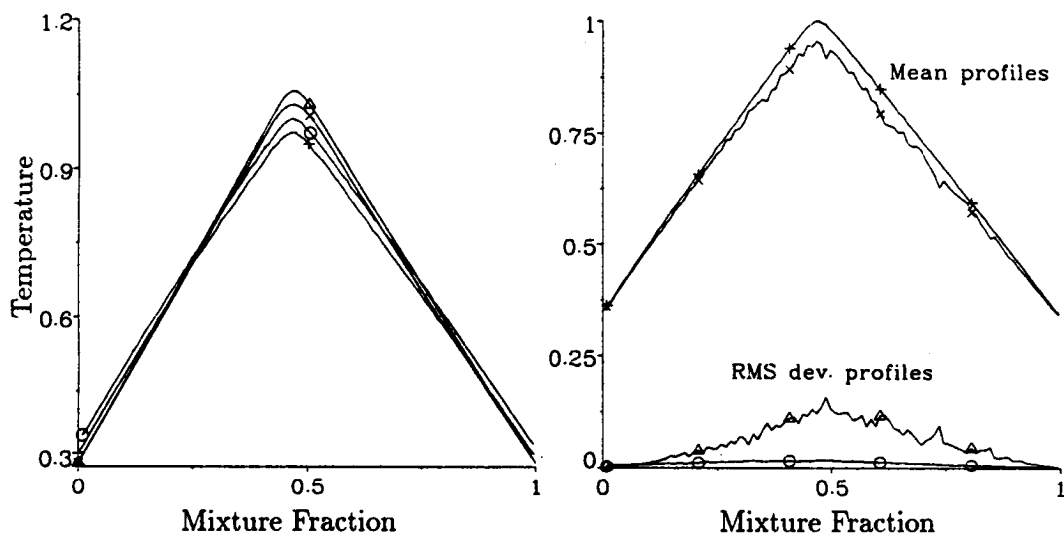
FIGURE 8.   Comparison of modeled and observed conditional statistics for temperature at different calculation times. (Left) Modeled and observed mean profiles from two-step chemistry cases : + - DNS at $t/\tau_t = 1/3$, o - DNS at $t/\tau_t = 1$, × - CMC at $t/\tau_t = 1/3$, $\triangle$ - CMC at $t/\tau_t = 1$. (Right) Observed mean and RMS deviations at $t/\tau_t = 1$ in one- and two-step chemistry cases : + - mean from two-step, × - mean from one-step, o RMS dev. from two-step, $\triangle$ - RMS dev. from one-step.
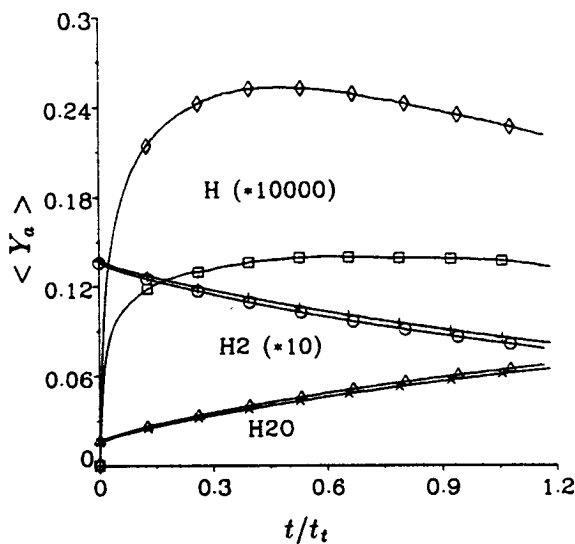
FIGURE 9.   Time history of unconditional mean chemical yields from model and simulation : $\sqcap$ - DNS $H(*10000)$, $\diamondsuit$ - CMC $H(*10000)$, o - DNS $H_2(*10)$, + - CMC $H_2(*10)$, × - DNS H_2O, $\triangle$ - CMC H_2O.

very rich mixture fractions, noted earlier, tends to cause the predicted H profile to be flattened at rich mixture fractions. In the right-hand plot of Fig. 7, the observed root mean square deviation profiles are plotted in comparison with the mean profiles. From this plot it appears that the absolute level of the deviational profiles decreases with time in accordance with the mean profiles.

On the left-hand side of Fig. 8, conditional mean temperature profiles are compared for various times in the CMC and DNS two-step chemical calculations. The model profiles are somewhat higher than the DNS measured profiles; however, the difference is substantially less than that seen in the one-step chemistry case. Also in contrast to the one-step chemistry comparison, both sets of profiles increase in magnitude with time. This is another indication of the fact that the two-step formulation gives rise to a chemical system that is less perturbed by mixing processes when compared to a similar case with one-step chemistry. This fact is highlighted in the right-hand plot of Fig. 8, where conditional mean temperature data is compared between DNS simulations with one- and two-step chemistry at a time of $t = \tau_t$. Not only is the mean profile greater in the two-step case, but the corresponding root mean square deviation profile is much lower.

It appears that the more robust nature of the two-step chemical mechanism lends itself better to CMC modeling, in the cases studied here, than its one-step counterpart. This is because the two-step mechanism is less perturbed by the level of mixing intensity with consequently smaller mixing induced deviations from the conditionally averaged reactive scalar values. This reduction in the size of conditional deviations thus improves the accuracy of the conditional mean chemical closure.

It is reasonable to assert that under more intense mixing conditions, that CMC models employing the two-step chemical mechanism would deviate to a larger degree from corresponding DNS observations. At very much higher mixing rates, the first order chemical closure would be invalidated altogether as the chemical system verges on extinction (see Bilger 1991, 1993).

3.2 Observed differential diffusion behavior

All of the DNS data and model predictions presented so far have been restricted to cases with uniform molecular diffusivity for all species ($Le_\alpha = 1$, $Pr = 0.75$). The DNS data presented in this section was computed with constant non-uniform Lewis numbers determined from counterflow laminar diffusion flames (see Smooke 1990). A Fickian diffusion approximation was used for all species, except nitrogen, which was the predominant background species for which the Lewis numbers were defined.

One of the most notable aspects of comparing general simulation behavior, with and without differential diffusion, is the absence of a unique mixture fraction definition in the former case. Fig. 10 illustrates this fact by plotting the scatter of points for two different conserved scalars, one based upon the mass fraction of an inert species (N_2) and the other based upon a combination of hydrogen and oxygen atomic mass fractions, at a time of $t/\tau_t = 1$. Instead of adhering to the constant mixing line (unit-slope line passing through the origin), the computed points follow the characteristic sigmoidal (reversed in this case) trace of differentially diffused
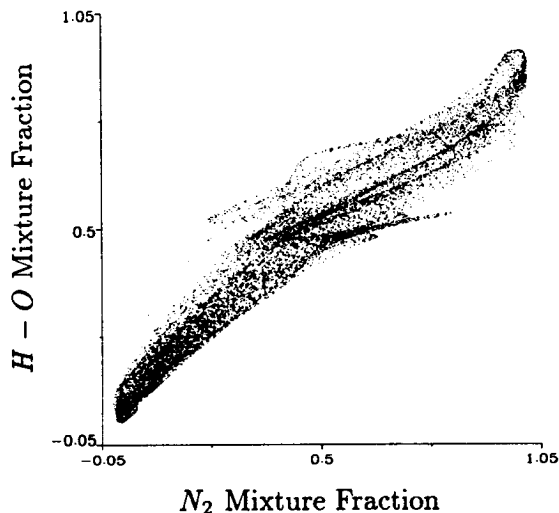
FIGURE 10.   Scatter plot of mixture fractions based on N_2 mass fraction and H-O atomic mass fractions, for differential diffusion simulation at time $t/\tau_t = 1$.

conserved scalars. The reason for this behavior can be understood when it is revealed that the $H - O$ mixture fraction has a positive linear relation to the light hydrogen bearing species and a negative linear relation to the heavier oxygen bearing species. Being lighter and more mobile than the other species, H and H_2 tend to diffuse more rapidly to lean (N_2-based) mixture fractions than O_2 can diffuse to rich (N_2-based) mixture fractions. The result is that the $H - O$ mixture fraction values increases at lean N_2-based mixture fractions and simultaneously decrease at rich values.

The chemical yields of the two step chemistry simulations are compared for cases with and without differential diffusion in Fig. 11. It is apparent that the differential diffusion case predicts a slightly greater reactant consumption rate, but with a less discernible increase in major production formation. It would appear that the additional reactants consumed by the differential diffusion case go towards creating the obvious excess of the radical species H. The temperature and pressure traces for the two simulations are very close; however, the differential diffusion case appears to have very slightly lower values. A clear difference is apparent between the two unmixedness traces (unmixedness of normalized N_2 mass fraction), with the decay coefficient in the differential diffusion case being around ~ 0.86 of the coefficient in the uniform diffusivity case.

Conditional statistics were calculated using an N_2-based mixture fraction definition, and are plotted in Figs. 12 and 13 for H radical mass fraction and temperature, respectively. It is apparent from Fig. 12 that the conditional mean H radical profiles from the differentially diffusive (diff-diff) case are somewhat lower than the uniform diffusivity results on the rich side of stoichiometric. At the same time, the opposite
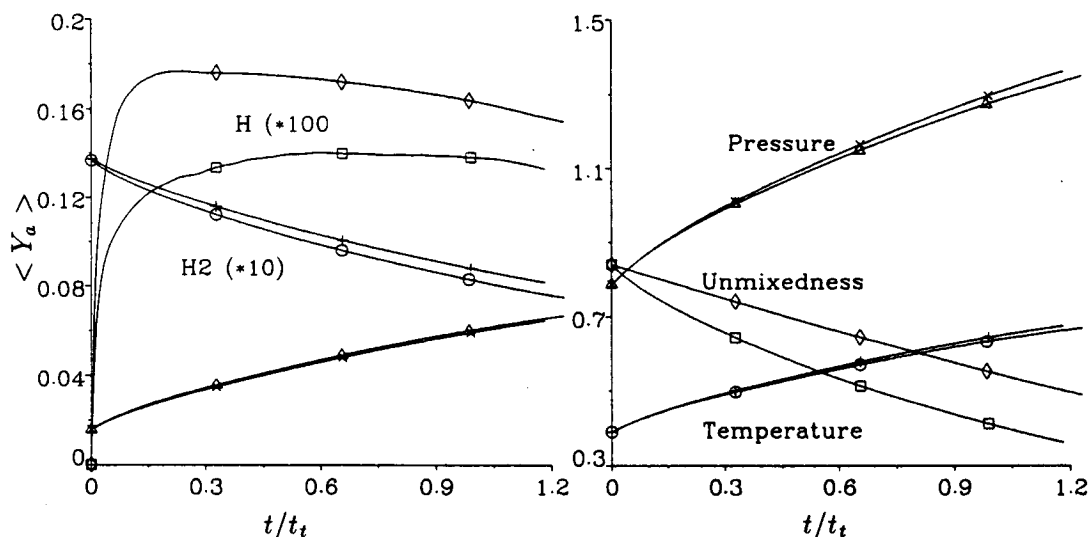
FIGURE 11. Time history of unconditional mean chemical yields from two-step chemistry simulations with and without differential diffusion. (Left) $\Diamond$ - dd $H(*10^5)$, $\sqcap$ - ud $H(*10^5)$, o - dd $H_2(*10)$, + - ud $H_2(*10)$, $\triangle$ - dd H_2O, $\times$ - ud H_2O. (Right) $\Diamond$ - dd unmixedness, $\sqcap$ - ud unmixedness, o - dd temperature, + - ud temperature, $\triangle$ - dd pressure, $\times$ - ud pressure.

is true on the lean side, where the differentially diffusive radicals have permeated this oxidizer-rich zone to a greater extent.

The mean temperature profiles from the diff-diff cases reflect the greater incursion of H radical into the lean zone, in that they are significantly elevated over the uniform diffusivity profiles. The presence of greater radical numbers allows the exothermic global reaction to proceed at a more rapid rate, thereby liberating more heat. It is clear that the root mean square deviations in the diff-diff case are much greater than in the corresponding uniform diffusivity cases. Since temperature is strongly dependent on reaction activity and this is in turn dependent on radical availability, these temperature deviations may be related to the disparate mixing behavior of H radical and N_2 (the conserved scalar) with the latter doing a poor job of tracking the mean transport of the former.

Finally it is interesting to compare the N_2-based mixture fraction PDFs observed in each simulation case. The PDFs plotted in Fig. 14 are from the time $t = \tau_t$ and embody the main difference between the diff-diff and uniform diffusivity behavior. The diff-diff PDF equation has a non-zero source term arising out the definition of N_2 mass fraction as the residual mass not accounted for by the reactive species mass fractions. This source term averages across mixture fraction space to provide a zero mean contribution, but serves to inflate the PDF at some mixture fractions. The source term (not plotted) has a sharp peak just to the lean side of stoichiometric, which results from H and H_2 incursion, and this peak causes the diff-diff case's
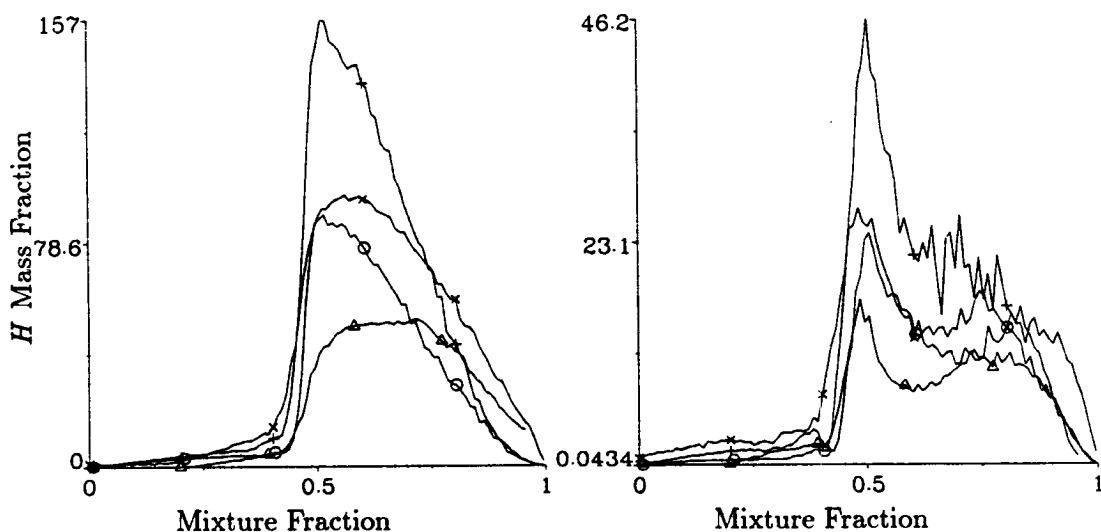
FIGURE 12. Comparison of observed conditional mean (left) and RMS deviations (right) for H radical mass fraction in cases with and without differential diffusion at different calculation times : $+$ - ud at $t/\tau_t = 1/3$, $\times$ - dd at $t/\tau_t = 1/3$, $\circ$ - ud at $t/\tau_t = 1$, $\triangle$ - dd at $t/\tau_t = 1$.
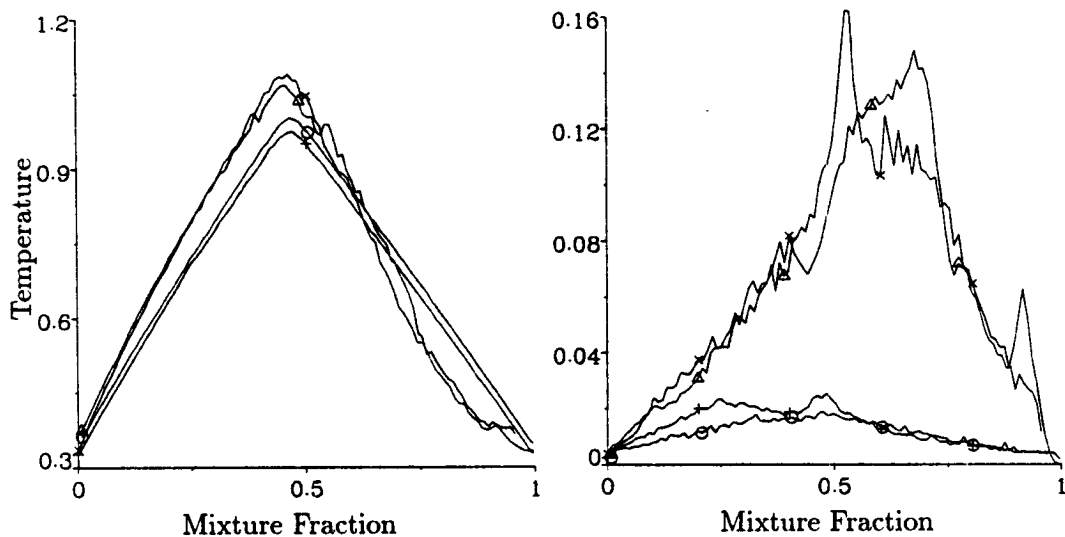
FIGURE 13. Comparison of observed conditional mean (left) and RMS deviations (right) for temperature in cases with and without differential diffusion at different calculation times : $+$ - ud at $t/\tau_t = 1/3$, $\times$ - dd at $t/\tau_t = 1/3$, $\circ$ - ud at $t/\tau_t = 1$, $\triangle$ - dd at $t/\tau_t = 1$.
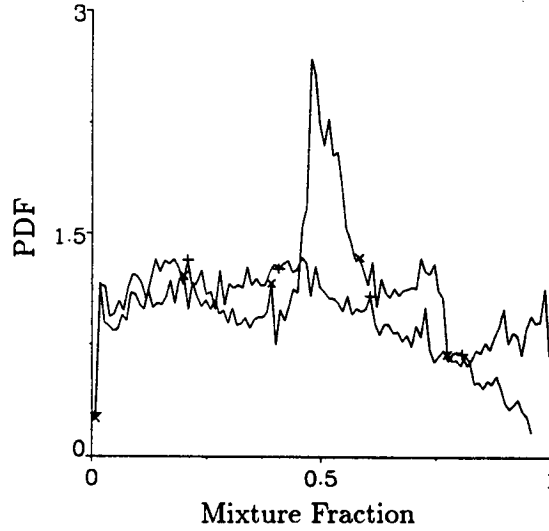
FIGURE 14.   Comparison of N_2-based mixture fraction PDFs from uniform and non-uniform molecular diffusivity simulations at time $t = \tau_t$: $+$ - uniform diffusivity, $\times$ - differential diffusivity

PDF to increase at this mixture fraction.

4. Discussion

Much of current turbulent nonpremixed combustion modeling relies on the existence of a unique mixture fraction, particularly the Joint PDF method (Pope 1985, 1991, Chen *et al.* 1990), and, of course, the CMC method (Smith 1994, Smith *et al.* 1995). Rationales have been put forth that suggest differential diffusion effects are small at high Reynolds numbers; however, experimental evidence suggests that they are substantial even in jet diffusion flames with Reynolds numbers as high as 30000 (Smith *et al.* 1993).

Let us briefly examine the impact of differential diffusion on the CMC method and discuss the additional modeling issues which arise. The equation for a composite conserved scalar ($\xi \equiv \sum_{\alpha=1}^{N} a_\alpha Y_\alpha$) is given by,

$$\frac{\partial}{\partial t}(\rho \xi) + \frac{\partial}{\partial x_i}(\rho u_i \xi) = \frac{\partial}{\partial x_j}(\rho D_\xi \frac{\partial \xi}{\partial x_j}) + \dot{s}_\xi \tag{15}$$

where $\dot{s}_\xi$ is a differential diffusion source term equal to

$$\dot{s}_\xi \equiv \frac{\partial}{\partial x_j}(\rho \sum_{\alpha=1}^{N} a_\alpha (D_\alpha - D_\xi)\frac{\partial Y_\alpha}{\partial x_j}). \tag{16}$$

From this equation it can be shown that the corresponding PDF equation is given by,

$$\frac{\partial}{\partial t}(< \rho \mid \eta > P_\eta) + \frac{\partial}{\partial x_i}(< \rho u_i \mid \eta > P_\eta) + e_\xi \tag{17}$$

and following the methodology of Klimenko (1990) yields the following CMC equation.

$$< \rho \mid \eta > \frac{\partial Q_\alpha}{\partial t} + < \rho u_i \mid \eta > \frac{\partial Q_\alpha}{\partial x_i} = \frac{1}{2} < \rho \chi \mid \eta > \frac{\partial^2 Q_\alpha}{\partial \eta^2} + < \rho \dot{w}_\alpha \mid \eta > + e_q^* + e_Q^*$$

(18)

The residual terms e_q^* and e_Q^* are defined as,

$$e_q^* \equiv \frac{1}{P_\eta} [\frac{\partial}{\partial x_j}(< \rho u_i' y_\alpha' \mid \eta > P_\eta) - \frac{\partial}{\partial \eta}(< \dot{s}_\xi' y_\alpha' \mid \eta > P_\eta)]$$

(19)

and

$$e_Q^* \equiv < \frac{\partial}{\partial x_j}(\rho(D_\alpha - D_\xi)\frac{\partial Y_\alpha}{\partial x_j} \mid \eta > - < \dot{s}_\xi \mid \eta > \frac{\partial Q_\alpha}{\partial \eta}.$$

(20)

The additional terms in the CMC and PDF equations are dependent on the definition of mixture fraction selected as the conditioning variable. Note that the e_Q^* term becomes small at high Reynolds numbers, but it is not clear that the same can be said for e_q^*.

The choice of a conserved scalar as a conditioning variable is governed by two criteria. Firstly, the scalar should be representative of the molecular transport of as many important chemical species as possible so as to minimize deviations from the resultant conditional averages. Secondly, in order to be able to model the evolution of the conserved scalar PDF (and thereby determine $< \rho \chi \mid \eta >$) in a simple manner, the mixture fraction source term $\dot{s}_\xi$ should be as small as possible. These criteria may prove to be conflicting. For example, it is possible to use an inert tracer species as a conserved scalar, thereby making $\dot{s}_\xi$ identically zero, but as this definition does not include any of the reactive species that are being tracked, deviations from the conditional means may be too great to effect a chemical source term closure.

Klimenko (1994) provides an equation for the conditional mean square deviation θ_α from a conditional mean reactive scalar Q_α in isotropic turbulence. This equation is slightly modified in the presence of differential molecular diffusivity to become,

$$< \rho \mid \eta > \frac{\partial \theta_\alpha}{\partial t} - \frac{1}{2} < \rho \chi \mid \eta > \frac{\partial \theta_\alpha}{\partial \eta} = < \rho \dot{w}_\alpha' y_\alpha' \mid \eta > -2 < D_\alpha(\frac{\partial y_\alpha'}{\partial x_i})^2 \mid \eta > + e_\theta^* + e_\Theta^*.$$

(21)

where the residual terms are analogous to e_q^* and e_Q^* but involve the conditional mean deviation rather than the conditional mean. The instantaneous change and transport of the conditional mean deviation is balanced against a chemical-instability source term, a deviational dissipation term, and residuals. Where the Reynolds number is moderate and the choice of conserved scalar is poor, the residuals will tend to increase the level of deviations. When combined with the nonlinear amplification provided by the chemical term, this added source of conditional deviation can cause levels to increase substantially (see Section 3.2) and thereby invalidate any first order chemical closure.

It may be that the chemical source term $< \rho \dot{w}_\alpha \mid \eta >$ can be closed using a second order method such as that applied by Li and Bilger (1993) to atmospheric pollutant

reactions in a turbulent mixing layer. However, in that case the chemistry was isothermal and one-step in nature and did not have significant differential diffusion. At higher Reynolds numbers the effect of differential diffusion is diminished, and it may be that practical devices that can be highly turbulent do not require a diff-diff treatment. At higher Reynolds numbers, however, deviations arise in Eq. 21 because of mixing interference via the chemical instability term (see Section 3.1), and it may be necessary to develop doubly conditional moment closures in order to model these conditions.

5. Conclusions and future plans

In this study, predictions from the CMC method for modeling turbulent non-premixed combustion were compared to DNS data for hydrogen burning in an isotropic decaying turbulent field. One- and two-step chemical mechanisms were used in both the model and simulation in order to study the effect of chemical complexity upon first order CMC chemical closure.

It was found that the one-step chemical mechanism was hindered to a greater extent over the two-step mechanism, under identical mixing conditions, as a result of a breakdown in the one-step assumption for radical partial equilibrium. This interference by the mixing processes lead to larger deviations from conditional mean reactive scalar profiles. This in turn made the one-step chemical system harder to model with the CMC method than the two-step system under the same mixing conditions.

The addition of differential molecular diffusivity to the analysis tended to increase the level of reactive scalar deviations from conditional means under the conditions studied. The different rates of species transport tended to modify the overall rate of chemical reaction in the hydrogen system. The lack of a unique conserved scalar as a conditioning variable caused conditional mean scalar profiles to shift in mixture fraction space according to the choice of conserved scalar.

It was suggested that the increase in conditional deviations that arise from differential diffusion effects is a potential source of serious in implementing a conditionally averaged first order chemical closure.

The future plan for this modeling project can be outlined as follows:

• Perform three-dimensional simulation under same kind of conditions to include the vortex stretching mechanism and improve the size of the statistical sample.

• Develop model refinements for treating differential diffusion—may require solving for conditional deviations.

• Investigate doubly-conditional moment closure methods in spatially degenerate case. This will allow high intensity near-extinction behavior to be examined.

• Use flexible chemical module for other mechanisms such as $H_2 - CO$.

REFERENCES

BILGER, R. W. 1982 Molecular Transport Effects in Turbulent Diffusion Flames at Moderate Reynolds Number. *J AIAA*, **20**, 962-970.

BILGER, R. W. 1989 Turbulent Diffusion Flames. *Ann. Rev. Fluid. Mech.*, **21**, 101-135.

BILGER, R. W. 1991 Conditional Moment Methods for Turbulent Reacting Flow using Crocco Variable Conditions. *Charles Kolling Report TNF99*, the University of Sydney.

BILGER, R. W. 1993 Conditional Moment Methods for Turbulent Reacting Flow. *Phys. Fluids*, **5**, 436-444.

CHEN, J.-Y., DIBBLE, R. W., BILGER, R. W. 1990 PDF Modelling of Turbulent Nonpremixed CO/H2/N2 Jet Flames with Reduced Mechanisms. *Twenty-Third Symposium (International) on Combustion*, the Combustion Institute, Pittsburgh, 775-780.

CORREA, S. M. 1993 A Review of NOx Formation under Gas-Turbine Combustion Conditions. *Comb. Sci. Tech.*, **87**, 329-362.

GIRIMAJI, S. S. 1991 Assumed Beta-pdf Model for Turbulent Mixing: Validation and Extension to Multiple Scalar Mixing. *Comb. Sci. and Tech.*, **78**, 177-196.

KLIMENKO, A. YU. 1990 Multicomponent Diffusion of Various Admixtures in Turbulent Flow. *Fluid Dynamics* **25**, 327-334.

KLIMENKO, A. YU. 1992 Conditional Moment Closure and Diffusion in Conserved Scalar Phase Space. *ECOLEN Scientific Research Lab Paper*, Moscow, Russia.

KLIMENKO, A. YU. 1994 Conditional Moment Closure and Large-Scale Fluctuations of Scalar Dissipation. *Fluid Dynamics*, **28**, 630-637.

KLIMENKO, A. YU., BILGER, R. W. 1992 Relationship between conserved scalar pdfs and scalar dissipation in turbulent flows. *Charles Kolling Report TNF101*, the University of Sydney.

LELE, S. 1992 Compact finite difference schemes with spectral-like resolution. *J. Comp. Phys.* **103**, 16.

LI, J. D., BILGER, R. W. 1993 Measurement and Predictions of the Conditional Variance in a Turbulent Reactive-Scalar Mixing Layer. *Phys. of Fluids*, **5**, 3255-3264.

MANTEL, T., 1994 Fundamental mechanisms in premixed flame propagation via vortex-flame interactions - numerical simulations. *Annual Research Briefs - 1994*, Center for Turbulence Research, NASA Ames/Stanford Univ.

POINSOT, T., LELE, S. 1992 Boundary conditions for direct simulations of compressible viscous flows. *J. Comp. Phys.*, **101**, 104.

POPE, S. B. 1985 PDF Methods for Turbulent Flows. *Prog. Energy Comb. Sci.*, **11**, 119-192.

POPE, S. B. 1991 Computations of Turbulent Combustion: Progress and Challenges. *Twenty-Third Symposium (International) on Combustion*, Combustion Institute, Pittsburgh. 591-612.

RUETSCH, G. R. 1994 Flame propagation under partially premixed conditions. *Annual Research Briefs - 1994*, Center for Turbulence Research, NASA Ames/Stanford Univ.

SMITH, L. L., DIBBLE, R. W., TALBOT, L., BARLOW, R. S., CARTER, C. D. 1993 Laser Raman Scattering Measurements of Differential Molecular Diffusion in Turbulent Nonpremixed Jet Flames of H_2/CO_2 Fuel. *Comb. Flame*, **100**, 153-160.

SMITH, N. S. A. 1994 *Development of the Conditional Moment Closure Method for Modelling Turbulent Combustion.* PhD Thesis, University of Sydney.

SMITH, N. S. A., BILGER, R. W., CARTER, C. D., BARLOW, R. S., CHEN, J.-Y., 1995 A Comparison of CMC and PDF Modelling Predictions with Experimental Nitric Oxide LIF/Raman Measurements in a Turbulent H_2 Jet Flame. *Comb. Sci. Tech.*, **105**, 357-375.

VERVISCH, L. 1992 Study and modeling of finite rate chemistry effects in turbulent nonpremixed flames. *Annual Research Briefs - 1992*, Center for Turbulence Research, NASA Ames/Stanford Univ.

YEUNG, P. K., POPE, S. B. 1993 Differential Diffusion of Passive Scalars in Isotropic Turbulence. *Phys. Fluids*, **5**, 2467-2478.

Page intentionally left blank

Effects of confinement on partially premixed flames

By G. R. Ruetsch AND J. E. Broadwell

1. Motivation and objectives

Partially premixed combustion is an intermediate regime between the limiting cases of premixed and nonpremixed combustion. Although combustion problems are generally approached from one of these two limiting cases, there are many practical situations where flames cannot be considered as purely premixed or nonpremixed, and thus the partially premixed approach must be used.

In partially premixed combustion, mechanisms from the premixed and nonpremixed regimes can coexist, and as a result some interesting new phenomena can arise. One such phenomenon is the flame stabilization in laminar mixing layers by triple flames. One of the first observations of triple flames was made by Phillips (1965), who investigated a triple flame propagating in a methane mixing layer. Kioni *et al.* (1993) also examined triple flames both experimentally and numerically. There have also been numerous analytical studies on the shape and propagation of triple flames under various assumptions by Dold (1989), Dold *et al.* (1991), and Hartley and Dold (1991). In terms of modeling, Müller *et al.* (1994) have combined the flamelet formulations for premixed and nonpremixed combustion in order to treat lifted diffusion flames. One common feature in the analytical and numerical studies mentioned above is the assumption of zero heat release, which is necessary to make the problem tractable. The effect of heat release on triple flames was investigated by Ruetsch *et al.* (1995), where for the unconfined case, flame speeds larger than their premixed counterparts were found.

One of the most important practical situations in which these conditions arise is in lifted turbulent jet diffusion flames. At a critical velocity the burning zone of a fuel jet lifts offfrom the nozzle, moves to increasing distances as the jet velocity increases, and finally blows off. The mechanisms that control these phenomena, i.e. that determine the *stability* of these flames, are still not understood.

In addition to regions where diffusion flame stabilization takes place, partially premixed conditions also exist during the ignition process in nonpremixed systems. Numerical simulations by Réveillon *et al.* (1994) of the ignition process in a weakly stirred mixture of fuel and oxidizer show that triple flames propagate along lines of stoichiometric mixture fraction throughout the fluid. In addition, Peters (1994) notes that NO_x emissions are likely to be large in such transient cases, and therefore an understanding of triple flames can provide information concerning pollutant formation.

This study extends the work previously done and examines the effects of lateral confinement on partially premixed flames. Once again, we study both the flame structure and propagation.

1.1 Numerical simulation and flow configuration

We use direct numerical simulations to solve the fully compressible Navier-Stokes equations. The simulation uses a two-dimensional version of the code developed by Trouve (1991). This code uses the high-order compact finite difference scheme of Lele (1992) for spatial differentiation, the third order Runge-Kutta scheme of Wray for time advancement, and the Navier-Stokes characteristic boundary conditions method of Poinsot and Lele (1992). Below we summarize some of the important features and assumptions of the code relevant to this work; for further details on the numerical method readers are referred to Lele (1992) and Poinsot and Lele (1992).

The chemical scheme we consider is represented by a one-step global reaction between a fuel and oxidizer:

$$F + O \longrightarrow P$$
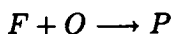
where we have assumed unity stoichiometric coefficients for simplicity. The reaction rate behaves according to the Arrhenius form:

$$\dot{w} = K \rho Y_F \rho Y_O \exp\left(-\frac{T_{ac}}{T}\right)$$

where ρ is the density, T_{ac} is the activation temperature, K is the pre-exponential factor, and Y_F and Y_O are the fuel and oxidizer mass fractions. Following Williams (1986), we can write this reaction rate as

$$\dot{w} = \Lambda \rho Y_F \rho Y_O \exp\left(-\frac{\beta(1-\theta)}{1 - \alpha(1-\theta)}\right)$$

where the reduced pre-exponential factor(Λ), heat release parameter(α), Zel'dovich number(β), and reduced temperature(θ) are defined by:

$$\Lambda = K \exp(-\beta/\alpha); \quad \alpha = \frac{T_f - T_0}{T_f}; \quad \beta = \frac{\alpha T_{ac}}{T_f}; \quad \theta = \frac{T - T_0}{T_f - T_0}$$

with T_f being the adiabatic flame temperature and T_0 taken in the ambient flow. In this study we hold the Zel'dovich number constant at $\beta = 8$ and use a heat release parameter of $\alpha = 0.75$.

The transport coefficients in the simulations are temperature dependent. This temperature dependence is expressed through the molecular viscosity, μ, given by:

$$\mu = \mu_0 \left(\frac{T}{T_0}\right)^a$$

with $a = 0.76$. The temperature dependence of the thermal conductivity, λ, and the mass diffusivities, $\mathcal{D}_k$, are obtained by requiring the Lewis and Prandtl numbers to be constant:

$$Le_k = \frac{\lambda}{\rho \mathcal{D}_k c_p}; \qquad Pr = \frac{\mu c_p}{\lambda},$$
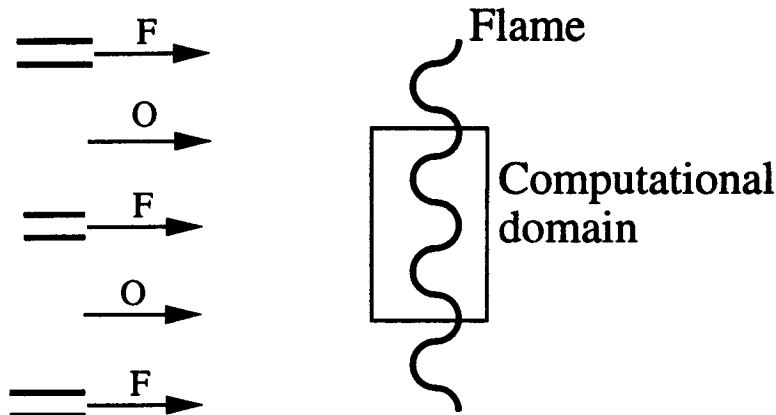
FIGURE 1. Computational domain used in the simulations. This domain represents a portion of a flame subjected to a periodic lateral variation in mixture fraction. The confinement is therefore accounted for by the periodic lateral boundary conditions.

where $k = F, O$ refers to either the fuel or the oxidizer species. We assume unity Lewis numbers throughout this study.

We solve the compressible Navier-Stokes equations in the two-dimensional domain depicted in Fig. 1. At the boundaries in the horizontal direction we use an inflow boundary condition on the left and nearly-perfect reflective boundary conditions, required to avoid pressure drift, at the outflow. In the lateral direction, in order to simulate the effects of confinement, we use periodic boundary conditions. This is in contrast to previous work on triple flames, which used nonreflecting boundary conditions in the lateral direction.

Within this domain we initialize the flow with a planar premixed flame, where the mixture fraction, defined as

$$Z = \frac{1 + Y_F - Y_O}{2},$$

is everywhere equal to its stoichiometric value, $Z_s = 0.5$. The incoming flow is uniform and set equal to the premixed laminar flame speed, S_L^0, which is maintained throughout the simulation. Also associated with the flame is the premixed flame thickness, δ_L^0.

After the flow and flame are initialized, a sinusoidal perturbation is added to the uniform stoichiometric mixture fraction. This perturbation is not small, as we consider values for the overall range of Z at the inlet from $\Delta Z = 0.2$ to $\Delta Z = 1.0$. In all cases, we maintain a overall equivalence ratio of one.

1.2 Calculation of the instantaneous flame speed

A useful diagnostic is the instantaneous flame speed at any point in the flow. We compute this by a method previously used to stabilize triple flames (Ruetsch

et al. 1995), which is summarized below. The basis of this method comes from the the Hamilton-Jacobi equation for the G-field developed by Kerstein *et al.* (1989):

$$\rho \frac{DG}{Dt} = \rho V |\nabla G|.$$

Here G is the field variable whose level surfaces represent the interfaces or flame surfaces, and V is the local propagation of these surfaces, or local flame speed.

The finite thickness flames with heat release we consider in this study do not obey the G-equation; however, we can apply the Hamilton-Jacobi equation in our simulations if we construct an appropriate G field. We should remark here that the G-equation applies to premixed flames; therefore, G can be interpreted as a progress variable in finite thickness flames. We therefore define the progress variable c as:

$$c = 1 - (Y_F + Y_O)$$

which ranges from zero in the unburnt gases to unity in completely burnt gases. From the convective-diffusive equation for a scalar field we then obtain:

$$\rho \frac{Dc}{Dt} = \frac{\partial}{\partial x_i} \left(\rho \mathcal{D} \frac{\partial c}{\partial x_i} \right) + \dot{w}_c$$

where $\dot{w}_c = -(\dot{w}_F + \dot{w}_O)$. Equating $\rho Dc/DT$ and $\rho DG/Dt$ along with $|\nabla G|$ and $|\nabla c|$, and solving for the relative progression velocity of the iso-progress variable surface, V, we obtain:

$$V = \frac{1}{\rho|\nabla c|} \frac{\partial}{\partial x_i} \left(\rho \mathcal{D} \frac{\partial c}{\partial x_i} \right) + \frac{1}{\rho|\nabla c|} \dot{w}_c$$

This relation gives the propagation speed of a progress variable isosurface along its normal oriented towards the unburnt gas. Thus the components of the progress variable isosurface propagation are given by:

$$\mathbf{v} = -\frac{\nabla c}{|\nabla c|} V$$

The sum of the local fluid velocity, $\mathbf{u}$, and the progress variable isosurface velocity, $\mathbf{v}$, indicates whether the flame is progressing or receding.

At this point we should clarify some terminology regarding flame speeds. Poinsot *et al.* (1991) showed that there are several flame speeds which describe flame propagation in a premixed laminar flame tip. Ruetsch *et al.* (1995) also indicated that there are also different flames speeds depending on whether or not one includes the flow redirection in front of the flame resulting from heat release. In this study we are concerned with two flame speeds. The local flame speed is simply $|V|$, whereas the propagation speed, assuming the configuration in Fig. 1, is defined as:

$$S_L = U_{INLET} - (u_x + v_x)$$

where the x-components of the $\mathbf{u}$ and $\mathbf{v}$ fields are u_x and v_x, and $U_{INLET} = u_x$ evaluated at the inlet. It is important to differentiate between these two flame speeds, since the local flame speed is important in terms of the chemistry, and the propagation speed determines how the flame moves as a whole.

2. Accomplishments

We begin our study of partially premixed flames by first reviewing characteristics of unconfined flames, followed by a qualitative comparison between the unconfined and confined cases. We then focus on the global propagation of confined flames, which is followed by a discussion of the mechanism for flame stabilization in the regions farthest from stoichiometry.

2.1 Review of unconfined partially premixed flames

In this section we briefly review material associated with the unconfined partially premixed flames. For a more thorough review see Ruetsch *et al.* (1995). In the unconfined case, where lateral flow out of the side boundaries occurs, we subject a premixed flame to a gradient in Z (using a *tanh* profile), which results in a single triple flame composed of two premixed and one diffusion wing. Aside from the change in the flame structure, the flame speed also changes when the flame is subjected to a gradient in mixture fraction. The increase in flame speed is a direct result of heat released in the flame. For thin flames, the flame speed and expansion ratios scale as:

$$\frac{S_L}{S_L^0} \sim \sqrt{\frac{\rho_U}{\rho_B}}; \qquad \frac{\delta_B}{\delta_U} \sim \frac{\rho_U}{\rho_B}$$

where the subscripts U and B refer to the unburned and burned regions of the flow, and δ denotes the lateral distance between a pair of streamlines. These relations were derived for the two-dimensional case. In general, however, one expects fluctuations of the mixture fraction to be three-dimensional. The analysis performed in the planar two-dimensional case can be redone for the axisymmetric case. This results in the following relations:

$$\frac{S_L}{S_L^0} \sim \sqrt{\frac{\rho_U}{\rho_B}}; \qquad \frac{r_B}{r_U} \sim \sqrt{\frac{\rho_U}{\rho_B}}.$$

where r is the radial coordinate of a streamline. Therefore, for the unconfined case we obtain the same increase in flame speed for a given amount of heat release, or density ratio. The only difference is in the length scale ratio for streamline divergence.

2.2 Confined vs. unconfined flames

Figure 2 compares the streamline, pressure field, and reaction rate for both confined and unconfined cases. Because the confined case uses a sinusoidal perturbation in mixture fraction about stoichiometric conditions, we observe two lateral locations where the mixture is at stoichiometric values, hence two triple flames. Because the lateral expansion observed in the unconfined case is absent in the confined case, the streamline patterns are substantially different. Because the streamlines can diverge in the unconfined cases, the pressure can recover laterally, and no global pressure drop is observed across the flame. For the confined flame, this is not the case. The major pressure difference occurring in this case is the drop across the flame, similar to that of a planar premixed flame. In addition to the pressure drop across the
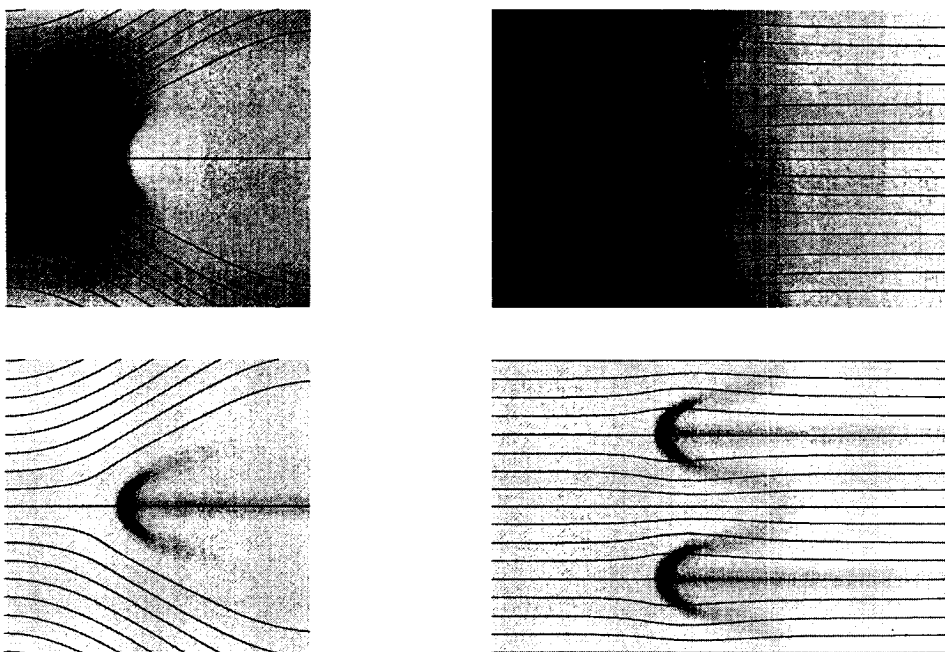
FIGURE 2.   Pressure (top) and reaction rate (bottom) gray scale images with streamline superposed for the unconfined (left) and confined (right) cases. (Higher values correspond to darker regions.) The global divergence of streamlines in the unconfined case is absent in the confined runs, where only a small local divergence in front of the flame is observed. The global pressure drop across the flame in the confined case is absent in the unconfined results.

flame, we observe a pressure rise in front of the flame centered around the stoichiometric streamlines. This is similar to the region in front of the triple point of the unconfined flame, but is much smaller in magnitude. In the unconfined case, this pressure rise is associated with a deceleration of the horizontal velocity that is directly responsible for the increase in propagation of the triple flame structure as a whole. The main question here is whether or not the confined flame observes an increase in flame speed.

2.3 Propagation of confined flames

Time series of the propagation speeds at the stoichiometric point, or leading edge, and the point farthest from stoichiometry, or flame trough, are given in Fig. 3. When the premixed flame is initially subjected to the variation in mixture fraction, the flame response is qualitatively similar to an unconfined flame at the leading edge, in that the propagation speed increases. The flame trough experiences the opposite trend; the flame speed decreases. This behavior is necessary for the flame shape to change, but is only a transient feature. As the flame has time to adjust to the change in mixture fraction gradient, the flame speed returns to that of the premixed case in both the leading edge and trough. The transient time scale for
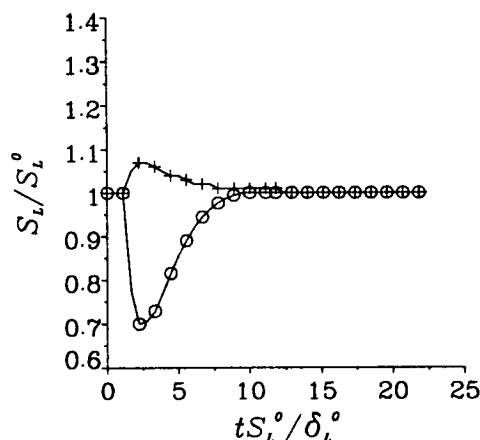
FIGURE 3. Time series of flame speed at the leading edge (+) and flame trough (o) when exposed to a variable mixture fraction. When the mixture fraction is first felt by the flame, the leading edge's flame speed increases, and the trough's flame speed decreases. After some time, both converge to the premixed planar flame speed, S_L^0. The values of Z in the troughs are 0.44 and 0.56.

the change depends on the value of ΔZ, where the larger values require a longer times to relax to the premixed flame speed.

The mixture fraction varies from $0.4 < Z < 0.6$ at the inlet. Simulations with larger ranges of the mixture fraction were performed up to and including $0 < Z < 1$ at the inlet. However, it is important to realize that these values correspond to inlet conditions. Because of the diffusive nature of the flows we consider, these ranges in mixture fraction are greatly reduced by the time the flow reaches the flame. As a result, values ranging from $.29 < Z < .71$ were achieved at the flame surface, and in all cases the flame speeds in both the leading edge and trough converged to the same values, indicating a saturation of flame deformation. Furthermore, these values are within three percent of the premixed laminar flame speed. Thus, for the confined case, no long term change in flame speed occurs when exposing the flame to a perturbation in the mixture fraction.

2.4 Stabilization of the flame trough

Of particular interest is how the flame in the trough is stabilized. To aid in exploring this phenomenon, it is instructive to compare what occurs in the trough of a partially premixed flame to its one-dimensional counterpart. Figure 4 compares the velocity, reduced temperature, and reaction rate in the trough of a partially premixed flame with the same profiles for a one-dimensional flame stabilized with the same reactant composition. There are several differences between these two cases. From the velocity profiles, it is apparent that the flame in the trough of the two-dimensional flow is stabilized in a higher velocity than the one-dimensional
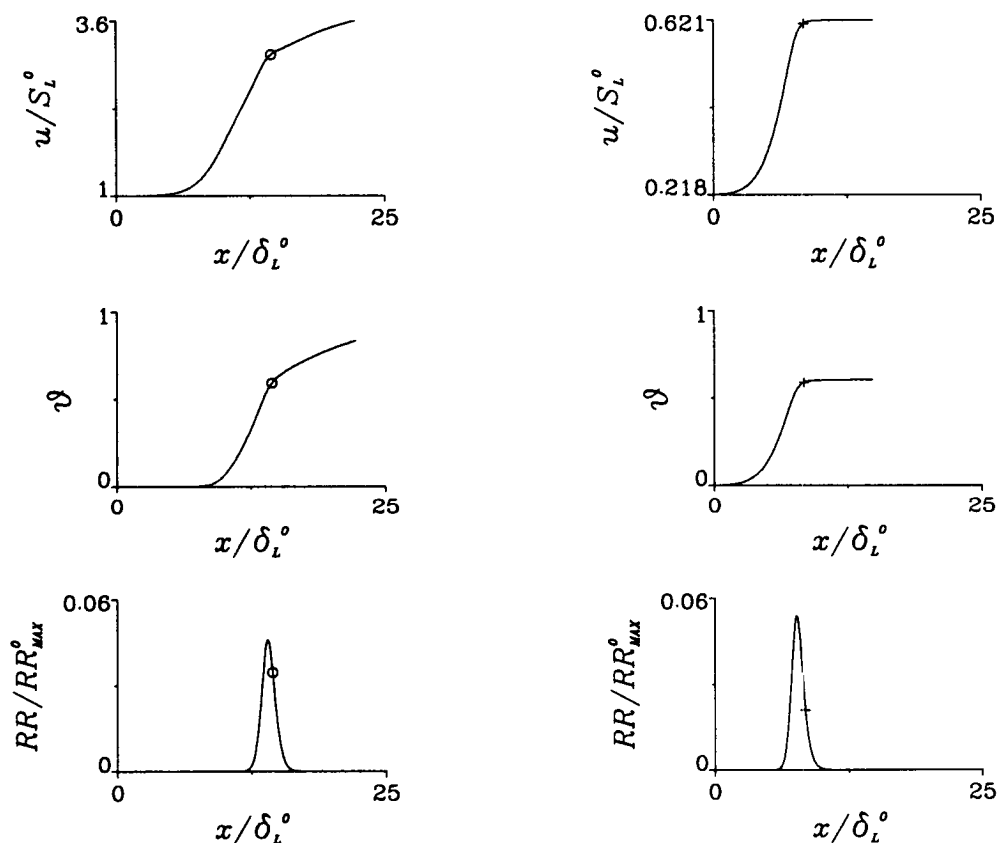
FIGURE 4.   Velocity, reduced temperature, and reaction rate through the flame trough of a two-dimensional flame (left) and for a one-dimensional flame under with the same mixture fraction as in the trough of the two-dimensional case (right). The velocity in the two-dimensional case is larger than in the one-dimensional case. The velocity and temperature profiles in the two-dimensional case show and increase through the flame front, and then a smaller rate of increase afterwards, due to the lateral diffusion of temperature and species.

flame. In addition to the magnitude difference, the shapes of the profiles also differ. The increase in the velocity and reduced temperature can be broken into two regions in the two-dimensional case. The transition between these two regions is marked in Fig. 4. The first region corresponds to the one-dimensional flame, where the chemical reaction is responsible for the increase in these properties. The second region, where the velocity and temperature increase more slowly, is absent in the one-dimensional case. This region results from the lateral conduction of temperature and species into the trough region. The diffusion of reactants into this region shifts the reaction rate back relative to the transition point marked in the figure.

    The comparison between one-dimensional flames and slices though the trough of two-dimensional flames can be extended to examine the effect of the mixture
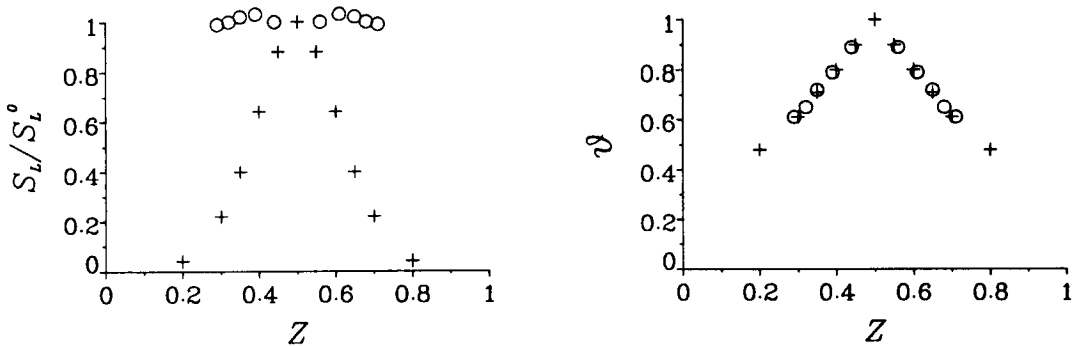
FIGURE 5.   Flame speed (left) and reduced temperature (right) in the trough of two-dimensional partially premixed flames (o) and for stabilized one-dimensional flames (+) at various mixture fractions.

fraction range on flame speed. The transition points for the temperature profiles were calculated for several values of ΔZ at the inlet, along with stabilized one-dimensional flames at various ΔZ. These are displayed in Fig. 5, along with the propagation speed of the flames, i.e. the velocity at the inlet, not at the transition point. The propagation speed plot shows that the two-dimensional cases maintain a flame speed close to the planar premixed flame speed at stoichiometric conditions. One possible mechanism for maintaining this flame speed is that the lateral heat conduction is driving the temperature at the transition point higher, which, for Arrhenius kinetics would exponentially increase the flame speed. However, this appears not to be the case, as we see that the one- and two-dimensional reduced temperatures collapse well onto the same curve. Furthermore, the reaction rates are roughly equal in these two cases, as is evident from Fig. 4.

We can utilize concepts from premixed combustion concerning the laminar flame tip by Poinsot *et al.* (1991) to aid in understanding the stabilization process in the trough region. In their investigation, they identified three mechanisms which may increase the flame speed: the chemical, diffusive, and hydrodynamic mechanisms. For unity Lewis numbers they found the chemical mechanism, which is related to the reaction rate, is small. This is apparent in our case from the reaction rate plot in Fig. 4. The diffusive mechanism corresponds to a leakage of fuel across streamtube boundaries. This mechanism is present; however, the fact that we are using a two-species reaction complicates its interpretation. Furthermore, the diffusion process causes a "leakage" across streamlines in a direction that would tend to decrease the propagation speed. The hydrodynamic mechanism is related to an isothermal area expansion and is signified by a lateral flow divergence. From the streamline pattern in Fig. 2, we see that this does occur in the trough region. One can also see the effect of the hydrodynamic mechanism on the temperature profile in Fig. 4 for the two-dimensional and one-dimensional cases. The flame thickness, based on the maximum temperature gradient, is much larger due to the lateral heat conduction in

the two-dimensional case. This larger flame thickness also indicates the presence of the hydrodynamic mechanism, (cf. Fig. 7 of Poinsot *et al.* 1995). The hydrodynamic mechanism of flame stabilization in the trough region is aided in the confined case by the fact that the streamtubes must return to their original thickness behind the flame. Since an expansion occurs in front of the leading edge, the contraction along the streamline furthest from stoichiometric conditions must occur at that horizontal location. This contracted region then expands farther downstream, through the flame trough, thus enhancing the hydrodynamic mechanism.

2.5 Relevance to turbulent jet flames

In this last section we digress from confined flames and discuss recent experimental work on turbulent jet flames and the applicability of triple flames in turbulence. The recent study of Schefer *et al.* (1994) of lifted flames at Reynolds numbers of 7,000 to 12,000 have found that the reaction zone is a smooth, thin, connected sheet surrounding the jet. Furthermore, measurements of the fuel concentration fields show that the flame lies on or near the stoichiometric contour in a region where the velocity significantly exceeds the laminar premixed flame propagation speed. All of these observations are consistent with the conclusion that the flame is, at least at these Reynolds numbers, a triple flame. Strong support for this conclusion is provided by the preliminary PIV experiments by Muñiz and Mungal (1995) of a methane jet burning in coflowing air. They find that the flame is stabilized in a region in which the measured velocity is approximately the triple flame speed for these gases. Therefore, it appears that triple flames are likely candidates for diffusion flame stabilization.

3. Future work

The ability to calculate partially premixed flames in a confined flow presents opportunities to study many different phenomena. To this point we have considered flows with overall equivalence ratios of unity. We can extend the study to examine extinction phenomena with global equivalence ratios far from stoichiometric conditions. To explore this regime, one would have to abandon the single-step chemistry model for a multistep reduced chemical scheme.

Another phenomenon that can be investigated in partially premixed combustion is the effect of non-unity Lewis numbers on flame speed. The confined partially premixed simulations provide and effective and efficient means of achieving large flame curvature. Simulations in this area are currently under way.

Acknowledgments

REFERENCES

DOLD, J. W. 1989 Flame propagation in a nonuniform mixture: analysis of a slowly varying triple flame. *Combust. & Flame.* **76**, 71.

DOLD, J. W., HARTLEY, L. J. & GREEN, D. 1991 Dynamics of laminar triple-flamelet structures in non-premixed turbulent combustion. *Dynamical Issues in Combustion Theory.* Springer-Verlag, 83.

HARTLEY, L. J. & DOLD, W. 1991 Flame propagation in a nonuniform mixture: analysis of a propagating triple-flame. *Comb. Sci. & Tech.* **80**, 23.

KERSTEIN, A. K., ASHURST, WM. T., & WILLIAMS, F. A. 1988 Field equation for interface propagation in an unsteady homogeneous flow field. *Phys. Rev. A.* **37**, 2728.

KIONI, P. N., ROGG, B., BRAY, K. N. C. & LIÑÁN, A. 1993 Flame spread in laminar mixing layers: the triple flame. *Combust. & Flame.* **95**, 276.

LELE, S. 1992 Compact finite difference schemes with spectral-like resolution. *J. Comp. Phys.* **103**, 16.

MÜLLER, C. M., BRIETBACH, H., AND PETERS, N. 1994 Partially premixed turbulent flame propagation in jet flames. *25th International Symposium on Combustion.* p. 1099

MUÑIZ, L., AND MUNGAL, M. G. Private communication.

PHILLIPS, H. 1965 Flame in a buoyant methane layer. *10th International Symposium on Combustion.* p. 1277

POINSOT, T. & LELE, S. 1992 Boundary conditions for direct simulations of compressible viscous flows. *J. Comp. Phys.* **101**, 104.

POINSOT, T., ECHEKKI, T., AND MUNGAL, M. G. 1992 A study of the laminar flame tip and implications for premixed turbulent combustion. *Comb. Sci. & Tech.* **81**, 45.

RÉVEILLON, J., DOMINGO, P., & VERVISCH, L. 1994 Autoignition in non-uniform mixture. To be published.

RUETSCH, G. R., VERVISCH, L., AND LIÑÁN, A. 1995 Effects of heat release on triple flames. *Phys. Fluids.* **7**, 1447.

SCHEFER, R. W., NAMAZIAN, M., AND KELLY, J. 1994 Stabilization of lifted jet flames. *Combust. & Flame.* **99**, 75.

TROUVE, A. 1991 Simulation of flame-turbulence interaction in premixed combustion. *Annual Research Briefs 1991.* Center for Turbulence Research, NASA Ames/Stanford Univ..

WILLIAMS, F. A. *Combustion Theory* Addison-Wesley, NY, 1986.

WRAY, A. A. Private communication.

Page intentionally left blank

Dynamics and structure of
turbulent premixed flames

By R. W. Bilger[1], N. Swaminathan[1], G. R. Ruetsch, AND N. S. A. Smith

1. Motivation and objectives

In earlier work (Mantel & Bilger, 1994) the structure of the turbulent premixed flame was investigated using statistics based on conditional averaging with the reaction progress variable as the conditioning variable. The DNS data base of Trouvé and Poinsot (1994) was used in this investigation. Attention was focused on the conditional dissipation and conditional axial velocity in the flame with a view to modeling these quantities for use in the conditional moment closure (CMC) approach to analysis of kinetics in premixed flames (Bilger, 1993). Two remarkable findings were made: there was almost no acceleration of the axial velocity in the flame front itself; and the conditional scalar dissipation remained as high, or higher, than that found in laminar premixed flames. The first finding was surprising since in laminar flames all the fluid acceleration occurs through the flame front, and this could be expected also for turbulent premixed flames at the flamelet limit. The finding gave hope of inventing a new approach to the dynamics of turbulent premixed flames through use of rapid distortion theory or an unsteady Bernoulli equation. This could lead to a new second order closure for turbulent premixed flames. The second finding was contrary to our measurements with laser diagnostics in lean hydrocarbon flames where it is found that conditional scalar dissipation drops dramatically below that for laminar flamelets when the turbulence intensity becomes high. Such behavior was not explainable with a one-step kinetic model, even at non-unity Lewis number. It could be due to depletion of H2 from the reaction zone by preferential diffusion. The capacity of the flame to generate radicals is critically dependent on the levels of H2 present (Bilger, *et al.*, 1991). It seemed that a DNS computation with a multistep reduced mechanism would be worthwhile if a way could be found to make this feasible.

Truly innovative approaches to complex problems often come only when there is the opportunity to work close at hand with the (in this case numerical) experimental data. Not only can one spot patterns and relationships in the data which could be important, but one can also get to know the limitations of the technique being used, so that when the next experiment is being designed it will address resolvable questions. A three-year grant from the Australian Research Council has enabled us to develop a small capability at the University of Sydney to work on DNS of turbulent reacting flow, and to analyze data bases generated at CTR. Collaboration between the University of Sydney and CTR is essential to this project and finding

---

1 The University of Sydney, Australia

a workable *modus operandum* for this collaboration, given the constraints involved, has been a major objective of the past year's effort.

The overall objectives of the project are: (1) to obtain a quantitative understanding of the dynamics of turbulent premixed flames at high turbulence levels with a view to developing improved second order closure models; and (2) to carry out new DNS experiments on turbulent premixed flames using a carefully chosen multistep reduced mechanism for the chemical kinetics, with a view to elucidating the laser diagnostic findings that are contrary to the findings for DNS using one-step kinetics. In this first year the objectives have been to make the existing CTR data base more accessible to coworkers at the University of Sydney, to make progress on understanding the dynamics of the flame in this existing CTR data base, and to carefully construct a suitable multistep reduced mechanism for use in a new set of DNS experiments on turbulent premixed flames.

2. Accomplishments

2.1 Accessing the data base

A Fortran 77 program has been written that allows easy access to the DNS data base of Trouvé and Poinsot (1994) from the computers at NAS and also allows efficient computation of derivatives of the data and conditional statistics. It can also be used on the DEC Alpha workstations used at the University of Sydney for this work, but with the limitation that data transfer and storage is limited and further coding has to be written for converting the subroutines that calculate derivatives. So far we have only one field at one time for the unity Lewis number case available in Sydney at 32-bit accuracy. Some processing has been achieved with this at Sydney, but more memory is needed before we can do processing that requires several arrays to be stored at the one time. A further 64 MBytes of RAM will become available soon and this will remove this limitation. It is proposed to write most of the Trouvé and Poinsot data base on tape at 32 bit accuracy and transport it to Sydney in this form.

2.2 Dynamics of the flame

2.2.1 Introduction

During the time that the senior research fellow (Bilger) was at CTR, a good deal of progress was made investigating the velocity and pressure field in the Trouvé and Poinsot flame. It was found that the pressure difference across this flame is small and the acceleration of the mean flow comes from the normal Reynolds stress. This dominance of the normal Reynolds stress makes it seem likely that the use of rapid distortion theory or an unsteady Bernoulli equation will not be successful.

Efforts to progress further were frustrated by apparent anomalies in any balances that contained the reaction rate. This problem took some time to uncover as most balances involve time dependent terms, and these were unavailable without running the original code, the new Fortran 90 version not then being available. The flame is not statistically stationary and the time dependent term in any averaged equation can be quite significant. An equation for the dilatation in the flow was derived which

has no unsteady term, and this showed that there was an error in the parameters being used. This has only been cleared up in the last month or so. The limitations on accessing the data base at Sydney are such that limited processing has only been possible up to now, but it is expected that this problem will be overcome soon.

The results for the dilatation equation are interesting in themselves and are presented here in detail.

2.2.2 Dilatation equation

Instantaneous reaction rate in turbulent flows is related to local value of scalar dissipation rate as demonstrated by Bilger (1976) in the fast chemistry limit and by Peters (1983) for finite rate chemistry for diffusion flames. In the high Da (Damkohler number) limit, Bray (1980) showed the same dependency for premixed flames. Hence, scalar dissipation rate is a crucial quantity in reacting flows. Recently, this quantity has attracted a quite a few modeling studies (Chen *et al.* 1989, Girimaji 1992). Mantel and Bilger (1994) analyzed DNS data base of Trouvé and Poinsot (1994) to comprehend the behavior of scalar dissipation rate in turbulent premixed flames. They observed that the behavior of scalar dissipation rate is independent of the position inside the turbulent flame brush. Here, we demonstrate that the conditional scalar dissipation rate can be obtained from the conditional dilatation equation for premixed flames, knowing the probability density function of the progress variable.

To ease the comparisons of the results with DNS, we make all the quantities in the following discussion dimensionless, unless otherwise specified, by using acoustic scales as in Trouvé and Poinsot (1994). One can write the mass conservation equation as

$$\nabla \cdot \mathbf{u} = \rho \frac{\partial(1/\rho)}{\partial t} + \rho \mathbf{u} \cdot \nabla(1/\rho), \tag{1}$$

where ρ and $\mathbf{u}$ respectively denote density and velocity vector. By making use of the equation of state and defining the reaction progress variable c as

$$c = (T - T_u)/(T_b - T_u) = \frac{1 - \alpha}{\alpha} \left[(\gamma - 1)T - 1 \right],$$

where α is a heat release parameter (Williams 1985), one can write Eq. (1) as

$$\nabla \cdot \mathbf{u} = \frac{\alpha}{1 - \alpha} \left[\rho \frac{\partial c}{\partial t} + \rho \mathbf{u} \cdot \nabla c \right]. \tag{2}$$

Substituting the governing equation for c in Eq. (2), one can obtain

$$\nabla \cdot \mathbf{u} = \frac{\alpha}{1 - \alpha} \left[\dot{\omega}_c + \frac{1}{RePr} \nabla \cdot \mu \nabla c \right], \tag{3}$$

where $\dot{\omega}_c$ and μ are respectively the reaction rate of c and the local dynamic viscosity of the fluid (Trouvé & Poinsot 1994). This equation is referred to as the dilatation
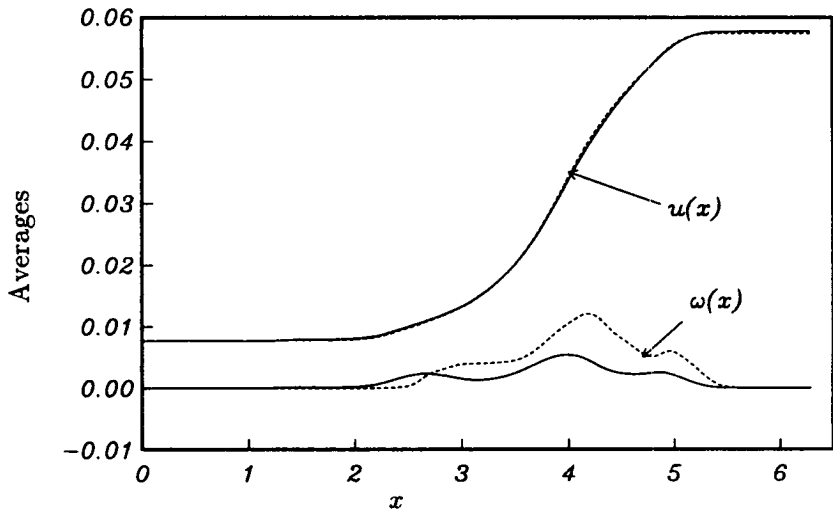
FIGURE 1. Variation of average velocity ($\overline{u}$), reaction rate ($\overline{\dot{\omega}_c}$), and diffusive flux along the inhomogeneous direction x. $\overline{u}$: ——— , DNS; - - - - , Eq.(4), unmarked line diffusive flux. See equation (4).

equation in the following discussions. Averaging this equation, after noting the statistical one-dimensionality of the DNS (Trouvé & Poinsot 1994), yields

$$\overline{u}(x,t) = \overline{u}(-\infty, t) + \frac{\alpha}{1-\alpha} \int_{-\infty}^{x} \overline{\dot{\omega}_c}(x',t)dx' + \frac{\alpha}{1-\alpha} \frac{1}{RePr} \overline{\mu \partial c / \partial x}. \qquad (4)$$

The average velocity $\overline{u}(x,t)$ obtained from the above equation is compared with DNS results in Fig. 1 for $Re = 1000, Pr = 0.75, Le = 1$, and $\alpha = 0.75$ at $t = 4.5$. Time is dimensionless with respect to initial eddy turnover time (Trouvé & Poinsot 1994). The agreement is excellent and encourages us to proceed further.

2.2.3 Conditional dilatation equation

Following Klimenko (1990), the conditioning process can be expressed using a Dirac delta function $\Psi = \delta(c[\mathbf{x}, t] - \zeta)$, where c and ζ are respectively progress variable and its sample space variable. Using this notation, the conditional average of any quantity B can be written as $< B\Psi > = < B|\zeta > P_\zeta$, where P_ζ denote the probability density function of progress variable. After applying the rules for the differentiation of the delta function, we can obtain the conditional dilatation equation as

$$\nabla \cdot [< \mathbf{u}|\zeta > P_\zeta] = -\frac{\partial}{\partial \zeta}(< \mathbf{u} \cdot \nabla c|\zeta > P_\zeta) + \frac{\alpha}{1-\alpha} < \dot{\omega}_c|\zeta > P_\zeta$$
$$+ \frac{\alpha}{1-\alpha}\frac{1}{RePr}D_\zeta P_\zeta, \qquad (5)$$

where D_ζ is the conditional diffusion expressed as $D_\zeta = < \nabla \cdot \mu \nabla c | \zeta >$. For statistically 1-D flow (as in the DNS) Eq. (5) can be written as

$$
\begin{aligned}
D_\zeta P_\zeta &= RePr \frac{1-\alpha}{\alpha} \left[\frac{\partial}{\partial x} (< u | \zeta > P_\zeta) + \frac{\partial}{\partial \zeta} (< \mathbf{u} \cdot \nabla c | \zeta > P_\zeta) \right] \\
&\quad - RePr < \dot{\omega}_c | \zeta > P_\zeta \qquad\qquad (6) \\
&= \frac{\partial}{\partial \zeta} (N_\zeta P_\zeta) + \frac{\partial}{\partial x} \left(< \mu \frac{\partial c}{\partial x} | \zeta > P_\zeta \right) \simeq \frac{\partial}{\partial \zeta} (N_\zeta P_\zeta).
\end{aligned}
$$

The second part of the above equation is obtained by relating the conditional diffusion to conditional dissipation N_ζ. In principle, one can get the conditional dissipation rate from the above equation.

2.3 Multistep reduced mechanism

2.3.1 Formulation

Possibilities of direct numerical predictions of turbulent reacting flows, even in simple geometries, with multistep elementary kinetic mechanisms are remote with the current computational hardware. Hence, researchers often simplify the chemical reactions to a single global step. Direct simulations with single-step chemistry (Trouvé & Poinsot 1994, Swaminathan *et al.*, 1995, Givi 1989), although simplified in certain sense, have given us valuable insight into the different physical processes involved in reacting flows. To further our understanding, direct simulations with a systematically reduced kinetic scheme would be of great interest. Mahalingam *et al.* (1995) have simulated turbulent nonpremixed flames using a two-step chemical scheme which is similar to the Zeldovich-Liñan mechanism. Here, we present a systematically reduced two-step scheme (Peters & Williams 1987, Williams 1991) for hydrocarbon flames from the direct numerical simulation point of view.

Peters (1985) has shown the strategy of reducing full kinetics to a simplified four-step mechanism. Simplification strategy consists of order of magnitude arguments, steady state, and partial equilibrium approximations for appropriate minor species. This reduced mechanism has been used in computational (Bilger *et al.* 1990, Peters & Kee 1987) and asymptotic (Peters & Williams 1987, Seshadri & Peters 1988) studies of laminar flames. These studies improved our understanding of flame structure and extinction mechanisms. For example, a laminar diffusion flame modeled by a single global step extinguishes at high strain rates after allowing fuel to leak through the reaction zone, whereas studies with four-step chemistry indicate that the oxidizer leaks through the reaction zone due to radical depletion on its rich side. These differences indicate that direct simulations with a reduced mechanism would further improve our understanding of turbulent flames and thereby allow us to construct more accurate models for engineering predictions. Due to the computational requirements, we further reduce a four-step mechanism to two steps as discussed below. Reducing a full mechanism to four steps can be found elsewhere (Peters 1991, Bilger *et al.* 1990).

Table 1. Elementary steps involved and their rate constants

Step	Reaction	A	b	E
1	$CH_4 + H \longrightarrow CH_3 + H_2$	6.6E+08	1.6	10840.0
2	$CO + OH \rightleftharpoons CO_2 + H$	1.2E+07	1.4	-730.0
3	$H + O_2 + M \longrightarrow HO_2 + M$	3.6E+17	-0.72	0.0
4	$H + O_2 \rightleftharpoons OH + O$	8.3E+13	0.0	14413.0

$K = AT^b \exp[-E/RT]$, cal-mol-cm-sec-K

Here we start with the four steps given by Bilger *et al.* (1990). These four steps are

$$CH_4 + 2H + H_2O \longrightarrow CO + 4H_2 \qquad\qquad I$$

$$CO + H_2O \rightleftharpoons CO_2 + H_2 \qquad\qquad II$$

$$2H_2 + O_2 \longrightarrow 2H_2O \qquad\qquad III$$

$$3H_2 + O_2 \longrightarrow 2H_2O + 2H. \qquad\qquad IV$$
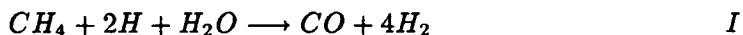
The rates of these four steps are given as linear combinations of some elementary reactions. Excluding all but the most elementary steps, the rate expression given by Bilger *et al.* (1990) can be expressed as

$$\dot{\omega}_I = \dot{\omega}_1, \qquad \dot{\omega}_{II} = \dot{\omega}_2,$$

$$\dot{\omega}_{III} = \dot{\omega}_3, \qquad \dot{\omega}_{IV} = \dot{\omega}_4,$$

where the roman and arabic subscripts respectively denote global and elementary steps. These elementary steps with their rate constants are given in Table 1.

The pressure dependence of elementary step 3 allows us to make a steady state approximation for H atom at pressures typically above one atmosphere. This assumption renders

$$[H]^2 = K_c \frac{[O_2][H_2]^3}{[H_2O]^2} \left[1 - \lambda \frac{[CH_4]}{[O_2]} \right], \qquad (7)$$

where K_c is a combination of equilibrium constants of elementary reactions involved in making partial equilibrium approximation of OH and steady state approximation for O atoms (Bilger *et al.* 1990, Peters & Kee 1987). The ratio of rate constants of elementary steps one to four is denoted by λ and its magnitude is about four for a temperature range of interest. Stoichiometry of the resulting reaction rate expressions of individual species lead us to a three-step mechanism given by (Peters & Williams 1987)

$$CH_4 + O_2 \longrightarrow CO + H_2 + H_2O$$

$$CO + H_2O \rightleftharpoons CO_2 + H_2$$

$$2H_2 + O_2 \longrightarrow 2H_2O.$$
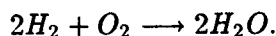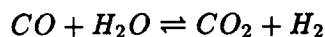
This mechanism can further be reduced to two steps by making partial equilibrium approximations for the water–gas shift reaction. With this assumption, the reaction rates of individual species are given as

$$\dot{\omega}_{CH_4} = -\dot{\omega}_I, \quad \dot{\omega}_{O_2} = -(\dot{\omega}_I + \dot{\omega}_{III})$$

$$\dot{\omega}_{H_2} = -2(\dot{\omega}_I - \dot{\omega}_{III})/(1 + \alpha), \quad \dot{\omega}_{CO} = -2\alpha(\dot{\omega}_I - \dot{\omega}_{III})/(1 + \alpha)$$

$$\dot{\omega}_{CO_2} = -[(1 - \alpha)\dot{\omega}_I + 2\alpha\dot{\omega}_{III}]/(1 + \alpha), \quad \dot{\omega}_{H_2O} = -2[\alpha\dot{\omega}_I + \dot{\omega}_{III}]/(1 + \alpha),$$

where α is ratio of CO to H_2 concentrations at partial equilibrium of water–gas shift reaction and is assumed to be a constant across the reaction zone. Stoichiometry coefficients in the above rate expressions give the two steps as

$$CH_4 + O_2 \longrightarrow \frac{2}{1 + \alpha}[H_2 + \alpha CO] + \frac{1 - \alpha}{1 + \alpha}CO_2 + \frac{2\alpha}{1 + \alpha}H_2O \quad .$$

$$O_2 + \frac{2}{1 + \alpha}[H_2 + \alpha CO] \longrightarrow \frac{2\alpha}{1 + \alpha}CO_2 + \frac{2}{1 + \alpha}H_2O.$$
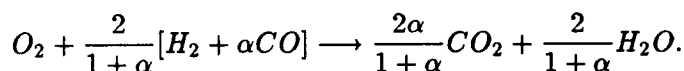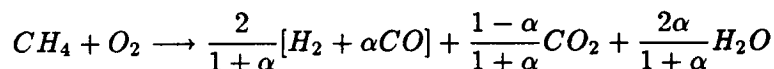
Laminar flame calculations (Bilger *et al.* 1991) with a skeletal mechanism suggest that α is $O(1)$. Hence the above two steps become

$$CH_4 + O_2 \longrightarrow [H_2 + CO] + H_2O$$

$$O_2 + [H_2 + CO] \longrightarrow H_2O + CO_2.$$
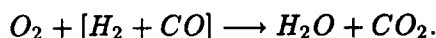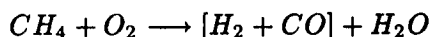
In this mechanism, $[H_2 + CO]$ clearly plays a role of intermediates. Hence, by denoting them as I, CH_4 as F, O_2 as Oxi, H as R, and the remaining species as product P, we get

$$F + Oxi \longrightarrow I + P \qquad \qquad I'$$

$$Oxi + I \longrightarrow 2P. \qquad \qquad II'$$

Reaction rates of these steps, according to the elementary reactions involved, are given as $\dot{\omega}_{I'} = K_1[F][R]$ and $\dot{\omega}_{II'} = K_3'[Oxi][R]$. Radical concentration $[R]$ is given by a modified form of Eq. (7) as suggested by Peters (1995):

$$[R] = K_r[Oxi]^{0.5}[I]^{1.5} \exp(-a\lambda[F]/[Oxi]),$$

where K_r is related to the equilibrium constant K_c, and a is a constant. This form is used to avoid the discontinuity which is implicit in the steady state approximation for H atom (see Eq. (7)) as this will give problems in DNS. By matching the flame speed eigen value for premixed flames (Peters & Williams 1987) or extinction scalar dissipation rate at stoichiometric mixture fraction for diffusion flames (Seshadri & Peters, 1988), one can obtain $a = \sqrt{15/4}$. One can also show that the first and second step of the above two-step mechanism release 40% and 60%, respectively, of the overall heat release. Structure of nonpremixed flames with the above two steps is presented in the following discussions.
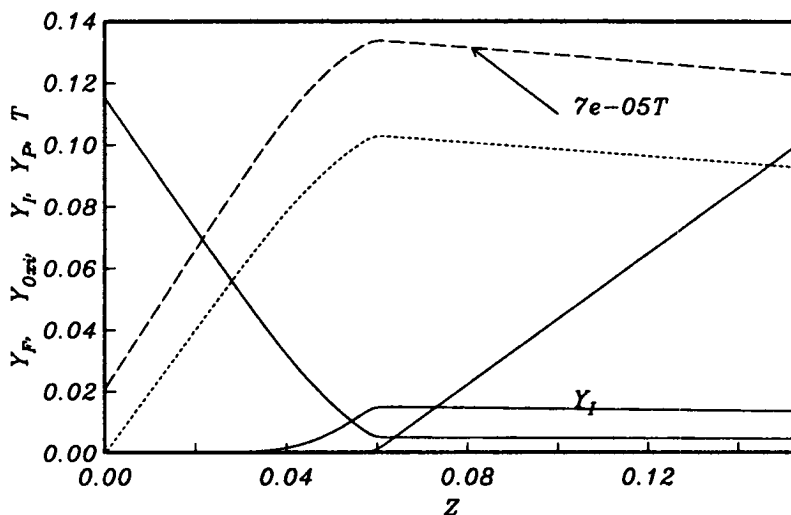
FIGURE 2.   Structure of a laminar (Tsuji) methane-air diffusion flame for a strain rate value of 100 sec^{-1}.
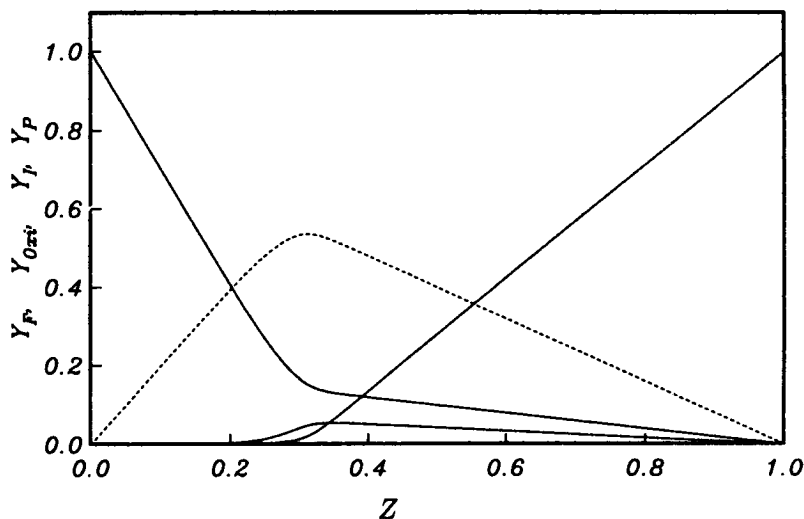
FIGURE 3.   Structure of a laminar diffusion flame used as an initial field for DNS of turbulent nonpremixed flame.

2.3.2 Nonpremixed flame structure

Calculation of Tsuji type laminar diffusion flames are carried out to understand the laminar flame structure and its relation to different rate constants involved. Figure 2 depicts the structure of a methane–air flame at a strain rate of 100 sec^{-1} in mixture fraction space.

The rate constants are derived from those given in Table 1. The specific moles are normalized by the free stream value of fuel species. Radical concentration is about ten times lower than the intermediate concentration. The intermediate is formed
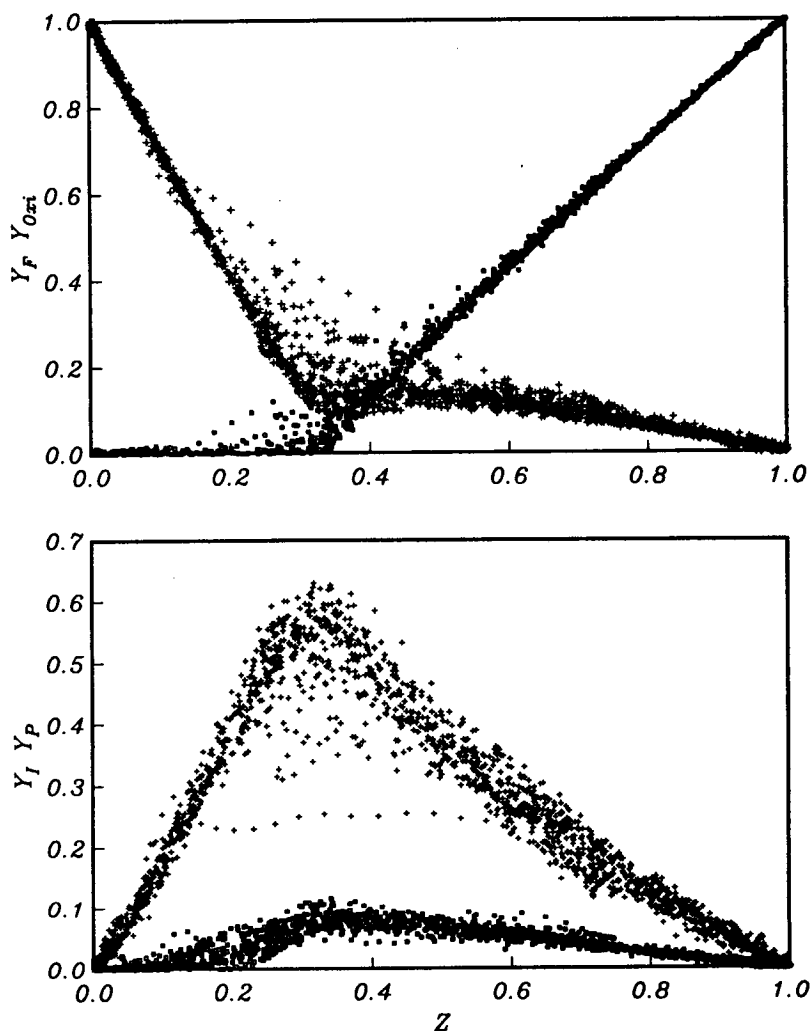
FIGURE 4. Turbulent nonpremixed flame structure with two-step kinetics at $t = 1.5$. Time t is made dimensionless with eddy turnover time at scalar field initialization.

on the rich side of the reaction zone while it is consumed on the lean side. The maximum temperature is about 1900 K, while the free stream value is 300 K. The size of fuel depletion zone in mixture fraction space is about one fifth of oxidizer consumption zone. This flame structure is consistent with Bilger *et al.*'s (1991) calculation using a skeletal mechanism.

The value of stoichiometric mixture fraction can be increased, to ease resolution requirements in DNS, by diluting the reactant streams. The combination of an oxidizer stream having 50% O_2 and 50% N_2 by weight and a fuel stream of 25% methane and 75% Argon by weight has a mixture fraction stoichiometric value of

1/3. These mixtures have equal molecular weights and densities which are the same as that of air. These attributes are attractive for direct simulations of turbulent nonpremixed flames with low heat release. The structure of a laminar diffusion flame for the above reactants is shown in Fig. 3. The rate constants for this calculation are evaluated at 1800 K. This structure is used to initialize DNS calculations using a psuedospectral algorithm (Swaminathan et al. 1995). The structure of the turbulent flame in mixture fraction space is shown in Fig. 4 in the form of scatter plot. The scatter in the values of specific moles is due to unsteady effects. More analysis of this calculation is expected to guide us to design a better experiment.

3. Future work

Our immediate goal is to settle the parameter values to be used in the two-step reduced mechanism for DNS. Laminar and two-dimensional turbulent premixed flames will be tested with the new Fortran 90 compressible code (see Ruetsch and Broadwell 1995, Smith 1995), and then 'production' runs will be made in three dimensions with various values chosen for the Lewis number of the intermediate. The simulation conditions chosen will be similar to those of Trouvé and Poinsot but hopefully with an inflow boundary condition of non-decaying turbulence. Given sufficient computational resources, it is hoped that the 'production' runs can be completed in time for analysis in the 1996 CTR Summer Program.

We will also pursue the goal of making the whole of the existing data base available in Sydney. As soon as the expanded memory for our DEC Alpha is available we will return to analysis of the conditionally averaged momentum, energy, Reynolds stress, and Reynolds flux equations. It is still considered likely that a new approach to second order closure will be found.

REFERENCES

BILGER, R. W. 1976 The Structure of Diffusion Flames. *Comb. Sci. Tech.* **13**, 155-170.

BILGER, R. W. 1993 Conditional Moment Closure Modelling and Advanced Laser Measurements. *In Turbulence and Molecular processes in Combustion.* T. Takeno (Ed), Elsevier,267-285.

BILGER, R. W. STARNER, S. H. & KEE, R. J. 1990 On Reduced Mechanisms for Methane-Air Combustion in Nonpremixed Flames. *Comb.& Flame.* **80**, 135-149.

BILGER, R. W. ESLER, M. B. & STARNER, S. H. 1991 On Reduced Mechanisms for Methane-Air Combustion (M. D. Smooke, Ed.). *Lecture Notes in Physics.* **384**, 86-110, Springer–Verlag.

BRAY, K. N. C. 1980 Turbulent Reacting Flows with Premixed Reactants. *Topics in Applied Physics.* **44**, Springer–Verlag, 115-183.

CHEN, H. CHEN, S. & KRAICHNAN, R. H. 1989 Probability Distribution of a Stochastically Advected Scalar Field. *Phys. Rev. Lett.* **63**, 2657-2660.

GIRIMAJI, S. S. 1992 On the Modeling of Scalar Diffusion in Isotropic Turbulence. *Phys. Fluids A.* **4**, 2529-2537.

KLIMENKO, A. 1990 Multicomponent Diffusion of Various Admixtures in Turbulent Flow. *Fluid Dynamics.* **25**, 327-334.

MAHALINGAM, S. CHEN, J. H & VERVISCH, L. 1995 Finite-rate Chemistry and Transient effects in Direct Numerical Simulation of Turbulent Nonpremixed Flames. *Comb. & Flame.* **102**, 285-297.

MANTEL, T. & BILGER R. W. 1994 Conditional Statistics in a Turbulent Premixed Flame Derived from Direct Numerical Simulation. *Annual Research Briefs-1994.* Center for Turbulence Research, NASA Ames/Stanford Univ., 3-27.

PETERS, N. 1995 Personal Communications.

PETERS, N. 1983 Local Quenching Due to Flame Stretch and Non-Premixed Turbulent Combustion. *Combust. Sci. Tech.* **30**, 1-17.

PETERS, N. & KEE, R. J. 1987 The Computation of Stretched Laminar Methane-Air Diffusion Flames Using a Reduced Four-Step Mechanism. *Combustion and Flame.* **68**, 17-29.

PETERS, N. & WILLIAMS, F. A. 1987 The Asymptotic Structure of Stoichiometric Methane-Air Flames. *Comb. & Flame.* **185-207.**

PETERS, N. 1985 in Numerical Simulation of Combustion Phenomena (R. Glowinski, B. Larrouturou, and R. Temam, Eds.). *Lecture Notes in Physics.* **241**, 90-109, Springer-Verlag.

RUETSCH, G. R., BROADWELL J. 1995 Effects of confinement on partially premixed flames. *Annual Research Briefs-1995.* Center for Turbulence Research, NASA Ames/Stanford Univ..

SESHADRI, K. & PETERS, N. 1988 Asymptotic Structure and Extinction of Methane-Air Diffusion Flames. *Comb. & Flame.* **73**, 23-44.

SMITH N. S. A. 1995 Modeling complex chemical effects in turbulent nonpremixed combustion. *Annual Research Briefs-1995.* Center for Turbulence Research, NASA Ames/Stanford Univ.

SWAMINATHAN, N. MAHALINGAM, S. & KERR, R. M. 1995 Structure of Nonpremixed Reaction Zones in Numerical Isotropic Turbulence. *To appear in Theo. Comp. Fluid Dynamics.*

TROUVÉ, A. & POINSOT, T. 1994 The Evolution Equation for the Flame Surface Density in Turbulent Premixed Combustion. *J. Fluid Mech.* **278**, 1-31.

WILLIAMS, F. A. 1991 Overview of Asymptotics for Methane Flames (M. D. Smooke, Ed.). *Lecture Notes in Physics.* **384**, 68–85, Springer–Verlag.

Page intentionally left blank

Study of turbulent premixed flame propagation using a laminar flamelet model

By H. G. Im

1. Motivation and objectives

The laminar flamelet concept in turbulent reacting flows is considered applicable to many practical combustion systems (Liñán & Williams 1993). For turbulent premixed combustion, the laminar flamelet regime is valid when turbulent Karlovitz number is less than unity, which is equivalent to stating that the characteristic thickness of the flame is less than that of a Kolmogorov eddy; this is known as the Klimov-Williams criterion (Williams 1985). In such a case, the flame maintains its laminar structure, and the effect of turbulent flow is merely to wrinkle and strain the flame front. The propagating wrinkled premixed flame can then be described as an infinitesimally thin surface dividing the unburnt fresh mixture and the burnt product.

It has been suggested (Kerstein *et al.* 1988) that such a propagating front can be represented as a level contour of a continuous function G, whose governing equation, derived using the Huygens' principle, is

$$\rho\frac{\partial G}{\partial t} + \rho u_j \frac{\partial G}{\partial x_j} = \rho s_L |\nabla G|. \tag{1}$$

Here s_L is the well-defined laminar flame speed which is generally not a constant, but can be modified by the effect of flame stretch. By introducing the Markstein length $\mathcal{L}$ (Pelce & Clavin 1982), an asymptotic analysis gives an expression for s_L:

$$s_L = s_L^\circ - s_L^\circ \mathcal{L} \nabla \cdot \mathbf{n} + \mathcal{L}\mathbf{n} \cdot (\nabla \mathbf{n}) \cdot \mathbf{n}, \tag{2}$$

where $\mathbf{n} = -\nabla G/|\nabla G|$ is the normal vector to the surface pointing toward the unburnt mixture. The Markstein length is of the order of flame thickness $\lambda/\rho c_p s_L$ defined usually in terms of unburnt mixture properties. Here λ is the thermal conductivity and c_p the specific heat.

There are several advantages to using the G-equation model rather than direct numerical simulation with Arrhenius-type chemistry. First, since the flame front is described by a contour of the smooth function G, complex topology changes in the propagating front can be easily captured by solving the transport equation for G, instead of tracking the corrugated front. Secondly, since the numerical stiffness due to the Arrhenius chemistry with large activation energy is removed in favor of a flamelet whose structure is given *a priori*, the computational effort can be significantly reduced with an appropriate discontinuity-capturing numerical scheme. Furthermore, the diffusional-thermal modification of the flame structure is accounted for by the flame-speed relation (2) in a parametric manner; the coupling

between the hydrodynamic field and the flame-structure is simply accounted for by the parameter $\mathcal{L}$. This is important in validating the existing predictions of turbulent flame speed, most of which are based on the constant s_L assumption. Finally, by eliminating the nonlinear reaction terms from the conservation equations, the system can be more easily adapted to large-eddy simulation based on the dynamic subgrid-scale modeling principle. A preliminary attempt at such modeling will be discussed in a later section.

From a fundamental standpoint, the G-equation model serves as a useful tool for understanding some issues in turbulent premixed combustion. One such issue is the determination of turbulent flame speed, s_T, as a function of flow quantities such as the turbulence intensity, u'. Although there are theoretical models and experimental observations, the agreement among the various results is far from being satisfactory. Thus far, perhaps the only concensus is that s_T increases with u' initially, then tends to level off at larger u', which is often called "bending" behavior (Bradley 1992).

Most theoretical models of s_T in the flamelet regime are based on Damköhler's (1940) proposition that the increase in the flame speed is proportional to the area increase, which in turn can be related to the turbulence intensity. This suggests

$$s_T/s_L = A_T/A_L \sim 1 + C(u'/s_L)^q, \qquad (3)$$

where A_T is the total surface area of the wrinkled front and A_L the cross-section area normal to the direction of propagation. Based on this proposition, Clavin & Williams (1979) derived $q = 2$ from geometrical considerations, while Yakhot's renormalization group theory (1988a) yields the same result in the weak turbulence limit. Recently, Kerstein & Ashurst (1992) proposed $q = 4/3$ by considering the random nature of turbulent flows. This result was further supported by their numerical study (Kerstein & Ashurst 1994).

All of these arguments are based on the constant density assumption so the effect of heat release generated by chemical reaction has not been taken into account. Variable density introduces additional complexities, one being that the coupling between flow and flame must be dealt with. Recently, Cambray & Joulin (1992), in a semi-analytic study of the model equation by Michelson & Sivashinsky (1977), demonstrated that, at least if $u' \leq O(s_L)$, the turbulent burning velocity is noticeably enhanced by hydrodynamic instability. Their numerical results suggest the value q of about 0.3 in the weak turbulence range. If validated by further studies, this result may show that the "bending" behavior may be the effect of thermal-expansion induced wrinkling, which diminishes at higher u'.

Therefore, in this study we attempt to provide a useful database for understanding these issues in turbulent premixed combustion. In particular, the effect of thermal expansion is investigated by fully coupling the G-equation with the flow field. In the following section, the formulation of the variable-density version of the G-equation model is presented, and some numerical results are discussed for premixed flames propagating in a harmonic inlet velocity flow field and a pair of counter-rotating vortices. The results of the former problem are consistent with those of Cambray & Joulin (1992), while the study of the flame-vortex interaction also reveals interesting

behaviors regarding the vorticity produced by flame. Finally, a subgrid-scale model for the G-equation based on the dynamic modeling concept is proposed.

2. Accomplishments

2.1 The G-equation model with heat release

2.1.1 Formulation

Throughout this study, we define the flame front as the contour, $G = 0$, of a continuous function $G(\mathbf{x}, t)$, where $G < (>) 0$ is defined as the unburnt (burnt) side. The species equation is then substituted by the G-equation which can be written in conservative form as (Williams 1985)

$$\frac{\partial}{\partial t}(\rho G) + \frac{\partial}{\partial x_j}(\rho u_j G) = \rho s_L |\nabla G|. \tag{4}$$

Using the flame-speed relation (2) with the definition $\mathbf{n} = -\nabla G/|\nabla G|$, we obtain (Peters 1992)

$$\frac{\partial}{\partial t}(\rho G) + \frac{\partial}{\partial x_j}(\rho u_j G) = \rho_0 s_L^\circ \left(|\nabla G| + \mathcal{L}\nabla^2 G - \mathcal{L}\frac{\partial \ln |\nabla G|}{\partial x_j}\frac{\partial G}{\partial x_j} \right)$$

$$+ \rho\mathcal{L}\frac{1}{|\nabla G|}\frac{\partial u_k}{\partial x_j}\frac{\partial G}{\partial x_j}\frac{\partial G}{\partial x_k} \tag{5}$$

where the subscript 0 denotes the condition at the unburnt mixture, s_L° the plane laminar flame speed, and we use the approximation $\rho s_L = \rho_0 s_L^\circ = $ constant. Equation (5) accounts for the effect of the flame stretch given by the results (2).

To include the effect of thermal expansion, we introduce the *total energy*

$$e = \frac{1}{2}u_i^2 + c_v T + q[1 - \mathcal{H}(G)] \tag{6}$$

where $\mathcal{H}$ is the Heaviside function. This implies that as the flow crosses the flame ($G = 0$), an amount of chemical energy q is converted to thermal energy, thereby creating jumps in the density and temperature. The conservation equation for the total energy is free of reaction term, *i.e.*

$$\frac{\partial}{\partial t}(\rho e) + \frac{\partial}{\partial x_j}[(\rho e + P)u_j] = \frac{\partial}{\partial x_j}(u_i \tau_{ij}) - \frac{\partial}{\partial x_i}\left(\lambda\frac{\partial T}{\partial x_i}\right), \tag{7}$$

where P is the pressure, τ_{ij} the stress tensor, and the heat flux is given by Fourier's law.

The rest of the system consists of the continuity equation

$$\frac{\partial \rho}{\partial t} + \frac{\partial}{\partial x_i}(\rho u_i) = 0, \tag{8}$$

the momentum equation

$$\frac{\partial}{\partial t}\left(\rho u_i\right) + \frac{\partial}{\partial x_j}\left(u_j \rho u_i\right) = -\frac{\partial P}{\partial x_i} + \frac{\partial \tau_{ij}}{\partial x_j}, \qquad (9)$$

and the equation of state

$$P = \rho RT. \qquad (10)$$

In the present numerical simulations, the discontinuity is removed by replacing the Heaviside function by the smooth function

$$\mathcal{H}(G) \approx [1 + \tanh(G/\delta|\nabla G|)], \qquad (11)$$

where δ is a small parameter of the order of the flame thickness.

The fully-compressible system (5)–(10) is solved using a high order compact scheme (Lele 1992) for spatial derivatives and a third order Runge-Kutta scheme (Wray 1990). Boundary conditions are treated following the method of Poinsot and Lele (1992). For one-dimensional calculations, the initial condition for the G function is

$$G(x) = \begin{cases} -1, & \text{if } x - x_f < -W; \\ \sin[\pi(x - x_f)/2W], & \text{if } |x - x_f| \leq W; \\ 1, & \text{if } x - x_f > W, \end{cases} \qquad (12)$$

and the boundary condition on G is treated in the same way as the other scalar variables. Here W is the thickness of the G profile. The converged one-dimensional solution is used as the initial condition for the two-dimensional calculation.

Figure 1 shows schematics of the two model problems considered, namely the flame response to (a) a steady harmonic velocity fluctuation, and (b) a pair of counter-rotating vortices. Some results for each model problem are presented and discussed below.

2.1.2 Harmonic inlet velocity

As shown in Fig. 1(a), we impose a steady harmonic inlet velocity profile

$$u(x = 0, t) = s_L^\circ + u' \cos(2\pi y). \qquad (13)$$

For $u' = 0$, the G-field remains fixed at the initial condition. In a simulation, at $t = 0$ a finite value of u' is imposed at the inlet boundary; this velocity fluctuation then produces a curved front. The calculation proceeds until a final state is attained, in which the flame area does not change and the front moves toward the unburnt mixture due to the enhanced propagation rate. In the present calculation we used the parameter values $Re_a = (aL/\nu)_0 = 2000$, where a is the speed of sound, unity for the Prandtl and Lewis numbers, and $s_L^\circ/a = 0.05$. The results depend on the Markstein length $\mathcal{L}$ through the flame-speed variation (see (2)). To minimize this flame-structure effect and to extract the behavior of the flame in the Huygens' limit, we choose $\mathcal{L}/L = 0.01$ in the present calculation, where L is the width of the channel shown in Fig. 1(a).
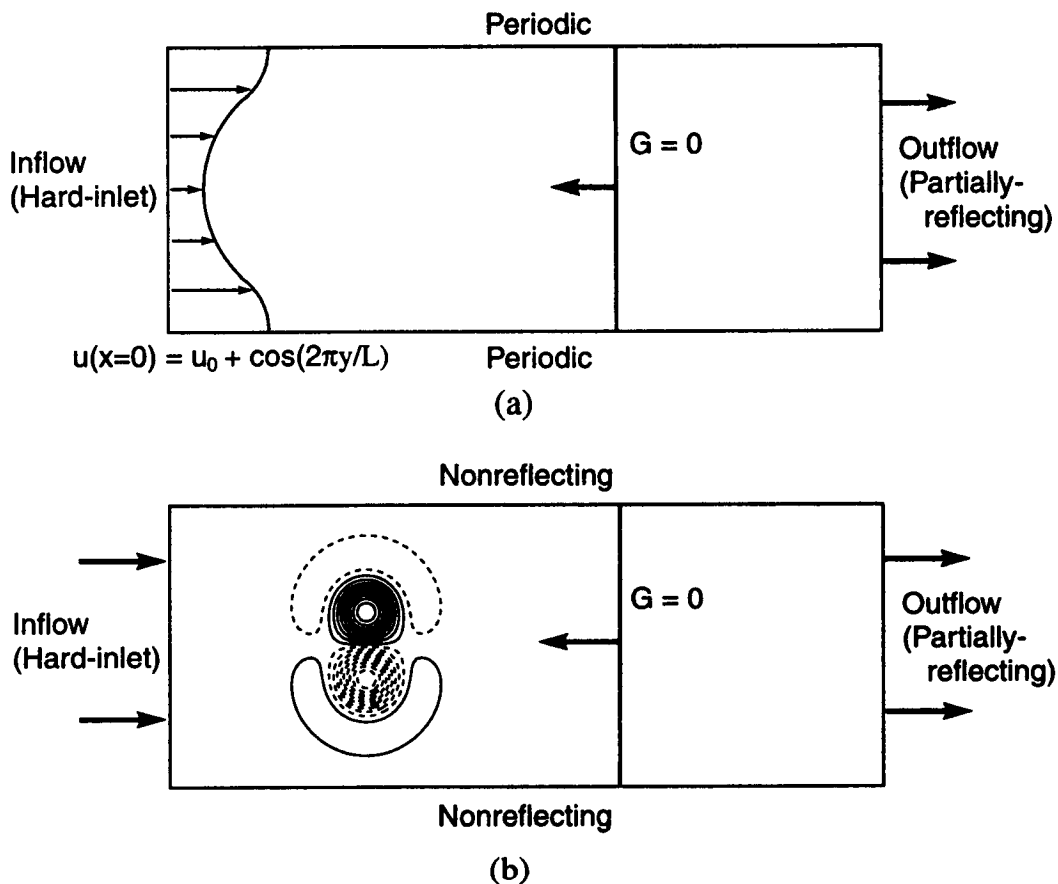
FIGURE 1. Schematics of the model problems and computational conditions: (a) flame propagating into the steady harmonic inlet velocity, (b) flame-vortex interaction, where the solid and dotted curves respectively denote positive and negative vorticities.

Figure 2 shows the final state of the flame fronts represented by the $G = 0$ contours for the inlet perturbations of $u'/s_L^\circ = 0$ and 0.3. Here $\alpha = (\rho_u - \rho_b)/\rho_u$ is the heat release parameter; $\alpha = 0$ for the zero heat-release case and $\alpha = 0.5$ when the downstream temperature is twice the upstream temperature. It is seen that the flames with heat release ($\alpha = 0.5$) are more curved than those without heat release ($\alpha = 0$). This is due to the hydrodynamic instability mechanism known as the Landau-Darrieus effect (Williams 1985). At a hydrodynamic discontinuity with constant propagation speed, thermal expansion induces a deflection of streamlines such that the convex front is further accelerated. Although the linear stability analysis predicts that the perturbation of the front grows indefinitely, in reality it saturates as nonlinear effects come into play. Figure 2 clearly demonstrates
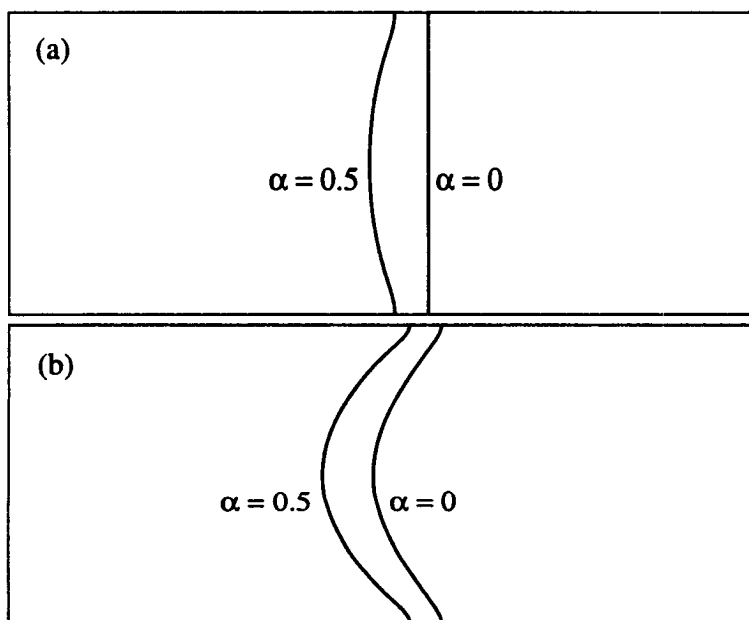
FIGURE 2.   Flame fronts described as $G = 0$ contours subject to the steady harmonic inlet velocity for (a) $u'/s_L^\circ = 0$ and (b) $u'/s_L^\circ = 0.3$. Shown in each figure are the cases for zero heat release ($\alpha = 0$) and for $\alpha = 0.5$.

such behavior, and the flame propagating with larger heat release exhibits more wrinkling. In particular, it is of interest to note from Fig. 2(a) that with heat release the flame front does not remain planar even if inlet velocity perturbation is absent ($u' = 0$), consistent with the result of Cambray & Joulin (1992).

In Fig. 3 we plot the area ratio (A_T/A_L) as a function of the magnitude of velocity fluctuation (u'/s_L°) for the configuration shown in Fig. 1(a). At present, the range of u'/s_L° is limited due to numerical difficulty that arises when u' significantly exceeds s_L° so that the front forms sharp curvature. Nevertheless, Fig. 3 confirms the results of Cambray & Joulin (1992) in that there is an additional flame-speed enhancement due to thermal expansion for weak turbulence ($u'/s_L^\circ < 1$). For larger velocity fluctuations, it is expected that the effect of thermal expansion induced self-wrinkling of the front will be less prominent as the large convective flow field dominates the flame behavior, which may be a possible mechanism for the "bending" behavior. Further improvement in the numerical methodology to capture more excessive wrinkled front is required to obtain a more conclusive database regarding this issue.

2.1.3 Flame-vortex interaction

To further investigate the coupling between a flame and a flow via density variation, we adopt the flame-vortex interaction as a model problem, as was previously studied by Poinsot et al. (1991). In particular, the emphasis is on fundamental issues such as the flame front response to the vortical flows and attenuation and
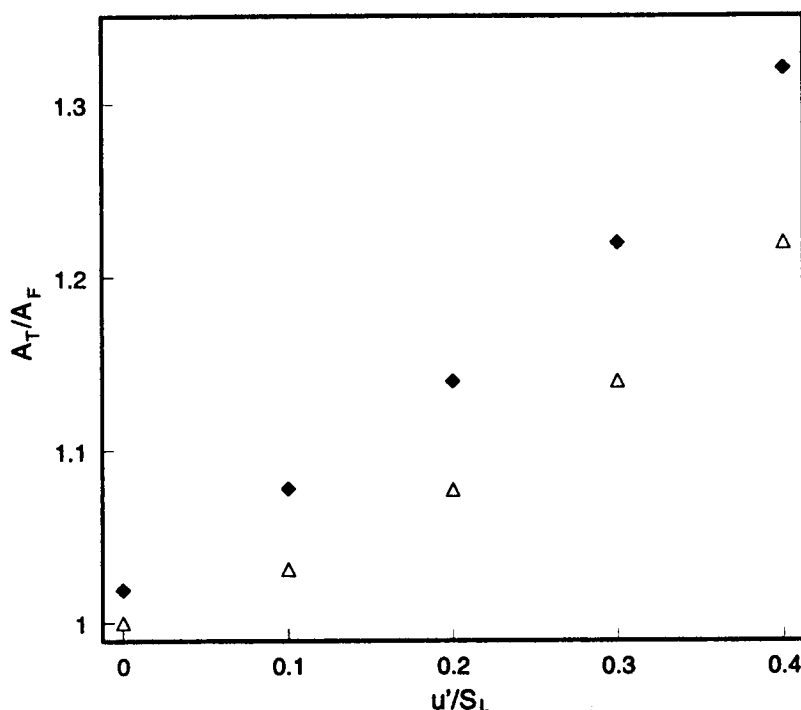
FIGURE 3. Nondimensional total flame-front area vs. nondimensional velocity fluctuation. Open symbols are for zero heat release ($\alpha = 0$) and solid symbols for $\alpha = 0.5$.

generation of vorticity by the flame due to thermal expansion. As shown in Fig. 1(b), at $t = 0$ we introduce a pair of counter-rotating vortices into the uniform flow field with $u_0 = s_L^\circ$, far upstream of the flame. Then, due to the mean flow as well as the flow induced by the vortices, the vortex pair drifts downstream and passes through the propagating flame front, while preserving symmetry. The initial circulation, Γ, of the vortices adopted in this study is given by

$$\Gamma(r) = \pm 2\pi \Psi \frac{r^2}{\sigma^2} \exp\left(-\frac{r^2}{\sigma^2}\right), \tag{14}$$

where r is the distance from the vortex center and σ the characteristic radius of the vortex. Here we define the strength of the vortex u' by the maximum circumferential velocity at $t = 0$. Other parameter values used in this study are $Re_a = 1000$, $Pr = Sc = 0.75$, $\mu/\mu_0 = (T/T_0)^{0.76}$, $s_L^\circ/a = 0.02$, $\mathcal{L}/(\lambda/\rho c_p s_L^\circ)_0 = 0.1$. The vortex diameter is initially about three times larger than the flame thickness and grows in time by diffusive transport.

Figures 4 and 5 show the snapshots of the flame front and vorticity contours at the instant that the flame is most wrinkled by the vortex, for two vortex strengths, $(u'/s_L^\circ)_{t=0} = 2.4$ and 4.8. In each figure, (a) is for the cold flame case ($\alpha = 0$)

FIGURE 4.   Flame-vortex interaction for $u'/s_L^\circ = 2.4$, (a) $\alpha = 0$ and (b) $\alpha = 0.75$. Top and bottom figures respectively denote flame fronts $(G = 0)$ and vorticity. The solid and dotted curves respectively denote counterclockwise and clockwise vorticity.

and (b) for $\alpha = 0.75$. Although not presented here, the results of the G-equation model have been compared to that with the one-step Arrhenius chemistry, and it was found that the G-equation captures the essential physics of the flame and flow responses. It is also remarked that, due to the rapid decrease in the tangential velocity for the initial field (14), an additional vortex pair with opposite sign is formed behind the incident vortex pair. Although it may be unphysical, this fast-decaying vortex requires a smaller computational domain, and thus adopted in this qualitative study.

Figure 4 is for the lower vortex strength. It is seen that, while the vortices Fig. 4(a) preserve their original shapes through the flame, in Fig. 4(b) the vortices are significantly elongated behind the flame due to thermal expansion accelerating the flow. Furthermore, in this case it is interesting to note that the sign of the vorticity is reversed as the vortex passes through the flame. This demonstrates the vorticity generation due to the baroclinic torque mechanism arising from the fact that the pressure and density gradients are not parallel across the curved flame. In this configuration the flame-generated vorticity is opposite to the incident vorticity. Therefore, for the case shown in Fig. 4(b), the incident vortices is overridden by the flame-generated vortices and cannot survive the flame. Consequently, the reversed velocity field induced by the flame-generated vorticity tends to push the retarded flame front forward, yielding a less wrinkled front compared to the cold-flame case shown in Fig. 4(a). The results agrees qualitatively with a recent experimental observation (Mueller *et al.* 1995).

Figure 5 shows the case of a stronger vortex, $u'/s_L^\circ = 4.8$. The front becomes
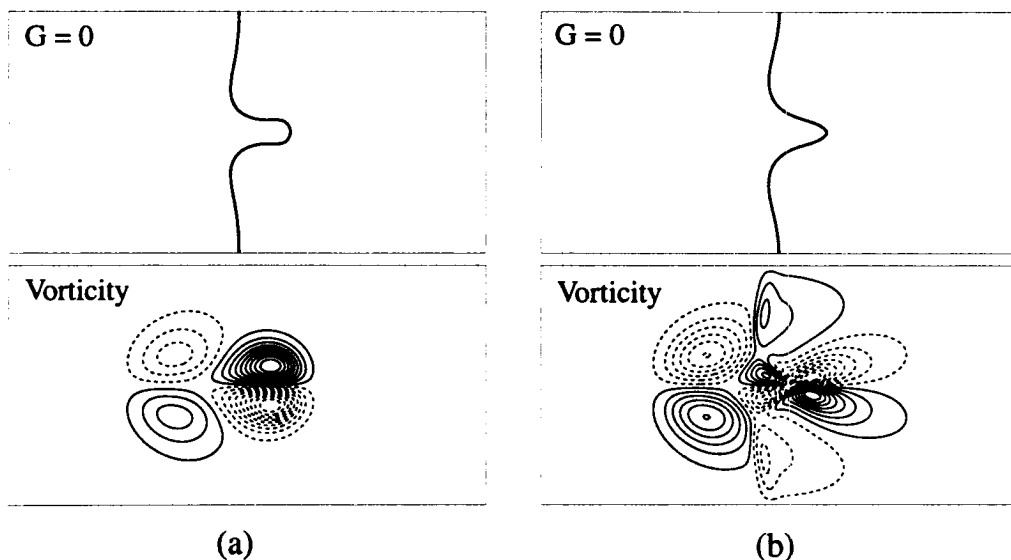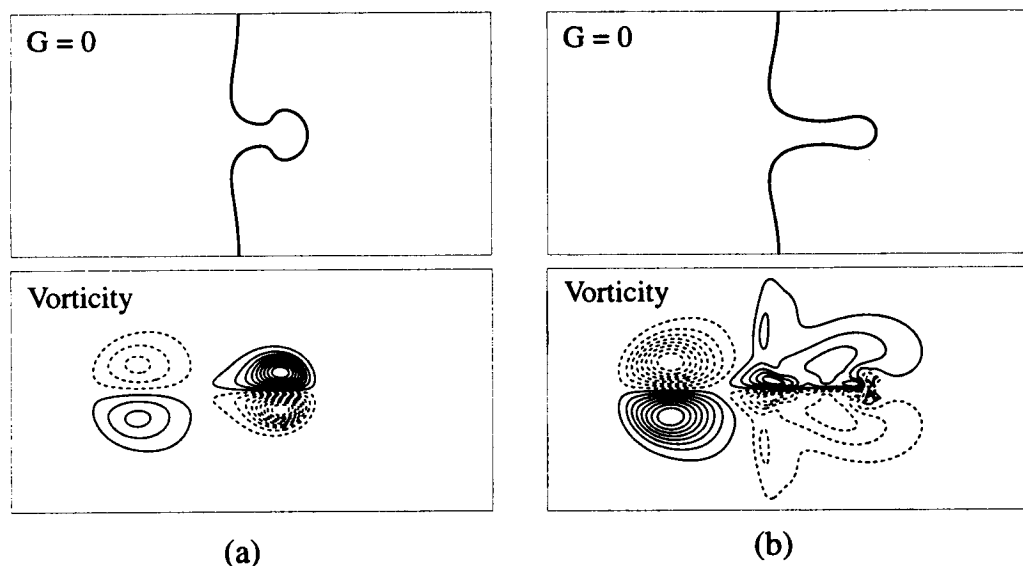
FIGURE 5. Flame-vortex interaction for $u'/s_L^0 = 4.8$, (a) $\alpha = 0$ and (b) $\alpha = 0.75$. Top and bottom figures respectively denote flame fronts ($G = 0$) and vorticity. The solid and dotted curves respectively denote counterclockwise and clockwise vorticity.

more wrinkled. Consistent with the results in Fig. 4, it is seen that the flame-front wrinkling is less severe in the $\alpha = 0.75$ case. Unlike Fig. 4(b), however, the incident vortices shown in Fig. 5(b) are sufficiently strong to survive the flame, except around the sharply curved front where the flame-generated vorticity is most intense. Although the vorticity downstream of the flame has the same sign as the incident vorticity, the strength of the vorticity is considerably weakened. The mechanisms of the vorticity attenuation by the flame are the aforementioned flame-generated vorticity and volume expansion, which spreads out the vortical region while preserving the total circulation (cf. Mueller *et al.* 1995). These front-stabilizing effects may be partly responsible for the experimentally observed "bending" behavior of s_T at high turbulence levels, along with the hydrodynamic effect discussed in the previous subsection.

2.2 Dynamic subgrid-scale modeling for the G-equation

The main idea of the G-equation is to model flame structure as asymptotically thin front. This eliminates the highly nonlinear reaction terms and facilitates modeling for large-eddy simulation. In high Reynolds-number flows, a turbulent premixed flame can be viewed as a wrinkled flame "brush" propagating with velocity s_T. Several previous studies have attempted to derive explicit expressions for $s_T(u')$ (Clavin & Williams 1979, Yakhot 1988a, Kerstein and Ashurst 1992). If u' represents the grid-size averaged quantity, this approach is analogous to the original Smagorinsky's subgrid scale model for Navier-Stokes equation in which the eddy viscosity coefficient is given *a priori*. Unfortunately, the existing theoretical and empirical results for $s_T(u')$ do not agree with one another, so that finding the correct functional form

of $s_T(u')$ remains an open question. Even if the question is resolved, there will still be a constant to be determined.

In this section we suggest a new subgrid-scale model for the G-equation based on the dynamic modeling principle developed recently (Germano *et al.* 1991, Moin *et al.* 1991). One of the prerequisite conditions for the application of dynamic subgrid-scale modeling is that the equation be scale-invariant so that the subgrid quantities can be extrapolated from two adjacent scales. The scale-invariance of the G-equation has been discussed in the previous studies (Pocheau 1992, Yakhot 1988b), and was employed in renormalization group theory to derive an explicit formula for $s_T(u')$ (Yakhot 1988a). We shall skip detailed discussion of this issue.

We start from the simplest incompressible form of the G-equation;

$$\frac{\partial G}{\partial t} + \frac{\partial}{\partial x_j}(u_j G) = s_L |\nabla G|, \qquad (15)$$

where, although not essential, s_L is assumed to be constant. Following previous works, we define the "grid" filter $\bar{\mathcal{G}}$ and the "test" filter $\hat{\mathcal{G}}$ respectively as

$$\bar{f}(\mathbf{x}) = \int f(\mathbf{x}') \bar{\mathcal{G}}(\mathbf{x}, \mathbf{x}') d\mathbf{x}', \quad \hat{f}(\mathbf{x}) = \int f(\mathbf{x}') \hat{\mathcal{G}}(\mathbf{x}, \mathbf{x}') d\mathbf{x}', \qquad (16)$$

where the width of the test filter, $\hat{\bar{\Delta}}$, is larger than that of the grid filter, $\bar{\Delta}$. By applying the grid filter to (16), we obtain

$$\frac{\partial \bar{G}}{\partial t} + \frac{\partial}{\partial x_j}(\bar{u}_j \bar{G}) = -\frac{\partial}{\partial x_j}(\overline{u_j G} - \bar{u}\bar{G}) + s_L \overline{|\nabla G|}. \qquad (17)$$

Here both the subgrid scalar flux $\overline{u_j G} - \bar{u}_j \bar{G}$ and the filtered modulus term $\overline{|\nabla G|}$ need to be modeled. We proceed with applying the test filter, then (17) becomes

$$\frac{\partial \hat{\bar{G}}}{\partial t} + \frac{\partial}{\partial x_j}\left(\hat{\bar{u}}_j \hat{\bar{G}}\right) = -\frac{\partial}{\partial x_j}\left(\widehat{\overline{u_j G}} - \hat{\bar{u}}_j \hat{\bar{G}}\right) + s_L \widehat{\overline{|\nabla G|}}. \qquad (18)$$

In (17) and (18), it is the filtered modulus term, $\overline{|\nabla G|}$ that makes the subgrid scale modeling of the G-equation difficult compared to other scalar equations. The simplest solution is to eliminate this term by applying the test filter to (17) and subtract from (18), yielding

$$(18) - \widehat{(17)} = -\frac{\partial}{\partial x_j}\left(\widehat{\bar{u}_j \bar{G}} - \hat{\bar{u}}_j \hat{\bar{G}}\right), \qquad (19)$$

where all the quantities on RHS can now be calculated directly from the large-eddy grid solutions.

We now need to introduce a model to represent the subgrid-scale quantities of the G-equation. To this end, we adopt the viewpoint described at the beginning of

the subsection, *i.e.* that, on the large-eddy scale, the turbulent flame brush can be represented as a thick front which propagates at speed s_T. Equations (17) and (18) can then be written as

$$\frac{\partial \bar{G}}{\partial t} + \frac{\partial}{\partial x_j} \left(\bar{u}_j \bar{G} \right) = \bar{s}_T |\nabla \bar{G}|, \tag{20}$$

$$\frac{\partial \hat{\bar{G}}}{\partial t} + \frac{\partial}{\partial x_j} \left(\hat{\bar{u}}_j \hat{\bar{G}} \right) = \hat{\bar{s}}_T |\nabla \hat{\bar{G}}|, \tag{21}$$

where $\bar{s}_T$ and $\hat{\bar{s}}_T$ respectively represent the speed of the flame brush at $\bar{\Delta}$ and $\hat{\bar{\Delta}}$ scales. To relate s_T with the turbulence intensity u', we choose a linear form

$$\bar{s}_T / s_L \approx 1 + C(u'/s_L). \tag{22}$$

Even if the linear form is not correct, the error may be adjusted by the constant C through the dynamic procedure.

As in the eddy-viscosity model, we further assume $u' \sim \bar{\Delta} |\bar{S}|$, where $|\bar{S}| = |2\bar{S}_{ij}\bar{S}_{ij}|^{1/2}$ of the large scale strain rate tensor

$$\bar{S}_{ij} = \frac{1}{2} \left(\frac{\partial \bar{u}_i}{\partial x_j} + \frac{\partial \bar{u}_j}{\partial x_i} \right). \tag{23}$$

Therefore, $\bar{s}_T$ and $\hat{\bar{s}}_T$ can be modeled as

$$\frac{\bar{s}_T}{s_L} = 1 + C_G \left(\frac{\bar{\Delta} |\bar{S}|}{s_L} \right), \tag{24}$$

$$\frac{\hat{\bar{s}}_T}{s_L} = 1 + C_G \left(\frac{\hat{\bar{\Delta}} |\hat{\bar{S}}|}{s_L} \right). \tag{25}$$

Substituting (24) and (25) into (20) and (21) and combining with (19) we obtain

$$\left\{ 1 + C_G \left(\frac{\hat{\bar{\Delta}} |\hat{\bar{S}}|}{s_L} \right) \right\} |\nabla \hat{\bar{G}}| - \widehat{\left\{ 1 + C_G \left(\frac{\bar{\Delta} |\bar{S}|}{s_L} \right) \right\} |\nabla \bar{G}|} = -\frac{1}{s_L} \frac{\partial}{\partial x_j} \left(\widehat{\bar{u}_j \bar{G}} - \hat{\bar{u}}_j \hat{\bar{G}} \right), \tag{26}$$

which we wish to use to determine the constant C_G. This is a version of Germano's identity (Germano *et al.* 1991) for the G-equation. Unlike Germano's identity used in the Navier-Stokes and other scalar equations, however, here we subtract the entire equations (17) and (18) instead of treating the subgrid stress terms only, in order to eliminate the modulus term $\widehat{|\nabla G|}$ which is difficult to model. Consequently, the resulting identity (26) is a single scalar equation for a single unknown parameter C_G, rather than the three equations arising from the models for other scalar equations.

As in previous work on dynamic subgrid-scale models, the constant C_G is, in general, a function of space and time. Therefore, C_G cannot be taken out of the test filter, and (26) is an integral equation. However, if the problem of interest has at least one homogeneous direction, then C_G can be assumed to be a function of the other coordinates and can be removed from the test filter. For example, in the case of premixed flame propagating through a channel that is homogeneous in y- and z-directions, $C_G = C_G(x,t)$ so that

$$C_G(x_0,t) \left\{ \left(\frac{\hat{\bar{\Delta}} |\hat{\bar{S}}|}{s_L} \right) |\nabla \hat{\bar{G}}| - \widehat{\left(\frac{\bar{\Delta} |\bar{S}|}{s_L} \right) |\nabla \bar{G}|} \right\} = \widehat{|\nabla \bar{G}|} - |\nabla \hat{\bar{G}}| - \frac{1}{s_L} \frac{\partial}{\partial x_j} \left(\widehat{\bar{u}_j \bar{G}} - \hat{\bar{u}}_j \hat{\bar{G}} \right),$$

$$(27)$$

which is a simpler algebraic equation.

The modeling proposed in this study is for the simplest constant-density case. However, it is anticipated that the same principle can be extended to incorporate variable density consideration. The validity of the model is currently under investigation for the incompressible G-equation model in homogeneous turbulence.

3. Future work

In this study the G-equation model has been applied to several fundamental problems relevant to turbulent premixed combustion in the laminar flamelet regime. Furthermore, a preliminary dynamic subgrid-scale model for the G-equation has been proposed. These ideas need to be further improved to be applied to practical high-Reynolds number premixed combustion systems.

From the standpoint of computational efficiency, the numerical techniques used in the present study appear to have a limited application in the practical turbulent reacting flows, partly due to necessity of resolving the abrupt changes in the dependent variables across the flame front. It is anticipated that a more efficient discontinuity-capturing numerical scheme will greatly reduce the computational cost, thereby allowing more extensive parametric studies of fundamental issues such as turbulent flame speed.

As the next step in the application of the large-eddy simulation to combustion, the dynamic subgrid-scale model for the G-equation suggested in this study should be validated by the direct numerical simulation of the passive G-equation in a turbulent flow. If it proves to be successful, then further study is needed to extend the model to account for the effects of thermal expansion and variable flame speed.

REFERENCES

BRADLEY, D. 1992 How fast can we burn? *Twenty-Fourth Symposium (International) on Combustion*, The Combustion Institute, pp. 247-262.

CAMBRAY, P. & JOULIN, G. 1992 On moderately-forced premixed flames. *Twenty-Fourth Symposium (International) on Combustion*, The Combustion Institute, pp. 61-67.

CLAVIN, P. & WILLIAMS, F. A. 1979 Theory of premixed-flame propagation in large-scale turbulence. *J. Fluid Mech.* **90**, 589.

DAMKÖHLER, G. 1940 *Z. Elektrochem.* **46**, 601.

GERMANO, M., PIOMELLI, U., MOIN, P. & CABOT, W. H. 1991 A dynamic subgrid-scale eddy viscosity model. *Phys. Fluids A.* **3**, 1760.

KERSTEIN, A. R. & ASHURST, WM. T. 1992 Propagation rate of growing interfaces in stirred fluids. *Phys. Rev. Lett.* **68**, 934.

KERSTEIN, A. R. & ASHURST, WM. T. 1994 Passage rates of propagating interfaces in randomly advected media and heterogeneous media. *Phys. Rev. E.* **50**, 1100.

KERSTEIN, A. R., ASHURST, WM. T., & WILLIAMS, F. A. 1988 Field equation for interface propagation in an unsteady homogeneous flow field. *Phys. Rev. A.* **37**, 2728.

LELE, S. 1992 Compact finite difference schemes with spectral-like resolution. *J. Comp. Phys.* **103**, 16.

LIÑÁN, A. & WILLIAMS, F. A. 1993 *Fundamental aspects of combustion*, Oxford University Press.

MICHELSON, D. M. & SIVASHINSKY, G. I. 1977 Non-linear analysis of hydrodynamic instability in laminar flames; Part II: numerical experiments. *Acta Astronautica.* **4**, 1207.

MOIN, P., SQUIRES, K., CABOT, W. & LEE, S. 1991 A dynamic subgrid-scale model for compressible turbulence and scalar transport. *Phys. Fluids A.* **3**, 2746.

MUELLER, C. J., DRISCOLL, J. F., REUSS, D. L., DRAKE, M. C. & ROSALIK, M. E. 1995 Generation and attenuation of vorticity by flames: Measured vorticity field time evolution during a premixed flame-vortex interaction. *Fall Technical Meeting of the Western States Section of the Combustion Institute*, Paper 95F-217, Stanford University, Stanford, CA, Oct. 30-31.

PELCE, P. AND CLAVIN, P. 1982 Influence of hydrodynamics and diffusion upon the stability limits of laminar premixed flames. *J. Fluid Mech.* **124**, 219.

PETERS, N. 1992 A spectral closure for premixed turbulent combustion in the flamelet regime. *J. Fluid Mech.* **242**, 611.

POINSOT, T. & LELE, S. 1992 Boundary conditions for direct simulations of compressible viscous flows. *J. Comp. Phys.* **101**, 104.

POCHEAU, A. 1992 Front propagation in a turbulent medium. *Europhysics Letters.* **20**, 401.

WILLIAMS, F. A. 1985 *Combustion Theory*, 2nd ed., Addison-Wesley.

WRAY, A. A. 1990 Minimal storage time-advancement schemes for spectral methods. *Internal Report*, NASA Ames.

YAKHOT, V. 1988a Propagation velocity of premixed turbulent flames. *Comb. Sci. & Tech.* **60**, 191.

YAKHOT, V. 1988b Scale invariant solutions of the theory of thin turbulent flame propagation. *Comb. Sci. & Tech.* **62**, 127.

Numerical study of boundary layer interaction with shocks – method improvement and test computation

By N. A. Adams

1. Motivation and objectives

The general motivation of this work has been outlined in Adams (1994). The objective is the development of a high-order and high-resolution method for the direct numerical simulation of shock turbulent-boundary-layer interaction. Details concerning the spatial discretization of the convective terms can be found in Adams and Shariff (1995). The computer code based on this method as introduced in Adams (1994) was formulated in Cartesian coordinates and thus has been limited to simple rectangular domains. For more general two-dimensional geometries, as a compression corner, an extension to generalized coordinates is necessary. To keep the requirements or limitations for grid generation low, the extended formulation should allow for non-orthogonal grids. Still, for simplicity and cost efficiency, periodicity can be assumed in one cross-flow direction.

For easy vectorization, the compact-ENO coupling algorithm as used in Adams (1994) treated whole planes normal to the derivative direction with the ENO scheme whenever at least one point of this plane satisfied the detection criterion. This is apparently too restrictive for more general geometries and more complex shock patterns. Here we introduce a localized compact-ENO coupling algorithm, which is efficient as long as the overall number of grid points treated by the ENO scheme is small compared to the total number of grid points.

Validation and test computations with the final code are performed to assess the efficiency and suitability of the computer code for the problems of interest. We define a set of parameters where a direct numerical simulation of a turbulent boundary layer along a compression corner with reasonably fine resolution is affordable.

2. Accomplishments

2.1 Generalized coordinates

The fundamental equations solved are the conservation equations for mass, momentum, and energy in generalized coordinates

$$\frac{\partial}{\partial t}\frac{U}{J} + \frac{\partial}{\partial x}\frac{F_E}{J} + \frac{\partial}{\partial y}\frac{G_E}{J} + \frac{\partial}{\partial z}\frac{H_E}{J} = \frac{\partial}{\partial x}\frac{F_S}{J} + \frac{\partial}{\partial y}\frac{G_S}{J} + \frac{\partial}{\partial z}\frac{H_S}{J} \qquad (1)$$

where the conservative variables are

$$U = \begin{bmatrix} \rho \\ \rho u \\ \rho v \\ \rho w \\ E \end{bmatrix} \ , \tag{2}$$

with $E = \frac{1}{\kappa-1}p + \frac{\rho}{2}(u^2 + v^2 + w^2)$. Considering only spanwise periodic configurations we limit the coordinate generalization to the (x, z)-plane. The convective fluxes are given by

$$F_E = \begin{bmatrix} \rho(u\xi_x + w\xi_z) \\ \rho u(u\xi_x + w\xi_z) + p\xi_x \\ \rho v(u\xi_x + w\xi_z) \\ \rho w(u\xi_x + w\xi_z) \\ (E + p)(u\xi_x + w\xi_z) \end{bmatrix} \ , \tag{3}$$

and similarly for G_E and H_E. The viscous fluxes are given by

$$F_S = \begin{bmatrix} \tau_{xx}\xi_x + \tau_{xz}\xi_z \\ \tau_{xy} \\ \tau_{xz}\xi_x + \tau_{zz}\xi_z \\ -q_x\xi_x - q_z\xi_z + (u\tau_{xx} + v\tau_{xy} + w\tau_{xz})\xi_x + (u\tau_{xz} + v\tau_{yz} + w\tau_{zz})\xi_z \end{bmatrix} \ , \tag{4}$$

and similarly G_S and H_S. The Jacobian of the coordinate transformation is

$$J = \xi_x\zeta_z - \xi_z\zeta_x \ . \tag{5}$$

The stresses are defined as

$$\tau_{xx} = \frac{\mu}{Re}\left[\frac{4}{3}\left(\frac{\partial u}{\partial \xi}\xi_x + \frac{\partial u}{\partial \zeta}\zeta_x\right) - \frac{2}{3}\frac{\partial v}{\partial \eta}\eta_y - \frac{2}{3}\left(\frac{\partial w}{\partial \xi}\xi_z + \frac{\partial w}{\partial \zeta}\zeta_z\right)\right] \ , \tag{6}$$

with analogous definitions for τ_{yy} and τ_{zz} ;

$$\tau_{xy} = \frac{\mu}{Re}\left[\left(\frac{\partial v}{\partial \xi}\xi_x + \frac{\partial v}{\partial \zeta}\zeta_x\right) + \frac{\partial u}{\partial \eta}\eta_y\right] \ , \tag{7}$$

and similarly for τ_{xz}, τ_{yz}, and τ_{zz}. The heat fluxes are defined as

$$q_x = -\frac{\mu}{(\kappa-1)M_\infty^2 PrRe}\left(\frac{\partial T}{\partial \xi}\xi_x + \frac{\partial T}{\partial \zeta}\zeta_x\right) \ , \tag{8}$$

q_y and q_z analogously. The viscosity is calculated according to Sutherland's law. We also assume the thermal equation of state for perfect gases to be valid.

Given a wall-normal temperature gradient distribution $\partial T/\partial n$, a von Neumann condition for the temperature is imposed by setting

$$T_\zeta = \frac{\sqrt{\zeta_x^2 + \zeta_z^2}\frac{\partial T}{\partial n} - (\xi_x\zeta_x + \xi_z\zeta_z)\frac{\partial T}{\partial \xi}}{\zeta_x^2 + \zeta_z^2} \tag{9}$$

whenever it appears during the computation of heat flux and stress terms (due to the temperature dependence of the viscosity).

2.2 Grid generation

For the generation of an analytic mapping of the computational domain onto the physical domain we follow a simple algebraic procedure. We restrict our interest to channel-like geometries where lower and upper boundary can be approximated by simple functions. The mapping is non-conformal and thus the orthogonal partition of the computational domain will be mapped onto a non-orthogonal partition of the physical domain in general. The mapping consists of two steps: (1) the computational domain $\{\xi, \zeta\} \in [0,1] \times [0,1]$ with a uniformly spaced partitioning is mapped onto an intermediate space with non-uniform partitioning $\{s, t\} \in [0,1] \times [0,1]$; (2) the intermediate space $\{s, t\}$ is mapped onto the physical space $\{x, z\}$. Using a linear blending function between lower and upper boundary, we define this latter mapping function by

$$x(\xi, \zeta) = (1-t)x_l(s) + tx_u(s) \tag{10}$$

$$z(\xi, \zeta) = tz_l(s) + (1-t)z_u(s) , \tag{11}$$

the indices l and u indicate that the functions are to be taken at the lower and upper boundary, respectively. The components of the Jacobi matrix are then given by

$$\frac{\partial(x, z)}{\partial(\xi, \zeta)} = \begin{bmatrix} \frac{\partial x}{\partial \xi} & \frac{\partial x}{\partial \zeta} \\ \frac{\partial z}{\partial \xi} & \frac{\partial z}{\partial \zeta} \end{bmatrix} . \tag{12}$$

Later the metric coefficients will be needed, which are the components of the inverse Jacobi matrix,

$$\frac{\partial(\xi, \zeta)}{\partial(x, z)} = \mathrm{Adj}\left(\frac{\partial(x, z)}{\partial(\xi, \zeta)}\right) \left[\mathrm{Det}\left(\frac{\partial(x, z)}{\partial(\xi, \zeta)}\right)\right]^{-1} \tag{13}$$

and the Jacobian

$$J(\xi, \zeta) = \mathrm{Det}\left(\frac{\partial(\xi, \zeta)}{\partial(x, z)}\right) . \tag{14}$$

For the point distributions along the parameter lines $s(\xi)$ along the lower and upper boundary, we define

$$s(\xi) = a\xi + b + c_1 \sinh[g_3(\xi)] \tag{15}$$

and its derivative

$$\frac{ds(\xi)}{d\xi} = a + \frac{c_1}{c_3} \cosh[g_3(\xi)] . \tag{16}$$

The following abbreviations are used:

$$g_3(\xi) = \frac{\xi - c_2}{c_3} \tag{17}$$

$$a = 1 - c_1 \left[\sinh\left(\frac{c_2}{c_3}\right) + \sinh\left(\frac{1-c_2}{c_3}\right)\right] \tag{18}$$

$$b = c_1 \sinh\left(\frac{c_2}{c_3}\right) . \tag{19}$$

If we consider compression corner geometries, then c_1 and c_3 are parameters that tune the grid point condensation around the corner point x_c. It coincides with the zero of $\sinh[g_3(\xi)]$, which is the condition from which c_2 is computed by solving

$$x_c - x(c_2) = 0 \tag{20}$$

for c_2. Knowing all parameters we define the variation of x along the lower or upper boundary in terms of the parameter s as

$$x(s) = Ls , \tag{21}$$

where L is the maximum value x assumes on the lower or upper boundary, respectively. Having obtained $x(s)$ we get $z(s)$ in the following manner.

$$z(x) = d_2 \left[x + \frac{1}{d_1} \ln\left(\cosh\left(d_1 x - x_c\right)\right) + d_3 \right] . \tag{22}$$

A corner singularity in the mapping is avoided by prescribing a finite curvature r_c at $\{x_c, 0\}$. The ramp endpoint is given by $\{L, \sin(\phi)(L - x_c)\}$, where ϕ is the ramp angle in physical space $\{x, z\}$. The parameter d_2 is computed from the condition

$$z(L) = \sin(\phi)(L - x_c) . \tag{23}$$

Finally one sets

$$d_1 = \frac{(1 + d_2^2)^{\frac{3}{2}}}{r_c} \tag{24}$$

and

$$d_3 = -\frac{d_2}{d_1}\ln(\cosh(d_1 x_c)) . \tag{25}$$

In the transversal direction we introduce the parameter function $t(\zeta)$

$$t(\zeta) = \frac{z_{1/2}}{z_1} h_1(\zeta) \left[\left(1 - \frac{z_{1/2}}{z_1}\right) + h_1(\zeta) \left(\frac{2z_{1/2}}{h1} - 1\right) \right]^{-1} \tag{26}$$

and its derivative

$$\frac{dt(\zeta)}{d\zeta} = \frac{z_{1/2}}{z_1} \left(\frac{1 - z_{1/2}}{z_1}\right) \left(c + \frac{e_1}{e_3} \cosh(h_2(\zeta))\right) \times \tag{27}$$

$$\times \left[\left(1 - \frac{z_{1/2}}{z_1}\right) + \left(\frac{2z_{1/2}}{z_1} - 1\right) h_1(\zeta) \right]^{-2} . \tag{28}$$

Herein following abbreviations and parameters are used: e_1 and e_3 control the grid stretching at a point $\{0, z_{mv}\}$ similar to d_1 and d_3; about half of the grid points are between $\{0,0\}$ and $\{0, z_{1/2}\}$. $\{0, z_1\}$ is the upper-left corner point. The auxiliary functions h_1 and h_2 are defined as

$$h_1(\zeta) = c\zeta + d + e_1 \sinh(h_2(\zeta)) \tag{29}$$

and

$$h_2(\zeta) = \frac{\zeta - e_2}{e_3} . \tag{30}$$

The constants c and d are given by

$$c = 1 - e_1 \left[\sinh\left(\frac{1-e_2}{e_3}\right) + \sinh\left(\frac{e_2}{e_3}\right) \right] \tag{31}$$

and

$$d = e_1 \sinh\left(\frac{e_2}{e_3}\right) . \tag{32}$$

Given z_{mv}, the parameter e_2 is computed from the condition that the argument of $z(\zeta) = z_{mv}$ coincides with $h_2(\zeta) = 0$, i.e. e_2 is obtained by solving

$$z_{mv} - z_1 t(e_2) = 0 . \tag{33}$$

2.3 Local compact-ENO coupling

The principle of the coupling between ENO-scheme and the compact finite-difference scheme is discussed in Adams and Shariff (1995). The actual implementation with a reasonable capability for vector optimization is more involved. Let us consider the one dimensional and one component problem. Given the flux F on the grid $\{x_j\}$, its derivative for x is approximated by

$$\frac{\partial F}{\partial x} \doteq P_N[F] = \mathbf{M}_L^{-1} \mathbf{M}_R F \tag{34}$$

Assume that $\{x\}_E = \{x_p, \ldots, x_q\}_1 \cup \cdots \cup \{x_r, \ldots, x_s\}_{n_E}$ is the union of regions of points where the flux derivatives are approximated by the ENO scheme. If a shock detection algorithm has detected a point x_i to be treated by the ENO scheme, v_i is set true and we define a topology vector Υ by

$$\Upsilon = \{v_i\} . \tag{35}$$

This vector has n_E unity blocks with dimensions $N_{n_E} \geq 2N_{sep}+1$, where N_{sep} is the dimension of the padding on both sides of ENO regions (Adams and Shariff, 1995). Whenever we have $v_i = 1$ for a certain grid point, we calculate $P_N[F]_i = P_N^{ENO}[F]_i$ from the ENO scheme.

The effect of the compact-ENO coupling on Eq. (34) is that the ith component of $\mathbf{M}_R F$ is replaced by the flux derivative at i calculated with the ENO scheme whenever v_i is 1. The row i of $\mathbf{M}_L$ has then to become unity so that the ENO flux derivative $P_N^{ENO}[F]$ is exactly returned when Eq. (34) is solved for $P_N[F]$. We defining a correction matrix $\mathbf{BCD}$, which changes the rows i of $\mathbf{M}_L$ to unity whenever v_i is true by its dyadic decomposition into the matrices $\mathbf{B}$, $\mathbf{D}$, and $\mathbf{C}$, the dimensions of which are given below. With this definition the fundamental equation for the computation of flux derivatives of the hybrid scheme can be written as

$$(\mathbf{M}_L - \mathbf{BDC})P_N[F] = \mathbf{M}_R F + \Upsilon(P_N^{ENO}[F] - \mathbf{M}_R F) . \tag{36}$$

The rank of the correction matrix $\mathbf{BCD}$ is $\sum_{\nu=1}^{n_E} N_\nu = m_E$. It is evident that Eq. (36) returns the ENO flux derivatives exactly at points i whenever $v_i = 1$.

To solve Eq. (36) efficiently we make use of the identity by Frobenius and Schur (Zurmühl and Falk, 1984, pg. 308,312) which allows to compute $(\mathbf{M}_L - \mathbf{BDC})^{-1}$ by using the inverse of $\mathbf{M}_L$ corrected by a the inverse of a rank m_E matrix $\mathbf{R}$. If $m_E << N$ this procedure is more efficient for multi-dimensional problems by using the precomputed inverse of $\mathbf{M}_L$ than inverting the LHS-matrix of Eq. (36).

The matrices $\mathbf{B}$, $\mathbf{D}$ and $\mathbf{C}$ are defined as follows:

$$\underbrace{\mathbf{B}}_{m_E \times N} = \sum_{\nu=1}^{m_E} \Upsilon \mathbf{e}_\nu^T , \tag{37}$$

$$\underbrace{\mathbf{D}}_{m_E \times m_E} = \underbrace{\mathbf{I}}_{m_E \times m_E} = \mathbf{I}_{m_E} \tag{38}$$

and

$$\underbrace{\mathbf{C}}_{m_E \times N} = \mathbf{B}^T(\mathbf{M}_L - \mathbf{I}) . \tag{39}$$

Here we define $\mathbf{e}_\nu$ as the m_E-component vector with its ν component equal to unity the rest being zero.

The solution algorithm for Eq. (36) according to (Zurmühl and Falk, 1984) is the following:

(0.) calculate the uncorrected solution vector $\mathbf{y}$ from

$$\mathbf{M}_L \mathbf{y} = \mathbf{M}_R F + \Upsilon(P_N^{ENO}[F] - \mathbf{M}_R F)$$

by direct inversion using the precomputed LU-decomposition of $\mathbf{M}_L$;

(1.) compute matrix $\mathbf{V}$ from

$$\mathbf{M}_L \mathbf{V} = \mathbf{B}$$

by direct inversion using the precomputed LU-decomposition of $\mathbf{M}_L$;

(2.) generate the rank m_E correction matrix $\mathbf{R}$ from

$$\mathbf{R} = \mathbf{I}_{m_E} - \mathbf{CV} ;$$

TABLE 1. Flow parameters for $M_\infty = 6$ ramp.

quantity	value	comment
T_∞^*	57.32K	free stream temperature
M_∞	6	free stream Mach number
p_∞^*	681.15Pa	free stream pressure
Pr	0.7	Prandtl number
κ	1.4	ratio of specific heats
R	287.03	gas constant
μ_∞^*	$3.77 \cdot 10^{-6}$kg/m/s	free stream viscosity
S^*	110.4K	Sutherland constant
Re_{ξ_0}	100000	running length Reynolds number
Re_{δ_1}	5255	reference Reynolds number
δ_1^*	$5.2554 \cdot 10^{-4}$m	reference length
ξ_0	19.03	inflow dist. from lead. edge
L_1	57.14	length of first ramp segment
L_2	120	length of second ramp segment
ϕ	7.5^o	ramp deflection angle

(3.) get the solution correction vector $\mathbf{z}$ from

$$\mathbf{Rz} = \mathbf{Cy}$$

(note that $\mathbf{R}$ is usually fully occupied so that this procedure is only efficient if $m_E \ll N$);
(4.) find the solution vector from

$$P_N[F] = \mathbf{y} + \mathbf{z} \ .$$

For a multidimensional problem all points in index planes normal to the derivative direction are gathered and a vector loop is spanned over these.

2.4 Code validation

Similar to Adams (1994) we validate the generalized coordinate code by comparison with a steady state solution. Experimental and numerical data for comparison are taken from the computational and experimental results of a laminar boundary layer along a 7.5^o compression corner at $M_\infty = 6$ by Simeonides *et al.* (1994). We emphasize that for the results presented in this section time-accurate and low-dissipation methods have been used. The computations have thus been halted before a true steady state has been reached (residual about 10^{-4}). The flow parameters are given in Table 1 (reference length is δ_1^*, dimensional quantities are marked with a star).

In Fig. 2 the grid generated by the algorithm in section 2.2 is shown (each 4th grid line). The grid is condensed towards the wall and towards the kink of the
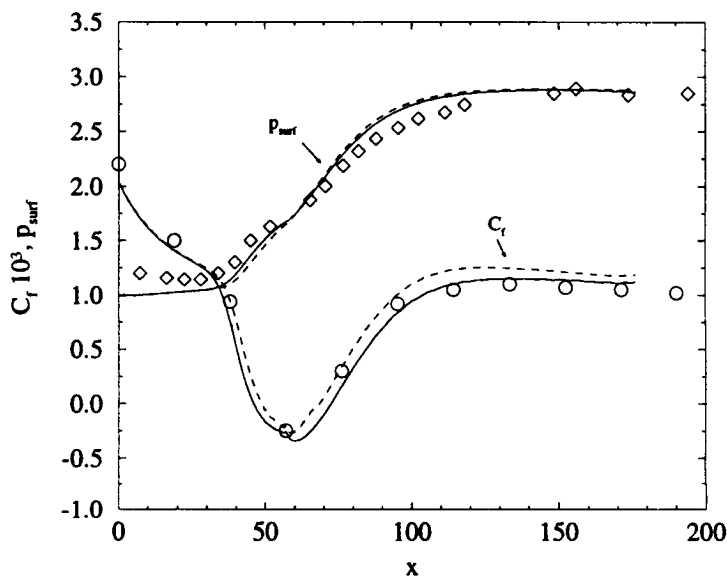
FIGURE 1. Skin friction and surface pressure, 7.5^o laminar compression corner at $M_\infty = 6$. Symbols: ---- , ENO3TVDR3; ——— , CUHDE4R3; $\diamond$, Simeonides *et al.*, exp.; o , Simeonides *et al.*, comput.

ramp. As initial condition we take outside of the boundary layer the solution of the inviscid deflection problem, while near the wall a boundary layer from a similarity solution is given (ignoring the adverse pressure gradient on the inclined segment of the ramp). As boundary conditions we fix at the inflow the initial condition for all primitive variables giving the correct number of 5 conditions for the Navier-Stokes equations (Oliger & Sundström, 1978). At the outflow we prescribe perfectly non-reflecting boundary conditions (Thompson, 1987). At the upper boundary freestream conditions for all flow variables are prescribed.

The computation is started with $N_x = 151$ and $N_z = 61$. After 1000 iterations with a 3rd order LLF-ENO scheme, the resolution is increased to $N_x = 351$ and $N_z = 121$ and the computation is continued for 12000 time steps. Finally, we switch to the hybrid scheme (5th compact upwind, 4th order LLF-ENO) and continue for another 16000 iterations. For the shock detection parameters we use $\beta_x = 5$ and $\beta_z = 5$. The agreement between the computational and experimental results of Simeonides *et al.* (1994) and the present results is satisfactory, Fig. 1. A small inflow transient is caused by the fact that we prescribe a boundary layer profile at inflow. This is to match the procedure in later DNS. In Simeonides *et al.* (1994) the plate leading edge is included in the computational domain.

Figure 3 shows a quasi-Schlieren plot (merely the norm of the density gradient) when the computations were halted. Both the separation shock and the main ramp shock are clearly visible.
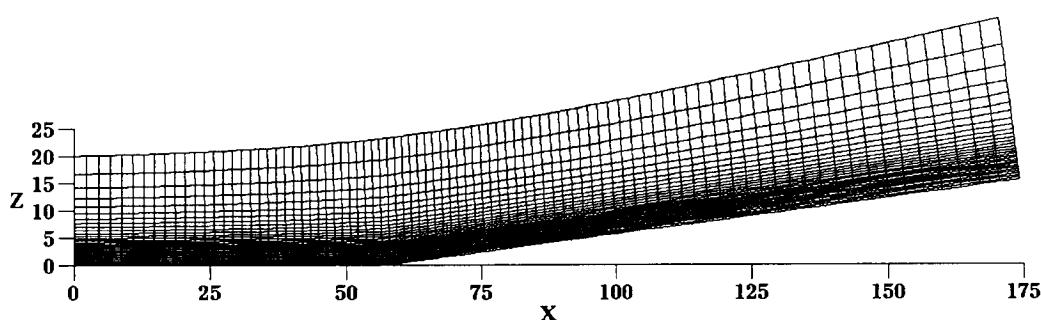
FIGURE 2. Grid for 7.5° ramp, each 4th grid line shown.
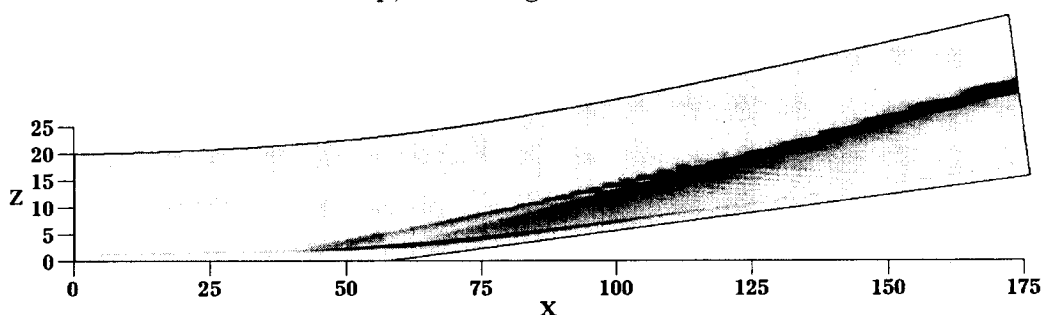
FIGURE 3. Quasi-Schlieren plot (intensity proportional to norm of density gradient).

2.5 Test computation – flat plate

A test computation of a turbulent boundary layer along a flat plate at $M_\infty = 3$ has been performed. The Reynolds number is $Re_{\delta_1} = 10000$, where δ_1 is the laminar displacement thickness corresponding to the inflow station, which is also the reference length. We take as reference length the displacement thickness from a laminar similarity solution since it is uniquely defined corresponding to a downstream station measured from the plate leading edge. The flow parameters are given in Table 2. Discretization is $N_x = 351$, $N_y = 41$ and $N_z = 121$.

The inflow data are generated from the temporal simulation data of Guo and Adams (1994) using Taylor's hypothesis. Initial condition is a laminar similarity solution which is also the reference solution used in the sponge region $48 < x \leq 56$ (Adams, 1994). The computation extends over 8000 time steps. Time step size is about $\Delta_t = 0.1069\ t^+$. The output data are sampled over the final 4400 time steps, starting after the inflow plane has been convected through the outflow. The time sampling interval is about 470 t^+.

For a comparison we refer to the inflow boundary layer profile of the experimental data at higher Reynolds number for a 25° compression corner of Zheltovodov *et al.* (1990). In Table 3 we compare data from simulation and experiment. In Fig. 4 we compare mean flow profiles (spanwise and ensemble averaged) at the

N. A. Adams

TABLE 2. Flow parameters for $M_\infty = 3$ flat plate.

quantity	value	comment
T_∞^*	115K	
M_∞	3	
Pr	0.72	
κ	1.4	
R	287.03	
μ_∞^*	$7.98 \cdot 10^{-6} \mathrm{kg/m/s}$	
S^*	110.4K	
Re_{δ_1}	10000	
δ_1^*	$4.0830 \cdot 10^{-4} \mathrm{m}$	
ξ_0	338.32	inflow station
L_x	56	streamwise box-length
L_y	4	spanwise box-length
L_z	25	wall-normal box-length

TABLE 3. Boundary layer data for flat plate, C_f is the skin friction coefficient, v^+ is the friction velocity, l^+ is the wall unit, Δ^+ is the grid spacing in wall units (for the wall-normal direction z it is the distance of the first point away from the wall), and δ_1 is the turbulent displacement thickness.

quantity	$x = 10.08$	$x = 25.12$	$x = 40.00$	exp
C_f	$0.27 \cdot 10^{-2}$	$0.28 \cdot 10^{-2}$	$0.26 \cdot 10^{-2}$	$0.15 \cdot 10^{-2}$
v^+	0.0595	0.0605	0.0576	0.0442
l^+	0.0107	0.0101	0.0098	0.0075
Δ_x^+	17.41 l^+	18.47 l^+	19.02 l^+	–
Δ_y^+	9.33 l^+	9.89 l^+	10.19 l^+	–
Δ_z^+	4.89 l^+	5.18 l^+	5.34 l^+	–
δ_1	1.53	1.56	1.55	1.93

same streamwise stations as in Table 3 with the experiment.

In general the quality of the simulation data is unsatisfactory. This is due to several reasons. One is the large distance of the first grid point away from the wall, which results in a poor approximation of wall-normal gradients. Another is the relatively small streamwise extent of the computational domain, which is only about 10 turbulent boundary layer thicknesses, considering the fact that the outflow sponge affects about another 1.5 boundary layer thicknesses, even less. The downstream extent of the inflow transient cannot be clearly assessed. Also, we make the same observation as in Guo and Adams (1994) that there is a mass defect visible in the profiles from the simulation in the lower boundary layer half. This
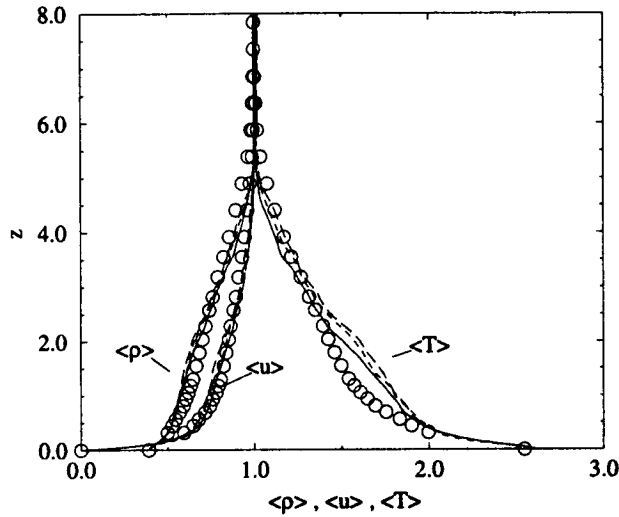
FIGURE 4. Mean flow profiles for $M_\infty = 3$ flat plate. Symbols: ———— , $x = 10$; ———— , $x = 25$; ——— , $x = 40$; ○ , exp.

is attributed to the too small streamwise extent, which apparently does not allow for the appropriate evolution of streamwise streaks. The computational cost was $32\mu s/(N_{point}\ N_{timestep})$ for a single CRAY C90 CPU.

3. Future plans

From the numerical experiments mentioned in the previous section, we estimate a set of parameters where a direct numerical simulation of a compression corner is feasible. A direct numerical simulation at these parameters will be attempted while an accompanying large-eddy simulation is under consideration by K. Mahesh (CTR).

3.1 DNS parameters and cost estimate

The Reynolds number with respect to the turbulent displacement thickness at inflow is about 6000. Turbulent boundary layer thickness and turbulent displacement thickness can be estimated as about 600 l^+ and 210 l^+, respectively. With an expected discretization of $N_x = 601$, $N_y = 51$, and $N_z = 141$, we estimate $\Delta_x = 15\ l^+$ and $\Delta_z = 10\ l^+$. With an estimated $T_{pass} = 300\ t^+$ for the inflow plane to be convected through the domain, a time step of about $\Delta_t = 0.06\ t^+$, and a code performance of about $38\mu s/(N_{point}\ N_{timestep})$ on a single CRAY C90 CPU, we require an estimated 265 hours per T_{pass}.

Acknowledgments

TABLE 4. Flow parameters for $M_\infty = 3$ ramp.

quantity	value	comment
T_∞^*	115K	
M_∞	3	
Pr	0.72	
κ	1.4	
R	287.03	
μ_∞^*	$7.98 \cdot 10^{-6}$kg/m/s	
S^*	110.4K	
Re_{δ_1}	4000	
δ_1^*	$1.6331 \cdot 10^{-4}$m	reference length
ξ_0	135.33	inflow station
L_1	45	length of first ramp segment
L_2	45	length of second ramp segment
ϕ	18	ramp deflection angle

REFERENCES

ADAMS, N. A. 1994 Numerical study of boundary layer interaction with shocks – method and code validation. In *CTR Annual Research Briefs 1994*, Center for Turbulence Research, NASA Ames/Stanford Univ.

ADAMS, N. A. & SHARIFF, K. 1995 A high-resolution hybrid compact-ENO scheme for shock-turbulence interaction problems. *CTR Manuscript 155*, Center for Turbulence Research, NASA Ames/Stanford Univ. (submitted to *J. Comp. Phys*).

BLAISDELL, G. A. & MANSOUR, N. N. & REYNOLDS W. C. 1991 Numerical simulations of compressible homogeneous turbulence.*Report* TF-50, Mechanical Engineering, Stanford University, Stanford, California.

GUO, Y. & ADAMS, N. A. 1994 Numerical investigation of supersonic turbulent boundary layers with high wall temperature. *Proc. 1992 Summer Program*, Center for Turbulence Research, NASA Ames/Stanford Univ.

OLIGER, J. & SUNDSTRÖM, A. 1978 Theoretical and practical aspects of some initial boundary value problems in fluid dynamics. *SIAM J. Appl. Math.* 35, 419–446.

THOMPSON, K. W. 1987 Time dependent boundary conditions for hyperbolic systems. *J. Comput. Phys.* **68**, 1–24.

ZHELTOVODOV, A. A., ZAYLICHNY, E. G., TROFIMOV, V. M. & YAKOVLEV, V. N. 1990 An experimental documentation of supersonic turbulent flows in the vicinity of sloping forward and backward facing steps. In Settles, G. S., & Dodson, L. J. 1994 Supersonic and hypersonic shock / boundary-layer interaction database. *AIAA Journal* **32**, 1377–1383.

ZURMÜHL, R. AND FALK, S. 1984 Matrizen und ihre Anwendungen 1: Grundlagen. Fifth edition, Springer Verlag, Berlin.

Appendix A. Split form of the convective fluxes

A typical indication of underresolution (thus of aliasing errors) of a direct numerical simulation of a compressible flow, solving the compressible Navier-Stokes equations, is the appearance of regions with negative temperature (or pressure). This is related to a local imbalance of internal (potential) and kinetic energy, caused mostly by aliasing errors. It has been observed by Blaisdell *et al.* (1991) that for the pseudospectral computation of derivatives of convolutions of dependent variables, as $\partial(fg)$, the aliasing error is reduced by using the identity $\partial(fg) = 1/2(\partial(fg) + 1/2 + f\partial g + 1/2g\partial f$. For finite-difference schemes the coefficients of the discrete Fourier series for the derivative have to be multiplied by the integer modified wavenumber, which becomes a function of the integer wavenumber; for dissipative schemes this modified wavenumber is complex. In this appendix we briefly investigate the effect of a split form of the convective fluxes for a dissipative finite-difference schemes. From numerical experimentation with coarsely resolved computations for a flat plate, we see that for the upwind scheme used above aliasing errors are even more critical for the split formulation than for the conservative form.

First we derive the expressions for pseudospectral convolution in terms of discrete Fourier series for a Fourier scheme (in the following the summations $\sum_{n+m=k}$ and $\sum_{n+m=k\pm N}$ are always to be taken over $m, n = -N/2, ..., -N/2 - 1$)

$$\partial_x(fg) = \sum_{k=-\frac{N}{2}}^{\frac{N}{2}-1} ik \left(\sum_{m+n=k} \hat{f}_m \hat{g}_n + \sum_{m+n=k\pm N} \hat{f}_m \hat{g}_n \right) e^{ikx} \qquad (A.1)$$

and

$$\frac{1}{2}\partial_x(fg) + \frac{1}{2}g\partial_x f + \frac{1}{2}f\partial_x g =$$

$$= \sum_{k=-\frac{N}{2}}^{\frac{N}{2}-1} \left(\sum_{m+n=k} i\frac{1}{2}(k+m+n)\hat{f}_m \hat{g}_n + \sum_{m+n=k\pm N} i\frac{1}{2}(k+m+n)\hat{f}_m \hat{g}_n \right) e^{ikx}$$

$$= \sum_{k=-\frac{N}{2}}^{\frac{N}{2}-1} \left(\sum_{m+n=k} ik\hat{f}_m \hat{g}_n + \sum_{m+n=k\pm N} i(k \pm \frac{N}{2})\hat{f}_m \hat{g}_n \right) e^{ikx} . \qquad (A.2)$$

For a finite difference schemes this reads

$$\partial_x(fg) = \sum_{k=-\frac{N}{2}}^{\frac{N}{2}-1} i\tilde{k}(k) \left(\sum_{m+n=k} \hat{f}_m \hat{g}_n + \sum_{m+n=k\pm N} \hat{f}_m \hat{g}_n \right) e^{ikx} \qquad (A.3)$$

and

$$\frac{1}{2}\partial_x(fg) + \frac{1}{2}\partial_x fg + \frac{1}{2}f\partial_x g =$$

$$= \sum_{k=-\frac{N}{2}}^{\frac{N}{2}-1} \left(\sum_{m+n=k} \mathrm{i}\frac{1}{2}(\tilde{k}(k) + \tilde{m}(m) + \tilde{n}(n))\hat{f}_m\hat{g}_n + \right.$$

$$\left. + \sum_{m+n=k\pm N} \mathrm{i}\frac{1}{2}(\tilde{k}(k) + \tilde{m}(m) + \tilde{n}(n))\hat{f}_m\hat{g}_n \right) e^{\mathrm{i}kx} \; . \qquad (A.4)$$

Using the symmetry properties of the dispersion function and of the dissipation function, we restrict the following to $0 \leq \xi \leq \pi$. We approximate the modified wavenumber $\tilde{\xi}(\xi)$ piecewise linearly by

$$\tilde{\xi}(\xi) \simeq \left\{ \begin{array}{ll} \xi & , \text{ if } \xi \leq \Xi \\ \frac{\pi-\xi}{\pi-\Xi}\Xi + \mathrm{i}\frac{\Xi-\xi}{\pi-\Xi}\tilde{D} & , \text{ if } \Xi < \xi \leq \pi \end{array} \right. \qquad (A.5)$$

The integer modified wavenumber $\tilde{k}(k)$ is then obtained as

$$\tilde{k}(k) \simeq \left\{ \begin{array}{ll} k & , \text{ if } k \leq K \\ \frac{N-2k}{N-2K}K + \mathrm{i}\frac{2K-2k}{N-2K}D & , \text{ if } K < k \leq \frac{N}{2} \end{array} \right. \qquad (A.6)$$

For the split formulation we get:
Case (1) $-K \leq k \leq K$:

$$\frac{1}{2}\partial_x(fg) + \frac{1}{2}\partial_x fg + \frac{1}{2}f\partial_x g =$$

$$= \sum_{k=-\frac{N}{2}}^{\frac{N}{2}-1} \left[\mathrm{i}\left(\sum_{m+n=k} \underbrace{k}_{\text{I}}\hat{f}_m\hat{g}_n + \sum_{m+n=k\pm N} \left(k \pm \frac{N}{2}\right)\hat{f}_m\hat{g}_n \right) \right] e^{\mathrm{i}kx} \qquad (A.7)$$

Case (2) $K < k \leq \frac{N}{2}$:

$$\frac{1}{2}\partial_x(fg) + \frac{1}{2}g\partial_x f + \frac{1}{2}f\partial_x g =$$

$$= \sum_{k=-\frac{N}{2}}^{\frac{N}{2}-1} \left[\sum_{m+n=k} \underbrace{-\frac{3K-2k}{N-2K}D}_{\text{VI}}\hat{f}_m\hat{g}_n + \sum_{m+n=k\pm N} \underbrace{-\frac{3K \mp N - 2k}{N-2K}D}_{\text{VII}}\hat{f}_m\hat{g}_n + \right.$$

$$\left. + \mathrm{i}\left(\sum_{m+n=k} \underbrace{\frac{\frac{3}{2}N-2k}{N-2K}K}_{\text{II}}\hat{f}_m\hat{g}_n + \sum_{m+n=k\pm N} \underbrace{\frac{(\frac{3}{2}\mp 1)N - 2k}{N-2K}K}_{\text{III}}\hat{f}_m\hat{g}_n \right) \right] e^{\mathrm{i}kx} \; . \quad (A.8)$$

For the non-split formulation we get:
Case (1) $-K \leq k \leq K$:

$$\partial_x(fg) =$$

$$= \sum_{k=-\frac{N}{2}}^{\frac{N}{2}-1} \left[\mathrm{i} \left(\sum_{m+n=k} \underbrace{k}_{\text{IV}} \hat{f}_m \hat{g}_n + \sum_{m+n=k\pm N} k \hat{f}_m \hat{g}_n \right) \right] e^{\mathrm{i}kx} \qquad (A.9)$$

Case (2.) $K < k \leq \frac{N}{2}$:

$$\partial_x(fg) =$$

$$= \sum_{k=-\frac{N}{2}}^{\frac{N}{2}-1} \left[\sum_{m+n=k} \underbrace{-\frac{2K-2k}{N-2K} D}_{\text{VIII}} \hat{f}_m \hat{g}_n + \sum_{m+n=k\pm N} -\frac{2K-2k}{N-2K} D \hat{f}_m \hat{g}_n + \right.$$

$$\left. + \mathrm{i} \left(\sum_{m+n=k} \underbrace{\frac{N-2k}{N-2K} K}_{\text{V}} \hat{f}_m \hat{g}_n + \sum_{m+n=k\pm N} \frac{N-2k}{N-2K} K \hat{f}_m \hat{g}_n \right) \right] e^{\mathrm{i}kx} \ . \qquad (A.10)$$
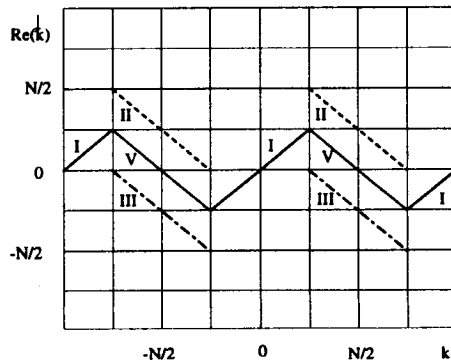
FIGURE 5. Sketch of the dispersion for non-split and split formulation.
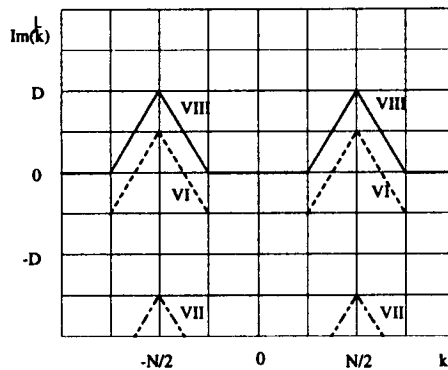
FIGURE 6. Sketch of the dissipation for non-split and split formulation.

The factors in the above Fourier sums have character of modified wavenumbers and represent the wave properties (dispersion and dissipation) of the particular Fourier mode. We now inspect particular factors. Considering the first terms on the left-hand sides first, we see that the split formulation generates the spurious wave (II,VI) while the non-split formulation generates (V,VIII). From the dispersion shown in Fig. 5 it is evident that II and V contribute by aliasing to the resolved spectrum. The spurious waves (II,VI) from the split formulation however, are partially amplified (negative dissipation) while the spurious waves from the non-split formulation are damped. From the second terms on the right-hand side we see that the split formulation generates another pair of spurious waves which contribute to the resolved spectrum by aliasing which is also amplified (III,VII). We conclude that the non-split formulation for an upwind scheme can exhibit spurious waves which are amplified contrary to the non-split form. This is due to the fact that the modified wavenumber for dissipative schemes is complex.

Fast multipole methods for three-dimensional N-body problems

By P. Koumoutsakos

1. Motivation and objectives

We are developing computational tools for the simulations of three-dimensional flows past bodies undergoing arbitrary motions. High resolution viscous vortex methods have been developed that allow for extended simulations of two-dimensional configurations such as vortex generators. Our objective is to extend this methodology to three dimensions and develop a robust computational scheme for the simulation of such flows.

A fundamental issue in the use of vortex methods is the ability of employing efficiently large numbers of computational elements to resolve the large range of scales that exist in complex flows. The traditional cost of the method scales as $\mathcal{O}(N^2)$ as the N computational elements/particles induce velocities at each other, making the method unacceptable for simulations involving more than a few tens of thousands of particles. In the last decade fast methods have been developed that have operation counts of $\mathcal{O}(N\log N)$ (Barnes and Hut, 1986) or $\mathcal{O}(N)$ (Greengard and Rohklin, 1987) (referred to as BH and GR respectively) depending on the details of the algorithm. These methods are based on the observation that the effect of a cluster of particles at a certain distance may be approximated by a finite series expansion. In order to exploit this observation we need to decompose the element population spatially into clusters of particles and build a hierarchy of clusters (a tree data structure) - smaller neighboring clusters combine to form a cluster of the next size up in the hierarchy and so on. This hierarchy of clusters allows one to determine efficiently when the approximation is valid. This algorithm is an N-body solver that appears in many fields of engineering and science. Some examples of its diverse use are in astrophysics (Salmon and Warren 1992), molecular dynamics (Ding, Karasawa and Goddard 1992), micromagnetics (Yuan and Bertram 1992), boundary element simulations of electromagnetic problems (Kuster 1993), Nabors, Kim and White 1992), computer animation (Kuhn and Muller 1993), etc. More recently these N-body solvers have been implemented and applied in simulations involving vortex methods. Koumoutsakos and Leonard (1995) implemented the GR scheme in two dimensions for vector computer architectures allowing for simulations of bluff body flows using millions of particles. Winckelmans *et al.* (1995) presented three-dimensional, viscous simulations of interacting vortex rings, using vortons and an implementation of a BH scheme for parallel computer architectures. Bhatt *et al.* (1995) presented a vortex filament method to perform inviscid vortex ring interactions, with an alternative implementation of a BH scheme for a Connection Machine parallel computer architecture.

Historically the method of BH was first implemented for large scale astrophysical simulations. Several N-body algorithms are extensions of tree codes originally

developed for gravitational interactions. This has been motivated not only by the ease of implementation to a variety of applications, but also by the fact that in three dimensions the scheme of GR suffers from the large computational cost of $\mathcal{O}(\mathrm{p}^4)$ associated with the translation of a p-th order multipole expansion. This cost has prohibited the use of large numbers of terms in the multipole expansions and lead to the general adoption of the BH method for N-body solvers. In a related effort to simplify the multipole expansion schemes, Anderson (1992) presented a computational scheme based on the Poisson Integral formula (hereafter referred to as PI). Greengard (1988) presented a strategy to reformulate the translation of the expansions as a convolution operators, thus enabling the use of FFT's and the reduction of the computational cost to $\mathcal{O}(\mathrm{p}^2)$ operations. This strategy has been concisely summarized and extended in the work of Epton and Dembart (1995). Having overcome the $\mathcal{O}(\mathrm{p}^4)$ difficulty, we believe that it is beneficial to follow the GR strategy as by using large number of expansions we avoid the costly pairwise interactions. The pairwise interactions determine the cost of the algorithm, and we try to minimize their number by using large numbers of expansions. Note that a large number of pairwise interactions may lead to algorithms of say $\mathcal{O}(\mathrm{N}^{1.1})$ that would be inefficient for simulations involving hundreds of millions of particles (Bhatt *et al.*, 1995). The efficiency of the approach of using large numbers of terms in the expansions has been shown by our implementation of the method in two dimensions (Koumoutsakos 1996).

The objective of this report is to present a summary of the GR multipole expansion scheme with efficient $\mathcal{O}(\mathrm{p}^2)$ multipole translations for general N-body problems. We discuss and compare the efficiency of computing the expansions based on the GR and the PI formulations. We document also the implementation of a suitable tree data structure for vector computer architectures by extending our previous work on the two-dimensional algorithm to strategies for a three-dimensional algorithm.

2. Accomplishments

We present a summary of the multipole expansions technique as presented by Greengard and Rohklin (1987) and Anderson (1992). We conduct some preliminary computations to assess the accuracy and efficiency of the two techniques and describe the fast multipole translation theory following Epton and Dembart (1995). Finally we describe our tree data structure and its implementation so as to take advantage of vector computer architectures.

2.1 The Greengard-Rohklin formulation

In order to introduce the subject of multipole expansions, we consider a unit source at a point $\mathrm{Q}(\vec{x}')$ (Fig. 1). This unit source induces a potential at point $\mathrm{P}(\vec{x})$ given by:

$$\Psi(\mathrm{P};\mathrm{Q}) = \Psi(\vec{x};\vec{x}') = \frac{1}{\mid \vec{x} - \vec{x}' \mid} \tag{1}$$

where the spherical coordinates of $\vec{x}$ and $\vec{x}'$ are given by (r, θ, ϕ) and (ρ, α, β) respectively. The distance between the two points is denoted by R and the angle
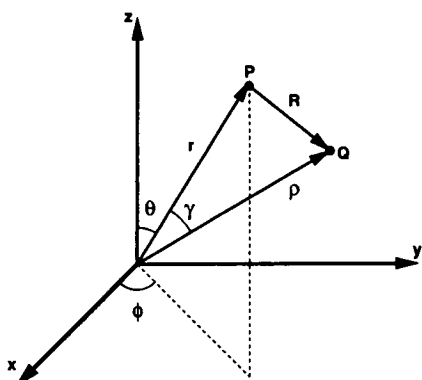
FIGURE 1. Coordinate definition for multipole expansion.

between vectors $\vec{x}$ and $\vec{x}'$ is denoted γ. If we define $\mu = \rho/r$ and $u = \cos\gamma$ then the potential at point Q may be expressed as:

$$\Psi(P;Q) = \frac{1}{R} = \frac{1}{r\sqrt{1 - 2u\mu + \mu^2}} \tag{2}$$

For $\mu = \rho/r < 1$, we use the generating formula for Legendre polynomials P_n so that the potential is expressed as:

$$\Psi(P;Q) = \sum_{n=0}^{\infty} \frac{\rho^n}{r^{n+1}} P_n(u) \tag{3}$$

This equation describes the *far field* potential at a point P, due to a charge of unit strength centered at Q. To obtain a computationally tractable formulation we proceed to express the Legendre functions in terms of *spherical harmonics*:

$$P_n(\cos\gamma) = \sum_{m=-n}^{n} Y_n^{-m}(\alpha, \beta) \, Y_n^m(\theta, \varphi) \tag{4}$$

and the *spherical harmonics* in terms of the *associated Legendre polynomials*:

$$Y_n^m(\theta, \varphi) = \sqrt{\frac{(n - |m|)!}{(n + |m|)!}} P_n^{|m|} \cos(\theta) \, e^{im\varphi} \tag{5}$$

The following numerically stable formulas are used for calculations:

$$(n - m)P_n^m(u) = (2n - 1) \, u \, P_{n-1}^m(u) - (n + m - 1) \, P_{n-2}^m(u) \tag{6}$$

and

$$P_m^m(u) = (-1)^m (2m - 1)!(1 - u^2)^{\frac{m}{2}} \tag{7}$$

and

$$P_m^m(u) = (-1)^m (2m - 1)!(1 - u^2)^{\frac{m}{2}} \tag{7}$$

Summarizing then we see that the *far field representation* of the potential induced by a collection of N_v sources centered around Q with coordinates $(\rho_i, \alpha_i, \beta_i)$ is expressed as:

$$\Psi(P; \{q_i\}) = \sum_{n=0}^{\infty} \sum_{m=-n}^{n} \frac{M_n^m}{r^{n+1}} Y_n^m(\theta, \varphi) \tag{8}$$

where:

$$M_n^m = \sum_{i=1}^{N_v} q_i \, \rho_i^n \, Y_n^{-m}(\alpha_i, \beta_i) \tag{9}$$

Note that if we wish to form a *local expansion* of the field around the origin then we express $1/R$ as:

$$\frac{1}{R} = \frac{1}{\rho \sqrt{1 - 2\frac{r}{\rho}u + (\frac{r}{\rho})^2}}$$
$$= \sum_{n=0}^{\infty} \frac{r^n}{\rho^{n+1}} P_n(u) \tag{10}$$

2.2 Translation of multipole expansions

Once the multipole expansions due to a collection of sources have been computed, one is usually interested in computing the far-field coefficients of the same collection expanded about some other point, say S, so that the potential would be represented as:

$$\Psi(S; P) = \sum_{n=0}^{\infty} \sum_{m=-n}^{n} \frac{L_n^m}{\sigma^{n+1}} Y_n^m(\Theta, \Phi) \tag{11}$$

where (σ, Θ, Φ) are the spherical coordinates of the distance between points P and S.

This defines the translation problem for multipole expansions for fast multipole methods. Following Greengard (1988) and Epton and Dembart (1994) we present a concise summary of the theory underlying the translation of multipole expansions. We make use of the following definitions of harmonic outer functions O_n^m and inner functions I_n^m:

$$O_n^m(\vec{x}) = O_n^m(r, \theta, \varphi) = \frac{(-1)^n i^{|m|}}{A_n^m} \frac{Y_n^m(\theta, \varphi)}{r^{n+1}} \tag{12}$$

$$I_n^m(\vec{x}) = I_n^m(r, \theta, \varphi) = i^{-|m|} A_n^m r^n Y_n^m(\theta, \varphi) \tag{13}$$

More specifically for $|\vec{x}| > |\vec{x'}|$ we obtain:

$$O_n^m(\vec{x} - \vec{x'}) = \sum_{n'=0}^{\infty} \sum_{m'=-n'}^{n'} (-1)^{n'} I_{n'}^{-m'}(\vec{x'}) \, O_{n+n'}^{m+m'}(\vec{x}) \tag{14}$$
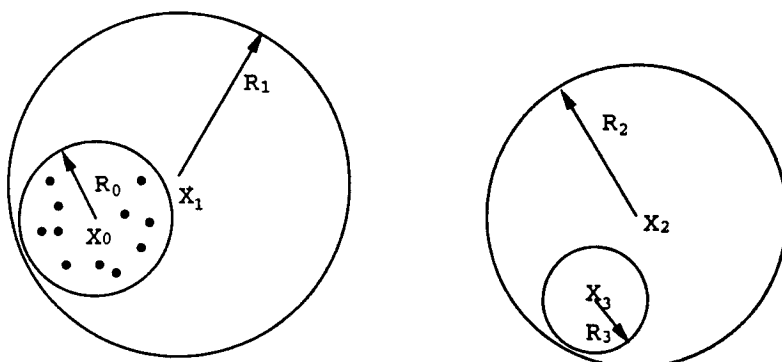
FIGURE 2. Sketch for the translation of the multipole expansions.

and for the inner expansions we get that:

$$I_n^m(\vec{x} - \vec{x'}) = \sum_{n'=0}^{\infty} \sum_{m'=-n'}^{n'} (-1)^{n'} \, I_{n'}^{m'}(\vec{x'}) \, I_{n-n'}^{m-m'}(\vec{x}) \tag{15}$$

so now we may express the equation for the potential induced at point $\vec{x}$ from a unit source at point $\vec{x'}$ as:

$$\frac{1}{|\vec{x} - \vec{x'}|} = O_o^o(\vec{x} - \vec{x'})$$

In order to further exhibit the formulation of these translation operators we consider the configuration shown in Fig. 2. We wish to determine the potential induced by a collection of sources within a sphere centered at $\vec{x_0}$ and having radius R_0 (denoted as $s(\vec{x_0}, R_0)$) to a collection of points/sources within a sphere $s(\vec{x_3}, R_3)$. This is achieved in the following steps:

(i)We compute a set of multipole expansion coefficients C_n^m (using Eq. 8) for the *far-field representation* of a set of sources distributed within $s(\vec{x_0}, R_0)$ Then the *far field* representation of the field induced by this cluster of particles at a location $\vec{x}$ is given by:

$$\Psi(\vec{x}) = \sum_{n=0}^{\infty} \sum_{m=-n}^{n} C_n^m \, O_n^{-m}(\vec{x} - \vec{x_0}) \tag{16}$$

(ii) We translate the *Outer* expansion about $\vec{x_0}$ to an *Outer* expansion about $\vec{x_1}$ (*child to parent*):

$$\psi(\vec{x}) = \sum_{l=0}^{\infty} \sum_{j=-l}^{l} D_l^j \, O_l^{-j}(\vec{x} - \vec{x_1}) \tag{17}$$

where

$$D_l^j = \sum_{n=0}^{l} \sum_{m=-n}^{n} C_n^m \, I_{l-n}^{j-m}(\vec{x_1} - \vec{x_0}) \tag{18}$$

(iii) We translate the *Outer* expansion about $\vec{x_1}$ to an *Inner* expansion about $\vec{x_2}$ (*box - box* interaction):

$$\psi(\vec{x}) = \sum_{l=0}^{\infty} \sum_{j=-l}^{l} E_l^j \ I_l^j(\vec{x} - \vec{x_2}) \qquad (19)$$

where

$$E_l^j = \sum_{n=0}^{l} \sum_{m=-n}^{n} D_n^m \ O_{l+n}^{-j-m}(\vec{x_2} - \vec{x_1}) \qquad (20)$$

(iv) We translate the *Inner* expansion about $\vec{x_2}$ to an *Inner* expansion about $\vec{x_3}$ (*parent to child*):

$$\psi(\vec{x}) = \sum_{l=0}^{\infty} \sum_{j=-l}^{l} F_l^j \ I_l^j(\vec{x} - \vec{x_3}) \qquad (21)$$

where

$$F_l^j = \sum_{n=0}^{l} \sum_{m=-n}^{n} E_n^m \ I_{n-l}^{m-j}(\vec{x_3} - \vec{x_2}) \qquad (22)$$

(v) Once the coefficients of the multipole expansions have been computed in the sphere $s(\vec{x_3}, R_3)$ we perform a *local expansion* using Eq. 10 to compute the potential at the individual points.

The above representations for the translation operations of spherical harmonics reveal that they require the evaluation of double summations that are essentially **convolution** operations over the coefficients of the expansions and can essentially be computed using 2-D FFT's.

2.3 The Poisson integral method

In order to approximate the potential due to a collection of particles Anderson (1992) proposed an alternative simplified technique. This technique is based on the observation that a harmonic function (Ψ) external to a sphere of radius R may be described using its boundary values $g(R\vec{s})$ on the surface of the sphere. So given a point $\vec{x}$ and $\vec{x_p}$ a point on the *unit* sphere that points in the direction of $\vec{x}$ then:

$$\Psi(\vec{x}) = \frac{1}{4\pi} \int_{S^2} \left[\sum_{n=0}^{\infty} (2n+1)(\frac{R}{r})^{n+1} P_n(\vec{s} \cdot \vec{x_p}) \right] g(R\vec{s}) \ ds \qquad (23)$$

where S^2 denotes the surface of the unit sphere and P_n is the n-th order Legendre polynomial. We use a quadrature formula to integrate the function on the surface of the sphere with K integration points $\vec{s_i}$ and weights w_i to obtain an approximation of the form:

$$\Psi(\vec{x}) \approx \frac{1}{4\pi} \sum_{i=1}^{K} \left[\sum_{n=0}^{M} (2n+1)(\frac{R}{r})^{n+1} P_n(\vec{s_i} \cdot \vec{x_p}) \right] g(R\vec{s_i}) \ w_i \qquad (24)$$
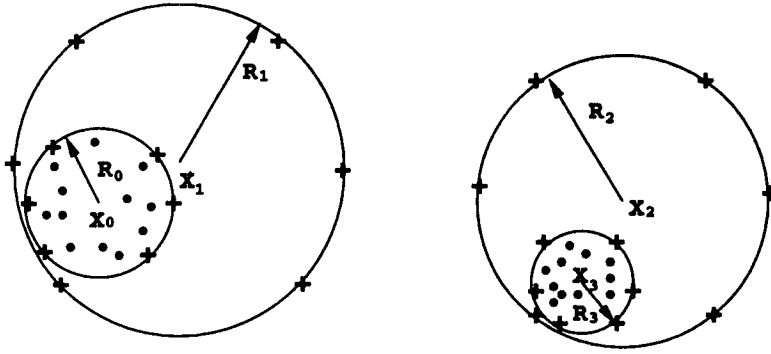
FIGURE 3.   Sketch for the translation of the multipole expansions using the PI technique.

In order to compute the far field multipole expansion of a cluster of particles based on this formulation, the function $g(R\vec{s})$ is determined on certain quadrature points on the surface of a sphere using the direct interactions of the potential induced by the sources onto the evaluation points. Subsequently these coefficients are used in Eq. 24 to compute the potential induced at distances sufficiently large compared to the radius of the cluster. In order to translate the expansions the above formula may be used again by considering the coefficients of $g(R\vec{s_i})$ on the inner sphere to be sources themselves. The method is completed by observing that a local expansion approximation may be constructed using the following formula. Note that the expansions are in terms of r/R in this formula.

$$\Psi(\vec{x}) \approx \frac{1}{4\pi} \sum_{i=1}^{K} \left[\sum_{n=0}^{M} (2n+1)(\frac{r}{R})^n P_n(\vec{s_i} \cdot \vec{x_p}) \right] g(R\vec{s_i}) \, w_i \qquad (25)$$

Anderson (1992) showed that approximations with $M = 2p + 1$ terms may be compared with multipole schemes that have p terms retained in the expansions. The strength of this method relies on its simplicity and its easy extension from two to three dimensions. This is exhibited by considering the implementation of this technique in the context of an $\mathcal{O}(N)$ algorithm for the computation of the potential field induced by a set of particles within a sphere $s(\vec{x_0}, R_0)$ to a cluster of points in $s(\vec{x_0}, R_0)$ (Fig. 4). This interaction is performed in the following steps:

   (i) The potential induced by the particles (denoted by dots) is computed on quadrature points properly selected on the surface of the enclosing sphere (denoted by +), thus constructing the function $g(R_0\vec{s_i})$

   (ii) The potential induced by the quadrature points on $s(\vec{x_0}, R_0)$ is computed on the quadrature points of $s(\vec{x_1}, R_1)$ using Eq. 24.

   (iii) The coefficients $g(R_1\vec{s_i})$ are considered to be sources themselves so that the coefficients $g(R_2\vec{s_i})$ are computed using Eq. 24.

   (iv) The coefficients $g(R_3\vec{s_i})$ are computed subsequently by performing a *local expansion* from the quadrature points on sphere $s(\vec{x_2}, R_2)$ to the quadrature points on the sphere $s(\vec{x_2}, R_2)$ using Eq. 25.
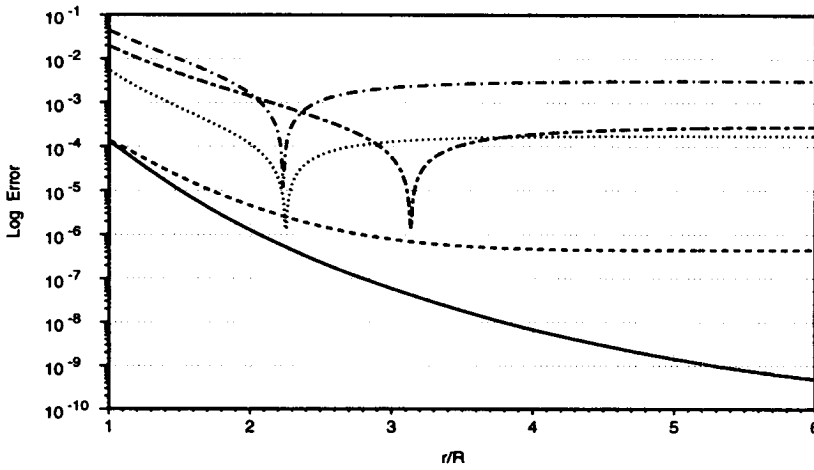
FIGURE 4. Relative error of the GR and PI multipole expansion schemes. Symbols: (GR):———— : $P = 8$; (PI): - - - - : $m = 14$, ········ : $m = 9$, —·—· $m = 7$, —·— : $m = 5$.

(v) By using Eq. 25 the potential on the particles inside the sphere $s(\vec{x_3}, R_3)$ is computed using the coefficients $g(R_3 \vec{s_i})$.

The simplicity of the formulas implemented in this technique make it an attractive alternative to the multipole expansion method of GR. We consider below a comparison of the two methods in terms of their accuracy and computational cost.

2.4 Computational cost

The computational cost, associated with the multipole expansions of the GR scheme, scales as $\mathcal{O}(p^2 N)$ for the multipole- particle operations and as $\mathcal{O}(\log N \, p^2)$ for the multipole translation operations using the convolution formulation discussed above. For the Poisson Integral formulation, assuming K integration points and M terms in the Poisson kernel, the cost scales as $\mathcal{O}(K \times M \times N)$ for the particle-multipole interactions and as $\mathcal{O}(K \times K \times M)$ for the multipole translation.

Both algorithms have error terms that scale as $(R/r)^{L+1}$ where L corresponds to p terms in the multipole method and to $M + 1$ for the Poisson Integral scheme. The number of the required integration points (K) corresponding to 5th, 7th, 9th, and 14th order quadrature formulas require 12, 24, 32, and 72 points respectively or approximately $K \approx 2 m^2/5$ points for an m-th order integration formula. So in order to achieve the same accuracy with the PI method as with the multipole scheme we require that $m \approx M \approx P$. This then implies a computational cost of $\mathcal{O}(p^3 N)$ for the particle-multipole interactions while it implies a $\mathcal{O}(\log N \, p^5)$ cost associated with the multipole translations.

Although such estimates depend on the particular implementation of the method, it is evident that for the same order of accuracy the multipole method with fast translation operations would lead to much faster computations, especially for large

expansion orders. Moreover, in the particular implementation of the methods it was easier to unroll the computational loops involving the particle multipole interactions for the GR scheme than the respective operations in the PI scheme. In Fig. 4 we present also the relative error as computed by the two methods using P = 8 and different values of m in the Poisson Integral method.

In the following table we present some representative timing results for the construction of the multipole expansions as well as for the particle-multipole interactions. A number of N particles was distributed randomly inside a cube of side 2 and the potential was evaluated on L points uniformly distributed along a line extending from the center of the cube and along one of its sides. The first line corresponds to the CPU time required for the construction of the multipol e expansions while the second line corresponds to the CPU time required to perform the particle-multipole expansions. It is observed then that using the GR multipole expansion scheme an order of magnitude faster calculations are achieved for the same order of accuracy. This dictates the use of the GR technique for computations using multipole expansions.

2.5 Tree data structures

A key issue in the implementation of fast multipole methods is the associated data structure and the computer platform. The present methodology has been successfully implemented for vector computer architectures and several of its feat ures could be carried over to parallel platforms involving large numbers of vector processors. The scheme of GR relies in a predetermined tree data structure and a large number of terms to be kept in the expansions while the scheme of BH determines the interaction list while traversing the tree data structure, and a tradeoff is made between the number of terms kept in the expansions (usually two to four) and the distance at which the expansions are favored over direct interactions.

In order to exploit the observation that the effect of a cluster of particles at a certain distance may be approximated by a finite sum of series expansions using the equations described above, we need to organize the particles in a hierarchy of clusters. This hierarchy of clusters allows one to efficiently determine when the approximation is valid. In order to establish the particle clusters one may resort to a tree building algorithm.

The straightforward method of computing the pairwise interaction of all particles requires $\mathcal{O}(N^2)$ operations for N vortex elements. In the last decade fast methods have been developed that have operation counts of $\mathcal{O}(N\log N)$ (Barnes and Hut, 1986) or $\mathcal{O}(N)$ (Greengard and Rohklin, 1987) depending on the details of the algorithm. The basic idea of these methods is to decompose the element population spatially into clusters of particles and build a hierarchy of clusters or a tree - smaller neighboring clusters combine to form a cluster of the next size up in the hierarchy and so on.

The contribution of a cluster of particles to the potential of a given vortex can then be computed to desired accuracy if the particle is sufficiently far from the cluster in proportion to the size of the cluster and a sufficiently large number of terms in the multipole expansion is taken. This is the essence of the 'particle-box'

N	L	m = 5	m = 7	m = 9	m = 14	Multipoles P = 8
10^5	10^5	0.0708	0.1397	0.1863	0.4191	0.1023
		0.5268	0.5844	0.6395	1.0870	0.0959
10^6	10^6	0.7111	1.4219	1.8968	4.2680	1.0251
		5.2724	5.8516	6.4145	10.8925	0.9585

FIGURE 5.   Computational cost of the FMM and Poisson integral method.

method, requiring $\mathcal{O}(N\log N)$ operations. One then tries to minimize the work required by maximizing the size of the cluster used while keeping the number of terms in the expansion within a reasonable limit and maintaining a certain degree of accuracy.

The 'box-box' scheme goes one step further as it accounts for box-box interactions as well. These interactions are in the form of shifting the expansions of a certain cluster with the desired accuracy to the center of another cluster. Then those expansions are used to determine the velocities of the particles in the second cluster. This has as an effect the minimization of the tree traversals for the individual particles requiring only $\mathcal{O}(N)$ operations.

In order to construct the tree data structure, the three-dimensional space is considered to be a cube enclosing all computational elements. We apply the operation of continuously subdividing a cube into eight identical cubes until each cube has only a certain maximum number of particles in it or the maximum allowable level of subdivisions has been reached.

The hierarchy of boxes defines a tree data structure which is common for both algorithms. The tree construction proceeds level by level starting at the finest level of the particles and proceeding upwards to coarser box levels. Due to the simplicity of the geometry of the computational domain, the addressing of the elements of the data structure is facilitated significantly. As the construction proceeds pointers are assigned to the boxes so that there is direct addressing of the first and last particle index in them as well as direct access to their children and parents. This facilitates the computation of the expansion coefficients of the children from the expansions of the parents for the *BB* algorithm and the expansions of the parents from those of the children for the *PB*

The data structure is used to determine when the expansions are to be used and when pairwise interactions have to be calculated. It helps in communicating to the computer the geometric distribution of the particles in the computational domain. The particles reside at the finest level of the structure. Clusters of particles form the interior nodes of the tree and hierarchical relations are established. The data

structure adds to the otherwise minimal memory requirements of the vortex method.

The tree has to be reconstructed at every step as the particles change positions in the domain. There are several ways that nearby particles could be clustered together and some of the decisions to be made are:

The center of expansions. In the present study the geometric center of the cells is used as it facilitates the addressing of the data structure.

The cluster size. In the present algorithms we follow a hybrid strategy as we keep at least L_{min} particles per box until we reach a predetermined finest level of boxes. The number L_{min} may be chosen by the user depending on the particle population and configuration so as to achieve an optimal computational cost.

Addressing the clusters. As particles are usually associated with a certain box, it is efficient to sort the particle locations in the memory so that *particles that belong to the same box occupy adjacent locations in the memory devoted to the particle arrays.* Such memory allocation enhances the vectorization significantly as very often we loop over particles of the same box (e.g., to construct the expansions at the finest level, or to compute interactions) and the loops have an optimum stride of one.

Description of the Algorithms:

In both algorithms, described herein, we may distinguish three stages:

- Building the data structure (tree).
- Establishing the interaction lists (by non-recursively descending the tree).
- Pairwise interactions for all particles in the domain.

The building of the data structure is common for both algorithms, but they differ in the tree descent and the pairwise interactions. Care has been exercised at all stages to maximize vectorization. In our respective two-dimensional implementation, the building of the data structure consumes about $5 - 7\%$ of the time, the descent consumes another $5 - 10\%$ so that the largest amount is spent in computing the pairwise interactions.

2.6 The particle-box algorithm

Step 1. Building the data structure (tree)

Step 1a : For each of the cubes at each level that are not further subdivided, we compute the p-terms of the multipole expansions. These expansions are used to describe the influence of the particles at locations that are well separated from their cluster.

Step 1b : The expansions of all parent boxes are constructed by shifting the expansion coefficients of their children. The tree is traversed upwards in this stage. Rather than constructing the expansions of all the members of a family (that is traverse each branch until the root is reached) we *construct the expansions of all parent boxes at each level simultaneously.* This enables long loops over the parent boxes at each level. Care is taken so that the procedure is fully vectorized by taking advantage of the regularity of the data structure and the addressing of the boxes in the memory. Moreover, the regularity of the data structure allows us to precompute many coefficients that are necessary for the expansions. Straightforward implementation of these translations leads to computational cost of $\mathcal{O}(p^4)$. This has been

the major reason that most implementations of the algorithm have employed only up to p=3 terms in the multipole expansions. However, such an approach results in large numbers of particle-particle interactions and hence a large computational cost. We implement the technique proposed by Greengard (1988) (see above) to reduce the computational cost of this translation to $\mathcal{O}(p^2)$ operations, by observing that this translation amounts to a convolution, and employ FFT's.

Step 2. Establishing of interaction lists

In the present algorithm a **breadth-first** search is performed at each level to establish the interaction lists of each particle (cell). This search is facilitated by the regularity of the data structure and the identification arrays of the cells in the tree. At each level interaction lists are established for the particles (cells) by looping across the cells of a certain level.

Note that this depth-first search for interaction lists is further facilitated by the fact that every particle belongs to a childless box. It is easy then to observe that *all particles in the same box share the same interaction list, which is comprised of members of the tree that belong to coarser levels*. In this way the tree is traversed upwards for all particles in a childless box together and downwards separately for each particle. It is evident that this procedure is more efficient for uniformly clustered configurations of particles because there would be more particles that belong to childless boxes at the finest level.

Step 3. Computation of the interactions.

Once the interaction lists have been established, the velocities of the particles are computed by looping over the elements of the lists. For particles that have the same boxes in their interaction list, this is performed simultaneously so that memory referencing is minimized. Moreover by systematically traversing the tree, the particle-particle interactions are made symmetric so that the cost of this computation is halved. The *cost* of this step is $\mathcal{O}(Np^2)$.

2.7 The box-box algorithm.

This scheme is similar to the *PB* scheme except that here every node of the tree assumes the role of a particle. In other words, interactions are not limited to particle-particle and particle-box but interactions between boxes are considered as well. Those interactions are in the form of shifting the expansion coefficients of one box into another and the interaction lists are established with respect to the locations of every node of the tree.

The scheme distinguishes five categories of interacting elements of the tree with respect to a cell denoted by **c**.

• **List 1:** All childless boxes neighboring **c**.

• **List 2:** Children of colleagues (boxes of the same size) of **c**'s parents that are well separated from **c**. All such boxes belong to the same level with **c**.

• **List 3:** Descendants (not only children) of **c**'s colleagues , whose parents are adjacent to **c** but are not adjacent to **c** themselves. All such boxes belong to finer levels.

• **List 4:** All boxes such that box **c** belongs to *their* List 3. All such boxes are childless and belong to coarser levels.

•**List 5:** All boxes well separated from **c's** parents. Boxes in this category do not interact directly with the cell **c**.

If the cell **c** is childless it may have interacting pairs that belong to all four lists. However if it is a parent it is associated with boxes that belong to lists 2 and 4 as described above. These observations are directly applied in our algorithm and we may distinguish again the following 4 steps.

Step 1: Building the data structure.

This procedure is the same as for the *PB* scheme. This fact enables us to compare directly the two algorithms and assess their efficiency.

Step 2: Construction of interaction lists.

To establish the interaction lists we proceed again level by level, starting at the coarsest level. For each level we distinguish childless and parent boxes. In establishing lists 1 and 3 we need only loop over childless boxes whereas to establish lists 2 and 4 we loop over all cells that are active in a certain level.

Step 2a: Here we establish lists 1 and 3. We start at the level of the parents of box **c** and we proceed level by level examining again breadth first, until we reach the finest level of the structure (the particles). The elements of lists 1 are basically the particles and account for the particle-particle interactions. Care is exercised so that this computation is symmetric, and we need to traverse the tree *downwards only* thus minimizing the search cost. The elements of List 3 are the boxes and are accountable for the particle-box interactions in this scheme.

Step 2b: Here we establish interaction lists 2 and 4 for all boxes in the hierarchy. We start at the coarsest possible level and proceed downward until reaching the level of box **c** to establish the interaction lists. To do so for a certain box we start by examining boxes that are not well separated from their parents (otherwise they would have been dealt with at the coarser level). Subsequently the children of those boxes are examined to establish interaction lists.

Step 3: Computations of the interactions

In this scheme we consider three kinds of interactions: the box-box, particle-box, and particle-particle interactions. The latter two categories were discussed in the previous section. For the box-box interactions once the respective interaction lists have been established (with members of lists 2 and 4), we need to transfer those expansions down to the ones of the children and add them to the existing ones. This procedure is vectorized by looping over the number of boxes at each level. The use of pointers to access the children of each box enhances this vectorization. Note that an arbitrarily high number of expansions can be calculated efficiently by unrolling the loop over the number of expansions into the previously mentioned loop.

3. Conclusions and future work

We are in the process of developing a three-dimensional N-body problem solver with the objective of applying it to the solution of engineering problems involving boundary element methods. This solver would be mainly used for the implementation of vortex methods for three-dimensional simulations involving unsteady flows past complex moving configurations. Furthermore, of particular interest is the

application of the code to simulations of rarefied flows using molecular dynamics methods. The code is envisioned as a computational tool that would easily enable the transition between continuum flows and flows using molecular dynamics.

REFERENCES

ANDERSON, C. R. 1992 An Implementation of the fast multipole method without multipoles. *SIAM J. Sci. Stat. Comp.* **13**, 923-947.

BARNES, J. & HUT, P. 1986 A Hierarchical $\mathcal{O}$(NlogN) force-calculation algorithm Nature. *324.* **446-449.**

BHATT, S., LIU, P., FERNANDEZ, V. & ZABUSKY, N. 1995 Tree codes for vortex dynamics: Application of a programming framework. *Workshop on Solving Irregular Problems on Parallel Machines.* Santa Barbara, April 25-28.

DING, H-Q., KARASAWA, N. & GODDARD, W. A. III 1992 Atomic level simulations on a million particles: The cell multipole method for Coulomb and London nonbond interactions. *J. Chem. Phys.* **97**, 4309-4315.

EPTON, M. A. & DEMBART, B. 1995 Multipole Translation Theory for the Three-Dimensional Laplace and Helmholtz Equations. *SIAM J. Sci. Stat. Comp.* **16**, 865-897.

GREENGARD, L. 1988 On the efficient implementation of fast multipole algorithms. *Dept. of Computer Science Report 602.* Yale University.

GREENGARD, L. & ROHKLIN, V. 1987 Rapid Evaluation of Potential Fields in Three Dimensions. *Dept. of Computer Science Report 515.* Yale University.

KOUMOUTSAKOS, P. & LEONARD, A. 1995 High Resolution simulations of the flow past an impulsively started cylinder. *J. Fluid Mech.* **96**, 1-32.

KUHN, V., & MULLER, W. 1993 Advanced Object-oriented Methods and Concepts for Simulation of Multi-body Systems. *J. Visual. & Comp. Anim.* **4**, 95-111.

KUSTER, N. 1993 Multiple Multipole Method for Simulating EM Problems Involving Biological Bodies. *IEEE Trans. Biomed. Engr.* **40**, 611-620.

NABORS, K., KIM, S. & WHITE, J. 1992 Fast Capacitance Extraction of General Three-Dimensional Structures. *IEEE Trans. Microwave Theory and Tech.* **40**, 1496-1506.

SALMON, J. K. & WARREN, M 1994 Skeletons from the treecode closet. *J. Comp. Phys.* **111**, 136-155.

YUAN, S. & BERTRAM, N. 1992 Fast Algorithms for Micromagnetics. *IEEE Trans. Magnetics.* **28**, 2031-2036.

WINCKELMANS, G. S., SALMON, J. K., WARREN, M. S., LEONARD, A. & JODOIN, B. 1995 Application of fast parallel and sequential tree codes to computing three-dimensional flows with the vortex element and boundary elements method. *Proc. of 2nd International Workshop on Vortex Flows and Related Numerical Methods.* Montreal, August 20-24.

Some progress in large-eddy simulation using the 3-D vortex particle method

By G. S. Winckelmans

1. Summary of motivation, accomplishments, and future plans

This two-month visit at CTR was devoted to investigating possibilities in LES modeling in the context of the 3-D vortex particle method (=vortex element method, VEM) for unbounded flows. A dedicated code was developed for that purpose. Although $O(N^2)$ and thus slow, it offers the advantage that it can easily be modified to try out many ideas on problems involving up to $N \approx 10^4$ particles. Energy spectrums (which require $O(N^2)$ operations per wavenumber) are also computed. Progress was realized in the following areas: particle redistribution schemes, relaxation schemes to maintain the solenoidal condition on the particle vorticity field, simple LES models and their VEM extension, possible new avenues in LES. Model problems that involve strong interaction between vortex tubes were computed, together with diagnostics: total vorticity, linear and angular impulse, energy and energy spectrum, enstrophy. More work is needed, however, especially regarding relaxation schemes and further validation and development of LES models for VEM. Finally, what works well will eventually have to be incorporated into the fast parallel tree code.

2. The 3-D VEM method

We use the 3-D regularized vortex particle method (=vortex element method, VEM) as in Winckelmans & Leonard (1993). The particle representation of the vorticity field is then taken as

$$\tilde{\omega}_\sigma(\mathbf{x}, t) = \sum_s \frac{1}{\sigma^3} \zeta \left(\frac{\|\mathbf{x} - \mathbf{x}^s(t)\|}{\sigma} \right) \gamma^s(t) \tag{1}$$

with $\gamma^s(t) = \omega^s(t) \operatorname{vol}^s$ the particle strength, ζ the regularization function, and σ the core size. All particles have the same core size, and it remains constant in time. Particles usually have the same volume of fluid, vol, associated with them (e.g., vol $= h^3$ for particles initially on an $h \times h \times h$ lattice). Sometimes however, the discretization of an initial condition (such as a torus for discretizing a vortex ring) leads to particle volumes that are not quite identical, see e.g., Winckelmans & Leonard (1993). Since the flow is incompressible, the particle volume remains constant in time. We also define the singular (delta-function) particle representation of the vorticity field as

$$\tilde{\omega}(\mathbf{x}, t) = \sum_s \delta(\mathbf{x} - \mathbf{x}^s(t)) \gamma^s(t). \tag{2}$$

The velocity field, $\mathbf{u}_\sigma$, is computed from the particle representation of the vorticity field as the curl of the vector potential, $\tilde{\psi}_\sigma$, which solves $\nabla^2 \tilde{\psi}_\sigma = -\tilde{\omega}_\sigma$. Hence it is divergence-free.

Vortex elements are convected by the local velocity

$$\frac{d}{dt}\mathbf{x}^q(t) = \mathbf{u}_\sigma(\mathbf{x}^q(t), t) , \tag{3}$$

and their strength is subjected to 3-D stretching by the local velocity gradient. The general mixed scheme is obtained as (Winckelmans 1989, Winckelmans & Leonard 1988, 1989, 1993),

$$\frac{d}{dt}\gamma^q(t) = \left(\alpha \, \nabla\mathbf{u}_\sigma(\mathbf{x}^q(t), t) + (1 - \alpha) \, (\nabla\mathbf{u}_\sigma(\mathbf{x}^q(t), t))^T \right) \cdot \gamma^q(t) . \tag{4}$$

Three different cases are: $\alpha = 1$ for the classical scheme, $\alpha = 0$ for the transpose scheme, and $\alpha = 0.5$ for the symmetric scheme.

For the present version of the VEM code, Gaussian smoothing is used (Leonard 1985, Winckelmans 1989, Winckelmans & Leonard 1993):

$$\zeta(\rho) = \left(\frac{1}{2\pi} \right)^{3/2} e^{-\frac{\rho^2}{2}} , \tag{5a}$$

$$G(\rho) = \frac{1}{4\pi \, \rho} \operatorname{erf}\left(\frac{\rho}{\sqrt{2}} \right) , \tag{5b}$$

$$K(\rho) = \frac{1}{\rho^2} \left(G(\rho) - \zeta(\rho) \right) , \tag{5c}$$

$$F(\rho) = \frac{1}{\rho^2} \left(3K(\rho) - \zeta(\rho) \right) , \tag{5d}$$

with ζ the vorticity smoothing function, G the Green's function for the vector potential ($=$ streamfunction), K the Biot-Savart function for the velocity evaluation, F a function used in evaluating the velocity gradient, and $\rho = r/\sigma$ the dimensionless distance. This choice leads to a second order method, provided $0 < h/\sigma \leq 1$.

The error function $\operatorname{erf}(x)$ is computed using e^{-x^2} and Eq. 7.1.26 in Abramowitz and Stegun (1972). For small ρ, Taylor series expansions are used to evaluate G, K, and F. Notice that, in general, switching from $f = f_a$ if $x < x_0$ to $f = f_b$ if $x \geq x_0$ is programmed without an "if" statement by making use of a Heaviside function:

$$f = f_a + (f_b - f_a) \frac{1}{2}(1 + \operatorname{sign}(1, x - x_0)) . \tag{6}$$

With the particle strength exchange scheme for viscous diffusion (Mas-Gallic 1987, Degond & Mas-Gallic 1989), we have:

$$\frac{d}{dt}\gamma^q(t) = \cdots$$
$$+ \frac{2\nu}{\sigma^2} \sum_s (\operatorname{vol}^q \gamma^s(t) - \operatorname{vol}^s \gamma^q(t)) \frac{1}{\sigma^3} \eta\left(\frac{\|\mathbf{x}^s(t) - \mathbf{x}^q(t)\|}{\sigma} \right) , \tag{7}$$

where $\eta(\rho) = -\frac{1}{\rho}\frac{d}{d\rho}\zeta(\rho)$. Note that the Gaussian smoothing is the only one for which $\eta(\rho) = \zeta(\rho)$. (It is also the natural kernel for the diffusion equation (Winckelmans & Leonard 1993).) For non-uniform diffusion coefficients (such as in LES), the formulation simply becomes:

$$\frac{d}{dt}\gamma^q(t) = \cdots$$

$$+\frac{1}{\sigma^2}\sum_s \left(\nu(\mathbf{x}^s(t)) + \nu(\mathbf{x}^q(t))\right)\left(\text{vol}^q\,\gamma^s(t) - \text{vol}^s\,\gamma^q(t)\right)\frac{1}{\sigma^3}\eta\left(\frac{\|\mathbf{x}^s(t) - \mathbf{x}^q(t)\|}{\sigma}\right).$$

$$(8)$$

2.1 Particle redistribution schemes

One needs to maintain the condition that particle cores overlap. In some cases, this calls for a particle redistribution scheme. The high order Λ_2 scheme used by Koumoutsakos (1993) and Koumoutsakos & Leonard (1992, 1995) was adopted. It consists of replacing the whole set of vortex particles by a new set. The new particles are located on an $h \times h \times h$ lattice (hence all particles have vol $= h^3$). Consider first the normalized 1-D problem with unit spacing. Then, in the $\Lambda_2(x)$ scheme, an old particle located at $-\frac{1}{2} \le x \le \frac{1}{2}$ gives $-\frac{1}{2}x(1-x)$ of its strength to the new particle located at -1, $(1-x)(1+x)$ of its strength to the new particle located at 0, and $\frac{1}{2}x(1+x)$ to the new particle located at 1. This scheme is such that:

$$x^n = (-1)^n\left(-\frac{1}{2}x(1-x)\right) + (0)^n\left((1-x)(1+x)\right) + (1)^n\left(\frac{1}{2}x(1+x)\right) \quad (9)$$

for $n = 0, 1, 2$. In 3-D, one applies the scheme as $\Lambda_2(x)\,\Lambda_2(y)\,\Lambda_2(z)$. This scheme then conserves exactly total vorticity, $\boldsymbol{\Omega} = \int_V \omega\,d\mathbf{x} = \sum_s \gamma^s$, linear impulse, $\mathbf{I} = \frac{1}{2}\int_V \mathbf{x} \times \omega\,d\mathbf{x} = \frac{1}{2}\sum_s \mathbf{x}^s \times \gamma^s$, and angular impulse, $\mathbf{A} = \frac{1}{3}\int_V \mathbf{x} \times (\mathbf{x} \times \omega)\,d\mathbf{x} = \frac{1}{3}\sum_s \mathbf{x}^s \times (\mathbf{x}^s \times \gamma^s)$. It usually performs very well on energy conservation and well on enstrophy conservation.

Notice that a simpler scheme is the Λ_1 scheme: in that case, an old particle located at $-\frac{1}{2} \le x \le \frac{1}{2}$ gives $\frac{1}{2} - x$ of its strength to the new particle located at $-\frac{1}{2}$, and $\frac{1}{2} + x$ to the new particle located at $\frac{1}{2}$. This scheme is such that:

$$x^n = \left(-\frac{1}{2}\right)^n\left(\frac{1}{2} - x\right) + \left(\frac{1}{2}\right)^n\left(\frac{1}{2} + x\right) \quad (10)$$

for $n = 0, 1$. Again, in 3-D, one applies the scheme as $\Lambda_1(x)\,\Lambda_1(y)\,\Lambda_1(z)$. This scheme then conserves exactly total vorticity and linear impulse. It does not conserve angular impulse. It usually performs poorly on energy conservation and very poorly on enstrophy conservation. We do not recommend its use.

The Λ_2 scheme has been incorporated in the fast 3-D parallel tree code as well (Winckelmans *et al.* 1995). Particle redistribution is programmed using the tree code data structure. It runs very efficiently. Its cost is much less than the cost associated with the field evaluation.

2.2 Relaxation schemes for the particle vorticity field

The particle representation of the vorticity field, $\tilde{\omega}_\sigma$, does not constitute a generally divergence-free basis (Saffman & Meiron 1986, Winckelmans & Leonard 1988, 1993). Thus, although the initial particle discretization of a vorticity field can be made very near divergence-free, this condition does not necessarily remain satisfied in long time computations. A relaxation scheme can be applied, if and when necessary, which ensures that the particle field, $\tilde{\omega}_\sigma$, remains a good representation of the true divergence-free vorticity field, $\omega_\sigma = \nabla \times \mathbf{u}_\sigma$. Different approaches have been proposed (Winckelmans 1989, Pedrizzetti 1992, Winckelmans & Leonard 1993).

Notice first that, once computed, the velocity gradient tensor, $\nabla \mathbf{u}_\sigma$, contains all the necessary components to evaluate the true vorticity field at the particle locations. This vorticity field is then used in both relaxation schemes considered here. Notice also that $\omega_\sigma = \nabla \times \mathbf{u}_\sigma = \nabla \times (\nabla \times \tilde{\psi}_\sigma) = -\nabla^2 \tilde{\psi}_\sigma + \nabla(\nabla \cdot \tilde{\psi}_\sigma)$. Recalling that $\nabla^2 \tilde{\psi}_\sigma = -\tilde{\omega}_\sigma$, it follows that $\nabla(\nabla \cdot \tilde{\psi}_\sigma) = \omega_\sigma - \tilde{\omega}_\sigma$.

The P-relaxation scheme (Pedrizzetti 1992) was developed in the framework of singular vortex particles. It is modified to be used in the context of regularized vortex particles. At every time step, the particle strength vector is modified using the filtering:

$$\gamma_{\text{new}}^q = (1 - f\,\Delta t)\,\gamma^q + f\,\Delta t\, \frac{\omega_\sigma(\mathbf{x}^q)}{\|\omega_\sigma(\mathbf{x}^q)\|} \|\gamma^q\| \tag{11}$$

where $\omega_\sigma(\mathbf{x}^q)$ is the true local vorticity field and where f is a frequency factor. The time scale $1/f$ must be "tuned" with respect to the time scale(s) of the physical phenomena under study to give satisfactory results. This relaxation scheme basically acts as a "spring" that tries to maintain the particle strength vector aligned with the true vorticity vector. This simple scheme is such that: (1) It doesn't do anything to the particle strength vector if that vector is aligned with the vorticity vector; (2) It is a simple local operation on the particle strength vector. No system of linear equations involving neighbor particles needs to be solved.

The W-relaxation scheme (Winckelmans 1989, Winckelmans & Leonard 1993) is based on the functional representation of the vorticity field: one requires that, at particle locations, the particle vorticity field be equal to the true vorticity field:

$$\sum_s \frac{1}{\sigma^3} \zeta\left(\frac{\|\mathbf{x}^q - \mathbf{x}^s\|}{\sigma} \right) \gamma_{\text{new}}^s = \omega_\sigma(\mathbf{x}^q) \,. \tag{12}$$

This scheme is best applied after the particle redistribution scheme . The fact that the particles are then well-aligned on a regular lattice greatly favors the reconstruction of a smooth function from the particle strengths.

It is also best to use Gaussian smoothing as this smoothing permits a "good-quality" reconstruction of a smooth function from the particle strengths in the whole range of core overlapping: $0 < h/\sigma \leq 1.5$. With other smoothings, the window of acceptable h/σ is much narrower.

The W-scheme amounts to solving a system of linear equations involving only near neighbors. This is done using an iterative method such as Relaxed-Jacobi (in

the tree code) or Relaxed Gauss-Seidel. Notice that the matrix is not diagonally dominant. Actually, with Gaussian smoothing and particles on a regular lattice in d-dimension, the diagonal dominance is violated as soon as $\left(\left(\frac{1}{2\pi}\right)^{1/2}\frac{h}{\sigma}\right)^d \leq \frac{1}{2}$: In 1-D, this means $h/\sigma \leq 1.25$. In 2-D, $h/\sigma \leq 1.77$, and in 3-D, $h/\sigma \leq 1.99$. Thus: (1) The higher the dimension, the worse the non-diagonal dominance; (2) The smaller h/σ, the worse the non-diagonal dominance. Since we operate here in 3-D, and at $h/\sigma = 0.75 - 1.0$ or so (to satisfy the core overlapping condition), we definitely do not have diagonal dominance.

At this point, the efficient iterative solution of this system is still a subject of active research (A. Leonard, private communication). There appears to be an "operating window" of h/σ where, although not diagonally dominant, all eigenvalues of the matrix are still real and positive. In that case, iterative solvers (with or without preconditioning) can be developed. For instance, it is known that the Gauss-Seidel iteration converges for any symmetric, positive definite matrix (Golub and Van Loan 1983). The matrix here is symmetric. It is also positive-definite as long as all eigenvalues remain real and positive.

2.3 Time integration

For time integration, the $O\left((\Delta t)^2\right)$ Adams-Bashforth scheme (AB2) is used. Since this scheme is not self-starting, an $O\left((\Delta t)^2\right)$ Runge-Kutta scheme (RK2) is used for the first time step (after the initial condition or after each use of the particle redistribution scheme). This approach allows one to maintain second order accuracy. Numerical experiments have indeed shown that an $O\left(\Delta t\right)$ Euler scheme for the start-up step is simply not acceptable. The RK2 scheme is efficiently programmed as follows: Euler predictor, Trapezoidal-rule corrector.

3. Energy, enstrophy, and their spectrum

A formulation developed by Leonard (1976 unpublished, private communication) (see also Leonard 1985, Shariff *et al.* 1989), is used to compute the energy spectrum. Although developed in the context of vortex filament methods (for which the filament vorticity field is, by construction, equal to the true vorticity field), the formulation also applies to vortex particle methods as long as the particle vorticity field, $\tilde{\omega}_\sigma$, remains a good representation of the true vorticity field, ω_σ. If this condition is violated, then the evaluation of the energy and of its spectrum becomes very complex, see e.g., Winckelmans (1989), Winckelmans & Leonard (1993), Kiya (1993).

With Gaussian smoothing, the energy spectrum is finally obtained as

$$E(k) = e^{-\frac{(k\sigma)^2}{2}} \hat{E}(k) \quad \text{with} \quad \hat{E}(k) = \left(\frac{1}{2\pi}\right)^2 \sum_q \sum_s \frac{\sin\left(k\|\mathbf{x}^q - \mathbf{x}^s\|\right)}{k\|\mathbf{x}^q - \mathbf{x}^s\|} \gamma^q \cdot \gamma^s ,$$

(13)

and the total energy as (Winckelmans & Leonard 1993)

$$E = \int_0^\infty E(k)\,dk = \frac{1}{2} \sum_q \sum_s \frac{1}{4\pi\|\mathbf{x}^q - \mathbf{x}^s\|} \operatorname{erf}\left(\frac{\|\mathbf{x}^q - \mathbf{x}^s\|}{\sqrt{2}\,\sigma}\right) \gamma^q \cdot \gamma^s$$

$$= \frac{1}{2} \int_V \tilde{\psi}_\sigma \cdot \tilde{\omega} \, d\mathbf{x} = \frac{1}{2} \int_V \tilde{\psi}_{\frac{\sigma}{\sqrt{2}}} \cdot \tilde{\omega}_{\frac{\sigma}{\sqrt{2}}} \, d\mathbf{x} \ . \tag{14}$$

The enstrophy spectrum is $\mathcal{E}(k) = k^2 \, E(k)$ and the total enstrophy is (Winckelmans & Leonard 1993)

$$\mathcal{E} = \int_0^\infty k^2 \, E(k) \, dk = \frac{1}{2} \sum_q \sum_s \left(\frac{1}{2\pi}\right)^{3/2} \frac{1}{\sigma^3} \exp\left(-\frac{\|\mathbf{x}^q - \mathbf{x}^s\|^2}{2\,\sigma^2}\right) \gamma^q \cdot \gamma^s$$

$$= \frac{1}{2} \int_V \tilde{\omega}_\sigma \cdot \tilde{\omega} \, d\mathbf{x} = \frac{1}{2} \int_V \tilde{\omega}_{\frac{\sigma}{\sqrt{2}}} \cdot \tilde{\omega}_{\frac{\sigma}{\sqrt{2}}} \, d\mathbf{x} \ . \tag{15}$$

Notice that the cost associated with evaluating the energy spectrum is $O(N^2)$ for each k.

A special case is the vortex ring of circulation Γ and radius R (Leonard 1985). In that case we obtain for the energy spectrum of the infinitely thin vortex ring:

$$\hat{E}(k) = \left(\frac{1}{2\pi}\right)^2 2\pi \, (\Gamma R)^2 \int_{-\pi}^\pi \frac{\sin\left(2kR\left|\sin\frac{\phi}{2}\right|\right)}{2kR\left|\sin\frac{\phi}{2}\right|} \cos\phi \, d\phi$$

$$= \left(\frac{1}{2\pi}\right)^2 4\pi \, (\Gamma R)^2 \int_0^\pi \frac{\sin\left(2kR\sin\frac{\phi}{2}\right)}{2kR\sin\frac{\phi}{2}} \cos\phi \, d\phi$$

$$= \left(\frac{1}{2\pi}\right)^2 4\pi \, (\Gamma R)^2 \frac{1}{kR} \left[\int_0^1 \sin(2kR\mu) \frac{(1-\mu^2)^{1/2}}{\mu} d\mu\right.$$

$$\left. - \int_0^1 \sin(2kR\mu) \frac{\mu}{(1-\mu^2)^{1/2}} d\mu\right]$$

$$= \left(\frac{1}{2\pi}\right)^2 4\pi \, (\Gamma R)^2 \frac{\pi}{2} \left[\left(1 + \sum_{n=1}^\infty \frac{1}{(2n+1)} \frac{(-(kR)^2)^n}{(n+1)! \, n!}\right) - \frac{J_1(2kR)}{kR}\right]$$

$$= -(\Gamma R)^2 \sum_{n=1}^\infty \frac{n}{(2n+1)} \frac{(-(kR)^2)^n}{(n+1)! \, n!} \ . \tag{16}$$

This complements a result presented in Leonard (1985):

$$\hat{E}(k) = (\Gamma R)^2 \frac{1}{2} \int_1^1 J_1^2\left(kR\left(1-\mu^2\right)^{1/2}\right) d\mu \ . \tag{17}$$

The spectrum, computed using a particle discretization of the vortex ring, is presented in Fig. 1. For small kR, $\hat{E}(k) = \frac{(kR)^2}{6}$. For large kR, $\hat{E}(k)$ asymptotes to $\frac{(kR)^{-1}}{2}$ (Leonard 1985). The fact that $\hat{E} \sim (kR)^2$ for small kR is a consequence of the non-zero linear impulse associated with the vortex ring, e.g., see Phillips (1956).
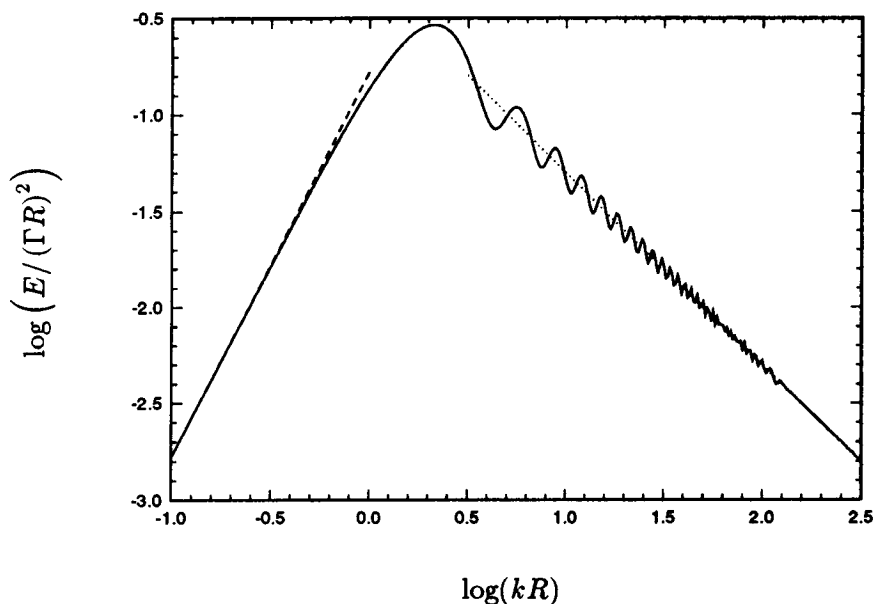
FIGURE 1. Energy spectrum of a singular vortex ring: ——— ; $(kR)^2/6$: – – – – ; $(kR)^{-1}/2$: ⋯⋯⋯ .

It is found numerically that for a given wavenumber, k, the spacing, h, between the particles used to discretize a ring only needs to satisfy $kh \leq 5$ or so in order for the discrete sum, Eq. (13), to correctly capture the exact integral, Eq. (16). This is very surprising (and not understood at this time) because the integrand varies quite a bit from one particle to the next (1 versus roughly $\frac{\sin(kh)}{kh}$).

For comparison with the single vortex ring, the spectrum of two opposite rings is shown in Fig. 2.

In that case, the linear impulse is zero and one finds that $\hat{E} \sim (kR)^4$. Actually, with sufficient symmetry, one can even create a system with $\hat{E} \sim (kR)^8$. This was obtained by considering six vortex rings on the surface of a cube, see Fig. 3. Finally, we find that all vortex loop configurations considered lead to a spectrum $\hat{E}(k) \sim k^{-1}$ for large k and that this appears to remain so when they evolve in time using VEM, inviscid or viscous (including LES), see Section 5.

4. LES and the possible extension to vortex methods

We consider turbulent flows away from solid boundaries. We also consider the general vorticity formulation (Winckelmans 1989, Winckelmans & Leonard 1993), together with an LES formulation which conserves the zero vorticity divergence (Mansour *et al.* 1978):

$$\frac{D}{Dt}\omega_i = \left(\alpha\frac{\partial u_i}{\partial x_j} + (1-\alpha)\frac{\partial u_j}{\partial x_i}\right)\omega_j + \frac{\partial}{\partial x_j}\left(\nu_{\text{turb}}\left(\frac{\partial \omega_i}{\partial x_j} - \frac{\partial \omega_j}{\partial x_i}\right)\right) \qquad (18)$$
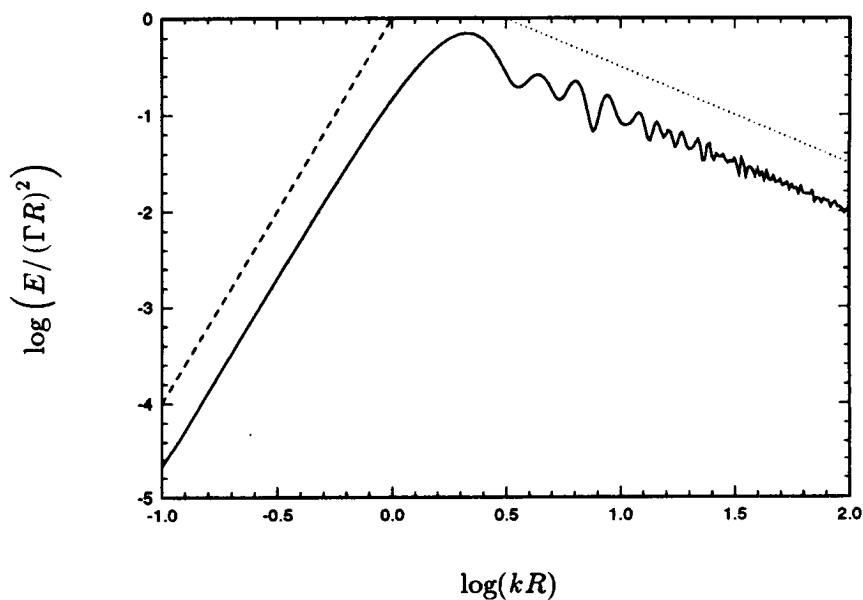
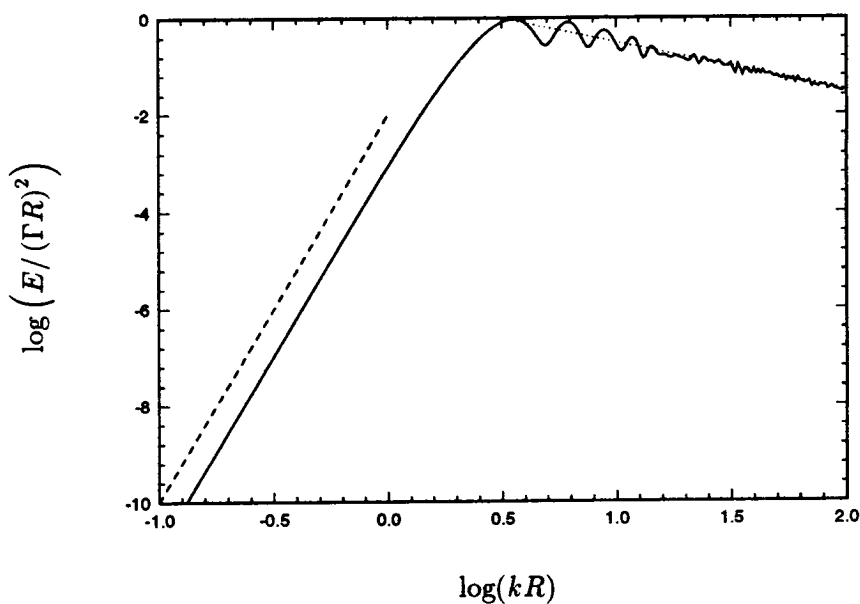FIGURE 2. Energy spectrum of two opposite singular vortex rings with spacing $S/R = 1.25$: ———— ; $(kR)^4$: – – – – ; $(kR)^{-1}$: ········ .

FIGURE 3. Energy spectrum of six singular vortex rings on the surface of a cube of size $S/R = 1.25$: ———— ; $(kR)^8$: – – – – ; $(kR)^{-1}$: ········ .

for any α. The symmetric case $\alpha = 1/2$ leads to $S_{ij}\omega_j$ for the 3-D stretching, with S_{ij} the rate-of-strain tensor.

In the basic LES Smagorinsky's model, the turbulence eddy-viscosity is taken as

$$\nu_{\text{turb}} = (C_s\, h)^2 \,(2\, S_{ij}S_{ij})^{1/2} \tag{19}$$

with $S_{ij}S_{ij} = S^2 \geq 0$. Typically, C_s lies in the range $0.1 - 0.24$ (Rogallo & Moin 1984, Lesieur *et al.* 1995). Consider the eigenvalues λ_1, λ_2, and λ_3 of the rate-of-strain tensor, with $\lambda_1 + \lambda_2 + \lambda_3 = S_{ii} = \nabla \cdot \mathbf{u} = 0$. The model then produces an eddy-viscosity

$$\nu_{\text{turb}} = (C_s\, h)^2 \,\left(2\left(\lambda_1^2 + \lambda_2^2 + \lambda_3^2\right)\right)^{1/2} \;. \tag{20}$$

We certainly agree with Lesieur *et al.* (1995) that "this simple eddy-viscosity hypothesis is extremely arbitrary, and substantial progress in LES might be achieved by relaxing this assumption". For the time being, however, a simple extension to particle methods of this eddy-viscosity LES model is considered. Since our σ-regularization of the vortex particle method is basically a Gaussian filter, it appears natural to replace the usual Eulerian grid filter h by the particle core size σ (Recall that $h/\sigma = O(1)$) and to take:

$$\nu_{\text{turb}} = (C_s\, \sigma)^2 \,(2\, S_{ij}S_{ij})^{1/2} \;. \tag{21}$$

Other simple ways of constructing an LES eddy-viscosity have been proposed, e.g., the model based on local enstrophy of Mansour *et al.* (1978):

$$\nu_{\text{turb}} = (C_v\, h)^2 \,(\omega_i\omega_i)^{\frac{1}{2}} \tag{22}$$

with $\omega_i\omega_i = \omega^2 \geq 0$ and $C_v \approx C_s$ ($C_v \approx 0.2$ in Mansour *et al.* 1978). If we recall the vector identity,

$$S^2 = \frac{1}{2}\omega^2 + \nabla \cdot (\nabla \cdot (\mathbf{u}\,\mathbf{u})) \tag{23}$$

together with the Euler equations,

$$\frac{\partial \mathbf{u}}{\partial t} + \nabla \cdot (\mathbf{u}\,\mathbf{u}) \approx -\nabla P \;, \tag{24}$$

it appears that, to first order, the two models differ by $\frac{1}{2}\omega^2 - S^2 \approx \nabla^2 P$. This is an interesting result as it could be used to explain the differences in the behavior of these two models depending on the pressure's Laplacian. Indeed, although $\frac{1}{2}\omega^2$ and S^2 are both positive-definite, their difference, $\nabla^2 P$, can have any sign.

A third model based on the relative rate of change of local enstrophy due to 3-D stretching of vortex lines,

$$\frac{1}{\omega_i\omega_i}\frac{D}{Dt}\left(\omega_i\omega_i\right) = 2\frac{\omega_i S_{ij}\omega_j}{\omega_i\omega_i} \;, \tag{25}$$

could also be constructed, e.g.,

$$\nu_{\text{turb}} = (C_w \, h)^2 \, 2 \frac{\omega_i S_{ij} \omega_j}{\omega_i \omega_i} \tag{26}$$

This model has the property that it "selects" the eigenvalues used to compute the eddy-viscosity according to the relative orientation between the vorticity vector, ω, and the principal axes (eigen vectors) of the rate-of-strain tensor. Indeed, writing the components of the vorticity vector in the system of principal axes as $(\omega_1, \omega_2, \omega_3)$, this model becomes

$$\nu_{\text{turb}} = (C_w \, h)^2 \, 2 \left(\frac{\lambda_1 \omega_1^2 + \lambda_2 \omega_2^2 + \lambda_3 \omega_3^2}{\omega_1^2 + \omega_2^2 + \omega_3^2} \right). \tag{27}$$

Hence a vorticity-weighted average of the eigenvalues is used to produce the eddy-viscosity. This model produces a negative eddy-viscosity in regions where enstrophy is decreasing (i.e., where vorticity is compressed). Since this is undesirable, one should use $|\omega_i S_{ij} \omega_j|$ (version 1) or $\max(0, \omega_i S_{ij} \omega_j)$ (version 2) instead of $\omega_i S_{ij} \omega_j$ (version 0).

In axisymmetric strain ($\lambda_1 = \lambda_2 = -\lambda/2$ and $\lambda_3 = \lambda$), the classical LES model gives $(C_s \, h)^2 \, \sqrt{3} \, |\lambda|$, regardless of the orientation of the vorticity vector. If vorticity is aligned with the direction of highest rate-of-strain, the "selective" model (version 1) gives $(C_w \, h)^2 \, 2 \, |\lambda|$. If vorticity is perpendicular to that direction, it gives $(C_w \, h)^2 \, |\lambda|$. Since $1 \leq \sqrt{3} \leq 2$, this result also suggests that using $C_w = C_s$ as a first "calibration" for the selective model is a fairly good choice.

In DNS of the Euler equations, the emergence of flat pancake-like structures ("potato chips") that shrink exponentially in time is also observed, e.g., Brachet *et al.* (1992). In that case, two eigenvalues become exponentially large, $\lambda_1 \approx \lambda \left(-\frac{1}{2} - e^{t/T} \right)$, $\lambda_3 \approx \lambda \left(-\frac{1}{2} + e^{t/T} \right)$, while the intermediate eigenvalue, $\lambda_2 \approx \lambda$, remains roughly constant. During this self-similar collapse, it is observed that the vorticity tends to remain aligned with the eigenvector corresponding to the intermediate eigenvalue. Instabilities similar to those leading to streamwise vortices in the context of free shear layers are expected to subsequently concentrate the vorticity and produce isolated vortex filaments. Modeling such flows with LES, a classical model would produce, during the collapse phase, an exponentially large eddy-viscosity (hence kill the collapse phase in its early stages by dissipating the energy rapidly) while the selective model would produce a fairly constant eddy-viscosity (hence dissipate the energy at the end of the collapse phase). Thus, the two models would behave quite differently.

Finally, mixed-schemes that are a judicious combination of the above models could also be considered. Whatever the choice, they would have to be validated somehow (e.g., using DNS data), including the determination of the "constants".

One interesting question is whether one of the simple models above (or a suitable mix of them) can produce better results than what is so far obtained with the classical Smagorinsky's model.

Note that the vortex method also has potential for the development of a dynamic LES model, in the same spirit as in Germano *et al.* (1991), Ghosal *et al.* (1992), Moin & Jiminez (1993), Ghosal & Moin (1994), Moin *et al.* (1994), Ghosal *et al.* (1995). For instance, one could compute the velocity fields and derivatives from the particle locations and strengths by using Gaussian smoothing at two levels: e.g., a filter of width σ and a filter of width 2σ. This information could then be used to "compute" C_s in a way similar to what is done so far with dynamic LES in grid methods. One must recall, however, that the vortex method with Gaussian smoothing is a second-order method. If dynamic LES requires higher order methods (as it may . . . , Ghosal, private communication), it might not be feasible in the context of VEM.

5. Fast and slow VEM codes

A fast parallel oct-tree code, originally developed for three-dimensional N-body gravitational problems (Salmon 1990, Salmon & Warren 1994, Warren & Salmon 1995) has been modified into a fast N-vortex code for vortex flow computations using the vortex particle method combined with the particle strength exchange scheme for viscous diffusion, with the Λ_2 particle redistribution scheme, and with both P- and W-relaxation schemes (Salmon, Warren & Winckelmans 1994, Winckelmans *et al.* 1995a,b,c,d).

Gravitation, VEM, etc. are all $O(N^2)$ in complexity: for each of the N elements, find the derivatives of the field induced by all N elements. This is the expensive part of the computation. The other tasks (particle strength exchange scheme, particle redistribution, etc.) are all fairly local operations and are not computationally expensive. The use of fast tree codes in 2-D and 3-D reduces the computing cost associated with all evaluations from $O(N^2)$ to something much more tractable: $O(N \log N)$, or $O(N^{1+\epsilon})$ with $\epsilon << 1$, or even $O(N)$, depending on the complexity of the implementation. The "big-O" notation can, however, be misleading for practical values of N and desired level of accuracy. In our implementations of the VEM, multipole expansions of order $p = 2$ are used (i.e., monopole + dipole + quadrupole). Particular attention is given to ensuring that the error introduced by the use of multipole expansion approximations remains below a desired level for all evaluations. A run-time parameter, ϵ_{tol}, determines the maximum allowed error bound for any particular multipole evaluation.

The tree code is written entirely in ANSI C and has been ported to several parallel and sequential platforms. Problems with $N = O(10^4 - 10^6)$ and beyond are computed on parallel supercomputers. Problems with $N = O(10^3 - 10^5)$ are also computed on the "degenerate" parallel case of single processor workstations.

For the present two-month "exploratory" work at CTR, it was decided to stick with a slow $O(N^2)$ VEM code. (Actually, an all-new VEM code was written for that purpose.) Recall that computing an energy spectrum is also an $O(N^2)$ operation for each wavenumber k anyway. Although this $O(N^2)$ code sets a limit of $N \approx 10^4$ on the number of particles (even on a CRAY C90), it provides for an easy and convenient way of experimenting with many ideas: different LES models, different particle redistribution schemes, different relaxation schemes, etc.

6. Some computational results

6.1 Twelve rings compact vortex system

We consider a "compact" vortex system which, by construction, has the following desirable properties: zero vorticity (as always in 3-D), zero linear impulse, zero angular impulse, and zero helicity, $H = \frac{1}{2} \int_V \mathbf{u}_\sigma \times \tilde{\omega} \, d\mathbf{x}$. Initially, it is formed of twelve circular vortex rings, each of circulation $\Gamma = 1$: six rings of radius $R = 0.6$ (38 sections per ring, with 9 particles per section (1 in the center with circulation $\Gamma/2$, and 8 around the center, at a distance $r_c = 0.123$ and with circulation $\Gamma/16$) laid on the surface of an outer cube of size $S = 1$ and with self-induced velocity directing them towards the cube's center, and six rings of radius $R = 0.3$ (19 sections per ring, again with 9 particles per section) laid on the surface of an inner cube of size $S = 0.5$ and with self-induced velocity directing them away from the cube's center. The total number of particles is $N = 3078$. The spacing between particles along the ring is $h \approx 0.10$. The two cubes share the same center. The outer cube is directed along $\hat{\mathbf{e}}_x = (1, 0, 0)$, $\hat{\mathbf{e}}_y = (0, 0, 1)$ and $\hat{\mathbf{e}}_z = \mathbf{e}_x \times \mathbf{e}_y$. To break the symmetry, the inner cube is arbitrarily oriented along $\hat{\mathbf{e}}_x$, $\hat{\mathbf{e}}_y$, $\hat{\mathbf{e}}_z$, with $\hat{\mathbf{e}}_x = \left(\frac{1}{2}, \frac{\sqrt{3}}{4}, -\frac{3}{4} \right)$, $\hat{\mathbf{e}}'_y = \left(0, \frac{\sqrt{3}}{2}, \frac{1}{2} \right)$, $\mathbf{e}_z = \hat{\mathbf{e}}_x \times \hat{\mathbf{e}}'_y$, $\hat{\mathbf{e}}_z = \mathbf{e}_z / \|\mathbf{e}_z\|$ and $\hat{\mathbf{e}}_y = \hat{\mathbf{e}}_z \times \hat{\mathbf{e}}_x$.

To ensure core overlapping for a long time, a large value of $\sigma = 0.20$ is used (hence $h/\sigma \approx 0.5$). The time step is $\Delta t = 0.02$. The symmetric stretching scheme is used, $\alpha = 0.5$. The LES model of Eq. (21) is used, with $C_s = 0.1$. The W-relaxation scheme is used every 10 time steps (with 50 Gauss-Seidel iterations).

Initially, the energy is $E = 1.428$ and the enstrophy $\mathcal{E} = 46.21$. Following classical definition of (isotropic) turbulence, the integral length scale is obtained as

$$L = \frac{3\pi}{4} \frac{\int_0^\infty k^{-1} E(k) \, dk}{E} = 0.490 \qquad (28)$$

and the Taylor microscale as

$$\lambda = \left(5 \frac{E}{\mathcal{E}} \right)^{1/2} = 0.393 . \qquad (29)$$

At first, a run without particle redistribution is conducted up to $t = 4$. Contour plots are presented in Fig. 4. The histograms of energy and enstrophy are provided in Fig. 5.

The energy decays due to LES diffusion. Due to vortex stretching, the enstrophy first increases. It then decreases due to vortex reconnection by viscous diffusion. Notice that two enstrophy curves are presented. The $\mathcal{E}$-curve refers to enstrophy as defined by Eq. (15). The $\mathcal{E}_b$-curve refers to enstrophy defined as

$$\mathcal{E}_b = \frac{1}{2} \int_V \omega_\sigma \cdot \tilde{\omega} \, d\mathbf{x} . \qquad (30)$$

As long as the particle vorticity field, $\tilde{\omega}_\sigma$, remains a good representation of the divergence-free field, ω_σ, the two curves remain identical. Their difference is thus a

FIGURE 4.   Twelve rings interaction. 3-D contour plots of $\omega_\sigma = 2.0$ at $t = 0.0$ and 2.0 .
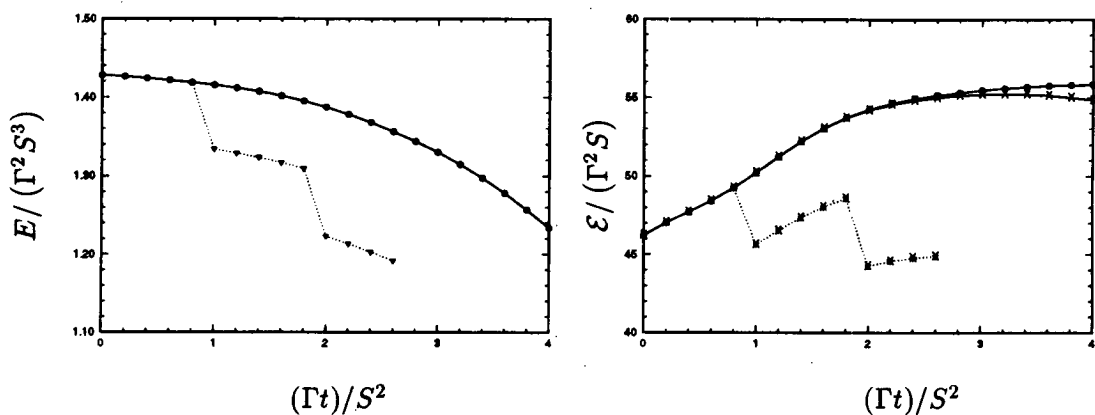
FIGURE 5.   Twelve rings interaction. ———— : without redistribution: E and $\mathcal{E}$: ● , $\mathcal{E}_b$: × ; ········ : with Λ_1 redistribution: E and $\mathcal{E}$: ▲ (inverted), $\mathcal{E}_b$: × .
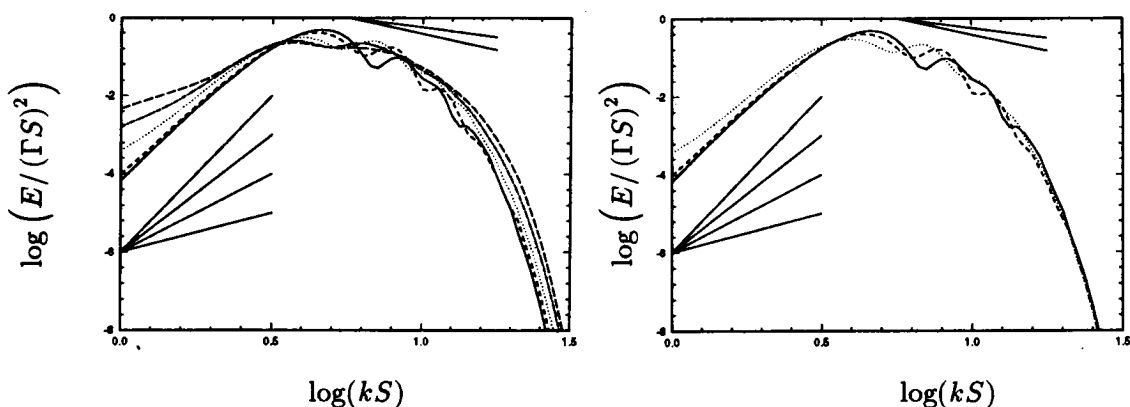
FIGURE 6.   Twelve rings interaction. Energy spectrums: $t = 0$: ———— , $t = 1$: ---- , $t = 2$: ········ , $t = 3$: —·— , $t = 4$: ---- ; k^8, k^6, k^4, k^2, k^{-1}, $k^{-5/3}$: ———— .

global indication of problems with $\tilde{\omega}_\sigma \neq \omega_\sigma$. In the present case, it is seen that the W-relaxation scheme does a fairly good job at keeping $\tilde{\omega}_\sigma \approx \omega_\sigma$ up to $t \approx 2$ or so.

Energy spectrums are provided in Fig. 6. It is seen that the high end of the spectrum starts filling up at $t \approx 2$ or so. This is also indicative of problems with $\tilde{\omega}_\sigma \neq \omega_\sigma$. This is confirmed by a close look, for all particles, at the amplitude of $\tilde{\omega}_\sigma$ and ω_σ and at their relative orientation. It is also seen that the low end of the spectrum does not remain well-behaved as time evolves. The behavior is physically acceptable as long as it remains above $(kS)^4$. The fact that it evolves to $(kS)^2$ indicates that spurious creation of linear impulse has occurred. This is confirmed by a close look at the histogram of $\mathbf{I}(t)$. Finally, total vorticity, $\Omega(t)$, also does not remain zero as it should. This could be somewhat improved by using the transpose scheme, $\alpha = 0$, instead of the symmetric scheme (Winckelmans 1989, Winckelmans
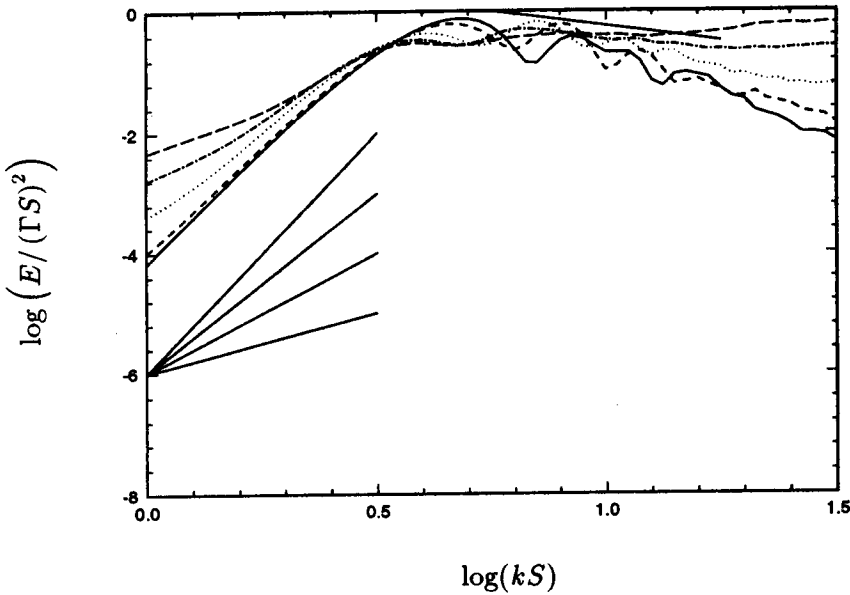
FIGURE 7. Twelve rings interaction. Unfiltered energy spectrums: $t = 0$: —— , $t = 1$: ---- , $t = 2$: ········ , $t = 3$: —·— , $t = 4$: ——— ; k^8, k^6, k^4, k^2, k^{-1}: —— .

& Leonard 1993). The W-relaxation scheme, however, does not conserve Ω. Again, all the above "symptoms" are indicative of problems with $\tilde{\omega}_\sigma \neq \omega_\sigma$.

For comparison, a run with Λ_1 particle redistribution every 50 time steps (and with $h = 0.10$) is also carried out. From $N = 3078$ at $t = 0$, this leads to $N = 6590$ at $t = 1$, and to $N = 11160$ at $t = 2$. Because of the $O(N^2)$ code, the computation cannot be carried out much further than $t = 2$, and is ended at $t = 2.6$. Histograms of energy and enstrophy are provided in Fig. 5. The conclusion is that the Λ_1 scheme is definitely not acceptable: it dissipates too much energy and enstrophy. In particular, it totally overshadows the amount of energy dissipated by the LES model. Another interesting result is that the correspondence $\tilde{\omega}_\sigma = \omega_\sigma$ is better maintained with particle redistribution than without. This confirms that the W-scheme is indeed best applied when combined with redistribution. Energy spectrums are also provided in Fig. 6. This time, the high end of the spectrum is still fine at $t = 2$. So far, the low end of the spectrum also behaves fine. Although the Λ_1 scheme exactly conserves Ω and $\mathbf{I}$, it is likely that spurious creation of Ω and $\mathbf{I}$ will also occur eventually due to the W-relaxation scheme and to the symmetric stretching scheme.

One conclusion so far is the following: If one is to do controlled LES with the VEM, it must be that the energy dissipation due to redistribution or relaxation is less than the one due to LES. A good run might be to use the Λ_2 scheme every 10 or 20 steps. (This scheme indeed conserves much better energy and enstrophy, see

below.) This could not be done with the present $O(N^2)$ code, however, due to the large increase in the number of particles required.

Another conclusion is that the W-scheme does not conserve Ω and $\mathbf{I}$. (Neither does the P-scheme.) One further improvement would be to develop a relaxation scheme which conserves Ω (and, if possible, also conserves $\mathbf{I}$).

One question arises regarding the "inertial" range of such vortex tubes interactions. Is there a $(kS)^{-5/3}$ Kolmogorov range that develops? In Kiya (1993), it is argued that yes, there is. We claim that no, there is not. In considering the filtered energy spectrum, $E(kS)$, of Fig. 6, it is hard to tell whether there is a Kolmogorov range or not. One finds the answer by considering instead the unfiltered energy spectrum, $\hat{E}(kS)$, of Fig. 7. Then, there is a clear indication that (1) the computation blows up (see comments above), and (2) as long as it doesn't blow up, the spectrum remains as $(kS)^{-1}$. This point will become clearer below, on a computation that replicates the one presented in Kiya.

6.2 Six rings compact vortex system

We consider next another compact vortex system with zero vorticity, zero linear impulse, zero angular impulse, and zero helicity. Initially, it is formed of six vortex rings, each of circulation $\Gamma = 1$ and of radius $R = 0.6$ (38 sections per ring, with 9 particles per section (1 in the center with circulation $\Gamma/2$, and 8 around the center, at a distance $r_c = 0.123$ and with circulation $\Gamma/16$) laid on the surface of an outer cube of size $S = 1$ and with self-induced velocity directing them towards the cube's center. The rings are elliptical (in order to break the symmetry) with $ab = R^2$ and $a/b = 1.25$ (top), 0.80 (left), 1.33 (bottom), 0.75 (right), 0.85 (front) and 0.90 (back). The total number of particles is $N = 2052$. The spacing between particles along the ring is $h \approx 0.10$.

A value of $\sigma = 0.14142 \approx \sqrt{2}h$ is used (hence $h/\sigma \approx 0.707$). The time step is $\Delta t = 0.025$ and the computations are carried out up to $t = 4$. The symmetric scheme is used, $\alpha = 0.5$. The LES model of Eq. (21) is used, with $C_s = 0.2$. The W-relaxation scheme is used every 10 time steps (with 50 Gauss-Seidel iterations).

Initially, the energy is $E = 1.745$ and the enstrophy $\mathcal{E} = 65.39$ (hence $\lambda = 0.365$). Notice that the application of the Λ_1 scheme to that perfectly fine initial condition leads to $E = 1.642$ (loss of 6%) and $\mathcal{E} = 57.91$ (loss of 11%) . For comparison the application of the Λ_2 scheme leads to $E = 1.741$ (loss of 0.24%) and $\mathcal{E} = 64.84$ (loss of 0.83%). This illustrates the superiority of the Λ_2 scheme over the Λ_1 scheme, regardless of the time evolution of the vortex system.

Three runs were done: one without particle redistribution, one with Λ_2 redistribution at $t = 2$, and one with Λ_1 redistribution at $t = 2$. Contour plots for the first run are presented in Fig. 8.

The histograms of energy and enstrophy are provided in Fig. 9. Again, the energy decays due to LES diffusion. Due to vortex stretching, the enstrophy first increases. It then decreases due to vortex reconnection by viscous diffusion. As long as $\tilde{\omega}_\sigma$ remains close to ω_σ (here up to $t \approx 2$), the two curves, $\mathcal{E}$ and $\mathcal{E}_b$ remain identical. The Λ_1 scheme is again clearly unacceptable. The Λ_2 scheme performs much better. However, it is believed that it should have been used more often (i.e.,
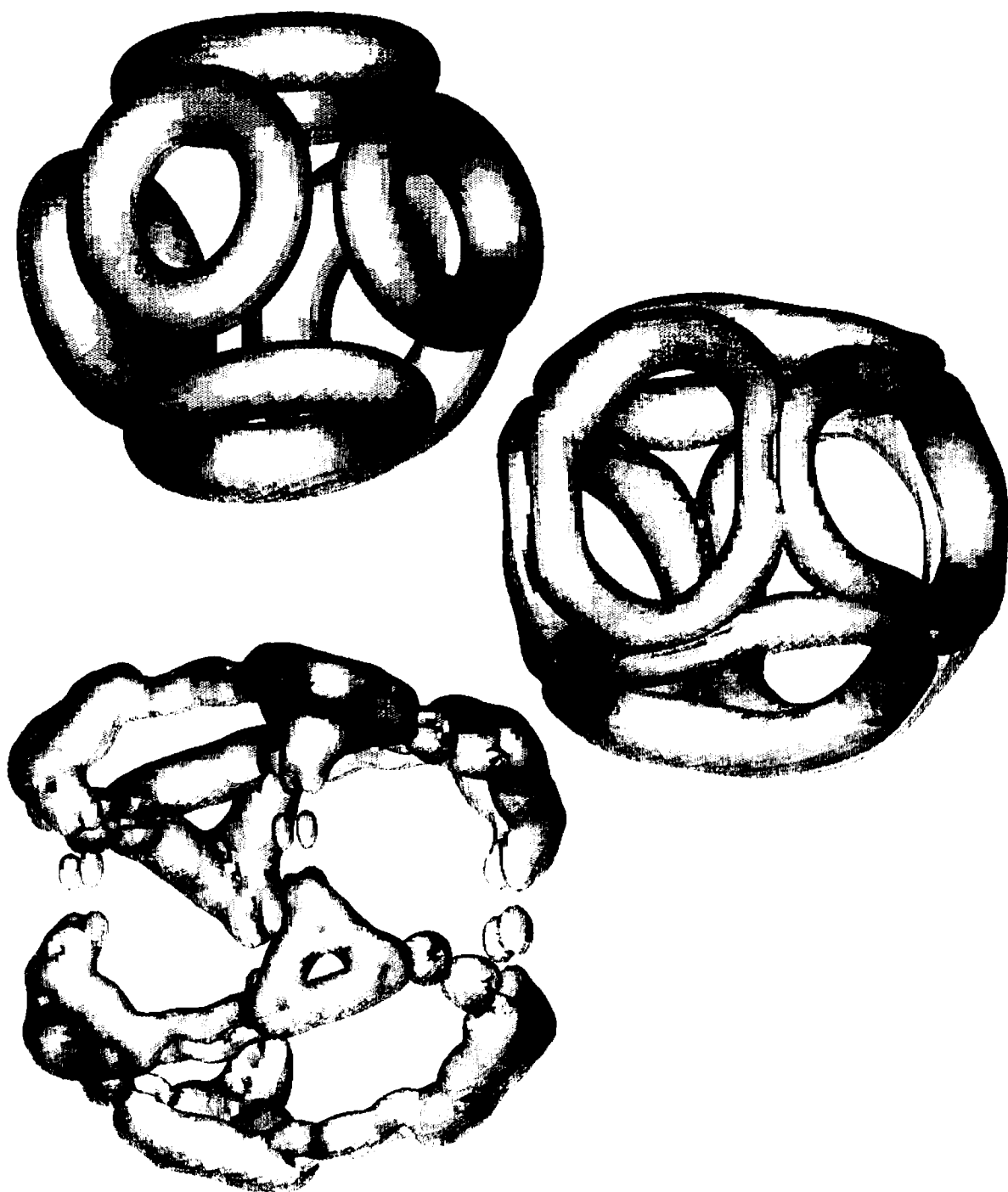
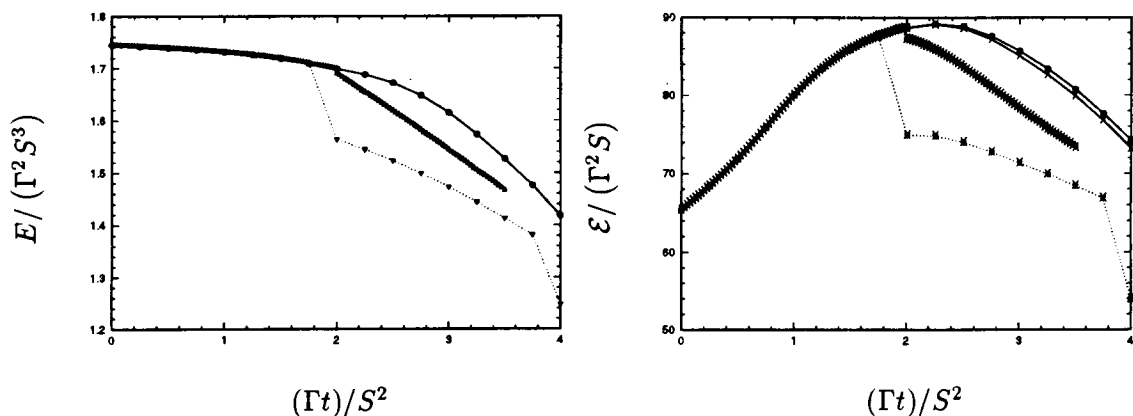FIGURE 8. Six rings interaction. 3-D contour plots of $\omega_\sigma = 2.0$ at $t = 0.0, 2.0$ and 4.0 .

FIGURE 9. Six rings interaction. ——— : without redistribution: E and $\mathcal{E}$: • , $\mathcal{E}_b$: × ; ········ : with Λ_1 redistribution: E and $\mathcal{E}$: ▲ (inverted), $\mathcal{E}_b$: × ; ———— : with Λ_2 redistribution: E and $\mathcal{E}$: ▲ , $\mathcal{E}_b$: × .
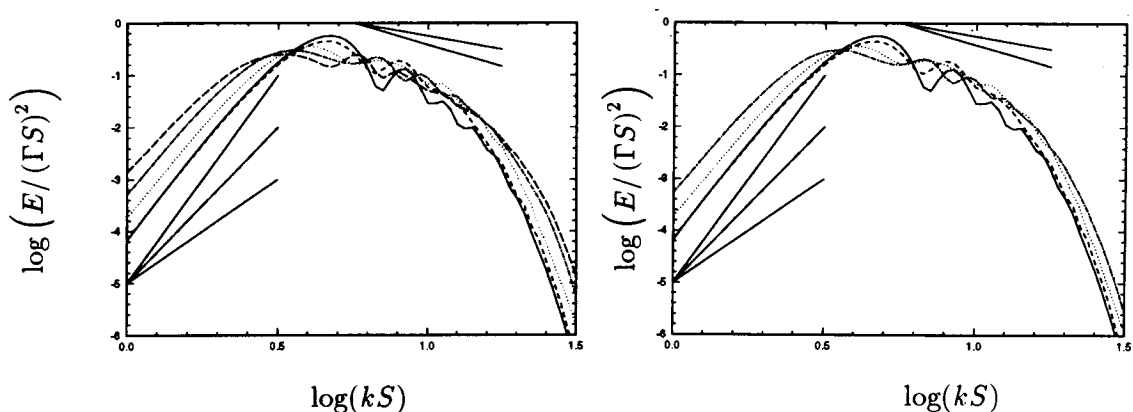
FIGURE 10. Six rings interaction. Energy spectrums: $t = 0$: ——— , $t = 1$: ———— , $t = 2$: ········ , $t = 3$: —·—· , $t = 4$: ——— ; k^8, k^6, k^4, k^{-1}, $k^{-5/3}$: ——— .

every 10 or 20 steps instead of every 80 steps) to give a better performance. Again, this could not be done, due to the $O(N^2)$ computational cost of the code. Finally, the correspondence $\tilde{\omega}_\sigma = \omega_\sigma$ (and hence $\mathcal{E} = \mathcal{E}_b$) is again better maintained with redistribution than without.

The energy spectrums are provided in Fig. 10. The high end of the spectrum starts filling up at $t \approx 2$. This is again indicative of problems with $\tilde{\omega}_\sigma \neq \omega_\sigma$ and is confirmed by a close look at both $\tilde{\omega}_\sigma$ and ω_σ for all particles. The low end of the spectrum remains well-behaved as time evolves, with very little spurious creation of linear impulse and of total vorticity. The six rings interaction here constitutes a "gentler" problem than the previous twelve rings interaction.

Again, regarding the "inertial" range of these vortex tubes interactions, it is again closer to a $(kS)^{-1}$ behavior (filtered by the Gaussian) than to a $(kS)^{-5/3}$

Kolmogorov behavior.

6.3 Six thin rings inviscid vortex system

To settle the issue, a run that replicates Kiya (1993) is also done. In that case, six circular rings of radius $R = 1$ and of circulation $\Gamma = 1$ are laid on the surface of the cube of size $S = 1.25$. Each ring is discretized using a single line of 256 particles (hence $h \approx 0.0245$. In Kiya, the high order algebraic smoothing is used, with $\sigma^\star = 0.10$. Recalling that the self-induced velocity of such a ring is obtained as (Leonard 1985, Winckelmans 1989)

$$U = \frac{\Gamma}{4\pi R} \left[\ln \left(\frac{8R}{\sigma^\star} \right) - \frac{1}{2} \right] \tag{31}$$

whereas the velocity of the ring with Gaussian smoothing is (Leonard 1985, Winckelmans 1989)

$$U = \frac{\Gamma}{4\pi R} \left[\ln \left(\frac{8R}{\sigma} \right) - 1.058 \right] , \tag{32}$$

the proper scaling requires that our computation be done with $\sigma = 0.05724$. Thus, these are much thinner rings than before. Hence a wider "inertial" range is expected.

The computation is carried up to $t = 1.5$, with $\Delta t = 0.01$. Again, the symmetric scheme is used, $\alpha = 0.5$. This is also a simple VEM computation. Hence, no relaxation scheme, and no redistribution scheme. Finally, this is an inviscid computation. Hence, no LES.

The energy spectrums are provided in Fig. 11. As claimed by Kiya, the filtered spectrum, $E(kR)$ suggests a $(kR)^{-5/3}$ behavior. This is purely due to the filter, however. Indeed, from examining the unfiltered spectrums, $\hat{E}(kR)$, it is clear that (1) the behavior remains as $(kR)^{-1}$ for a long time (forever?), and (2) the computation eventually blows up (as was the case in Kiya). The histograms of energy and enstrophy are provided in Fig. 12. From the difference between the curves $\mathcal{E}$ and $\mathcal{E}_b$, it appears that the computation blows up at $t \approx 1.2$.

In conclusion, it appears that interactions involving only vortex tubes lead to a k^{-1} behavior. It may require the interaction between both vortex tubes and vortex sheets to obtain a Kolmogorov-like spectrum. A model involving spiral vortices (i.e., rolled-up vortex sheets) is presented in Lundgren (1982).

6.4 DNS of two rings fusion using the fast parallel tree code

This work was not done while at CTR. It was done in collaboration with Salmon, Warren and Leonard (Winckelmans *et al.* 1995d). It is also presented here in order to illustrate the capabilities of the fast parallel VEM code. We consider a high resolution DNS of the fusion of two vortex rings: radius $R = 1$, circulation $\Gamma = 1$, Gaussian vorticity distribution with $\sigma_R = 0.10$, spacing of the two rings center to center $S = 2.70$, angle of each ring w.r.t. vertical $= 20$ degs. Each ring is discretized with 126 sections and 225 particles per section (i.e., 7 layers, see Winckelmans & Leonard 1993). The inter-particle spacing is then $h \approx 0.05$. The computations were run with $\Delta t = 0.05$, $\sigma = 0.0625$, $\alpha = 0$, $\nu = 0.0025$ (i.e., $Re = \Gamma/\nu = 400$) on
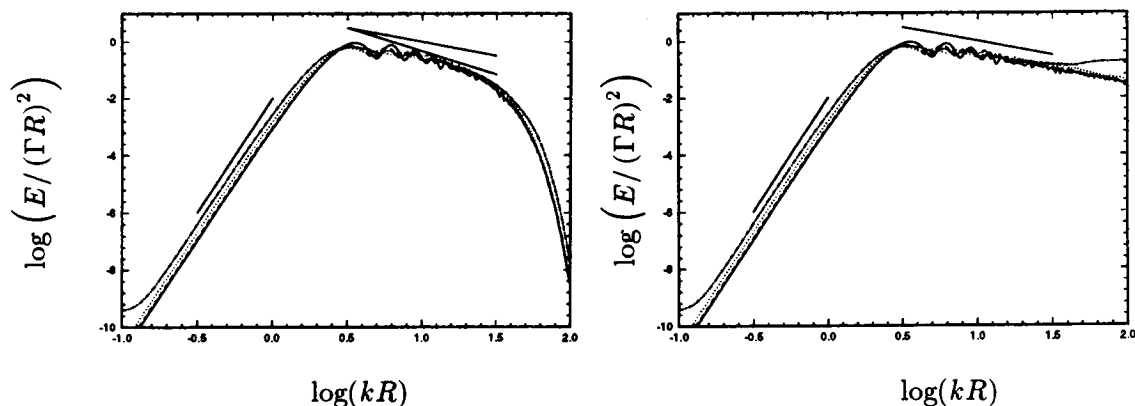
FIGURE 11.   Six thin rings inviscid interaction. Filtered and unfiltered energy spectrums: $t = 0$: ———— , $t = 0.5$: ---- , $t = 1$: ········ , $t = 1.5$: —·— ; k^8, k^{-1}, $k^{-5/3}$: ———— .
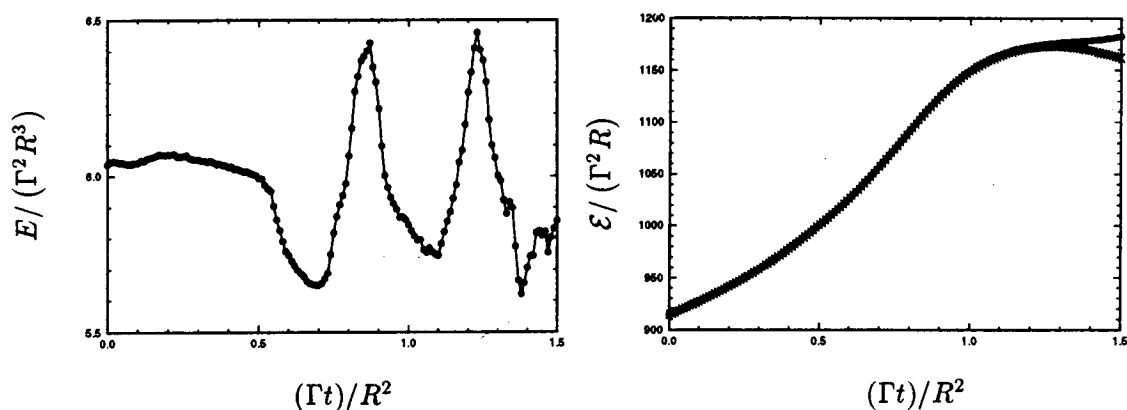

FIGURE 12.   Six thin rings inviscid interaction. ———— : without redistribution: E and $\mathcal{E}$: • , $\mathcal{E}_b$: × .

both 32 nodes of the NAS IBM-SP2 and 64 nodes of the Caltech Intel Paragon. Initially, there were 56,700 particles (19 CPU secs per step on SP2-32 and 68 on Paragon-64). The Λ_2 particle redistribution scheme with $h = 0.05$ was used every 10 time steps. At the end of the run, there were 218,696 particles (87 CPU secs per step on SP2-32 and 236 on Paragon-64). The velocity error was roughly 0.0006 for the mean over all elements, and 0.0008 for the max.

It is seen in Fig. 13 that the diffusion scheme, when combined with the high order particle redistribution scheme, correctly captures the fusion process: First, the energy and enstrophy losses associated with the Λ_2 scheme are small enough that they cannot be seen in the histograms. (They can only slightly be seen when they are differentiated numerically.) Second, the normalized energy decay rate remains (almost) equal to the enstrophy, as it should. For comparison, a run without particle
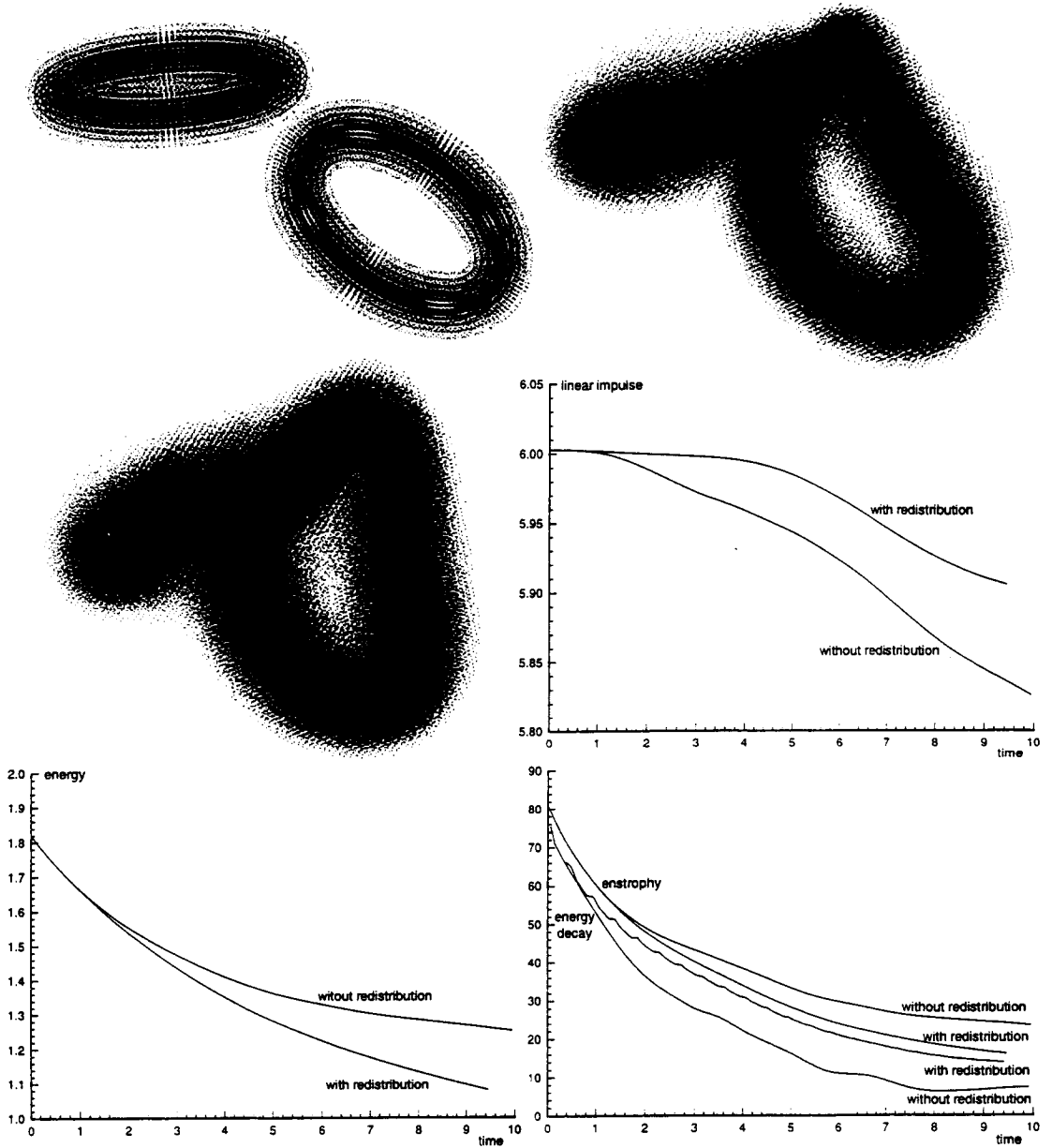
FIGURE 13. Fusion of two vortex rings. 3-D view of the particle strengths at $t = 0.0, 5.4, 9.0$; Histogram of linear impulse, I_z, of energy, E, of enstrophy, $\mathcal{E}$, and of $-\frac{1}{\nu}\frac{dE}{dt}$.

redistribution was also done, see histograms in Fig. 13. In that case, the energy decay rate is clearly incorrect. Finally, the conservation of linear impulse is also much improved by the use of the redistribution scheme. Yet, even with particle redistribution, linear impulse starts decreasing at $t \approx 4$. It is believed that $\tilde{\omega}_\sigma$ is then beginning to deviate from ω_σ.

At this point, we are also experimenting with the two relaxation schemes when used in conjunction with the redistribution scheme. Results obtained so far are encouraging, yet too preliminary to be reported.

7. Conclusions

The VEM method has gone a long way since its early stages: accurate viscous diffusion, particle redistribution schemes, relaxation schemes for the particle vorticity field, fast and accurate field evaluation on both sequential and parallel platforms. This work is still in progress. The time has come to start developing LES models suitable to VEM. During this two-month visit at CTR, a dedicated $O(N^2)$ LES-VEM code was developed. Although slow, this code could be modified rapidly in order to experiment with many different schemes and ideas. Energy spectrums could also be computed. Some progress was accomplished in the following areas: (1) LES models and how to incorporate them into VEM, (2) energy spectrums and how to compute them, (3) particle redistribution schemes, (4) relaxation schemes. More work is needed, however, especially regarding (1) relaxation schemes and (2) further validation and development of LES models for VEM (which also requires that they eventually be incorporated into the fast parallel tree code.)

It is believed that, when combined with recent developments in vortex techniques for wall-bounded flows (Pépin 1990, Koumoutsakos 1993, Koumoutsakos & Leonard 1992, 1995, Koumoutsakos *et al.* 1994), a matured and well-developed methodology will permit the simulation of 3-D unsteady problems of engineering interest: flow past airfoils including vortex wake, and flow past bluff bodies including vortex wake. These body/wake computations will require the merging of the VEM code with a Boundary Element Method (BEM) in order to determine, at each time step, the vorticity flux required at solid boundaries in order to satisfy no-slip.

REFERENCES

ABRAMOWITZ, M. & STEGUN, I. E. 1972 *Handbook of Mathematical Functions With Formulas, Graphs, and Mathematical Tables.* Applied Mathematics Series 55, Tenth Printing. National Bureau of Standards.

BRACHET, M. E., MENEGUZZI, M., VINCENT, A., POLITANO, H. & SULEM, P. L. 1992 Numerical evidence of smooth self-similar dynamics and possibility of subsequent collapse for three-dimensional ideal flows. *Phys. Fluids A.* 4(12), 2845–2854.

DEGOND, P. & MAS-GALLIC, S. 1989 The weighted particle method for convection-diffusion equations, Part I: the case of an isotropic viscosity, Part II: the anisotropic case. *Math. Comput.* **53**, 485–526.

GERMANO, M., PIOMELLI, U., MOIN, P. & CABOT, W. 1991 A dynamic subgrid-scale eddy-viscosity model. *Phys. Fluids A.* **3**(7), 1760.

GHOSAL, S., LUND, T. S. & MOIN, P. 1992 A local dynamic model for large-eddy simulation. *Annu. Res. Briefs*, Center for Turbulence Research, Stanford Univ. & NASA Ames, 3–25.

GHOSAL, S. & MOIN, P. 1995 The basic equations for the large-eddy simulation of turbulent flows in complex geometry. *J. Comput. Phys.* **118**, 24–37.

GHOSAL, S., LUND, T. S., MOIN, P. & AKSELVOLL, K. A. 1995 A dynamic localization model for large-eddy simulation of turbulent flows. *J. Fluid Mech.* **286**, 229–255.

GOLUB, G. H. & VAN LOAN, C. F. 1983 *Matrix Computations*. John Hopkins Univ. Press.

KIYA, M. 1993 Simulating three-dimensional vortex motion by a vortex blob method. *Sādhanā.* **18**(3,4), 531–552.

KOUMOUTSAKOS, P. & LEONARD, A. 1992 Direct numerical simulations using vortex methods. *Proc. NATO Advanced Research Workshop: Vortex Flows and Related Numerical Methods*, Grenoble, France, 1992, 15–19.

KOUMOUTSAKOS, P. 1993 *Direct numerical simulations of unsteady separated flows using vortex methods.* Ph.D. thesis, California Institute of Technology.

KOUMOUTSAKOS, P., LEONARD, A. & PÉPIN, F. 1994 Viscous boundary conditions for vortex methods. *J. Comput. Phys.* **113**(1), 52–61.

KOUMOUTSAKOS, P. & LEONARD, A. 1995 High resolution simulations of the flow around an impulsively started cylinder using vortex methods. *J. Fluid Mech.* **296**, 1–38.

LEONARD, A. 1980 Review: Vortex methods for flow simulation. *J. Comput. Phys.* **37**(3), 289–335.

LEONARD, A. 1985 Computing three-dimensional incompressible flows with vortex elements. *Annu. Rev. Fluid Mech.* **17**, 523–559.

LESIEUR, M., COMTE, P. & MÉTAIS, O. 1995 Numerical simulations of coherent vortices in turbulence. *Applied Mechanics Rev.* **48**(3), 121–149.

LUNDGREN, T. S. 1982 Strained spiral vortex model for turbulent fine structure. *Phys. Fluids.* **25**(12), 2193–2203.

MANSOUR, N. N., FERZIGER, J. H. & REYNOLDS, W. C. 1978 *Large-eddy simulation of a turbulent mixing layer.* Report TF-11, Thermosciences Div., Dept. of Mech. Eng., Stanford University.

MAS-GALLIC, S. 1987 *Contribution à l'analyse numérique des méthodes particulaires.* Thèse d'Etat, Université Paris VI.

MOIN, P. & JIMINEZ, J. 1993 Large eddy simulation of complex turbulent flows. *AIAA 24th Fluid Dynamics Conference*, Orlando, Fl., AIAA paper 93-3099.

Moin, P., Carati, D., Lund, T., Ghosal, S, & Akselvoll, K. 1994 Developments and applications of dynamic models for large eddy simulation of complex flows. *74th Fluid Dynamics Symposium on Application of Direct and Large Eddy Simulation to Transition and Turbulence*, Chania, Crete, Greece, AGARD-CP-551, 1-1-9.

Pedrizzetti, G. 1992 Insight into singular vortex flows. *Fluid Dyn. Res.* **10,** 101-115.

Pépin, F. 1990 *Simulation of flow past an impulsively started cylinder using a discrete vortex method.* Ph.D. thesis, California Institute of Technology.

Phillips, O. M. 1956 The final period of decay of non-homogeneous turbulence. *Proc. Cambridge Phil. Soc.* **52**(1), 135-151.

Rogallo R. S. & Moin, P. 1984 Numerical simulation of turbulent flows. *Annu. Rev. Fluid Mech.* **16,** 99-137.

Saffman, P. G. & Meiron, D. I. 1986 Difficulties with three-dimensional weak solutions for inviscid incompressible flow. *Phys. Fluids.* **29**(8), 2373-2375.

Salmon, J. K. 1990 *Parallel hierarchical N-body methods.* Ph.D. thesis, California Institute of Technology.

Salmon, J. K. & Warren, M. S. 1994 Skeletons from the treecode closet. *J. Comput. Phys.* **111**(1), 136-155.

Salmon, J. K., Warren, M. S. & Winckelmans, G. S. 1994 Fast parallel tree codes for gravitational and fluid dynamical N-body problems. *Int. J. Supercomputer Applications.* **8**(2), 129-142.

Shariff, K., Leonard, A. & Ferziger, J. H. 1989 *Dynamics of a class of vortex rings.* NASA Technical Memorandum 102257, Ames Research Center.

Warren, M. S. & Salmon, J. K. 1995 A Parallel, Portable and Versatile Treecode. *Proc. Seventh SIAM Conference on Parallel Processing for Scientific Computing*, San Francisco, CA, 15-17 Feb., 1995, 319-324.

Winckelmans, G. S. & Leonard, A. 1988 Weak solutions of the three-dimensional vorticity equation with vortex singularities. *Phys. Fluids, Letters.* **31**(7), 1838-1839.

Winckelmans, G. S. & Leonard, A. 1989 Improved vortex methods for three-dimensional flows. *SIAM Workshop on Mathematical Aspects of Vortex Dynamics*, Leesburg, VA, April, 1988, *SIAM Proc. Series*, R. E. Caflisch ed., 25-35.

Winckelmans, G. S. 1989 *Topics in vortex methods for the computation of three- and two-dimensional incompressible unsteady flows.* Ph.D. thesis, California Institute of Technology.

Winckelmans, G. S. 1993 Comments on a paper by Kiya et al. on the numerical simulation of pseudo-elliptical vortex rings using the vortex particle method. *Fluid Dyn. Res., Brief Comm.* **12,** 57-60.

WINCKELMANS, G. S. & LEONARD, A. 1993 Contributions to vortex particle methods for the computation of three-dimensional incompressible unsteady flows. *J. Comput. Phys.* **109**(2), 247–273.

WINCKELMANS, G. S., SALMON, J. K., WARREN, M. S. & LEONARD, A. 1995 The fast solution of three-dimensional fluid dynamical N-body problems using parallel tree codes: vortex element method and boundary element method. *Proc. Seventh SIAM Conference on Parallel Processing for Scientific Computing*, San Francisco, CA, 15–17 Feb., 1995, 301–306.

WINCKELMANS, G. S., SALMON, J. K., LEONARD, A. & WARREN, M. S. 1995 Three-dimensional vortex particle and panel methods: Fast tree-code solvers with active error control for arbitrary distributions/geometries. *Proc. Forum on Vortex Methods for Engineering Applications*, Albuquerque, NM, 22–24 Feb., 1995, 25-43.

WINCKELMANS, G. S., SALMON, J. K., LEONARD, A. & WARREN, M. S. 1995 Simulations of airfoil three-dimensional vortex wakes via fast vortex particle parallel and sequential tree codes. In *Proc. Third Annual Conference of the CFD Society of Canada*, Banff, Alberta, 25–27 June, 1995, 349–356.

WINCKELMANS, G. S., SALMON, J. K., WARREN, M. S., LEONARD, A. & JODOIN, B. Application of fast parallel and sequential tree codes to computing three-dimensional flows with the vortex element and boundary element methods. To appear in *Proc. Second International Workshop on Vortex Flows and Related Numerical Methods*, Montréal, Canada, 20–24 August, 1995 (submitted Sept. 95).

Page intentionally left blank

Tensoral present and future

By Eliot Dresselhaus

1. Motivation and objectives

The coding of high-performance fluids simulations requires significant knowledge of both numerical and computational details. The magnitude and complexity of low-level details is often enough to discourage many *users* of turbulence data wishing to study more important, higher-level fluid dynamical questions. These same complexities are often a practical barrier to simulation *experts* who develop, verify and maintain the codes which generate this data. Future fluids codes, with high resolution and complex geometries, are likely to involve far more coding complexity.

My research — the design and implementation of the `Tensoral` computer language — aims to greatly ease the coding of today's simulation and post-processing codes and at the same time provide a general computational tool for future simulations.

2. The current `Tensoral`

`Tensoral` is a very high-level language. To the user seeking to analyze turbulence data, `Tensoral` speaks the language of the Navier–Stokes equation: three dimensional tensor calculus and statistics. With `Tensoral` a user can perform efficient high-level analysis of simulation data without any knowledge of the underlying numerical and computational complexities necessary to manipulate this data.

The simulation expert is responsible for teaching `Tensoral` how to realize this tensor language with executable computer code. Specifically, such an expert must code the basic building blocks of a numerical method in a `Tensoral` "back-end." A back-end defines how a fluid field is to be represented on a particular computer system and how operations (e.g. derivatives, integrals, statistics, etc.) are to be performed on this representation. Once these building blocks are in place, post-processing and simulation codes can be constructed from them using the `Tensoral` compiler.

The current implementation of `Tensoral` — described in detail in previous CTR research briefs — can generate efficient code for general computations involving the arithmetic, statistics, and calculus of numerically represented tensor fields. Currently, the only complete back-end is for isotropic turbulence. In principal, the current language and compiler is sufficient to meet the needs of today's users and experts alike. In practice, however, the current language and compiler has significant limitations.

The current `Tensoral` is not coherent. Inside `Tensoral` there is a language the user sees (tensors) and a language that experts sees (the back-end language). Coding with the current back-end language is practically difficult and conceptually obscure. This inhibits the generation of new back-ends with the current system.

The current `Tensoral` is not modular. Back-ends cannot share code in a flexible way. As many of the codes at CTR use similar numerical and data management strategies, this lack of modularity is a significant problem.

3. The new `Tensoral`

The new `Tensoral`, a generalization and renovation of the current system, is presently being developed. The new system is both coherent and modular. For the remainder of this document we outline the new system and give specific examples of its abstractions. In particular, we introduce the E programming language, in which the new `Tensoral` is implemented. Next we introduce abstractions for tensor representation and for the data management of large arrays. Along the way we show how several different numerical strategies employed at CTR are realized with these abstractions.

3.1 Coherence: C within E

The new `Tensoral` software has a coherent structure. In the new system users and experts both see the same language. Users see high-level abstractions such as tensors embedded in C syntax. Experts define new abstractions in terms of lower-level abstractions, also embedded in C syntax. Thus, the new system has no separate back-end language. This new general programming system — called E— distills and generalizes the basic programming ideas of the current `Tensoral`. The new `Tensoral` will be implemented in this new system.

The E compiler scans blocks of C code delimited by {} brackets for special syntax, for example tensor or back-end syntax. This syntax is then associated with further E code which itself may contain other special syntax. This process continues recursively until all special syntax is resolved into C code. The resulting C code is then organized for efficient execution. This basic plan allows for very general high-level computations to be hierarchically reduced into low-level computations.

3.2 Modularity: Syntax within E

New abstractions in E are introduced by adding new syntax to the system. Syntax rules matched by the compiler are transformed into E code which may contain yet other syntax rules.

E's programmable syntax allows for notation to be suited to the problem at hand. Languages with fixed syntax (e.g. C or Fortran) require problems to be translated this fixed syntax. E encourages problems to be expressed in their most natural syntactic form. For example, mathematical formulae could be notated with TeX syntax, two-dimensional computer graphics operations could be notated with `Postscript` syntax, etc. What ever the syntax, the compiler reduces this syntax eventually into executable code.

3.3 Tensors and their representation

Variables in `Tensoral` — such as a fluid velocity field — are instances of the `tensor` abstraction which we describe here. Tensors are indexed: they have rank and dimension. Tensors depend on `coordinate` directions. Tensor arithmetic is

performed point-wise. Derivatives, integrals and averaging may be taken with respect to these coordinates. Coordinates are defined by the values they may take as well as by how functions of them are to be represented.

Suppose a programmer wants a real valued function f of a variable $0 < t < 1$, represented on a fixed grid of size I by values $f(t_i)$, $t_i = i/I$, $i = 0 \ldots I - 1$. A coordinate t is introduced

```
coordinate t = 0 .. 1, size I;
```

and f is declared to depend on t

```
real f(t);
```

The function f may be added to other functions (compatibly represented), may be differentiated with a finite difference stencil, averaged, etc.

Of course functions may depend on more than one coordinate and may be represented by orthogonal function expansions or by splines (rather than on a fixed grid). For example, the isotropic turbulence simulation represents velocity fields by N^3 Fourier coefficients in a cube:

```
fourier coordinate x y z = 0 .. 2pi, size N;
```

The coordinate system for the channel flow simulation would need a Chebyshev direction:

```
chebyshev coordinate w = -1 .. 1, size N;
```

The `fourier` and `chebyshev` (and other) packages contains all of the relevant details of how tensor representations are realized, how derivatives are taken, how the Laplace operator is inverted given boundary conditions, etc.

Once these coordinate systems have been defined tensors may be declared to depend on them. With coordinates as above, an isotropic velocity field u would be declared as `real u_i(xyz)`, a channel flow field as `real v_i(xwz)`. Such tensors, once declared, may now be used for computation.

3.4 Split arrays

Fluids simulations represent velocity fields with a small number of large three-dimensional arrays. To attain the highest possible resolution these arrays must be as large as possible. Modern computer systems have finite resources: typically, $\approx 10^2$ processors connected by a fast network, each processor having $\approx 10^6$ fast storage elements (e.g. RAM) and $\approx 10^9$ slow storage elements (e.g. disk or tape). One of the painful details of high-resolution coding is fitting the largest possible problem onto a given set of computational resources.

Such large problems are fit on specific computer systems by splitting arrays so that only one or two dimensional fragments of the entire array are in fast memory at a time. The remainder of the array can only be accessed through communication with other processors or by accessing mass storage (disk or tape).

How an array is to be split may depend on what operations are being performed on it. Transform (e.g. spectral and spline) methods typically require that the

array direction being transformed be in local memory. Such methods may require different array geometries for each direction to be transformed. Data management operations must be introduced to put data in the right geometry at the right time.

The new `Tensoral` has a general high-level abstraction for such split multi-dimensional arrays. Split arrays are general. They may be used in `Tensoral` back-ends for representing tensors or may be used elsewhere. Just as a `tensor` is referenced via a `coordinate` system, `Tensoral` arrays are referenced via array indices. Indices are declared

```
index x = 1 ..  nx;
```

and arrays declared as functions of these indices `float f[x]`. Indices may be `split` in a hierarchical and programmable manner. Declarations

```
index y = 1 ..  ny | cpu;
index z = 1 ..  nz | cpu;
```

would introduce indices x and z that are split across processor in a multi-computer. cpu refers to a package which knows how interface with inter-processor communication software in the operating system. Splitting packages would be provided for various inter-processor communication schemes or for communication with mass storage devices (such as disks or tapes). Once a system of indices are introduced, arrays may be declared (`float f[xyz]`, `g[xyz]`) and operated upon (`f = g + 1`).

When arrays are referenced, splittings may be explicitly given. Thus, `f[xy|z]` would generate code so that each `cpu` had `xy` planes of data (for a "planes" code); `f[x|yz]` would generate code so that each `cpu` had `x` pencils of data (for "pencil" codes). This allows for explicit control over data management.

5. Status

It is clear that the system outlined here is a powerful and general extension of the current `Tensoral` system. Current work focuses on realizing the design presented here.

Appendix

ROSTER

<u>NAME/TERM</u>   <u>AREA OF RESEARCH</u>

POSTDOCTORAL FELLOWS

NAME/TERM		AREA OF RESEARCH
ADAMS, Dr. Nikolaus 10/93-10/95	(Ph.D, Theoretical Fluid Mechanics, 1993, DLR, Göttingen)	Boundary layer interaction with shocks
GHOSAL, Dr. Sandip 2/92-9/95	(Ph.D. Physics, 1992, Columbia University)	Analysis of numerical errors in LES
GODEFERD, Fabien 6/95-8/95	(Ph.D. Fluid Mechanics, 1994, Ecole Centrale Lyon)	Rotating turbulence
IM, Dr. Hong Geun 10/94-present	(Ph.D. Mechanical & Aersospace Engr., 1994, Princeton University)	Turbulent combustion
JANSEN, Dr. Kenneth 9/93-present	(Ph.D. Mechanical Engr, 1993, Stanford)	Large-eddy simulation of complex flows
KALTENBACH, Dr. Hans-Jakob 9/92-10/95	(Ph.D. Atmospheric Physics, 1992, DLR)	Large-eddy simulation
KOUMOUTSAKOS, Dr. Petros 8/94-present	(Ph.D. Aeronautics & Applied Mathematics, 1992, California Institute of Technology)	Numerical simulation via vortex methods
MITTAL, Dr. Rajat 6/95-present	(Ph.D. Theoretical & Applied Mechanics, 1995, U. Illinois)	Large-eddy simulation
OBERLACK, Dr. Martin 5/95-present	(Ph.D. Mechanical Engineering, 1995, RWTH Aachen)	Turbulence modeling

RUETSCH, Dr. Gregory 9/93-present	(Ph.D. Applied Mathematics, 1991, Brown University)	Turbulent combustion
SMITH, Nigel S. A. 10/94-present	(Ph.D. Mechanical & Mechatronic Engr., 1994, University of Sydney)	Turbulent combustion

RESEARCH ASSOCIATES

CABOT, Dr. William H. 3/88-present	(Ph.D. Physics, 1983, University of Rochester)	Large-eddy simulation and convection
DRESSELHAUS, Dr. Eliot 9/91-present	(Ph.D. Applied Mathematics, 1991, Columbia University)	Postprocessing and computer languages
LUND, Dr. Thomas S. 11/90-present	(Ph.D. Aero-Astro, 1987, Stanford)	Large-eddy simulation
SADDOUGHI, Dr. Seyed G. 6/91-9/95	(Ph.D. Mechanical Engineering, 1989, The University of Melbourne)	Development of on-demand vortex generators
WANG, Dr. Meng 9/92-present	(Ph.D. Mechanical Engr., 1989, Univ. of Colorado)	Aerodynamic noise

SR. VISITING FELLOWS

BILGER, Prof. Robert W. 1/95-4/95	University of Sydney	Turbulent combustion
BLACKWELDER, Prof. Ron F. 9/94-12/94	University of Southern California	Control of bounded shear flows
CHOI, Prof. Haecheon 1/95, 7/95	Seoul National University	Large-eddy simulation of complex flows
CAMBON, Dr. Claude 7/95-8/95	Ecole Centrale Lyon	Rotating turbulence
GEORGE, Prof. William K. 10/94, 1/95	SUNY-Buffalo	Analysis of turbulent mixing layers

LILLEY, Prof. Geoffrey M. 5/95-present	University of Southampton	Aeroacoustics
MORINISHI, Dr. Youhei 3/95-present	University of Tokyo	High order methods for LES
ORLANDI, Prof. Paolo	University of Rome	Rotating pipe flow
POINSOT, Dr. Thierry 8/95	CERFACS	Turbulent combustion
VEYNANTE, Dr. Denis 8/95	Ecole Centrale Paris	Turbulent combustion
WINCKELMANS, Dr. Gregoire 5/95-6/95	University of Sherbrooke	3D vortex particle methods

SR. RESEARCH FELLOWS

BROADWELL, Dr. James E. 1/94-present		Turbulent combustion
DURBIN, Dr. Paul 1/90-present		Turbulence modeling
JIMENEZ, Prof. Javier 8/95-12/95		Subgrid-scale modeling
YAGLOM, Prof. Akiva 7/95-present		Writing of 2nd edition, "Statistical Fluid Mechanics"

GRADUATE STUDENTS

BUICE, Carl 7/95-present		Experimental study of diffuser flow
SHAH, Kishan 7/95-present		Subgrid-scale modeling
SHABANY, Younes 7/95-present		Turbulence modeling

1995 ADVISORY COMMITTEE

Prof. George K. Batchelor
DAMTP, Univ. of Cambridge

Mr. Ronald Bengelink
Boeing Commercial Airplane Group

Dr. Richard G. Bradley, Jr.
Lockheed

Prof. Eugene Covert
Massachusetts Institute of Technology

Dr. Spiro Lekoudis
Office of Naval Research

Prof. John L. Lumley   (Chair)
Cornell University

Dr. James M. McMichael
Air Force Office of Scientific Research

Prof. Norbert Peters
RWTH - Aachen

Prof. Richard A. Seebass
Univ. Colorado at Boulder

Dr. John Howe (Ex-officio)
NASA Ames Research Center

1995 STEERING COMMITTEE

Prof. Dean R. Chapman
Department of Aeronautics & Astronautics
Stanford University

Dr. Paul A. Durbin
Senior Research Fellow
Center for Turbulence Research

Dr. Dochan Kwak
Chief, Advanced Computational Methods
Branch, NASA Ames Research Center

Prof. Javier Jimenez
Senior Visiting Fellow, 8/95-12/95
Center for Turbulence Research,
Professor, Fluid Mechanics,
University of Madrid

Dr. Nagi N. Mansour
Turbulence Physics & Modeling Branch,
NASA Ames Research Center

Mr. Joseph G. Marvin
NASA Turbulence & Transition
Technical Program Manager

Prof. Parviz Moin
Director, Center for Turbulence
Research
Professor, Mechanical Engineering,
Stanford
Sr. Staff Scientist, NASA Ames
Research Center

Prof. William C. Reynolds
Program Coordinator, Center for
Turbulence Research
Professor, Mechanical Engineering,
Stanford
Sr. Staff Scientist, NASA Ames
Research Center